

Book of abstracts of the International Workshop on Computational Nanotechnology 2023



**IWCN June 12th-16th, 2023
Barcelona (Spain)**



International Workshop on
Computational Nanotechnology

June 12th-16th, 2023 Barcelona (Spain)

Book of abstracts of the International Workshop on Computational Nanotechnology 2023

Authors:

ORIOLS PLADEVALL, XAVIER
ABADAL BERINI, GABRIEL
CARTOIXÀ SOLER, XAVIER
CUMMINGS, ARON
DESTEFANI, CARLOS FERNANDO
JIMÉNEZ JIMÉNEZ, DAVID
MARTÍN MARTÍNEZ, JAVIER
RODRÍGUEZ MARTÍNEZ, ROSANA
BENALI, ABDELILAH

ISBN: 978-84-09-51107-5



FOREWORD

Casa Convalescència, Barcelona,

June 12, 2023

I would like to welcome all participants to the International Workshop on Computational Nanotechnology (IWCN 2023) that will take place in Barcelona (Spain). This is the 22nd edition of a series of conferences that started more than 30 years ago. The workshop serves as a unique platform for researchers, scholars, and practitioners to exchange ideas, present cutting-edge advancements, and foster collaborations that push the boundaries of this interdisciplinary field.

The workshop's agenda has been thoughtfully crafted to encompass a broad spectrum of topics, ranging from first principles modeling and simulation methods to the development of advanced algorithms and software tools for nanoscale phenomena.

Your help is needed for a fruitful conference. International conferences are the modern forums for exchanging forefront scientific knowledge. At the frontiers of research our knowledge is still unstable, somehow immature and, certainly, not free from controversies. I encourage all participants to promote discussions and ask and answer questions in a friendly atmosphere. We are all on the same team, playing the fascinating game of unraveling the mysteries of the nanoscale world.

I would also like to encourage all participants (especially those who are in Barcelona for the first time) to discover our city. Barcelona is famous worldwide for its modernist architecture. Indeed, the conference site (casa Convalescència) is one example of the modernist style. This is one of the reasons for choosing this place to hold the conference.

Finally, I would like to thank our sponsors SILVACO and MINISTERIO DE CIENCIA E INNOVACION. Special thanks to the local, national, program and advisory committees for their constant help and support.

I really wish all of you a pleasant and scientifically fruitful stay in Barcelona during this week.

Yours faithfully,



Xavier Oriols

Chair IWCN 2023

GENERAL CHAIR

Xavier Oriols	Universidad Autonoma de Barcelona
---------------	-----------------------------------

LOCAL COMMITTEE

Gabriel Abadal	Universidad Autonoma de Barcelona
Abdelilah Benali	Universidad Autonoma de Barcelona
Aron Cummings	Catalan Institute of Nanoscience and Nanotechnology
Carlos Destefani	Universidad Autonoma de Barcelona
Javier Martin	Universidad Autonoma de Barcelona
Rosana Rodríguez	Universidad Autonoma de Barcelona

NATIONAL COMMITTEE

Xavier Cartoixà	Universidad Autonoma de Barcelona
Antonio García-Loureiro	Universidad de Santiago de Compostela
Andrés Godoy	Universidad de Granada
Tomás González	Universidad de Salamanca
David Jiménez	Universidad Autonoma de Barcelona
Stephan Roche	Catalan Institute of Nanoscience and Nanotechnology
Riccardo Rurali	Institut de Ciència de Materials de Barcelona (ICMAB-CSIC)

PROGRAM COMMITTEE

Anant M. P. Anantram	University of Washington	USA
Rossella Brunetti	Università degli Studi di Modena e Reggio Emilia	Italy
Massimo V. Fischetti	University of Texas at Dallas	USA
Andrés Godoy	Universidad de Granada	Spain
Tomás González	Universidad de Salamanca	Spain
Sung-Min Hong	Gwangju Institute of Science and Technology	Korea
Ming-Yi Lee	Macronix International Co.	Taiwan
Fabienne Michelini	Aix-Marseille University	France
Hideki Minari	Sony	Japan
Elisa Molinari	Università degli Studi di Modena e Reggio Emilia	Italy
Riccardo Rurali	Institute of Materials Science from Barcelona	Spain
Clivia Sotomayor Torres	ICREA and Catalan Institute of Nanoscience and Nanotechnology	Spain
Victor A. Sverdlov	Technical University Vienna	Austria
Xavier Waintal	CEA Grenoble	France
Alison Walker	University of Bath	UK
Katsuhisa Yoshida	Research Center for Computational Science and Informatics (Resonanc Corp.)	Japan

ADVISORY COMMITTEE

Marc Bescond	Aix-Marseille University/CNRS	France
György Csaba	Pázmány Péter Catholic University	Hungary
Aldo Di Carlo	University of Rome "Tor Vergata"	Italy
Philippe Dollfus	CNRS/University of Paris-Saclay	France
David Ferry	Arizona State University	USA
Stephen Goodnick	Arizona State University	USA
Karol Kalna	Swansea University	UK
Robert Kelsall	University of Leeds	UK
Gerhard Klimeck	Purdue University	USA
Irena Knezevic	University of Wisconsin	USA
Hans Kosina	TU Wien	Austria
Tillmann Kubis	Purdue University	USA
Paolo Lugli	Free University of Bozen-Bolzano	Italy
Massimo Macucci	University of Pisa	Italy
Nobuya Mori	Osaka University	Japan
Xavier Oriols	Universidad Autonoma de Barcelona	Spain
Wolfgang Porod	University of Notre Dame	USA
Nobuyuki Sano	Tsukuba University	Japan
Siegfried Selberherr	TU Wien	Austria
Mincheol Shin	KAIST	Korea
William Vandenberghe	University of Texas at Dallas	USA
Dragica Vasileska	Arizona State University	USA
Josef Weinbub	TU Wien	Austria

COLABORATORS



**VNIVERSIDAD
D SALAMANCA**

CAMPUS DE EXCELENCIA INTERNACIONAL



ugr

Universidad
de **Granada**



SPONSORS

SILVACO



INVITED SPEAKERS

AB-INITIO THERMAL TRANSPORT CALCULATIONS FOR CRYSTALS AND NANOSTRUCTURES BASED ON THE BOLTZMANN TRANSPORT EQUATION

Jesus Carrete, TU Wien (Austria)

WHERE IS SEMICONDUCTOR TECHNOLOGY HEADING? A VIEW FROM THE INDUSTRY AND IMPLICATIONS ON COMPUTATIONAL NANOTECHNOLOGY

Carlos H. Diaz, Senior Director in R&D (TSMC)

UNVEILING QUANTUM PHASE TRANSITION BY DISORDER AND DEFECTS IN 2D MATERIALS: JACUTINGAITE FAMILY

Adalberto Fazzio, Brazilian Center for Research in Energy and Materials (Brazil)

TREATING NON-EQUILIBRIUM GREEN'S FUNCTIONS WITH A MONTE CARLO METHOD

David K. Ferry, Arizona State University (USA)

PROCESS SIMULATION IN MICRO- AND NANO-ELECTRONICS

Lado Filipovic, Institute for Microelectronics (Austria)

QUANTUM PHOTODETECTORS

Francois Léonard, Sandia National Laboratories (USA)

MULTISCALE MODELLING AND COMPUTATIONAL SPECTROSCOPY

Kersti Hermansson, Uppsala University (Sweden)

IMPACTS OF BAND STRUCTURES AND SCATTERING PROCESSES ON HIGH-FIELD CARRIER TRANSPORT IN WIDE BANDGAP SEMICONDUCTORS

Nobuya Mori, Osaka University (Japan)

MACHINE LEARNING FOR MATERIALS AND DEVICE SIMULATIONS

Alison B. Walker, University of Bath (UK)

MEMRISTORS WITH THOUSANDS OF CONDUCTANCE LEVELS FOR ANALOG COMPUTING

J. Joshua Yang, Future of Computing Institute, University of Southern California

ARTIFICIAL INTELLIGENCE AT FC BARCELONA

Jordi Mompart, Director of Research at FC Barcelona

LSQUANT: LINEAR SCALING QUANTUM TRANSPORT METHODOLOGIES

Jose Hugo Garcia, ICN2 (Spain)

MS-DFT: QUANTUM TRANSPORT FROM A MULTI-SPACE EXCITATION VIEWPOINT

Yong-Hoon Kim, KAIST (Republic of Korea)

NEMO: FROM ESOTERIC QUANTUM THEORY TO INDUSTRIAL TRANSISTOR DESIGNS AND GLOBAL IMPACT

Gerhard Klimeck, Purdue University (USA)

TKWANT: A SOFTWARE PACKAGE FOR TIME-DEPENDENT QUANTUM TRANSPORT

Thomas Kloss, Neel Institute (France)

TRANSIESTA: ADVANCED APPLICATIONS IN ELECTROCHEMISTRY AND SPINTRONICS

Pablo Ordejon, ICN2 (Spain)

QUANTUM ESPRESSO: FROM DENSITY-FUNCTIONAL THEORY TO DUAL WAVE-PARTICLE TRANSPORT AND DEVICE SIMULATION

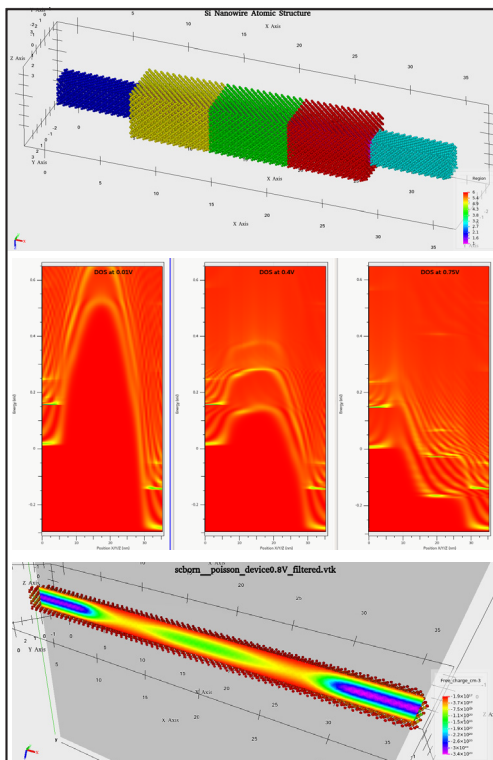
Michele Simoncelli, University of Cambridge (UK)

Victory Atomistic

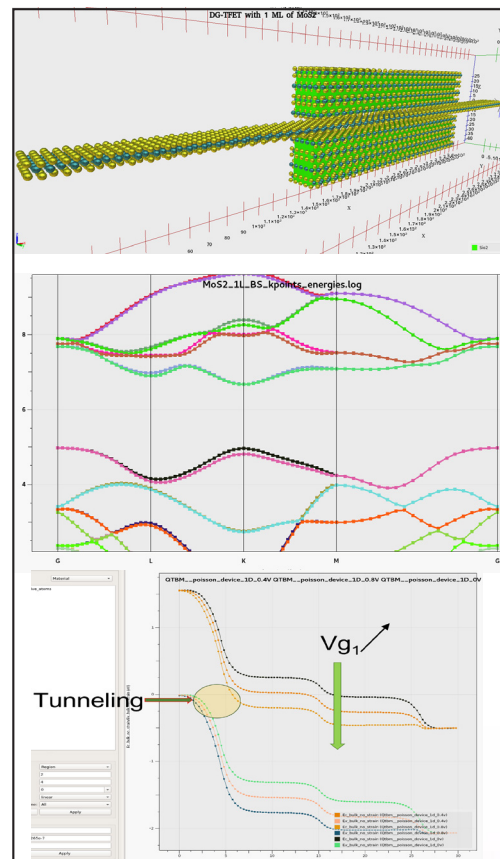
Nanostructure Material and Quantum Device Simulator

Device simulator functional at atomic resolution for 2D and 3D materials

- Integrated into Silvaco's TCAD DeckBuild environment
- Advanced visualization with companion tool VictoryVisual
- Multiple physics solvers
 - o Self-consistent Poisson-Schrödinger,
 - o Force-field relaxation, strain-dependent calculation
 - o Quantum Transmission Boundary Method (QTBM)
 - o Non-Equilibrium Green's Function (NEGF)
 - o Electron-phonon and phonon-phonon self-energies
 - o Mode-space and low-rank approximation compatible with scattering
 - o Büttiker-probes method
- Electronic structure calculations: band-structure, density of states, transmission probability.
- Atomic prediction of potentials, charges, mobilities and band edge shifts, that can serve as input to traditional TCAD
- Device simulation of MOSFET, TFET, and LED thanks to device templates and meta-solvers
- I(V) characteristics, density of states, and current density resolved in space and energy
- Amazon cloud-ready, parallel MPI/OpenMP runs in batch mode.



A silicon nanowire FET with 20 orbitals per atom and 8 000 atoms with modespace and electron-phonon scattering: visualization of the NEGF results with Victory Visual
Top: NWFET structure with spacers
Middle: Density of States resolved in space and energy for different grid voltages
Bottom: Free charges in the NWFET



Dual-gate TFET with one monolayer of MoS2 – Top: device structure with insulator (green), Mo (blue) and S (yellow) atoms
Middle: Band Structure of the Wannier Hamiltonian
Bottom: TFET 1D band profile function of the gate voltage applied

Silvaco is a leading provider of TCAD, EDA software and semiconductor design IP, used for process and device development for advanced semiconductors, power IC, display, memory, and SoC designs. Silvaco is headquartered in Santa Clara, California and has a global presence with offices located in North America, Europe, Brazil, China, Japan, Korea, Singapore, and Taiwan.

SILVACO

www.silvaco.com

INDEX

Monday, June 12

Session: Quantum transport simulators

TKWANT: A SOFTWARE PACKAGE FOR TIME-DEPENDENT QUANTUM TRANSPORT1

Thomas Kloss (INVITED)

Neel Institute (France)

NEMO: FROM ESOTERIC QUANTUM THEORY TO INDUSTRIAL TRANSISTOR

DESIGNS AND GLOBAL IMPACT.....2

Gerhard Klimeck (INVITED)

Purdue University (USA)

LSQUANT: LINEAR SCALING QUANTUM TRANSPORT4

Jose Hugo Garcia (INVITED)

ICN2 (Spain)

MS-DFT: QUANTUM TRANSPORT FROM A MULTI-SPACE EXCITATION VIEWPOINT5

Yong-Hoon Kim (INVITED)

KAIST (Republic of Korea)

TRANSIESTA: ADVANCED APPLICATIONS IN ELECTROCHEMISTRY AND SPINTRONICS6

Pablo Ordejón (INVITED)

ICN2 (Spain)

QUANTUM ESPRESSO: FROM DENSITY-FUNCTIONAL THEORY TO DUAL

WAVE-PARTICLE TRANSPORT AND DEVICE SIMULATION7

Michele Simoncelli (INVITED)

University of Cambridge (UK)

Tuesday, June 13

Session: Quantum materials

UNVEILING QUANTUM PHASE TRANSITION BY DISORDER AND DEFECTS

IN 2D MATERIALS: JACUTINGAITE FAMILY8

Adalberto Fazzio (INVITED)

Brazilian Center for Research in Energy and Materials (Brazil)

Haiku graphene nanoribbons with tunable topology.....9

Rodrigo E. Menchón (1), Pedro Brandimarte (1), Daniel Sánchez-Portal (1,2) and Aran Garcia-Lekue (1,3)

(1) Donostia International Physics Center (DIPC), 20018 Donostia-San Sebastián, Spain (2) Centro de Física de Materiales CSIC-UPV/EHU, 20018 Donostia-San Sebastián, Spain (3) Ikerbasque, Basque Foundation for Science, 48013 Bilbao, Spain

Hot electron dynamics in graphene –a linear scaling atomistic approach10

Luis Manuel Canonico Armas, Aron W. Cummings and Stephan Roche

Catalan Institute of Nanoscience and Nanotechnology (ICN2), CSIC and BIST, Campus UAB, Bellaterra, 08193 Barcelona, Spain

Localized states, spin-polarisation and transport in graphene grain boundaries11

Aleksander Bach Lorentzen, Mads Brandbyge

Dept. of Physics, Technical University of Denmark (DTU) DK-2800 Kongens Lyngby, Denmark

Image-Force Barrier Lowering of Contact Resistance for Two-Dimensional Materials:

Direct Determination and Method of Images on a Cone Manifold13

Sarah R. Evans (1) Emeric Deylgat (1,2,3), Edward Chen (4) and William G. Vandenberghe(1)

(1) Department of Materials Science and Engineering, The University of Texas at Dallas. (2) Department Physics, KU Leuven, (3) Imec, Kapeldreef 75, 3001 Heverlee, Belgium, (4) Corporate Research, Taiwan Semiconductor Manufacturing Company Ltd., Taiwan.

Spin-valley transport in magnetic 2D materials through multiscale simulations15

D. Soriano (1), D. Marian (2), D. K. Dubey (2), E. Cannavò (2), E. G. Marin (3), and G. Fiori (2)

(1) Departamento de Física Aplicada, Universidad de Alicante, 03690 Alicante, Spain (2) Dipartimento di Ingegneria dell'Informazione, Università di Pisa, Via G. Caruso 16, Pisa, 16122, Italy (3) Departamento de Electrónica, Universidad de Granada, Avenida Fuente Nueva s/n, Granada, 18071, Spain

Session: Quantum electron transport

TREATING NON-EQUILIBRIUM GREEN'S FUNCTIONS WITH

A MONTE CARLO METHOD (INVITED)17

David K. Ferry (INVITED)

Arizona State University (USA)

Non-Equilibrium Green's Functions Basis in Multiband Models for Broken-Gap Antimonide-Based Tunneling Devices	19
T. Sato (1,2), S. Birner (1), C. Jirauschek (2), and T. Grange (3)	
(1) nextnano GmbH, Konrad-Zuse-Platz 8, 81829 München, Germany (2) TUM School of Computation, Information and Technology, Technical University of Munich, Hans-Pilgry-Straße 1, 85748 Garching b. München, Germany (3) nextnano Lab, 12 chemin des prunelles, 38700 Corenc, France	
A phenomenological method to reduce NEGF simulation from 3D to 1D for lateral translation invariant systems.....	21
A. Martinez (1) and J.R. Barker (2)	
(1) Department of Electrical and Electronic Engineering, Swansea University, Bay Campus , UK (2) James Watt School of Engineering, University of Glasgow, Glasgow G12 8LT, UK	
Delta-layer tunnel junctions in semiconductors for charge sensing	23
J.P. Mendez and D. Mamaluy	
Cognitive & Emerging Computing, Sandia National Laboratories, Albuquerque, USA	
A novel structure of Cooling Nano-devices: The Quantum Cascade Cooler.....	25
G. Etesse (1), C. Salhani (2,3), X. Zhu (2), N. Cavassilas (1), F. Michelini (1) , K. Hirakawa (2,3), and M. Bescond (1,2)	
(1) Aix Marseille Université, CNRS, IM2NP UMR 7334, 133997 Marseille, France (2) Institute of Industrial Science, University of Tokyo, Japan (3) LIMMS-CNRS, IRL 2820, Tokyo, Japan	
Weak values: a new paradigm to characterize nanoscale systems.....	27
Xabier Oianguren-Asua, Carlos F. Destefani and Xavier Oriols	
Departament d'Enginyeria Electrònica, Universitat Autònoma de Barcelona, 08193 Bellaterra, Barcelona, Spain.	

Session: Machine Learning

MACHINE LEARNING FOR MATERIALS AND DEVICE SIMULATIONS.....	29
Alison B. Walker (INVITED)	
University of Bath (UK)	
First-Principles Multiscale Modeling Enabled by Machine Learning Interatomic Potentials.....	30
B. Mortazavi (1,2), and X. Zhuang (1,2)	
(1) Department of Mathematics and Physics, Leibniz Universität Hannover, Appelstraße 11,30167 Hannover, Germany. (2) Cluster of Excellence PhoenixD (Photonics, Optics, And Engineering–Innovation Across Disciplines), Gottfried Wilhelm Leibniz Universität Hannover, Hannover, Germany	
Design of Oscillatory Neural Networks by Machine Learning Algorithms	32
Tamas Rudner (1), Gyorgy Csaba (1), Wolfgang Porod (2)	
(1) Faculty of Information Technology and Bionics, Pázmány University Budapest, Hungary. (2) Department of Electrical Engineering, University of Notre Dame, USA	

Automatic optimization of doping profile for high performance Single-Photon

Avalanche Diodes 34

Rémi Helleboid (1,2), Jérôme Saint-Martin (1), Marco Pala (1), Philippe Dollfus (1), Denis Rideau (2), Gabriel Mugny (2), Isobel Nicholson (2), Jeremy Grebot (2)

(1) C2N, Université Paris-Saclay – CNRS, Palaiseau, France (2) STMicroelectronics, Crolles, France – Edinburgh, United-Kingdom

Machine learning based analysis of collective diffusion in inorganic

solid-state electrolytes..... 36

Cibrán López Álvarez (1,2,3), Riccardo Rurali (3) and Claudio Cazorla (1,2)

(1) Departament de Física, Universitat Politècnica de Catalunya, 08034 Barcelona, Spain, (2) Barcelona Research Center in Multiscale Science and Engineering, Universitat Politècnica de Catalunya, 08019 Barcelona, Spain (3) Institut de Ciència de Materials de Barcelona, ICMAB–CSIC, Campus UAB, 08193 Bellaterra, Spain

Session: Growth and interface processes

PROCESS SIMULATION IN MICRO- AND NANO-ELECTRONICS..... 38

Lado Filipovic (INVITED)

Institute for Microelectronics (Austria)

An Efficient Atomistic Method for Micro-Scale Film Growth from the Vapor Phase 40

E.E. Lorenz (1,2) and J. Schuster (1)

(1) Fraunhofer Institute for Electronic Nanosystems, Technologie-Campus 3, 09126 Chemnitz, Germany (2) Center for Microtechnologies, Chemnitz University of Technology, 09126 Chemnitz, Germany

Interfacial and structural characterization of polymer – electrolyte systems

using classical Molecular Dynamics 42

M.A. Salvador (1), Elena Degoli (2), Alice Ruini (1) and Rita Magri (2)

(1) Dipartimento di Scienze Fisiche, Informatiche e Matematiche, Università di Modena e Reggio Emilia, MO, Italy (2) Dipartimento di Scienze e Metodi dell'Ingegneria, Università di Modena e Reggio Emilia, RE, Italy

3D Multi-Level-Set Simulation of Bottom Dielectric Isolation Process for Forksheet FETs 44

In Ki Kim and Sung-Min Hong

School of Electrical Engineering and Computer Science, Gwangju Institute of Science and Technology (GIST), Gwangju, Cheomdangwagiro-123, South Korea

Theory of Electric Enthalpy of Formation in Electrified Interface..... 46

Ryong-Gyu Lee, Juho Lee, Hyeonwoo Yeo and Yong-Hoon Kim

School of Electrical Engineering, Korea Advanced Institute of Science and Technology, 291 Daehak-ro, Yuseong-gu, Daejeon 34141, Korea

Wednesday, June 14

Session: Thermal transport and dissipation

AB-INITIO THERMAL TRANSPORT CALCULATIONS FOR CRYSTALS AND NANOSTRUCTURES BASED ON THE BOLTZMANN TRANSPORT EQUATION 48

Jesus Carrete (INVITED)

TU Wien (Austria)

Full Band Monte Carlo simulation of transient and stationary thermal transport in GaAs porous nanostructures based on ab initio calculation 50

Junbum Park (1), Lorenzo Paulatto (2), Marco Pala (1), and Jerome Saint-Martin (1)

(1) C2N, Université Paris-Saclay, CNRS, 91120, Palaiseau, France (2) IMPMC, Sorbonne Université, CNRS, 75252, Paris, France

BTE-Barna: first-principles thermal simulation of devices based on 2D materials 52

M. Raya-Morenoz (1), X. Cartoixà (2) and J. Carrete (3)

(1) Institut de Ciència de Materials de Barcelona (ICMAB-CSIC), Campus UAB, 08193 Bellaterra, Spain (2) Departament d'Enginyeria Electrònica, Universitat Autònoma de Barcelona, 08193 Bellaterra, Spain (3) Institute of Materials Chemistry, TU Wien, A-1060 Vienna, Austria

Dynamics of Long-Wavelength Phonons Near Boundaries and Interfaces in Nanomaterials 54

L. Avazpour, M.K. Eryilmaz, and I. Knezevic

Department of Electrical and Computer Engineering, University of Wisconsin – Madison Madison, WI 53706 USA

Strong anharmonicity at the origin of anomalous thermal conductivity in Cs₂NaYbCl₆ 56

Antonio Cappai, Claudio Meli, Francesco Quochi, Michele Saba, Daniela Marongiu and Luciano Colombo

Dipartimento di Fisica, Università di Cagliari, Italy

Temperature-induced boomerang effect of electron flow in semiconductor heterostructures 58

C. Belabbas (1), A. Crépieux (2), N. Cavassilas (1), F. Michelin¹, X. Zhu (3), C. Salhani (3,4), G. Etesse (1), K. Hirakawa (3, 4, 5) and M. Bescond (1,3)

(1) IM2NP UMR-CNRS, Aix Marseille Université, Université de Toulon, Marseille, France. (2) Aix Marseille Univ, Université de Toulon, CNRS, CPT, Marseille, France (3) Institute of Industrial Science, University of Tokyo, Japan, (4) LIMMS-CNRS, IRL 2820, Tokyo, Japan

Session: Semiclassical electron transport

IMPACTS OF BAND STRUCTURES AND SCATTERING PROCESSES ON HIGH-FIELD CARRIER TRANSPORT IN WIDE BANDGAP SEMICONDUCTORS 60

Nobuya Mori (INVITED)

Osaka University (Japan)

Effect of Electron-Electron Scattering on the Energy Distribution in Semiconductor

Devices.....62

Hans Kosina and Josef Gull

Institute for Microelectronics, TU Wien, Gußhausstraße 27–29, 1040 Wien, Austria

Efficient ab initio electronic transport methods64

Z. Li, P. Graziosi (2) and N. Neophytou (1)

(2) School of Engineering, University of Warwick, Coventry, CV4 7AL, UK (2) CNR-Bologna, Italy

Modelling of Schottky-Barrier Diodes Operating under Strong Reverse-Bias Conditions66

B. Orfao, B. G. Vasallo, S. Pérez, J. Mateos, and T. González

Dpto. De Física Aplicada and USAL-NANOLAB, Universidad de Salamanca, 37008 Salamanca, Spain

Influence of Deformation Potential Scattering on Impact Ionization in Ultra-Wide

Bandgap Materials.....68

J. Shoemaker, R. Vatan, T. Biswas, A. Singh, M. Saraniti, S.M. Goodnick

Arizona State University, Tempe, AZ, USA

Upper Valley and Degeneracy Interplay on the Mobility of Transition Metal

Dichalcogenides: Insights from Monte Carlo Simulation70

José M. Iglesias (1), Karol Kalna (2), Raúl Rengel (3) and Elena Pascual (3)

(1) Department of Applied Mathematics, University of Salamanca, 37008 Salamanca, Spain (2) Nanoelectronic Devices Computational Group, Faculty of Science & Engineering, Swansea University, Swansea SA1 8EN, Wales, United Kingdom (3) Department of Applied Physics, University of Salamanca, 37008 Salamanca, Spain

Session: Advanced nanoelectronics

WHERE IS SEMICONDUCTOR TECHNOLOGY HEADING? A VIEW FROM THE INDUSTRY AND

IMPLICATIONS ON COMPUTATIONAL NANOTECHNOLOGY.....72

Carlos H. Diaz (INVITED)

Senior Director in R&D (TSMC)

Nanowire transport and edge passivation74

P. Blaise (1), T. Kubis (2), E. Guichard (1)

(1) Silvaco Inc., Santa Clara, CA 95054, USA and Montbonnot-Saint-Martin, 38330, FRANCE (2) School of Electrical and Computer Engineering, Purdue University, West Lafayette, IN 47907, USA

Modeling Self-Heating Effects in 28 nm Technology Node Fully-Depleted SOI Devices76

Z. Wang (1), D. Vasileska (1), C.S. Soares (2), G.I. Wirth (2), M.A. Pavanello (3) and M. Povolotskyi (4)

(1) Arizona State University, Tempe, AZ, USA (2) UFRGS, Porto Alegre, Brazil (3) Centro Universitario FEI, Sao Bernardo do Campo, Brazil (4) Jacobs, Hanover, MD, USA

Closing the “10-100 eV Gap” for Electron Thermalization in GaN Devices from

First Principles 78

Dallin O. Nielsen (1), Chris G. Van de Walle (2), Sokrates T. Pantelides (3,4), Ronald D. Schrimpf (4), Daniel M. Fleetwood (4), and Massimo V. Fischetti (1)

(1) Department of Materials Science and Engineering, University of Texas at Dallas (2) Materials Department, University of California, Santa Barbara (3) Department of Physics and Astronomy, Vanderbilt University (4) Department of Electrical and Computer Engineering, Vanderbilt University

3D Quantum Corrected Monte Carlo Simulation of n-FinFETs 80

C. S. Soares (1), G. F. Furtado (2), A. C. J. Rossetto (3), G. I. Wirth, D. Vasileska (4).

(1) Programa de Pós-Graduação em Microeletrônica Universidade Federal do Rio Grande do Sul Porto Alegre, Brazil. (2) Silvaco, Porto Alegre, RS, Brazil. (3) Centro de Desenvolvimento Tecnológico Universidade Federal de Pelotas Pelotas, Brazil (4) Department of Electrical Engineering Arizona State University Tempe, USA

Session: Quantum electron transport II

Edge-states interferometers in graphene nanoribbons: a time-dependent modelling 82

G. Forghieri (1), P. Bordone (1), and A. Bertoni (2)

(1) Università di Modena e Reggio Emilia, via Campi, 213/A, Modena, Italy (2) Istituto Nanoscienze – CNR, Modena, Italy

A Coupled Electrostatic – Quantum Transport Framework for Exascale Systems 84

S. S. Sawant (1), F. Léonard (2), J. Yao (1), and A. Nonaka (1)

(1) Lawrence Berkeley National Laboratory, Berkeley, California, 94720, USA (2) Sandia National Laboratories, Livermore, California, 94550, USA

Acoustic phonon modulation of terahertz quantum cascade lasers 86

A. Demic (1), A. Valavanis (1), J. Bailey (2), P. Dean (1), L. H. Li (1), A. G. Davies (1), E. H. Linfield (1), P. Harrison (3), J. E. Cunningham (1), A. Kent (2)

(1) School of Electronic and Electrical Engineering, University of Leeds, Leeds LS2 9JT, UK (2) School of Physics and Astronomy, University of Nottingham, Nottingham NG7 2RD, UK (3) School of Computing and Engineering, University of Huddersfield, Huddersfield HD1 3DH, UK

Simulation of Single-Electron Shuttling for Spin-Qubit Transport in a SiGe Quantum Bus 88

L. Ermoneit (1), B. Schmidt (1), J. Fuhrmann(1), T. Koprucki (1), L. R. Schreiber (2), and M. Kantner (2)

(1) Weierstrass Institute for Applied Analysis and Stochastics, Mohrenstr. 39, 10117 Berlin, Germany (2) ARA-FIT Institute for Quantum Information, Forschungszentrum Jülich GmbH and Institute of Physics, RWTH Aachen University, Otto-Blumenthal-Str., 52074 Aachen, Germany

Coherent Wigner Dynamics of a Superposition State in a Tunable Barrier Quantum Dot 90

M. Ballicchia, M. Nedjalkov, and J. Weinbub

Institute for Microelectronics, TU Wien, Gußhausstraße 27–29, 1040 Wien, Austria

Incorporation of the Tight Binding Hamiltonian into Quantum Liouville-type Equations 92

C. Abdi, M. Pech, and D. Schulz

Chair for High Frequency Techniques, TU Dortmund, Friedrich-Wöhler-Weg 4, 44227 Dortmund, Germany

Thursday, June 15

Session: Engineered nanomaterials and nanostructures

MULTISCALE MODELLING AND COMPUTATIONAL SPECTROSCOPY 94

Kersti Hermansson (INVITED)

Uppsala University (Sweden)

Solving Kohn-Sham Equations of Heterobilayer Systems Beyond 1000 Atoms:

Twist Angle-dependent Piezoelectricity 96

Han-Wei Hsiao, Namita Narendra, and Tillmann Kubis

Elmore Family School of Electrical and Computer Engineering, Purdue University, West Lafayette, IN, USA

Anomalous transient blue-shift in the internal stretch mode of CO on Pd(111) 98

Raul Bombín (1,2,3), Alberto S. Muzas (2), Dino Novko (4), J. Iñaki Juaristi (1,2,5) and Maite Alducin (1,5)

(1) Centro de Física de Materiales CFM/MPC (CSIC-UPV/EHU), Donostia-San Sebastián, Spain (2) Departamento de Polímeros y Materiales Avanzados: Física, Química y Tecnología, Facultad de Químicas (UPV/EHU), Donostia-San Sebastián, Spain (3) Departament de Física, Universitat Politècnica de Catalunya, Barcelona, Spain (4) Institute of Physics, Zagreb, Croatia (5) Donostia International Physics Center (DIPC), Donostia-San Sebastián, Spain

Ab initio calculation of mobility degradation caused by Si-vacancies in

SiC/SiO₂ channels 100

Colin Kälin, Mathieu Luisier

Integrated Systems Laboratory, ETH Zürich, Switzerland

Modelling the electrical conductivity of carbon nanotube films 102

T.R. Durrant (1,2), D.Z. Gao (2), Y. Giret (2) and A.L. Shluger (1)

(1) Department of Physics and Astronomy, University College London. Gower Street, London WC1E 6BT, UK (2) Nanolayers Research Computing Ltd.1 Granville Court, Granville Road, London N12 0HL, UK

Electric fields for tuning molecular orientation in TPD-modified glasses 104

Marta Rodríguez-López (1), Antonio, Cappai (2), Claudio Melis (2), Luciano Colombo (2), Javier Rodríguez-Viejo (1), Marta Gonzalez-Silveira (1).

(1) Group of Thermal properties of Nanoscale Materials (GTNaM), Universitat Autònoma de Barcelona (UAB) & Catalan Institute of Nanoscience and Nanotechnology (ICN2), Barcelona, Spain. (2) Dipartimento di Fisica, Università di Cagliari, Cittadella Universitaria, Monserrato (Ca), Italy.

Session: 2D materials and devices

Shot noise in disordered graphene samples 106

P. Marconcini (1), D. Logoteta (2) and M. Macucci (1)

(1) Dipartimento di Ingegneria dell'Informazione, Università di Pisa, Via Caruso 16, 56122 Pisa, Italy (2) Dipartimento di Ingegneria dell'Informazione, Elettronica e Telecomunicazioni (DIET), Università di Roma La Sapienza, via Eudossiana 18, 00184 Roma

Engineering of Charge Current Flow in Nanoporous Graphenes 108

I. Alcón (1), A. Cummings (1) and S. Roche (1,2)

(1) Catalan Institute of Nanoscience and Nanotechnology (ICN2), Campus UAB, Bellaterra, 08193 Barcelona, Spain (2) ICREA, Institució Catalana de Recerca i Estudis Avançats, 08070 Barcelona, Spain

Recombination Time in Drift-Diffusion Models of Graphene Field-Effect Transistors..... 110

Pedro C. Feijoo (1,2), Ferney A. Chaves (2) and David Jiménez (2)

(1) Departamento de Matemática Aplicada a la Ingeniería Industrial, C/José Gutiérrez Abascal 2, 28006 Madrid, Universidad Politécnica de Madrid (2) Departament d'Enginyeria Electrònica, C/ de les Sitges s/n, 08193 Cerdanyola del Vallès (Barcelona), Universitat Autònoma de Barcelona, Spain

Numerical simulation of terahertz carrier dynamics in monolayer MoS₂ 112

Shuva Mitra, Laleh Avazpour, and Irena Knezevic

Department of Electrical and Computer Engineering University of Wisconsin-Madison, Madison, WI 53706, USA

Quantum Transport Study of Metal-TMD Contacts: Role of the Dielectric Environment..... 114

Pranay Kumar Reddy Baikadi (1), Peter Reyntjens (1,2), Maarten L. Van de Put (2) and William G. Vandenberghe (1)

(1) Department of Materials Science and Engineering, The University of Texas, Dallas, TX, USA (2) Department of Material Engineering, KU Leuven, Belgium

Electrothermal Properties of 2D Materials..... 116

S. Klein (1), Z. Aksamija (2)

(1) University of Massachusetts, Amherst, MA, USA, (2) University of Utah, Salt Lake City, UT, USA

First-principles study of water molecules at the electrified graphene surface..... 118

Hyeonwoo Yeo, Juho Lee, Ryong Gyu Lee, Seunghyun Yu, and Yong-Hoon Kim

School of Electrical Engineering, Korea Advanced Institute of Science and Technology (KAIST), 291 Daehak-ro, Yuseong-gu, Daejeon 34141, Korea

Session: Special session in honor of David K. Ferry

Wigner Transport in Magnetic Fields 119

M. Ballicchia, C. Etl, M. Nedjalkov, and J. Weinbub

Institute for Microelectronics, TU Wien, Gußhausstraße 27–29, 1040 Wien, Austria

Kirchhoff Coupling Generates ATP, the Chemical Energy of Life 121

Robert Eisenberg

Illinois Institute of Technology, Rush University, University of Illinois, Chicago IL USA

50 Years in the Semiconductor Underground: A Retrospective 123

Stephen Goodnick (1) , Paolo Lugli (2) Dragica Vasileska (3), Irena Knezevic (4) and Wolfgang Porod (5)

(1) Arizona State University (USA), (2) University of Bolzano (Italy), (3) Arizona State University (USA), (4) University of Wisconsin-Madison (USA) and (5) Notre Dame University (USA).

Friday, June 16

Session: Neuromorphic computing

MEMRISTORS WITH THOUSANDS OF CONDUCTANCE LEVELS FOR ANALOG COMPUTING	124
J. Joshua Yang (INVITED)	
Future of Computing Institute University of Southern California (USA)	
Probabilistic modelling of resistive switching in emerging ReRAM cells.....	125
Y. V. Pershin (1) and V. A. Slipko (2)	
(1) Department of Physics and Astronomy, University of South Carolina, Columbia, SC 29208, USA (2) Institute of Physics, Opole University, Opole 45-052	
Compact modelling of memristors for neuromorphic circuit simulation.....	127
F. Aguirre, J. Suñé and E. Miranda	
Departament d'Enginyeria Electrònica. Universitat Autònoma de Barcelona Campus de Bellaterra, 08193-Bellaterra (SPAIN)	
Molecular dynamics simulation of the full operation cycle of a HfO₂-based RRAM cell	129
X. Cartoixà (1) , M. L. Urquiza (1,2), Md M. Islam (3), A. C. T. van Duin (4), and A. Strachan (5)	
(1) Departament d'Enginyeria Electrònica, Universitat Autònoma de Barcelona, 08193 Bellaterra (Barcelona), Spain, (2) Laboratoire des Solides Irradiés, École Polytechnique, Institut Polytechnique de Paris, Paris, France (3) Department of Mechanical Engineering, Wayne State University, Detroit, Michigan 48202, USA (4) Department of Mechanical Engineering, Pennsylvania State University, 240 Research East Building, University Park Pennsylvania 16802, USA (5) School of Materials Engineering, Purdue University, West Lafayette, Indiana 47907 USA	
Multiscale Modelling of Dielectric Breakdown in Amorphous HfO₂	131
Jack Strand (1,2) and Alexander Shluger (1)	
(1) Department of Physics and Astronomy, University College London, Gower Street, London WC1E 6BT, UK (2) Nanolayers Research Computing Ltd, 1 Granville Court, Granville Road, London, England, N12 0HL	
Termination-Dependence of Resistive Switching in SrTiO₃-based Valence Change Memory	133
M. Mladenovic, M. Kaniselman, C. Weilenmann, A. Emboras, and M. Luisier	
Integrated Systems Laboratory, ETH Zürich, Gloriastrasse 35, 8092, Zürich, Switzerland	
Temperature-Dependent Electric Switching of Chalcogenide Memories Below the ns Limit	135
R. Brunetti, M. Rudan, and C. Jacoboni	
FIM Department, University of Modena and Reggio Emilia, Modena, Italy, DEI Department, University of Bologna, Bologna, Italy	

Session: Electrons under electromagnetic fields

QUANTUM PHOTODETECTORS 137

Francois Léonard (INVITED)
Sandia National Laboratories (USA)

Impact of hBN-encapsulation on light absorption in 2D-TMD-based photodetectors..... 138

A. A. Díaz-Burgos, A. Toral-López, J. Cuesta, E.G. Marín, F. Pasadas, F.G. Ruiz, A. Godoy
Departamento de Electrónica y Tecnología de Computadores, Universidad de Granada, Granada, Spain

Dual-Potential Finite-Difference Method for Electrodynamics

Within Multiphysics Solvers 140

S. W. Belling, L. Avazpour and I. Knezevic
Department of Electrical and Computer Engineering, University of Wisconsin – Madison Madison, WI 53706 USA

Polaritonic features in the THz displacement current through RTDs in microcavities 142

C. F. Destefani (1), M. Villani (1), X. Cartoixà (1), M. Feiginov (2), and X. Oriols (1)
(1) Department of Electronic Engineering, Universitat Autònoma de Barcelona, Spain (2) Department of Electrical Engineering and Information Technology, Technische Universitat Wien, Austria

Switching Performance of Mo-based pMTJ and dsMTJ structures 144

B.Pruckner (1) S.Fiorentini (1), N.Jorstad (2), T.Hadamek (1), S.Selberherr (2), W.Goes (3), and V.Sverdlov (1,2)
(1) Christian Doppler Laboratory for Nonvolatile Magnetoresistive Memory and Logic at the (2) Institute for Microelectronics, TU Wien, Gußhausstraße 27–29, A-1040 Wien, Austria (3) Silvaco Europe, Cambridge, United Kingdom

Deterministic Approach for Skyrmionic Dynamics at Non-zero Temperatures 146

C. Navau, J. Castell-Queralt, L. Gonzalez-Gómez, N. Del-Valle
Departament de Física, Universitat Autònoma de Barcelona, 08193 Bellaterra, Barcelona, Catalonia, Spain

Poster sessions

Tuesday, June 13

Poster session I

Mach-Zehnder-like interferometry with graphene nanoribbon networks..... 147

Sofia Sanz (1), Nick Papior (2), Geza Giedke (3,4), Daniel Sanchez-Portal (5), Mads Brandbyge (1), Thomas Frederiksen (3,4)
(1) Department of Physics, DTU, DK-2800 Kgs. Lyngby, Denmark, (2)DTU Computing Center DK-2800 Kgs. Lyngby, Denmark, (3) Donostia International Physics Center (DIPC), E-20018, Donostia-San Sebastian, Spain, (4) IKERBASQUE,

Two conductivity regimes in semiconductor δ -layer tunnel junctions 149

D. Mamaluy and J.P. Mendez

Cognitive & Emerging Computing, Sandia National Laboratories, Albuquerque, USA

Charge Transport Properties of Cytochrome b562 on Gold Interfaces 151

G.N. Jonnalagadda, Z. Futera

Faculty of Science, University of South Bohemia, Branisovska 1760, 370 05 Ceske Budejovice, Czech Republic

Coherent and Incoherent Electron Transport through Protein Junctions

Investigated by DFT-based Approaches..... 153

Z. Futera

Faculty of Science, University of South Bohemia, Branisovska 1760, 370 05 Ceske Budejovice, Czech Republic

Schrödinger Equation Solver Based on Data-Driven Physics-Informed Generic

Building Blocks 155

Martin Veresko, Ming-Cheng Cheng

Department of ECE, Clarkson University, 8 Clarkson Ave, Potsdam NT, United States

Considerations on Treating Polar-Optical Phonon Scattering in Real Space..... 157

D. K. Ferry

School of Electrical, Computer, and Energy Engineering, Arizona State University, Tempe, AZ 25287-6206 USA

Spin-selective transport phenomena in helical molecular wires..... 159

R. Korytá (1), Š. Marek (1), J. van Ruitenbeekz (2) and F. Eversy (3)

(1) Charles University, Czech Republic, (2) Institute of Theoretical Physics, University of Regensburg, Germany (3) Huygens-Kamerlingh Onnes Laboratory, Leiden University, Netherlands

Efficient Method to Obtain Target Bias Solutions of 6F2 DRAM Cells with Geometric Fluctuations..... 161

Geonho Park, Seung-Cheol Han, and Sung-Min Hong

School of Electrical Engineering and Computer Science, Gwangju Institute of Science and Technology

First-principles Study on As Antisites in InGaAs Alloys, GaAs and InAs 163

Yucheol Cho, Gyeongdo Ham and Daeshik Kim*

School of Electrical Engineering, Korea Advanced Institute of Science and Technology, Daejeon, 34141, South Korea

First-Principles investigation of polytypic defects in InP..... 165

Christian Dam Vedel (1,2) , Søren Smidstrup (2), Vihar P. Georgiev (1)

(1) Device Modelling Group, School of Engineering, University of Glasgow, United Kingdom (2) Synopsys Denmark ApS, Copenhagen, Denmark

Multiscale simulations of ink-jet printed devices..... 167

D. Marian (1), P. K. Dubey (1), M. Perucchini (1), E. G. Marin (2), and G. Fiori (1)

(1) Dipartimento di Ingegneria dell'Informazione, Università di Pisa, Via G. Caruso 16, Pisa, 16122, Italy (2) Departamento de Electrónica, Universidad de Granada, Avenida Fuente Nueva s/n, Granada, 18071, Spain

An extended Hueckel theory parameterization of Germanium for doped SiGe alloys 169

D. Dick (1,3), F. Fuchs (2,3), S. Gemming (3,4) and J. Schuster (1,2,3)

(1) Center for Microtechnologies, Chemnitz University of Technology, Chemnitz, Germany (2) Fraunhofer Institute for Electronic Nano Systems (ENAS), Chemnitz, Germany (3) Center for Materials, Architectures and Integration of Nanomembranes (MAIN), Chemnitz University of Technology, Chemnitz, Germany (4) Institute of Physics, Chemnitz University of Technology, Chemnitz, Germany

Time-Domain Computation of the Linewidth Enhancement Factor in

Multi-Quantum-Well Semiconductor Optical Amplifiers..... 171

Ö.E. Aşırım, C. Jirauschek

TUM School of Computation, Information and Technology, Technical University of Munich, Hans-Piloyt Straße 1, 85748 Garching, Germany

Multiscale simulation of high harmonic generation using artificial intelligence 173

Javier Serrano, José Miguel Pablos-Marín and Carlos Hernández-García

Grupo de Investigación en Aplicaciones del Láser y Fotónica, Departamento de Física Aplicada Universidad de Salamanca, Pl. Merced s/n, E-37008 Salamanca, Spain

Application of Discontinuous Galerkin Methods onto Quantum-Liouville

type Equations..... 175

V. Ganiu, D. Schulz

Chair for High Frequency Techniques, TU Dortmund, Friedrich-Woehler-Weg 4, 44227 Dortmund, Germany

Wednesday, June 14

Poster session II

Full-Band Device Simulator with Real-Space Treatment of the Short-Range Coulomb Interactions for Modeling 4H-SiC VDMOS Devices..... 177

Dragica Vasileska and Chi-Yin Cheng

School of Electrical, Computer and Energy Engineering Arizona State University, Tempe, AZ 85287-5706

Schottky barriers in one-dimensional field-effect transistors: a model-based

Characterization 179

Anibal Pacheco-Sanchez, David Jiménez

Departament d'Enginyeria Electrònica, Escola d'Enginyeria, Universitat Autònoma de Barcelona, Bellaterra 08193, Spain.

Silicon passivation of zigzag graphene edge enabling robust spin-polarized

nanogap quantum transport 181

Juho Lee, Seunghyun Yu and Yong-Hoon Kim

School of Electrical Engineering, Korea Advanced Institute of Science and Technology (KAIST), 291 Daehak-ro, Yuseong-gu, Daejeon 34141, Korea

Monte Carlo Simulations of Electrons in Al₄SiC₄ Ternary Carbide 182

K. Kalna (1) and D. Chaussende (2)

(1) NanoDeCo Group, Dept. Electronic & Electrical Engineering, Faculty of Science & Engineering, Swansea University, Swansea, SA1 8EN, Wales, United Kingdom (2) Université Grenoble Alpes, CNRS, Grenoble INP, SIMaP, 38000 Grenoble, France

Ab initio heat dynamics in phonon-based dark matter detectors 184

M. Raya-Moreno (1), B. J. Kavanagh (2), E. Vilanova (1), L. Fàbrega (1) and R. Rurali (1)

(1) Institut de Ciència de Materials de Barcelona (ICMAB-CSIC), Campus UAB, 08193 Bellaterra, Spain (2) Instituto de Física de Cantabria (IFCA, UC-CSIC), Av. De los Castros, 39005 Santander, Spain

Ab initio effective dragged thermoelectric properties in Si nanowires 186

M. Raya-Moreno (1), R. Rurali (1) and X. Cartoixà (2)

(1) Institut de Ciència de Materials de Barcelona (ICMABCSIC), Campus UAB, 08193 Bellaterra, Spain (2) Departament d'Enginyeria Electrònica, Universitat Autònoma de Barcelona, 08193 Bellaterra, Spain

Phonon transport across Ge/GaAs heterojunctions by nonequilibrium

molecular dynamics 188

T. Albrigi and R. Rurali

Institut de Ciència de Materials de Barcelona (ICMAB-CSIC) Campus UAB, 08193 Bellaterra, Spain

Electrothermal simulations of a thermal sensor integrated with a 4H-SiC JFET 190

D. Monaghan, A. Martinez and M. Jennings

Department of Electrical and Electronic Engineering, Swansea University, UK Swansea, UK

Effects of structural arrangements on thermoelectric properties of SiX (X=N,P,As,Sb,Bi) monolayers 192

Subhradip Ghosh, and Himanshu Murari

Department of Physics, Indian Institute of Technology Guwahati, Guwahati-781039, India

Analysis of Wave speed in magneto-thermoelastic nonlocal micropolar

orthotropic medium 194

Anand Kumar Yadav (1) and Sangeeta Kumari (2)

(1) Shishu Niketan Model Senior Secondary School, Sector 22-D, Chandigarh, India (2) Department of mathematics, Chandigarh University, Gharuan, Punjab, India

Towards a semi-classical simulator for the energy distribution functions in optically

excited hot carrier semiconductor devices 196

J. R. Barker (1) and A. M. Martinez (2)

(1) James Watt School of Engineering, University of Glasgow, Glasgow G12 8LT, UK (2) Department of Electrical and Electronic Engineering, Swansea University, Bay Campus, UK

Breakdown of GaN-based Planar Gunn Diodes investigated through a Combined Deep Learning-Monte Carlo Model 198

S. García-Sánchez, R. Rengel, S. Pérez, T. González and J. Mateos

Applied Physics Department and NANOLAB, Universidad de Salamanca, Salamanca 37008, Spain

DECaNT Numerical Tool for Exciton Dynamics in Carbon Nanotube Films..... 200

S. S. Sanders, S. W. Belling and I. Knezevic

Department of Electrical and Computer Engineering, University of Wisconsin – Madison Madison, WI 53706, USA

Efficient Monte Carlo Electron Transport Formalism for Highly Nanostructured Materials 202

Pankaj Priyadarshi and Neophytos Neophytou

School of Engineering, University of Warwick, Coventry, CV4 7AL, United Kingdom

Thermal and electrical properties of nanocrystalline superionic $\text{Na}_x\text{Cu}_{1.75\text{S}}$ ($x=0.1, 0.15, 0.2, 0.25$) compounds 204

M.M. Kubenova, K.A. Kuterbekov, M.Kh. Balapanov, A.M. Kabyshev, K.Zh. Bekmyrza, Zh.A. Mukhan and A.K. Kulanov

L.N. Gumilyov Eurasian National University, 010008 Astana, Kazakhstan

Extending the small-signal modelling of GFETs to ambipolarity regime 206

Nikolaos Mavredakis, Anibal Pacheco-Sanchez, David Jiménez

N. Mavredakis, A. Pacheco and D. Jiménez are with the Departament d'Enginyeria Electrònica, Escola d'Enginyeria, Universitat Autònoma de Barcelona, Bellaterra 08193, Spain.

Thursday, June 15

Poster session III

Simulation-based Optimization of a Sensor-Indenter System for Thin Layer Crack Detection 208

F. Tremmel (1), O. Nagler (1), C. Kutter (2), and R. Holmer (3)

(1) Infineon Technologies AG, Am Campeon 1-15, 85579 Neubiberg, Germany (2) Polytronic Systems (EMFT) Institute of Physics, UniBw München, Germany (3) Faculty of Electrical Engineering and Information Technology, OTH Regensburg, Germany

Functionalized TaS₂ for thermoelectric applications: an ab-initio investigation 210

Francesco Siddi, Antonio Cappai, Luciano Colombo and Claudio Melis

Department of Physics, University of Cagliari, Italy

Monte Carlo Solution to Excess Noise and Spatial Blur in Amorphous Selenium Thin-films 212

Dragica Vasileska (1), Atreyo Mukherjee (2), and Amir H. Goldan (3)

(1) School of Electrical, Computer and Energy Engineering, Arizona State University, AZ, US (2) Department of Electrical Engineering, Stony Brook University, NY, US (3) Department of Radiology, Weill Cornell Medical College, Cornell University, New York, NY, USA

Impurity- and remote-phonon-limited mobility in TMD monolayers 214

Shoaib Mansoori, Sanjay Gopalan, and Massimo V. Fischetti

Department of Materials Science and Engineering, The University of Texas at Dallas, 800 W. Campbell Rd., Richardson, TX 75080

Self-consistent k.p band structure in doped core-shell nanowires with type-I, type-II and broken-gap radial heterointerfaces 216

A. Vezzosi (1), A. Bertoni (2), and G. Goldoni(1, 2)

(1) Università di Modena e Reggio Emilia, via Campi, 213/A, Modena, Italy (2) Istituto Nanoscienze – CNR, Modena, Italy

A Sunlight Cooling Device Based on a 2D van der Waals Heterojunction 218

P. Dalla Valle, M. Bescond, F. Michelini, and N. Cavassilas.

Aix Marseille Université, CNRS, Université de Toulon, IM2NP UMR 7334, 13397, Marseille, France

Revealing the Thermal and Mechanical Properties of Amorphous Boron Nitride..... 220

Onurcan Kaya, Ivan Cole and Stephan Roche

Catalan Institute of Nanoscience and Nanotechnology (ICN2), CSIC and BIST, Campus UAB, Bellaterra, 08193 Barcelona, Spain

Resistance calculation in metal-2D contacts: Accuracy of numerical integration..... 222

Peter Reyntjens (1,2,3), Pranay Baikadi (2), Raseong Kim (4), Maarten Van de Put (3), Bart Sorée (1,3,5) and William G. Vandenberghe (2)

(1) Department of Electrical Engineering, KULeuven (2) Department of Materials Science, UT Dallas (3) Imec (4) Components Research, Intel Corporation, Hillsboro, OR 97124 USA (5) Department of Physics, Universiteit Antwerpen

FiPo FDTD Algorithm: Modeling Electric and Magnetic Fields with Potentials

A and ϕ for Quantum Transport Solvers 224

L. Avazpour, M.L. King, S.W. Belling, and I. Knezevic

Department of Electrical and Computer Engineering University of Wisconsin-Madison, Madison, WI 53706, USA

Noise impact on memristor performance: improvement of neuromorphic binary STDP 226

E. Salvador (1), R. Rodriguez (1), E. Miranda (1), J. Martin-Martinez (1), A. Rubio (2), V. Ntinis (2), G. Ch. Sirakoulis (3), A. Crespo-Yepes (1), M. Nafria (1)

(1) Electronic Engineering Department, Universitat Autònoma de Barcelona, 08193 Bellaterra, Spain (2) Electronic Engineering Department, Universitat Politècnica de Catalunya, 08034, Barcelona, Spain (3) Dept. of Electrical & Computer Engineering, Democritus University of Thrace, 67100, Xanthi, Greece

Control of the local magnetic states in graphene with voltage and gating 228

Fei Gao (1,2), Yu Zhang (3), Lin He (3), Shiwu Gao (4) and Mads Brandbyge (1)

(1) Department of Physics, Technical University of Denmark, DK-2800 Kongens Lyngby, Denmark (2) Donostia International Physics Center (DIPC), 20018 Donostia-San Sebastián, Spain (3) Center for Advanced Quantum Studies, Department of Physics, Beijing Normal University, 100875 Beijing, China (4) Beijing Computational Science Research Center, 100193 Beijing, China

General Maxwell-Bloch modelling of self-induced transparency in N-level atom..... 230

A. Demic (1), T.B Gill (1), M.A. Talukder (2), D. Indjin (1), P. Dean (1)

(1) School of Electronic and Electrical Engineering, University of Leeds, Leeds LS2 9JT, UK (2) Electrical and Electronic Engineering, Bangladesh University of Engineering and Technology, Dhaka-1205, Bangladesh

Electronic and Magnetic Properties of Eu doped GaN nanowires: An Ab-initio

study for spin-optoelectronic applications 232

V. K. Gudelli and I. S. Roqan

Physical Sciences and Engineering Division, King Abdullah University of Science and Technology, Thuwal-23955-6900, Saudi Arabia

From radiofrequency to infrared antennas: downscaling

a rectangular loop geometry..... 234

D.K. Maram, J. Garcia, R. Ruiz, X. Cartoixà, G. Abadal

Dept. Enginyeria Electrònica, Campus UAB, 08193-Bellaterra, Spain;

Thursday, June 15

Gala dinner invited speaker

ARTIFICIAL INTELLIGENCE AT FC BARCELONA 236

Jordi Mompart (INVITED)

Director of Research at FC Barcelona

INDEX OF AUTHORS CONTRIBUTING TO THE IWCN 2023

TKWANT: A SOFTWARE PACKAGE FOR TIME-DEPENDENT QUANTUM TRANSPORT

Thomas Kloss, Neel Institute (France)

Tkwant is a Python package for the simulation of quantum nanoelectronic devices to which external time-dependent perturbations are applied. Tkwant is an extension of the Kwant package (<https://kwant-project.org/>) and can handle the same types of systems: discrete tight-binding-like models that consist of an arbitrary central region connected to semi-infinite electrodes.

For such systems, Tkwant provides algorithms to simulate time-dependent manybody expectation values, such as densities and currents.

In this talk I will present the theoretical framework behind Tkwant, which is based on a wave-function approach.

For non-interacting systems, the wave-function approach is mathematically fully equivalent to the nonequilibrium Green's function formalism, but it is much better suited for numerical simulations in terms of scaling.

I will show some examples of typical Tkwant applications as well as a recent extension to include interactions as a time-dependent mean-field.

Tkwant is free software distributed under a BSD license and can be found at

<https://tkwant.kwant-project.org/>.

NEMO: From Esoteric Quantum Theory to Industrial Transistor Designs and Global Impact

Gerhard Klimeck

Network for Computational Nanotechnology and School of Electrical and Computer Engineering,
Purdue University, West Lafayette, IN 47907, USA
e-mail: gekco@purdue.edu

ABSTRACT

Today's nano-scaled transistor have been explored and designed with full quantum transport modeling tools utilizing an atomistic basis. The NEMO5 tool set has been integrated into the in-house Intel design suite [1] and is being commercialized by Silvaco [2]. Other technology leaders such as Samsung and TSMC have built their own in-house tools adopting NEMO approaches. Non-Equilibrium Green Functions (NEGF) for quantum transport with an atomistic basis (typically tight binding) are now the widely accepted standard. NEMO results were the basis for the 2004 rotated substrate technology at Texas Instruments [3] impacting chips in over a billion cell phones. Over 25,000 nanoHUB users have explored nanoscale devices such as nanowires, ultra-thin-body transistors, and quantum dots using NEMO/OMEN tools on nanoHUB.org. They use simple-to-use apps in the first end-to-end scientific computing cloud. Over half of nanoHUB's simulation users explore device and modeling concepts in formal classrooms in over 180 institutions globally. Atomistic device simulation, quantum transport with NEGF and million atom electronic structure simulations were deemed too expensive by the community. Dissemination of easy-to-use app versions of NEMO (and other codes) were deemed to be useless for research and for education. nanoHUB and NEMO have changed fundamental approaches and underlying assumptions: paradigm shifts. This presentation will highlight some of the key hurdles, insights, and developments that drove these paradigm shifts.

KEY INSIGHTS IN QUANTUM TRANSPORT

Today's 3D FinFETs [4] or nanosheet transistors have the same 5nm central length characteristics as 1D resonant tunneling diodes

(RTDs). The quantitative and predictive modeling of 1D RTDs (1994-1997) has defined the standards needed for today's 3D nano-transistors.

Realistic devices are extended. It is not good enough to model a central component of a quantum device. Instead, the central component is embedded in large source and drain regions that have their own quantum and scattering physics that is just as important as the central device. We developed an approach to partition realistic devices for full quantum transport [5].

Incoherent scattering is critical in the source/drain regions. Decoherence and scattering effects are intellectually challenging and have been the focus of RTD models in the central device region. For high performance devices such scattering is much less important than the relaxation effects in the contacts [6].

Effective mass approaches are not predictive. At the 5nm scale a heterostructure does not only form a new device but a new composite material. Effects such as non-parabolicity, band-to-band coupling, crystal orientation, and quantization through geometry allow designers to create a new composite material with new bandgaps, effective masses that cannot be predicted by bulk effective mass approaches. Atomistic basis sets are critically needed, even though transport might just happen in the conduction band. Effective mass models can be tuned to specific atomistic representations but cannot be predictive [6-8]. The establishment of experimentally validated atomistic basis sets via genetic algorithms has been critical [9].

KEY INSIGHTS IN TOOL & DATA SHARING

The typical "products" of a research-oriented faculty member are the creation of new knowledge and graduate students. Papers usually just lead to other papers even in engineering departments. In general tools and data are not shared. As a result, most computational science or engineering papers

cannot even be duplicated, calling into question their scientific merit. nanoHUB was created to share computational tools with the community such that others can duplicate results and use tools to drive new research or use in education.

Simplified user interfaces enable broad use. Most small research codes are written by one person for one person without any consideration of reuse or dissemination. Larger research codes and even commercial codes are often extremely complex that require months of tool training. nanoHUB has developed Rappture [10] and Sim2Is [11] environments that enable the encapsulation of such codes in simple-to-use user interfaces with reduced complexities. Over 2,600 research papers cite nanoHUB with over 68,000 secondary citations (h-index 121). Over 55% of nanoHUB simulation users are in formal classrooms.

nanoHUB tools – a new publication type. The Web-of-Science and Google Scholar have listed nanoHUB tools since 2017 creating an academic incentive to publish new tool & data artifacts. The US government has moved to federal requirements to share data if the research is funded by the government.

CONCLUSION

In the past 30+ years I have strived to create “products” that other researchers and educators can use. NEMO has created paradigm shifts in how people understand and model devices and has

had impact on billions of people through chips in computing and communication devices since 2002. nanoHUB has created paradigm shifts by creating new types of publications and by enabling researchers and educators to use NEMO and hundreds of other tools.

ACKNOWLEDGMENT

This work would not have been possible without my hundreds of collaborators who helped to build, test drive, break, and rebuild NEMO/OMEN [5-9,12-14] and nanoHUB [10,11]. I have the deepest appreciation for their hard work, dedication and in most cases their personal friendship. The citations here just cover some of the fundamental developments. Citations to these papers lead to hundreds of application publications enabled by my collaborators and friends.

REFERENCES

- [1] Mark Stettler *et al.*, *IEDM*, 39.1.1 (2019)
- [2] Silvaco – Victory Atomistic, silvaco.com
- [3] RC Bowen *et al.*, US patent 7,268,399 (2004)
- [4] G. Yeap *et al.*, *IEDM*, 36.7.1 (2019)
- [5] G. Klimeck, *et al.*, *APL Lett.* **67**, 2539 (1995)
- [6] RC Bowen, *et al.*, *JAP* **81**, 3207 (1997)
- [7] Jing Wang, *et al.*, *APL*. **86**, 093113 (2005)
- [8] M Luisier, *et al.*, *Phys. Rev. B* **74**, 205323 (2006);
- [9] G Klimeck *et al.*, *Superlatt. and Microstr.*, **27**, 77, (2000)
- [10] G Klimeck, *et al.*, *IEEE CISE*, Vol. **10**, 17 (2008)
- [11] M. Hunt *et al.*, *PLoS ONE* **17**(3): e0264492.
- [12] R Lake, *et al.*, *JAP* **81**, 7845 (1997)
- [13] G. Klimeck, *et al.*, *Computer Modeling in Engineering and Science (CMES)* **3**, 601-642 (2002).
- [14] S Steiger *et al.*, *IEEE Tr. Nanotechn.*, **10**, 1464, (2011)



Fig. 1. nanoHUB user map representative of year 2016. Red circles designate users viewing lectures, tutorials, or homework assignments. Yellow dots are simulation users. Green dots indicate 4,100+ authors of 1,700+ scientific publications citing nanoHUB through 2016. Dot sizes correspond to number of users, and lines show author-to-author connections proving research collaboration networks. (b) U.S. enlarged. (c) a collage of typical nanoHUB interactive tool sessions and 3D-rendered interactively explorable results (quantum dots, carbon nanotubes, nanowires).

LSQUANT: Linear Scaling Quantum Transport Methodologies

Jose H. Garcia

Catalan Institute of Nanoscience and Nanotechnology, Barcelona, Spain

e-mail: josehugo.garcia@icn2.cat

ABSTRACT SUBMISSION

In this session we will present a recently developed linear scaling or order- n computational techniques for quantum transport simulations name LSQUANT. We will be focusing on explaining the general formalism of the Kubo formula, and how in the noninteracting picture it converges in the Kubo-Greenwood for electrical conductivities and Kubo-Bastin for the Hall conductivity. We will also give further highlights regarding the trade-off between computational cost and accuracy of these numerical schemes and will consider also disordered linear chain and graphene to reinforce the content.

INTRODUCTION

The development of materials and devices relies on a balanced triad of experimentation, theory, and numerical simulations. The focus here is electronic devices, with a key focus on understanding the flow of electrons in response to an electric field, a central question in condensed matter physics that links to the performance of a myriad of devices. To accurately simulate electronic transport in complex materials and devices at the length scales observed in experiments, two elements are necessary: a realistic depiction of the structure and electronic properties of the material in question, and an efficient numerical method for simulating electronic transport.

Ab initio methods like density functional theory (DFT) have been successful in describing various properties of a wide range of materials, but their computational cost limits their application to large systems. This is where quasiparticle-based real-space tight-binding (TB) models come in, allowing for efficient numerical simulation.

The review focuses on efficient numerical calculations of the Kubo and Kubo-Bastin formulas for the electrical and Hall conductivities.

These have been used in a wide array of realistic models of disordered and two-dimensional materials, multilayer graphene, organic semiconductors, conducting polymers, quasicrystals, silicon nanowires, carbon nanotubes, and three-dimensional models of topological insulators. Charge, spin, and Hall transport coefficients have been numerically computed in different transport regimes. These methods have proven to be a cornerstone for the simulation of quantum transport in complex situations, especially in the presence of weak magnetic fields and for disordered systems containing many millions of atoms.

Here, we will give a comprehensive description of the most efficient linear-scaling algorithms for studying electronic transport in complex forms of disordered materials. It is intended to serve as a valuable resource for future developers and users of such methodologies, which can be applied to a large variety of materials of current interest for fundamental science and advanced technologies.

THE SESSION

In this session we will go through the theory of quantum transport methodologies based on the Kubo formula. We will briefly go into the theory of tight binding Hamiltonians and how to construct inputs for the LSQUANT¹ code. We will provide a tutorial of how to perform quantum transport calculations and what are the key parameters to make realistic simulations. At the end we will discuss scalability and potential extensions of the method.

REFERENCES

- [1] Z Fan, JH Garcia, AW Cummings, JE Barrios-Vargas, M Panhans, A Harju, F Ortmann, S Roche. *Linear scaling quantum transport methodologies*, Physics Reports Volume **903**, (2021).

¹<https://www.lsquant.org/>

MS-DFT: Quantum transport from a multi-space excitation viewpoint

Yong-Hoon Kim

School of Electrical Engineering, Korea Advanced Institute of Science and Technology (KAIST),
Daejeon 305-701, Korea
E-mail : *y.h.kim@kaist.ac.kr*

ABSTRACT

For the simulation of non-equilibrium open junction systems under finite bias in a first-principles manner, there exist several motivations to seek an alternative to the standard approach of combining density functional theory (DFT) and nonequilibrium Green's function (NEGF) formalisms. For example, for graphene electrode-based van der Waals 2D tunneling transistors, *ab initio* simulations are currently not possible due to the inherent limitations of the DFT-NEGF method [1-2]. In this presentation, I will discuss the formulation and applications of the multi-space constrained-search DFT (MS-DFT) that we have been developing at KAIST for the past decade plus [1-4]. Seeking an alternative to the standard Landauer picture for quantum transport, we first propose a viewpoint that maps quantum transport processes to space-resolved (drain-to-source) optical excitation counterparts. The multi-space excitation picture for quantum transport then allows the formulation of microcanonical approaches for quantum transport, and the resulting MS-DFT provides unique opportunities in understanding and designing nanoscale devices such as the graphene-based 2D tunneling transistor in operando conditions. Importantly, unlike in the grand-canonical DFT-NEGF, the non-equilibrium total energy as well as quasi-Fermi levels and voltage drop profile can be obtained within the microcanonical MS-DFT [3,4]. Several extensions and applications of MS-DFT will be also outlined.

REFERENCES

- [1] H. S. Kim & Kim, Y.-H., "Constrained-search density functional study of quantum transport in two-dimensional vertical heterostructures", arXiv:1808.03608 [cond-mat.mes-hall] (2018).
- [2] T. H. Kim, J. Lee, R. Lee, & Y.-H. Kim, "Gate-versus defect-induced voltage drop and negative differential resistance in vertical graphene heterostructures", *Npj Comput. Mater.* **8**, 50 (2022).
- [3] J. Lee, H. S. Kim, and Y.-H. Kim, "Multi-space excitation as an alternative to the Landauer picture for non-equilibrium quantum transport", *Adv. Sci.* **7**, 2001038 (2020).
- [4] J. Lee, H. Yeo, and Y.-H. Kim, "Quasi-Fermi level splitting in nanoscale junctions from *ab initio*", *Proc. Natl. Acad. Sci. U. S. A.* **117**, 10142 (2020)

TranSIESTA: Advanced Applications in Electrochemistry and Spintronics

Pablo Ordejón

Catalan Institute of Nanoscience and Nanotechnology - ICN2 (CSIC-BIST)

Campus UAB, 08193 Cerdanyola del Valles, Barcelona (Spain)

e-mail: pablo.ordejon@icn2.cat

SIESTA [1,2] is a Density Functional Theory (DFT) code that uses localized, numerical atomic orbitals as a basis set, and is designed to be able to deal with systems with very large numbers of atoms. One of the distinctive features of SIESTA compared with other DFT codes is the possibility to deal with open systems connected to semi-infinite electrodes at different electrochemical potentials. This non-equilibrium situation is handled through the use of the Non-Equilibrium Green's Functions (NEGF) formalism combined with DFT [3]. This is implemented in the TranSIESTA module of SIESTA, and was originally developed to describe electronic transport in nanoscale devices in molecular electronics and nanoelectronics, where quantum effects (ballistic transport, tunneling, conductance quantization, quantum confinement, etc) are of paramount importance [4]. TranSIESTA was continuously improved, with more efficient numerical algorithms and capabilities, like the possibility of including bias voltages through gates, and multiterminal setups [5].

Recent work has recently enhanced the applicability of TranSIESTA to problems beyond electronic transport. Two of these will be the topic of this talk. The first one is the study of electrochemical processes, where an electrolyte is in contact with metallic electrodes which are subject to external voltages. These problems are formally very similar to those involving electronic transport in nanoelectronic devices (as the electrodes are subject to different electrochemical potentials) although in this case the electrical current is due to the ionic dynamics at the electrolyte and the chemical reactions at the electrolyte-electrode interface. The second topic is that of spintronics, involving spin polarized currents. TranSIESTA has been revamped to be able to treat with such problems, not only including spin polarization, but also the description of non-collinear spin states (where the direction of magnetization can change in space, like in the case of ferromagnetic domain walls), and spin-orbit effects, which are key for spintronic applications.

- [1] J. M. Soler, E. Artacho, J. D. Gale, A. García, J. Junquera, P. Ordejón and D. Sánchez-Portal, *The SIESTA method for ab initio order-N materials simulation*, J. Phys.: Cond. Mat. **14**, 2745–79 (2002)
<https://doi.org/10.1088/0953-8984/14/11/302>
- [2] A. García *et al.*, *SIESTA: Recent developments and applications*, J. Chem. Phys. **152**, 204108 (2020)
<https://doi.org/10.1063/5.0005077>
- [3] M. Brandbyge, J. L. Mozos, P. Ordejón, J. Taylor, K. Stokbro, *Density-functional method for nonequilibrium electron transport*, Phys. Rev. B **65**, 165401 (2002)
<https://doi.org/10.1103/PhysRevB.65.165401>
- [4] K. Stokbro, J. Taylor, M. Brandbyge and P. Ordejón, *TranSIESTA - A spice for molecular electronics*, Annals of the New York Academy of Sciences **1006**, 212-226 (2003)
<https://doi.org/10.1196/annals.1292.014>
- [5] N. Papior, N. Lorente, Th. Frederiksen, A. García and M. Brandbyge, *Improvements on non-equilibrium and transport Green function techniques: The next-generation TranSIESTA*, Computer Physics Communications **212**, 8 (2017)
<https://doi.org/10.1016/j.cpc.2016.09.022>

Quantum ESPRESSO: from density-functional theory to dual wave-particle transport and device simulation

Michele Simoncelli

Theory of Condensed Matter Group of the Cavendish Laboratory, University of Cambridge (UK)

ABSTRACT

Understanding and quantitatively predicting transport phenomena in solids, involving for example charge or heat, from first principles is crucial to design devices for energy conversion or management. In general, the functioning of these devices is governed by an interplay between microscopic, intrinsic materials' properties (determined by the atomistic structure and composition) and macroscopic device properties (such as shape and boundary conditions). We present recent advances in Quantum ESPRESSO, an open-source density-functional-theory (DFT) software, that are relevant for the bottom-up, multiscale simulation of devices. First, we discuss how to compute from DFT all the parameters entering in the microscopic Wigner formulation for transport in solids. This formulation encompasses the emergence and coexistence of particle-like and wave-like conduction mechanisms, enabling quantitative predictions for the intrinsic thermal (electrical) conductivity of solids ranging from crystals to glasses (semiconductors to metals). We then discuss how this microscopic formulation can be coarse-grained into continuum models that describe, at a reduced computational cost, how the shape and size of the device affect transport. Finally, we show that these continuum models can be parameterized from DFT, and rationalize non-diffusive, viscous transport phenomena recently observed in devices made of layered materials.

REFERENCES

- Dragašević & Simoncelli. *arXiv:2303.12777* (2023).
Harper, Iwanowski, Payne, & Simoncelli. *arXiv:2303.08637* (2023).
Simoncelli, Mauri, & Marzari. *NPJ Comput. Mater.* and *arXiv:2209.11201* (2023, in press).
Simoncelli, Marzari, & Mauri. *Phys. Rev. X* **12** (2022).
Simoncelli, Marzari, & Cepellotti. *Phys. Rev. X* **10** (2020).
Simoncelli, Marzari, and Mauri. *Nat. Phys.* **15** (2019).
Giannozzi et al., *J. Phys. Condens. Matter* **46** (2017).

Unveiling quantum phase transition by disorder and defects in 2D-materials: Jacutingaite family

Adalberto Fazzio

Ilum School of Science, CNPEM, Campinas, Brazil

Transition metal dichalcogenides have been the subject of numerous studies addressing technological applications and fundamental issues. Between this class of materials, a single-layer PtSe₂ is a semiconductor with a trivial bandgap. In contrast, its counterpart with 25% of Se atoms substituted by Hg, Pt₂HgSe₃ (jacutingaite, a naturally occurring mineral), is a 2D topological insulator with a large bandgap. We investigate the energetic stability and the topological transition in Pt(Hg_xSe_{1-x})₂ as a function of alloy concentration and the distribution of Hg atoms embedded in the PtSe₂ host. Our findings reveal the dependence of the topological phase on the alloy concentration and robustness regarding the distribution of Hg ordered and random configuration. And also show that vacancies randomly distributed induce a quantum transition trivial to topological in doped materials. Finally, we discuss a fundamental issue is whether a topological insulator protected by time-reversal is robust enough under a transformation to an amorphous state. The crucial role of translational symmetries in building the theory of topological insulators raises the question: to what extent is translational symmetry necessary for a topological state to retain its properties?

Haiku graphene nanoribbons with tunable topology

Rodrigo E. Menchón¹, Pedro Brandimarte¹, Daniel Sánchez-Portal^{1,2} and Aran Garcia-Lekue^{1,3}

¹Donostia International Physics Center (DIPC), 20018 Donostia-San Sebastián, Spain

²Centro de Física de Materiales CSIC-UPV/EHU, 20018 Donostia-San Sebastián, Spain

³Ikerbasque, Basque Foundation for Science, 48013 Bilbao, Spain

e-mail: daniel.sanchez@ehu.es

Recent advances on surface-assisted synthesis open the door to engineering topological phases in atomically precise graphene nanoribbons (GNRs). However, to fully exploit their potential, a rational design is needed to achieve GNRs with optimal properties for spintronics or quantum computing applications.

Here we explore a novel family of armchair GNRs, which we name haiku-AGNRs, consisting of 5- and 7-atom wide segments. Based on ab initio simulations, we predict a tunable topological phase dependent on the density of the 7-atom wide segments, with the concomitant emergence or quenching of topological end and interface states [1]. Moreover, we derive a generalized Su-Schrieffer-Heeger (SSH) model that allows to treat haiku-AGNRs of technologically relevant lengths, thus providing valuable information for the devise of future experiments. Finally, we also present some results for B-doped periodic haiku-AGNRs in comparison with experiments performed at Prof. Pascual's lab in nanoGUNE, San Sebastian (Spain) [2].

ACKNOWLEDGMENT

The authors gratefully acknowledge financial support from Grant PID2019-107338RB-C66 funded by MCIN/AEI/10.13039/501100011033, the European Union (EU) H2020 program through the FET Open project SPRING (Grant Agreement No. 863098), and the IKUR Strategy under the collaboration agreement between Ikerbasque Foundation and DIPC on behalf of the Department of Education of the Basque Government.

REFERENCES

- [1] R. E. Menchón, P. Brandimarte, D. Sánchez-Portal, and A. Garcia-Lekue, *Haiku graphene nanoribbons as novel platforms for tunable topology*, submitted 2023
- [2] N. Friedrich, R. E. Menchón, I. Pozo, J. Hieulle, A. Vegliante, J. Li, D. Sánchez-Portal, D. Peña, A. Garcia-Lekue and J. I. Pascual, *Addressing electron spins*

embedded in metallic graphene nanoribbons, ACS Nano 16, 14819-14826 (2022)

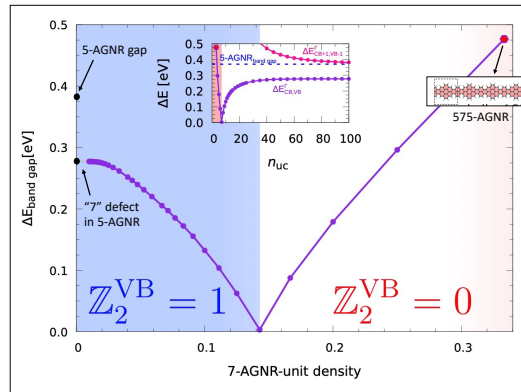


Fig. 1. DFT-SIESTA band gap of $7-(5\text{-AGNR})_{n_{uc}}$ as a function of the density ($1/n_{uc}$) of 7 widenings for periodic haiku ribbons with supercells containing n_{uc} 5-AGNR unit cells. The band gap closes separating the topological and the trivial phases. The inset highlights the presence of a defect level localized around isolated 7-widenings for very dilute systems. Notice that the labels 575-AGNR and $7-(5\text{-AGNR})_3$ denote the same system.

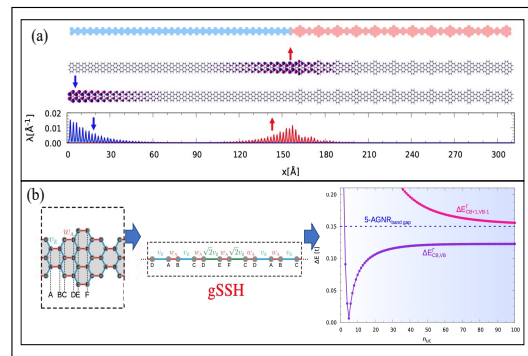


Fig. 2. (a) DFT-SIESTA calculation of the spin polarized end states appearing at the boundaries of the 5-AGNR portion of a mixed 5-AGNR/575-AGNR long ribbon. (b) Same as the inset in Fig. 1 but computed with a simple SSH model derived from a first-neighbors π -tight-binding description.

Hot electron dynamics in graphene – a linear-scaling atomistic approach

Luis Manuel Canonico Armas, Aron W. Cummings and Stephan Roche
Catalan Institute of Nanoscience and Nanotechnology (ICN2), CSIC and BIST,
Campus UAB, Bellaterra, 08193 Barcelona, Spain
luis.canonico@icn2.cat

Graphene holds significant promise for a variety of applications. In particular, graphene photodetectors have been shown to be very fast, highly sensitive, and consume minimal power, making them extremely promising for next-generation optical communication technologies [1].

Hot electrons – electrons whose temperature is higher than the surrounding lattice – play a fundamental role in such graphene photodetectors. A variety of theories and measurements have been developed and conducted to understand the main factors controlling the dynamics and relaxation of hot carriers in graphene, but fundamental questions remain to be examined [2].

In this talk, we present our development of a numerical simulation tool that can capture the dynamics of hot carriers in graphene with arbitrary lattice vibrations, defects, and disorder. Our methods are linear-scaling, meaning we can simulate systems with millions of atoms – this permits an atomic description of the system while allowing for system sizes that approach the experimental scale. Such a tool will allow for a deeper fundamental understanding of hot carrier dynamics in graphene, as well as reveal strategies for the control of such dynamics, with an eye toward future applications in photodetection, optical communications, and energy conversion.



Fig. 1. Schematic representation of the self-consistency cycle for the atomistic simulation of coupled charge and ion dynamics

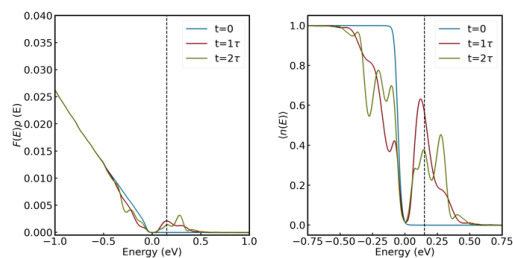


Fig. 2. Time and energy resolved phonon absorption in monolayer graphene.

ACKNOWLEDGMENT

This work was supported by project ECONWHET, reference PID2019-106684GB-I00, funded by MCIN/AEI/10.13039/501100011033/y by "ERDF A way of making Europe" and the Army Research Office under Grant Number W911NF-21-1-0004. ICN2 is supported by the Severo Ochoa Centres of Excellence programme, Grant CEX2021-001214-S, funded by MCIN/AEI/10.13039.501100011033

REFERENCES

- [1] M. Romagnoli, V. Sorianello, M. Midrio, F.H.L. Koppens, C. Huyghebaert, D. Neumaier, P. Galli, W. Templ, A. D'Errico, and A.C. Ferrari, *Nat. Rev. Mater.*, 3, 392 (2018).
- [2] M. Massicotte, G. Soavi, A. Principi, and K.-J. Tielrooij, *Nanoscale*, 13, 8376 (2021).

Localized states, spin-polarisation and transport in graphene grain boundaries

Aleksander Bach Lorentzen, Mads Brandbyge
 Dept. of Physics, Technical University of Denmark (DTU)
 DK-2800 Kongens Lyngby, Denmark
 e-mail: abalo@dtu.dk

INTRODUCTION

Grain boundaries (GBs) are abundant in graphene grown by CVD [1]. One may, as a start, consider GBs as bi-crystal interfaces, with a mis-orientation (twist-angle), θ . The GBs display a remarkable complexity of reconstructions with varying degrees of order along the GB, and it can host localized states [2]–[4]. GBs may display a transport gap up to ~ 1 eV around the Dirac point due to momentum mismatch along the GB (k_{\perp}), tied to θ [5], [6]. However, the role of the GB structure as a scatterer on the transport is less understood [7], together with the experimental evidence for f.ex. the quasi-localized and magnetic states [8], and their relation to buckling, gating, and finite bias effects. Here we present a work-flow for DFT-NEGF enabling screening of the transport properties and electronic structure of many GBs.

I. METHOD

The generation of GB geometries and setup of DFT-NEGF [9] is non-trivial for the mis-oriented crystals acting as electrodes, cf. Fig. 1. We have devised a work-flow starting from (i) randomly matched geometries, (ii) two relaxation steps, (iii) electronic structure and transport characterization with DFT-NEGF [9], see Fig. 2. We generated ca. 150 GBs, and have studied the effect of carriers doping (gating), and finite bias.

II. RESULTS

In Fig. 3 and Fig. 4 we present an example of k_{\perp} -resolved device DOS and transmission functions. While these are dominated by the overlapping electrode Dirac-cones, we find that intricate structure show up both inside the gapped *and* conductive regions. This is related to 1D/quasi-1D electronic

states localized at the GB, resulting in 1D bands, which may be dispersionless. We calculate the wave-functions of these bound states at the peaks in the DOS (at energy ϵ and k_{\perp}) by solving the "quasi-particle"-type equation involving the device Hamiltonian (H_d) and electrode self-energies (Σ),

$$[H_d + \frac{1}{2}(\Sigma(\epsilon) + \Sigma^{\dagger}(\epsilon))] \psi^{QP} = \epsilon \psi^{QP} \quad (1)$$

Roughly, four types of GBs appear from the dataset when considering their conductive properties: Transparent, opaque, insulating and spin-filtering GBs. Availability of transmission channels in conjunction with the local electronic structure and out-of-plane buckling produce these different classes. Opaque GBs often display the bound states cutting into the 2D-continuum, which show interference effects in the transmission function. We find that these bound states are sensitive to gating, giving a gate-dependent transmission (Fig. 4). We also find that the bound states can be affected by applying even a small bias (Fig. 3) Finally, a high spin-filtering has been found for GBs with large buckling (Fig. 5).

REFERENCES

- [1] L. Tapasztó *et al.*, *App. Phys. Lett.* **100**(5), 053114 (2012).
- [2] C. Ophus *et al.*, *Phys. Rev. B*, **92**, 205402 (2015).
- [3] J. Lahiri, *et al.*, *Nature Nanotech.* **5**, 326 (2010).
- [4] A. Luican-Mayer *et al.* *2D Mater.* **3**(3), 031005 (2016).
- [5] O. V. Yazyev, S. G. Louie, *Nature Mater.* **9**, 806 (2010); *Phys. Rev. B* **81**, 195420 (2010).
- [6] D. Perera, J. Rohrer, *Nanoscale*, **13**, 7709 (2021).
- [7] P. Vancsó *et al.*, *CARBON* **64**, 101 (2013).
- [8] K. Hsieh *et al.*, *Phys. Rev. Lett.* **126**, 206803 (2021).
- [9] A. Garcia *et al.*, *J. Chem. Phys.* **152**, 204108 (2020); N. Papior *et al.*, *Comp. Phys. Comm.*, **212**, 8, (2017); M. Brandbyge *et al.*, *Phys. Rev. B* **65**, 165401 (2002);

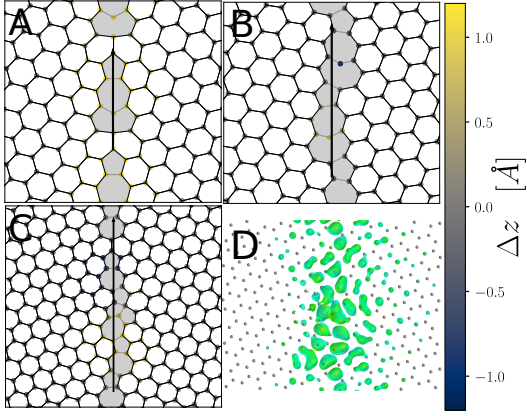


Fig. 1. Examples of bi-crystal grain boundaries with different twist-angle, θ . Transport direction is left-right. A) $\theta = 32.20^\circ$. B) $\theta = 42.10^\circ$. C) $\theta = 26.01^\circ$. D) Quasi-particle state (cf. Eq. (1)) of GB in panel C with $E = +0.23\text{eV}$ at $k_\perp = 0$.

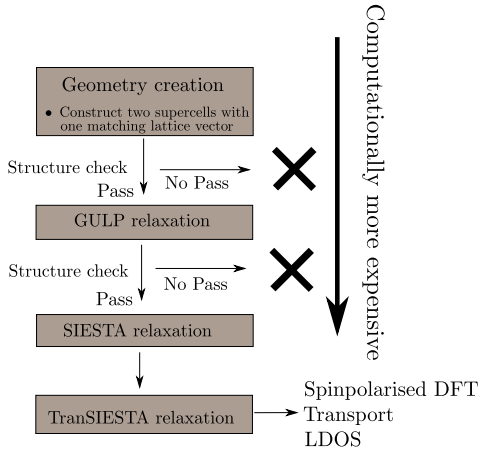


Fig. 2. Flow-chart for GB creation and transport calculation with DFT-NEGF. The method is utilising the Siesta scripting package `siesta_python`, the Siesta-code and the force-field code GULP [J.D. Gale, A.L. Rohl, *Molecular Simul.* **29** 291 (2003)]. The structure check involves checking if there are more than three angles outside the bound $100^\circ < \theta < 160^\circ$ in the 2D plane of the structure. All atoms within $|x| < 8\text{\AA}$ of the GB can relax freely in three dimensions. In the 3rd step (SIESTA) the left/right groups of atoms with $|x| > 8\text{\AA}$ relax rigidly together.

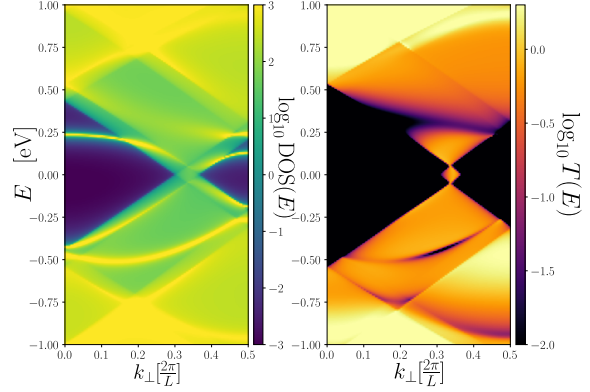


Fig. 3. Out-of-equilibrium k_\perp -resolved density-of-states(left) and transmission function (right) of the GB in Fig. 1C. Chemical potentials set to $\mu_L = -\mu_R = 0.1\text{eV}$. Presence of Fano-type resonances in the transmission can be seen as black arcs.

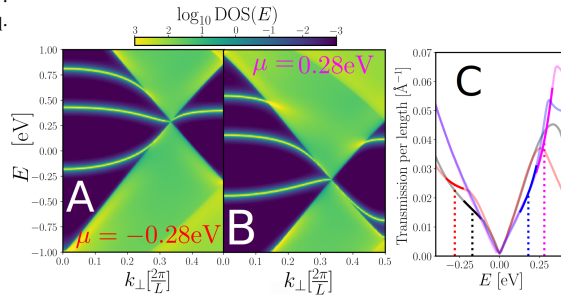


Fig. 4. A-B) k_\perp -resolved DOS for p - and n -type doping of GB in Fig. 1A. C) The effect of gating on the Transmission through the GB. As the localised state is pushed into the continuum by gating, more electrons can tunnel through the GB. Red: $\mu = -0.28\text{eV}$, black: $\mu = -0.17\text{eV}$, blue: $\mu = 0.18\text{eV}$, magenta: $\mu = 0.28\text{eV}$. μ is measured relative to the Dirac point.

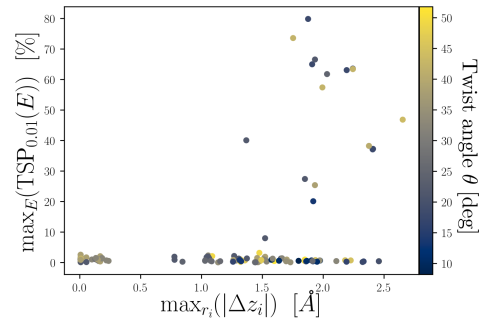


Fig. 5. Spin-polarisation coefficient $\text{TSP}_{0.01}$ where $\text{TSP}_\delta(\epsilon) = \left| \frac{T_r(\epsilon) - T_l(\epsilon)}{T_r(\epsilon) + T_l(\epsilon) + \delta} \right|$, versus maximal out-of-plane buckling relative to average z of each structure. Maximum taken for $-0.5\text{eV} < E < 0.5\text{eV}$. 146 points in plot.

Image-Force Barrier Lowering of Contact Resistance for Two-Dimensional Materials: Direct Determination and Method of Images on a Cone Manifold

Sarah R. Evans,¹ Emeric Deylgat,^{1,2,3} Edward Chen,⁴ and William G. Vandenberghe¹

¹*Department of Materials Science and Engineering, The University of Texas at Dallas.*

²*Department Physics, KU Leuven,*

³*Imec, Kapeldreef 75, 3001 Heverlee, Belgium,*

⁴*Corporate Research, Taiwan Semiconductor Manufacturing Company Ltd., Taiwan.*

Introduction: Two-dimensional (2D) semiconducting materials have received an enormous amount of attention in the last couple of decades. [1] However, high contact resistance experienced by 2D material contacts severely inhibit practical device applications. Thus, finding methods to lower contact resistance is imperative to several 2D applications such as improving nanotube performance,[2] connecting high-mobility graphene structures through metallic contacts,[3] and improving electrical contacts.[4] Recently, we found that the permittivity of the surrounding material can enhance the Schottky barrier lowering up to 50 times.[5] Despite the importance of IFBL to the contact resistance of devices at the nanoscale, it is often ignored when analyzing the Schottky barrier height. However, the reason for neglecting IFBL is because to date, there exists no way to model the majority of contact geometries with the method of images, which requires specific geometric symmetry about the metal and the electron.

In this abstract, we present a general solution for determining the IFBL energy which can be applied to an electron near a geometry of metal with surfaces separated by an angle Ω . First, we solve Poisson's equation using the appropriate boundary conditions and then we prove that our solution can be obtained using the method of images, provided a cone-manifold space is used.

Methods: Figure 1 demonstrates the geometry of a 2D top-contact, which is experimentally the most prevalent approach. It is an example of a contact geometry for which there exists no known expression of IFBL because the method of images cannot be used. The coordinate system used in the derivation is also shown.

We determine IFBL energy by solving Eq. (1) in Figure 6 as a function of position with (r, θ, z) in addition to the location of the exciting electron, (r_0, θ_0, z_0) . We are only interested in the obtaining V_I , or the potential resulting from the charge induced on the metal by the nearby electron. Thus, we will take the potential of the entire system, V , and subtract out the Coulomb potential of the electron, V_C , to obtain V_I , as seen in Figure 2. We assume a solution of the form $V(r, \theta, z) = R(r)\Theta(\theta)Z(z)$ and solve Poisson's equation using the Kontorovich-Lebedev transform.[6] Equations (2) and (3) demonstrate the resulting solutions for $\Theta(\theta)$, (2) using the boundary conditions for a point charge in free space and (3) for a point charge in near a metal wedge. After subtracting V_C from V , the contributions of the metal are

isolated and the resulting V_I is depicted in Eq. (4). Finally, we set $r = r_0$, $\theta = \theta_0$ and $z = z_0$, and the final equation for image potential energy is determined as Eq. (5).

Next, we expand method of images over a non-Euclidean space to prove that we can obtain the same result. We consider a cone manifold space where we 'unfold' our metal such that it always appears flat to the electron and an image charge can now easily be placed, as illustrated in Figure 4. Solving again for $\Theta(\theta)$, this time with boundary conditions that consider the cone manifold space, we obtain Eq. (6). The method of images now immediately yields the potential for the system by adding the same potential of the charge with an opposite sign on the other side of the metal plate. The resulting IFBL energy is shown in Eq. (7) and can be proven equal to Eq. (5) through trigonometric identities.

Results: Figure 3 plots the IFBL with $\Omega = 3\pi/2$ and $\epsilon = 3.9\epsilon_0$, which is the permittivity of SiO_2 . We find that far from the corner, the IFBL of a bulk contact is recovered and that the IFBL weakens as the corner is approached. From visual inspection, we see that the Schottky barrier can be lowered by more than 0.1eV due to IFBL, which could improve contact resistance by orders of magnitude. In Figure 5, we consider several different contact geometries and show by how much the IFBL scales compared to a bulk contact. We find that the IFBL can be increased by a factor of 2.69 relative to a bulk contact provided an optimal geometry is used.

Conclusion: In summary, we determined a general solution for the IFBL emerging from two metals separated by an angle Ω and expand the method of images using a cone manifold space. We show that IFBL can provide significant improvement to contact resistance and demonstrate how fabricating contacts to 2D materials with an optimized contact angle should significantly reduce the contact resistance. Additionally, because IFBL is scaled by permittivity, our results highlight the importance of choosing a low-permittivity dielectric surrounding the 2D material.

Acknowledgements: This material is based upon work supported by the Taiwan Semiconductor Manufacturing Company, Ltd.

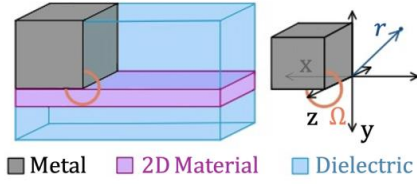


Figure 1: Illustration of a metal making a side contact to a 2D semiconductor and the coordinate system used in our derivation

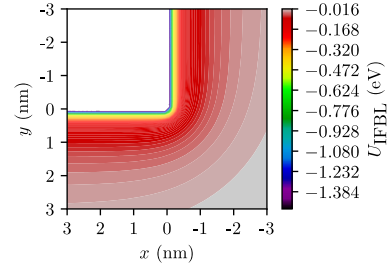


Figure 3: Plot of IFBL energy of an electron as a function of x and y with $\Omega = 3\pi/2$ and $\epsilon = 3.9\epsilon_0$, which is the permittivity of SiO_2

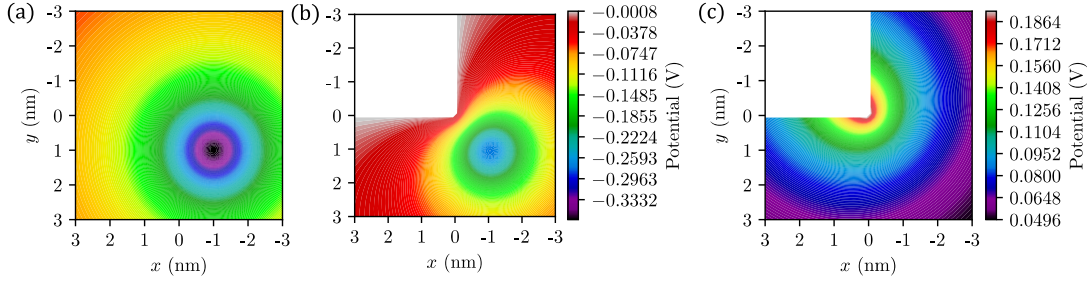


Figure 2: Graphs taken at $z = 0$ of (a) V_C , the potential caused by a single electron located at $(r_0, \theta_0, z_0) = (\sqrt{2}, 3\pi/4, 1)$, b) V , the potential an electron experiences in the presence of a metal wedge with $\Omega = 3\pi/2$, and c) V_I , the attractive potential exerted by the metal wedge due to the presence of the electron. Note that $V_I = V - V_C$.

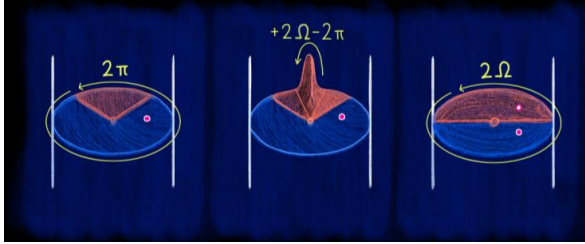


Figure 4: Illustration on how expanding Euclidean space with an additional $2\Omega - 2\pi$ in the metal region yields a cone manifold (right) where the method of images can be used. An electron is represented with a pink dot; its image with a white dot.

	Ω	θ	$U_{\text{IFBL}}/(-e^2/(16\pi\epsilon r))$
a	π	$\pi/2$	1
b	π	θ	$\csc(\theta)$
c	2π	π	$2/\pi \approx 0.63$
d	$3\pi/2$	π (or $\pi/2$)	$6 - 2/\sqrt{3} \approx 0.85$
e	$4\pi/3$	π	$8\sqrt{3}/9 + 1/\pi - 3/4 \approx 2.21$
f	2π	$3\pi/2$	$1/\pi + 1/2 \approx 0.82$
g	$3\pi/2$	$\Omega/2 = 3\pi/4$	$2 + 2\sqrt{2} - 16\sqrt{3}/9 \approx 0.74$
h	$4\pi/3$	$\Omega/2 = 2\pi/3$	$4/\sqrt{3} - 3/2 \approx 0.81$
i	$2\pi/3$	$\Omega/2 = \pi/3$	$4\sqrt{3}/9 + 2/\pi \approx 1.41$
j	$\pi/2$	$\Omega/2 = \pi/4$	$2\sqrt{2} - 1 \approx 1.8$
k	$\pi/3$	$\Omega/2 = \pi/6$	$5 - 4/\sqrt{3} \approx 2.69$

Figure 5: Table showing various Ω and θ combinations, where Ω indicates the shape of the metal and θ is the angle of the semiconductor. We evaluate the resulting IFBL energy compared to bulk contact IFBL (a).

$$\begin{aligned}
 U_{\text{IFBL}}(r, \theta) &= - \int_0^{-e} \frac{q}{e} V_I(r_0, \theta_0, z_0; r, \theta, z) dq = -\frac{1}{2} e V_I \quad (1) & V_I &= \frac{e}{4\pi\epsilon\sqrt{r r_0}} \int_0^\infty d\alpha P_{\alpha-1/2} \left(\frac{(z-z_0)^2 + r_0^2 + r^2}{2rr_0} \right) \quad (4) \\
 \Theta_{\text{L};\alpha}(\theta; \theta_0) &= \frac{\sinh(\alpha\theta) \cosh(\alpha(\pi - (\Omega - \theta_0)))}{\alpha \sinh(\alpha\pi) \sinh(\alpha\Omega)} \quad (2) & & \left(\frac{\sinh(\alpha\theta) \cosh(\alpha(\pi - (\Omega - \theta_0)))}{\sinh(\alpha\Omega) \cosh(\alpha\pi)} \right. \\
 &+ \frac{\sinh(\alpha(\Omega - \theta)) \cosh(\alpha(\pi - \theta_0))}{\alpha \sinh(\alpha\pi) \sinh(\alpha\Omega)} & & \left. + \frac{\sinh(\alpha(\Omega - \theta)) \cosh(\alpha(\pi - \theta_0))}{\sinh(\alpha\Omega) \cosh(\alpha\pi)} \right) \\
 \Theta_{\text{C};\alpha}(\theta; \theta_0) &= - \frac{\cosh(\alpha(\pi - |\theta - \theta_0|))}{\alpha \sinh(\alpha\pi)} \quad (3) & \Theta_{\text{C};\alpha}^\oplus(\theta; \theta_0) &= - \frac{\cosh(\alpha(\Omega - |\theta - \theta_0|))}{\alpha \sinh(\alpha\Omega)} \quad (6) \\
 U_{\text{IFBL}}(r, \theta) &= \frac{-e^2}{8\pi\epsilon r} \int_0^\infty d\alpha \left(\frac{\sinh(\alpha\theta) \cosh(\alpha(\pi - (\Omega - \theta)))}{\sinh(\alpha\Omega) \cosh(\alpha\pi)} + \frac{\sinh(\alpha(\Omega - \theta)) \cosh(\alpha(\pi - \theta))}{\sinh(\alpha\Omega) \cosh(\alpha\pi)} \right) \quad (5) \\
 U_{\text{IFBL}}(r, \theta) &= \frac{-e^2}{8\pi\epsilon r} \int_0^\infty d\alpha \frac{\cosh(\alpha(\Omega - 2\theta)) \sinh(\alpha\pi) + \sinh(\alpha(\Omega - \pi))}{\sinh(\alpha\Omega) \cosh(\alpha\pi)} \quad (7)
 \end{aligned}$$

Figure 6: Equations used in the derivation

References:

- [1] G. Fiori, *et al.*, "Electronics based on two-dimensional materials," *Nature nanotechnology*, 2014
- [2] R. Hafizi, *et al.*, "Band structure and contact resistance of carbon nanotubes deformed by a metal contact," *Phys. Rev. Lett.*, 2017
- [3] T. Cusati, *et al.*, "Electrical properties of graphene-metal contacts," *Scientific Reports*, 2017
- [4] A. Allain, *et al.*, "Electrical contacts to two-dimensional semiconductors," *Nature materials*, 2015
- [5] M. Brahma, *et al.*, "Contacts to two-dimensional materials: Image forces, dielectric environment, and back-gate," in *VLSI-TSA*, 2022
- [6] M. Kontorovich and N. Lebedev, "On the one method of solution for some problems in diffraction theory and related problems," *J Exp Theor Phys*, 1938

Spin-valley transport in magnetic 2D materials through multiscale simulations

D. Soriano[§], D. Marian^{†*}, D. K. Dubey[†], E. Cannavò[†], E. G. Marin[‡], and G. Fiori[†]

[§] Departamento de Física Aplicada, Universidad de Alicante, 03690 Alicante, Spain

[†] Dipartimento di Ingegneria dell'Informazione, Università di Pisa, Via G. Caruso 16, Pisa, 16122, Italy

[‡] Departamento de Electrónica, Universidad de Granada, Avenida Fuente Nueva s/n, Granada, 18071, Spain

*e-mail: damiano.marian@gmail.com

INTRODUCTION

Recently, two-dimensional (2D) magnetic materials have attracted great attention for their magnetic, electrical and physical properties that can open new paths for the design of nanoscale spintronic and valleytronic devices [1]. In particular, bilayer CrI₃ outstands for its antiferromagnetic ground state and with weak interlayer coupling which allows to switch the magnetic ground state by applying an external electric field [2]. In addition, the possibility to interface 2D magnetic materials with other van der Waals materials such as transition metal dichalcogenides has opened new possibilities for the observation of new and exciting physical phenomena. Here we present two proof-of-concept devices, a double split-gate device based on bilayer CrI₃ and then a valleytronic device based on CrBr₃-encapsulated WSe₂.

METHOD

In order to investigate the proposed device concept and evaluate its performance as a spin-valve transistor, we use a multiscale approach combining *ab-initio* DFT calculations, using Quantum Espresso suite [3], maximally localized Wannier functions [4] and non-equilibrium transport calculations using the Green's functions approach. The transport through the devices is solved self-consistently with the device electrostatics using the NanoTCAD ViDES [5] device simulation code.

DISCUSSION

The first device based on bilayer CrI₃ is reported in Fig. 1 (top). The first two gates (V_{g1}) act as control electrodes for the spin filtering, selecting either spin-up or spin-down carriers depending on

the electric field orientation, while the second two gates (V_{g2}) turn ON and OFF the selected spin current, effectively acting as a spin detector as schematically depicted in Fig. 1 (bottom). In Fig. 2 we present the spin-polarized current (a) and difference between the I_{up} and the I_{down} (b) for different values of $V_{g1/2}$, demonstrating the tunability of the spin-polarized current through gates. The second device is presented in Fig. 3 and it is based on CrBr₃/WSe₂/CrBr₃ van der Waals trilayer heterostructure. It leverages on the valley splitting that takes place in the conduction band of WSe₂ due to the hybridization with the spin-polarized bands of the CrBr₃ layers. The valley splitting can be controlled through the relative orientation of the magnetization in both CrBr₃ layers, leading to K, K', or 0 valley-polarized devices (Fig. 4).

CONCLUSION

We have presented two proof-of-concept devices, a double split-gate device which is able to both filter (> 99%) and select ON/OFF the spin current up to a ratio of $\approx 10^2$, based on bilayer CrI₃ and a valleytronic device based on CrBr₃-encapsulated WSe₂. The latter shows an unprecedented valley splitting of ~ 100 meV, able to be tuned by the relative magnetization of the encapsulating layers.

ACKNOWLEDGMENT

The authors gratefully acknowledge Graphene Flagship Core 3 (Contract No. 881603).

REFERENCES

- [1] C. Gong et al., *Nature*, **546**, 265 (2017).
- [2] S. Jiang et al., *Nat. Mater.*, **17**, 406 (2018).
- [3] P. Giannozzi, et al., *J.Phys.:Cond.Matt.* **21**, 395502 (2009).
- [4] G. Pizzi, et al., *J.Phys.:Cond.Matt.* **32**, 165902 (2020).
- [5] <http://vides.nanotcad.com/vides/>

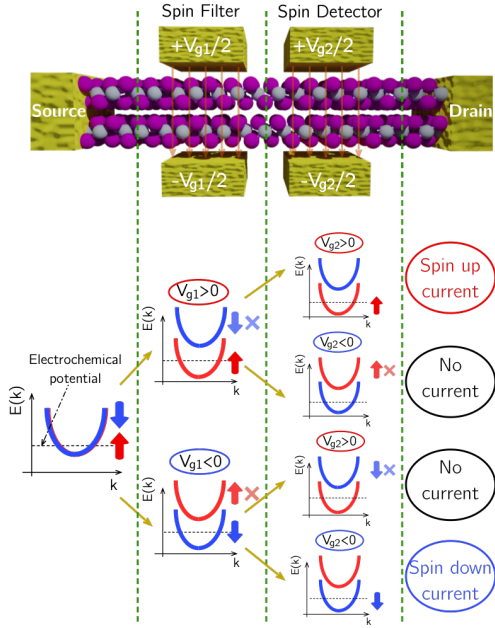


Fig. 1. (Top) Schematic of the device architecture. (Bottom) Pictorial sketch of the spin-polarized bottom of the conduction band structure for the filtering and detecting mechanism for different values of V_{g1} and V_{g2} .

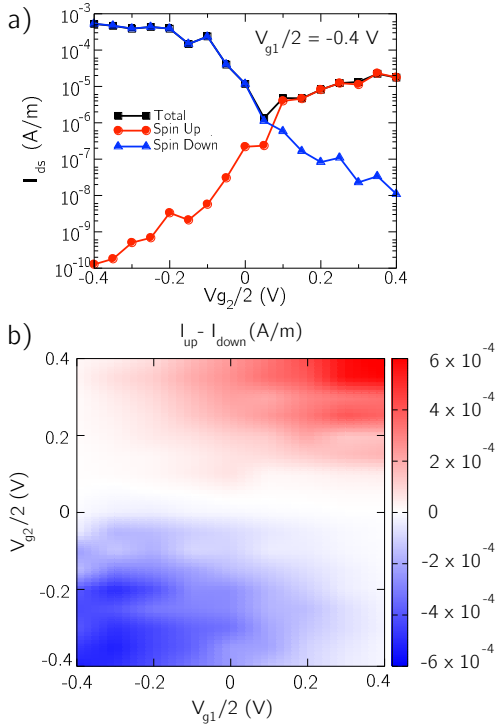


Fig. 2. Total, spin up and spin down currents as a function of V_{g2} for $V_{g1}/2 = -0.4$ V. b) Color map of the difference between spin up current (I_{up}) and spin down current (I_{down}) as a function of V_{g1} and V_{g2} .

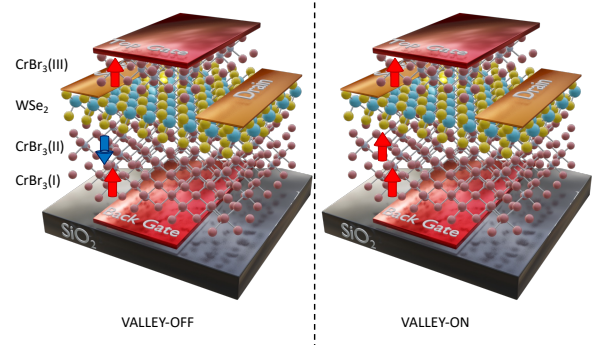


Fig. 3. Schematics of the proposed proof-of-concept valleytronic field-effect transistor.

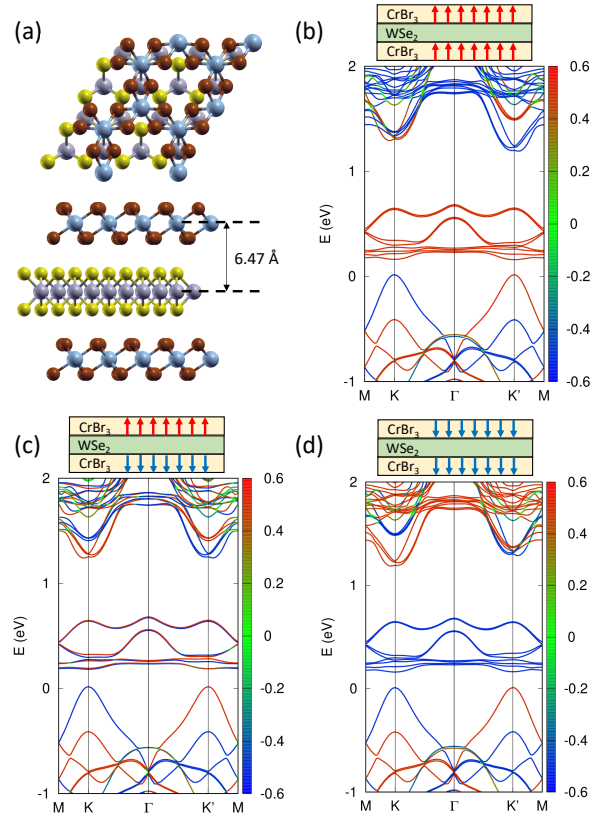


Fig. 4. (a) Details of the stacking configuration of $\text{CrBr}_3/\text{WSe}_2/\text{CrBr}_3$ trilayer heterostructure. Gray and yellow spheres correspond to W and Se atoms, respectively. Blue and brown spheres correspond to Cr and Br atoms, respectively. First-principles band structure for three different magnetic orientations: (b) CrBr_3 layers are co-polarized up, (c) CrBr_3 layers are counter-polarized, and (d) CrBr_3 layers are co-polarized down. Insets illustrate the magnetic configurations of the CrBr_3 layers in each case.

Treating Non-Equilibrium Green's Functions with a Monte Carlo Method

D. K. Ferry

School of Electrical, Computer, and Energy Engineering, Arizona State University,
Tempe, AZ 25287-6206 USA
e-mail: ferry@asu.edu

ABSTRACT SUBMISSION

The use of ensemble Monte Carlo (EMC) methods for the simulation of transport in semiconductor devices has become extensive over the past few decades. This method allows for simulation utilizing particles while addressing the full physics within the device, leaving the computational difficulties to the computer. Here, a particle EMC approach to NEGF is discussed, and preliminary results are obtained for quantum transport in Si at 300 K.

INTRODUCTION

From the beginning, there has been a rich history for the use of particles in quantum mechanics, ranging from Kennard to Feynman. The use of particles in the EMC approach has become standard in studying the operation and performance of semiconductor devices. However, today one of the most popular approaches to quantum transport and quantum distributions, especially in devices, is thought to be non-equilibrium Green's functions (NEGF). But, these functions bring considerable computational difficulty to any transport problem. Here, the Airy transform is used to formulate the important "less-than" Green's function in a manner that is amenable to solution via EMC techniques.

MODEL

In this work, a continuous *Airy transform* is used. The Airy transform of a function $f(\mathbf{r}, z)$ is given as

$$F(\mathbf{k}, s) = \int d^2\mathbf{r} \int \frac{dz}{2\pi L} e^{i\mathbf{k}\cdot\mathbf{r}} \text{Ai}\left(\frac{z-s}{L}\right) f(\mathbf{r}, z).$$

Use of this transform allows us to rewrite the less-than function in the generalized Kadanoff-Baym manner as [1]

$$G^<(\mathbf{k}, s, \omega) = A(\mathbf{k}, s, \omega) f(s, \omega)$$

with

$$f(s, \omega) = \frac{\Sigma^<(s, \omega)}{2\text{Im}\{\Sigma_r(s, \omega)\}}.$$

THE SILICON PROPERTIES

To illustrate this new EMC approach to solving for NEGF, the case of Si will be considered. While the situation for electrons in the conduction band is complicated by the multi-valley nature of this band, the scattering processes themselves are very local and do not require some of the more complicated higher-order corrections. Scattering by acoustic and f - and g -intervalley phonons are considered. Non-parabolic bands are considered.

The imaginary parts of the retarded self-energy is shown in Fig. 1 for an applied electric field of 50 kV/cm. In Fig. 2, the spectral density is shown for this same field. An important aspect of the present EMC approach is that drift time is replaced by drift distance [2]. This drift distance is then used to determine the drift time needed to evaluate the change in particle momentum. In Fig. 3, the average drift distance is shown as a function of the electric field. Figure 4 shows the drift velocity as a function of electric field, and the distribution function at 50 kV/cm is shown in Fig. 5.

CONCLUSION

The use of the ensemble Monte Carlo process has been shown to be effective in evaluating non-equilibrium Green's functions in a fast and effective approach. Methods to extend this to both inhomogeneous material, such as devices, and to polar optical phonons are under consideration and represent future work on this topic.

REFERENCES

- [1] R. Bertoni, A. M. Kriman, and D. K. Ferry, *Airy Coordinate Approach for Nonequilibrium Green's Functions in High Field Quantum Transport*, Phys. Rev. B 41, 1390 (1990).
- [2] D. K. Ferry, *Using Ensemble Monte Carlo Methods to Evaluate Nonequilibrium Green's Functions*, submitted for publication.

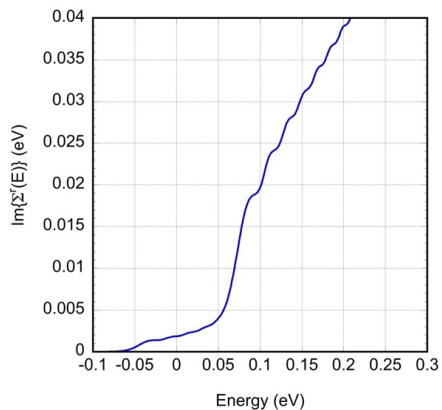


Fig. 1. Imaginary part of the self-energy in Si at 50 kV/cm and 300K.

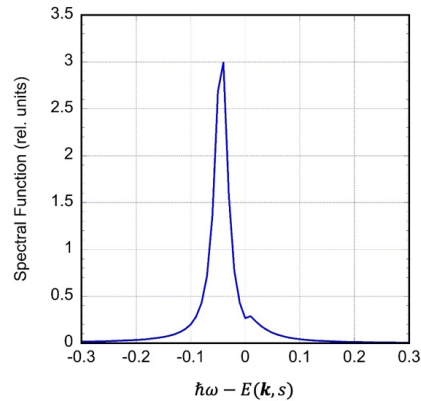


Fig. 2. The spectral density for a field of 50 kV/cm and 300 K.

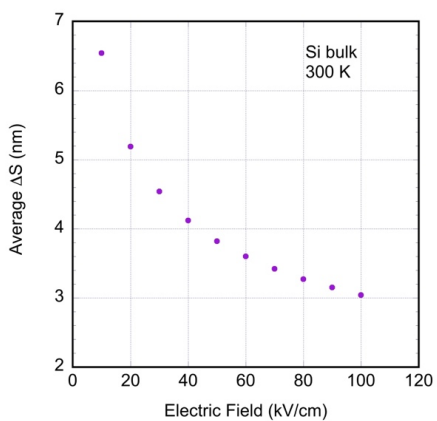


Fig. 3. Drift distance as a function of the electric field. This distance is averaged over 10^5 particles and 200 iterations.

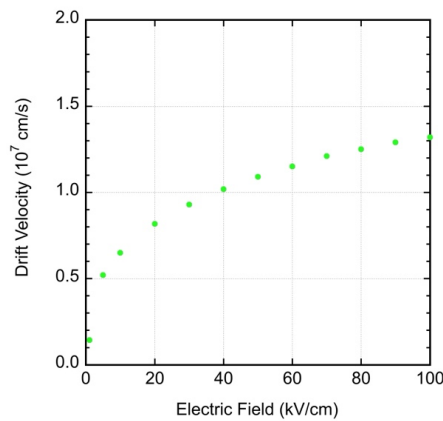


Fig. 4. The drift velocity in Si at 300 K as a function of the applied electric field.

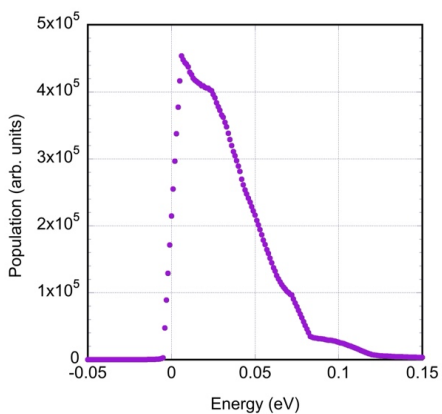


Fig. 3. Distribution function for Si with a field of 50 kV/cm and at 300 K.

Non-Equilibrium Green's Functions Basis in Multiband Models for Broken-Gap Antimonide-Based Tunneling Devices

T. Sato^{*†}, S. Birner^{*}, C. Jirauschek[†], and T. Grange[‡]

^{*}nextnano GmbH, Konrad-Zuse-Platz 8, 81829 München, Germany

[†]TUM School of Computation, Information and Technology, Technical University of Munich, Hans-Piloty-Straße 1, 85748 Garching b. München, Germany

[‡]nextnano Lab, 12 chemin des prunelles, 38700 Corenc, France
e-mail: takuma.sato@nextnano.com

Interband cascade lasers (ICLs) and detectors have shown promising properties for mid-infrared gas sensing applications. However, some of the performance degradations cannot be explained by known principles, particularly for longer wavelengths, in which the gas molecules relevant for medical and industrial purposes have their vibrational modes [1]. A rigorous theoretical modelling of the tunneling carrier transport, including the coupling of the conduction and valence bands, is desired for optimization of this class of devices.

The dynamics of electrons and holes in the ICL active region involve tunneling through potential barriers and their recombination (generation). Carriers in small- or closed-bandgap semiconductor heterostructures can be described by multiband models of the Schrödinger equation such as the 8-band $\mathbf{k} \cdot \mathbf{p}$ method (Fig. 1).

Two-point Green's functions (GFs) enable evaluation of the statistical average of time-dependent physical quantities since the expectation value of a product of field operators equals the sum of all pairwise contractions (Wick's theorem). The non-equilibrium Green's function (NEGF) formalism allows to include scattering mechanisms in devices under steady-state operation without relying on phenomenological parameters.

NEGF simulation of dissipative carrier transport using the 8-band model has been addressed recently [2]. The bottleneck is the numerical load caused by an increased number of basis states, required by the presence of the non-negligible interband coupling. The size of the problem can be

reduced by switching the basis from the full real space grid [3] to a selected set of relevant states in the nanostructure such as the Wannier function basis [4], [5], [6].

Here, we present our extension of our NEGF solver nextnano.NEGF from intersubband to interband tunneling devices, with a focus on the basis functions of the GFs. We discuss how to capture the in-plane wavevector dependence, the influence of the interband coupling, and how to obtain the basis functions well describing the actual quasiparticles of the system, while minimizing the numerical overhead required in the following NEGF self-consistent loop.

We acknowledge funding from the European Union's Horizon 2020 MSCA research and innovation programme under grant agreement no. 956548 (QUANTIMONY).

REFERENCES

- [1] J. R. Meyer, W. W. Bewley, C. L. Canedy, C. S. Kim, M. Kim, C. D. Merritt, and I. Vurgaftman. The interband cascade laser. *Photonics*, 7(3), 2020.
- [2] F. Bertazzi, A. Tibaldi, M. Goano, J. A. G. Montoya, and E. Bellotti. Nonequilibrium Green's function modeling of type-II superlattice detectors and its connection to semiclassical approaches. *Phys. Rev. Appl.*, 14:014083, 2020.
- [3] T. Kubis, C. Yeh, P. Vogl, A. Benz, G. Fasching, and C. Deutsch. Theory of nonequilibrium quantum transport and energy dissipation in terahertz quantum cascade lasers. *Phys. Rev. B*, 79:195323, 2009.
- [4] S.-C. Lee and A. Wacker. Nonequilibrium Green's function theory for transport and gain properties of quantum cascade structures. *Phys. Rev. B*, 66:245314, 2002.

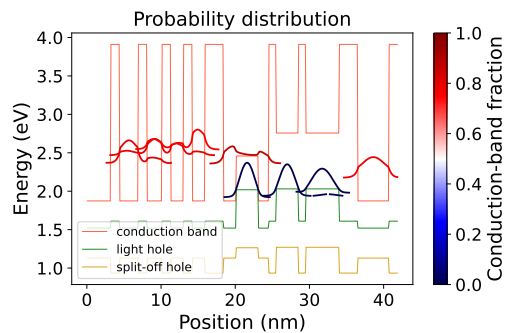


Fig. 1. Carrier probability distribution of lasing states (center), electron injector (left) and hole injector (right) in an interband cascade laser of Ref. [7] simulated by the 8-band $\mathbf{k} \cdot \mathbf{p}$ solver of the nextnano.NEGF. The color scheme of the wavefunctions signifies the fraction of the conduction-band components in the solutions.

- [5] L. Zeng, Y. He, M. Povolotskyi, X. Liu, G. Klimeck, and T. Kubis. Low rank approximation method for efficient Green's function calculation of dissipative quantum transport. *J. Appl. Phys.*, 113(21):213707, 2013.
- [6] T. Grange. Electron transport in quantum wire superlattices. *Phys. Rev. B*, 89:165310, 2014.
- [7] I. Vurgaftman, W. W. Bewley, C. L. Canedy, C. S. Kim, M. Kim, C. D. Merritt, J. Abell, J. R. Lindle, and J. R. Meyer. Rebalancing of internally generated carriers for mid-infrared interband cascade lasers with very low power consumption. *Nat. Comm.*, 2(1):585, 2011.

A phenomenological method to reduce NEGF simulation from 3D to 1D for lateral translation invariant systems

A. Martinez and J.R. Barker*

Department of Electrical and Electronic Engineering, Swansea University, Bay Campus, UK

*James Watt School of Engineering, University of Glasgow, Glasgow G12 8LT, UK

e-mail: a.e.martinez@swansea.ac.uk

ABSTRACT

In this work we present a methodology for calculate the current-voltage characteristics of devices within the Non-equilibrium Green's Function Formalism (NEGF). The methodology is valid for lateral translational invariant (TI) systems in the direction perpendicular to the transport direction. The calculation of a 3D system is reduced to a 1D. One essential feature of the method is that it allows the use of the recursive algorithm for the reduced 1D retarded Green G^R and lesser $G^<$ matrices for block triangular Hamiltonians. It is exact for ballistic systems. However, for system with photon/phonon interactions, the approximations reside between the Kadanoff-Baym ansatz [1] and the exact 3D methodology. For elastic scattering the method is explicit current conserving. However, for inelastic scattering conditions needs to be supplied to ensured current conservation. Application to a pn junction will be presented.

INTRODUCTION

Simulation of current voltage characteristics of semiconductor devices has mainly used Drift-Diffusion (DD) based simulators. Commercial 2D simulators for 3D space invariant systems were realisable by the 80s. This is possible as the DD equations are not energy resolved and are essentially model a density charge fluid with drift and diffusion currents. With the increase of computational power 3D simulations were possible for several hundred microns systems using DD. However, even today, three dimensional (3D) NEGF simulations of devices are almost prohibited for relatively large systems. For the case of space invariant system, simulation of 3D system requires the simulation of a number

of copies of 1D system (uncoupled mode), of a coupled set of 1D systems. This is possible for narrow systems as nanowires or even Finfets. However, for large cross-sections or bulk-like devices these methods prohibitive and larges copies of 1D systems deed to be simulated (see QCLasers). A method presented in ref [2] allowed for the reduction of 3D to 1D for TI system. Even if approximated, the method is ingenious, however the reduced 1D system required the calculation of the full NEGF matrices i.e. the equations are not suitable for the use of the recursive algorithm [3].

MODEL AND CONCLUSION

The method proposed here projects the 3D NEGF problem to an equivalent 1D NEGF problem. The method assumes that the retarded scattering self-energy Σ^R is a function of $E-E_t$, where E is the carrier total energy and E_t the transversal energy. The resultant 1D equations are the same Keldysh equations (for G^R and $G^<$) as the standard NEGF and therefore the recursive algorithm can be used. However, the scattering self-energies needs to be renormalized to the 3D weight. In addition, the Keldysh equations [4] do not contain E_t and therefore the 3D problem is reduced to the calculation of a pure 1D problem. The 1D $G^<$ needs to be renormalized and integrated to produce the 3D density and current. This means that a large 3D problem of μm size may be considered. The methodology is current conserving for elastic scattering (or phase breaking scattering). For inelastic scattering the method needs further refinements to ensure current conservation. The method would be applied to calculate the current voltage characteristic of a GaSb n - p junction diode. Ballistic, Dissipative and recombination limited current would be studied.

REFERENCES

- [1] Quantum Statistical Mechanics. L. P. Kadanoff and G. Baym. (New York : W. A. Benjamin, Inc., 1962.)
- [2] R. Lake and S. Datta, *Non-equilibrium Green's-function method applied to double-barrier resonant-tunnelling diodes*, Phys. Rev. B **45**, 6670 (1992).
- [3] A. Svizhenko et al *Two dimensional quantum mechanical model of nano-transistors*, Journal of Applied Physics, vol. 91, no. 4, pp. 2343-2354 (2002).
- [4] L. V Keldysh, *Diagram technique for non-equilibrium processes*, Sov. Phys. JETP (**20**), P. 1018, (1965)

Delta-layer tunnel junctions in semiconductors for charge sensing

J.P. Mendez and D. Mamaluy

Cognitive & Emerging Computing, Sandia National Laboratories, Albuquerque, USA

e-mail: jpmende@sandia.gov

INTRODUCTION

At Sandia National Laboratories, a lot of effort has been dedicated to what we have denominated Atomic Precision Advanced Manufacturing (APAM) to explore new opportunities for Beyond Moore computing. APAM allows us to create 2D doped regions (δ -layers) in a semiconductor. Simultaneously, we have also explored other new opportunities that δ -layers might offer. In particular, the use of δ -layers in semiconductors for charge sensing. In this work, we will show that the presence of a single charge near the tunnel gap in a Si: P δ -layer tunnel junction is easily detected by electrical current measurements.

QUANTUM TRANSPORT FRAMEWORK

Our open-system quantum transport framework [1,2,3] relies on a self-consistent solution of Poisson-open system Schrödinger equation in the effective mass approximation and the Non-Equilibrium Green's Function (NEGF) formalism. To reduce the computational cost of these intensive calculations, we utilize the Contact Block Reduction (CBR) method [1,2,3], which is an efficient method to calculate the electronic transmission function of an arbitrarily shaped, multi-terminal open device and scales linearly with the size of the system.

DISCUSSION AND CONCLUSIONS

Our device (see Fig. 1) consists of two highly-conductive P δ -layers separated by an intrinsic gap embedded in Si, which corresponds to a lightly doped Si body and Si cap. The δ -layers are in contact with a source and drain respectively.

Fig. 2 shows the computed electrical current through the device for different positions of an electrical charge in the middle plane ($y=W/2$). As one can notice, the electrical current is not affected

when the charge is located very far from the tunnel gap (the current without the charge is $1.4e-7$ A). However, the electrical current increases considerably when the charge is around the tunnel gap. Indeed, the maximum current is reached when the charge is in the middle of the tunnel gap, which is approx. 18 times higher for just a single charge.

Fig. 3 shows the local density of states for Si: P δ -layer tunnel junctions. We postulate that the extreme sensitivity of the δ -layer tunnel junction to the presence of charges is due to the strong quantization of the conduction band (shown schematically as white dashed lines in the figure) for these highly-confined systems. As a result, the presence of a single charge near the tunnel gap can be translated into a strong effect on the current.

In conclusion, we have shown that a single charge near the intrinsic gap of a Si: P δ -layer tunnel junction can be easily detected by electric current measurements. Therefore, this results shed light on new opportunities for highly-confined systems in semiconductors to be used for sensing charges in many applications.

ACKNOWLEDGMENT

SNL is managed and operated by NTESS under DOE NNSA contract DE-NA0003525.

REFERENCES

- [1] H. R. Khan, et al., *3D NEGF quantum transport simulator for modeling ballistic transport in nano FinFETs*, Journal of Physics: Conference Series 54, 784–796 (2007).
- [2] D. Mamaluy, and X. Gao, *The fundamental downscaling limit of field effect transistors*, Appl. Phys. Lett. 106, 193503 (2015).
- [3] X. Gao, et al., *Efficient self-consistent quantum transport simulator for quantum devices*, Appl. Phys. 115, 133707 (2014).

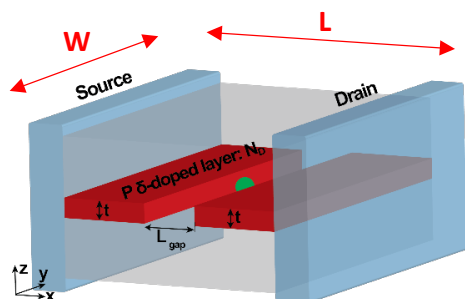


Fig. 1. Si:P δ -layer tunnel junction (TJ). The electrical charge is represented as a green sphere in the figure.

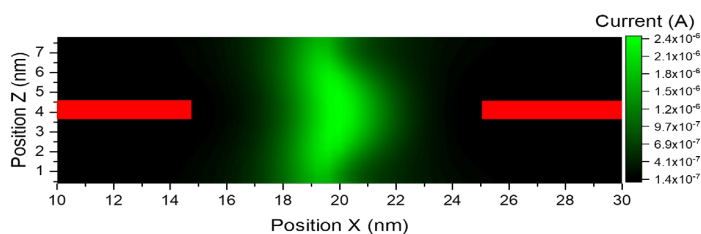


Fig. 2. Computed electrical current for different position of the electrical charge in the middle plane ($y=W/2$). The applied voltage is 100mV. Note that the current without the charge is $1.4e-7$ A

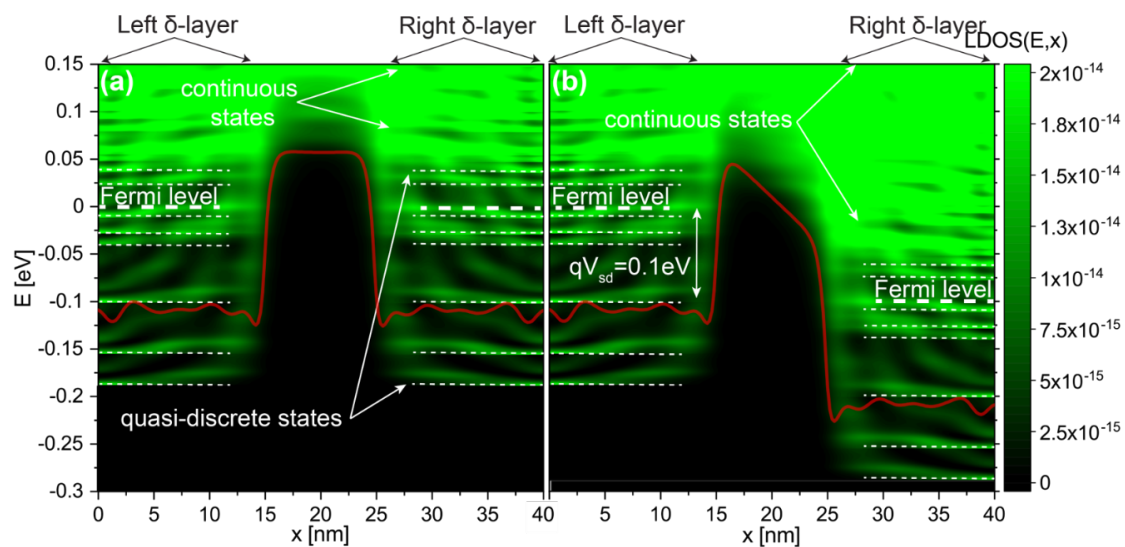


Fig. 3. Local density of state (LDOS) for δ -layer tunnel junction device shown in Fig. 1: (a) for an applied of 1 mV; (b) for an applied of 100mV. The semi-quantized states in the conduction band are indicated with dashed lines.

A novel structure of Cooling Nano-devices: The Quantum Cascade Cooler

G. Etesse^{1,*}, C. Salhani^{2,3}, X. Zhu², N. Cavassilas¹, F. Michelini¹,
K. Hirakawa^{2,3}, and M. Bescond^{1,2,*}

¹Aix Marseille Université, CNRS, IM2NP UMR 7334, 133997 Marseille, France

²Institute of Industrial Science, University of Tokyo, Japan

³LIMMS-CNRS, IRL 2820, Tokyo, Japan

* gueric.ettesse@univ-amu.fr and marc.bescond@cnrs.fr

INTRODUCTION

We propose and study an innovative heterostructure as a cooling nanodevice based on tunneling filtering and thermionic emission. The structure, whose layers are made of AlGaAs (Fig.1) with varying Al concentration, is designed to exhibit progressively higher quantized states within two consecutive quantum wells (QWs). By applying a bias voltage between the two contacts, we induce a net current, and we “force” electrons to absorb phonons during successive transmissions before being extracted from the last well. Derived from a previously investigated structure [1], the “Quantum Cascade Cooler” is expected to yield increased efficiencies when compared to single quantum well structures as each electron now have to absorb multiple phonons on their way to the collector.

MODEL AND DISCUSSIONS

In order to investigate the properties of such structure, we use an in-house code which couples self-consistently non-equilibrium Green’s function formalism for electron, heat equation and Poisson equation [1]. We include the interactions between the electrons and both acoustic phonons (elastic) and polar optical phonons (inelastic) [2] through the use of self-energies. This self-consistent approach yields important electronic properties to understand the underlying physics in such device. For instance, we can see that the designed resonant tunnelling way across the QW states that can be observed in figure 2-a) shapes the electron flow represented in figure 2-b).

We subsequently determine the temperature of electrons (usually different from the lattice one in out-of-equilibrium regimes) by using the virtual Büttiker probes [3]. The principle of the latter is to

weakly couple a probe to the active region of the structure of interest. We then cancel both the carrier and heat current between the probe and the system by modifying the electron temperature and electrochemical potential of the probe. The probe will be in local equilibrium with the structure, even though the device operates far from equilibrium.

With this method we calculate, in each quantum well, the average electron temperature (Fig.3-a) for which we observe anticorrelated oscillations. We relate the latter to the energy difference W between the ground state of successive QWs (Fig.3-b) and notice that the period of the oscillations corresponds to the energy of an optical phonon ($\hbar\omega_{LO} = 35$ meV). We propose that these oscillations are the result of the competition between the phonon assisted transmitted and reflected electron flow in the second QW. This point will be discussed in detail during the workshop.

CONCLUSION

By numerically investigating the cooling properties of an AlGaAs based heterostructure, we manage to provide a proof of concept for the Quantum Cascade Cooler and propose an interpretation of the polar optical phonon energy dependency on the cooling behaviour.

REFERENCES

- [1] M.Bescond et al. *Thermionic cooling devices based on resonant-tunneling AlGaAs/GaAs heterostructure* J. Phys.: Condens. Matter 30, 064005 (2018).
- [2] M.Moussavou, et. al. *Physically based diagonal treatment of polar optical phonon self-energy: performance assessment of III-V double-gate transistors* Phys. Rev. Appl. 10, 064023 (2018).
- [3] A. Shastry and C. A. Stafford, *Temperature and voltage measurement in quantum systems far from equilibrium* Phys. Rev. B 94, 155433 (2016).

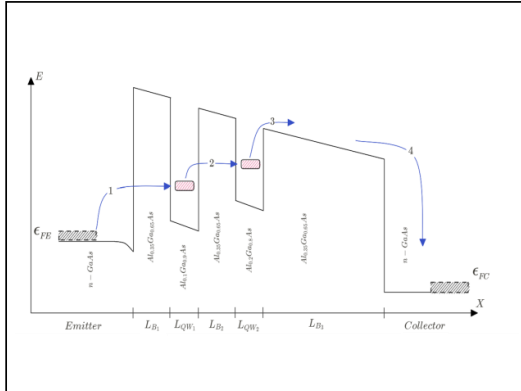


Fig. 1. Sketch of the considered Quantum Cascade Cooler heterostructure under potential bias. The red dashed rectangles represent the QW states, while E_{FE} and E_{FC} are the Fermi levels of the emitter and collector respectively. For all the considered devices, doping in the emitter and the collector is 10^{18} cm^{-3} . $L_{B1} = L_{B2} = 6 \text{ nm}$, $L_{QW1} = L_{QW2} = 5 \text{ nm}$, $L_{B3} = 30 \text{ nm}$. Blue arrows highlight intended pathway for the electron flow.

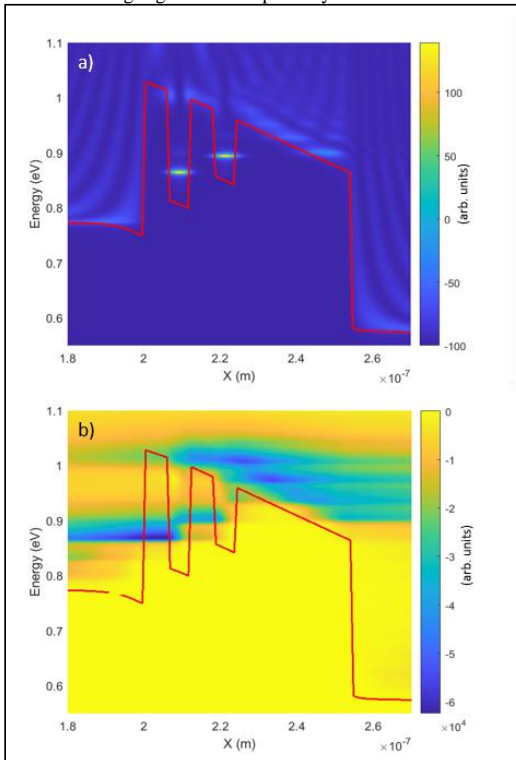


Fig. 2. a) Local density of states of the device. b) Electron current spectrum going from the left to the right. In both figures, the red solid red lines represent the potential profile of the structure ($V = 0.2 \text{ V}$). $E_{FE} = 0.8 \text{ eV}$ and $E_{FC} = 0.6 \text{ eV}$

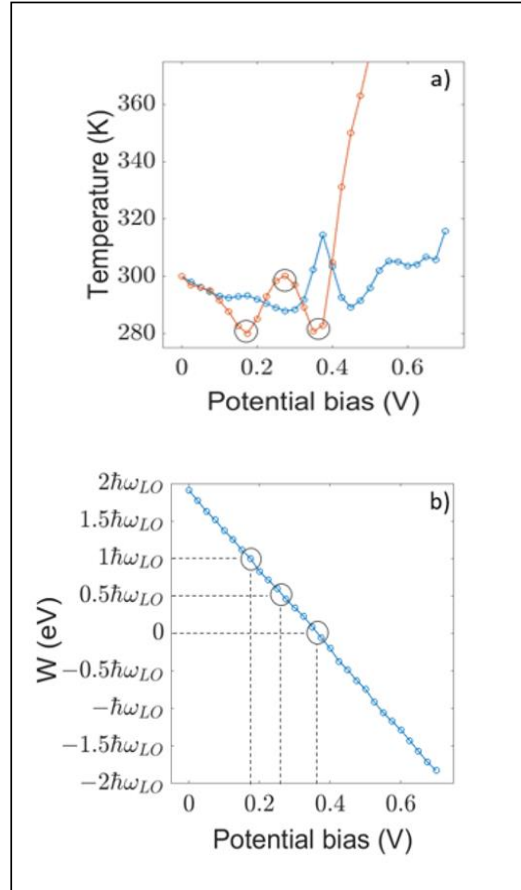


Fig. 3. a) Average temperature in the first (blue) and second (orange) QW as a function of bias. b) Energy difference W between the ground states of the first and second quantum wells as a function of bias (>0 when QW₂'s ground state is above QW₁'s). Black circles and black dotted lines highlight biases and energy differences corresponding to extrema of temperature respectively.

ACKNOWLEDGEMENT

This work was supported by the GELATO ANR project (ANR-21-CE50-0017)

Weak values: a new paradigm to characterize nanoscale systems

Xabier Oianguren-Asua, Carlos F. Destefani and Xavier Oriols

Departament d'Enginyeria Electrònica, Universitat Autònoma de Barcelona, 08193 Bellaterra, Barcelona, Spain.
e.mail: Xavier.oriols@uab.es

INTRODUCTION

Since their introduction more than 30 years ago, weak values are gradually transitioning from a theoretical curiosity to a practical tool in both, physical and computational experiments, allowing an unprecedented characterization of quantum systems. Weak values can provide information of quantum systems beyond those provided by the traditional expectation or correlation values of Hermitian operators. As such, they open an unexplored paradigm to give experimentally meaningful microscopic properties to nanoscale systems in computational simulations. Several examples will be presented in this workshop [1-5].

EXPERIMENTAL AND THEORETICAL WEAK VALUES

From the experimental point of view, the weak value is a complex number that can be obtained in the laboratory through a well-defined operational protocol, consisting in a weak measurement of a property plus a subsequent strong measurement of another property, for an ensemble of identically prepared quantum systems $|\Psi\rangle$. The novelty of the weak values appears when such measured properties belong to non-commuting operators [3]. From a theoretical point of view, when for example, the first (weak) measurement is of the momentum linked to the operator \hat{p} , and the second (strong) measurement is of the position x , the weak value is defined as

$$p(x) = \langle x | \hat{p} | \Psi \rangle / \langle x | \Psi \rangle,$$

which can be interpreted as a distribution of momenta along the position x . This weak value turns out to coincide with the (Bohmian) velocity in Bohmian theory [3]. In fact, the computation of momentum weak values (post selected in position) appears quite naturally in different formulations of quantum hydrodynamics.

NOVEL CHARACTERIZATION OF NANOSCALE SYSTEMS

In this workshop, we will present several examples where these weak values allow the computational simulation (and thus prediction) of empirical properties of nanoscale systems, that were seemingly inaccessible from standard expectation or correlations values. Among others, they allow:

- (i) A natural extension of the classical Monte Carlo technique for electron transport to quantum systems through well-defined trajectories [1]. See Fig. 1.
- (ii) Pure-state “unravellings” in non-Markovian open quantum systems, using conditional states [4].
- (iii) A non-contextual definition of the quantum work operator for quantum thermodynamics [3], and of two-time correlations for non-commuting observables [3].
- (iv) The computation of the dwell-time in the active region of nanoscale devices [2] (see an example for graphene in Fig 2).
- (v) The understanding of quantum thermalization of many-body systems, by distinguishing two components of the kinetic energy [5]. See Fig. 3.

CONCLUSION

Weak values allow us to simulate new practical properties that can be later tested in the laboratory. As such, we argue that they will become essential tools for computational nanotechnology in the forthcoming years.

REFERENCES

- [1] D. Marian, N. Zanghì, and X. Oriols, Phys. Rev. Lett. 116, 110404 (2016).
- [2] D. Pandey, M.Villani, E. Colomes, Z. Zhan and X.Oriols, Sci. Technol. 34, 034002 (2019).
- [3] D. Pandey, R. Sampaio, T. Ala-Nissila, G. Albareda, and X. Oriols, Phys. Rev. A 103, 052219 (2021).
- [4] D. Pandey, E. Colomes, G. Albareda, X. Oriols, Entropy 21(12), 1148 (2019).
- [5] C. F. Destefani and X. Oriols, Phys. Rev. A 107, 012213 (2023).

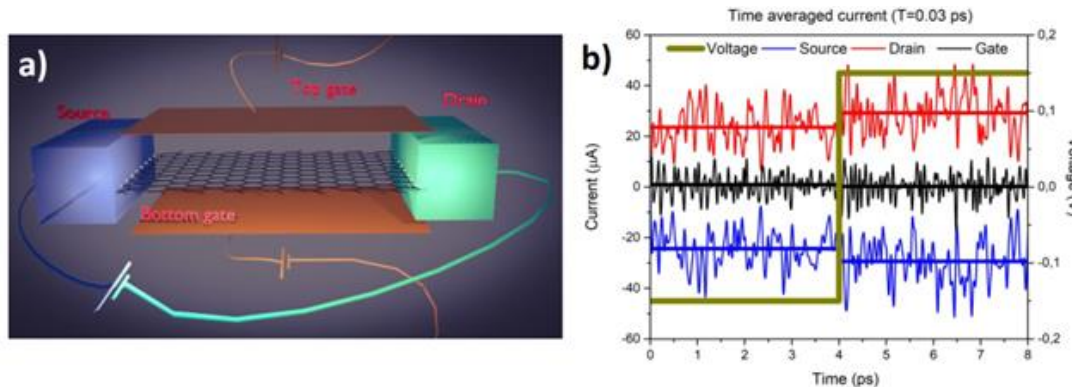


Fig. 1: (a) Schematic representation of the graphene-based FET, with a channel composed of a single-crystal monolayer graphene. (b) The high frequency lines are the instantaneous currents (time-averaged at a window of 0.03 ps) as a function of time, computed from the dynamics of Bohmian trajectories. The straight lines are due to a wider averaging window of 4 ps, where we can clearly assert the binary response. We can conclude that 4 ps is a reasonable operating time for the transistor.

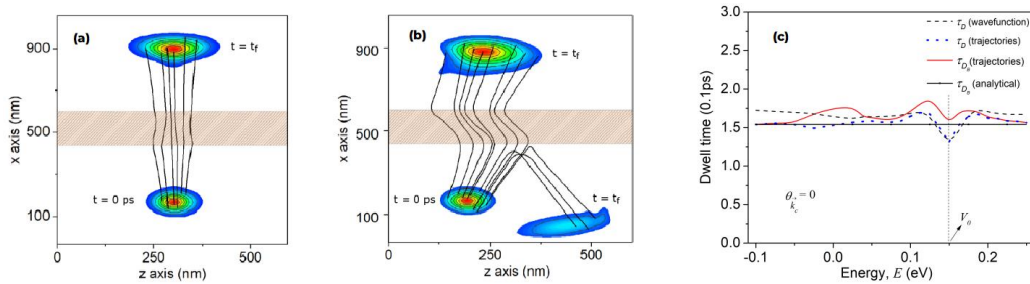


Fig. 2: A conditional wave packet in graphene impinges upon a barrier (shaded orange region) suffering Klein tunneling with an incident angle of zero degrees (a) and 15 degrees (b). The ability to use trajectories allows us the unambiguous definition of the dwell time of electrons in graphene, as seen in (c) for the incident angle of (a) as a function of the central energy of the wave packet. Such a time, unambiguously computed from measurable weak values, directly determines the high frequency behavior of nanoscale devices.

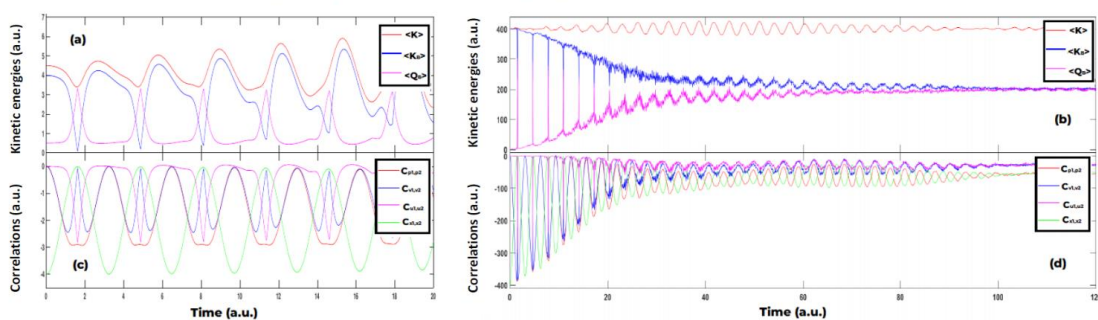


Fig. 3: (a) Expectation and correlation values of the dynamics of two particles in an harmonic trap. Left panels: a few initial cycles under no disorder showing a periodic behavior; Right panels: whole dynamics under disorder showing thermalization. Panels (a), (b) for kinetic energies comparison: Orthodox (K), Bohmian (KB), quantum potential (QB) energies. Panels (c), (d) for correlations: momentum $C_{p1,p2}$, Bohmian velocity $C_{v1,v2}$, osmotic velocity $C_{u1,u2}$, position $C_{x1,x2}$ correlations. The result $\langle K \rangle / 2 = \langle KB \rangle = \langle QB \rangle$ is a signature of thermalization, even when $\langle K \rangle$ is constant, that can only be accessed through weak values.

Machine Learning For Materials And Device Simulations

Alison Walker, Department of Physics, University of Bath, UK

I will describe the application of machine learning methods in a new context. Specifically, how we address a scientific question that enables comparison between physics-based simulation and measurements in a way that can straightforwardly be generalized. Our method allows for uncertainty in the model input parameters, an area rarely discussed in materials modelling.

In this talk I will demonstrate a novel use of Bayesian Optimisation to relate simulation model results to experimental measurements on charge-carrier dynamics in the lead halide perovskite semiconductor methyl-ammonium lead iodide MAPbI_3 . Halide perovskite solar cells are highly topical as they have rapidly emerged as leading contenders in photovoltaic technology. We show how Bayesian Optimisation can efficiently search the model input space of a simulation to minimise the difference between the simulation output and a set of experimental results. This method also allows an explicit evaluation of the probability that the simulation can reproduce the measured experimental results in the region of input space defined by the uncertainty in each input parameter. I will show how mesoscale simulation models of charge transport in lead halide perovskites, using an ensemble Monte Carlo approach based on Boltzmann transport theory, can provide insight into mobility-limiting mechanisms. Figure 1 [1] demonstrates how the method can also quantify the effective importance (the "inverse length-scales" of the figure) of each input parameter in determining the simulation outcomes.

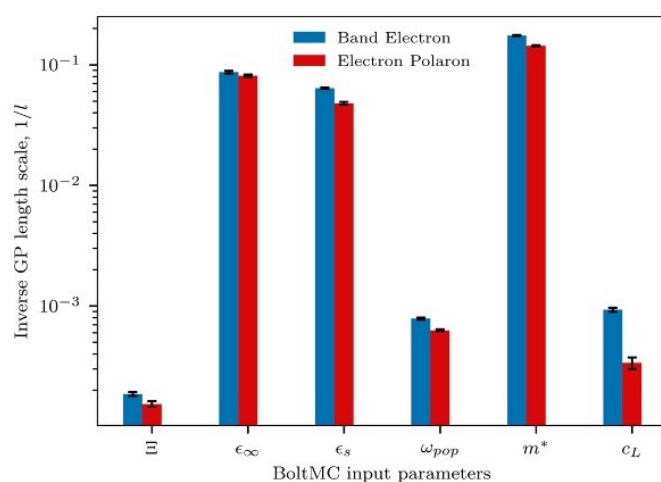


Figure 1. Inverse length-scales of the covariance function for each simulation input parameter, plotted such that larger values indicate larger output (mobility) sensitivity to that parameter. Error bars show standard error in the mean in black. Ξ is the acoustic deformation potential, ϵ_∞ (ϵ_s) the high (low) frequency permittivity, ω_{pop} the polar optical phonon frequency, m^* the effective mass and c_L the elastic constant.

1. S. G. McCallum, J. E. Lerpinière, K O Jensen, P. Friederich, A. B. Walker APL Machine Learning (2023) in review

First-Principles Multiscale Modeling Enabled by Machine Learning Interatomic Potentials

B. Mortazavi*, and X. Zhuang

Department of Mathematics and Physics, Leibniz Universität Hannover,
Appelstraße 11, 30167 Hannover, Germany.

Cluster of Excellence PhoenixD (Photonics, Optics, And Engineering–Innovation Across Disciplines),
Gottfried Wilhelm Leibniz Universität Hannover, Hannover, Germany
e-mail: bohayra.mortazavi@gmail.com

ABSTRACT SUBMISSION

In the conventional and everyday-life finite element (FE) simulations of engineering systems and products, prior to starting the calculations, materials and interactions properties are required to be provided as inputs to the models. On this basis, the development of accurate and robust theoretical approaches for elaborated examinations of various material properties, is highly advantageous in order to enhance the design process and minimize the necessity of complex experimental tests. Since the birth of the concept of machine learning interatomic potentials (MLIPs) in 2007 by Behler, and Parrinello [1], a growing interest has been developed to the replacement of empirical interatomic potentials (EIPs) with MLIPs, in order to conduct more accurate and reliable molecular dynamics calculations. As an exciting novel progress, recently the applications of MLIPs have been extended towards the exploration of the thermal transport and mechanical properties, providing novel opportunities not heretofore efficiently achievable, neither by EIPs nor by density functional theory (DFT) calculations. In this work, we first illustrate that how the combination of EIPs with FE multiscale simulations, could provide useful vision on the thermal and mechanical responses of nanostructured materials at the continuum level. Next, by considering several examples of recent studies, the robustness of MLIPs in the analysis of the mechanical and thermal properties will be discussed, and their superiority over EIPs and DFT methods will be emphasized. It will be finally highlighted that MLIPs furthermore offer astonishing capabilities to marry the robustness of DFT method with continuum mechanics, enabling the first-principles

multiscale modeling of mechanical and thermal properties [2,3] of nanostructures at continuum level, with minimal prior physical knowledge, DFT level of accuracy and affordable computational costs.

METHODOLOGY

The first-principles multiscale modeling of mechanical and thermal conduction properties [2,3], comprises four major steps, which are schematically shown in Figure 1. In the first step, DFT simulations are carried out over stress-free and strained atomic configurations under varying temperatures to prepare required training datasets. Next, MLIPs are fitted using the two-step passive training approach [2,3]. To obtain the mechanical or thermal properties of pristine and heterostructure phases at room temperature, MLIP-based classical molecular dynamics calculations are employed. In the final step, on the basis of data provided by MLIP-based molecular dynamics simulations, the heat transport and/or mechanical responses of macroscopic heterostructures can be examined using the continuum FE method.

CONCLUSION

Machine learning interatomic potentials enabled first-principles multiscale modeling is believed to inherit an outstanding prospect to develop fully computerized platforms, to design and optimize novel materials and structures, with enhanced performances.

ACKNOWLEDGMENT

This research is funded by the Deutsche Forschungsgemeinschaft (DFG, German Research Foundation) under Germany's Excellence Strategy within the Cluster of Excellence PhoenixD (EXC 2122, Project ID 390833453).

REFERENCES

- [1] J. Behler, M. Parrinello, *Generalized Neural-Network Representation of High-Dimensional Potential-Energy Surfaces*, Phys. Rev. Lett. **98**, 146401 (2007).
- [2] B. Mortazavi, M. Silani, E. V Podryabinkin, T. Rabczuk, X. Zhuang, A. V Shapeev, *First-Principles Multiscale Modeling of Mechanical Properties in Graphene/Borophene Heterostructures Empowered by Machine-Learning Interatomic Potentials*, Adv. Mater. **33**, 2102807 (2021).
- [3] B. Mortazavi, E. V Podryabinkin, S. Roche, T. Rabczuk, X. Zhuang, A. V Shapeev, *Machine-learning interatomic potentials enable first-principles multiscale modeling of lattice thermal conductivity in graphene/borophene heterostructures*, Mater. Horizons. **7**, 2359 (2020).

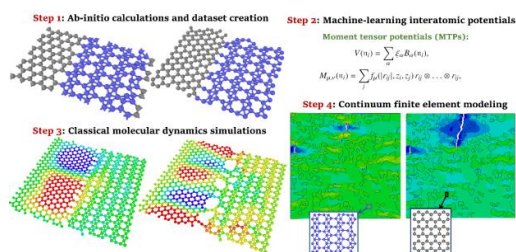


Fig. 1. Main steps to conduct the first-principles multiscale modeling of mechanical properties (reprinted from [2], copyright 2021, John Wiley & Sons).

Design of Oscillatory Neural Networks by Machine Learning Algorithms

Tamas Rudner, Gyorgy Csaba, Wolfgang Porod*

Faculty of Information Technology and Bionics, Pázmány University Budapest, Hungary

*Department of Electrical Engineering, University of Notre Dame, USA

INTRODUCTION

Hardware accelerators for neuromorphic computing are in large demand. It is widely accepted that analog circuits could implement neural networks far more efficiently than the now omnipresent digital circuits, and they are better suited for analog sensory inputs. Despite this, analog circuits do not enjoy widespread adoption as it is difficult to implement robust, low-power analog circuitry in a deeply-scaled CMOS technology.

Oscillatory Neural Networks (ONNs) may be free from impediments of traditional analog circuitry [1], and they are also realizable by relatively straightforward nanoscale hardware. ONNs are however disadvantaged by the fact that only very few applications have been realized by them so far, and these applications require fully connected networks, which are not easily scalable to larger numbers of oscillators.

In this work, we demonstrate how state-of-the-art ONNs can be designed by machine learning techniques, opening the way to new applications and simple, realizable network topologies. As an example, we demonstrate a Hopfield-network-like associative memory [2] that uses only nearest neighbor interconnections and that significantly outperforms Hopfield nets trained by Hebbian learning method.

DESIGN OF ONNS BY BPTT

Backpropagation through time (BPTT) is a numerical technique to engineer the parameters of a dynamical system for a particular task. In order to use BPTT on an ONN circuit, we built a differential-equation-based compact model of ring oscillators (ROs), following [3]. This model is solved by torchdiffEq [4], in such a way that BPTT can run on the computational tree. This computing framework can automatically design the resistors which interconnect ROs so that the RO phases converge to a certain pattern. For a simple two RO case the procedure is illustrated in Fig 1. For many

oscillators the BPTT can be used to engineer the couplings in such a way that classification on the MNIST database [5] is achieved. To test our method on MNIST each pixel of the input handwritten digits is applied as an input phase to nearest-neighbor connected oscillator network on a 14x14 grid.

The loss function can be defined so that the ONN acts as an associative memory – in that case phases representing the handwritten digits should converge to the image of an ideally-shaped digit. The resulting network is functionally equivalent to a fully-interconnected Hopfield network trained by Hebbian learning, but performs this function using much fewer interconnections (see Fig. 2) and at a higher rate of correct classification.

Alternatively, the classification can be done by summing up oscillator outputs and recognize digits by the appearance of a high-amplitude output signal (see Fig. 3). For a single layer, the network achieves a 70% classification accuracy on the MNIST dataset, but an accuracy above 92% can be achieved by adding a very simple second classifier layer consisting of only 40 neurons.

In conclusion, we developed an ‘in silico’ training method for ONNs. The designed network can act as an energy efficient first layer of a neuromorphic processing pipeline.

We acknowledge financial support from Intel corporation via the THWAI program.

REFERENCES

- [1] Csaba, G., & Porod, W. (2020). Coupled oscillators for computing: A review and perspective. *Applied physics reviews*, 7(1), 011302.
- [2] Abernot, M., & Todri-Saniai, A. (2023). Simulation and implementation of two-layer oscillatory neural networks for image edge detection: bidirectional and feedforward architectures. *Neuromorphic Computing and Engineering*.
- [3] Lai, X., & Roychowdhury, J. Analytical equations for predicting injection locking in LC and ring oscillators. In *Proc. of the IEEE 2005 Custom Int. Circuits Conf*, 2005.
- [4] Chen, Ricky T. Q.: torchdiffEq <https://github.com/rtqichen/torchdiffEq> (2018)
- [5] <http://yann.lecun.com/exdb/mnist/>

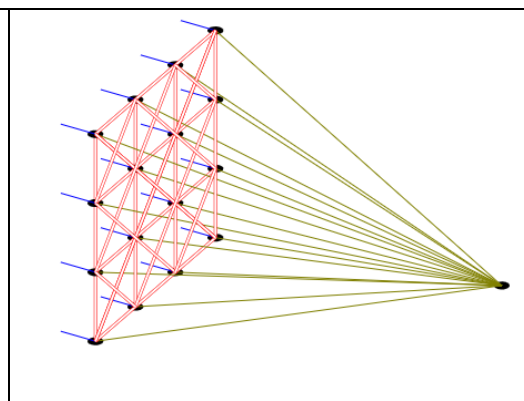
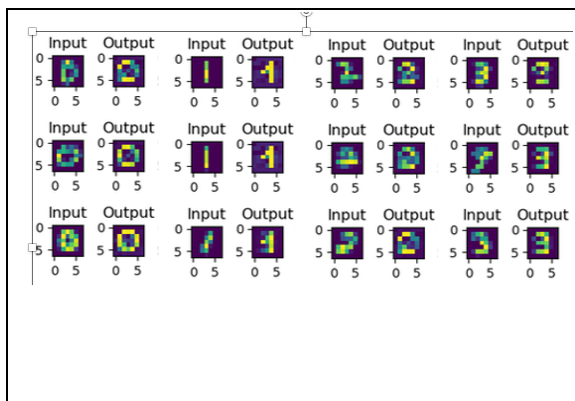
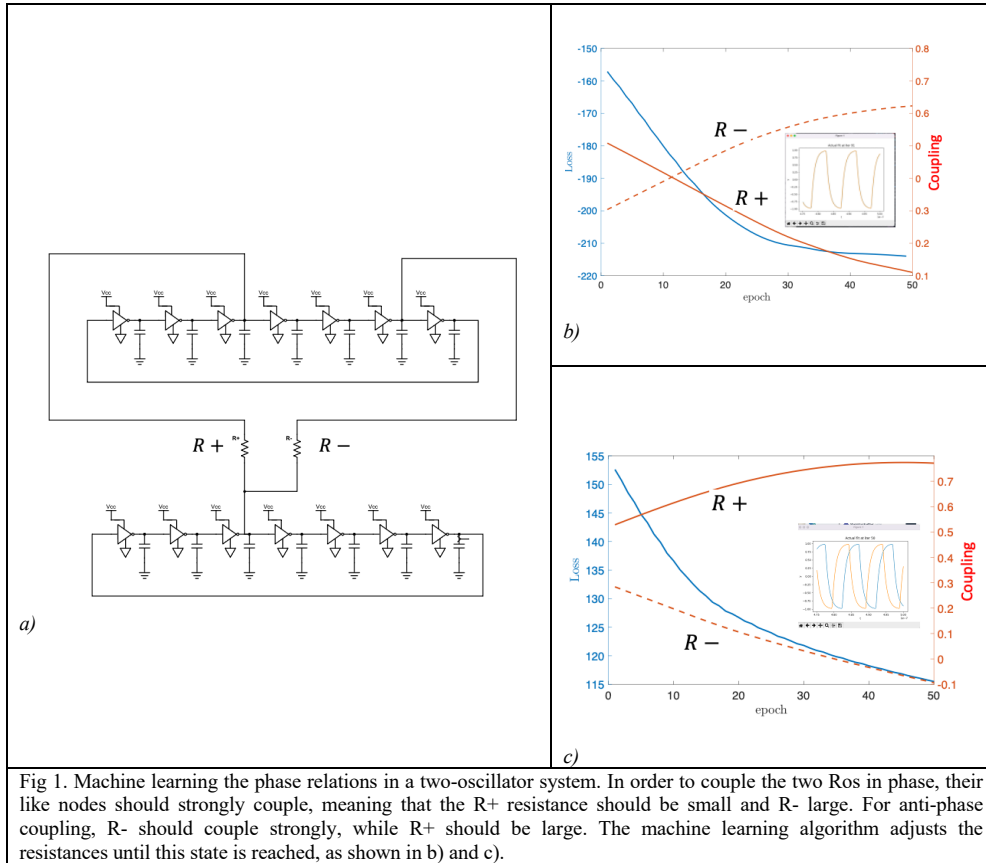


Fig 2. Associative function in a nearest-neighbor interconnected ONN. The images show the phase with respect to a reference oscillator. In most (but not all) cases the distorted digits (handwritten images) converge to the target digits.

Fig 3. It is possible to get a single classification output by summing up all oscillator nodes. With appropriate learning parameters, this configuration leads to the highest accuracy.

Automatic optimization of doping profile for high performance Single-Photon Avalanche Diodes

Rémi Helleboid*[†], Jérôme Saint-Martin*, Marco Pala*, Philippe Dollfus*,
Denis Rideau[†], Gabriel Mugny[†], Isobel Nicholson[†], Jeremy Grebot[†]

*C2N, Université Paris-Saclay - CNRS, Palaiseau, France

[†]STMICROELECTRONICS, CROLLES, FRANCE - EDINBURGH, UNITED-KINGDOM

Abstract—A method to efficiently optimize doping profile for high performance Single-Photon Avalanche Diodes is presented. The method aims at maximizing the photon detection efficiency while minimizing the timing jitter and keeping the breakdown voltage in a reasonable range by optimizing the doping profile of the device. Two different optimization methods are compared, and their performances are evaluated on a one-dimensional model of a Si-SPAD.

INTRODUCTION

Single-Photon Avalanche Diodes (SPADs) are optoelectronic devices that aim at detecting light with a single photon sensitivity. They are used in a wide range of applications such as optical time-of-flight (TOF) ranging, optical communication, and optical imaging. SPADs are usually made of a p-n junction operated in reverse bias to generate a strong electric field in the active region that can trigger self-sustained generations of carriers by impact ionization process, which leads to a detectable current pulse. The voltage at which the avalanche breakdown occurs is called the breakdown voltage (BV) and must be kept in a reasonable neighborhood of 20V for a Si device to be used in embedded applications. The SPAD is then operated at an excess bias voltage (VEX) of around 3V above the BV. The probability for an optically generated electron-hole pair to generate an avalanche is called the avalanche breakdown probability (BrP). The statistical distribution of timing between the generation of the electron-hole pair and its detection is called the timing jitter.

MODEL AND OPTIMIZATION

For efficiency purposes, we consider a one-dimensional model of a SPAD, that represents a cut in the middle of the device along its depth. Given a doping profile, the electrostatic potential is computed by solving the Poisson equation using an iterative Newton scheme coupled with a finite difference method. The BrP and the BV are computed using the McIntyre model as described in [1]. The timing jitter performance is evaluated by measuring the extension of the depletion region, also called depletion width (DW) region in the device. The relevance of this proxy will be discussed at the conference. The optimization process then consists in finding the doping profile that maximizes the BrP and

minimizing the timing jitter, together with a breakdown voltage constraint. Formally we minimize the following function:

$$F(\mathbf{W}) = \beta \cdot (\text{BV} - \text{BV}_{\text{Target}})^2 - \alpha \cdot \text{BrP}_{\text{VEX}=3\text{V}} - \gamma \text{DW}_{\text{VEX}=3\text{V}}$$

where \mathbf{W} is the input doping profile and α , β and γ are the weights of the three objectives. The doping profile is described through a set of parameters, as shown in Fig. 1. The cost function is expected to depend in complex ways on the doping profile parameters, admitting many local minima, saddle points and an ill-defined gradient. The optimization process has therefore to be performed with global optimization methods that do not require the knowledge of the gradient of the cost function. Hereafter, we compare two different methods: a Simulated Annealing (SA) method and a Particle Swarm Optimization (PSO) method [2]. An illustration of the PSO method is shown in Fig. 2 and the electric field resulting from the optimization process is shown in Fig. 3. All the steps are implemented in an in-house C++ program which takes advantage of the parallelization capabilities of modern CPUs.

RESULTS AND DISCUSSION

The cost function evolution during the optimization process is plotted in Fig. 4. Both methods are able to decrease the cost function, at different rates. The PSO method has the advantage of showing a regular decrease of the cost function, while the SA method shows a more erratic behavior. This feature may be useful to pick an intermediate point in the optimization process that satisfies a desired compromise between the different figures of merit (see Fig. 5).

In conclusion, we have demonstrated that it is possible to optimize the doping profile of a SPAD to maximize the photon detection efficiency while minimizing the timing jitter using a simple one-dimensional model of the device. This work is a first step towards the optimization of SPAD on complex two- or three-dimensional geometries with more advanced models of device operation.

REFERENCES

- [1] R. Helleboid *et al.* *IEEE Journal of the Electron Devices Society*, vol. 10, pp. 584–592, 2022.
- [2] S. Luke, “Essentials of metaheuristics,” vol. 2, pp. 25, 55–58, Lulu Raleigh, 2013.

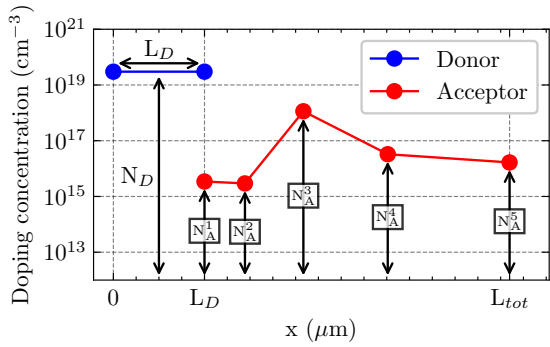


Fig. 1. Sketch of the doping profile structure. The N side is described by its length and level, while the P side is described by a piecewise exponential function defined by n_A acceptor levels (here $n_A=5$). The x coordinate of the points are not optimized and are chosen to be well distributed. The total number of variables to optimize is $N_{opt} = n_A+2$.

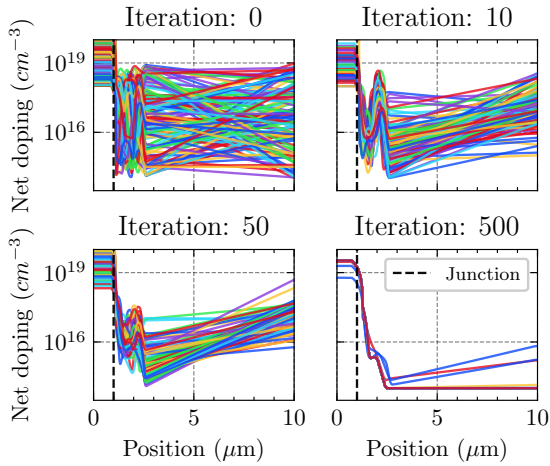


Fig. 2. Illustration of the PSO algorithm where each line represents a particle of the algorithm. The initial population is randomly generated (Iteration 0) and then evolves during the optimization process in order to find a global minimum. For visualization purposes, the $N+$ length L_D was kept constant.

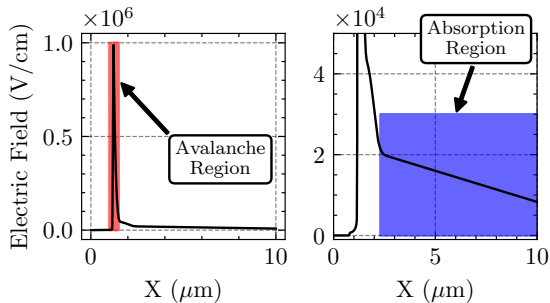


Fig. 3. Electric field at the end of the optimization process that favors depletion. (Right figure is a zoom of the left one.) The device is fully depleted in the absorption region as desired. Yet pushing the electric field within the back of the diode led to a reduction of the thickness of the avalanche region, causing a low breakdown probability (see Fig. 5).

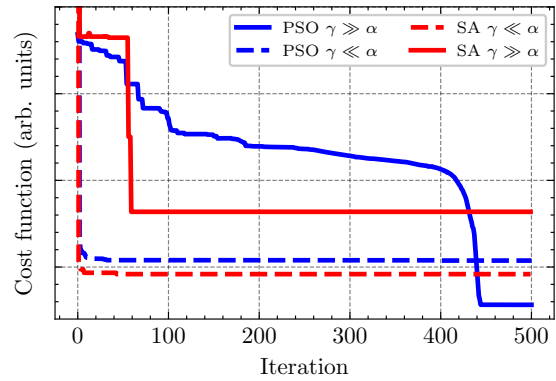


Fig. 4. Cost function evolution during the optimization process for the two methods. The convergence rate highly depends on the meta-parameters of the algorithm and makes it difficult to conclude on the best method. The best set of meta-parameters depends on the problem at hand and must be found empirically. The different α to γ ratios are discussed in Fig 5.

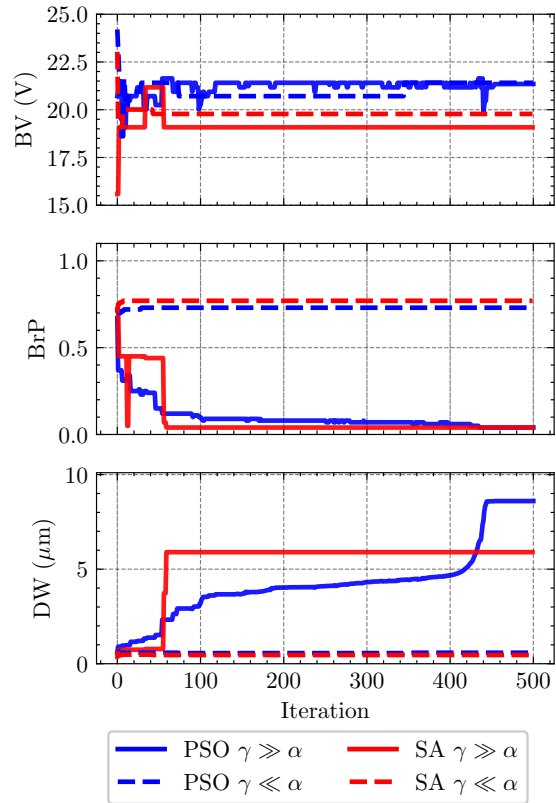


Fig. 5. Evolution of the different figures of merit of the SPAD that are optimized during the process for two different weights scenarios. The scenario $\gamma \gg \alpha$ favors the depletion width at the expense of the breakdown probability. The optimization is very efficient and leads to a fully depleted SPAD (see Fig. 3). In the scenario $\gamma \ll \alpha$, the optimization favors the BrP, and reaches an optimum very quickly. The scenario $\gamma = \alpha$ tends to favor the depletion width, and is not shown here.

Machine learning based analysis of collective diffusion in inorganic solid-state electrolytes

Cibrán López^{*†‡}, Riccardo Rurali[‡] and Claudio Cazorla^{*†}

^{*}Departament de Física, Universitat Politècnica de Catalunya, 08034 Barcelona, Spain

[†]Barcelona Research Center in Multiscale Science and Engineering,
Universitat Politècnica de Catalunya, 08019 Barcelona, Spain

[‡]Institut de Ciència de Materials de Barcelona, ICMAB-CSIC, Campus UAB, 08193 Bellaterra, Spain

STATE OF PURPOSE

Despite playing a central role in the design of high performance solid-state electrolytes (SSE), little is known about the processes governing ionic diffusion in these materials and the spatio-temporal correlations acting on migrating particles. Computer simulations can reproduce the trajectories of individual diffusing ions in real time with extraordinary accuracy, thus providing incredibly valuable atomistic data that in practice cannot be resolved by experiments.

However, the identification of hopping events in computer simulations typically relies on active supervision and definition of arbitrary material-dependent geometrical parameters, thus frustrating high throughput screenings of diffusing paths and mechanisms across simulation databases and the assessment of many-diffusing-ion correlations.

RESULTS

Here, we introduce a novel approach for analysing ion hopping events in molecular dynamics (MD) simulations in a facile and totally unsupervised manner, what would allow the extraction of completely new descriptors related to these diffusions. Our approach relies on the k-means clustering algorithm and allows to identify with precision which and when particles diffuse in a simulation and the exact migrating paths that they follow as well, as it is exemplified in Figure 1.

We apply such a powerful analysis tool to a comprehensive database of density functional theory *ab initio* MD (DFT-AIMD) simulations, analyzed in

a previous work [1], comprising several families of SSE and tens of millions of atomic configurations. By doing this, we are able to (1) quantify correlations between many diffusing ions, (2) identify predominant collective migrating mechanisms and (3) determine how specific and novel migration descriptors such as the length and duration of individual ionic hops correlate with the overall ion diffusion coefficients or structural properties of the material, all under realistic finite-temperature conditions.

For instance, the distribution of lengths of diffusions can be easily extracted for each family and the database in general, presenting slightly different trends, as shown in Figure 2. Gaining such insights points towards new, more efficient SSE, provided the close relation between this magnitudes and their diffusion performance.

Concretely, we show that the probability of finding N-correlated particles in a simulation decreases exponentially with N, proving that these correlations do not depend on temperature and are mostly pairwise for SSE, as shown in Figure 3. The fundamental mechanisms involved in such processes are also depicted and analysed.

DATA AND CODE AVAILABILITY

The analysis scripts resulting from this study have been made publicly available as a Python package, that is user-friendly and easily adaptable [2] to any desired MD code output, as well as the DFT-AIMD database [3].

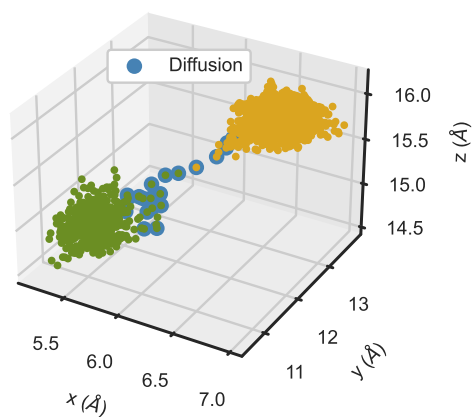


Fig. 1. Example of the performance of our unsupervised algorithm at extracting the diffusive path for one random particle of a DFT-AIMD simulation of $\text{Li}_7\text{La}_3\text{Zr}_2\text{O}_{12}$ at a temperature of 400K.

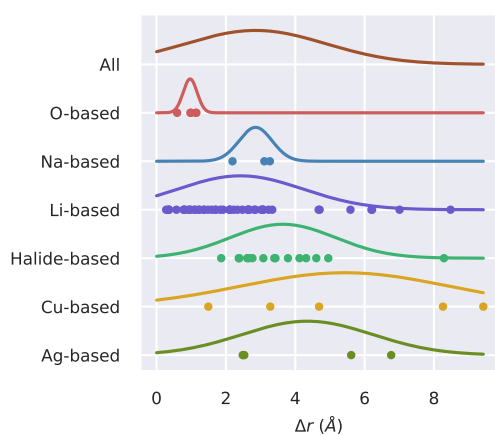


Fig. 2. Distribution of spatial lengths of diffusion for each family and the general DFT-AIMD database studied in the present work (labels from the left, accounting 'All' for the distribution of the set of all spatial lengths). This figure shows different tendencies for each family, as well as it exemplifies one of the analysis that can be easily extracted with the present approach.

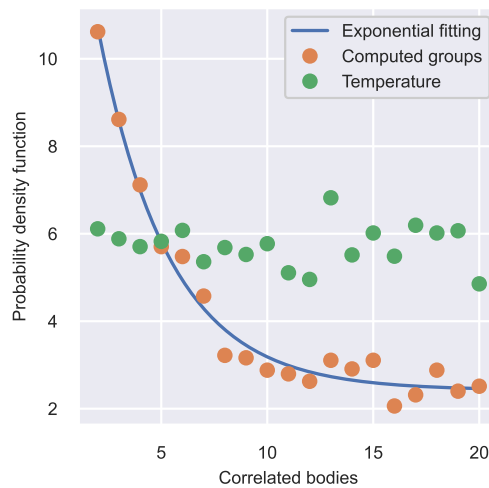


Fig. 3. The probability density function of finding N -correlated bodies for a MD simulation in SSE decreases exponentially with the number of involved bodies, independently of the temperature, with a fair predominance of pairwise correlations.

REFERENCES

- [1] C. López, A. Emperador, E. Saucedo, *et al.*, *Universal ion-transport descriptors and classes of inorganic solid-state electrolytes*, *Materials Horizons*, 2023, doi: 10.1039/D2MH01516A
- [2] C. López, R. Rurali, C. Cazorla, *Repository with all the developed codes*, 2023, url: <https://github.com/IonRepo/IonDiff>
- [3] C. López, A. Emperador, E. Saucedo, *et al.*, *DFT-AIMD database*, 2023, url: <https://superionic.upc.edu>

Process Simulation in Micro- and Nano-Electronics

L. Filipovic^{1*}, T. Reiter¹, X. Klemenschts^{2,3}, S. Leroch¹, R. Stella¹, O. Baumgartner³, A. Hössinger⁴

¹CDL for Multi-Scale Process Modeling of Semiconductor Devices and Sensors at the

²Institute for Microelectronics, TU Wien, Gußhausstraße 27-29/E360, 1040 Vienna, Austria

³Global TCAD Solutions, Bösendorferstraße 1/1/12, 1010 Vienna, Austria

⁴Silvaco Europe Ltd., Compass Point, St Ives, Cambridgeshire, PE27 5JL, United Kingdom

*E-mail: filipovic@iue.tuwien.ac.at

The continued transistor miniaturization, the introduction of novel materials and geometries in complementary semiconductor-metal-oxide (CMOS) fabrication, and the ever-increasing complexity of the processes required for modern integrated circuits (ICs) must be supported by proper process- and device-technology computer aided design (TCAD) tools. Improvements in performance, power efficiency, and area density (PPA) from one technology node to the next nowadays involves substantial architectural and material innovations through TCAD-supported design-technology co-optimization (DTCO) [1], [2] (cf. Fig. 1).

Process simulation does not describe a single modeling approach and the complexities involved often span over many time and size scales, require the integration of several frameworks and data structures, and demand the application of models which range from highly physical to simplified geometric reconstructions [3]. Here, we describe some critical methodologies including applying different surface and volume descriptions in the same framework, merging physical and geometric (compact) models, and the multi-scale integration of atomistic molecular dynamics (MD) for process TCAD.

Process simulation can refer to topography simulations (e.g., surface etching and deposition) or volume processes (e.g., ion implantation, annealing, diffusion, oxidation), each requiring a unique modeling approach. Topography motion is often represented implicitly using the level set (LS) method, while volume processes require an explicit volume representation. We present the ViennaPS framework (cf. Fig. 2) which combines these approaches, allowing to simultaneously solve volume and surface

problems. This allows to model, e.g., plasma impact damage during sputter etching [4] (cf. Fig. 3) and oxide redeposition during selective Si₃N₄ etching in 3D NAND structures [5].

For DTCO it is often necessary to provide quick process-aware structures, meaning that physical simulations are unfeasible. For this, we have pioneered the concept of process compact models, which are trained using combined measurements and physical simulations (cf. Fig. 4). The compact models can either be based on geometric equations whose inputs are functions of process parameters, or on process emulation through geometric advection, whereby the new surface is redrawn from each surface point, based on a known process-aware distribution [6]. The compact model approach has been applied to quantify the impact of fabrication conditions on the generation of air spacers at the 7 nm technology node and on their subsequent effect on the performance of a 5-stage ring oscillator (RO) [3]. The results (cf. Fig. 5) allow us to optimize the fabrication conditions towards improving PPA.

Finally, with the introduction of new materials, it has become increasingly important to study fabrication at the atomistic level, since experiments alone are too time- and cost-intensive. Therefore, a multi-scale link between atomistic MD and continuum TCAD modeling must be made. We are studying the formation of Al-doped 4H-SiC devices using this approach (cf. Fig. 6), whereby the atomistic analysis of the SiC film at different stages of the doping process (e.g., post ion implantation, post-annealing) must be analyzed. This allows to study the role of defects, interstitials, and vacancies on dopant activation and the subsequent fabrication steps.

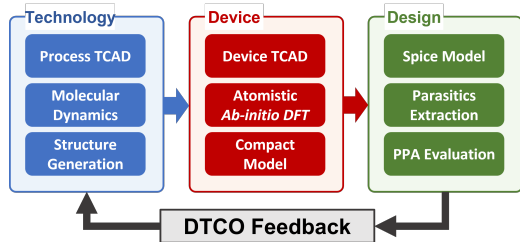


Fig. 1. Simplified DTCO flow for new designs, incorporating multi-scale process and device simulations as well as a feedback loop between circuit design and fabrication technology.

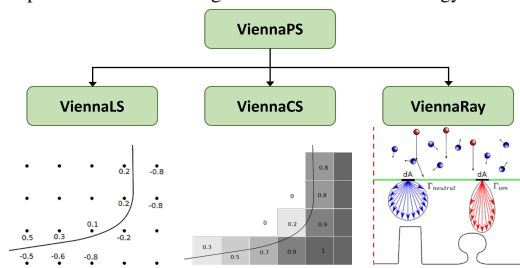


Fig. 2. Process simulation (PS) framework ViennaPS [7] including a level set (LS) surface definition, a cell set (CS) volume description, and a ray tracer for physical modeling.

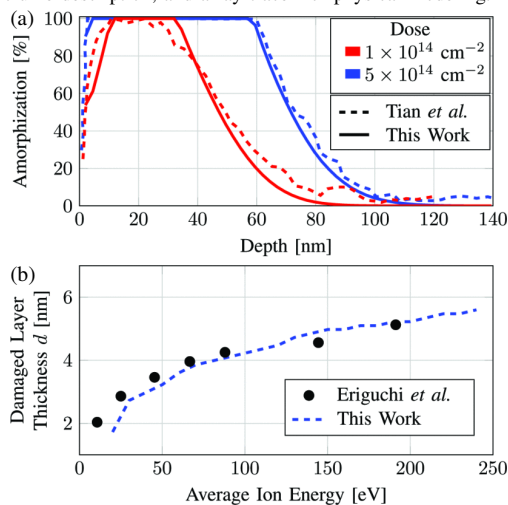


Fig. 3. (a) Comparison of the computed amorphization profile for high energy ions (50 keV) of an As implant process to the results obtained by Tian *et al.* [8]. (b) Impact of average ion energies on the thickness of the damaged (non-crystalline) layer compared to experimental data by Eriguchi *et al.* [9].

ACKNOWLEDGMENT

The financial support by the Austrian Federal Ministry for Digital and Economic Affairs, the National Foundation for Research, Technology and Development and the Christian Doppler Research Association is gratefully acknowledged. Support in part by the Austrian Research Promotion Agency FFG Project 878662 PASTE-DTCO. Many thanks for contributions from J. Piso, J. Bobinac, and B. Bamer.

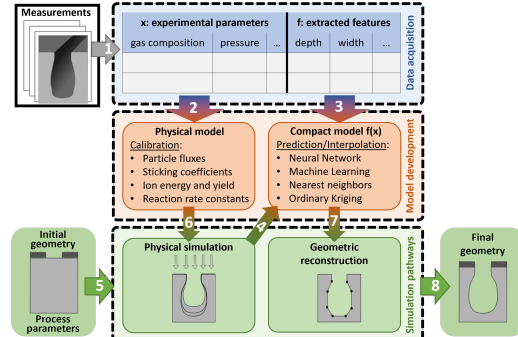


Fig. 4. For model generation, experimental data (1) is used to calibrate physical models (2), while a compact model is trained using experiments (3) and physical simulations (4). A simulation from initial conditions (5) can use a physical model (6) or a compact model (7) to obtain the final geometry (8).

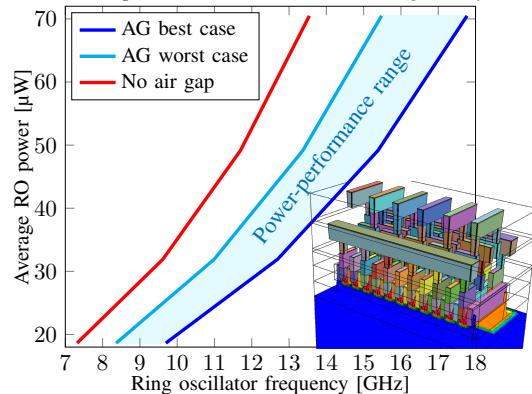


Fig. 5. Achieved power and performance for the 5-stage RO with no air gap (AG) and with an AG under the best and worst tested process conditions during spacer generation.

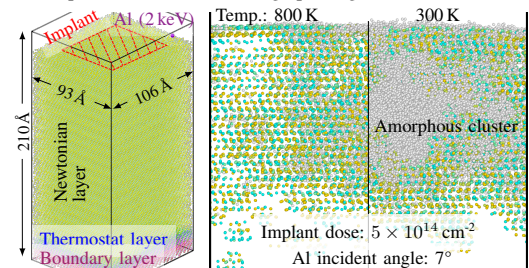


Fig. 6. MD setup of Al implantation in 4H-SiC (left) allows to study the resulting defects, vacancies, and interstitials (right).

REFERENCES

- [1] Z. Zhang *et al.*, in SNW, 2pp, 2019.
- [2] L. Yuan, in TSMC Blog, 2022.
- [3] L. Filipovic *et al.*, SSE **199**, No. 108527, 2023.
- [4] T. Reiter *et al.*, in IEEE IIRW, 5 pp, 2022.
- [5] Z. Zhou *et al.*, JIEC **119**, pp. 218–225, 2023.
- [6] X. Klemenschits *et al.*, CMAME **386**, No. 114196, 2021.
- [7] ViennaPS-1.2.0. <https://github.com/ViennaTools>.
- [8] S. Tian *et al.*, IEEE TED **45**(6), pp. 1226–1238, 1998.
- [9] K. Eriguchi *et al.*, JJAP **49**, No. 056203, 2010.

An Efficient Atomistic Method for Micro-Scale Film Growth from the Vapor Phase

E.E. Lorenz^{*†} and J. Schuster^{*}

^{*} Fraunhofer Institute for Electronic Nanosystems, Technologie-Campus 3, 09126 Chemnitz, Germany

[†] Center for Microtechnologies, Chemnitz University of Technology, 09126 Chemnitz, Germany

We present a multi-scale method for the simulation of vapor deposition processes in micrometer-sized structures with full atomistic representation. Our method couples Kinetic Monte Carlo (KMC) sampling at the microscale with Molecular Dynamics (MD) simulations at the nanoscale. Parallel efficiency is improved through a maintainable active surface graph representation, which accelerates the search for adsorption sites and enables seamless subdomains for MD simulations. The surrounding gas phase and growing surfaces are modeled geometrically and linked to the presented method.

Coupling Method: Fig. 1 shows the coupling method of the atomistic deposition model. Adsorption events are sampled using KMC methods at the active surface. Selected events are simulated using MD in subdomains around the adsorption site. After each event, the atoms are frozen and reinserted in-place into the global domain, and the active surface and the event candidates are updated. Seamless reinsertion is guaranteed through a shared boundary region between the domains.

KMC Adsorption Sampling: A direct method KMC algorithm is used to sample adsorption events with overestimating rate heuristics at the active surface. Since KMC is inherently sequential and MD simulations take some seconds to complete, placeholder Null events and limited time warping are used to evaluate events in parallel while preserving the system's KMC dynamics.

MD Adsorption Simulations: Each adsorption event is evaluated with an explicit LAMMPS MD simulation in a local subdomain around the adsorption site. The incident atom is placed above the adsorption site, with a velocity according to the process characteristics, and a NVE simulation with a bulk-only thermostat is performed. This allows for the accurate modelling of the adsorption process,

and yields film morphologies from MD force fields.

Surface Representation: An Alpha Shape representation of the growing surface is used as an acceleration structure for KMC candidate searches. The Alpha Shape is constructed from the Delaunay triangulation of the atom positions by omission of tetrahedra with circumradii $r_{\text{circ}} > \alpha$. Since this criterion limits the influence of each atom to a radius of 2α , the Alpha Shape construction can be performed in space-filling subdomains with overlapping boundaries of size 2α . This enables the seamless local update of the Alpha Shape after each MD simulation without the need for computationally expensive global re-triangulations.

Particle Transport in the Gas Phase: To incorporate gas phase particle transport and surfaces surrounding the atomistic region, the presented deposition model is linked to a geometric particle transport model in the free molecular flow regime. Particles are traced linearly between surfaces, and precomputed particle-surface interaction statistics are applied. Non-atomistic surrounding surfaces are modeled with a geometric surface growth model. Through the use of modern raytracing techniques and hardware acceleration, the surface sampling resolution from incident gas particles is improved.

Geometric Surface Growth: A Level Set method is used to represent the surrounding growing surface as a scalar field, and advance the surface according to the local growth rates as calculated from the particle-surface interactions, as shown in Fig. 2. Incident particle statistics for the atomistic method is then sampled in predefined surface regions.

REFERENCES

- [1] J. Gehre, *Coupling between stochastic particle transport models and topographic thin film growth*, Master Thesis, TU Chemnitz (2022). <https://nbn-resolving.org/urn:nbn:de:bsz:ch1-qucosa2-786436>

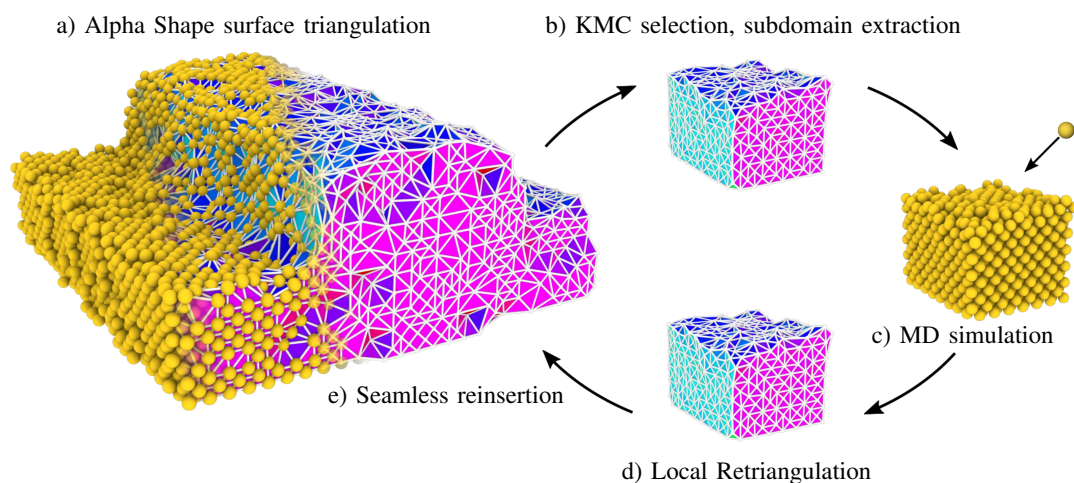


Fig. 1. Circular coupling method of the atomistic vapor deposition model: a) Global triangulation and Alpha Shape construction of the active surface b) KMC sampling of adsorption events at the active surface c) MD simulation around the adsorption site d) Local retriangulation of the subdomain e) Seamless reinsertion due to a shared domain boundary and the alpha criterion

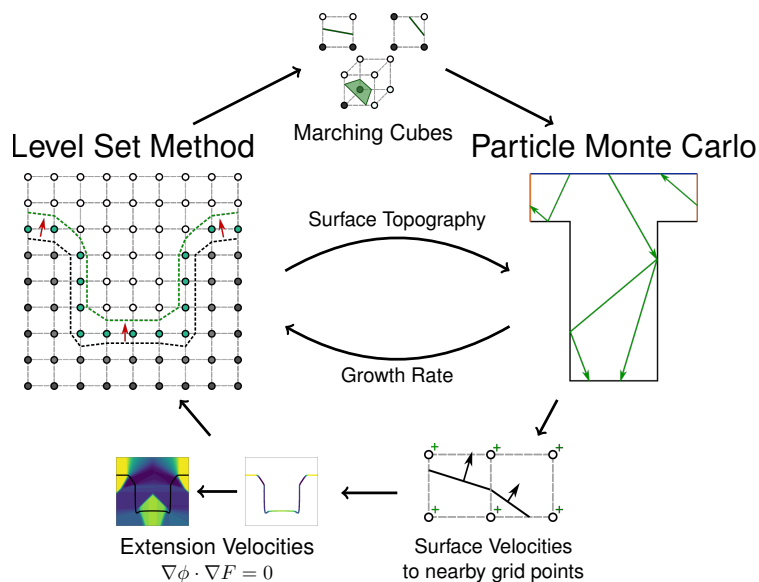


Fig. 2. Geometric surface growth model: Surface is maintained in the Level Set representation, and is advanced according to the local growth rate sampled from particle Monte Carlo simulations.

Interfacial and structural characterization of polymer - electrolyte systems using classical Molecular Dynamics

M.A. Salvador, Elena Degoli*, Alice Ruini, Rita Magri

Dipartimento di Scienze Fisiche, Informatiche e Matematiche, Università di Modena e Reggio Emilia, MO, Italy

*Dipartimento di Scienze e Metodi dell'Ingegneria, Università di Modena e Reggio Emilia, RE, Italy
e-mail: msalvado@unimore.it

ABSTRACT SUBMISSION

In this work we studied the interactions of a self-healing polymer, a combination of boronated polyaniline (B@Pani) monomers and polyvinyl acetate (PVA) trimers, and an electrolyte solution formed by a pyrrolidinium-based ionic liquid, with composition (Pyr16)_{0.5}(Li)_{0.5}-TFSI, using molecular dynamics calculations.

INTRODUCTION

The combination of ionic liquids and polymers are considered to be a promising alternative to improve the performance of Lithium-ion batteries, due to the association of chemical-physical properties such as the polymer mechanical stability, and the ionic liquid conductivity. However, limitations are related to the poor conductivity at room temperature, which depends upon the ion/salt concentration and polymers structure. To understand the properties of these mixtures, and, in particular, the polymer-electrolyte solution interface is of the outmost importance.

MODEL

The Boronated Pani (B@Pani) model was built from the leucoemeraldine base form of Pani monomer functionalized with -B(OH)₂. For the PVA model, we built a chain with 3 monomers, so that the size of B@Pani and PVA are similar. Neat ionic liquid (Pyr16-TFSI), ionic liquid plus Li electrolyte solutions (Pyr16-Li-TFSI), with half of Pyr16 replaced by lithium in a 1:1 proportion, were studied in previous works [3]. Our calculations were performed using the Gromacs software [1], with OPLS-AA force-field parameters for carbon, hydrogen and nitrogen, and the parameters for boron and oxygen of the boronated moiety were taken from the literature [2]. All results presented here were produced at 300 K temperature and 1 bar pressure.

SAMPLE SECTION

Once we had the electrolyte solution and polymer systems separately characterized, we modeled the mixture between electrolyte solutions and polymer, by (i) considering as solute either the polymers or the electrolyte, and (b) by building polymer/electrolyte well-defined interfaces and allowing the systems to relax. Results showed that when we have Pyr16-TFSI as solvent and B@Pani as solute, the Pyr16 cations are closer to the B@Pani monomers than the anions. We also obtained the density and pair correlation functions of the polymer phase and the electrolyte solutions. In the interface studies, we can see formation of a mixed phase 1 nm thick.

CONCLUSION

This work allowed us to understand the interactions between the constituents of the electrolyte solution (Pyr16, TFSI, Li) and the self-healing polymer (B@Pani-PVA), both in mixture and in interface models.

ACKNOWLEDGMENT

We thank our partners from BAT4EVER project (www.bat4ever.eu), developed in the scope of European Union's Horizon 2020 research and innovation program under grant agreement No. 957225. Thanks also IWCN.

REFERENCES

- [1] van der Spoel, et al., GROMACS: Fast, Flexible and Free. *J. Comp. Chem.*, 26, 2005, 1701–1719
- [2] Kurt, B., et al., Development of AMBER parameters for molecular dynamics simulations of boron compounds containing aromatic structure. *Chemical Physics Letters* 775 (2021) 138656
- [3] Salvador et al. Structural and dynamic characterization of Li-ionic liquid electrolyte solutions application in Li-ion batteries: a Molecular Dynamics Approach, to be submitted.

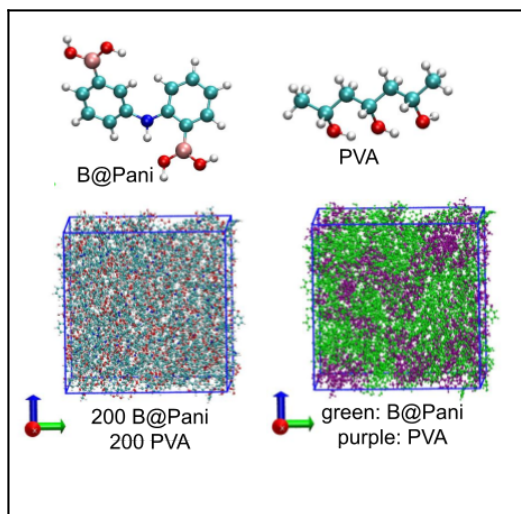


Figure 1: top: B@Pani and PVA models; bottom: box with 200 B@Pani and 200 PVA, ball-and-stick atomic representation and labelling by molecule.

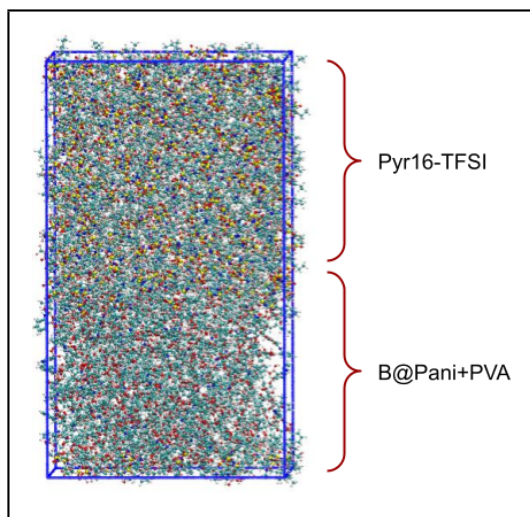


Figure 2: model of the polymer - electrolyte solution interface.

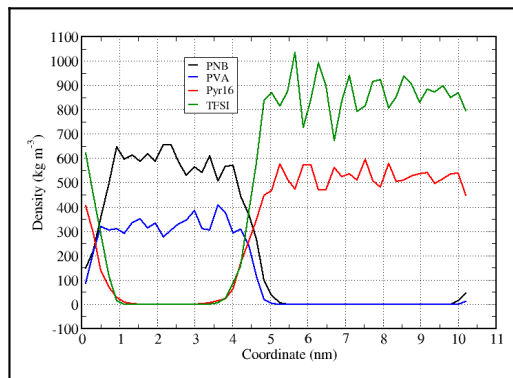


Figure 3: Number density of the system represented in Figure 2. X-axis in the graph represents the z direction in the box.

3D Multi-Level-Set Simulation of Bottom Dielectric Isolation Process for Forksheet FETs

In Ki Kim and Sung-Min Hong

School of Electrical Engineering and Computer Science, Gwangju Institute of Science and Technology (GIST), Gwangju, Cheomdangwagi-ro-123, South Korea
e-mail: smhong@gist.ac.kr

ABSTRACT

The effect of a Si separator layer in the bottom dielectric isolation (BDI) process for forksheet field effect transistors (FSFETs) has been numerically investigated by an in-house topology simulator based on the 3D multi-level-set method. From the simulation result, it is clearly seen that the geometric profile of $\text{Si}_{0.8}\text{Ge}_{0.2}$ sacrificial layer can be improved by adding the Si separator layer.

INTRODUCTION

The FSFET has emerged as a next generation device architecture with its N/P space scaling potential [1], [2]. The reduced N/P space in the FSFET can cause difficulty in an opposite polarity doping for the junction-based substrate isolation, and the challenging process can be eliminated by introducing the BDI [2]. However, the $\text{Si}_{0.8}\text{Ge}_{0.2}$ sacrificial layer may be damaged in the BDI process, causing problems in the gate contact formation process. Therefore, it is essential to examine the geometric profile of the device after the BDI process. The multi-level-set method can accurately represent and evaluate the boundary evolution of the multiple materials [3]. Hence, it is suitable to investigate the geometric profile of the FSFET after the BDI process.

In this work, we numerically simulate the BDI process of the FSFET with an in-house topology simulator based on the multi-level-set method and the effect of the thin Si separator is investigated with the simulation results.

MULTI-LEVEL-SET METHOD IMPLEMENTATION

In the multi-level-set method, several materials are represented by the multiple level-set function. In the method, the upper level-set contains the lower level-set and the topology change over time is calculated based on the top level-set function [3]. The surface velocity of top level-set is determined as the surface velocity of the exposed material, as shown in Fig. 1. Since the boundary of the material is extracted unsuitably for the device representation with the corresponding level-set function alone, the boundary extraction is performed by considering not only the corresponding layer level-set but also the lower layer level-set for the proper

boundary extraction, as shown in Fig. 2 (a). And, since time evolution scheme of the multi-level-set method may generate the unphysical thin layer, the thin layer correction scheme is employed for accurate boundary representation, as shown in Fig. 2 (b).

SIMULATION RESULT

The BDI process is simulated with the relevant process flow reported in [2]. The flow of the BDI process is shown in Fig. 3 and Fig. 4. The simulation has been conducted for the processes without the Si separator and with the Si separator, which are shown in Fig. 3 and Fig. 4, respectively. In the case without the Si separator, the $\text{Si}_{0.8}\text{Ge}_{0.2}$ sacrificial layer is etched with a sloped profile during the $\text{Si}_{0.5}\text{Ge}_{0.5}$ release process due to its low selectivity (7:1), which could cause difficulty in the gate contact formation process. It can be addressed by introducing a Si separator protecting the $\text{Si}_{0.8}\text{Ge}_{0.2}$ layer during the release process [2]. The case with the Si separator is represented in Fig. 4. In the process, it is seen that the $\text{Si}_{0.8}\text{Ge}_{0.2}$ layer exhibits a flat profile owing to the Si separator layer that has a high selectivity to $\text{Si}_{0.5}\text{Ge}_{0.5}$.

CONCLUSION

In conclusion, the BDI process of the FSFET has been simulated by using our in-house topology simulator based on the multi-level-set method. In the simulation, the effect of Si separator was successfully investigated and the results suggest that this method could be useful in the design of 3D logic device processes.

ACKNOWLEDGMENT

This work was supported by the National Research Foundation of Korea (NRF) through the Korean Government under Grant NRF-2020M3H4A3081800.

REFERENCES

- [1] H. Mertens et al., *Forksheet FETs for Advanced CMOS Scaling: Forksheet-Nanosheet Co-Integration and Dual Work Function Metal Gates at 17nm N-P space*, Symposium on VLSI Tech., pp. 1-2 (2021)
- [2] H. Mertens et al., *Forksheet FETs with Bottom Dielectric Isolation, Self-Aligned Gate Cut, and Isolation between Adjacent Source-Drain Structures*, IEDM Tech., pp. 23-1 (2022)
- [3] O. Ertl et al., *A Fast Level Set Framework for Large Three-Dimensional Topography Simulation*, Comput. Phys. Commun. 180, pp. 1242-1250 (2009)

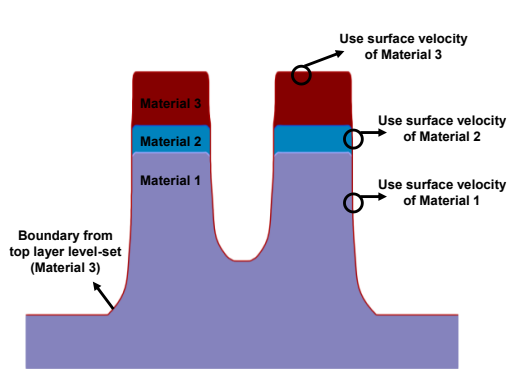


Fig. 1. Schematic of the multi-level-set method. It is shown in which surface velocity is used in the time evolution based on the top layer level-set.

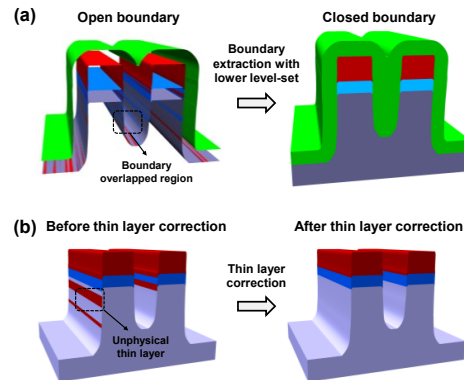


Fig. 2. (a) Closed boundary extraction based on the multiple level-set functions. (b) Correction of a unphysical thin layer.

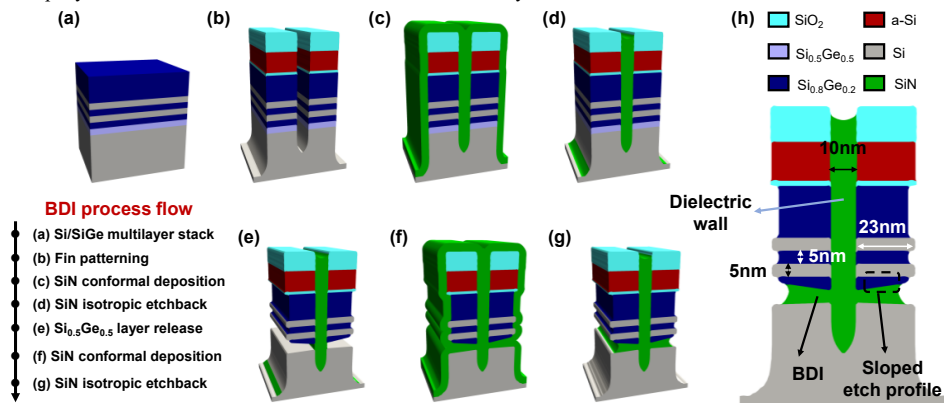


Fig. 3. (a)-(g) The BDI process simulation about the device without the Si separator. The process simulation was conducted by following the represented process flow. (h) Cross section of the simulated device structure.

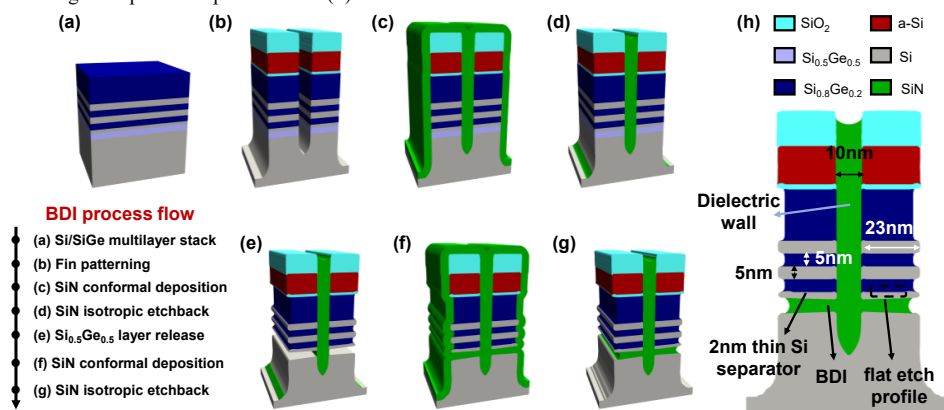


Fig. 4. (a)-(g) BDI process simulation about the device with the Si separator. The process simulation was conducted by following the represented process flow. (h) Cross section of the simulated device structure.

Theory of Electric Enthalpy of Formation in Electrified Interface

Ryong-Gyu Lee, Juho Lee, Hyeonwoo Yeo and Yong-Hoon Kim*

School of Electrical Engineering, Korea Advanced Institute of Science and Technology, 291 Daehak-ro, Yuseong-gu, Daejeon 34141, Korea

Email: ronggyulee@kaist.ac.kr

INTRODUCTION

The recent developments in the modern theory of polarization or density polarization functional theory have derived a well-established concept of the electric enthalpy providing a detailed understanding of the electrified interfaces in the field of electromechanics [1-3]. Despite their success, including the electrode potential effects on first-principles calculations remains a significant challenge due to the difficulty of incorporating the non-equilibrium electrostatic potential condition. While the non-equilibrium Green's function (NEGF) formalism coupled with density-functional theory (DFT) is adopted as a standard approach to finite-bias calculations, it has fundamental limitations raised from the grand-canonical condition which yields an ill-defined quantity of total energy. In this work, we establish a theory of the electric enthalpy based on the multi-space constrained-search DFT (MS-DFT) formalism [4] which allows the variational total energy of non-equilibrium states employing the microcanonical viewpoint. Within MS-DFT, we formulate the non-equilibrium electric enthalpy of the interface systems consisting of electrode and channel systems. Our framework is tested with gold and graphene-based nanocapacitor models by evaluating the biased-induced changes in electric enthalpy. This study will provide a quantitative understanding of the electrified interface's energetics which has critical implications for the development of advanced energy conversion and storage devices.

METHOD

As an alternative to DFT-NEGF scheme, the MS-DFT formalism is based on the microcanonical viewpoint which maps quantum transport processes to multi-space excitation counterparts that allows the variational total energy of a non-equilibrium

state of a junction model consisting of channel (C), left electrode (L), and right electrode (R), where their electrodes are at different electrochemical potentials of μ_L and μ_R .

In this study, we utilize the MS-DFT formalism to obtain L/C/R electron densities of total junction system under applied bias V_b , and thus we can formulate the electric field (\mathcal{E}_{L+R}^V) of the electrodes and dipole moment (\mathbf{p}_C^V) of C regions. We then calculate the non-equilibrium electric enthalpy of junction according to

$$\mathcal{F}_{L+C+R}^V = E_{L+C+R}^V - \mathcal{E}_{L+R}^V \cdot \mathbf{p}_C^V, \quad (1)$$

where E_{L+C+R}^V is the non-equilibrium total energy of the junction.

RESULTS

We first evaluate the capability of MS-DFT calculations to properly decompose the total electron densities of junction system into the L/C/R electron densities. As shown in Fig. 1, the electron density of nanocapacitor models are separated into electrode's and channel's electron densities. These quantities can properly reproduce the dielectric profiles obtain from the conventional finite-field approach (Fig. 2). We then apply our method to calculate the non-equilibrium enthalpy for a single water molecule placed next to Au(111) electrode and graphene surface (Fig. 3).

REFERENCES

- [1] R. D. King-Smith, and D. Vanderbilt, *Theory of polarization of crystalline solids*. Phys. Rev. B **47**, R1651–R1654 (1993).
- [2] I. Souza, J. Íñiguez, and D. Vanderbilt, *First-principles approach to insulators in finite electric fields*. Phys. Rev. Lett. **89**, 117602 (2002).
- [3] P. Umari, and A. Pasquarello, *Ab initio molecular dynamics in a finite homogeneous electric field*. Phys. Rev. Lett. **89**, 157602 (2002).
- [4] J. Lee, H. S. Kim, and Y.-H. Kim, *Multi-Space Excitation as an Alternative to the Landauer Picture for Nonequilibrium Quantum Transport*. Adv. Sci. **7**, 2001038 (2020).

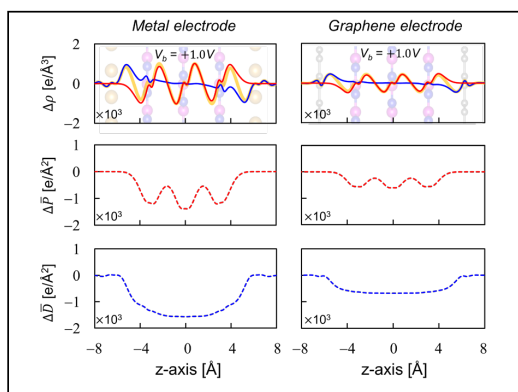


Fig. 1. Electric displacement and polarization of Au/hexagonal boron nitrides (hBN)/Au and graphene/hBN/graphene models

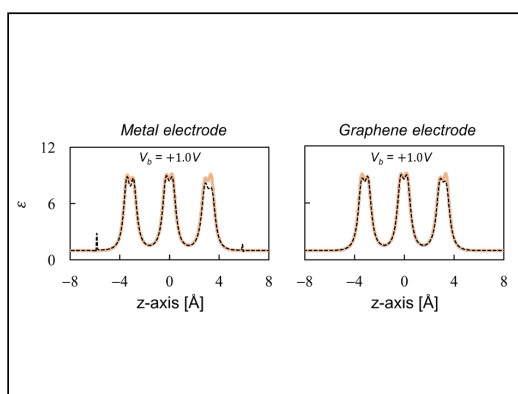


Fig. 2. Comparison of the dielectric profiles obtained through Fig. 1 (black dotted) and the finite field method (yellow).

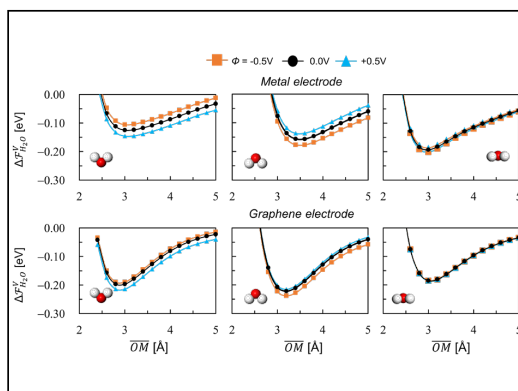


Fig. 3. The formation of enthalpy for single water molecule with different configurations placed next to Au electrode (top) and graphene surface (bottom).

Ab-initio Thermal Transport Calculations for Crystals and Nanostructures Based on the Boltzmann Transport Equation

J. Carrete

Institute of Materials Chemistry, TU Wien, A-1060 Vienna, Austria

e-mail: jesus.carrete.montana@tuwien.ac.at

MOTIVATION

Technological progress requires increasingly fine-tuned heat management strategies, be it to keep the operating temperatures of device parts optimized for long lifetimes or to extract higher performance from energy-scavenging cycles. This kind of context imposes new demands on computational materials science, which must be able to deliver predictive thermal transport calculations for new compounds, materials and devices, as opposed to just shedding light on existing solutions.

A PREDICTIVE ATOMISTIC APPROACH

In the last two decades, solutions to the Boltzmann transport equation (BTE) for phonons formulated based on inputs from density functional theory (DFT) have enabled the development of predictive thermal transport calculation workflows in an increasingly diverse catalog of situations dominated by lattice excitations. The first part of this presentation will consist in a guided tour of those developments viewed from a methodological angle but illustrated with relevant examples at each step. The starting point will be the solution for a perfect single crystal in the steady state [1], which serves to introduce most of the important quantities involved. I will then present the extension of this method to more realistic systems containing defects [2], which also affords excellent agreement with experiment, and show solutions for nanostructures, interfaces, models of electronic devices, time-dependent problems [3] and high-temperature phases [4].

THE MACHINE LEARNING (ML) REVOLUTION

This increase in model complexity can pose formidable computational challenges, which are

compounded by the need to scale horizontally as well, i.e., to scan collections of materials or ranges of parameter values while optimizing for a target application. I will illustrate how ML techniques can be of crucial help when exploring chemical and configurational space by detecting and exploiting regularities between systems with similar structures or compositions. ML force fields, regression models for the potential energy and the forces trained on DFT calculations, can decrease the computational cost of the ingredients required for a solution to the phonon BTE by orders of magnitude. One of the keys to enabling this is algorithmic differentiation (AD), a feature of the latest generation of ML frameworks. I will explain how AD opens the door to completely new kinds of workflows [5] of special relevance for thermal transport calculations.

BEYOND PHONONS

To conclude, I will discuss some fundamental limitations of BTE-based approaches when dealing with higher-order anharmonicity and more disordered structures, generalizations [6] and alternatives [7] to treat those systems, and the role that ML techniques can play in making those viable.

REFERENCES

- [1] W. Li, J. Carrete, N.A. Katcho, N. Mingo, *ShengBTE: A Solver of the Boltzmann Transport Equation for Phonons*, Computer Physics Communications **185**, 1747 (2014).
- [2] A. Katre, J. Carrete, B. Dongre, G.K.H. Madsen, N. Mingo, *Exceptionally Strong Phonon Scattering by B Substitution in Cubic SiC*, Physical Review Letters **119**, 075902 (2017).
- [3] J. Carrete, B. Vermeersch, A. Katre, A. van Roekeghem, T. Wang, G.K.H. Madsen, N. Mingo, *almaBTE: A Solver of the Space-Time Dependent Boltzmann Transport Equation for Phonons in Structured Materials*, Computer Physics Communications **220**, 351 (2017).

- [4] A. van Roekeghem, J. Carrete, N. Mingo, *Anomalous Thermal Conductivity and Suppression of Negative Thermal Expansion in ScF_3* , Physical Review B **94**, 020303(R) (2016).
- [5] S. Bichelmaier, J. Carrete, G.K.H. Madsen, *Evaluating the Efficiency of Power-Series Expansions as Model Potentials for Finite-Temperature Atomistic Calculations*, International Journal of Quantum Chemistry e27095 (2023).
- [6] M. Simoncelli, N. Marzari, F. Mauri, *Unified Theory of Thermal Transport in Crystals and Glasses*, Nature Physics **15**, 809 (2019).
- [7] R. Bertossa, F. Grasselli, L. Ercole, S. Baroni, *Theory and Numerical Simulation of Heat Transport in Multicomponent Systems*, Physical Review Letters **122**, 255901 (2019).

Full Band Monte Carlo simulation of transient and stationary thermal transport in GaAs porous nanostructures based on *ab initio* calculation

Junbum Park¹, Lorenzo Paulatto², Marco Pala¹, and Jerome Saint-Martin¹

¹C2N, Université Paris-Saclay, CNRS, 91120, Palaiseau, France

²IMPMC, Sorbonne Université, CNRS, 75252, Paris, France

e-mail: junbum.park@universite-paris-saclay.fr

INTRODUCTION

Semiconducting materials such as GaAs are a key technology for increasing the energy efficiency of electronic devices [1]. Despite significant progress in thermal transport modeling beyond Fourier's law, the analysis of the nanostructures with porous that fully capture their properties are still scarce [2].

In this work, we present a full-band Monte Carlo (MC) approach based on the Boltzmann's transport equation (BTE) for phonons using *ab initio* parameters. Thermal conductivity, transient and stationary properties of GaAs nanostructures are analyzed in all phonon transport regimes.

METHOD

All necessary material parameters including scattering rates are calculated by *ab initio* methods in the framework of the density functional theory (DFT) as implemented in Quantum ESPRESSO [3], as shown in Fig. 1.

To solve the BTE that describes the time evolution of the phonon distribution function, our home-made Monte Carlo simulator is used and detailed implementations are presented in [4]. In Fig. 2 investigated nanowires and nanofilms in both cross-plane and in-plane configurations are shown. Nanowires have only diffusive external boundaries that randomize the propagation direction of reflected phonons. To mimic the effect of nanopores in the simulated device, the boundaries of each nanopore are assumed to be diffusive.

RESULTS

We first investigate the dependence of thermal conductivity on the length, temperature and porosity in cross-plane nanofilms (CPNF). Our simulation results are compared to semi-analytical

models and experimental data in Fig. 3. The phonon transport gradually changes from a ballistic regime in ultra-short films to a diffusive one in long nanofilms, and thermal conductivity decreases depending on the porosity due to the degradation effect of nanopores. Figure 4 shows that the conductivity reduction is directly related to the number of rough boundaries when the heat transport is diffusive. The ratio of thermal conductivity of CPNF calculated by MC simulation to semi-analytical ballistic one is plotted in Fig. 5 (a) showing the degree of ballisticity of transport. The transient thermal response is investigated by analyzing the time evolution of heat flux density at different positions as shown in Fig. 5 (b). Finally, Fig. 6 shows the spectral contributions of the thermal flux for each device of different length. Optical phonons can contribute over 20% to thermal conductivity in ultra-short devices where ballistic transport dominates.

CONCLUSION

We have proposed a stochastic Monte Carlo algorithm parameterized with *ab initio* calculations efficient for predicting the thermal properties of diverse nanostructures at all time and dimension scales.

ACKNOWLEDGMENT

This work was supported by the French National Research Agency (ANR) as part of the "Investissements d'Avenir" program (Labex NanoSaclay, reference: ANR-10-LABX0035) and the Placho project grant (ANR-21-CE50-0008).

REFERENCES

- [1] S. Singh, et al, *APL Mater.* 7(3), 031104 (2019)
- [2] A. Ghukasyan, et al, *Nanomaterials.* 12(8), 1288 (2022)
- [3] P. Giannozzi, et al, *J. Phys.: Condens. Matter.* 21(39), 395502 (2009)
- [4] B. Davier, et al, *J. Phys.: Condens. Matter.* 30, 495902 (2018)
- [5] D. Strauch and B. Dörner, *J. Phys.: Condens. Matter.* 2(6), 1457 (1990)
- [6] A. V. Inyushkin, et al, *Semicond. Sci. Technol.* 18(7), 685 (2003)

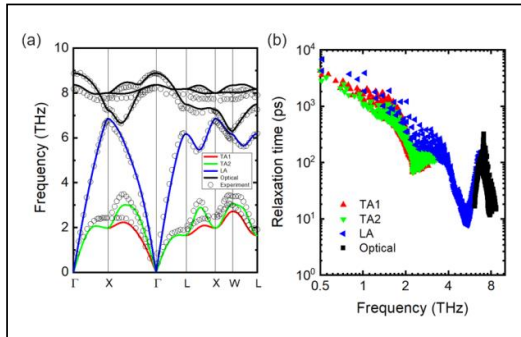


Fig. 1. (a) Calculated phonon dispersions for GaAs along the high symmetry paths and experiment data [5]. (b) Phonon relaxation times as a function of frequency at 300 K for different modes computed via DFPT.

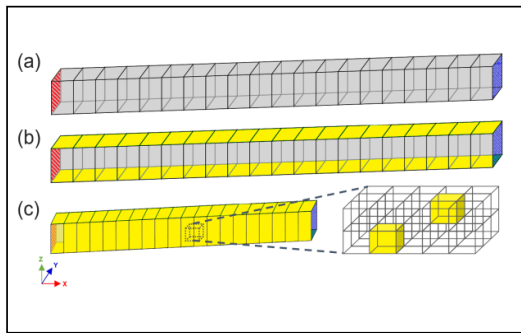


Fig. 2. (a) Nanofilm in cross-plane configuration (CPNF), (b) Nanofilm in in-plane configuration (IPNF), (c) Nanowire (NW) and partial diffusive internal structure for mimicking nanopores. Red/blue faces for hot/cold thermostats $T_H=302K$, $T_C=298K$, respectively. Yellow faces for diffusive boundaries.

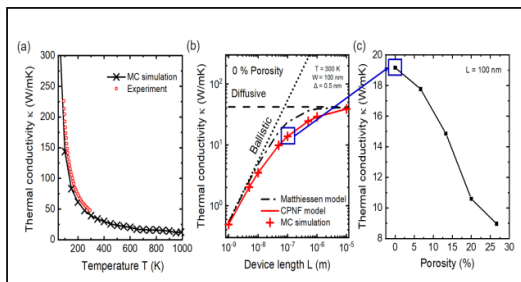


Fig. 3. (a) A comparison between the thermal conductivity of MC simulation results and experiment data [6]. (b) Thermal conductivity as a function of length and (c) the effect of nanopore density for CPNF.

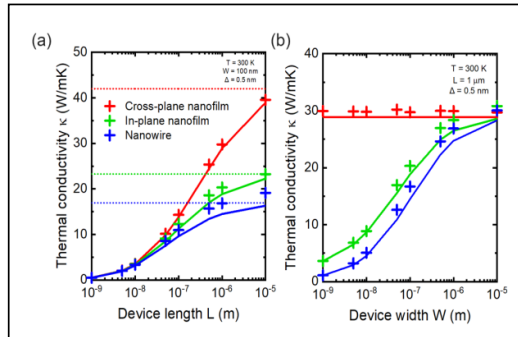


Fig. 4. Thermal conductivity κ as a function of (a) length L with 100 nm width and (b) width W with 1 μ m length for CP and IP nanofilms and for nanowires at 300 K. Solid and dotted lines represent for semi-analytical models and long-device thermal conductivity, respectively.

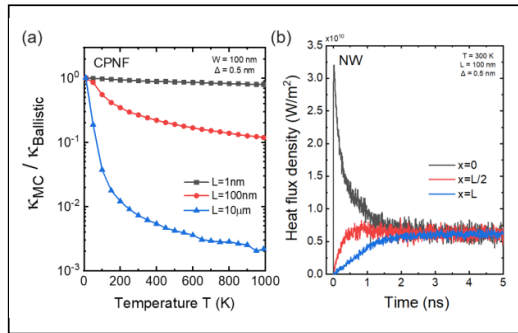


Fig. 5. (a) The Knudsen number calculated by MC simulation as a function of temperature for CPNF with three different device lengths. (b) Heat flux density as a function of time for NW of length 100 nm at three different positions along the x-axis.

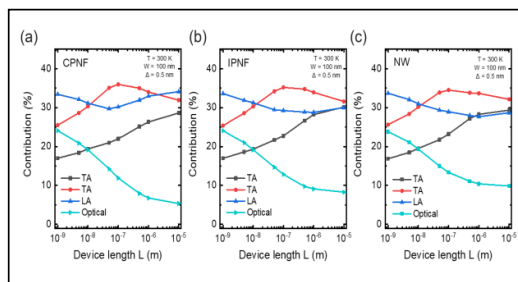


Fig. 6. Spectral contributions of each phonon mode to the total heat flux as a function of length for (a) CPNF, (b) IPNF, and (c) NW at 300 K.

BTE-Barna: first-principles thermal simulation of devices based on 2D materials

M. Raya-Moreno[‡], X. Cartoixà^{*}, and J. Carrete[†]

Institut de Ciència de Materials de Barcelona (ICMAB-CSIC), Campus UAB, 08193 Bellaterra, Spain

^{*}Departament d'Enginyeria Electrònica, Universitat Autònoma de Barcelona, 08193 Bellaterra, Spain

[†]Institute of Materials Chemistry, TU Wien, A-1060 Vienna, Austria

[‡]e-mail: mraya@icmab.es

The continuous shrinking of transistors and the associated increase in integration levels, as predicted by Moore's law [1], is pushing devices to their limits, not only physically but also in terms of heat dissipation. In this context, two-dimensional materials (2DMs), thanks to their excellent properties [2] and CMOS compatibility, are promising candidates to replace silicon in transistor channels [3], [4]. Therefore, accurate simulation of thermal transport in 2DM-based devices becomes essential to optimize heat management in such devices. Despite the existence of several open-source packages [5], [6], [7] solving the problem, i.e. the Peierls-Boltzmann transport equation, informed with *ab initio* data, none of them allow for the simulation of 2DM-based systems and/or simulation beyond the relaxation approximation time (RTA) which is known to provide a very poor description of thermal properties for 2DMs [8]. In this work, we present BTE-Barna [9]—freely available at <https://github.com/sousaw/BTE-Barna>—, a software package that extends the `almaBTE` [7] package to calculate the thermal properties of devices and systems based on 2DMs and other nanosystems. Amid all new features the most relevant are:

- 1) The iterative solver has been extended to provide the effective conductivity by partially suppressing the phonon lifetimes due to boundaries [10] for the case of nanoribbons and nanowires (3D materials).
- 2) The RTA Monte Carlo simulator was updated so that now it can address finite and/or periodic 2D systems under the effect of thermal gradients and isothermal reservoirs. Moreover, it now provides information for transient

and steady-state regimes for finite systems.

- 3) A beyond-RTA Monte Carlo simulator for 2D systems has been implemented in order to provide an accurate description in those cases when the RTA falls short. This innovation, in particular, has required the implementation of a completely different Monte Carlo formalism [11] in a much more efficient way than had previously been achieved using Krylov subspace methods.

To showcase the new capabilities we have used the simulators to highlight the differences in the heat flux profile for the case of Poiseuille flow in a nanoribbon, for the case of RTA and beyond the RTA (see Figs. 1-2) as well as to compute the effective thermal flux both with MC and the iterative solver (see Fig. 3). Additionally, we also show the capabilities of our simulators to investigate hydrodynamic effects for more complex structures [12], see, for instance, vorticity and negative resistance zones in Fig. 4.

REFERENCES

- [1] G. E. Moore, *Electronics* **38**, 114117 (1965).
- [2] M. Chhowalla *et al.*, *Nat. Rev. Mater.* **1**, 16052 (2016).
- [3] D. Akinwande *et al.*, *Nat. Commun.* **5**, 5678 (2014).
- [4] J. Jiang *et al.*, *IEEE J. Electron Devices Soc.* **7**, 878-887 (2019).
- [5] A. Togo *et al.*, *Phys. Rev. B* **91**, 094306 (2015).
- [6] W. Li *et al.*, *Comput. Phys. Commun.* **185**, 1747-1758 (2014).
- [7] J. Carrete *et al.*, *Comput. Phys. Commun.* **220**, 351-362 (2017).
- [8] A. Cepelloti *et al.*, *Nat. Commun.* **6**, 6400 (2015).
- [9] M. Raya-Moreno *et al.*, *Comput. Phys. Commun.* **281**, 108504 (2022).
- [10] W. Li *et al.*, *Phys. Rev. B* **85**, 195436 (2012).
- [11] C. Landon *et al.*, *Appl. Phys.* **116**, 163502 (2014).
- [12] M. Raya-Moreno *et al.*, *Phys. Rev. B* **106**, 014308 (2022).

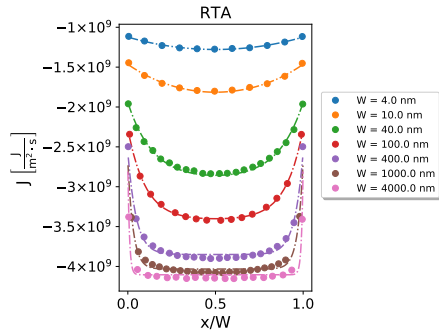


Fig. 1. Fitting to hydrodynamic equation (lines) of RTA-MC calculated heat flux (points) as a function of normalized position for phosphorene AC nanoribbons of different widths under the effect of $\nabla_{AC}T = 0.2 \text{ K nm}^{-1}$. Reproduced from Ref. [9].

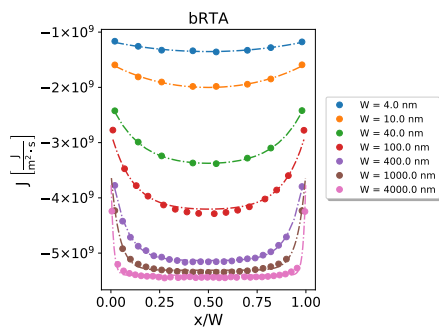


Fig. 2. Fitting to hydrodynamic equation (lines) of beyond the RTA-MC (bRTA) calculated heat flux (points) as a function of normalized position for phosphorene AC nanoribbons of different widths under the effect of $\nabla_{AC}T = 0.2 \text{ K nm}^{-1}$. Reproduced from Ref. [9].

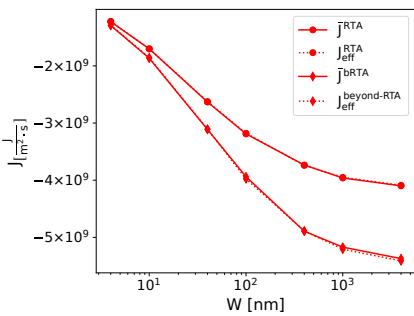


Fig. 3. Comparison between effective RTA and beyond-RTA heat fluxes for AC nanoribbons and the respective Monte Carlo obtained mean fluxes—RTA and bRTA, respectively—for a 0.2 K nm^{-1} gradient in the unbound direction. Reproduced from Ref. [9].

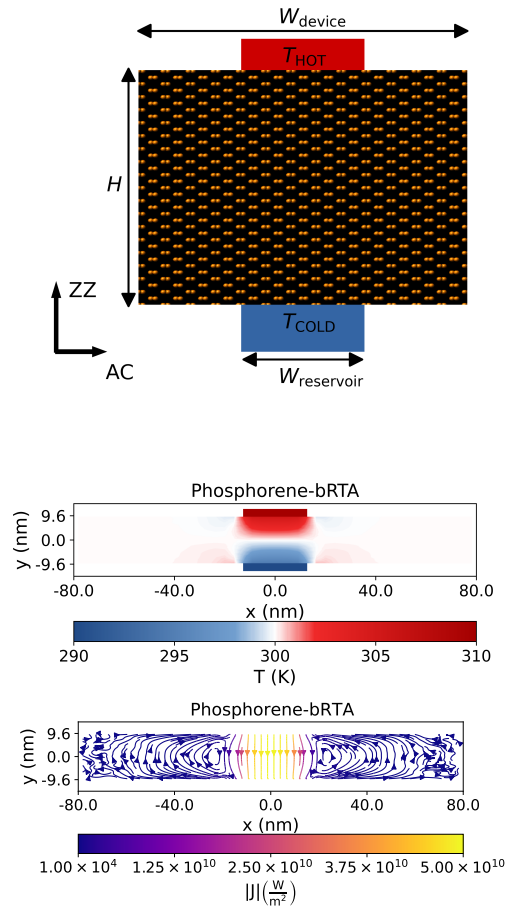


Fig. 4. Sketch of a Levitov configuration (top) with characteristic lengths H , $W_{\text{reservoir}}$ and W_{device} indicated. The transport axis, armchair (AC) and zigzag (ZZ), for phosphorene case are given as reference. The bRTA (i.e. beyond the RTA), steady-state thermal profiles (middle) and heat fluxes (bottom) illustrating vorticity for a ballistic phosphorene-based Levitov configuration with $W_{\text{reservoir}} = 25 \text{ nm}$, $W_{\text{device}} = 160 \text{ nm}$ and $H = 19.2 \text{ nm}$, $T_{\text{HOT}} = 310 \text{ K}$ and $T_{\text{COLD}} = 290 \text{ K}$. Adapted from Ref [12].

Dynamics of Long-Wavelength Phonons Near Boundaries and Interfaces in Nanomaterials

L. Avazpour, M.K. Eryilmaz, and I. Knezevic

Department of Electrical and Computer Engineering, University of Wisconsin – Madison
Madison, WI 53706

e-mail: laleh.avazpour@wisc.edu; irena.knezevic@wisc.edu

ABSTRACT

Long-wavelength phonons undergo infrequent phonon-phonon scattering and propagate ballistically over long distances in single-crystalline, high-quality bulk materials, thereby making a major contribution to thermal conductivity in these systems. The dynamics of long-wavelength phonons and their interaction with boundaries and interfaces can be accurately modeled within the elastic-continuum limit. We present our modeling of thermal transport in the long-wavelength limit in the presence of boundary and interface disorder that relies on the finite-difference time-domain (FDTD) solution to the elastic wave equation and is strongly informed by experiment. We show the emergence of phenomena such as the incoherent-to-coherent transition in thermal transport in III-V superlattices and the changes in the power-law dependence of phonon lifetime on frequency for rough nanowires and membranes with varying correlation types. The work illustrates the complexity of phonon interaction with disorder, and the utility and flexibility of numerical techniques such as the finite-difference time-domain (FDTD) method for elucidating the dynamics of phonons in nanomaterials.

ELASTIC-WAVE MODELING OF LONG-WAVELENGTH PHONON DYNAMICS

We present thermal transport in a) III-V alloy superlattices, such as those used in quantum cascade lasers, and in b) rough silicon nanowires. Our simulation work is corroborated with experimental data. We solve the elastic wave equation using the finite-difference time-domain (FDTD) technique in the velocity-stress formulation, starting from the code base we developed earlier [1]. Interface and boundary roughness are generated according to a correlation

type with a given rms roughness and correlation length [1].

To simulate thermal transport in InGaAs/InAlAs alloy superlattices, we performed FDTD calculations with several rms roughness values and correlation lengths, and all of which are close to experimental observations [2]. We then used these FDTD calculations as training data for a neural-network-based machine-learning algorithm in order to identify the optimal values of rms roughness and correlation lengths that give the best agreement between measurements and calculations. Both experiment and simulation show a cross-over between incoherent and coherent phonon transport in alloy superlattices as the interface density increases (Fig. 1).

As for transport in nanowires, a Gaussian longitudinal wave packet is launched at the center of a Si nanowire (Fig. 2) toward the rough interface formed between Si and Al (right boundary of the domain). The Gaussian pulse is centered around a certain frequency, typically one that coincides with a resonant mode. The Fourier transform of this signal is peaked around the launch frequency and its harmonics, and there is a notable broadening to it that depends on roughness properties. Each prominent peak is fitted with a Lorentzian to extract the line width, which corresponds to the scattering rate (inverse of scattering lifetime). Lifetime versus frequency power-law dependence carries valuable information about the interplay between wire dimensions and roughness features.

This work was funded by the AFOSR (award FA9550-22-1-0407), NSF (award 2212011), and the Splinter Professorship.

REFERENCES

- [1] L. N. Maurer, S. Mei, and I. Knezevic, *Phys. Rev. B* **94**, 045312 (2016).
- [2] C. Perez, et al., *Appl. Phys. Lett.* **121**, 232201 (2022).

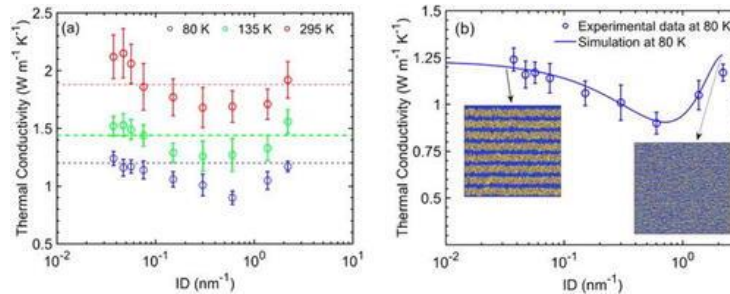


Fig. 1: (a) Experimental values of the cross-plane thermal conductivity at 80 K (blue), 135 K (green), and 295 K (red) vs interface density ranging from 0.0374 to 2.19 nm⁻¹. The dashed horizontal lines represent the reference values for the bulk quaternary alloys of the same stoichiometry as the SLs. (b) Experimental (open symbols) and modeling values (solid curve) for the cross-plane thermal conductivity as a function of interface at 80 K. Symbols are experimental averages, and error bars are the standard deviation of four measurements. Insets to panel (b) depict simulated structures with low and high interface densities. Reprinted with permission from AIP Publishing from Appl. Phys. Lett. 121, 232201 (2022).

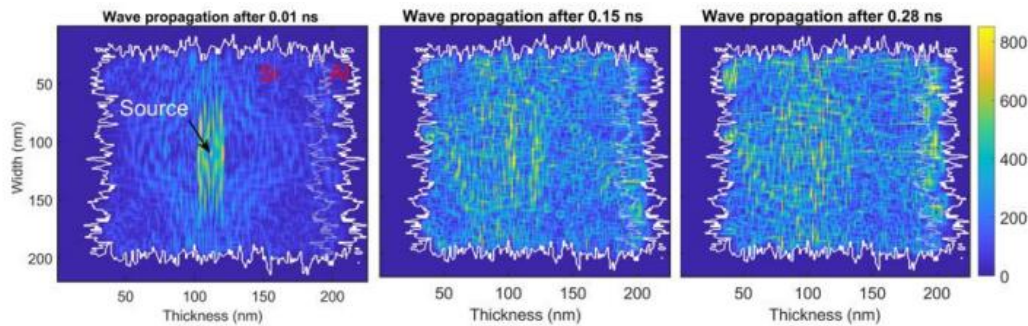


Fig. 2: (Preliminary work) A Gaussian wave packet launched from the center of a Si nanowire (170 nm width; 200 nm thickness) capped with Al (layer on the right). Snapshots taken 0.01 ns (left), 0.15 ns (center), and 0.28 ns (right) after launch. The rough surface is exponentially correlated with a correlation length of 1.7 nm (0.01 of the width) and rms roughness of 5 nm.

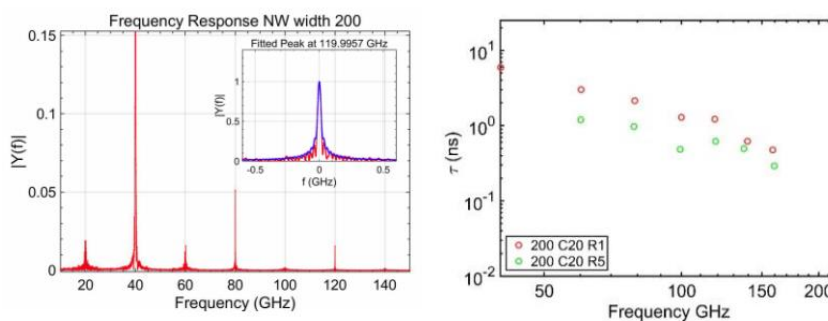


Fig. 3: (Left) Fourier transform of the time-resolved, spatially averaged velocity magnitude (divided by velocity magnitude of the launched Gaussian wave). Each prominent peak is fitted with a Lorentzian (see inset) whose width corresponds to the scattering rate, the inverse of lifetime due to roughness as averaged over the whole surface. (Right) Sample data presenting lifetime versus elastic-wave frequency for two different rms roughness (1 and 5 nm), but the same wire dimensions (200 nm x 200 nm) and correlation length (20 nm). The dependence of the lifetime on frequency carries important information about the interplay between aspect ratio of the wire cross section, the rms roughness, and the roughness correlation length and type.

Strong anharmonicity at the origin of anomalous thermal conductivity in $\text{Cs}_2\text{NaYbCl}_6$

Antonio Cappai *, Claudio Melis*, Francesco Quochi*,
Michele Saba *, Daniela Marongiu*, and Luciano Colombo*
Dipartimento di Fisica, Università di Cagliari, Italy

e-mail: luciano.colombo@dsf.unica.it

INTRODUCTION

Double halide perovskites have gained attention in recent years due to their potential applications in thermoelectric and energy-related devices [1], [2], [3]. In particular, it was recently found that specific perovskites exhibit anomalous dependence on temperature of thermal conductivity that deviates from the standard phonon-dominated behavior $\kappa(T) \sim T^{-1}$, as well as negative thermal expansion coefficients [4]. This deviation has been attributed to several factors such as structural disorder, lattice defects, and grain boundary scattering [5], [6].

Among double halide perovskites, rare earth-based perovskites (as $\text{Cs}_2\text{YbNaCl}_6$) have shown particularly interesting properties. The possibility to tune the electronic bandgap [7] combined with the intrinsically low thermal conductivities ($1 - 10 \text{ W m}^{-1} \text{ K}^{-1}$) make these systems very promising for thermoelectric applications.

METHODS

We perform a full ab-initio study of the (i) structural, (ii) electronic and (iii) lattice dynamical properties of $\text{Cs}_2\text{YbNaCl}_6$ by using the QuantumEspresso software suite [8], [9]. Ultrasoft pseudopotential (USPP), PBE functional and a plane wave basis set with an energy cut-off of 45Ry are adopted to describe the conventional cubic cell (40 atoms) used in this study.

The lattice dynamical properties, i.e. the phonon dispersion curves and the phonon lifetimes, are calculated using the finite-displacement (*frozen-phonon*) methodology as implemented in the Alamode software package [10]. Fourth-order anharmonicity is eventually included using the Self-Consistent Phonon approach (SCPH) [11]. The thermal conductivity $\kappa(T)$ is calculated by solving the Boltzmann Transport Equation in the Relaxation Time Approximation (BTE-RTA).

RESULTS

To validate the computational setup used to modelize the double perovskite structure, a series of benchmark calculations was conducted. The lattice parameter served as the figure of merit, and we achieved a remarkable agreement with the experiment within a margin of 0.6%. We then calculated the harmonic and anharmonic interatomic force constants to determine the phonon dispersion curves and lifetimes, respectively. Our observations revealed that when only cubic anharmonicity is considered to describe phonon scattering processes, the thermal conductivity at 300 K resulted in $0.25 \text{ W m}^{-1} \text{ K}^{-1}$, significantly underestimating the corresponding experimental value of $\kappa^{\text{exp}} = 0.55 \text{ W m}^{-1} \text{ K}^{-1}$. In contrast, when we included fourth-order anharmonicity using the SCPH method, we were able to (i) resolve the underestimation and (ii) explain the anomalous trend of $\kappa(T)$ observed in the experiment. Specifically, we attribute the failure of $T^{-\alpha}$ law in describing $\kappa(T)$ to an unusual increase in the phonon group velocity and lifetimes for $500\text{K} \leq T \leq 800\text{K}$.

ACKNOWLEDGMENT

We acknowledge financial support under the National Recovery and Resilience Plan (NRRP), Mission 4 Component 2 Investment 1.3 - Call for tender No.341 published on March 13, 2022) by the Italian Ministry of University and Research (MUR) funded by the European Union – NextGenerationEU. Award Number: Project code PE_00000021, Concession Decree No. 1561 adopted on October 11, 2022 by the Italian Ministry of University and Research (MUR), CUP F53C22000770007, Project title "NEST - Network 4 Energy Sustainable Transition"

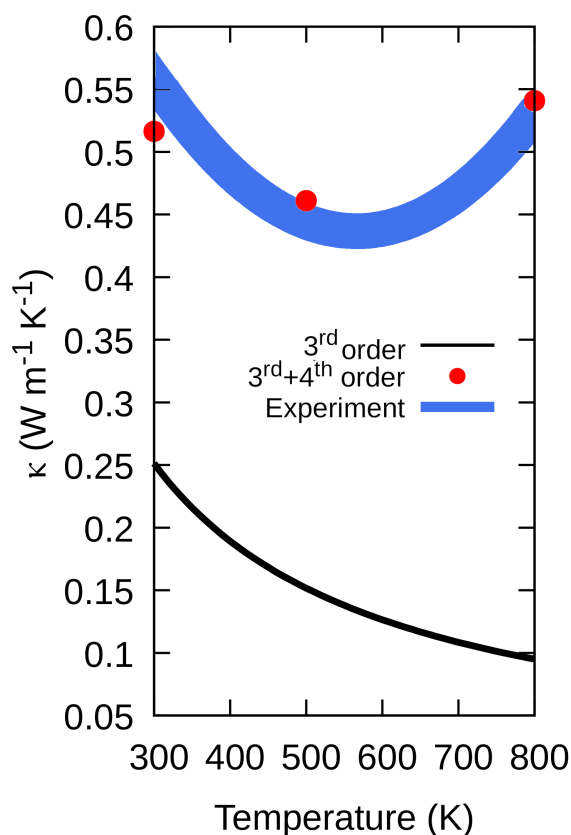


Fig. 1. $\text{Cs}_2\text{NaYbCl}_6$ thermal conductivity κ as a function of the temperature. The black line shows the theoretical prediction of $\kappa(T)$ based solely on cubic anharmonicity. The conspicuous underestimation of the anomalous experimental trend (blue band) is eventually resolved by the inclusion of fourth-order anharmonicity (red points)

REFERENCES

- [1] Fatemeh Heidari Gourji and Dhayalan Velauthapillai. A review on cs-based pb-free double halide perovskites: From theoretical and experimental studies to doping and applications. *Molecules*, 26(7):2010, 2021.
- [2] Sebastian F Hoefler, Gregor Trimmel, and Thomas Rath. Progress on lead-free metal halide perovskites for photovoltaic applications: a review. *Monatshefte für Chemie-Chemical Monthly*, 148:795–826, 2017.
- [3] Shadrack J Adjogri and Edson L Meyer. A review on lead-free hybrid halide perovskites as light absorbers for photovoltaic applications based on their structural, optical, and morphological properties. *Molecules*, 25(21):5039, 2020.
- [4] Ikuya Yamada, Kazuki Tsuchida, Kenya Ohgushi, Naoaki Hayashi, Jungeun Kim, Naruki Tsuji, Ryoji Takahashi, Masafumi Matsushita, Norimasa Nishiyama, Toru Inoue, et al. Giant negative thermal expansion in the iron perovskite $\text{srCu}_3\text{Fe}_4\text{O}_{12}$.

Angewandte Chemie International Edition, 50(29):6579–6582, 2011.

- [5] Tianjun Liu, Sheng-Ying Yue, Sinclair Ratnasingham, Thibault Degousée, Pritesh Varsini, Joe Briscoe, Martyn A. McLachlan, Ming Hu, and Oliver Fenwick. Unusual thermal boundary resistance in halide perovskites: A way to tune ultralow thermal conductivity for thermoelectrics. *ACS Applied Materials & Interfaces*, 11(50):47507–47515, 2019. PMID: 31752489.
- [6] Animesh Bhui, Tanmoy Ghosh, Koushik Pal, Kewal Singh Rana, Kaushik Kundu, Ajay Soni, and Kanishka Biswas. Intrinsically low thermal conductivity in the n-type vacancy-ordered double perovskite cs_2sn_6 : Octahedral rotation and anharmonic rattling. *Chemistry of Materials*, 34(7):3301–3310, 2022.
- [7] Adil Alshoaibi, Mohammed Benali Kanoun, Bakhtiar Ul Haq, Salem AlFaify, and Souraya Goumri-Said. Ytterbium doping effects into the ba and ti sites of perovskite barium titanate: Electronic structures and optical properties. *Results in Physics*, 18:103257, 2020.
- [8] P Giannozzi, S Baroni, and N Bonini. *J. phys.: Condens. matter*. 21, 2009.
- [9] Qian Zhang, Shuhui Tao, Ruowei Yi, Chunhui He, Cezhou Zhao, Weitao Su, Alexander Smogunov, Yannick J Dappe, Richard J Nichols, Li Yang, et al. P. giannozzi et al., advanced capabilities for materials modelling with quantum espresso. *J. Phys.: Condens. Matter*, 29:465901, 2017.
- [10] T Tadano, Y Gohda, and S Tsuneyuki. Anharmonic force constants extracted from first-principles molecular dynamics: applications to heat transfer simulations. *Journal of Physics: Condensed Matter*, 26(22):225402, may 2014.
- [11] Terumasa Tadano and Shinji Tsuneyuki. Self-consistent phonon calculations of lattice dynamical properties in cubic srTiO_3 with first-principles anharmonic force constants. *Phys. Rev. B*, 92:054301, Aug 2015.

Temperature-induced boomerang effect of electron flow in semiconductor heterostructures

C. Belabbas¹, A. Crépieux², N. Cavassilas¹, F. Michelini¹, X. Zhu³, C. Salhani^{3,4}, G. Etesse¹,
K. Hirakawa^{3,4,5}, and M. Bescond^{1,3}

⁽¹⁾ IM2NP UMR-CNRS, Aix Marseille Université, Université de Toulon, Marseille, France.

⁽²⁾ Aix Marseille Univ, Université de Toulon, CNRS, CPT, Marseille, France ⁽³⁾ Institute of Industrial Science, University of Tokyo, Japan, ⁽⁴⁾ LIMMS-CNRS, IRL 2820, Tokyo, Japan.

e-mail: marc.bescond@cnrs.fr

ABSTRACT SUBMISSION

We theoretically report a remarkable boomerang effect of electron flow when applying a lattice temperature gradient across an asymmetric double-barrier heterostructure.

INTRODUCTION

Thermoelectric devices consist in converting heat into electricity or vice versa. Those devices are based on the diffusive phonon and electron transport, and operate in close to equilibrium regime, where their produced power is obviously limited. The scenario is significantly different in nanostructures where carrier transport can be assumed as strongly ballistic. In this non-equilibrium regime, electron temperature may significantly differ from the lattice one, raising the opportunity to obtain devices with better performances than conventional thermoelectric structures. We recently demonstrated that an asymmetric double-barrier heterostructure can efficiently act on both the electronic and phononic bath's refrigeration when applied a bias between the emitter and collector contacts [1].

MODEL AND DISCUSSIONS

Here, we focus on the opposite effect, *i.e.* when a temperature gradient is applied between the collector and the emitter, and we study the induced electrical current properties (Fig. 1). We demonstrate that electrons are subject to an unexpected boomerang effect. Depending on the lattice temperature increase/decrease, electrons respectively absorb/emit a phonon and

subsequently go back to the reservoir from which they have been injected (Fig. 2).

Our simulation code, which self-consistently solves the non-equilibrium Green's function framework and the heat equation, is capable to calculate the electron temperature and electrochemical potential inside the device. By investigating those non-equilibrium thermodynamic quantities (Fig.3), we show that the boomerang effect is due to the sign inversion of the local electron distribution (Fig. 4). In particular, simulation results evidenced a variation of the electrochemical potential inside the device to compensate the temperature gradient, and to maintain the electrostatic neutrality in the access regions [2].

CONCLUSION

We report an original temperature gradient induced boomerang effect, able to control the direction flow of electrons in a given energy interval. Such a boomerang effect, while it does not (almost) transport electrons, transfers a high energy flux from a hot area to a colder one. Finally, our study demonstrates an additional validation of the virtual probe approach to determine thermodynamic properties in strongly non-equilibrium regime.

REFERENCES

- [1] M. Bescond, G. Dangoisse, X. Zhu, C. Salhani and K. Hirakawa, *Comprehensive analysis of electron evaporative cooling in double-barrier semiconductor heterostructures*, Phys. Rev. Appl. **17**, 014001 (2022).
- [2] C. Belabbas, A. Crépieux, N. Cavassilas, F. Michelini, X. Zhu, C. Salhani, G. Etesse, K. Hirakawa, and M. Bescond, *Temperature-induced boomerang effect of electronic flow in asymmetric double-barrier semiconductor heterostructures*, submitted (2023).

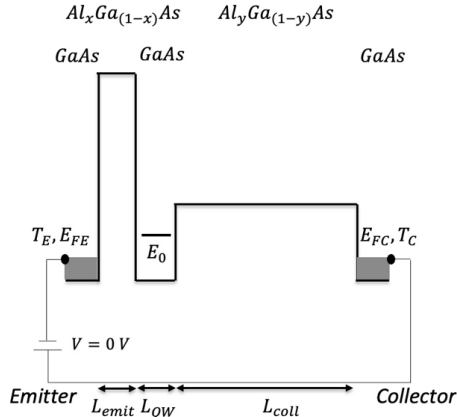


Fig. 1. Sketch of the considered asymmetric double-barrier heterostructure. L_{emit} , L_{QW} and L_{coll} refer to the thicknesses of the emitter barrier, the quantum well and the collector barrier respectively. E_0 is the quantum well state, while E_{FE} (T_E) and E_{FC} (T_C) are the Fermi levels (temperatures) of the emitter and collector respectively. For all the considered devices, doping in the emitter and the collector is 10^{18} cm $^{-3}$, $L_{emit}=L_{QW}=5$ nm and $L_{coll}=100$ nm.

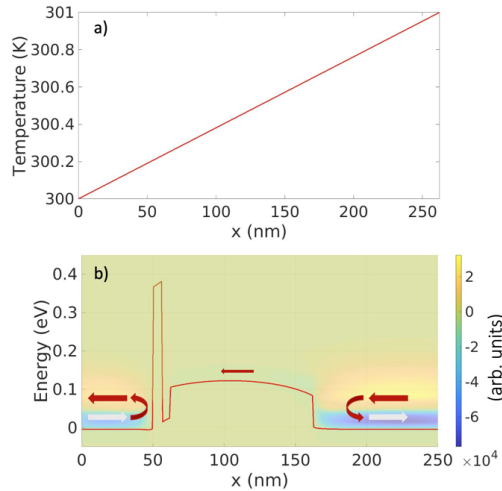


Fig. 2. a) Lattice temperature gradient along the device shown in Fig. 1. A temperature gradient of 1 K is applied between the emitter ($T_{emi}=300$ K) and collector ($T_{coll}=301$ K) reservoirs; b) Corresponding electron current spectrum. The solid red line represents the energy potential profile, while red and white arrows indicate the electron flow and reflection on the potential barrier. The smaller red arrow in the central region represents the total electron flow, going from right to left. No potential bias is applied ($V=0$ V).

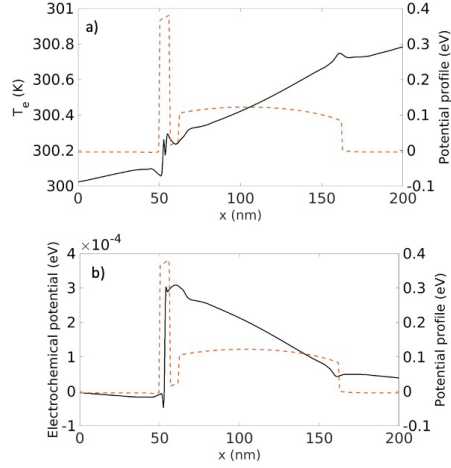


Fig. 3. a) Non-equilibrium electron temperature along the device and b) corresponding electrochemical potential when applying lattice temperature gradient of 1 K and no potential bias ($V=0$ V).

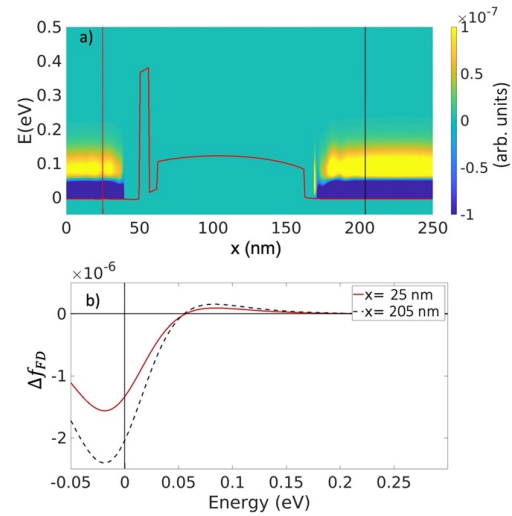


Fig. 4. a) Difference between two consecutive plans of the Fermi-Dirac distributions calculated with the electron temperature and chemical potential shown on Fig. 3-a) and -b) respectively; b) Vertical cuts of Fig. 4-a) at $x=25$ nm (red solid line) and $x=205$ nm (dashed line). The vertical black solid line defines the Fermi-levels of the emitter and collector (equal to each other since there is no applied bias).

ACKNOWLEDGMENT

This work was supported by the JSPS KAKENHI (JP 19K21957), the JSPS Core-to-Core Program (A. Advanced Research Networks), the GELATO project from ANR (ANR-21-CE50-0017) and AMUtech Institute of Aix-Marseille University.

Impacts of Band Structures and Scattering Processes on High-field Carrier Transport in Wide Bandgap Semiconductors

H. Tanaka*, T. Kimoto[†], N. Mori*

* Division of Electrical, Electronic and Infocommunications Engineering, Osaka University, Osaka, Japan
{mori, tanaka}@si.eei.eng.osaka-u.ac.jp

[†] Department of Electronic Science and Engineering, Kyoto University, Kyoto, Japan
kimoto@kuee.kyoto-u.ac.jp

ABSTRACT

In this talk, the results of our work on the impact of band structures and scattering processes on the high-field carrier transport properties of wide-bandgap semiconductors will be presented. Using a tunable band structure model, Monte Carlo simulation is performed to obtain transport characteristics including the impact ionization coefficients and the drift-velocities. It is shown that the smaller Brillouin zone width significantly reduces the impact ionization coefficients. The study also revealed that the impact ionization coefficient may show a positive temperature dependence when the Bloch oscillation occurs.

I. INTRODUCTION

Wide-bandgap semiconductors such as silicon carbide (SiC), gallium nitride (GaN), gallium oxide, and diamond have been attracting attention as materials suitable for power device applications toward an energy-saving and carbon-neutral society. Those materials have high breakdown electric field, which enables the simultaneous achievement of low resistivity and high blocking voltage. The high breakdown field of wide-bandgap semiconductors is usually considered to be attributed to their large bandgap (E_g). This is because that the main cause of the high-field breakdown is the avalanche multiplication of carriers through the impact ionization and it can occur when the carrier energy exceeds E_g . However, phenomena have been reported that cannot be explained only by this naïve scenario. For example, the electron impact ionization coefficient of 4H-SiC along the $\langle 0001 \rangle$ direction is known to be much smaller than that along the $\langle 11\bar{2}0 \rangle$ direction [1], [2] and the hole impact ionization coefficient [3]–[6], despite the common E_g for these

cases. The electron impact ionization coefficient of 4H-SiC along the $\langle 0001 \rangle$ direction is also smaller than a recently reported electron impact ionization coefficient of GaN [7], which has larger E_g . This suggests significant impacts of the band structure parameters such as the Brillouin zone (BZ) width and band-edge effective mass other than E_g . To clarify those issues, we conducted theoretical study on high-field transport characteristics by performing Monte Carlo simulation utilizing a tunable band structure model [8], [9].

II. MODEL

We employ a tunable band structure model with a dispersion:

$$E(\mathbf{k}) = \bigcup_{n=1}^N E_n(\mathbf{k}), \quad (1)$$

$$E_n(\mathbf{k}) = (n-1)\Delta E + \sum_{i=x,y,z} 2t_i[1 - \cos(k_i a_i)]. \quad (2)$$

Here, $\mathbf{k} = (k_x, k_y, k_z)$ is the wavevector, n is the band index, N is the total number of bands considered, ΔE is the energy interval between adjacent bands, and a_i is the lattice period along the i -direction. The transfer energy, t_i , is given by the band-edge effective mass m_i as $t_i = (\hbar/a_i)^2/(2m_i)$ ($i = x, y, z$). m_i is set to be $0.3m_0$. We assume an electric field, F , along the x -direction, and a_x is treated as a variable when investigating the impacts of the BZ width, $G_x = 2\pi/a_x$, along the k_x direction. Specifically, three values of 0.25 nm, 0.5 nm and 1 nm are considered as a_x , while $a_y = a_z = 0.5$ nm are fixed. For $a_x = 0.5$ nm, we set $N = 10$ and $\Delta E = 1$ eV. For other values of $a_x = 0.25$ nm and 1 nm, N and ΔE are set so as that both the total number of states and the total band width coincide with those of $a_x = 0.5$ nm.

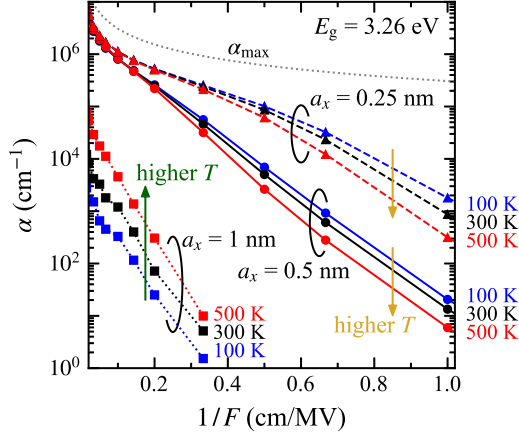


Fig. 1. Inverse electric field dependence of the impact ionization coefficients α with different BZ widths of $G_x = 2\pi/a_x$ for $E_g = 3.26$ eV. Results for $T = 100, 300, 500$ K are shown by blue, black, and red symbols, respectively. α for $G_x = 2\pi/(1\text{ nm})$ increases with T , while others decrease at higher T . The gray dotted line is the maximum impact ionization coefficient of $\alpha_{\max} = eF/E_g$.

We consider elastic acoustic and inelastic non-polar optical phonon scatterings. We assume that the scattering rates are proportional to the final density-of-states. In addition to the phonon scatterings, we take account of the impact ionization using the impact ionization rates with the form give by

$$W_{ii}(E) = a[(E - E_g)/E_0]^b, \quad (E > E_g), \quad (3)$$

with $a = 1.11 \times 10^{13} \text{ s}^{-1}$, $b = 3.38$, and $E_0 = 3.26$ eV.

We perform a full-band Monte Carlo simulation to calculate the drift velocity, v_d , and the impact ionization coefficient of electrons, α , assuming the above-mentioned band structures and scattering mechanisms including impact ionization.

III. RESULTS AND DISCUSSION

Figure 1 shows the impact ionization coefficient of electrons, α , as a function of the inverse electric field, F^{-1} . We see that α is larger for a larger BZ width $G_x = 2\pi/a_x$ (or smaller a_x). This can be attributed basically to the larger average group velocity along the x -direction. In addition, a smaller BZ width such as $G_x = 2\pi/(1\text{ nm})$ leads to easier occurrence of Bloch oscillations, which suppress the energy gain from the electric field and result in smaller α . As for the temperature dependence, α for $G_x = 2\pi/(0.25\text{ nm})$ and $2\pi/(0.5\text{ nm})$ decreases at higher temperatures due to enhanced phonon scatterings. On the contrary, α for $G_x = 2\pi/(1\text{ nm})$ increases

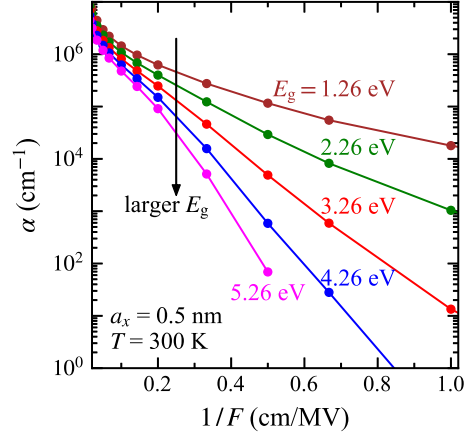


Fig. 2. Impact ionization coefficients α as a function of inverse electric field for different E_g , $a_x = 0.5$ nm and $T = 300$ K.

with temperature. The positive temperature dependence is related to Bloch oscillations.

In Fig. 2, E_g dependence of α is presented. As expected, the increase of E_g leads to smaller α . However, even the increase of E_g from 3.26 eV to 5.26 eV does not outperform the impacts of decrease of G_x from $2\pi/(0.5\text{ nm})$ to $2\pi/(1\text{ nm})$ (see Fig. 1). This indicates that the impacts of E_g on α is not so significant as those of the BZ width and group velocity, which may be an important aspect when discussing the material dependence of impact ionization coefficients.

In the talk, effects of scattering processes on the drift-velocities and the impact ionization coefficients will also be presented.

REFERENCES

- [1] T. Hatakeyama, T. Watanabe, T. Shinohe, K. Kojima, K. Arai, and N. Sano, Appl. Phys. Lett. **85**, 1380 (2004).
- [2] D. Stefanakis, X. Chi, T. Maeda, M. Kaneko, and T. Kimoto, IEEE Trans. Electron Devices **67**, 3740 (2020).
- [3] A. O. Konstantinov, Q. Wahab, N. Nordell, and U. Lindefelt, Appl. Phys. Lett. **71**, 90 (1997).
- [4] H. Niwa, J. Suda, and T. Kimoto, IEEE Trans. Electron Devices **62**, 3326 (2015).
- [5] T. Kimoto, H. Niwa, T. Okuda, E. Saito, Y. Zhao, S. Asada, and J. Suda, J. Phys. D: Appl. Phys. **51**, 363001 (2018).
- [6] Y. Zhao, H. Niwa, and T. Kimoto, Jpn. J. Appl. Phys. **58**, 018001 (2019).
- [7] T. Maeda, T. Narita, S. Yamada, T. Kachi, T. Kimoto, M. Horita, and J. Suda, J. Appl. Phys. **129**, 185702 (2021).
- [8] H. Tanaka, T. Kimoto, and N. Mori, Appl. Phys. Express **13**, 041006 (2020).
- [9] H. Tanaka, T. Kimoto, and N. Mori, J. Appl. Phys. **131**, 225701 (2022).

Effect of Electron-Electron Scattering on the Energy Distribution in Semiconductor Devices

Hans Kosina and Josef Gull

Institute for Microelectronics, TU Wien, Gußhausstraße 27–29, 1040 Wien, Austria

e-mail: hans.kosina@tuwien.ac.at

Physical modeling of hot carrier degradation of semiconductor devices requires accurate knowledge of the carrier distribution function. Childs et al. predicted that the high energy tail of the distribution function is strongly affected by electron-electron scattering (EES) [1]. This has been shown by numerically solving the Boltzmann equation, which is nonlinear in the presence of EES, using an iterative method. The following approximations were made: 1) an energy-dependent formalism with the isotropic part of the distribution function (DF) as the unknown is adopted; 2) the phonon energy is assumed to be much smaller than the kinetic energy. The iterative method is thus not applicable in the low energy range, where instead a Monte Carlo method is used; 3) in the out-scattering rate the contribution of the EES rate is neglected.

While 1) is required to keep the problem numerically tractable, the purpose of approximations 2) and 3) is unclear since they do not significantly simplify the problem, but can greatly change the results.

In this work we employ instead of the Boltzmann equation a two-particle kinetic equation which has the advantage of being linear also in the presence of EES. In [2] a two-particle Monte Carlo method for uniform electric field has been presented, which calculates trajectory pairs to sample the six-dimensional \mathbf{k} -space of the two particles. We have extended the stationary Monte Carlo algorithm so as to account for spatially varying electric fields.

The following numerical results were obtained assuming a single-valley band structure model and the material parameters of silicon. Fig. 1 shows the frequencies of different types of scattering events for uniform electric field. The frequencies of phonon absorption and emission do not change when EES is activated, despite EES being a dom-

inant scattering process. A similar observation can be made in Fig. 2 and Fig. 3. Mean velocity, mean energy, and also the DF as functions of the electric field are virtually not affected by EES.

The situation is different for non-uniform electric fields. Fig. 4 shows a simplified potential profile in a channel of 50nm length, along with a colormap of the DF. At positions A and B the local potential is, respectively, 0.5eV and 1.0eV lower than the potential maximum. Without EES, the DF exhibits a thermal tail, whereas EES reduces the slope of the tail as shown in Fig. 5.

The potential profile in [1] is similar to that in Fig. 4 and characterized by a channel length of 150nm and a potential drop of 1.5V. The positions where the potential drops by 0.5/1.0/1.5eV are designated as A/B/C, respectively. Fig. 6 shows the DF at these positions in the channel. EES results in an enhanced high energy tail, which confirms Childs' results qualitatively. The main difference is that our results indicate the deviation from the thermal tail to occur at significantly lower energies. By comparing Fig. 5 and Fig. 6 we find that the enhancement of the tail is weaker if the potential drop along the channel is smaller.

ACKNOWLEDGMENT

This work has been supported by the the Austrian Research Promotion Agency (FFG), contract 880672.

REFERENCES

- [1] P. Childs and C. Leung. *A one-dimensional solution of the Boltzmann transport equation including electron-electron interactions*, Journal of Applied Physics, **79**, 222 (1996).
- [2] G. Indalecio and H. Kosina, *Monte Carlo Simulation of Electron-Electron Interactions in Bulk Silicon*, in Scientific Computing in Electrical Engineering, Mathematics in Industry **32**, G. Nicosia, V. Romano (ed); Springer International Publishing, 125 (2020)

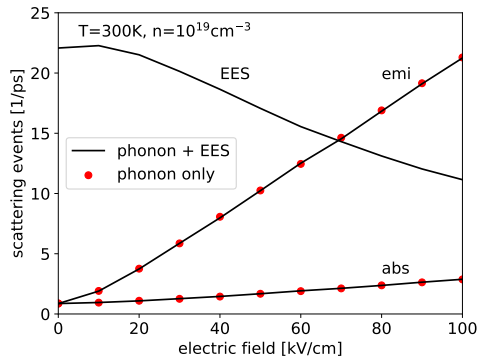


Fig. 1. Number of scattering events in a given time interval versus electric field for phonon emission, phonon absorption, and EES. Two simulations with and without EES are compared.

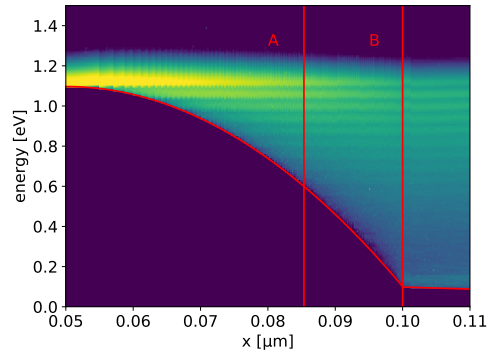


Fig. 4. Potential profile in a 50nm channel. The distribution function shown is calculated assuming phonon scattering only.

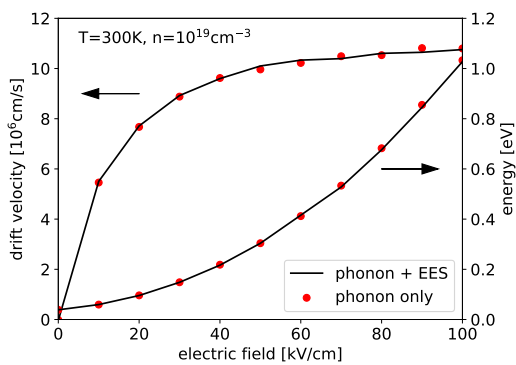


Fig. 2. Mean velocity and mean energy versus electric field. EES has no visible influence on the mean values.

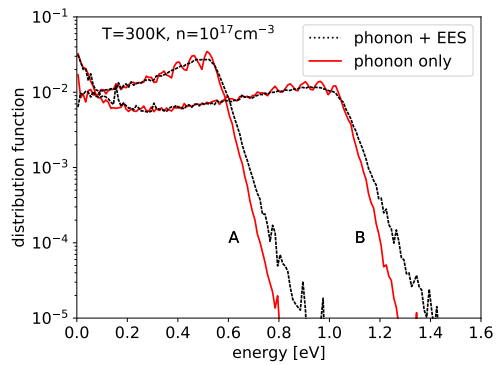


Fig. 5. Distribution functions at positions A and B in a 50nm channel, calculated with and without EES.

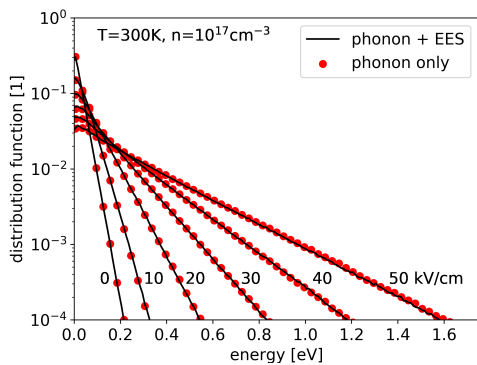


Fig. 3. Distribution functions for uniform electric field at different field strengths. EES has no visible influence.

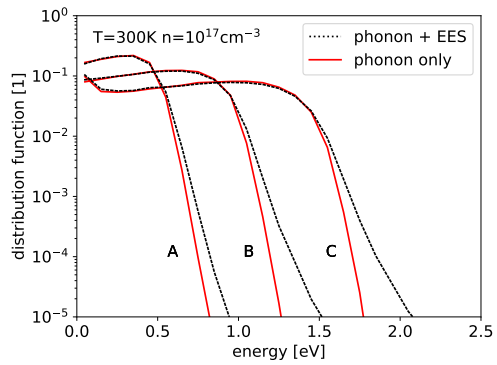


Fig. 6. Distribution functions at positions A, B, C in a 150nm channel, calculated with and without EES.

Efficient ab initio electronic transport methods

Z. Li, P. Graziosi*, and N. Neophytou

School of Engineering, University of Warwick, Coventry, CV4 7AL, UK

*CNR-Bologna, Italy

e-mail: n.neophytou@warwick.ac.uk

INTRODUCTION

Recently there has been an increase in efforts to compute the electronic properties of complex electronic structure materials for many applications, e.g. novel devices and energy materials. The typical process is to use the Boltzmann Transport equation (BTE) in the relaxation time approximation, while scattering rates are extracted at various degree of complexity and accuracy. The most accurate fully ab initio methods, however, are computationally extremely expensive and rarely used. Here we present a method to compute electronic transport from first principles in materials of arbitrary bandstructure.

METHODS

Typical ab initio calculations use Density Functional Theory (DFT) to extract the electronic structure, and then Density Functional Perturbation theory (DFPT) to extract the phonon attributes and the electron-phonon matrix elements. Dense electronic and phonon meshes are needed, which often are a result of interpolations, and up to billions of matrix element calculations are required. This makes the calculation very expensive. Scattering rates are then extracted and are used within the BTE. Instead of computing billions of matrix elements, we follow a practical approach, where we identify and compute a small relevant sample of required matrix elements, and use those to compute deformation potentials involving all relevant phonon modes. We then form the usual deformation potential scattering expressions to use within a BTE which considers numerically the full band electronic structure.

RESULTS

We show this for Si as an example in Figs 1-3 [1]. Only a narrow energy region around the electronic band extrema contributes to transport (red regions in Fig. 1), and only a small region in the phonon spectrum meets energy/momentum

conservation to facilitate transitions (red regions in Fig. 2). The corresponding matrix elements are shown in Fig. 3 for some valence (LA-blue and LO-red modes) and conduction (LO-green mode) band transitions. The slope of the LA mode will give the deformation potential for acoustic modes, while the value of the matrix element itself, that for optical modes. The green line clearly captures the fact that LO transitions are only inter-valley in Si (it is close to zero at Γ and finite at g). We use the deformation potentials to form scattering rates, and then use them within *ElecTra*, a full band BTE that we have developed [2]. The code takes into account all relevant transitions (intra/inter-band), for all relevant scattering mechanisms (elastic, inelastic, isotropic, anisotropic), as illustrated in Fig. 4. The computed Si hole mobility, entirely from first principles, is shown in Fig. 5, with excellent match to experiment (blue-squared line).

The method can be applied to materials with arbitrary band complexity. As an example we show in Fig. 6 the electronic and phononic bands for Mg_3Sb_2 (6a, b), and by identifying all relevant transition types between CBM energy surfaces (6c), we compute matrix elements for all phonon modes, indicating the dominant ones (box in 6d).

CONCLUSION

We presented an efficient and accurate ab initio method to extract electronic transport properties in materials with arbitrary band complexity.

ACKNOWLEDGMENT

This work received funding from the European Research Council (ERC) under the EU's H2020 research and innovation programme (GA 678763).

REFERENCES

- [1] Z. Li, P. Graziosi, and N. Neophytou, *Deformation potential extraction and computationally efficient mobility calculations in silicon from first principles*, Phys. Rev. B **104**, 19, 195201 (2021).
- [2] P. Graziosi, Z. Li, and N. Neophytou, *ElecTra code: Full band electronic transport properties of materials*, Computer Physics Communications **287**, 108670 (2023).

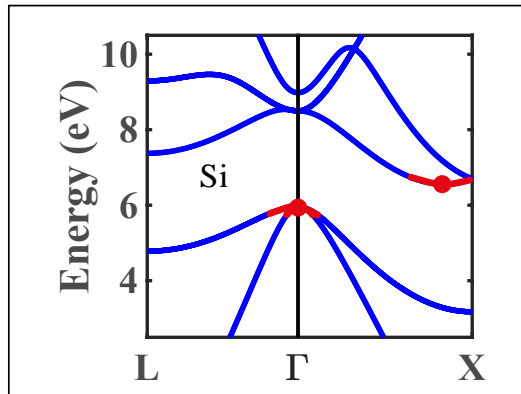


Fig. 1. Electronic structure of Si with relevant transport regions indicated in red [1].

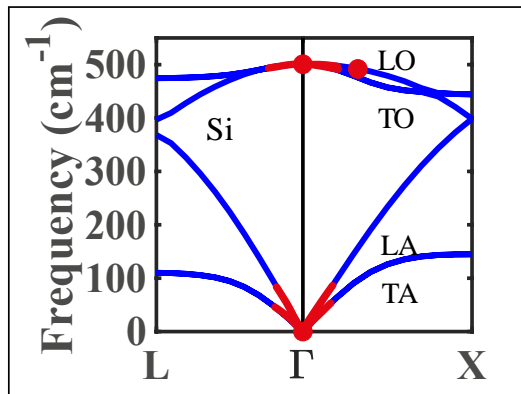


Fig. 2. Phonon spectrum of Si with scattering relevant regions indicated in red [1].

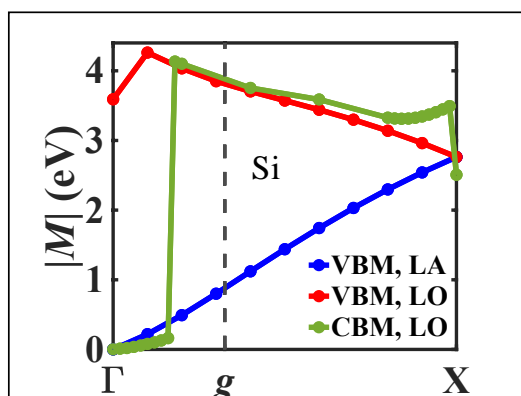


Fig. 3. Matrix elements involving LA and LO modes for the valence and conduction bands in Si [1]. For the CBM and LO mode, clearly the inter-valley nature of the g -process is evident (green line is zero close to Γ , and finite close to g)

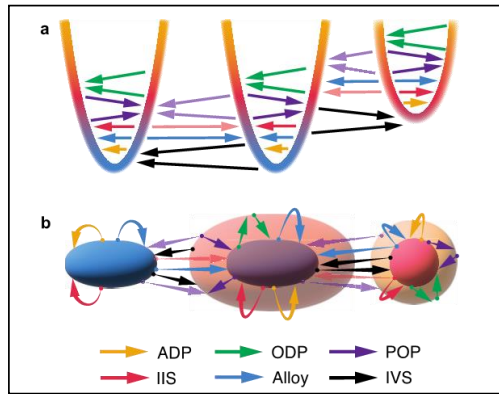


Fig. 4. Illustration of scattering transitions in *ElecTra* code: (a) intra/inter-valley and (b) elastic/inelastic transitions [2].

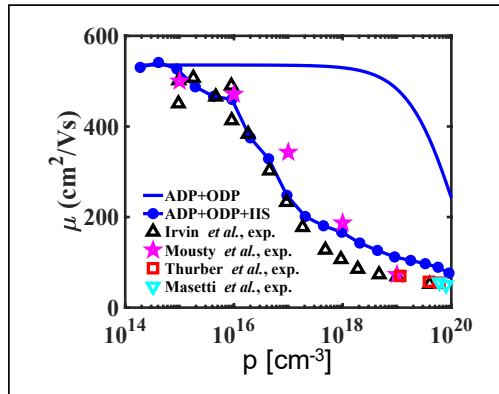


Fig. 5. Fully ab initio calculated Si hole mobility (blue lines) and comparison to experimental data [1].

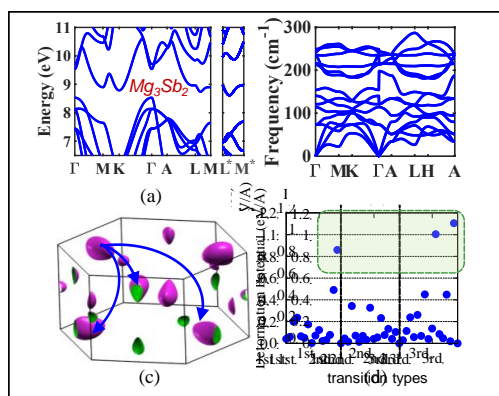


Fig. 6. Matrix element extraction in a complex band material Mg_3Sb_2 . (a-b) Electronic and phononic structure. (c) Three dominant transition types. (d) Matrix elements for each transition type involving all phonon branches.

Modelling of Schottky-Barrier Diodes Operating under Strong Reverse-Bias Conditions

B. Orfao, B. G. Vasallo, S. Pérez, J. Mateos, and T. González

Dpto. de Física Aplicada and USAL-NANOLAB, Universidad de Salamanca, 37008 Salamanca, Spain
e-mail: tomasg@usal.es

ABSTRACT

We report on a Monte Carlo (MC) model which includes the physical phenomena necessary to correctly simulate Schottky-barrier diodes (SBDs) operating under strong reverse-bias conditions, particularly relevant to regions of the diodes where a very high electron tunnel injection takes place, like the contact edge or surface inhomogeneities. The model is applied to the analysis of GaN diodes with 1D and (more realistic) 2D topologies.

INTRODUCTION

The correct modelling of reverse current in SBDs is essential to predict their breakdown. Ideal thermionic-emission and tunneling currents are typically estimated assuming full depletion (FD) in the semiconductor adjacent to the metal [1]. However, in regions of the diode surface where the number of injected electrons is very high, the FD assumption does not hold anymore. In such a case, the barrier profile determining electron tunnel injection must be self-consistently calculated with carrier concentration in the partially depleted region, being necessary the simulation of carrier transport. Impact ionization (II) initiated by the injected electrons, and also by the generated holes, is especially critical, since very high electric fields are reached, particularly in some regions like the contact edges [2]. In this work we address this issue for the case of GaN SBDs by means of MC simulations where all the involved physical effects are carefully modeled.

MODEL

The model includes tunnel injection with barrier lowering [3], electron and hole transport [4,5], with II implemented by means of the Keldysh approach [5], and self-consistency between the shape of the energy barrier and carrier concentration in the adjacent semiconductor [6].

RESULTS

Fig. 1 shows the I-V curves calculated at 300 K for a large-area GaN SBD (1D geometry, uniform in transversal direction) with active region length 1.0 μm , doping $4 \times 10^{17} \text{ cm}^{-3}$ and barrier height 0.6 eV. As observed, the FD assumption overestimates the current, and the contribution of the carriers generated by II events (triangles), calculated as the hole current at the Schottky contact (SC), becomes relevant for voltages beyond -40 V. As shown by Fig. 2, electrons injected by tunneling at the SC gain energy from the very high field inside the device [see Fig. 3(b)] and originate II events as they drift left. Generated holes, in turn, also originate II processes while moving right towards the SC. As a result, carrier concentrations exhibit the profiles shown in Fig. 3(a). Note the relevant differences existing between the results (current level, carrier concentration, electric field profile) obtained with and without considering II [6].

In more realistic diodes with 2D geometries, very high values of the electric field as those reached in the previous 1D structure are found near the contact edge, region at which avalanche breakdown may be initiated [2]. Such effects can be mitigated by the selection of an appropriate passivation dielectric [7]. Fig. 4 reports results corresponding to the small-area 2D GaN diode sketched in Fig. 4(a) [barrier height 0.5 eV, I-V curve in Fig. 4(b)]. Figs. 4(c) and (d) show the electron concentration for an applied voltage of -30 V considering air and Si_3N_4 as passivation dielectric. As observed, tunnel injection is much more pronounced at the contact edge, where the vertical electric field is stronger, this effect being reduced using a higher κ dielectric, like Si_3N_4 . Figs. 4(e) and (f), corresponding to -40 V and air as dielectric, show electron and hole concentration. For this bias the epilayer is totally depleted. The high hole density near the contact edge evidences that significant II is taking place, ultimately

leading to the avalanche breakdown of the device when the bias is further increased ($V_{break} \approx -68$ V).

ACKNOWLEDGMENTS

This work has been partially supported through Grant PID2020-115842RB-I00 funded by MCIN/AEI/10.13039/501100011033. B. Orfao thanks the PhD contract from the Junta de Castilla y León.

REFERENCES

[1] W. Li, D. Saraswat, Y. Long, K. Nomoto, D. Jena, and H. G. Xing, *Appl. Phys. Lett.* **116**, 192101 (2020).
 [2] X. Liu, F. Lin, J. Li, Y. Lin, J. Wu, H. Wang, X. Li, S. Huang, Q. Wang, H.-C. Chiu, and H. C. Kuo, *IEEE Trans. Electron. Dev.* **69**, 1938 (2022).
 [3] B. Orfao, G. Di Gioia, B. G. Vasallo, S. Pérez, J. Mateos, Y. Roelens, E. Frayssinet, Y. Cordier, M. Zaknoute, and T. González, *J. Appl. Phys.* **132**, 044502 (2022).
 [4] S. García, S. Pérez, I. Íñiguez-de-la-Torre, J. Mateos, and T. González, *J. Appl. Phys.* **115**, 044510 (2014).
 [5] S. Chen and G. Wang, *J. Appl. Phys.* **103**, 023703 (2008).
 [6] T. González, B. Orfao, S. Pérez, J. Mateos, and B. G. Vasallo, *Appl. Phys. Express* (2023). DOI:10.35848/1882-0786/acb9d4
 [7] B. Orfao, B. G. Vasallo, S. Pérez, J. Mateos, D. Moromelgar, M. Zaknoute, and T. González, *IEEE Trans Electron Dev.* **68**, 4296 (2021).

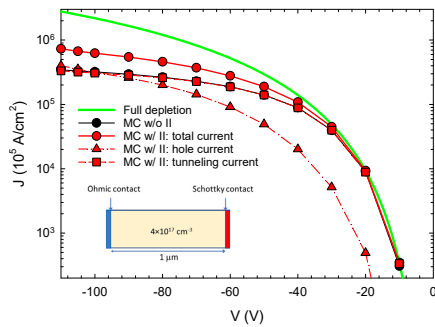


Fig. 1. I-V curve under reverse bias conditions calculated at 300 K for the diode in the inset using different models (FD assumption, MC without and with II) jointly with hole and tunneling contributions at the SC in the case of MC with II.

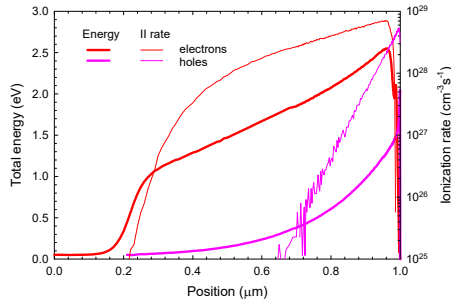


Fig. 2. Profiles of total average energy and II rate of electrons and holes for a bias voltage of -100 V.

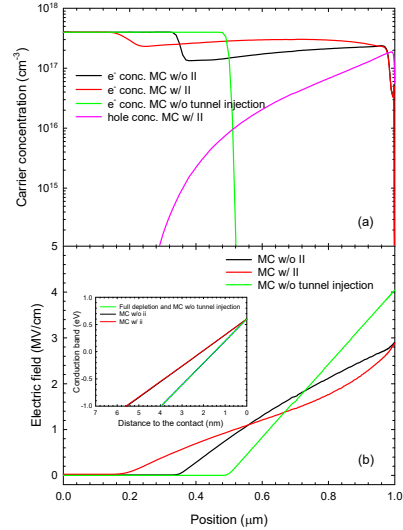


Fig. 3. (a) Profiles of carrier concentration for $V = -100$ V calculated with and without considering II in MC simulations, as well as without tunnel injection. (b) Corresponding electric field profiles. The inset shows the conduction band at the SC for the same cases (with the metal Fermi level as zero-energy reference) compared with the FD approximation.

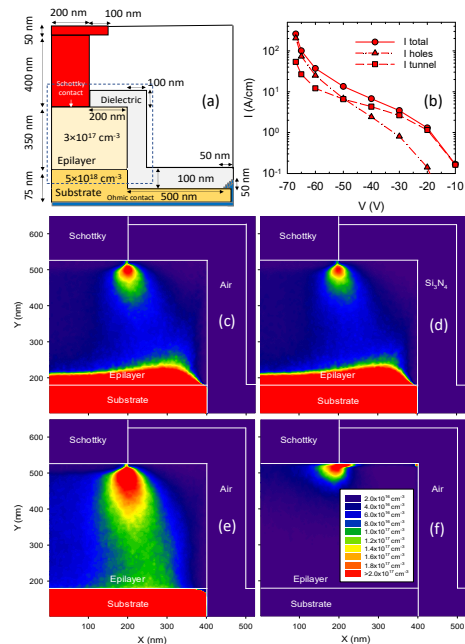


Fig. 4. (a) Sketch of the 2D diode. (b) I-V curve. Color maps of electron concentration for an applied voltage of -30 V in the area delimited in (a) by the dashed rectangle using: (c) air and (d) Si_3N_4 as passivation dielectrics. (e) Electron and (f) hole concentration for $V = -40$ V and air as dielectric.

Influence of Deformation Potential Scattering on Impact Ionization in Ultra-Wide Bandgap Materials

J. Shoemaker, R. Vatan, T. Biswas, A. Singh, M. Saraniti, S.M. Goodnick
Arizona State University, Tempe, AZ, USA
e-mail: stephen.goodnick@asu.edu

INTRODUCTION

A major advantage of ultra-wide band gap (UWBG) materials for power electronic applications are the predicted high breakdown voltages limited by avalanche breakdown due to impact ionization. However, experimental data on the impact ionization coefficients in these new class of materials is limited. Theoretical calculations of ionization coefficients using Monte Carlo methods are highly influenced by the choice of impact ionization and deformation potential scattering rates, which in turn are dependent on the electronic structures and phonon dispersions used as inputs. In the present paper, we present comparisons of the impact ionization and electron-phonon deformation potential scattering rates using various combinations of pseudopotential, electronic structure, and phonon dispersion inputs.

MODEL

The impact ionization and electron-phonon deformation potential scattering rates are computed from Fermi's golden rule. Electronic structures are computed from DFT using Quantum Espresso and from GW using BerkeleyGW. Phonon dispersions are calculated from DFPT using Quantum Espresso and from an empirically fitted valence force field model. K-vector dependent deformation potentials are computed using EPW in Quantum Espresso. The impact ionization coefficient is calculated from full band cellular Monte Carlo (CMC) simulation as shown in Fig. 3.

DISCUSSION

Although DFT produces a similar band structure to that from GW, Fig. 1 shows that there are notable differences between the two, even after correcting DFT's band-gap to match GW's. The influence of deformation potential inputs on the deformation scattering rate can be clearly seen in Fig. 2. Fig. 3 demonstrates that empirical models

such as VFF, although computationally inexpensive, have major differences from those computed from more fundamental methods. As seen in Fig. 4, the effect of different constant values chosen for the phonon deformation potentials shows a strong sensitivity of the impact ionization coefficient on the assumed deformation potentials, demonstrating the need for k-vector dependent deformation potentials from accurate phonon dispersion inputs.

CONCLUSION

Using inputs calculated from first principles methods can help to compensate for the shortage of experimental data available for newer materials such as UWBG semiconductors. More traditional approximations, such as constant deformation potential values and empirical electronic and phonon dispersions, aren't sufficiently accurate for predicting UWBG material ionization coefficients. GW electronic structures and DFPT phonon dispersions help to produce more accurate ionization coefficients, but it is important to compare the various choices for pseudopotential functions.

ACKNOWLEDGMENT

This work was supported as part of ULTRA, an Energy Frontier Research Center funded by the U.S. Department of Energy (DOE), Office of Science, Basic Energy Sciences (BES).

REFERENCES

- [1] Saraniti, Marco, and Stephen M. Goodnick. "Hybrid fullband cellular automaton/Monte Carlo approach for fast simulation of charge transport in semiconductors." *IEEE Transactions on Electron Devices* 47.10 (2000): 1909-1916.
- [2] Giannozzi, Paolo, et al. "QUANTUM ESPRESSO: a modular and open-source software project for quantum simulations of materials." *Journal of physics: Condensed matter* 21.39 (2009): 395502.

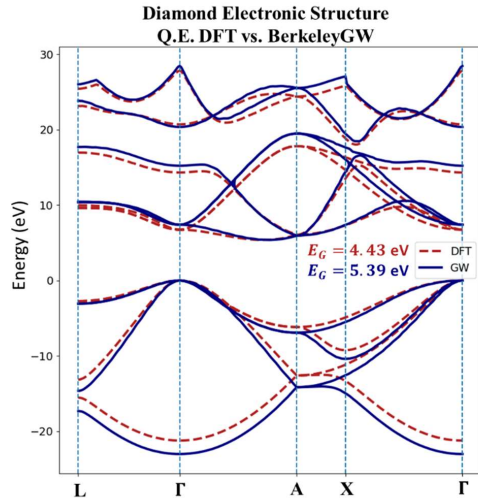


Fig. 1. Electronic structures computed from Density Functional Theory (DFT) using Quantum Espresso (red) and from GW using BerkeleyGW (blue). The DFT electronic structure conduction bands are shifted to match the GW-calculated band-gap (values shown on figure).

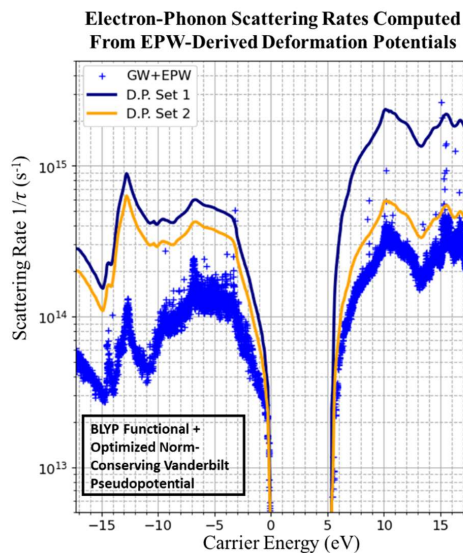


Fig. 2. Electron-Phonon scattering rates computed from EPW-derived deformation potentials, using GW energies and wavefunctions as input (blue). The phonon band structure is computed using DFPT in Quantum Espresso. Both sets of points calculated using a BLYP functional and optimized norm-conserving Vanderbilt pseudopotential input.

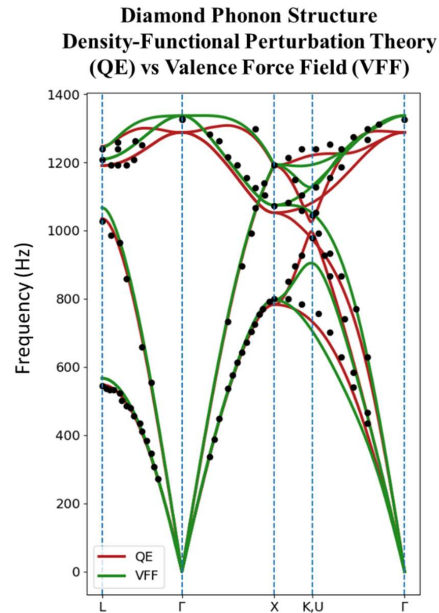


Fig. 3. Phonon dispersions computed from Density Functional Perturbation Theory (DFPT) using Quantum Espresso (red) and from Valence Force Field (VFF) model (green). The DFPT phonon structure is computed using a BLYP functional and optimized norm-conserving Vanderbilt pseudopotential input.

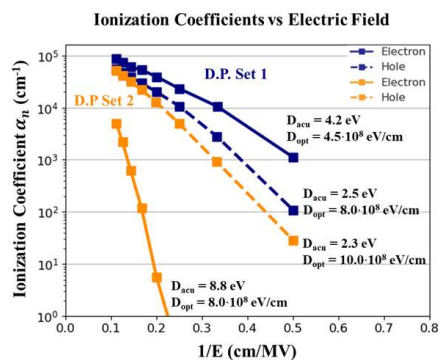


Fig. 4. Impact ionization coefficients from Monte Carlo simulations using two different sets of constant deformation potentials as input. The blue curves use the deformation potential scattering rate (shown in Fig. 2) computed from D.P. Set 1 (inset), and the orange curves use the rate computed from D.P. Set 2 as input. The resulting ionization coefficients are highly influenced by the choice of deformation potential values.

Upper Valley and Degeneracy Interplay on the Mobility of Transition Metal Dichalcogenides: Insights from Monte Carlo Simulation

José M. Iglesias⁽ⁱ⁾, Karol Kalna⁽ⁱⁱ⁾, Raúl Rengel⁽ⁱⁱⁱ⁾ and Elena Pascual⁽ⁱⁱⁱ⁾

⁽ⁱ⁾ Department of Applied Mathematics, University of Salamanca, 37008 Salamanca, Spain

⁽ⁱⁱ⁾ Nanoelectronic Devices Computational Group, Faculty of Science & Engineering, Swansea University, Swansea SA1 8EN, Wales, United Kingdom

⁽ⁱⁱⁱ⁾ Department of Applied Physics, University of Salamanca, 37008 Salamanca, Spain
e-mail: josem88@usal.es

INTRODUCTION

Carrier mobility and carrier high-field drift velocity of transition metal dichalcogenides (TMDs) are fundamental transport properties needed to advance the TMD device technology. Despite an ongoing research, significant disparities between experimental results and theoretical models persist, largely due to a significant surface-to-volume ratio of atomically thin TMDs, which renders them particularly susceptible to environmental factors.

In this study, we employed our in-house ensemble Monte Carlo (EMC) simulator to examine the impact of degeneracy and screening on a low-field electron mobility and a high-field electron drift velocity, specifically studying the influence of carrier concentration and temperature. We accounted for a full screening of scattering events, including intrinsic processes [1]. Our findings indicate that free carrier screening, along with other factors, plays a crucial role in comprehending the non-monotonic behavior of mobility as a function of carrier concentration in the most widely used TMDs, such as MoS₂ or WS₂.

MODEL

The in-house EMC simulator was successfully tested in previous research on various 2D materials [2-5]. The transport model employed a multi-band, multi-valley band structure, with the conduction band of TMD materials described by primary valleys (K points of the first Brillouin zone) and secondary valleys (Q points) utilizing parabolic dispersion relations in the vicinity of the valley

minima. In the valence band, the maxima are situated in the K points, as for direct gap materials, while the secondary valleys are located at the Γ point at lower energy (see Table 1). Effective masses for electrons and holes are derived from density functional theory calculations [6, 7]. Isotropic masses were considered for the K valleys, while longitudinal and transverse effective electron masses are considered for the Q valleys. This analytical description of the bands has demonstrated a good agreement with full-band models in EMC simulations for TMDs, while being more computationally efficient [8].

RESULTS

This study analyzed the effect of free carrier screening and degeneracy on the electronic transport properties of 2D TMD materials supported on a dielectric substrate. The EMC simulator showed that the mobility of electrons and holes exhibited a strong non-monotonic dependence (see Fig. 1) with carrier concentration n at the lowest temperature under study. The highest mobility for electrons was achieved at $T = 77$ K and $n = 5 \cdot 10^{12}$ cm⁻². At intermediate n values, the progressive increase in electron mobility up to maximum values is attributed to the effect of screening on intrinsic scattering mechanisms in the K valleys. At larger n , the mobility dropped due to the increasing proportion of electrons reaching the upper Q valleys, leading to additional electron scatterings. The electron drift velocity at high electric fields was influenced by the SPP scattering in the K valleys, acting as an effective energy relaxation mechanism.

REFERENCES

- [1] N. Ma and D. Jena, "Charge Scattering and Mobility in Atomically Thin Semiconductors," *Phys. Rev. X* **4**, 011043 (2014)
- [2] E. Pascual, J. M. Iglesias, M. J. Martín and R. Rengel, "Harmonic Extraction in Graphene: Monte Carlo Analysis of the Substrate Influence," *Materials* **14**, 5108 (2021)
- [3] E. M. Hamham, J. M. Iglesias, E. Pascual, M. J. Martín and R. Rengel, "Impact of the hot phonon effect on electronic transport in monolayer silicene," *Phys. Rev. X* **51**, 415102 (2018)
- [4] J. M. Iglesias, E. Pascual, M. J. Martín and R. Rengel, "High-order harmonic generation in 2D transition metal disulphides," *Appl. Phys. Lett.* **119**, 012101 (2021)
- [5] R. Rengel, O. Castelló, E. Pascual, M. J. Martín and J. M. Iglesias, "Monte Carlo study of noise velocity fluctuations and microscopic carrier transport in monolayer transition metal dichalcogenides," *J. Phys. D: Appl. Phys.* **53**, 395102 (2020)
- [6] X. Li, J. T. Mullen, Z. Jin, K. M. Borysenko, M. Buongiorno Nardelli and K. W. Kim, "Intrinsic electrical transport properties of monolayer silicene and MoS₂ from first principles," *Phys. Rev. B* **87**, 115418 (2013)
- [7] Z. Jin, X. Li, J. T. Mullen and K. W. Kim, "Intrinsic transport properties of electrons and holes in monolayer transition-metal dichalcogenides," *Phys. Rev. B* **90**, 045422 (2014)
- [8] A. Pilotto, P. Khakbaz, P. Palestri and D. Esseni, "Semi-classical transport in MoS₂ and MoS₂ transistors by a Monte Carlo approach," *Solid-State Electron.* **192**, 108295 (2022)

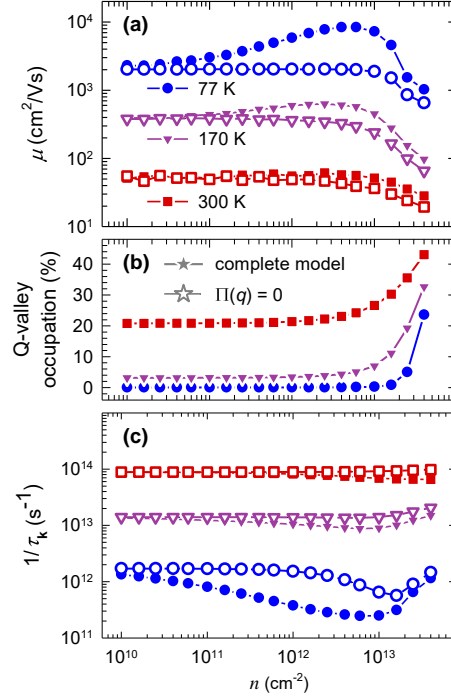


Fig. 1. (a) Low-field electron mobility, (b) upper (Q) valley occupation, and (c) inverse of momentum relaxation time due to scattering mechanisms at three different temperatures in monolayer MoS₂ supported on a SiO₂ substrate. Solid symbols relate to simulations accounting for all the phenomena of the EMC model, and open symbols to results where the screenings due to free carrier is omitted.

TMD	Conduction band			Valence band		
	m_K^* (u. of m_0)	$m_{Q,\parallel}^*, m_{Q,\perp}^*$ (u. of m_0)	$\epsilon_{0,Q} - \epsilon_{0,K}$ (meV)	m_K^* (u. of m_0)	m_{Γ}^* (u. of m_0)	$\epsilon_{0,K} - \epsilon_{0,\Gamma}$ (meV)
MoS ₂	0.50	0.62, 1.00	70	0.58	4.05	148
WS ₂	0.31	0.60, 0.60	67	0.42	4.07	173
MoSe ₂	0.64	0.80, 0.80	28	0.71	7.76	374
WSe ₂	0.39	0.64, 0.64	16	0.51	7.77	427

Table 1. Band structure parameters for the effective mass approximation in various TMDs.

Where is semiconductor technology heading? A view from industry and implications on computational nanotechnology

Carlos H. Díaz

R&D, Taiwan Semiconductor Manufacturing Company, Ltd., 121, Park Ave. 3, Hsinchu, Taiwan. Email: chdiaz@tsmc.com

Abstract – The quest for sustainable growth in computing performance and expanded functional capabilities of information technology and communication (ICT) products requires energy-efficiency improvements of underlying technologies in devices, systems, architectures, algorithms and software, and information representation and processing. This paper discusses emerging transistors, memories, and interconnect fabrics. The paper highlights open research areas, the necessary completeness of the metrics, and associated modeling challenges to identify viable alternatives to state-of-the-art technologies and their projected evolutionary paths.

Introduction

Bridging the gap between existing silicon nanotechnology and future VLSI needs innovations in devices and interconnect fabrics, each and all-cohesively enabling higher integration-density, performance improvements, and capabilities at lower power consumption cross-generations. Continued growth in computing capacity requires significant improvements in energy efficiency for it to be sustainable as illustrated in Fig.1 adapted from the SRC-SIA Decadal Plan of Semiconductors [1]. Artificial intelligence (AI) is a key element in the fourth industrial revolution. Increased cognitive capabilities are key to next generation AI, attaining them while decreasing the power consumption will be critical regardless of application domain as illustrated in Fig. 2. The quest for the necessary energy efficiency requires innovations at all levels from the basic technology structures and building blocks to the system architectures and algorithms. Research and development monumental efforts on silicon-based CMOS technology scaling continuously raise the bar that emerging devices and interconnects need to meet for value [2]. This paper overviews progress and research challenges for some of the leading emerging devices and interconnect fabrics.

Transistors

Power supply scaling is a critical knob in boosting energy efficiency from generation to generation, capacitance being the other. The optimal nominal operating voltage (minimum) for a given speed goal is bounded to the left by leakage power and to the right by active power as illustrated in Fig 3. To retain or improve switching speeds while also reducing power supply, materials with significantly better transport properties than silicon are needed as shown in Fig.3. Transistor structures such as stacked gate-all around channels will enable improved electrostatic control / steeper subthreshold slope than present Fin-FETs resulting in significant reduction of minimum operating voltages as shown in Fig. 4 [2]. Exploratory work on low-dimensional materials such as transition metal dichalcogenides [3], graphene nanoribbons [4,5], or carbon nanotubes [6,7] seeks to demonstrate higher than state-of-the-art drive current capability per unit footprint while also reducing transistor capacitances. Wafer-scale device-quality channel material synthesis - placement - patterning, reliable ultra-thin gate-dielectrics, gate-stacks supporting multiple work-functions, and thermally stable ultra-low resistivity contacts remain critical challenges. Figures 5 to 8 illustrate some of the best results to date for low dimensional materials. Despite these advancements, significant theoretical and experimental work still needed to identify true platform-viable alternatives to silicon-based CMOS transistors. Comprehensive and predictive fundamental transport models that can realistically project on and off-state capabilities including thermally and mechanically stable low-resistance

contacts remain imperative. Also key is accelerating the turn-around time (TAT) for fundamental screening of new materials synthesis and processing concepts through modeling.

Memory Elements and Arrays

A representative compute memory hierarchy of a computing system is shown in Fig. 9. Emerging memory devices in a given level of the memory hierarchy must outperform incumbent technologies on critical indexes to be considered promising alternatives. Those critical indexes include density, energy efficiency, speed, endurance, retention, environmental robustness, controllability, and complexity as proxy to cost/bit. SOT-MRAM is a potential alternative being explored as an SRAM alternative, demonstrating materials and cell structures with low-operating current while supporting tight write-error rates and magnetic immunity requirements remain challenging as illustrated in Fig. 10. Ferroelectric memories are also subject of active research for their high density and energy-efficiency potential [13], progress in understanding and resolution of endurance has recently being reported [14] as shown in Fig. 11. Emerging memory research and development demands ever increasing modeling capabilities to enable accurate, predictive, and fast TAT mapping of the design space including process variability, bit-error-rate, retention, and endurance metrics that along with power-performance-area (PPA) indicators are key to assert alternative memory cells across the memory hierarchy.

Interconnect fabrics

The resistance of vias, via-line interfaces, and lines represent a continuous challenge to the attainable chip-level performance and energy efficiency in advanced nodes. The search for materials with the goal of 2x or larger resistance reduction over elemental state-of-the-art solutions is a top challenge; yet when successful significant power-performance benefits are expected at the corresponding inception node as illustrated in Fig. 12. Inter-chip data movement (e.g. between external memory and processing units) is also an area of significant opportunities for elevating the system-level performance and energy efficiency. Scalable 3D-interconnect fabrics enabling increasingly higher intra and cross-die connection density as shown in Fig. 13 will be instrumental to denser VLSI systems supporting very high memory bandwidths [15,2].

Conclusion

Systems with increased levels of performance, functionality, and density will require increasingly more significant energy-efficiency innovations from software to process technology. Significant progress continues to be made in exploratory devices and interconnects. Yet challenges remain to attain proofs of concept which meet complete sets of critical metrics asserting their potential over evolutionary state-of-the-art silicon-based pathways. To this end experimental efforts compounded with a robust computational modelling framework remains imperative to efficient and effective research and pathfinding as illustrated in Fig. 14 [16].

References

- | | |
|--|--|
| [1] SRC Decadal Plan for Semiconductors. | [9] G. Pitner et al., Nano Letter, 2019. |
| [2] M. Liu, IEEE ISSCC, 2020. | [10] Q. Cao et al., Science, 2015 |
| [3] T.-A. Chen et al., Nature, 2020. | [11] A. Franklin, Nat. Nano, 2010 |
| [4] A. Way et al., J. Phys. Chem. Lett., 2019. | [12] S. Lin et al., IEEE IRPS, 2021. |
| [5] Z. Mutlu et al., ACS Nano, 2021. | [13] A. Tan et al., arXiv:2103.08806v1. |
| [6] J. Wang et al., Nature Catalysis, 2018. | [14] P. J. Liao et al., IEEE IRPS, 2021. |
| [7] G. Pitner et al., IEEE IEDM, 2020. | [15] D. Yu, IEEE ISSCC, 2021. |
| [8] Tang et al., VLSI Tech. Symp., 2017. | [16] J. Wu, et al., IEEE SISPAD 2021. |

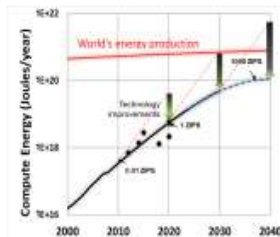


Fig. 1. Technology improvements will become increasingly important to sustain computational capacity growth over the next decades [1].

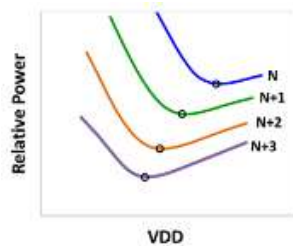


Fig. 2. Power supply scaling critical knob for cross-generation enhancements in energy-efficiency.

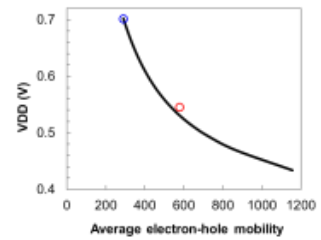


Fig. 3. Channel materials with significantly better transport properties critical to boost drive strength and circuit speed while scaling power supply.

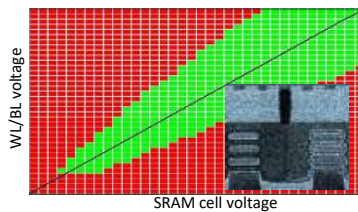


Fig. 4. Stacked gate-all-around channel structures to enable V_{DD} scaling beyond Fin-FETs, c.f. [2].

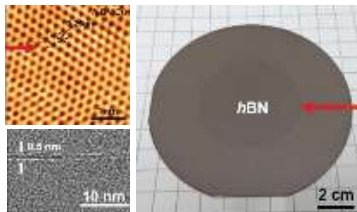


Fig. 5. Wafer-level synthesis demonstration of 2D channel materials and interlayer gate dielectrics [3].

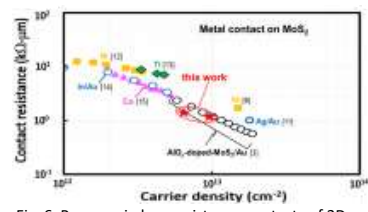


Fig. 6. Progress in low-resistance contacts of 2D TMDs [4]. Aside additional improvements in R_c, thermal stability, and CMOS capability also critical.

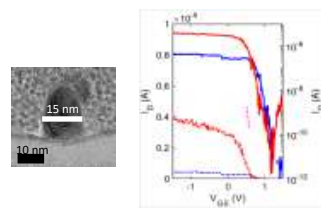


Fig. 7. Top-gated CNTs with ALD interlayer dielectric and HK attaining 65mV/dec @ L_g ~ 15 nm [7]. Progress on the synthesis of oriented and regularly spaced CNTs also continues to make inroads [6].

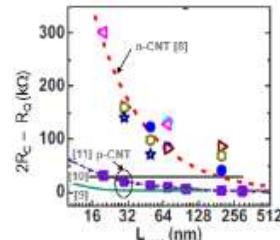


Fig. 8. Thermally stable low-resistance contacts for n/p-CNT transistors are subjects of active research.

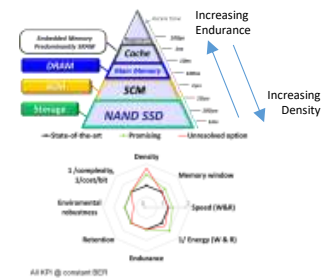


Fig. 9. Memory hierarchy and key research metrics.

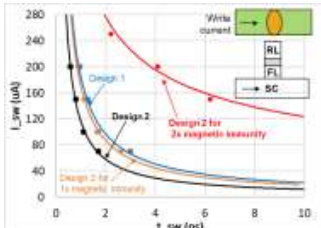


Fig. 10. SOT-MRAM type-Y cells support field-free operation. Low write current under density, magnetic immunity, write speed, and tight error requirements remain challenging.

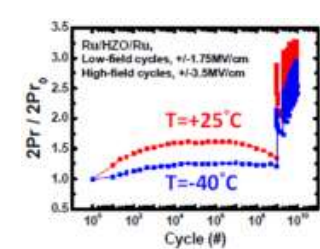


Fig. 11. Progress in fundamental understanding and approaches to high endurance ferroelectric memory cells has been reported, c.f. [14].

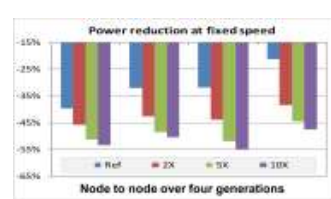


Fig. 12. Complex materials beyond elemental interconnect solutions continue to be searched with the goal of seeking 2x or larger via and line resistance reduction for significant chip-level power-performance benefits at inception node.

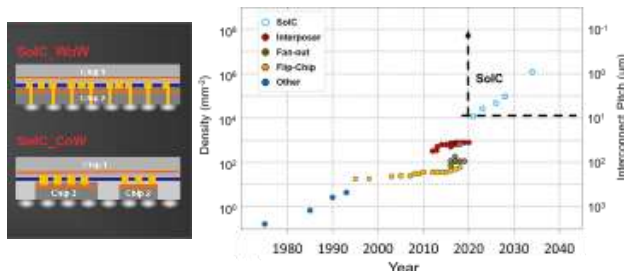


Fig. 13. New 3D stacking and interconnect fabrics will support sustainable I/O density increases.

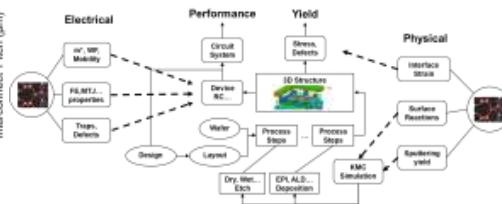


Fig. 14. A Virtual-Fab modeling framework.

Nanowire transport and edge passivation

P. Blaise¹, T. Kubis², E. Guichard¹

¹ Silvaco Inc., Santa Clara, CA 95054, USA and Montbonnot-Saint-Martin, 38330, FRANCE

² School of Electrical and Computer Engineering, Purdue University, West Lafayette, IN 47907, USA
e-mail: philippe.blaise@silvaco.com

ABSTRACT

The influence of edge passivation on quantum transport simulations of a silicon nanowire is revisited. Thanks to a combination of non-equilibrium Green's functions and state-of-the-art band structure calculations we extract I(V) characteristics of a p-doped and n-doped nanowire MOSFET (NWFET). A self-energy of passivation is parametrized, allowing us to gauge the impact of various edge chemistry on electrical characteristics.

INTRODUCTION

Non-equilibrium Green's functions (NEGF) allow us to perform a quantum transport simulation of an NWFET made of two leads and an active region, where carriers move according to a custom band structure (BS) [1].

One of the most efficient ways to describe the BS of a material is the Slater-Koster (SK) tight-binding (TB) model. The set of SK-TB parameters is usually based on accurate experimental measurements and can be extended to state-of-the-art density functional theory (DFT) data, including results of hybrid functionals [2].

We focus here on an NWFET structure made of pure Si [100] along the transport direction, with 3x3 nm² square cross-section. The two contacts are highly-doped Si with an intrinsic channel surrounded by SiO₂, see Fig. 1. NEGF calculations are performed using a recursive Green's function with low-rank approximation [3] and an sp³d⁵s* TB-basis. The transferability of the basis for correct description of the NW BS can be affected by the scheme employed to passivate the silicon dangling bonds. They are located around the nanowire, and to avoid too high complexity the Si/SiO₂ interface is usually not described explicitly.

MODEL

The BS obtained in DFT of the Si NW passivated with hydrogen are shown in Fig. 2 and

Fig. 3. Thanks to a self-energy technique [4] a fit to the DFT results is performed both for the valence and conduction bands. Note that this technique can be extended to a more complex Si/SiO₂ interface as shown Fig.4 obtained thanks to ab initio molecular dynamics [5] with the resulting band structure Fig. 5.

Taking into account the self-energy effect of passivation, the NEGF results for an n-doped and p-doped NWFET are shown Fig. 6 and Fig. 7 respectively. The passivation effect shows a decrease of the electronic current at high gate voltage and more pronounced for a p-NWFET.

CONCLUSION

Essentially the edges passivation of a nanowire can be included implicitly thanks to a custom self-energy. I(V) characteristics are influenced by the corresponding set of parameters, and conversely one can seek a good set of parameters as a function of passivation chemistry engineering.

ACKNOWLEDGMENT

We used the RCAC HPC resources @Purdue.

REFERENCES

- [1] R. Lake, G. Klimeck, R. C. Bowen and D. Jovanovic, *Single and multiband modeling of quantum electron transport through layered semiconductor devices*, J. Appl. Phys. vol. 81, pp. 7845-7869, (1997).
- [2] Y. Tan, M. Povolotskyi, T. Kubis, T.B. Boykin, and G. Klimeck, *Transferable tight-binding model for strained group IV and III-V materials and heterostructures*, Phys. Rev. B 94, 045311, (2016).
- [3] Lemus, D.A., Charles, J. & Kubis, T. *Mode-space-compatible inelastic scattering in atomistic nonequilibrium Green's function implementations*. J Comput Electron 19, 1389-1398 (2020).
- [4] Y. He, Y. Tan, Z. Jiang, M. Povolotskyi, G. Klimeck, and T. Kubis, *Surface Passivation in Empirical Tight Binding*, in IEEE Transactions on Electron Devices, vol. 63, no. 3, pp. 954-958, (2016).
- [5] J. M. Soler, E. Artacho, J.D. Gale, A. García, J. Junquera, P. Ordejón, and D. Sánchez-Portal, *The SIESTA method for ab initio order-N materials simulation*, J. Phys. Condens. Matter 14, 2745-2779 (2002).

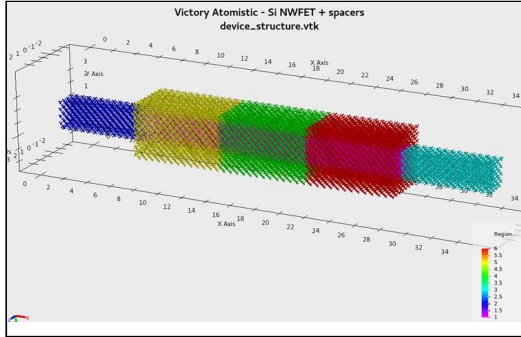


Fig. 1. MOSFET structure of a silicon nanowire oriented [100] with a square cross-section of $3 \times 3 \text{ nm}^2$.

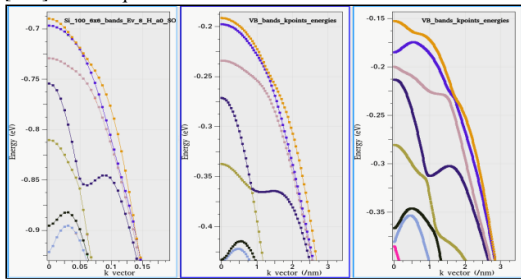


Fig. 2. Valence band structures of a slice of Si NW [100] obtained in DFT (left) and Tight-Binding (middle and right) with two different passivation schemes (fitted vs original).

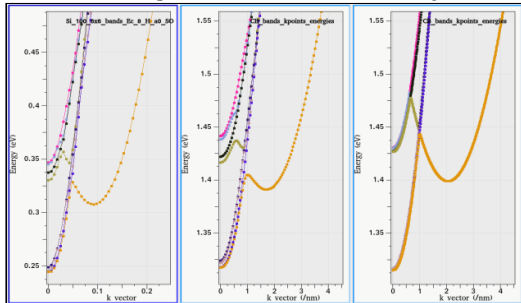


Fig. 3. Same as Fig. 2 for the valence band structures of a slice of Si NW [100] DFT (left), TB (middle and right).

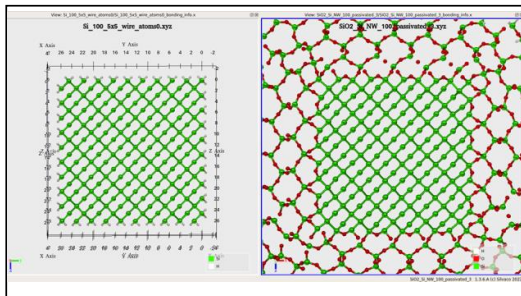


Fig. 4. Si NW [100] passivation of the dangling bonds with hydrogen atoms (left), with cristobalite SiO_2 (right).

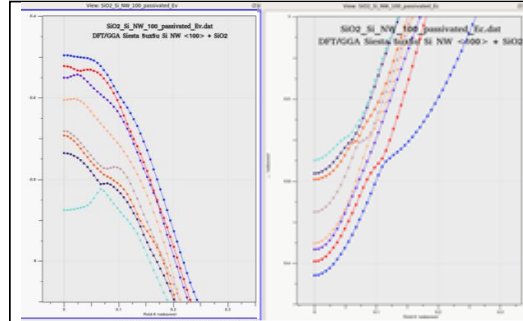


Fig. 5. Valence and conduction band structures of a slice of Si NW [100] (left and right respectively) with SiO_2 passivation obtained in DFT.

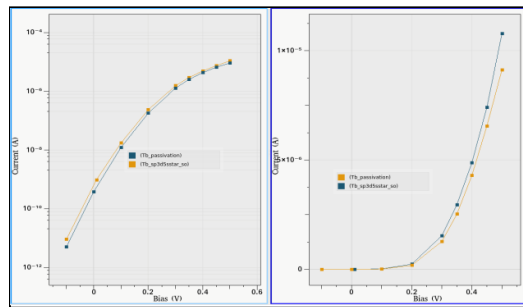


Fig. 6. I(V) curves of Si NW n-MOSFET with two different passivation schemes, one conventional with H- termination, and one that mimics the passivation obtained in DFT.

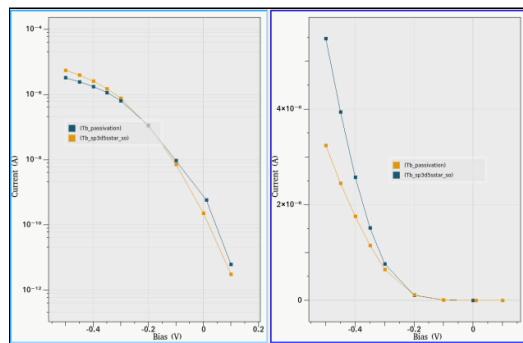


Fig. 7. I(V) curves of Si NW p-MOSFET with two different passivation schemes, one conventional with H- termination, one that mimics the passivation obtained in DFT.

Modeling Self-Heating Effects in 28 nm Technology Node Fully-Depleted SOI Devices

Z. Wang, D. Vasileska, C.S. Soares*, G.I. Wirth*, M.A. Pavanello** and M. Povolotskyi***

Arizona State University, Tempe, AZ, USA

*UFRGS, Porto Alegre, Brazil

**Centro Universitario FEI, Sao Bernardo do Campo, Brazil

*** Jacobs, Hanover, MD, USA

zwang581@asu.edu

Recently, excellent characteristics at 4.2K were demonstrated for Fully-Depleted (FD) SOI technologies. These electrical characteristics represent a great opportunity to use advanced CMOS in low-temperature environments such as space applications. Also, due to recent efforts to bring down quantum computing into mainstream technology, cryogenic control electronics for quantum computing is becoming of significant interest for low-temperature MOSFET operation.

In FDSOI devices the heat generated at the drain side is impeded by the low thermal conductivities of the buried oxide (BOX) and the thin Si layer constituting the channel (due to phonon boundary scattering). Self-heating effects (SHE) lead to a significant increase in the channel temperature when the device is in its on-state. The channel temperature increase can severely affect the device performance by reducing the carrier mobility. Extensive studies, both experimental [1] and theoretical [2], are already conducted and published for room temperature device operation. Also, experimental studies were performed recently to understand SHE in FDSOI devices at cryogenic temperatures [3]. Hence, there is a need for simulation software able to explain existing experimental data and make reliable predictions for FDSOI devices with different channel lengths, silicon film and BOX thickness at various temperatures.

For that purpose, we developed a thermal device simulator for modeling SHE in FDSOI devices at temperatures down to 78K. Details about the theoretical model of our electro-thermal device solver can be found in Ref. [2]. Briefly, we solve the electron Boltzmann Transport Equation (BTE) using the Monte Carlo method self-consistently with the energy balance equations for both the

acoustic and the optical phonons. We account for the partial ionization of the dopants and the temperature and the thickness dependence of the thermal conductivity.

The device structure of interest (28nm technology node with 30 nm physical channel length n-FDSOI device with 7 nm silicon film thickness, 1.2 nm effective gate oxide and 25 nm thickness of the BOX) is schematically shown in Fig. 1. Simulated transfer characteristics (Fig. 2) are first compared with available experimental data at $T=300\text{K}$ [3]. Excellent agreement is observed between the experimental and simulated data in both sub-threshold and linear regions of operation of the device. In Fig. 3, we show the simulated transfer characteristics at $T=78\text{K}$, 150K and 300K . We observe that, at lower temperatures, the threshold voltage slightly increases due to the partial ionization of the dopants, in agreement with the experimental findings [3]. The lattice temperature profile at ambient temperature $T=300\text{K}$, and for $V_{gs}=0.6\text{V}$ and $V_{ds}=0.9\text{V}$, is shown in Fig. 4. In these simulations it is assumed that the source and drain contacts are perfect absorbers of heat. In Fig. 5, we show a comparison of the simulated and the experimental excess temperature in the channel for various input powers and for ambient temperatures $T=78\text{K}$, 150K and 300K . Experimentally, self-heating was obtained using the well-known gate resistance thermometry technique [1]. In this method, the thin gate dielectric layer allows one to assume that the temperature of the channel and that of the gate electrode are almost the same. Even though simulated channel temperatures are slightly higher at lower input power than the experimentally extracted values, the slope of the two curves, which gives the thermal resistance, is very similar. The discrepancy between the experimental

and the simulated data is attributed to the uncertainties in the experimental device dimensions and the simplified zero heat flux boundary condition for the lattice temperature on the gate electrode.

In summary, this work intends to fill the gap in obtaining relevant simulation data concerning self-heating in advanced FDSOI transistors at various temperatures.

REFERENCES

- [1] K. Triantopoulos *et al.*, *Self-heating effect in FDSOI transistors down to cryogenic operation at 4.2K*, IEEE Trans. Electron Devices **66**, no. 8, pp. 3498-3505 (2019).
- [2] K. Raleva, D. Vasileska, S. M. Goodnick and M. Nedjalkov, *Modeling Thermal Effects in Nanodevices*, IEEE Trans. Electron Devices **55**, no. 6, pp. 1306-1316 (2008).
- [3] M. Casse *et al.*, *FDSOI for cryoCMOS electronics: device characterization towards compact model*, IEDM (2022).

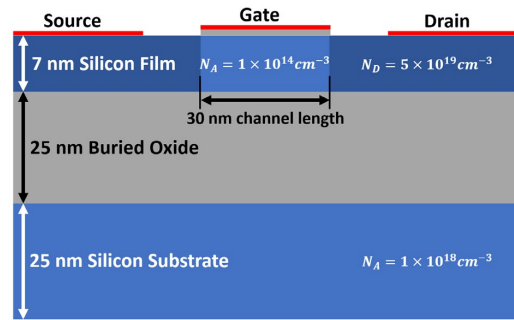


Fig. 1. FDSOI device structure being considered in this study.

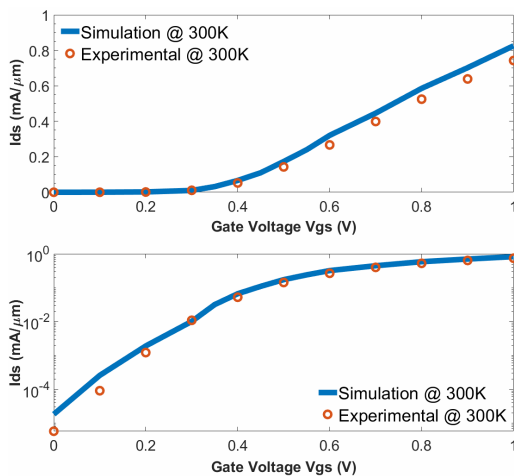


Fig. 2. Simulated transfer characteristics compared with available experimental data from Ref. [3] at T=300K. The applied drain voltage is Vds=0.9V.

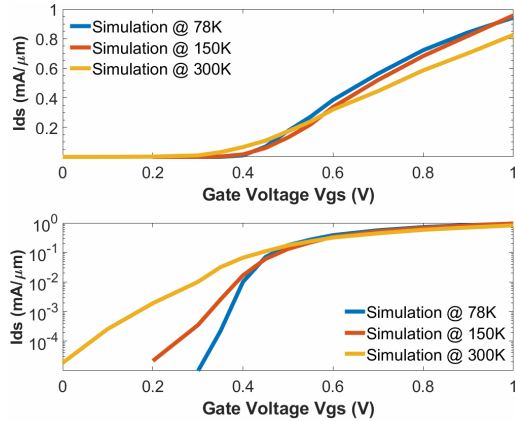


Fig. 3. Simulated transfer characteristics at 78K, 150K and 300K. The applied drain voltage is Vds=0.9V.

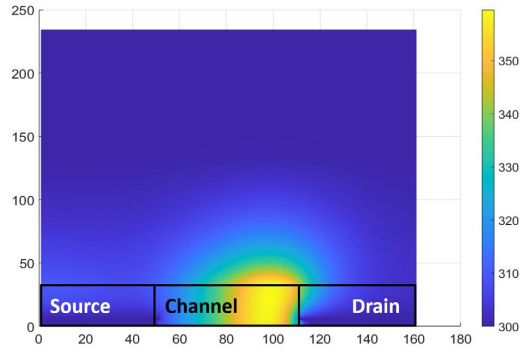


Fig. 4. Lattice temperature profile at ambient temperature T=300K for Vgs=0.6V and Vds=0.9V. We used boundary conditions with fixed temperature T=300K at source and drain contacts, and boundary condition with zero heat flux at the gate contact.

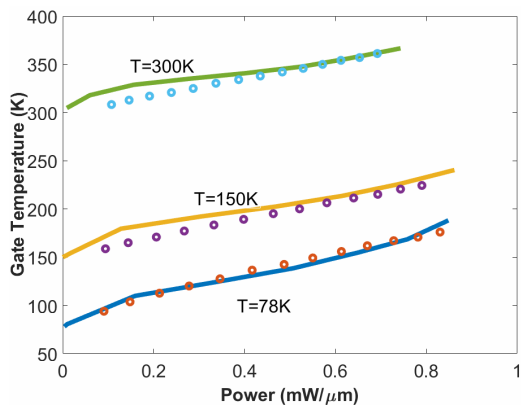


Fig. 5. Comparison of simulated (solid lines) and experimental (open circles) temperature under the gate for various input powers at T=78K, 150K and 300K.

Closing the “10-100 eV Gap” for Electron Thermalization in GaN Devices from First Principles

Dallin O. Nielsen¹, Chris G. Van de Walle², Sokrates T. Pantelides^{3,4}, Ronald D. Schrimpf⁴, Daniel M. Fleetwood⁴, and Massimo V. Fischetti¹

¹Department of Materials Science and Engineering, University of Texas at Dallas

²Materials Department, University of California, Santa Barbara

³Department of Physics and Astronomy, Vanderbilt University

⁴Department of Electrical and Computer Engineering, Vanderbilt University

Email: don170000@utdallas.edu

INTRODUCTION

Since the launch of Sputnik I in 1957, human presence in space has expanded greatly, and with it the demand for durable and reliable technologies, capable of operating in environments with high levels of radiation exposure. As a result, increased attention has been placed on radiation effects on electronic devices [1,2,3], and it has become necessary to improve the accuracy of computational models used to simulate these effects. The present work concentrates on radiation effects in GaN but can be extended to any material of interest.

The major focus of this work is to study theoretically the energy-loss processes that control the thermalization of hot electrons and/or electron-hole pairs that are generated by high-energy radiation in semiconductors. Current knowledge and capabilities cover both the high-energy range (energies above ~100 eV), where nuclear/particle-physics computational tools have been successfully applied [4], and the lower-energy range (below ~10 eV), which has been studied extensively by the electronic-device community [5]. The processes that control electron and hole thermalization in the

intermediate range are poorly known (the “10-100 eV gap”), with only a few studies (which used a free-electron model) showing losses to plasmons being the dominant process [6].

THEORETICAL MODELS

As electrons thermalize from the high-energy, free-electron regime into this intermediate range, they begin to feel the effects of the band structure, necessitating a first-principles calculation. Using the density functional theory (DFT) package Quantum ESPRESSO, we obtain the electronic band structure for 150 bands, reaching energies above 100 eV. We also calculate the phonon dispersion and the associated electron-phonon matrix elements to evaluate the electron- and hole-phonon scattering rates via Fermi’s Golden Rule (Fig. 1).

To deal with losses to plasmons and impact ionization, we utilize time-dependent DFT to calculate the dynamic dielectric function, $\epsilon(\mathbf{q}, \omega)$. Employing the fluctuation-dissipation theorem, we calculate the energy-loss rate (ELR), $1/\tau_n(\mathbf{k})$, of an electron in conduction band n with wavevector \mathbf{k} , in terms of the imaginary part of the inverse dielectric function [7,8,9]:

$$\frac{1}{\tau_n(\mathbf{k})} = \frac{2\pi}{\hbar} \sum_{n'} \int \frac{d\mathbf{q}}{(2\pi)^3} \frac{e^2 \hbar}{q^2} \int \frac{d\omega}{2\pi} \text{Im} \left[\frac{-1}{\epsilon(\mathbf{q}, \omega)} \right] \left\{ \frac{n(\omega)}{1+n(\omega)} \right\} \delta[E_n(\mathbf{k}) - E_{n'}(\mathbf{k} + \mathbf{q}) \pm \hbar\omega], \quad (1)$$

where $n(\omega)$ is the Bose-Einstein distribution function (Fig. 1). The loss function $\text{Im}[-1/\epsilon(\mathbf{q}, \omega)]$ exhibits peaks (shown in Fig. 2), associated with either plasmon losses or impact ionization. Plasmon peak positions yield the dispersion of the valence sp - and d -electron plasmons and their widths yield the plasmon lifetimes (Fig. 3).

MONTE CARLO SIMULATION

Using the above results in a full-band Monte Carlo program, we study the time dependence of the thermalization of electrons and high-energy hole generation in GaN. Using a synchronous ensemble, electrons are allowed to advance through time with

interaction mechanisms and subsequent final states being chosen stochastically. Electron-hole pairs are generated when impact ionization or plasmon emission is chosen. Thanks to the extremely short plasmon lifetimes (Fig. 3, bottom frame), we have assumed their immediate decay into electron-hole pairs. Full thermalization is achieved in ~1 ps (Fig. 4). Hot electrons produce pairs with an average energy of ~9.4 eV/pair, and spread ~ 10^{-7} m from their starting positions (important for device simulation).

ACKNOWLEDGMENT

This work was supported by the Air Force Office of Scientific Research: Award FA9550-21-0461, and

through the Center of Excellence in Radiation Effects: Award FA9550-22-1-0012.

REFERENCES

1. P. E. Dodd, IEEE Trans. Device Mater. Rel. **5**, 343 (2005).
2. A. F. Witulski, D. R. Ball, K. F. Galloway, A. Javanainen, J.-M. Lauenstein, A. L. Sternberg, and R. D. Schrimpf, IEEE Trans. Nuc. Sci. **65**, 1951 (2018).
3. D. M. Fleetwood, E. X. Zhang, R. D. Schrimpf and S. T. Pantelides, IEEE Trans. Nuc. Sci. **69**, 1105 (2022).

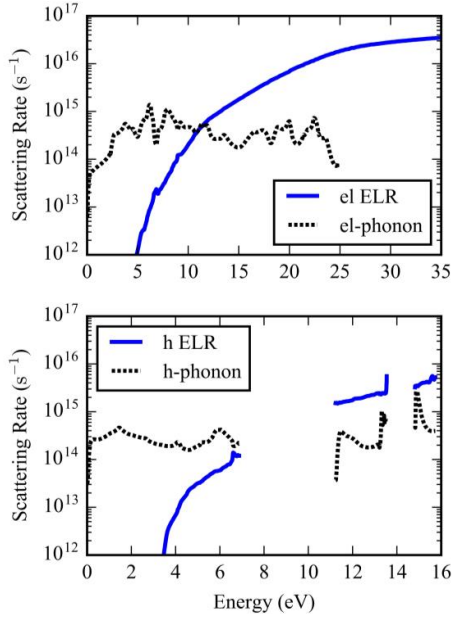


Fig. 1. Top: Electron-phonon scattering rate and electron energy-loss rate (ELR) plotted together. **Bottom:** Hole-phonon scattering rate and hole ELR. Gaps correspond to energy gaps in the valence bands.

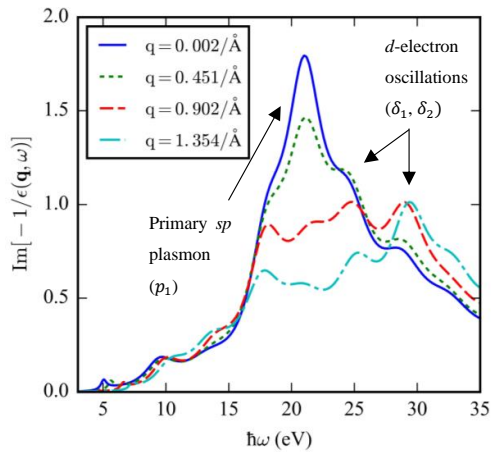


Fig. 2. Imaginary part of the inverse dielectric function of GaN calculated using the DFT package Quantum ESPRESSO. The function $\text{Im}[-1/\epsilon(\mathbf{q}, \omega)]$ is plotted vs. the energy, $\hbar\omega$, for the indicated values of \mathbf{q} . Plasmon peaks (p_1 , δ_1 , and δ_2) are indicated.

4. R. A. Reed, R. A. Weller, M. H. Mendenhall, D. M. Fleetwood, K. M. Warren, B. D. Sierawski, M. P. King, R. D. Schrimpf, and E. C. Auden, IEEE Trans. Nuc. Sci. **62**, 1441 (2015).
5. M. V. Fischetti, S. E. Laux, Phys. Rev. B **38**, 14 (1988).
6. D. Pines, Rev. Mod. Phys. **28**, 184 (1956).
7. J. J. Quinn and R. A. Ferrell, Phys. Rev. **112**, 812 (1958).
8. J. J. Quinn, Phys. Rev. **126**, 1453 (1962).
9. D. R. Penn, Phys. Rev. **35**, 482 (1987).

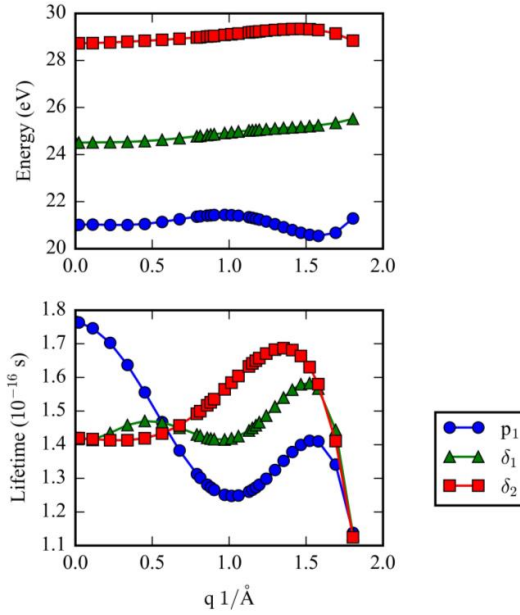


Fig. 3 Plasmon dispersion (top) and lifetime (bottom) obtained from the position and width of the quasi-Lorentzian peaks (p_1 , δ_1 , and δ_2) shown in Fig. 2.

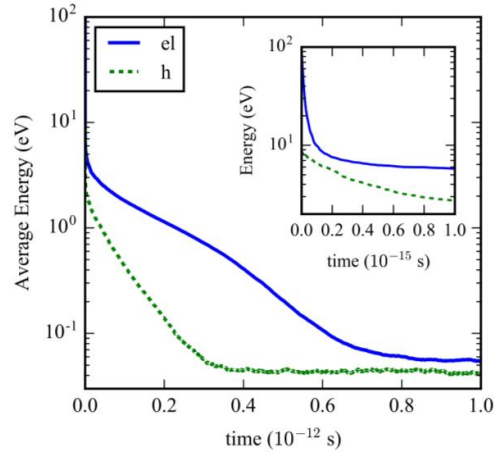


Fig. 4. Relaxation of electrons from a kinetic energy of 100 eV shown with the average energy of the generated holes throughout the thermalization process. **Embedded figure:** the first 10^{-15} s of the simulation.

3D Quantum Corrected Monte Carlo Simulation of n-FinFETs

C. S. Soares, G. F. Furtado*, A. C. J. Rossetto**, G. I. Wirth, D. Vasileska***

Programa de Pós-Graduação em Microeletrônica Universidade Federal do Rio Grande do Sul Porto Alegre, Brazil.

*Silvaco, Porto Alegre, RS, Brazil.

**Centro de Desenvolvimento Tecnológico Universidade Federal de Pelotas Pelotas, Brazil

***Department of Electrical Engineering Arizona State University Tempe, USA

e-mail: santos.soares@ufrgs.br

A Monte Carlo (MC) device simulator is an efficient tool to analyze the performance and reliability of transistors. However, to adequately model multi-gate transistors, such as n-FinFETs, in which electrons are confined along the fin height and width, a quantum correction (QC) must be included into the MC device simulator.

Previous works have successfully incorporated the Effective Potential model [1] as a QC into MC device simulators of planar devices [2]. In this work, we employ the Effective Potential model as a quantum correction to MC device simulator to consider the quantum confinement of electrons in n-FinFETs.

The Effective Potential approach [1] was developed to model space-quantization effects. The expression for the Effective Potential is derived by employing the density-matrix formalism, that allows one to estimate the potential of a system of electrons, assuming that the electrons are Gaussian wave packets. The Effective Potential is given by

$$V_{eff}(\mathbf{r}) = \int \frac{1}{(2\pi\sigma^2)^{3/2}} V(\mathbf{r}') \exp\left(-\frac{|\mathbf{r}-\mathbf{r}'|^2}{2\sigma^2}\right) d\mathbf{r}', \quad (1)$$

where σ is the smoothing parameter of the Effective Potential and $V(\mathbf{r})$ is the Hartree potential. To obtain the smoothing parameter, we employed the fitting method explained in Ref. [3]. From the definition of the Effective Potential, the carriers can be treated as zero-size particles that are exposed to this Effective Potential.

This QC was incorporated into the MC device simulator for n-FinFETs presented in Ref. [4]. In the quantum corrected MC device simulator, the Effective Potential is efficiently calculated using:

$$V_{eff}^{i,j,k} = \frac{1}{(2\pi\sigma^2)^{3/2}} \sum_{l,m,n} \left[(x_i, y_j, z_k) I_{i,j,k,l,m,n}^1 + (V(x_l, y_m, z_n) - V(x_i, y_j, z_k)) (I_{i,j,k,l,m,n}^2 + I_{i,j,k,l,m,n}^3 + I_{i,j,k,l,m,n}^4) \right], \quad (2)$$

where the index l,m,n refers to the neighbor points around i,j,k , V is the Hartree potential calculated by the Poisson solver, and $I_{i,j,k,l,m,n}^1$, $I_{i,j,k,l,m,n}^2$, $I_{i,j,k,l,m,n}^3$, and $I_{i,j,k,l,m,n}^4$ are error and exponential functions of the mesh spacing. The coefficients of Eq. (2) are calculated ahead of time, thus saving computational time. The flowchart of the simulator is shown in Fig. 1. The force that acts on the electrons in the transport is calculated from the Effective Potential.

The device structure of interest, represented in Fig 2, is an unintentionally doped FinFET with H_{Fin} and W_{Fin} of 42 nm and 8 nm, respectively, with $L = 18$ nm, and $EOT = 1.2$ nm. For this device, $\sigma = 0.45$ nm. Both semi-classical MC and quantum corrected MC simulators include random distribution of dopants. Fig. 3 shows the conduction band profile for a given dopant distribution. The impact of the random dopant distribution is clearly seen in the transfer characteristics of this device obtained by using the semi-classical MC simulator (Fig. 4) and the quantum corrected MC simulator (Fig. 5). From the semi-classical simulations, we calculate that the average threshold voltage is $V_T = 0.4368$ V, while the quantum corrected simulation gives $V_T = 0.4522$ V. The higher V_T obtained by using the QC model is expected due to the quantum-mechanical size quantization effects, that lead to smaller carrier density in the channel (see Fig. 6 for the average line density along the channel length).

In summary, we presented accurate and efficient methodology for studying transport in n-FinFET devices that adequately describes volume inversion in the channel and, at the same time, significantly reduces the computational time as opposed to a full Non-Equilibrium Green Function (NEGF) approach.

REFERENCES

- [1] D. K. Ferry, *The onset of quantization in ultra-submicron*

semiconductor devices, Superlattices & Microstructures **27**, 61 (2000).

[2] D. Vasileška, et al., *The Role of Quantization Effects on the Operation of 50 nm MOSFETs, 250 nm FIBMOS Devices and Narrow-Width SOI Device Structures*, Journal of Computational Electronics **1**, 453–465 (2002).

[3] C. S. Soares, et al., *Modeling Quantum Confinement in Multi-Gate Transistors with Effective Potential*, 36th SBMICRO Conference, Porto Alegre, Brazil (2022).

[4] G.F. Furtado, et al., *3-D TCAD Monte Carlo Device Simulator: State-of-the-art FinFET Simulation*, Journal of Integrated Circuits and Systems **16**, p. 1 (2021).

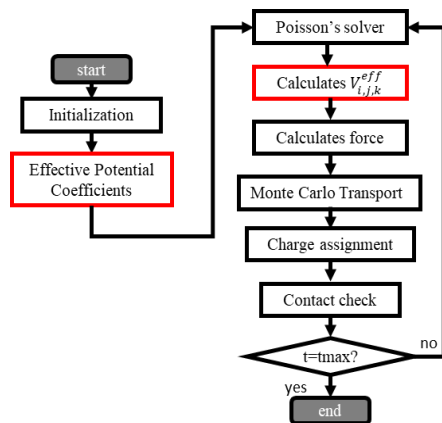


Fig. 1. Flowchart of the quantum corrected MC simulator.

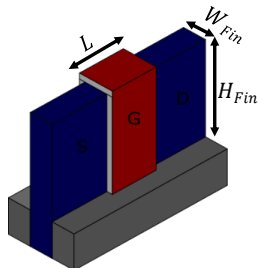


Fig. 2. Structure of the n-FinFET studied in this work.

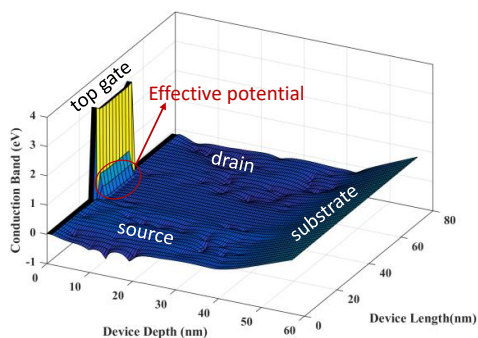


Fig. 3. Conduction band along the device length and depth at the middle of W_{FIN} . $V_B = V_S = 0$ V, $V_{DS} = 0.1$ V and $V_{GS} = 0.8$ V.

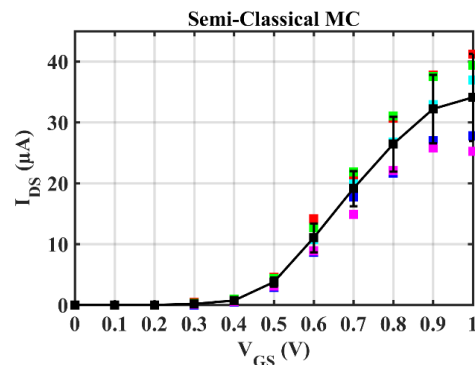


Fig. 4. Transfer characteristics obtained with semi-classical MC simulator for five devices with different random dopant distribution in the source, drain and channel. The average channel doping is 10^{15}cm^{-3} . Solid line is the averaged characteristic. $V_B = V_S = 0$ V and $V_{DS} = 0.1$ V.

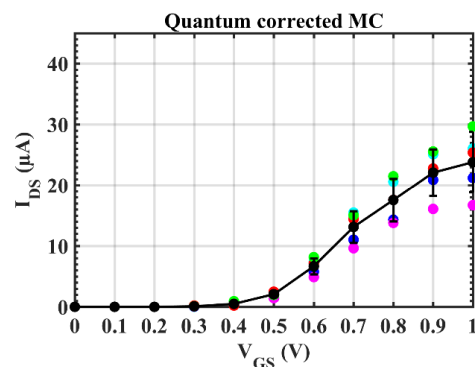


Fig. 5. Transfer characteristics obtained with the QC MC simulator for five devices with different random dopant distribution in the source, drain and channel. The average channel doping is 10^{15}cm^{-3} . $V_B = V_S = 0$ V and $V_{DS} = 0.1$ V.

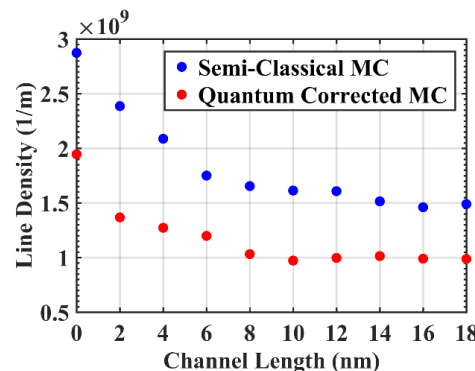


Fig. 6. Line density calculated using the semi-classical MC device simulator (blue) and quantum corrected MC device simulator (red). $V_B = V_S = 0$ V, $V_{DS} = 0.1$ V and $V_{GS} = 0.8$ V.

Edge-states interferometers in graphene nanoribbons: a time-dependent modeling

G. Forghieri¹, P. Bordone¹, and A. Bertoni²

¹ Università di Modena e Reggio Emilia, via Campi, 213/A, Modena, Italy

² Istituto Nanoscienze - CNR, Modena, Italy

e-mail: andrea.bertoni@nano.cnr.it

INTRODUCTION

Graphene has recently proved to be a reliable platform for electronic quantum optics in the integer quantum Hall regime[1], and offers promising perspectives for flying-qubit implementation of quantum computers[2]. Edge-state Mach-Zender interferometers (MZIs)[3] represents one of the simplest setups able to expose the wealth of physical phenomena stemming from the multi-valley bandstructure of graphene, as Klein tunneling and snake states in pn junctions. In the proposed contribution, we will present the methods and results of our time-dependent modeling of quasiparticle dynamics in graphene MZIs [4] based either on quantum point contacts or valley beam splitters (fig. 1). We will illustrate the reasons why a time-dependent approach, taking into account the real-space dispersion of the carriers, is necessary to fully assess the functional regimes of MZ devices.

MODEL AND METHOD

To obtain the exact evolution of the carrier quasiparticles injected in an edge state, we numerically integrate the corresponding time-dependent Schrödinger equation in the integer quantum Hall regime in graphene through the split-step Fourier method. We extended the latter approach to include the whole band structure in the proximity of the valleys in the first Brillouin zone, and consider the electronic wave function as a four-component spinor. This allows us to take into account the sublattice and valley degrees of freedom. The Hamiltonian is obtained within the $k\cdot p$ model, in which the bands are approximated by a linear dispersion near the valleys. An edge state is localized in the direction orthogonal to the nanoribbon boundary or to the pn junction, but it is delocalized in the transport direction. Since we aim at studying the time evolution of localized wave packets, we consider as the quasiparticle

initial state a localized linear combination of edge states in the transport direction.

RESULTS

Our simulations show that it is possible to control the transport regime of single particles along graphene pn junctions through the interplay between the energy of the injected carrier and the height of the junction itself (fig. 2), in turn, tailored by an external electrostatic field. The tuning of the cyclotron radius of the carrier in both regions of the junction makes it possible to either observe semiclassical snake-state trajectories or edge-state behavior, with Klein tunneling through a finite potential barrier. The energy dispersion of the localized wave packet allows to observe phase averaging at the end of the MZIs, a phenomenon which does not occur for delocalized currents[4].

We also highlight a transport regime in which the Edge Channels that constitute the interferometer cross periodically along the zigzag direction perpendicular to the nanoribbon boundary (fig.3). This phenomenon affects the frequency of Aharonov-Bohm oscillations and causes the visibility to drop significantly[4].

ACKNOWLEDGMENT

AB acknowledges partial financial support from the EU project IQubits (Call No. H2020-FETOPEN-2018-2019-2020-01, Project ID 829005). The authors acknowledge CINECA for HPC computing resources.

REFERENCES

- [1] M. Carrega, L. Chiroli, S. Heun, L. Sorba, Nat. Rev. Phys. 3, 698 (2021).
- [2] H. Edlbauer, J. Wang, T. Crozes, et al., EPJ Quantum Technol. 9, 21 (2022).
- [3] L. Bellentani, A. Beggi, P. Bordone, A. Bertoni, Phys. Rev. B 97, 205419 (2018).
- [4] G. Forghieri, P. Bordone, A. Bertoni, Phys. Rev. B 106, 165402 (2022).

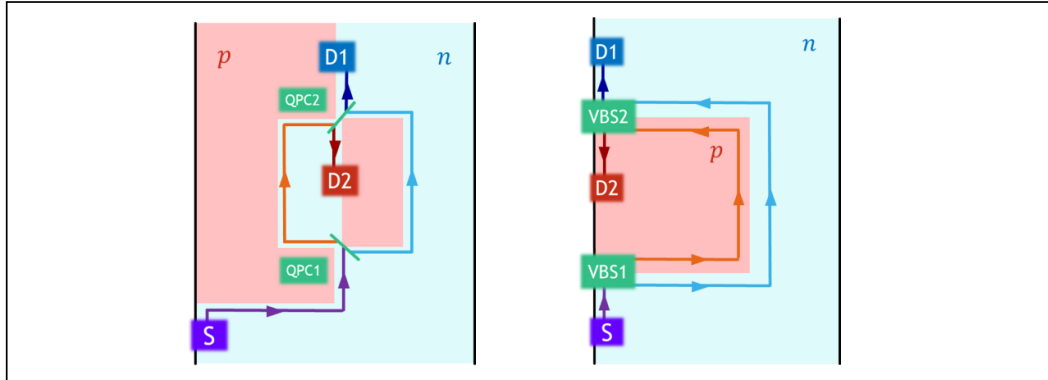


Fig. 1. MZIs for edge-states in graphene nanoribbons with armchair boundaries (black vertical lines) where the quasiparticles are injected from an excitation source (S) able to inject carriers with an energy broadening of 45 meV and detected in the two outputs of the interferometer (D1 and D2). Left panel: the two beam splitters are realized by two quantum point contacts (QPC1 and QPC2) where channels between two n -doped regions are quenched by the p -doped region. Right panel: the two valley beam splitters are realized by electrostatically aligning the electron-like and hole-like edge states where the n and p regions meet the boundary (VBS1 and VBS2) and the two edge states propagate in the same direction in the two regions with opposite doping.

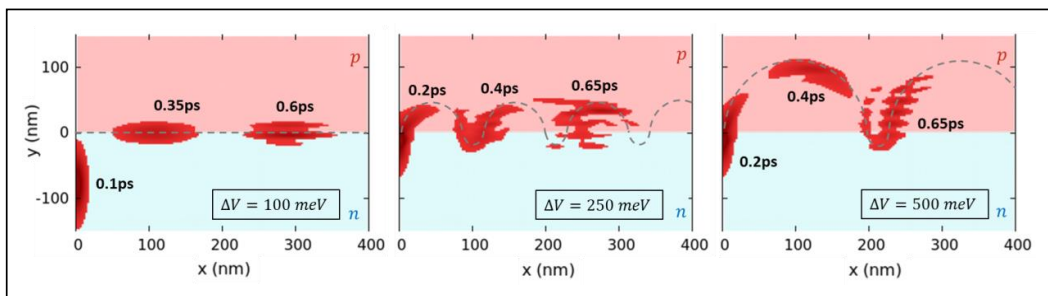


Fig. 2. Dynamics of a Gaussian wave packet of edge states at a pn junction of an armchair nanoribbon. The three panels show three cases, with different height ΔV of the potential step leading to different effective electrostatic doping in the two regions. The initial wave packet has an energy $E=51.4$ meV (left panel) and $E=77.5$ meV (center and right panels). The interplay between the potential energy difference among the junction and the packet energy gives rise to snake states, where electron-like and hole-like states are excited on the opposite sides of the junction.

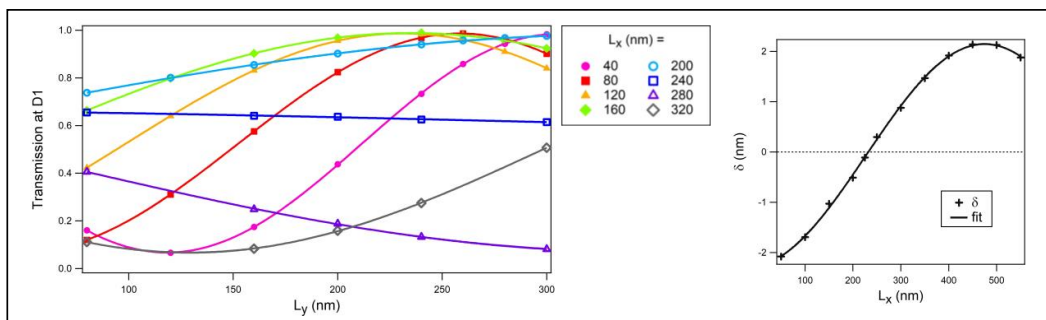


Fig. 3. Behaviour of Aharonov-Bohm oscillations in the interferometer on the right from fig. 1. The transmission probability at D1 (left panel) is reported as a function of the vertical dimension of the p region (L_y) for different values of the horizontal dimension (L_x). The frequency of the curves changes with L_x . The right panel shows the distance δ between the channels along L_y , which oscillates as a function of L_x .

A Coupled Electrostatic - Quantum Transport Framework for Exascale Systems

S. S. Sawant, F. Léonard*, J. Yao, and A. Nonaka

Lawrence Berkeley National Laboratory, Berkeley, California, 94720, USA

*Sandia National Laboratories, Livermore, California, 94550, USA

e-mail: saurabhsawant@lbl.gov

Advances in nanoscale sensors using field effect transistors (FETs) have numerous applications in various scientific fields, including astrophysics, biomedicine, and security. These applications require large numbers of FETs to operate together using superior channel materials like carbon nanotubes and silicon nanowires. To study the performance of these FETs, a software framework is needed that can efficiently utilize many-core/GPU architectures and scale effectively on exascale supercomputers.

This work presents our efforts to develop a self-consistently coupled electrostatic-quantum transport framework for exascale systems (see Fig. 1), and its demonstration in modeling multiple carbon nanotube FETs (CNTFETs) functionalized with quantum dots for a novel photodetector [1]. The framework includes an open-source, 3-D exascale electrostatic solver, eXstatic [2], which utilizes the GPU-enabled AMReX library [3] for calculating electrostatic potential. AMReX provides necessary functionalities for writing massively parallel, block-structured adaptive mesh refinement (AMR) applications. The eXstatic solver offers support for specifying intricate contact types through embedded boundaries as well as various domain boundaries (Dirichlet, Neumann, Robin, periodic) with an option to specify time-varying inputs. The solver provides routines for specifying atom locations of materials, gathering fields at these locations, and depositing charges onto the grid. The multigrid finite-volume approach used by eXstatic, in contrast to the commonly used fast Fourier transform based approach, enables the modeling of large-scale aperiodic array and stacks of FETs.

The framework has been extended to include a quantum transport module using the Nonequi-

librium Green's Function (NEGF) method, which will support GPU-enabled matrix operations. The module models contacts as semi-infinite leads and the electronic properties of carbon nanotubes are described through the tight-binding approximation. The framework will be demonstrated for its weak-scaling and its application in obtaining current-voltage characteristics of multiple CNTFETs functionalized with quantum dots. In the future, the NEGF module will be extended to include phonon scattering and time-dependent equations based on two-time Green's functions to model the dynamic conductance caused by the presence of point charges.

SUMMARY

A self-consistently coupled electrostatic-quantum transport framework is being developed that efficiently leverages many-core/GPU architectures and scales well on exascale systems.

ACKNOWLEDGMENT

This work is supported by the US Department of Energy, Office of Science, Office of Basic Energy Sciences, the Microelectronics Co-Design Research Program, under contract no. DE-AC02-05-CH11231.

REFERENCES

- [1] S. M. Young, M. Sarovar, and F. Léonard, "Nanoscale architecture for frequency-resolving single-photon detectors," 2022, submitted for publication, arXiv No: quant-ph/2205.05817, <https://arxiv.org/abs/2205.05817>.
- [2] eXstatic, <https://github.com/AMReX-Microelectronics/eXstatic>.
- [3] W. Zhang, A. Myers, K. Gott, A. Almgren, and J. Bell, "AMReX: Block-structured adaptive mesh refinement for multiphysics applications," *The International Journal of High Performance Computing Applications*, vol. 35, no. 6, pp. 508–526, 2021.

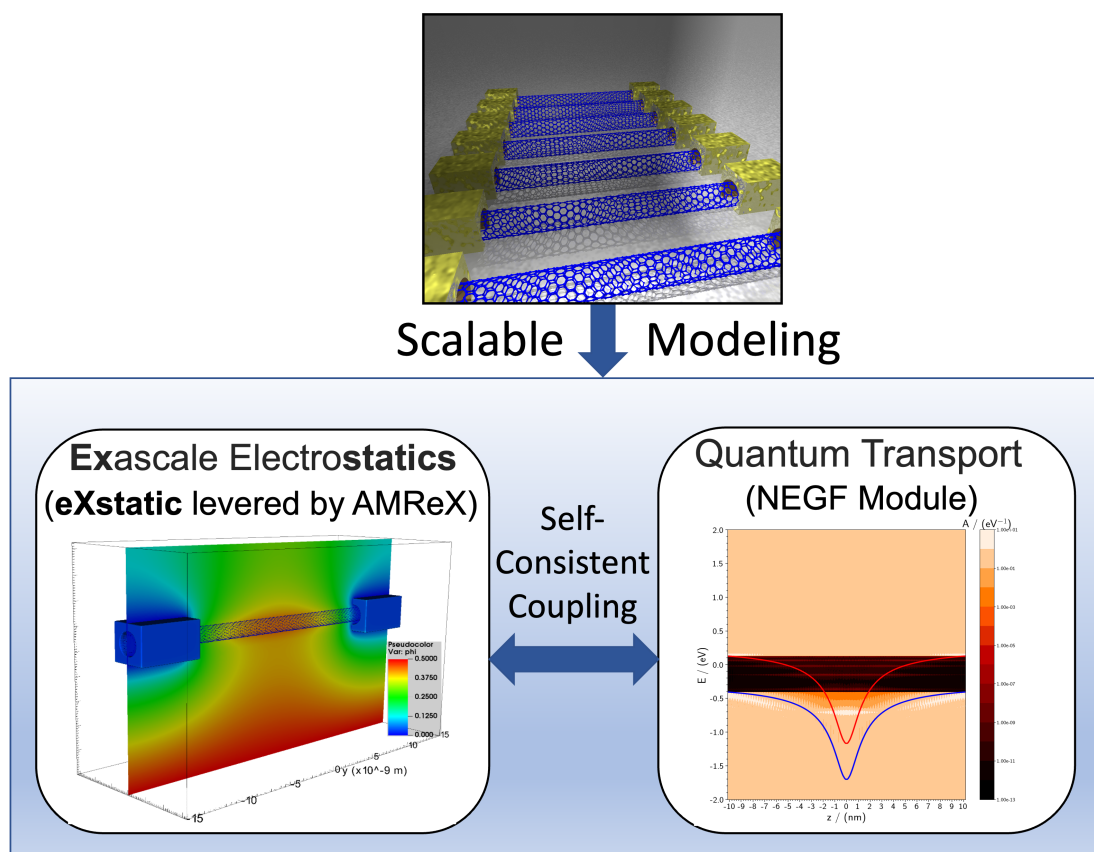


Fig. 1. A scalable approach to modeling multiple CNTFETs using the 3-D, open-source exascale electrostatic solver (eXstatic) and the self-consistently coupled quantum transport module based on the NEGF method.

Acoustic phonon modulation of terahertz quantum cascade lasers

A. Demić*, A. Valavanis*, J. Bailey†, P. Dean*,
L. H. Li*, A. G. Davies*, E. H. Linfield*, P. Harrison‡, J. E. Cunningham*, A. Kent†

* School of Electronic and Electrical Engineering, University of Leeds, Leeds LS2 9JT, UK

† School of Physics and Astronomy, University of Nottingham, Nottingham NG7 2RD, UK

‡ School of Computing and Engineering, University of Huddersfield, Huddersfield HD1 3DH, UK
e-mail: A.Demic@leeds.ac.uk

INTRODUCTION

We investigate theoretical methods for the analysis of acoustic phonon modes in arbitrary heterostructure superlattice and their effect on modulating transport in terahertz-frequency quantum-cascade lasers (THz QCLs). We solve the acoustic phonon wave equation via Fourier method to obtain excellent agreement with experimental results (Fig. 1-3). Our model is applicable to arbitrary heterostructure profile. The acoustic stop-bands in a THz QCL were measured via an ultrafast pump-probe spectroscopy technique, using a pair of mode-locked Ti:Sapphire Tsunami femtosecond lasers, tuned to a wavelength of 810 nm. We use the envelope of the obtained acoustic deformation potential as a perturbation to bandstructure potential (Fig. 4) to analyse electron transport in common THz QCLs active-region design schemes via density matrix approach [1]. We find that acoustic modes up to ~ 200 GHz are capable of significantly perturbing QCL transport (Fig. 5-6), highlighting their potential for ultra-fast modulation of laser emission. This agrees well with our demonstration by using externally generated acoustic pulses [2].

ACOUSTIC PHONON MODE MODELLING

We consider the acoustic wave equation [3]: $\frac{\partial}{\partial z} v_s^2(z) \frac{\partial}{\partial z} \psi(z, t) - \frac{\partial^2}{\partial t^2} \psi(z, t) = 0$ where $\psi(z, t)$ is the acoustic wave pressure and $v_s(z)$ is the acoustic velocity. This equation can be solved using a Fourier method, by assuming $\psi(z, t) = \psi_0 \psi_n(z) \exp(-i\omega_n t)$, where ψ_0 is the wave amplitude, ω_n the angular frequency and $p_n(z)$ the envelope of the acoustic wave:

$$-\frac{\partial}{\partial z} v_s^2(z) \frac{\partial}{\partial z} p_n(z) = \omega_n^2 p_n(z) \quad (1)$$

which can be discretised via finite-difference method. The obtained envelopes of the resonant phonon modes $p_n(z)$ are directly proportional to the local acoustic strain, and this can be added as a static deformation potential $V_{S_n}(z)$ to the Hamiltonian for an electron in the QCL:

$$V_{S_n}(z) = M \cdot p_n(z) \quad (2)$$

where M is a modulation strength constant.

REFERENCES

- [1] A. Demić *et.al.*, AIP Advances 9 no. 9, 095019 (2019).
- [2] A. Dunn *et.al.*, Nature communications 11 no. 1, 1 (2020).
- [3] P. Harrison and A. Valavanis, John Wiley & Sons, (2016).

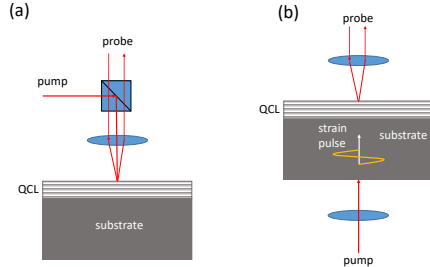


Fig. 1: Schematic illustrations of ASOPS experimental configurations, showing (a) reflection mode, and (b) transmission mode geometries.

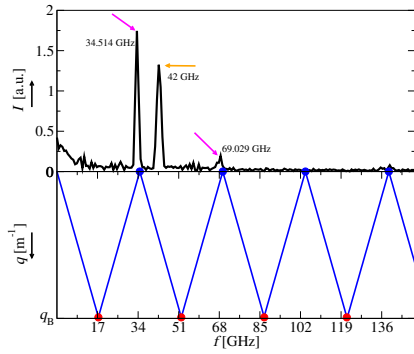


Fig. 2: Experimental probe reflectivity spectrum (top), obtained using a reflection-mode ASOPS geometry, and folded dispersion of the first Brillouin zone (bottom), obtained by solving Eq. (1) for a single period of the Hybrid THz QCL [2].

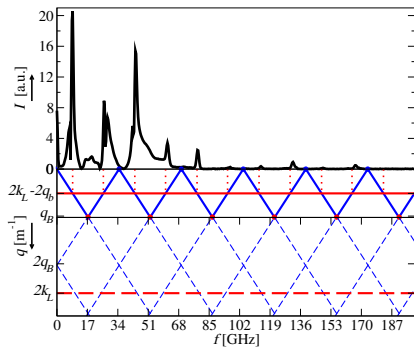


Fig. 3: Experimental probe reflectivity spectrum (top), using the transmission-mode ASOPS geometry, and acoustic dispersion resulting from model in Equation (1) (bottom). Solid blue lines represent the phonon dispersion, folded into the first Brillouin zone. The red dashed line corresponds to $q = 2k_L$, and the red solid line shows this folded into the first phonon Brillouin zone.

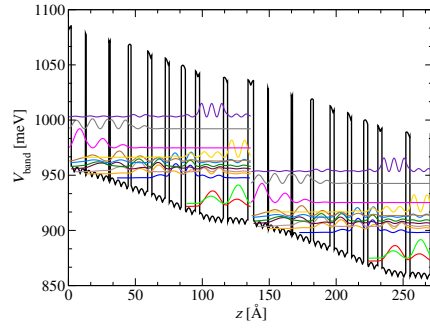


Fig. 4: Conduction band potential of a hybrid QCL design [2] with the addition of the 30th acoustic mode with modulation $M = 5$ meV. Two periods are shown at the resonance bias $K = 3.63 \frac{\text{kV}}{\text{cm}}$ along with the corresponding wavefunction moduli squared.

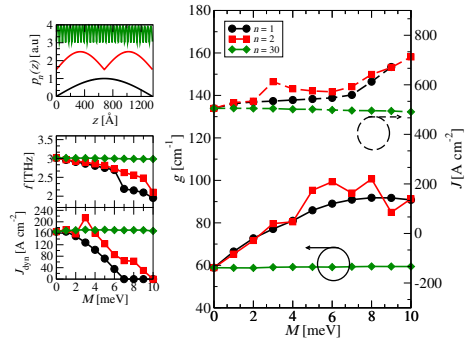


Fig. 5: Top inset: acoustic strain perturbation for mode index $n = 1, 2, 30$. Bottom insets: Frequency dependence (at NDR point) and dynamic range dependence, respectively, on modulation strength M for $n = 1, 2, 30$. Graph on the right: Full line traces illustrate material gain peaks from figure in a) as modulation M is varied for $n = 1, 2, 30$, while dashed lines illustrate current density peaks (NDR points) of the Hybrid THz QCL [2].

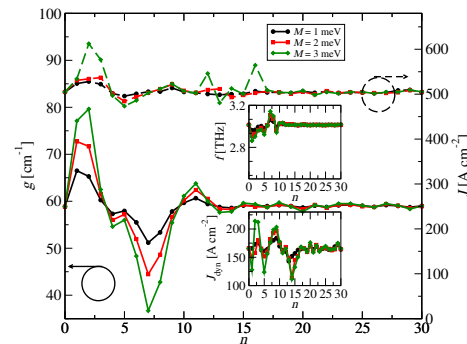


Fig. 6: Dependence of performance parameters for Hybrid THz QCL [2], as a function of acoustic mode index, using varying modulation strengths $M = 1, 2, 3$ meV. Results are shown for (a) emission frequency (at NDR point), (b) dynamic range, (c) peak gain, and (d) current density at the NDR point.

Simulation of Single-Electron Shuttling for Spin-Qubit Transport in a SiGe Quantum Bus

L. Ermoneit*, B. Schmidt*, J. Fuhrmann*, T. Koprucki*, L. R. Schreiber†, and M. Kantner*

*Weierstrass Institute for Applied Analysis and Stochastics, Mohrenstr. 39, 10117 Berlin, Germany
e-mail: ermoneit@wias-berlin.de, kantner@wias-berlin.de

†JARA-FIT Institute for Quantum Information, Forschungszentrum Jülich GmbH and
Institute of Physics, RWTH Aachen University, Otto-Blumenthal-Str., 52074 Aachen, Germany
e-mail: lars.schreiber@physik.rwth-aachen.de

INTRODUCTION

Spin qubits in gate-defined semiconductor quantum dots (QDs) are one of the major candidates for the realization of fault-tolerant universal quantum computers. Ongoing advances in the growth of SiGe heterostructures with isotopically purified ^{28}Si quantum wells have enabled exceptionally long coherence times. Moreover, the compatibility with industry standard fabrication technology opens up excellent prospects for scaling up SiGe-based quantum processors to very large numbers of qubits. Recently, small-scale devices have been demonstrated, which execute one- and two-qubit logic gates as well as initialization and read-out operations with high fidelity using all-electrical control.

The wiring and interconnection of large arrays of tunnel-coupled QDs, however, is a challenging problem as numerous control signals must be routed from external sources to every QD [1]. While control lines can be stacked in multiple layers, there are clear limitations in view of geometric constraints. A possible solution to this *fan-out problem* is partitioning of the qubit register into smaller QD arrays interconnected by coherent quantum links. Ref. [2] describes the design of such a scalable quantum bus, which allows to shuttle electrons using moving QDs along a one-dimensional channel in a *conveyor belt mode*, see Fig. 1. The quantum bus design provides sufficient space for QD wiring and classical on-chip control electronics.

NUMERICAL SIMULATION

We present a framework for device-scale simulation of qubit shuttling in a SiGe quantum bus. Our goal is to assess the transfer fidelity of the electron

and its spin state as it travels along the channel in the presence of material defects (*e.g.*, charged defects, interface inhomogeneity, etc.) and noise. The electrostatic potential of the control fields (clavier gates, screening gates, back gate), see Figs. 1–3, and the defect potential are computed by solving Poisson’s equation using the Julia-package `VoronoiFVM.jl` [3]. The potentials are passed to `WavePacket` [4] for numerical simulation of the electron using either the time-dependent Schrödinger equation or a Lindblad-type quantum master equation. The latter allows to include phonon-assisted relaxation from excited orbital and valley states. We discuss optimization of the device geometry and give an outlook on optimal control of gate voltages for optimal steering of the qubit to minimize the effects of perturbations.

ACKNOWLEDGMENT

This work received funding from the German Research Foundation under Germany’s Excellence Strategy – EXC 2046: MATH+ (project AA2-17).

REFERENCES

- [1] L. M. K. Vandersypen, H. Bluhm, J. S. Clarke, A. S. Dzurak, R. Ishihara, A. Morello, D. J. Reilly, L. R. Schreiber, and M. Veldhorst, *Interfacing spin qubits in quantum dots and donors—hot, dense, coherent*, npj Quantum Inf. **3**, 34 (2017)
- [2] V. Langrock, J. A. Krzywda, N. Focke, I. Seidler, L. R. Schreiber, and Ł. Cywiński, *Blueprint of a scalable spin qubit shuttle device for coherent mid-range qubit transfer in disordered Si/SiGe/SiO₂*, arXiv:2202.11793 (2022).
- [3] J. Fuhrmann, *VoronoiFVM.jl: Finite volume solver for coupled nonlinear partial differential equations*, DOI: 10.5281/zenodo.7615014 (2023)
- [4] B. Schmidt, and U. Lorenz, *WavePacket: A Matlab package for numerical quantum dynamics. I: Closed quantum systems and discrete variable representations*, Comput. Phys. Commun. **213**, 223–234 (2017).

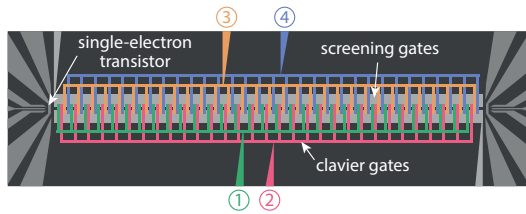


Fig. 1. Top view on the quantum bus, cf. [2]. Electrons are loaded and detected using single-electron transistors at both ends. By applying a sine-like pulse sequence on the clavier gate sets, a moving QD potential for qubit shuttling is formed.

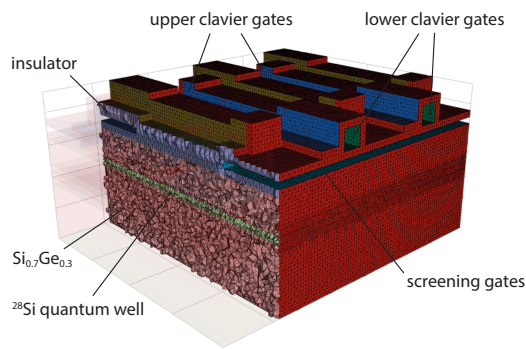


Fig. 2. Boundary conforming Delaunay mesh (generated with TetGen) for computation of the electrostatics problem using the finite volume method implemented in VoronoiFVM.jl [3].

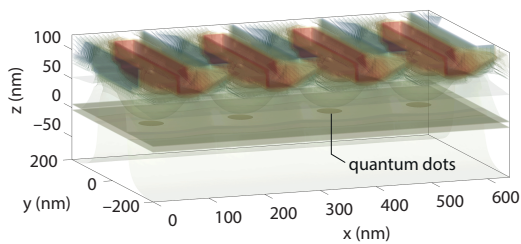


Fig. 3. Control potential generated by appropriate biasing of clavier gates and screening gates. A series of gate-defined quantum dots is formed in the center of the channel.

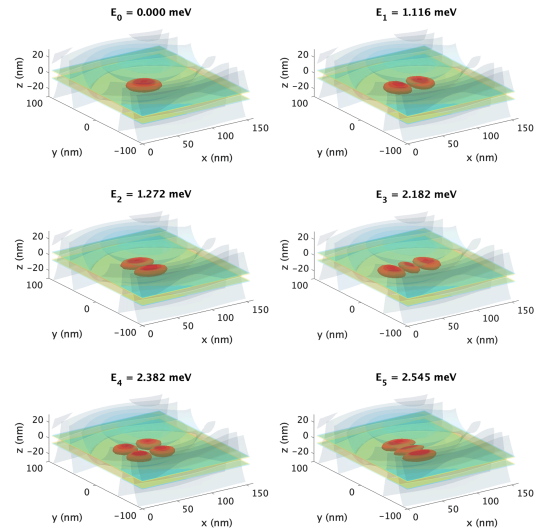


Fig. 4. Lowest energy bound states of an electron in a single periodic segment (four clavier gates) in a stationary frame computed using WavePacket [4]. The spectrum resembles that of a two-dimensional anisotropic harmonic oscillator.

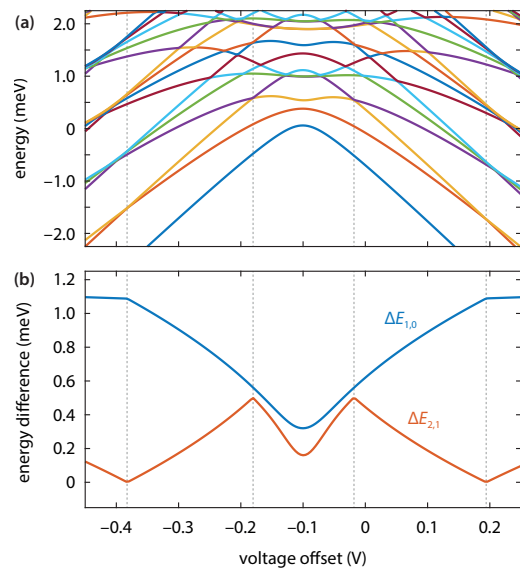


Fig. 5. (a) Bound state energies and (b) level separation as a function of the voltage amplitude offset between the lower and upper clavier gates. By tuning the voltage offset, the fundamental orbital splitting $\Delta E_{1,0}$ and the excited state degeneracy $\Delta E_{2,1}$ can be controlled.

Coherent Wigner Dynamics of a Superposition State in a Tunable Barrier Quantum Dot

M. Ballicchia, M. Nedjalkov, and J. Weinbub

Institute for Microelectronics, TU Wien, Gußhausstraße 27–29, 1040 Wien, Austria
e-mail: weinbub@iue.tuwien.ac.at

Tunable barrier quantum dots (QDs) are used in single electron sources [1], [2] which in turn are essential building blocks for electron quantum optics, quantum metrology, and quantum information processing [3]–[5]. The tunable barriers are realized by a two-gate structure along a nanowire [2]. The operational principle uses a pumping scheme of loading, capture, and ejection stages [6]: Understanding the coherent electron dynamics is vital for optimizing the overall performance.

In this work, we investigate the dynamics of the captured and ejected electron state by a Wigner simulation study [3], [7]–[9]. Extending previous work [10], here we consider the probability current and impact of different timings on the state evolution after ejection. Inspired by [6], we model a one-dimensional nanowire (200 nm) with a QD which is modeled by two Gaussian potential barriers placed at $x_1 = 25$ nm and $x_2 = 75$ nm (Fig. 1), where the first barrier has a $V_1 = 0.5$ eV and the second barrier a time-dependent $V_2(t)$, i.e., driven by a gate voltage (barrier width $w_{bar} = 5$ nm). Up to $V_2(t) = V_1$, the energy is quantized in the spatial domain Ω bounded by the two Gaussian barriers and the electron state can be obtained in principle by the stationary Schrödinger equation as a superposition of the orthonormal set of eigenfunctions ψ_n . Limiting our analysis to the first two eigenfunctions of the QD, ψ_1 and ψ_2 , as was done in [6], we get: $\Psi(x, t) = a_1\psi_1(x)e^{-\frac{i}{\hbar}\epsilon_1 t} + a_2\psi_2(x)e^{-\frac{i}{\hbar}\epsilon_2 t}$.

We use the wavefunction $\Psi(x, 0)$ to determine the density matrix at time $t = 0$ and consequently obtain the initial Wigner function $f_w(x, p, 0)$ which is then evolved by solving the Wigner equation [9]. The coherent dynamics of the superpo-

sition state are analyzed by considering the two first moments of the Wigner function, i.e., $n(x) = \int f_w(x, p)dp$ (probability density) and $J(x) = (1/m_{eff}) \int p f_w(x, p)dp$ (probability current).

We studied two scenarios: (1) Capture stage: $V_2(t)$ is kept constant and equal to V_1 . (2) Ejection stage: $V_2(t) = V_1 \cdot [1 - H(t - t_1)]$, where $H(t)$ is the Heaviside function and particularly consider $t_1 = 10$ fs and $t_1 = 400$ fs. Initial condition: The electron at $t = 0$ is bounded inside the QD with $a_1 = a_2 = 1/\sqrt{2}$ and the effective mass is $m_{eff} = 0.19 m_{el}$. Reg. (1), Fig. 1 shows the probability density (Wigner and verification with Schrödinger) after half a period of oscillation. The electron state oscillates from left to right and vice-versa with a period $T = 2\pi\hbar/(\epsilon_2 - \epsilon_1) \approx 500$ fs. Reg. (2), Fig. 2 shows the evolution of the probability density at $t = 500$ fs and $t = 700$ fs for $t_1 = 10$ fs, while Fig. 3 for $t_1 = 400$ fs. Different opening times t_1 clearly influence the shape of the probability density, potentially leading to separation or superimposition. Fig. 4 shows the probability current at $t = 500$ fs for both $t_1 = 10$ fs and $t_1 = 400$ fs. The first case shows clear peak separation, indicating the presence of significantly different velocities (energies) in the state. The latter case results in much more localization, higher magnitude, and almost no peak separation. We can thus show that a Wigner dynamics simulation is an attractive additional tool in designing the tunable barrier system for coherent single electron sources.

Acknowledgment: The financial support by the Austrian Science Fund (FWF): P33609 is gratefully acknowledged. The computational results have been achieved using the Vienna Scientific Cluster (VSC).

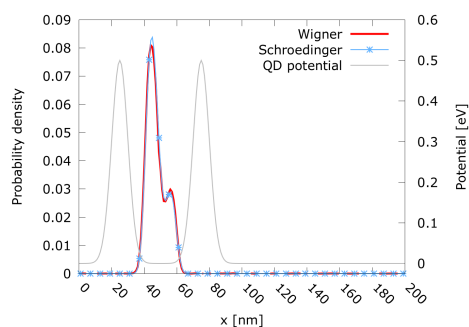


Fig. 1. Probability density of the superposition state at $t = 250$ fs: Comparison between Wigner and Schrödinger. The two peaks of the captured electron state oscillate with $T \approx 500$ fs.

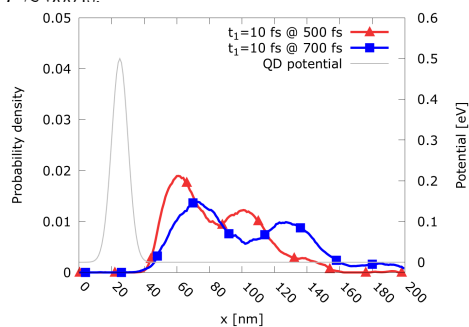


Fig. 2. Evolution along the channel of the electron superposition state ejected at $t_1 = 10$ fs: Probability density at $t = 500$ fs and $t = 700$ fs. The state's peak separation indicates the presence of significantly different velocities (energies) in the state (confirmed in Fig. 4).

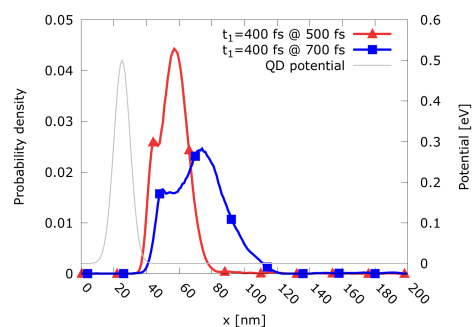


Fig. 3. Evolution along the channel of the electron superposition state ejected at $t_1 = 400$ fs: Probability density at $t = 500$ fs and $t = 700$ fs.

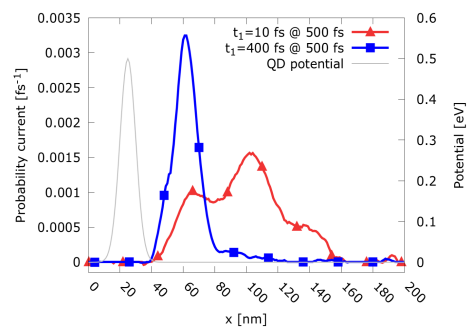


Fig. 4. Probability current at $t = 500$ fs. The case $t_1 = 10$ fs (red) clearly shows the presence of significantly different velocities (energies) in the state.

REFERENCES

- [1] G. Yamahata *et al.*, *Phys.Rev.B* **103**, 245306 (2021).
- [2] B. Kaestner *et al.*, *Rep.Prog.Phys.* **78**, 103901 (2015).
- [3] J. Weinbub *et al.*, *J.Phys.Condens.Mat.* **34**, 163001 (2022).
- [4] C. Bäuerle *et al.*, *Rep.Prog.Phys.* **81**, 056503 (2018).
- [5] H. Edlbauer *et al.*, *EPJ Quant.Techn.* **9** (2022).
- [6] G. Yamahata *et al.*, *Nat.Nanotech.* **14**, 1019 (2019).
- [7] M. Nedjalkov *et al.*, *Wigner Function Approach*, Springer, 289 (2011).
- [8] D.K. Ferry *et al.*, *The Wigner Function in Science and Technology*, IOP Publishing (2018).
- [9] J. Weinbub *et al.*, *Appl.Phys.Rev.* **5**, 041104 (2018).
- [10] M. Ballicchia *et al.*, *Proc. IEEE NANO*, 565 (2022).

Incorporation of the Tight Binding Hamiltonian into Quantum Liouville-type Equations

A. Abdi, M. Pech, and D. Schulz

Chair for High Frequency Techniques, TU Dortmund, Friedrich-Wöhler-Weg 4, 44227 Dortmund, Germany
e-mail: alan.abdi@tu-dortmund.de

Abstract—A novel numerical approach is introduced and validated for the determination of the statistical density matrix based on the Tight Binding Hamiltonian included in a Quantum Liouville-type equation. Besides the main advantage that the atomic structure is taken into account, a transport model results which, unlike the conventional Wigner equation, does not involve any loss of information in the domain of the density matrix.

INTRODUCTION

For the analysis of quantum mechanical transport, well-known models such as the Wigner Transport Equation (WTE), the Non-Equilibrium Green Function (NEGF) method or Quantum Liouville-type Equations (QLTE) have been developed. However, the use of a Tight Binding (TB) Hamiltonian as an addition for these models allows an atomistic view and thus considers the electronic structure of the materials used. The solution of the QLTE in combination with the TB Hamiltonian results in a density matrix defined on lattice points. On this basis computationally efficient algorithms can be realized.

MODEL

After incorporating the TB Hamiltonian into the Von-Neumann Equation (VNE) and applying the center of mass transformation, a transport equation for the density matrix in center mass coordinates χ and ξ results. As a consequence, a staggered grid formulation appears as depicted in Fig. 1 on which a formalism in the phase space can be established. For this purpose a transformation based on a set of plane wave functions with wave numbers k is carried out in ξ -direction for both sub-grids arriving at a QLTE [1]. The orthogonality of the basis is mandatory. With this resulting staggered grid formulation, all

of the density matrix information is contained in the transport equations [2]. The transport equations obtained are related to a formalism presented by Mains and Haddad [3], where the transformations chosen for each sub-grid are different. Unfortunately, the latter model leads to negative carrier densities and requires the use of a scattering model while this is not the case for the proposed approach.

DISCUSSION

Special attention needs to be paid with regard to boundary conditions. In χ -direction the inflow and outflow concept is applied onto both grids [2], whereas in ξ direction a Complex Absorbing Potential (CAP) is applied [4]. A resonant tunneling diode (Fig. 2) is now acting as a test device. In the flat band case, the model (referred to as TB-QLTE) shows good agreement with the results obtained from the NEGF method as it can be seen from Fig. 3 and 4. Combining the TB Hamiltonian with the QLTE seems to be a promising approach and shall be further investigated.

REFERENCES

- [1] L. Schulz, B. Inci, M. Pech, and D. Schulz, *Subdomain-based exponential integrators for quantum Liouville-type equations*, Journal of Computational Electronics **20**, 2070-2090 (2021).
- [2] W. Frensley *Boundary conditions for open quantum systems driven far from equilibrium*, Review of Modern Physics **62**, 745 (1990).
- [3] R. Mains, and G. Haddad *An Accurate Re-formulation of the Wigner Function Method for Quantum Transport Modeling*, Journal of Computational Physics **112**, 149-161 (1992).
- [4] L. Schulz, and D. Schulz, *Complex Absorbing Potential Formalism Accounting for Open Boundary Conditions Within the Wigner Transport Equation*, Ieee Transactions on Nanotechnology **18**, 830 - 838 (2019).

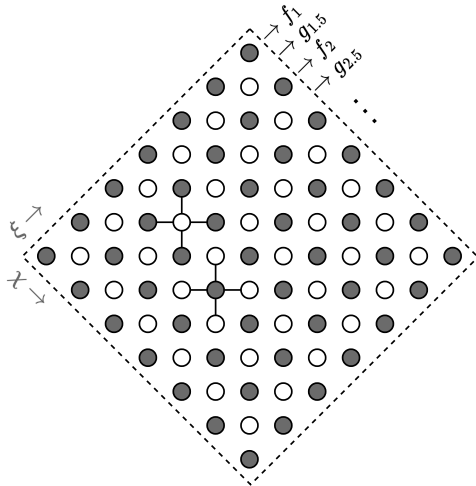


Fig. 1. Illustration of the staggered grid composed of the two subgrids (f-black and g-white) in the center-of-mass coordinates χ and ξ . The circles stand in for the elements of the density matrix. The coupling between the two grids is indicated for two grid points. When not at the boundary each element couples to four neighboring elements.

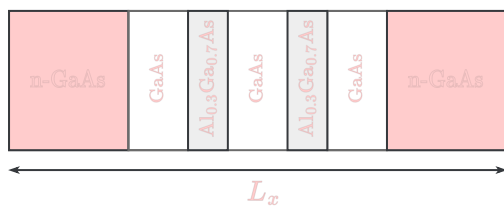


Fig. 2. Structure of a AlGaAs/GaAs resonant tunneling diode with a width of $L_x=152$ nm, barriers of 3.38 nm width and a quantum well of 4.5 nm width. The contacts are n-doped with a concentration of $N_D=2 \times 10^{18}$ cm⁻³. A spatially constant effective mass distribution with the effective mass of GaAs is assumed.

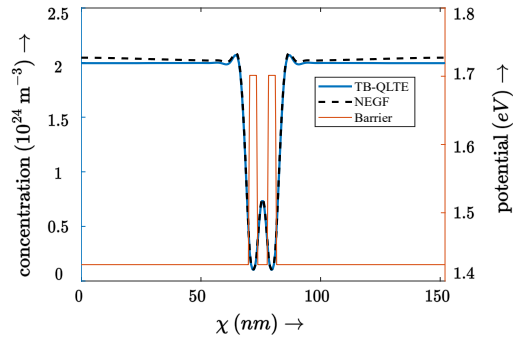


Fig. 3. The electron density from the use of TB-QLTE for one of the both grids is shown as a function of the coordinate χ . For the equilibrium case, the results are compared to those obtained from the NEGF method. The results agree very well. For the k-discretization $N_k = 200$ values were considered.

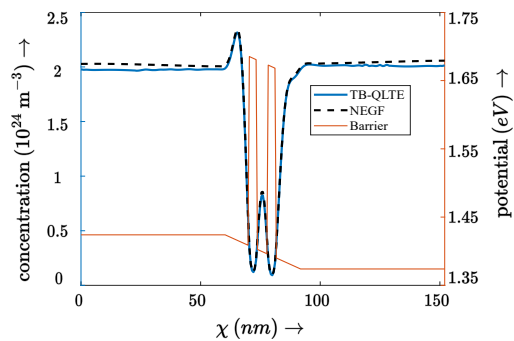


Fig. 4. The electron density from the use of TB-QLTE for one of the both grids is shown as a function of the coordinate χ with an applied voltage of 0.05 V. The results are compared to those obtained from the NEGF method. At this point it should be mentioned that the CAP has a considerable influence on the results, so it is important to choose a suitable parameter set for it. Further investigations with regard to the CAP and the boundary conditions will be presented.

Mutiscale modelling and Computational spectroscopy

K. Hermansson

Department of Chemistry-Ångström, Box 538, SE-75121 Uppsala, Sweden
e-mail: kersti@kemi.uu.se

ABSTRACT OF MY ABSTRACT

My presentation will deal with metal oxides with and without molecules "on top of them", and how we can use modelling of different flavours to acquire new knowledge where experiments need assistance. In particular I will mention multiscale modelling, simulated experiments (e.g. computational spectroscopy) and 'physics-based vs. data-driven' modelling.

METAL OXIDES AND MULTISCALE MODELLING

Metal oxide and their interfaces with molecules play crucial roles in technology, science, industry, and society. Metal-oxide-based catalysts, sensors and battery devices are just a few examples and finding the mechanisms that govern such functionalities is challenging. Here computer modelling can provide unique detail and insight.

Here I will describe some of our efforts to develop multiscale modelling protocols for metal oxide surfaces and nanoparticles (e.g. of CeO₂, ZnO and MgO). We combine a range of theoretical methods including DFT, tight-binding-DFT [1], and reactive force-field models [2]; cf **Fig. 1**. A key question is whether it is really possible to model redox-active metal oxides *without including the electrons*?

METAL OXIDES WITH MOLECULES

Cerium oxide (ceria) is a reducible metal oxide with intriguing chemical and physical properties. Experiments in the literature have shown that the oxygen storage capacity (OSC) of ceria at the nanoscale is strongly shape and size dependent [3,4]. An increased activity towards O₂ molecules has been observed for particles of exotic shapes (such as nanorods and nanocubes), and a increased OSC has been measured for very small nanoparticles (d < 5 nm). We combine density functional theory (DFT) calculations with micro-

kinetic modelling (MKM) to simulate O₂ temperature programmed desorption (TPD) and H₂ temperature programmed reduction (TPR) spectra for ceria nanoparticles (Refs. [5] and unpublished work). The chemical origin of this enhancement has been amply discussed in the literature. dramatically.

The H₂O molecule deserves special attention as hydroxylation/hydration changes the stabilities and reactivities of metal oxides, often with far-reaching consequences. Furthermore, water and surface OH groups are central in many applications of metal oxides, either as key actors or because they are omnipresent under ambient conditions. Water is discussed in the next section.

WATER ADSORPTION, DATABASES AND COMPUTATIONAL MOLECULAR SPECTROSCOPY – PREDICTION OR INSIGHT?

Vibrational spectroscopy is one of the most sensitive methods to explore bound OH groups, although interface systems constitute a particular challenge also for such spectroscopies. Access to robust correlation curves is essential in order to decipher structural information from IR spectra. We generate such correlation curves from DFT and AIMD calculations followed by quantum vibrational calculations (=> anharmonicity).

We have recently [6, 7] created two databases (**Fig. 2**) of structures and properties of OH groups of water and hydroxides (i) on metal oxide surfaces, and (ii) within the crystalline state. We use these databases to find *fundamental scientific relations* as well as *structure-property models* for frequency prediction, and assess the prediction capabilities of a range of descriptors (features). Starting from a machine-learning geometrical descriptor we gradually include more physics/chemistry flavor in the descriptor and examine how the frequency prediction power (and "insight content") vary (cf. **Fig. 3**).

MUCH WATER: HYDROPHOBICITY OF CERIA

If time allows, I will mention some recent results on why ceria with a lot of water "on top" can be hydrophobic (an experimental fact!) while the direct ceria-water interaction is in fact hydrophilic. [8]

CONCLUSION

Molecular and materials modelling on metal oxide systems can deliver new and unique data and valuable relations/models which save time and energy.

ACKNOWLEDGMENT

Acknowledgements go to all co-workers as listed in the Reference list, and to the Swedish Research Council, the National Academic Infrastructure for Supercomputing in Sweden (NAISS), the Swedish National Infrastructure for Computing (SNIC), and the National Strategic e-Science Research Program eSSSENCE.

REFERENCES

- [1] J. Kullgren, M. J. Wolf, K. Hermansson, Ch. Köhler, B. Aradi, Th. Frauenheim, and P. Broqvist, "Self-Consistent-Charge Density-Functional Tight-Binding (SCC-DFTB) Parameters for Ceria in 0D to 3D". *J. Phys. Chem. C* **121**, 4593 (2017).
- [2] B-H Kim, J Kullgren, MJ Wolf, K Hermansson, P Broqvist, *Multiscale Modeling of Agglomerated Ceria Nanoparticles: Interface Stability and Oxygen Vacancy Formation*, *Frontiers in Chemistry* **7**, Article 203 (2019).
- [3] Z. Wu, M. Li, J. Howe, H. M. Meyer, S. H. Overbury, *Probing Defect Sites on CeO₂ Nanocrystals with Well-Defined Surface Planes by Raman Spectroscopy and O₂ Adsorption*, *Langmuir* **26**, 16595 (2010).
- [4] N. K. Renuka, N. Harsha, T. Divya, *Supercharged ceria quantum dots with exceptionally high oxygen buffer action*, *RSC Adv.* **5**, 38837 (2015).
- [5] D. Du, J. Kullgren, K. Hermansson, P. Broqvist, *From Ceria Clusters to Nanoparticles: Superoxides and Supercharging*, *J. Phys. Chem. C* **123**, 1742 (2019).
- [6] A. Röckert, J. Kullgren, K. Hermansson, *Predicting Frequency from the External Chemical Environment: OH Vibrations on Hydrated and Hydroxylated Surfaces*, *J. Chem. Theory Comput.* **18**, 7683 (2022).
- [7] J. Kullgren, A. Röckert, K. Hermansson, *Water in crystals – a database for ML and a knowledge-base for vibrational prediction*, *J Phys. Chem. C*, Accepted 12 April (2023).
- [8] L. Agosta, D. Arismendi, M. Dzugutov, K. Hermansson, *Origin of the Hydrophobic Behaviour of Hydrophilic CeO₂*, *Angewandte Chemie Int. Ed. (Comm)* **3** April (2023).

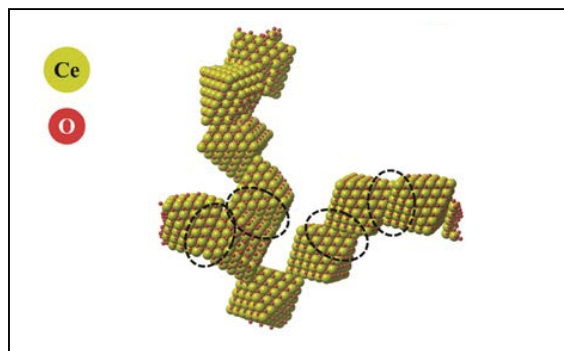


Fig. 1. Snapshot from a ReaxFF MD simulation of many Ce₁₃₂O₂₆₄ nanoparticles which agglomerate into a winding chain (remade from Ref. [2]).

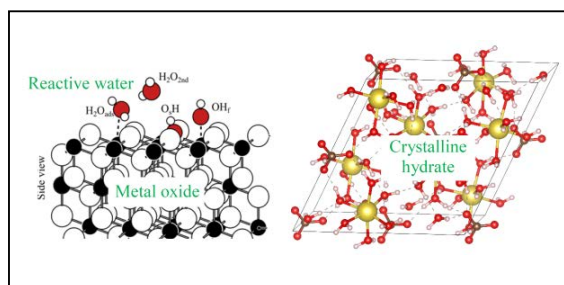


Fig. 2. We have created two databases of structures and properties of water and OH⁻ on metal oxide surfaces [6], and within crystalline hydrates and hydroxide [7]. From these we generate spectroscopic and other models/relations. All data were based on the same electronic structure (DFT) method.

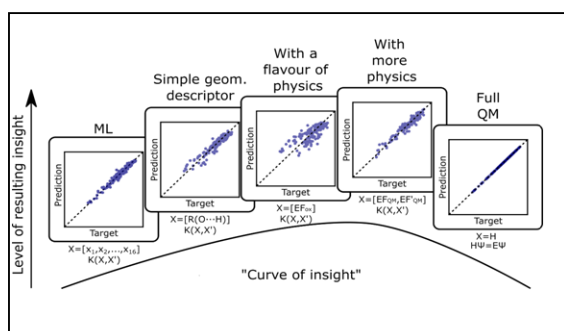


Fig. 3. Illustration of the progression of our descriptors in terms of the "amount" of physics coded into them and their respective level of insight. The scatter plots show the agreement between predictions and targeted reference values. (cf. Ref. 7).

Solving Kohn-Sham Equations of Heterobilayer Systems Beyond 1000 Atoms: Twist Angle-dependent Piezoelectricity

Han-Wei Hsiao, Namita Narendra, and Tillmann Kubis

Elmore Family School of Electrical and Computer Engineering, Purdue University, West Lafayette, IN, USA
e-mail: hsiao35@purdue.edu

ABSTRACT

We introduce an efficient density-functional tight-binding (DFTB) approach that allows converged piezoelectric coefficient predictions of relaxed, twisted two-dimensional (2D) heterobilayer systems beyond 1000 atoms on a single compute node. The results unveil controllable in-plane piezoelectricity in twisted hBN/hBP heterobilayers. The corresponding out-of-plane piezoelectric response, on the other hand, is mostly constant due to corrugations. We apply and extend this method to study twist angle-dependent piezoelectricity in hexagonal III-V/transition metal dichalcogenide (TMD) van der Waals heterostructures.

INTRODUCTION

Recent studies have demonstrated that stacking 2D monolayers may achieve a stronger piezoelectricity than the sum of the respective monolayers [1], [2]. There is experimental evidence that suggests that the twist angle is a relevant design and control factor for the piezoelectric coefficients of van der Waals heterostructures [3], [4]. This theoretical work assesses in high detail the impact of the twist angle on the piezoelectricity of 2D heterobilayer systems. We expand the DFTB method to predict the piezoelectric coefficients of twisted and corrugated 2D heterostructures with more than 1000 atoms. We showcase the method on twisted hBN/hBP heterostructures (see Fig. 1). Our calculations yield a periodic relationship between the in-plane piezoelectric coefficients and the corresponding twist angles. In contrast, the twist angle influences the average interlayer distance which in turn determines the out-of-plane piezoelectricity.

METHOD

We apply the third-order self-consistent DFTB method implemented in the DFTB+ software to solve the Kohn-Sham equations of systems beyond 1000 atoms [5]. The DFTB parameters (compression radii, exponents, on-site energies) and the internuclear repulsion energies are parameterized to precisely reproduce the electronic structures and the piezoelectric coefficients predicted by the hybrid HSE06 functional implemented in VASP [6]. All relevant long-range effects due to twist angles, corrugations, and strain effects are well-converged vs. the supercell size.

RESULTS AND DISCUSSION

Fig. 2 indicates that the interlayer distance gradually converges with the supercell size. This convergence affects all observables including piezoelectric coefficients. Initial supercells containing 1000+ atoms are required for a well-converged simulation. Fig. 3 shows that the calculated in-plane piezoelectric coefficients of the twisted bilayers deviate from the idealized analytical results for all twist angles due to charge transfer, break of inversion symmetry, corrugations, and nonlinear, twist angle dependence. The out-of plane piezoelectric response correlates with the average interlayer distance. That in turn fluctuates with the layer corrugations and depends nonlinearly on twist angles which prevents a smooth angle dependence (see Fig. 4).

CONCLUSION

The prediction of twist angle dependent piezoelectric coefficients of heterobilayers converges with supercell sizes of around 1000 atoms only. Our

calculations show that the in-plane piezoelectricity varies strongly with the twist angle. The out-of-plane piezoelectric response does not show systematic twist angle dependence due to pronounced corrugation. This method is currently being used to explore non-linear twist angle-dependent piezoelectricity in other 2D material combinations (e.g., hexagonal III-V/TMD heterobilayers).

REFERENCES

- [1] H. Zhu, Y. Wang, J. Xiao, M. Liu, S. Xiong, Z. Wong, Z. Ye, Y. Ye, X. Yin, and X. Zhang, "Observation of piezoelectricity in free-standing monolayer mos₂," *Nature nanotechnology*, vol. 10, 12 2014.
- [2] S. Yuan, W. Io, J. Mao, Y. Chen, X. Luo, and J. Hao, "Enhanced piezoelectric response of layered in 2 se 3 /mos 2 nanosheet-based van der waals heterostructures," *ACS Applied Nano Materials*, vol. 3, 11 2020.
- [3] K. Yasuda, X. Wang, K. Watanabe, T. Taniguchi, and P. Jarillo-Herrero, "Stacking-engineered ferroelectricity in bilayer boron nitride," *Science*, vol. 372, p. eabd3230, 05 2021.
- [4] Y. Li, X. Wang, D. Tang, X. Wang, K. Watanabe, T. Taniguchi, D. Gamelin, D. Cobden, M. Yankowitz, X. Xu, and J. Li, "Unraveling strain gradient induced electromechanical coupling in twisted double bilayer graphene moiré superlattices," *Advanced Materials*, p. 2105879, 12 2021.
- [5] B. Hourahine, B. Aradi, V. Blum, F. Bonafé, A. Buccheri, C. Camacho, C. Cevallos, M. Deshayé, T. Dumitrică, A. Dominguez Garcia, S. Ehlert, M. Elstner, T. Heide, J. Hermann, S. Irle, J. Julián, C. Köhler, T. Kowalczyk, T. Kubař, and T. Frauenheim, "Dftb+, a software package for efficient approximate density functional theory based atomistic simulations," *The Journal of Chemical Physics*, vol. 152, p. 124101, 03 2020.
- [6] G. Kresse and J. Hafner, "Ab initio molecular-dynamics simulation of the liquid-metal-amorphous-semiconductor transition in germanium," *Phys. Rev. B*, vol. 49, pp. 14 251–14 269, 05 1994.

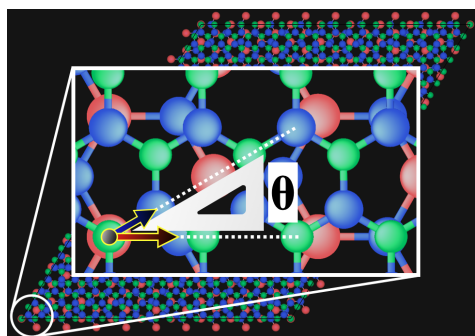


Fig. 1. Schematic of hBN/hBP heterostructure. The angle θ between the dipole vectors of hBN and hBP is the twist angle.

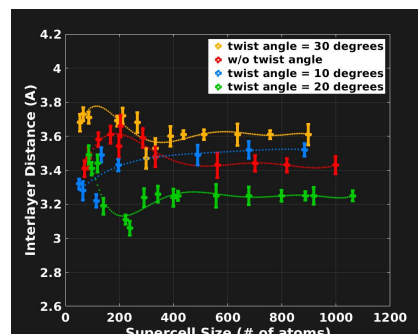


Fig. 2. Average interlayer distance as a function of supercell size. Typically, a supercell containing ~ 1000 atoms is necessary for well-converged simulations.

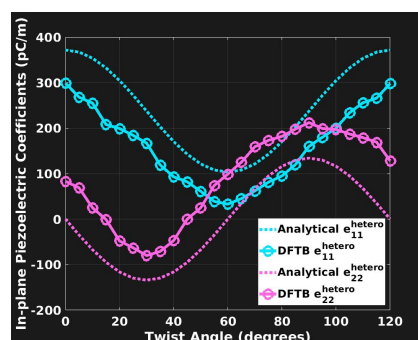


Fig. 3. In-plane piezoelectric coefficients e_{11} (blue) and e_{22} (red) vs. twist angle. The solid lines and the dotted lines are the DFTB results and the analytical formulas derived from isolated monolayers respectively.

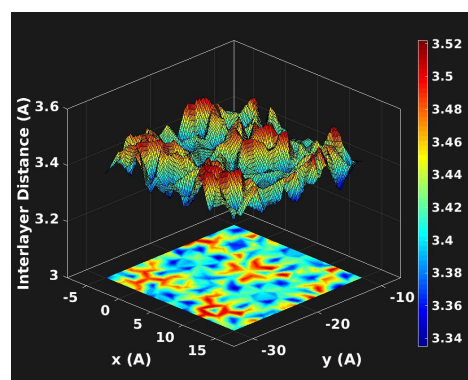


Fig. 4. Average interlayer spacing of the corrugated hBN/hBP heterobilayer twisted at $\theta = 10$ degrees. The interlayer spacing varies nonlinearly with twist angle, preventing a smooth correlation between e_{33} and twist angle.

Anomalous transient blue-shift in the internal stretch mode of CO on Pd(111)

Raul Bombín ^{*†‡}, Alberto S. Muzas [†], Dino Novko [§],
J. Iñaki Juaristi ^{*†¶} and Maite Alducin ^{*¶}

^{*} Centro de Física de Materiales CFM/MPC (CSIC-UPV/EHU), Donostia-San Sebastián, Spain

[†] Departamento de Polímeros y Materiales Avanzados: Física, Química y Tecnología, Facultad de Químicas (UPV/EHU), Donostia-San Sebastián, Spain

[‡] Departament de Física, Universitat Politècnica de Catalunya, Barcelona, Spain

[§] Institute of Physics, Zagreb, Croatia

[¶] Donostia International Physics Center (DIPC), Donostia-San Sebastián, Spain

The internal stretch mode (IS) of polar molecules adsorbed on metal surfaces, being decoupled in energy from the rest of vibrational modes of the system, can be monitored during a reaction using state-of-the-art time-resolved vibrational spectroscopy. This gives access to the subpicosecond dynamics occurring at the surface. On the other hand, from the theoretical point of view, these systems appear as an exceptional test-bed in which to benchmark the validity many-body theories with experimental data. Here we study non-adiabatic effects on the internal stretch mode of CO adsorbed on the Pd(111) surface by means of first principles calculations [1].

The theoretical treatment that we employ, including electron-hole pair excitations and electron-mediated coupling between the vibrational modes [3], [4], allows us to study the IS mode under pump-probe experimental conditions. This is achieved by evaluating the phonon self-energy as a sum of first- and second-order terms in the e-ph coupling

$$\pi_{\lambda}(\omega) = \pi_{\lambda}^{[1]}(\omega) + \pi_{\lambda}^{[2]}(\omega), \quad (1)$$

where $\pi_{\lambda}^{[1]}$ and $\pi_{\lambda}^{[2]}$ correspond to dominant inter-band and intra-band contributions, respectively. The first order accounts for nonadiabatic coupling (NC) to electron-hole pairs, while the second order corresponds to the so-called electron mediated phonon-phonon coupling (EMPPC). Within these two mechanisms it has been possible to simulate the conditions that a femtosecond infrared pump pulse generates on the CO/Cu(100) system, obtaining a remarkable agreement between theory and experiment [2], [3], [4].

To simulate the laser-induced nonthermal conditions in the CO/Pd(111) system, electron and phonon distributions are described, respectively, by Fermi-Dirac

and Bose-Einstein distributions. These distributions are completely defined by time-dependent electronic $T_e(t)$ and lattice $T_l(t)$ temperatures that are calculated with a two temperature model (TTM) [see Fig. 1(a)]. As it is shown in Fig. 1(b), our calculations for the CO/Pd(111) system predict an anomalous transient blue-shift in the internal stretch frequency that is followed in the picosecond regime by a red-shift. From Fig. 1 it becomes evident that the NC (EMPPC) contribution is driven by the changes in the electronic (lattice) temperature. We show that the initial blue-shift arises purely from temperature-dependent electronic structure effects, while the subsequent red-shift occurs due to the coupling to other phonon modes [1].

REFERENCES

- [1] R. Bombín, A. S. Muzas, D. Novko, J. I. Juaristi and M. Alducin, *Anomalous transient blueshift in the internal stretch mode of CO/Pd(111)*, arXiv:2211.12192 [[cond-mat.mtrl-sci](#)]
- [2] D. Novko, and M. Alducin, and M. Blanco-Rey, and J. I. Juaristi, *Effects of electronic relaxation processes on vibrational linewidths of adsorbates on surfaces: The case of CO/Cu(100)*, Phys. Rev. B **19**, 22306 (2016).
- [3] D. Novko. and M. Alducin and J. I. Juaristi, J. I., *Electron-Mediated Phonon-Phonon Coupling Drives the Vibrational Relaxation of CO on Cu(100)*, Phys. Rev. Lett. **120**, 156804 (2018).
- [4] D. Novko, and J. C. Tremblay, and M. Alducin, and J. I. Juaristi, *Ultrafast Transient Dynamics of Adsorbates on Surfaces Deciphered: The Case of CO on Cu(100)*, Phys. Rev. Lett. **122**, 016806 (2018).

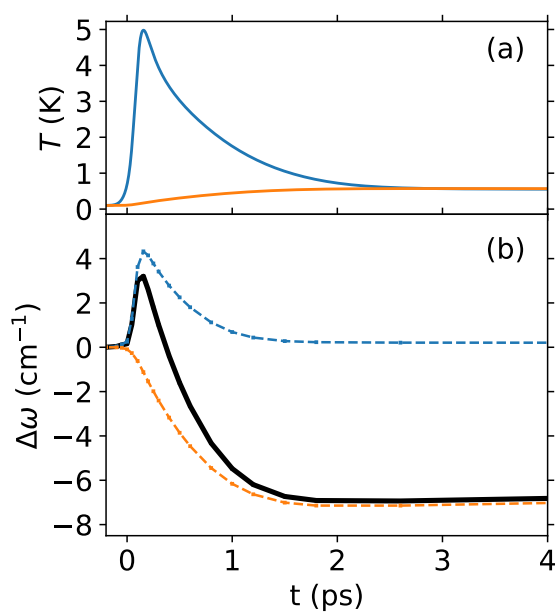


Fig. 1. Transient changes induced in CO/Pd(111) by a 450 nm pump pulse (100-fs duration and absorbed fluence of 40 J/m^2) that hits the surface at $t = 0.1$ ps. The initial temperature is 100 K. (a) Electron $T_e(t)$ (blue) and lattice $T_l(t)$ (orange) temperatures calculated with TTM. (b) Transient frequency shift of the CO IS mode: black line is $\Delta\omega(t)$ and dashed blue and orange lines are the contributions of the NC and EMPPC, respectively.

Ab initio calculation of mobility degradation caused by Si-vacancies in SiC/SiO₂ channels

Colin Kälin, Mathieu Luisier
Integrated Systems Laboratory, ETH Zürich, Switzerland
E-mail: ckaelin@iis.ee.ethz.ch

Introduction: Due to its wide bandgap, silicon carbide (SiC), in particular the 4H polytype, is a promising material for power semiconductor applications as it allows to build devices with higher breakdown voltages and lower losses than Si. However, SiC suffers from electron scattering caused by defects at the SiC/SiO₂ interface [1] or within the SiC channel which results in a lower channel mobility as compared to bulk SiC and a high specific ON-state resistance [2].

In this work, we present a method to create realistic SiC/SiO₂ interface structures using a reactive force field as well as (tight-binding) density functional theory DFT(B). We then investigate the influence of defects on the transport properties, focusing on Si-vacancies close to the interface [3]. These defects usually come from the transfer of Si atoms into the SiO₂ oxide layer. Finally, the mobility of the constructed structures is calculated. We demonstrate that these defects can be passivated and the carrier mobility partly restored.

Method: The chosen simulation approach is illustrated in Fig. 1(a). It consists of two main steps. 1) *Layer-by-layer technique:* As the goal is to examine the influence of Si-vacancies, defect-free SiC/SiO₂ interfaces should be created. For that purpose, silicon oxide (SiO₂) is grown on top of a 4H-SiC cell by depositing Si and O atoms in a layer-by-layer fashion (Fig. 1(b)). After each step, annealing with a reactive force field [4,5] is performed. In the end, the obtained structure is further relaxed with DFT(B) [6]. Defects, such as Si-vacancies, can finally be inserted at different positions.

2) *Mobility calculation:* Using DFT, the Hamiltonians and the overlap matrices of the produced "devices" are calculated and subsequently passed to a quantum transport solver [7] to calculate the electrical current flowing through them. The dR/dL

method [8] allows to determine the defect-limited mobility by calculating the resistance of channels with different lengths.

Results: The layer-by-layer technique proposed above allows to create practically defect-free interfaces as shown in Fig. 2(a). A Si-vacancy was introduced here close to the SiC/SiO₂ interface. The corresponding density-of-states is plotted in Fig. 2(b). Defect states around the conduction band are clearly visible.

Channels with Si-vacancies and after their passivation with nitrogen highlight the influence of the defects on the transport properties. In particular, Fig. 3(a) shows that the transmission function turns on at lower energies after passivation.

Mobility values for both structures were extracted with the dR/dL method. The results are given in Fig. 3(b). A significant improvement from 68.6 cm²/(Vs) to 130.9 cm²/(Vs) is observed when going from the defective to the repaired channel.

Conclusion: To investigate the influence of defects on the carrier transport of SiC/SiO₂ channels, we have developed a layer-by-layer deposition scheme and have used the resulting structures to calculate the mobility through a channel with Si-vacancies. Although nitrogen passivation enhances the mobility value, it is still far from its bulk counterpart (900 cm²/(Vs)), leaving room for further improvements.

References: [1] S. Iwase et al. Phys. Rev. B 95, 041302(R) (2017). [2] Y. Deng et al., J. Electron. Mater. 35, 618–624 (2006). [3] J. Cottom et al., J. Appl. Phys. 124, 045302 (2018). [4] A. P. Thompson et al., Comp Phys Comm 271, 10817 (2022). [5] D. A. Newsome et al., J. Phys. Chem. C, 116, 30, 16111–16121 (2012). [6] T. D. Kühne et al. J. Chem. Phys. 152, 194103 (2020). [7] M. Luisier et al. Phys. Rev. B 74, 205323 (2006). [8] K. Rim et al., IEDM, 1175775 (2002).

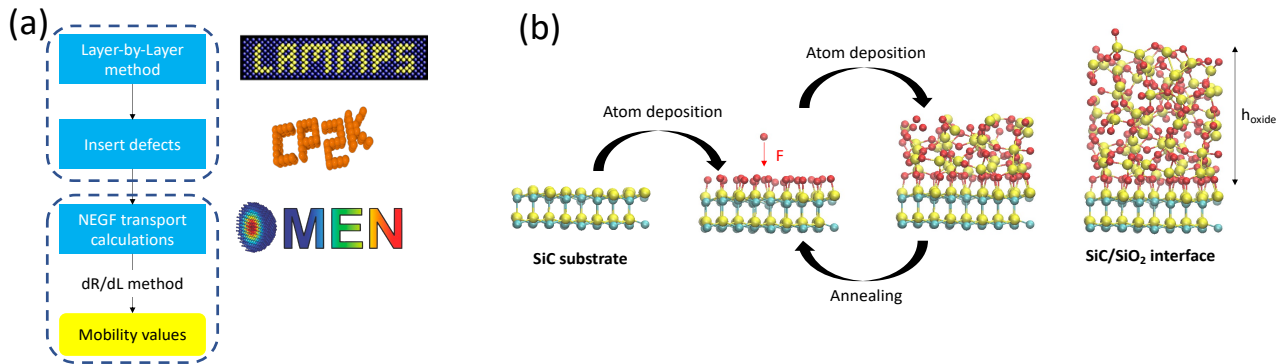


Fig. 1. (a) Illustration of the simulation method to study the transport properties of SiC/SiO₂ channels. A reactive force field is combined with DFT(B) to create realistic interfaces. The resulting Hamiltonian and overlap matrices are passed to an NEGF solver to calculate the mobility with the dR/dL technique. (b) Steps of the developed layer-by-layer procedure to grow SiO₂ onto SiC. Annealing is performed with a ReaxFF force field after the deposition of each atomic layer. Further relaxations of the structure with DFT(B) as implemented in CP2K [6] are not visualized here.

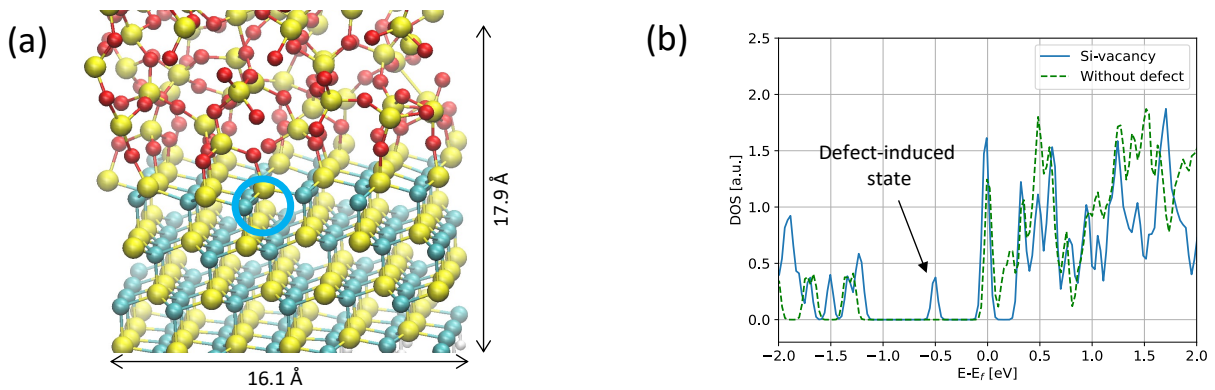


Fig. 2. (a) Exemplary interface structure created with the proposed layer-by-layer deposition technique. The blue circle indicates the location of a Si-vacancy that was introduced on purpose. (b) Density-of-states of the SiC/SiO₂ structure with (solid line) and without (dashed line) Si-vacancy.

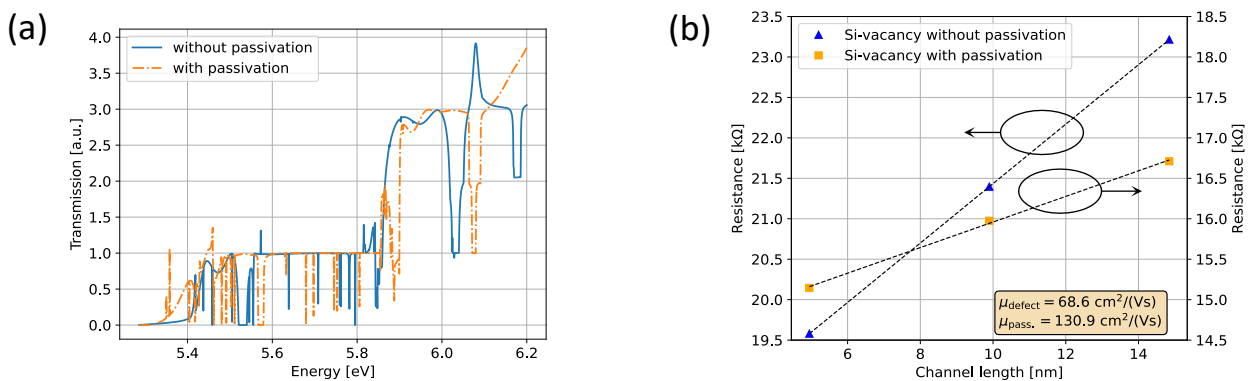


Fig. 3. (a) Transmission function through a SiC/SiO₂ channel with Si-vacancies before (solid line) and after (dashed-dotted line) passivation with nitrogen atoms. (b) Channel resistance as a function of the channel length. Results for the structure with Si vacancies before (triangles) and after passivation (squares) are compared. Lines are guides to the eyes. As expected, a linear resistance increase is obtained. The extracted mobilities with the dR/dL method are reported as inset.

Modelling the electrical conductivity of carbon nanotube films

T.R. Durrant^{1,2}, D.Z. Gao², Y. Giret² and A.L. Shluger¹

¹ Department of Physics and Astronomy, University College London, Gower Street, London WC1E 6BT, UK

² Nanolayers Research Computing Ltd, 1 Granville Court, Granville Road, London N12 0HL, UK
e-mail: thomas.durrant.14@ucl.ac.uk

ABSTRACT SUBMISSION

Carbon nanotubes (CNTs) are a fascinating material with very high electrical conductivity. In many practical applications, CNTs are deposited in a disorganized film. In order to model the electrical conductivity of such films, models of the electrical conductivity of individual CNT junctions must be combined with larger-scale models of their geometric structure. Such models elucidate the role that the CNT film structure has on electrical conductivity.

INTRODUCTION

Carbon nanotubes hold significant technological promise due to their extremely high electrical conductivities. This is due to metallic CNTs behaving as ballistic conductors, which enables highly energy efficient electrical devices to be constructed from them. One such example application is the use of a CNT film as resistance-changing element in non-volatile computer memory [1]. In such applications, the placement of individual CNTs is not directly controlled, and instead the electrical conductivity of a disorganized network of CNTs must be evaluated.

METHODOLOGY

The following steps were used to simulate the electrical conductivity of disordered CNT films:

(a) The intrinsic electrical conductivity of individual CNTs is high and the primary source of electrical resistance within CNT films is anticipated to occur at CNT-CNT junctions where electrons must tunnel from one CNT to another. In order to understand this tunneling resistance, a large library of CNT-CNT junction structures (Fig. 1) was simulated using density functional tight binding (DFTB) in combination with the non-equilibrium Green's function (NEGF) approach [2]. The results were used to generate an atomistic

conductivity model (Fig. 2) which was found to include a radius dependence (Fig. 3).

(b) Mesoscopic models of nanoscale CNT films were generated using coarse-grained molecular dynamics (MD). The procedure used to generate these models is described in Fig. 4. A library of CNT films was generated, and an example structure is shown in Fig. 5.

(c) The developed atomistic conductivity model developed in (a) was used in combination with larger-scale DFTB calculations in order to parameterize electrical conductivities between the mesoscopic segments employed in (b).

(d) The structural models generated in (b) were then combined with the electrical parameters established in (c) in order to produce a large-scale electrical model of the conductivity of a nanoscale CNT film, using the method of nodal analysis. An example simulation is shown in Fig. 6.

CONCLUSION

A numerical model for simulating the electrical conductivity of nanoscale CNT fabrics has been developed, by combining atomistic electrical conductivity calculations with larger scale mesoscopic structure simulations. This will enable an enhanced understanding of the electrical conductivity of CNT films to be developed.

ACKNOWLEDGMENT

We thank G. Bersuker and T. Rueckes for fruitful discussions and A.M. El-Sayed for assistance with mesoscopic structure generation.

REFERENCES

- [1] D. C. Glimer, T. Rueckes and L. Cleveland, *NRAM: a disruptive carbon-nanotube resistance-change memory* Nanotechnology **29** 134003 (2018).
- [2] T. R. Durrant, A.M. El-Sayed, D. Z. Gao, T. Rueckes, G. Bersuker, and A. L. Shluger, *Atomistic Modeling of the Electrical Conductivity of Single-Walled Carbon Nanotube Junctions* Phys. Status Solidi Rapid Res. Lett. **16** 2200118 (2022).

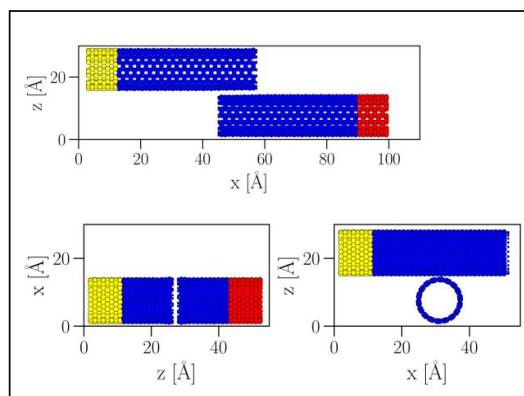


Fig. 1 Template CNT junction structures used to perform DFTB+NEGF electrical conductivity calculations. Red and yellow atoms denote the electrodes and blue the device region.

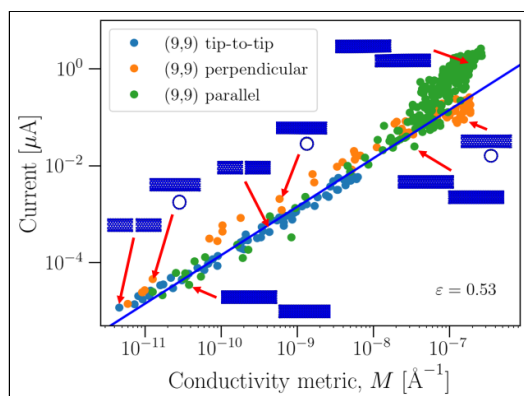


Fig. 2. Atomistic calculations of the electrical conductivity of CNT-CNT junction structures, calculated using DFTB+NEGF (markers). A simple model is fitted to the available data.

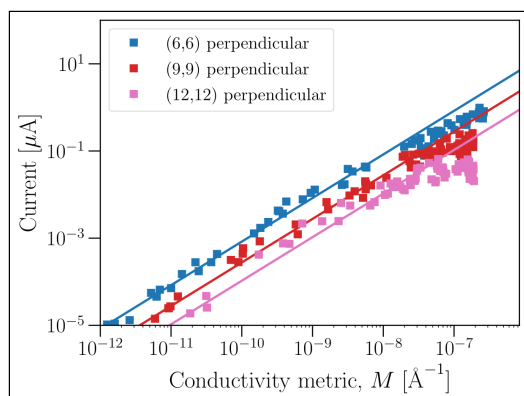


Fig. 3. The electrical conductivity of CNT junctions formed from armchair CNTs decreases with increasing CNT radius.

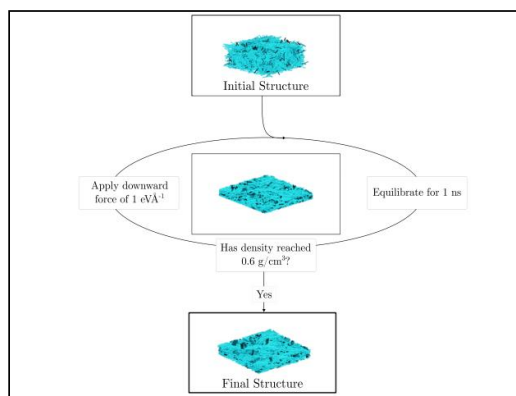


Fig. 4. Procedure to produce mesoscopic CNT film models. An initial random structure is generated and then sequentially compressed and equilibrated in order to produce films of the target density.

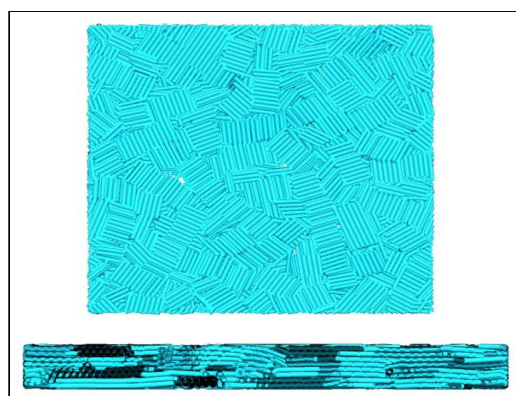


Fig. 5. Example mesoscopic model of a dense CNT film. This film demonstrates significant bundling between the CNTs. The degree of bundling depends on the CNTs used.

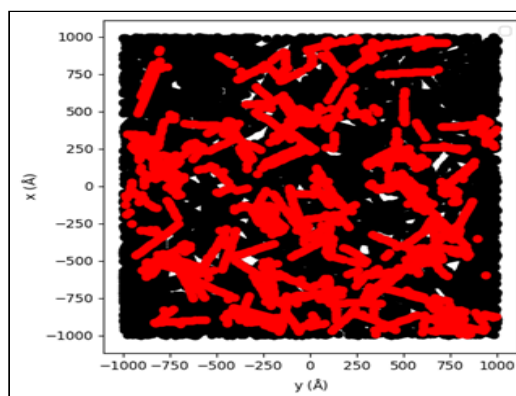


Fig. 6. Example calculation of the electrical conductivity through a film model, highlighting current carrying CNTs.

Electric fields for tuning molecular orientation in TPD-modified glasses

Marta Rodríguez-López^{1*}, Antonio, Cappai², Claudio Melis², Luciano Colombo², Javier Rodríguez-Viejo¹, Marta Gonzalez-Silveira¹.

¹ Group of Thermal properties of Nanoscale Materials (GTNaM), Universitat Autònoma de Barcelona (UAB) & Catalan Institute of Nanoscience and Nanotechnology (ICN2), Barcelona, Spain.

² Dipartimento di Fisica, Università di Cagliari, Cittadella Universitaria, Monserrato (Ca), Italy.

*E-mail: marta.rodriguez@uab.cat

INTRODUCTION

Molecular organic glasses are nowadays gaining attention due to the great advantages they present when used in the electronics industry, such as flexibility, freedom of choice of the underlying layers, low cost, easily control of the thickness and composition and simple fabrication process. However, their lack of efficiency and long-term stability prevent their presence in our daily life. These inconveniences can be solved if those glasses are prepared by Physical Vapor Deposition (PVD) [1]. This technique permits to tune glasses properties by changing the preparation conditions such as the deposition temperature and rate. One of the key attributes that can be tuned is the spatial orientation of the molecules in the glass, differing from the random distribution that a traditional isotropic glass would have, therefore enhancing the electrical, thermal and optical properties of the glassy materials [2,3]. The orientation is mostly determined by the deposition temperature during a PVD process, which is also involved in the stability of the glass. Therefore, it is desirable to decouple these two properties – in order to obtain ultrastable glasses in which the orientation of its molecules can be chosen as demanded by the final application.

MODEL

In this work, molecular dynamics simulations (performed by the LAMMPS package) are used for studying the electric field effect on the PVD process. Previous investigations already managed

to extract properties of vapor deposited glasses, as stability and anisotropy, by building up organic molecules with Lennard-Jones model potentials [4]. Our work goes one step further, as it simulates the realistic structures of the deposited molecules using the GAFF force field. External electric field is applied to the system in order to determine if it is possible to change the orientation imposed by the substrate temperature.

DESCRIPTION

We are studying how molecules in a simulated vapor deposited glass behave under the application of an external electric field of up to 10^9 V/m. The goal is to change the imposed orientation by the deposition temperature. To do so, the molecules used for this work are a modified version of the commercially available TPD, TPD-Br. This later molecule has a larger dipole moment while maintaining the shape and the semiconductor behavior. In this context, different situations have been investigated to extract when and under which conditions there is an effect of the field to the orientation of the dipole moment, including static and dynamic depositions of single and multiple molecules. Useful parameters obtained in the laboratory, such as the order parameter, can be extracted from the simulations too.

CONCLUSION

The work concludes that the effect of the electric field is produced at the top of the surface, where the degrees of freedom are reduced, taking advantage of the surface diffusion. These

simulations are a complement of an experimental work that intends to affect the orientation of the molecules in real systems. Therefore, the parameters obtained in the calculations can be compared to the ones obtained in the laboratory.

ACKNOWLEDGMENT

J.R.-V. and M.G.-S. acknowledge grant MAT2016-79759-R funded by MCIN/AEI/10.13039/501100011033 and 'ERDF A way of making Europe', and grant PID2020-117409RB-I00 funded by MCIN/AEI/10.13039/501100011033. M.R.-L. was in receipt of a FI-SDUR 2020 from AGAUR Agència de Gestió d'Ajuts Universitaris i de Recerca. A.C., C.M. and L.C. acknowledge financial support under the National Recovery and Resilience Plan (NRRP), Mission 4 Component 2 Investment 1.3 - Call for tender No.341 published on March 13, 2022) by the Italian Ministry of University and Research (MUR) funded by the European Union - NextGenerationEU. Award Number: Project code PE\00000021, Concession Decree No. 1561 adopted on October 11, 2022 by the Italian Ministry of Ministry of University and Research (MUR), CUP F53C22000770007, Project title "NEST - Network 4 Energy Sustainable Transition".

REFERENCES

- [1] S.F. Swallen, K.L. Kearns, M.K. Mapes et al., *Organic Glasses with Exceptional Thermodynamic and Kinetic Stability*. Science, 315.5810, 353-356 (2007).
- [2] D. Yokoyama. *Molecular orientation in small-molecule organic light-emitting diodes*. J. Mater. Chem. 21, 19187 (2011).
- [3] Joan Ràfols-Ribé, Riccardo Dettori et al., *Evidence of thermal transport anisotropy in stable glasses of vapor deposited organic molecules*. Phys. Rev. Materials **2**, 035603 (2018).
- [4] Lyubimov I., Antony L., Walters D. et al., *Orientalional anisotropy in simulated vapor-deposited molecular glasses*. The Journal of Chemical Physics, **143**(9), 094502 (2015).

Shot noise in disordered graphene samples

P. Marconcini*, D. Logoteta[†], and M. Macucci*

*Dipartimento di Ingegneria dell'Informazione, Università di Pisa, Via Caruso 16, 56122 Pisa, Italy

[†]Dipartimento di Ingegneria dell'Informazione, Elettronica e Telecomunicazioni (DIET),

Università di Roma La Sapienza, via Eudossiana 18, 00184 Roma

e-mail: macucci@mercurio.iet.uniipi.it

INTRODUCTION

One of the most promising applications for graphene is in the implementation of sensors, which benefit from the extremely high surface-to-volume ratio of a 2-dimensional material. In order to minimize the variance on the readout of such sensors, we need to reduce all sources of noise as much as possible. A noise contribution particularly relevant for samples with high aspect ratio (ratio of the width to the length) is shot noise, which is expected to have a very peculiar behavior as a function of the chemical potential, as predicted by Tworzidło *et al.* [1] and, therefore, as a function of the voltage applied to a gate electrostatically coupled to the graphene sheet. We developed an approach, based on an envelope function representation, enabling the simulation of samples of realistic size [2], [3].

SIMULATIONS AND COMPARISON WITH EXPERIMENTAL DATA

We consider a graphene sheet, with a width W and a length L , with two contacts (Fig. 1). Contacts are modeled with large potential steps.

In Fig. 2 we report the behavior of the Fano factor as a function of the Fermi energy for an ideal graphene sample 200 nm wide and 40 nm long (and thus with an aspect ratio $W/L = 5$) (red curve) and for the same sample in the presence of disorder due to a $5 \times 10^{11} \text{ cm}^{-2}$ concentration of charged impurities placed at a distance of 1 nm from the graphene sheet (green curve). The results for a flake that has the same aspect ratio ($W/L = 5$), but with a width of 1000 nm, is reported in Fig. 3: we notice that, while in the case of ideal graphene there is simply, as expected, a scaling in terms of the energy coordinate, for disordered graphene the behavior is quite different. This can be explained considering that, contrary to the device size, the spatial scale

of the disorder is unchanged. In Fig. 4 we report the behavior of the Fano factor for a 200 nm wide sample with $W/L = 1$, again for the ideal case (red curve) and with disorder (green curve).

In Fig. 5 we present a comparison between our simulations of the behavior of the Fano factor as a function of the backgate voltage and the experimental results by Danneau *et al.* [4]: we notice a reasonable agreement with the simulation for a disordered sample with an impurity density of $5 \times 10^{11} \text{ cm}^{-2}$ located 2.15 nm away from the graphene sheet. However, it is apparent that the behavior of the Fano factor is not the one due to the effect studied by Tworzidło *et al.*, but, rather, it is a consequence of the prevailing effect of the disorder. Finally, in Fig. 6 we show a comparison between the results obtained by DiCarlo *et al.* [5] and the same simulation as in Fig. 5: in this case the experimental data do not exhibit any significant variation of the Fano factor with the position of the Fermi level: most likely this is the consequence of an even stronger disorder.

ACKNOWLEDGMENT

This work was partially supported by the Italian Ministry for University and Research (MUR) in the framework of the “CrossLab” and of the “FoReLab” projects (Departments of Excellence).

REFERENCES

- [1] J. Tworzidło, B. Trauzettel, M. Titov, A. Rycerz, and C. W. J. Beenakker, *Phys. Rev. Lett.* **96**, 246802 (2006).
- [2] D. Logoteta, P. Marconcini, C. Bonati, M. Fagotti, and M. Macucci, *Phys. Rev. E* **89**, 063309 (2014).
- [3] P. Marconcini, D. Logoteta, and M. Macucci, *Phys. Rev. B* **104**, 155429 (2021).
- [4] R. Danneau, F. Wu, M. F. Craciun, S. Russo, M. Y. Tomi, J. Salmilehto, A. F. Morpurgo, and P. J. Hakonen, *Phys. Rev. Lett.* **100**, 196802 (2008).
- [5] L. DiCarlo, J. R. Williams, Y. Zhang, D. T. McClure, and C. M. Marcus, *Phys. Rev. Lett.* **100**, 156801 (2008).

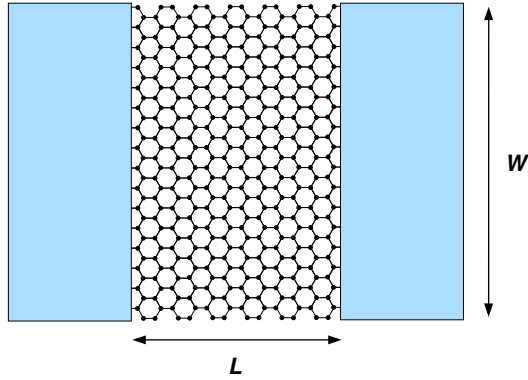


Fig. 1. Graphene sample

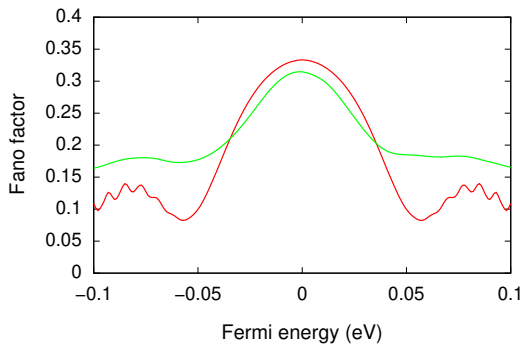


Fig. 2. Fano factor vs. Fermi energy for a graphene sample with $W/L = 5$ and $W = 200$ nm for an ideal sample (red curve) and a disordered sample (green curve)

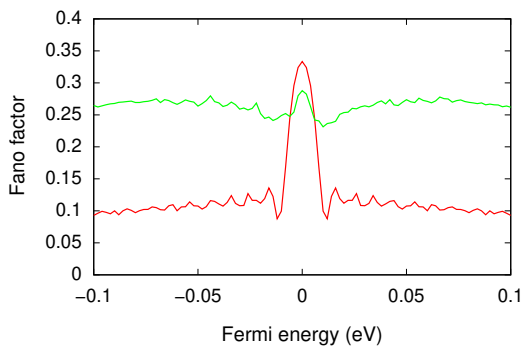


Fig. 3. Fano factor vs. Fermi energy for a graphene sample with $W/L = 5$ and $W = 1000$ nm for an ideal sample (red curve) and a disordered sample (green curve)

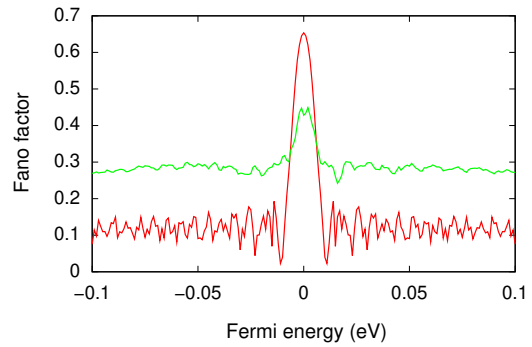


Fig. 4. Fano factor vs. Fermi energy for a graphene sample with $W/L = 1$ and $W = 200$ nm for an ideal sample (red curve) and a disordered sample (green curve)

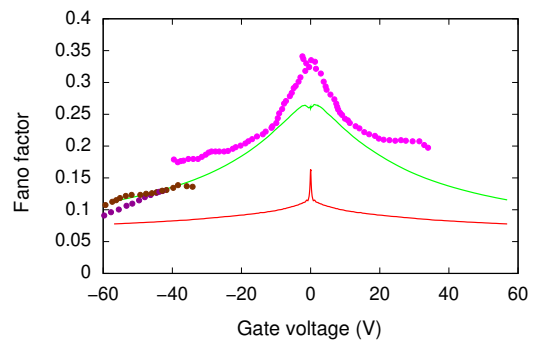


Fig. 5. Comparison between the results of the simulation and the experimental data by Danneau *et al.*

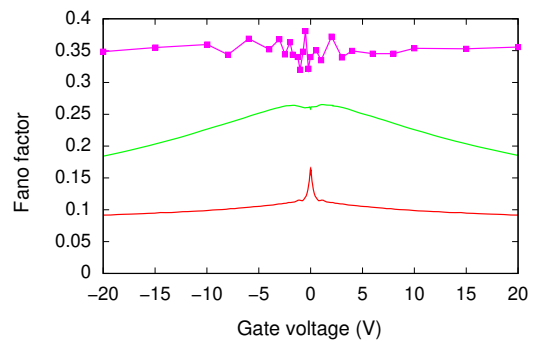


Fig. 6. Comparison between the results of the simulation and the experimental data by DiCarlo *et al.*

Engineering of Charge Current Flow in Nanoporous Graphenes

I. Alcón*, A. Cummings* and S. Roche**†

*Catalan Institute of Nanoscience and Nanotechnology (ICN2), Campus UAB, Bellaterra, 08193 Barcelona, Spain

†ICREA, Institució Catalana de Recerca i Estudis Avançats, 08070 Barcelona, Spain
e-mail: isaac.alcon@icn2.cat

ABSTRACT SUBMISSION

INTRODUCTION

During the last decade, on-surface fabricated graphene nanoribbons (GNRs) have gathered enormous attention due to their semiconducting π -conjugated nature and atomically precise structure.[1] GNRs are regularly characterized by means of scanning probe microscopy (SPM), which has also allowed to study exotic electronic quantum phases realized in these nanostructured materials.[2] A significant breakthrough in the same field was the fabrication of the nanoporous graphene (NPG) as a 2D array of laterally bonded GNRs,[3] as sketched in Fig. 1. This covalent integration of GNRs could enable complex electronic functionality at the nanoscale, particularly if one could tune the electronic coupling between GNRs within NPGs.

RESULTS

In this talk I will summarize recent efforts towards controlling current flow within NPGs either via rational chemical design[4] or via external means such as electrostatic gates.[5] Our most recent studies, based on quantum chemical calculations and large-scale transport simulations, generalize these ideas to other types of carbon nanostructures[6] and, importantly, demonstrate their applicability under practical use conditions, such as including the effect of electrostatic disorder or finite temperature (see Fig. 1).

CONCLUSION

A fundamental strategy to design carbon nanodevices with built-in externally tunable electronics is thus proposed, and should be key for future applications such as bio-chemical nanosensing and carbon nanoelectronics.

REFERENCES

- [1] Cai, J. *et al.* *Atomically precise bottom-up fabrication of graphene nanoribbons*, *Nature* **466**, 470–3 (2010).
- [2] Rizzo, D. J. *et al.* *Topological band engineering of graphene nanoribbons*, *Nature* **560**, 204–208 (2018)
- [3] Moreno, C. *et al.* *Bottom-up synthesis of multifunctional nanoporous graphene*, *Science* **360**, 199–203 (2018)
- [4] Calogero, G., Alcón, I., Papior, N., Jauho, A.-P. & Brandbyge, M. *Quantum Interference Engineering of Nanoporous Graphene for Carbon Nanocircuitry*, *J. Am. Chem. Soc.* **141**, 13081–13088 (2019)
- [5] Alcón, I., Calogero, G., Papior, N. & Brandbyge, M. *Electrochemical Control of Charge Current Flow in Nanoporous Graphene*, *Adv. Funct. Mater.* **31**, 2104031 (2021)
- [6] Alcón, I. *et al.* *Unveiling the Multiradical Character of the Biphenylene Network and Its Anisotropic Charge Transport*, *J. Am. Chem. Soc.* **144**, 8278–8285 (2022)

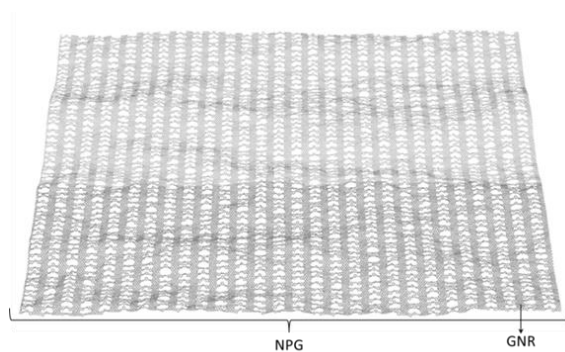


Fig. 1. NPGs are made as 2D arrays of laterally connected parallel GNRs.

Recombination Time in Drift-Diffusion Models of Graphene Field-Effect Transistors

Pedro C. Feijoo^{1,2,*}, Ferney A. Chaves², David Jiménez²

¹Departamento de Matemática Aplicada a la Ingeniería Industrial, C/José Gutiérrez Abascal 2, 28006 Madrid, Universidad Politécnica de Madrid

²Departament d'Enginyeria Electrònica, C/ de les Sitges s/n, 08193 Cerdanyola del Vallès (Barcelona), Universitat Autònoma de Barcelona

*e-mail: pc.feijoo@upm.es

1. Introduction

Graphene field-effect transistors (GFET) have been widely studied for applications in electronics, such as sensors or radiofrequency. Several physical models have been developed to explain the carrier transport in GFETs [1-3], but the way to introduce carrier generation-recombination is still in debate. Drift-diffusion models in graphene often use a single quasi-Fermi level for both electrons and holes as an approximation, assuming a very low recombination time, which is measured and calculated to be in the order of 1-100 ps [4]. This work presents a method to calculate the net recombination rate, adapted from semiconductor physics, which is applied to a self-consistent Poisson-drift-diffusion GFET model.

2. Methods

We study double-gate GFETs with a structure as presented in Fig. 1. Continuity equations for electron and hole current densities in the stationary state (J_n and J_p , respectively) can be expressed by the following equation:

$$\frac{dJ_n}{dy} = -\frac{dJ_p}{dy} = qU \quad (1)$$

where U is the net recombination rate of electron-hole pairs [5]. The total drain current density J_{DS} is the sum of the electron and hole current densities. Considering only band-to-band generation-recombination in graphene, we write the net recombination rate with a relaxation form, depending on the recombination time τ :

$$U = \frac{\partial(\Delta n)}{\partial t} = \frac{\partial(\Delta p)}{\partial t} = -\frac{n - n_{eq}}{\tau} \quad (2)$$

To calculate carrier concentration in equilibrium n_{eq} , we must assume the quasi-neutral approximation (the excess of electrons must equal the excess of holes, $\Delta n = \Delta p$). The parameters for simulations are listed in Table 1.

3. Results and discussion

We explore how recombination time affects graphene carrier transport. Transfer characteristics in Fig. 2 show that the recombination time mostly affects drain current at biases close to the Dirac point. Quasi-Fermi levels for electrons and holes at the Dirac bias are represented in Fig. 3. For τ above 1 ps, the two levels show a large separation, which decreases as τ is reduced and

eventually converge into the model of a single quasi-Fermi level for $\tau \rightarrow 0$. At the Dirac bias, electron and hole concentrations in the graphene channel are comparable, and their distribution as a function of τ can be observed in Fig. 4. The net recombination rate is represented in Fig. 5. This rate is null when the τ is large, as can be deduced from Eq. 2. However, for short times, the net recombination is maximum in the middle of the channel, where carrier concentration is minimum (see Fig. 4). The value of U at this point in the channel increases gradually as τ decreases.

4. Conclusions

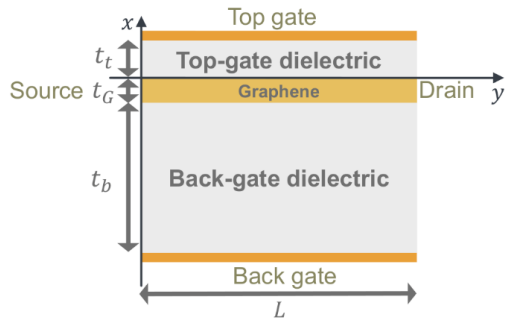
This work confirms that a single quasi-Fermi level for electrons and holes is a good approximation when recombination times are small enough. However, a sizeable separation between quasi-Fermi levels might appear for longer recombination times being the increase of the conductivity at the Dirac voltage the expected fingerprint.

Acknowledgements

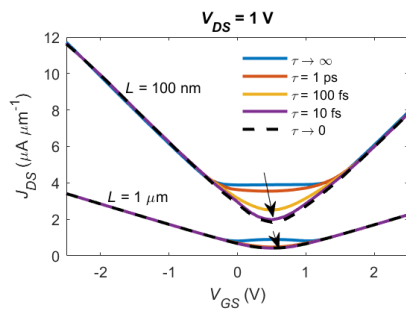
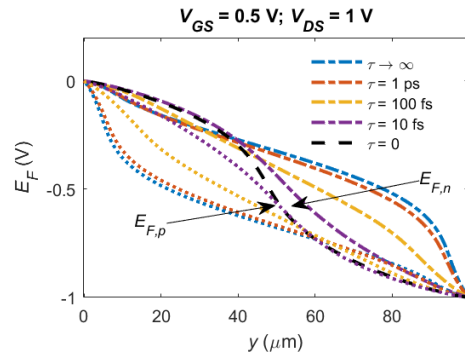
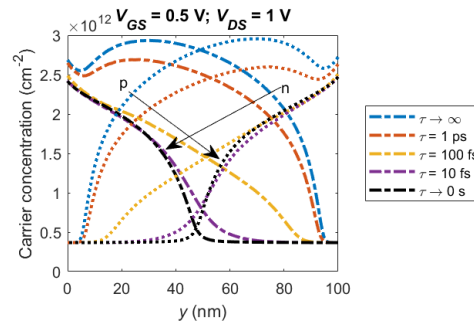
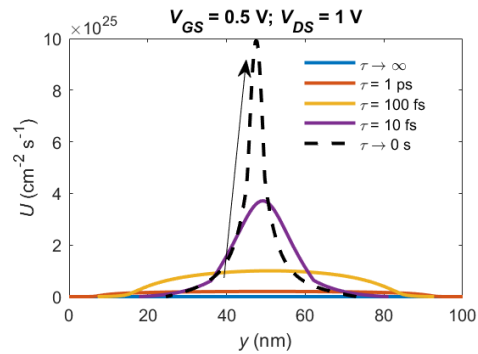
This work has received funding from the European Union's Horizon 2020 Research and Innovation Programme under Grant Agreement No. GrapheneCore3 881603, from the Spanish Government under the project PID2021-127840NB-I00 (MCIN/AEI/FEDER, UE) and from the European Union Regional Development Fund within the framework of the ERDF Operational Program of Catalonia 2014–2020 with the support of the Departament de Recerca i Universitat, with a grant of 50% of total cost eligible. GraphCAT project reference: 001-P-001702.

References

- [1] S. Thiele et al., J Appl Phys, vol. 110, no. 3, p. 034506, 2011.
- [2] C. Yu et al., IEEE Electron Device Lett, vol. 42, no. 2, pp. 268–271, 2021.
- [3] O. Habibpour, et al., IEEE Trans Electron Devices, vol. 59, no. 4, pp. 968–975, Apr. 2012.
- [4] P. Huang et al., Nature Comm, vol. 11, no. 863, 2020.
- [5] M. G. Ancona, IEEE Trans Electron Devices, vol. 57, no. 3, pp. 681–689, 2010.


Fig. 1. Schematic of the active region of the GFET.

Parameter	Symbol	Values
Channel length	L	100 nm, 1 μm
Top dielectric thickness	t_t	10 nm
Bottom dielectric thickness	t_b	285 nm
Top dielectric permittivity	ϵ_t	$9 \epsilon_0$
Bottom dielectric permittivity	ϵ_b	$3.9 \epsilon_0$
Source bias	V_S	0 V
Drain bias	V_D	1 V
Bottom gate bias	V_B	0 V
Flatband voltages	V_{gs0} and V_{bs0}	0 V
Low-field carrier mobility	μ_{LF}	$2000 \text{ cm}^2 \text{ V}^{-1} \text{ s}^{-1}$
Saturation velocity	v_{sat}	$6.59 \cdot 10^5 \text{ m s}^{-1}$
Saturation velocity parameter	β	1
Puddle concentration	σ_0	$3.67 \cdot 10^{11} \text{ cm}^{-2}$
Recombination times	τ	0, 10^{-14} , 10^{-13} , 10^{-12} , ∞ s
Temperature	T	300 K

Table 1. Main parameters used in the simulations.

Fig. 2. Transfer curves for different recombination times in GFETs with two channel lengths.

Fig. 3. Electron (dashed-dotted lines) and hole (dotted) quasi-Fermi levels at Dirac bias for different recombination times. As recombination time approaches 0 s, quasi-Fermi levels converge to a single curve.

Fig. 4. Electron (dashed-dotted lines) and hole (dotted) concentrations in the channel at Dirac bias for different recombination times.

Fig. 5. Net recombination in the channel at Dirac bias for different recombination times.

Numerical simulation of terahertz carrier dynamics in monolayer MoS₂

Shuva Mitra, Laleh Avazpour, and Irena Knezevic
 Department of Electrical and Computer Engineering
 University of Wisconsin-Madison, Madison, WI 53706, USA
 smitra8@wisc.edu, laleh.avazpour@wisc.edu, irena.knezevic@wisc.edu

I. INTRODUCTION

Among the rapidly advancing two-dimensional (2D) quantum materials, transition-metal dichalcogenides (TMDs) are attractive for their promising electronic properties [1], [2]. Monolayer molybdenum disulfide (MoS₂) is particularly suitable for electronic and optoelectronic applications, as it is a direct bandgap material, with additional advantages such as high on-off current ratio and speed [3]. The complex conductivity $\sigma(\omega)$, where ω is the angular frequency, is an important quantity that characterizes the electrical transport of materials under electrical and electromagnetic sources. The terahertz (THz) frequency range is particularly interesting because most 2D materials including TMDs have scattering rates in this range. The interplay between carrier transport and electromagnetic fields cannot be approximated by traditional time-dependent device simulation techniques, where electronic solvers are coupled with a quasi-electrostatic Poisson's solver because at THz frequencies, $\omega\tau \approx 1$, where τ is the effective carrier lifetime, makes the quasi-electrostatic approximation inaccurate.

In this paper, we analyze the frequency-dependent low-field THz-frequency electrical conductivity of monolayer MoS₂ both suspended and supported on different substrates [4]. Our numerical simulation tool employs the ensemble Monte Carlo (EMC) technique, widely used for diffusive carrier transport simulation, with the finite-difference-time-domain (FDTD) technique as the electromagnetic field solver. The EMC and FDTD source each other, where EMC incorporating various scattering mechanisms and updates charge and current densities based on calculated fields from FDTD, and FDTD updates fields based on the charge and current distributions from EMC. The EMC-FDTD technique was previously used to compute the THz conductivity of bulk silicon and graphene sheets [5], [6].

II. NUMERICAL MODEL

Figure 1 shows the numerical simulation domain. The domain consists of a single layer of MoS₂ with air in the top half and a dielectric in the bottom half. For the suspended case, the dielectric is also air, and for the supported case, we considered commonly used SiO₂ and hBN substrates. The horizontal planes at the top and bottom are terminated via convolutional perfectly matched layer (CPML) boundary conditions and the vertical planes via periodic boundary conditions to simulate a large semiconductor. Carrier transport is limited by acoustic and optical phonon scattering, as well as long-range Coulomb interaction with ionized impurities present in the MoS₂ layer and the substrate. The scattering rates are calculated under the deformation potential approximation with the effective mass extracted from tight-binding calculations. The time-dependent fields and currents are Fourier transformed to obtain the conductivity using

$$\sigma(\omega) = \frac{\tilde{\mathbf{E}}(\omega) \cdot \tilde{\mathbf{J}}^*(\omega)}{|\tilde{\mathbf{E}}(\omega)|^2}, \quad (1)$$

where $\tilde{\mathbf{E}}(\omega)$ and $\tilde{\mathbf{J}}(\omega)$ are the spatially averaged steady-state electric-field and current-density phasors.

We demonstrate the application of our technique here. Figure 2 shows the real part of $\sigma(\omega)$ for suspended MoS₂ at different carrier densities. The conductivity shows Drude-type behavior. $\text{Re}[\sigma(\omega)]$ increases at high carrier densities while the effective lifetime approaches the impurity-free value taking the screening of ionized impurities into account. Figure 3 shows the conductivity when the sample is placed on substrates. Remote phonon scattering lowers the conductivity. However, MoS₂ on a highly polar SiO₂ has a higher conductivity than on hBN at high frequencies and an overall flatter frequency dependence.

III. CONCLUSION

In conclusion, we presented a coupled EMC–FDTD technique to simulate terahertz frequency dynamics of monolayer MoS₂. This macroscopic simulation tool can be effective to understand frequency-dependent electronic transport and substrate effects on emerging 2D materials.

REFERENCES

- [1] G. Fiori, F. Bonaccorso, G. Iannaccone, T. Palacios, D. Neumaier, A. Seabaugh, S. K. Banerjee, and L. Colombo, “Electronics based on two-dimensional materials,” *Nature Nanotechnology*, vol. 9, no. 10, pp. 768–779, Oct. 2014. [Online]. Available: <https://doi.org/10.1038/nnano.2014.207>
- [2] D. Lembke, S. Bertolazzi, and A. Kis, “Single-layer mos₂ electronics,” *Accounts of Chemical Research*, vol. 48, no. 1, pp. 100–110, Jan. 2015. [Online]. Available: <https://doi.org/10.1021/ar500274q>
- [3] M. Amani, M. L. Chin, A. G. Birdwell, T. P. O’Regan, S. Najmaei, Z. Liu, P. M. Ajayan, J. Lou, and M. Dubey, “Electrical performance of monolayer MoS₂ field-effect transistors prepared by chemical vapor deposition,” *Applied Physics Letters*, vol. 102, no. 19, p. 193107, May 2013. [Online]. Available: <https://doi.org/10.1063/1.4804546>
- [4] S. Mitra, L. Avazpour, and I. Knezevic, “Terahertz conductivity of monolayer MoS₂,” *Journal of Computational Electronics*, 2023, in press.
- [5] K. J. Willis, S. C. Hagness, and I. Knezevic, “Terahertz conductivity of doped silicon calculated using the ensemble monte carlo/finite-difference time-domain simulation technique,” *Applied Physics Letters*, vol. 96, no. 6, p. 062106, 2010. [Online]. Available: <https://doi.org/10.1063/1.3308491>
- [6] N. Sule, K. J. Willis, S. C. Hagness, and I. Knezevic, “Terahertz-frequency electronic transport in graphene,” *Physical Review B*, vol. 90, no. 4, Jul. 2014. [Online]. Available: <https://doi.org/10.1103/physrevb.90.045431>

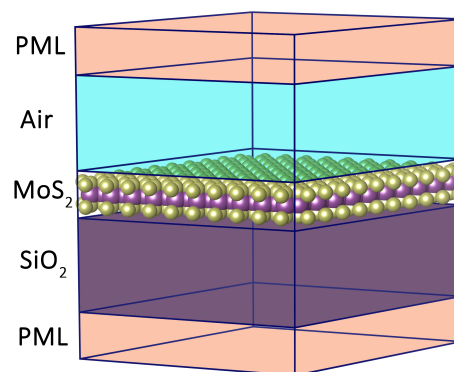


Fig. 1. Schematic of the three-dimensional (3D) simulation geometry of monolayer MoS₂ between air on top and SiO₂ substrate on bottom. The vertical boundaries have periodic boundary conditions.

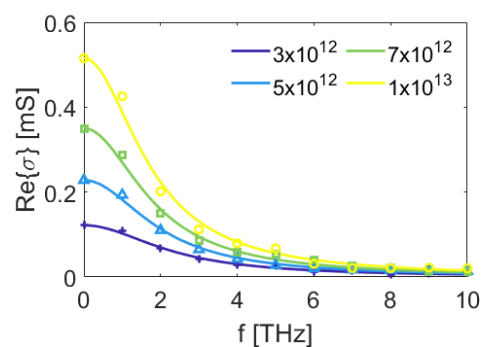


Fig. 2. Real part of $\sigma(\omega)$ as a function of terahertz frequency for different electron densities in suspended monolayer MoS₂. The impurity density throughout is 10^{12} cm⁻². The points are numerically calculated and the solid lines are Drude fits.

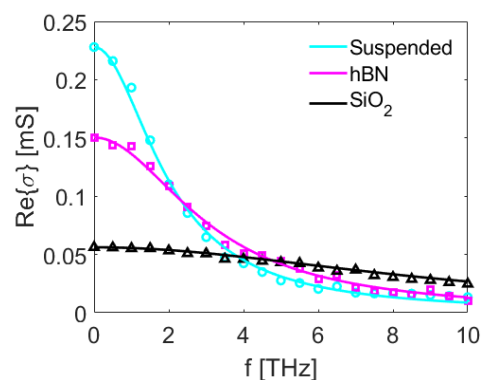


Fig. 3. Real part of $\sigma(\omega)$ versus frequency for MoS₂ that is suspended, supported on hBN, and supported on SiO₂.

Quantum Transport Study of Metal-TMD Contacts: Role of the Dielectric Environment

Pranay Kumar Reddy Baikadi¹, Peter Reyntjens^{1,2}, Maarten L. Van de Put² and William G. Vandenberghe¹

¹Department of Materials Science and Engineering, The University of Texas, Dallas, TX, USA

²Department of Material Engineering, KU Leuven, Belgium,
email: wxv101020@utdallas.edu

ABSTRACT

We use non-equilibrium Green's Function (NEGF) quantum transport simulations to calculate contact resistance of metal contacted to TMDs and investigate the impact of non-uniform dielectric environment along the transport direction. We investigated five dielectric combinations and find that a low- κ near the metal edge gives lower contact resistances.

INTRODUCTION

Over the years, many strategies such as heavily doping the TMD to increase tunneling current, using low workfunction metals such as Scandium [1] have been developed to reduce contact resistance (R_c) in top contacts. Most recently, semi-metal contacts to MoS₂ have been demonstrated, where a record low R_c of 123 $\Omega\text{-}\mu\text{m}$ was achieved for Bi-MoS₂ system [2]. In terms of modeling, Density Functional Theory (DFT) has been used to study metal-TMD interfaces. However, the large computational burden involved in DFT presents a severe limitation in studying lowly doped TMDs, where the depletion length is large. Moreover, solving the Poisson equation and using the WKB approximation, some of us showed that the dielectric environment plays a critical role in side contacts [3].

In this paper we perform quantum transport simulations of a top and bottom contacted TMD. We shed light on the importance of the dielectric environment for these structures and identify the most promising dielectric setup that results in good contacts.

MODEL

We first generate a commensurate unit cell of two layers of metal and a TMD monolayer, where an interlayer distance of ~ 2.5 Å is obtained by performing structural relaxation calculations using VASP [4]. The commensurate unit cell is repeated along the transport direction (x) but to realize a

top-contacted geometry, we remove the periodicity by applying a potential that eliminates a portion of metal above the TMD.

To perform self-consistent calculations, we apply a bias of 0.1 V to the right edge of the simulation domain. We model the electron density in the metal and TMD using (1) and (2) of Fig. 5. We model the TMD-contact current using the PETRA quantum transport code [5]. The self-consistent potential is used to construct the Hamiltonian in the NEGF formalism, where transmission is evaluated by applying quantum transmitting boundary conditions (QTBM). Equations for current and R_c are shown in Fig 5.

RESULTS

Fig. 1 shows the color plots of free charge density for four dielectric combinations. We see that systems with low- κ near the metal edge have smaller depletion widths. The band-diagrams shown in Fig. 2 reinforce this observation where the Schottky barrier height (SBH), measured at the metal edge, is lower for left-SiO₂ systems. The calculated R_c for five dielectric combinations is shown in Fig. 3, where left-low- κ systems have about 5 orders of magnitude lower R_c compared to their left-high- κ counterparts. In Fig. 4, we show the contact resistances as a function of left dielectric length (right dielectric being HfO₂). We observe an optimal length of at ~ 2 nm for which R_c is found to be the lowest.

CONCLUSIONS

Five different dielectric combinations are investigated for dual-metal TMD contacts. Having a low- κ near the metal edge was found to give low contact resistances.

REFERENCES

- [1] S. Das *et al.*, *Nano Lett.*, vol. 13, no. 1, pp. 100–105, Jan. 2013.
- [2] P.-C. Shen *et al.*, *Nature*, vol. 593, no. 7858, pp. 211–217, May 2021.
- [3] Brahma, Madhuchhanda, *et al.*, *2021 SISPAD*. IEEE, 2021.
- [4] G. Kresse *et al.*, *Phys. Rev. B* 47, 558 (1993); *ibid.* 49, 14 251 (1994).
- [5] M. L. Van de Put *et al.*, *Computer Physics Communications*, vol. 244, pp. 156–169, Nov. 2019.

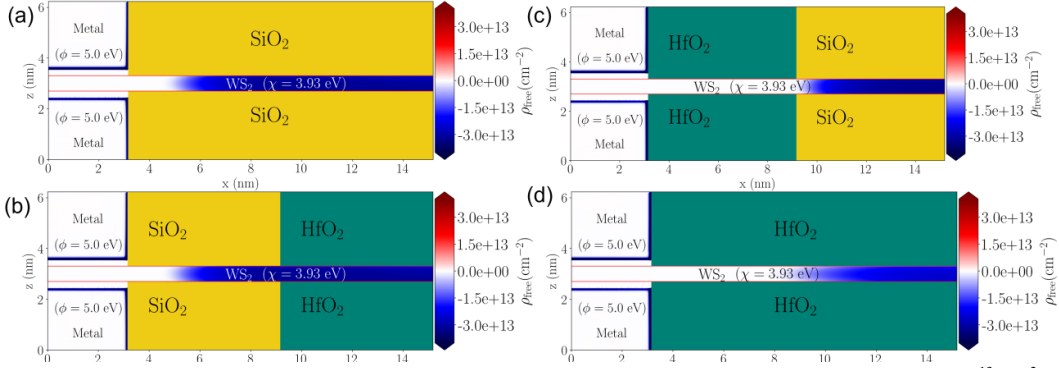


Figure 1. Color plots of free charge density for the four dielectric combinations. The TMD is n -doped to $1.73 \times 10^{13} \text{ cm}^{-2}$.

Configurations with low- κ environment closer to metal edge have smaller depletion widths.

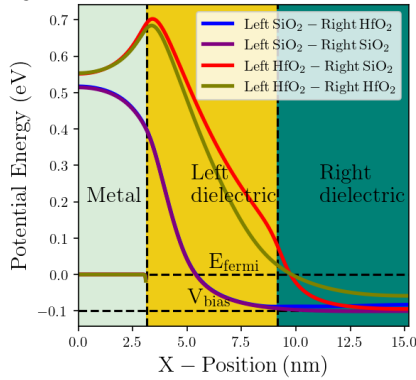


Figure 2. Band diagrams for the four different dielectric combinations, obtained by taking the cutlines (along the length of metal and TMD) of the mean of the self-consistent potential along the transverse direction (y). Systems with low- κ environment near the metal edge have lower barrier heights and smaller depletion widths.

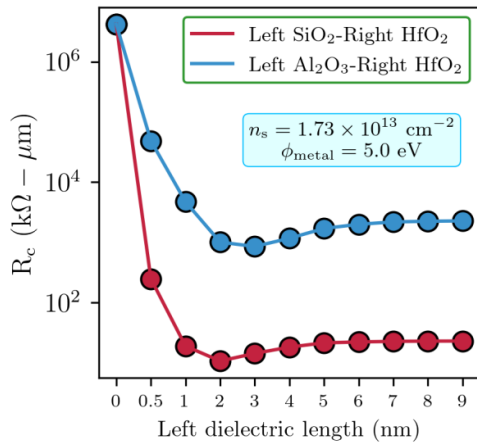


Figure 4. Contact resistance as a function of left dielectric length for metal-WS₂ system. For both cases, we observe an optimal left dielectric length of about 2 nm that gives the lowest R_c .

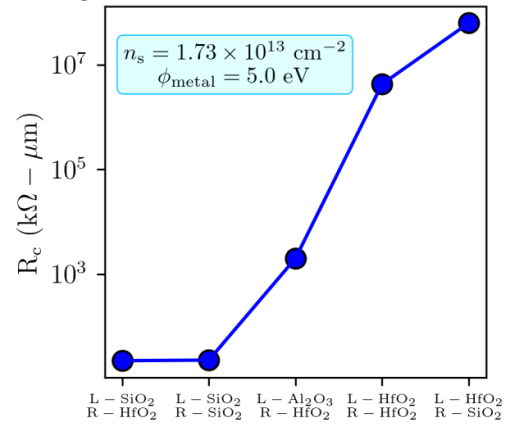


Figure 3. Calculated contact resistances for the four dielectric combinations. Left low- κ systems have the least contact resistances.

$$\rho = DOS_{\text{metal}} \times (E - \phi_{\text{metal}}) \quad (1)$$

$$\rho = \frac{m^* k_B T}{\pi \hbar^2} \ln \left(1 + e^{-\left(\frac{E - \chi - E_F}{k_B T}\right)} \right) \quad (2)$$

$$\nabla \cdot [\epsilon(\mathbf{r}) \nabla V(\mathbf{r})] = \rho[\mathbf{r}, V] + \rho_{\text{doping}}(\mathbf{r}) \quad (3)$$

$$[EM - H - \Sigma] \mathbf{c} = \mathbf{B} \quad (4)$$

$$I = \frac{2q}{h} \left(\int T(E) (f_L(E) - f_R(E)) dE \right) \quad (5)$$

Figure 5. Equations describing our methodology. (1) and (2) describe semiclassical modeling of free charge density in metal and TMD respectively. (3) is the non-linear Poisson equation used to find the potential self-consistently. (4) is then used to solve for the coefficients, \mathbf{c} , of the injected modes at energy E , from which transmission coefficients are extracted [5]. And (5) is used to calculate current through the contact, using the transmission coefficients calculated above, from which contact resistance, R_c , is extracted.

Acknowledgement: This material is based upon work supported by Intel Corporation. We acknowledge the Texas Advanced Computing Center (TACC) at The University of Texas at Austin for providing the high-performance computing resources.

Electrothermal Properties of 2D Materials

S. Klein¹, Z. Aksamija²

¹University of Massachusetts, Amherst, MA, USA, ²University of Utah, Salt Lake City, UT, USA,
email: zlatan.aksamija@utah.edu

Abstract—To keep downsizing transistors, new materials must be explored. 2D materials are appealing due to their thinness and bandgap. The relatively weak van der Waals forces between layers in 2D materials allow easy exfoliation and device fabrication but also result in poor heat transfer to the substrate, which is the main path for heat removal. The impaired thermal coupling is exacerbated in few-layer devices where heat dissipated in the layers further from the substrate encounters additional interlayer thermal resistance before reaching the substrate, which results in self-heating ($\Delta T \neq 0$ where ΔT is the temperature rise of the few-layer device) and degradation of mobility. This study explores the electrothermal properties of five materials (MoS₂, MoSe₂, WS₂, WSe₂, and 2D black phosphorous). We simulate various devices with self-heating with various V_{DS} and examine the effects on mobility and change in device temperature and compare to the isothermal case ($\Delta T = 0$). We observe that self-heating has a significant effect on temperature rise, layer-wise drain current, and effective mobility. We show that black phosphorous performs the best thermally and WSe₂ performs the best electrically. This study will inform future thermally aware designs of nano electronic devices based on 2D materials.

I. INTRODUCTION

As transistors continue to become smaller, traditional 3D materials such as silicon become problematic as quantum effects prevail [1]. New materials must be explored to continue downsizing semiconductors. 2D materials such as transition metal dichalcogenides (TMDs) and 2D black phosphorus (phosphorene) are attractive replacements as they are thin and contain a bandgap [2]. Mobility suffers in single-layer devices [3] due to charged impurity scattering from the substrate. To resolve this issue, few-layer stacks are explored, using the layers immediately above the first layer to encapsulate the bottom [4]. This results in improved mobility but creates more thermal issues. Heat removal is more difficult in upper layers as they are farthest from the substrate, which dissipates the most heat from the device [5], and the layers create additional interlayer thermal resistance [6] due to weak van der Waals forces between 2D layers [7]. This results in self-heating and a degradation of mobility.

In this study, the four TMDs (MoS₂, MoSe₂, WS₂, and WSe₂) as well as 2D black phosphorus (BP) are compared. We look at several electrical properties (drain current and mobility) and multiple thermal properties (temperature rise, joule heating, mobility degradation, TBC, and effective conductivity) to determine what material has the best balance between electrical and thermal performances.

II. METHODS

The device being simulated is a back-gated MOSFET, composed of 10 layers. The source and drain contacts are connected to the topmost layer with the substrate and gate below the bottommost layer. Each layer has a different resistance, voltage, and current flowing through it. The current encounters extra resistance via interlayer resistance as well as the contact resistance above the topmost layer. The device can be represented as a resistor network, composed of layer resistance, interlayer resistance, and contact resistance, which is used to calculate layer-wise voltage and current. We use the coupled Schrodinger-Poisson equations to calculate carrier concentration per layer (Q_i) and screening length per layer (λ_i), from which mobility per layer is calculated using $\mu_i = \mu_1 + (\mu_0 - \mu_1)(1 - c_i)$ where $c_i = c_{i-1} (\exp(-d_{ML}/\lambda_i))$ and d_{ML} is the thickness of the layer. We calculate layer-wise resistivity using $\rho_i = m/Q_i e \mu_i \cdot L_{channel}$ where m is the fraction of the channel not pinched off, e is the magnitude of the charge of an electron, and $L_{channel}$ is the length of the channel. We then calculate the total resistivity in the device by adding the interlayer resistances (R_{int}) and contact resistances in series with the layer resistivity and then add those values in parallel. Temperature rise per layer is calculated from

$$\Delta T_i = \left(\frac{P_i}{W_{ch} L_{ch}} \right) R_{BD,i} \left[1 - \frac{2L_{H,i}}{L_{ch}} \tanh \left(\frac{L_{ch}}{2L_{H,i}} \right) \right],$$

where $L_{H,i} = \sqrt{\kappa_{bulk} d_{ML} R_{BD,i}}$, $R_{BD,i}$ is the layer-wise thermal boundary resistance ($R_{BD,i} = 1/h_{BD,i}$), κ_{bulk} is the bulk thermal conductivity, and $W_{channel}$ is the channel width. The simulation is iterated until convergence is reached (Fig. 1).

III. RESULTS

We first look at the I_D-V_{DS} characteristics of the five materials for both the isothermal case and the self-heating case where $I_D = \sum I_i$ in Fig. 2. WS₂ has the most current and BP has the least in the isothermal case. However, current degradation due to self-heating is greatest for WS₂ and MoS₂, so WSe₂ has the most current in that case and MoS₂ has the least. Total joule heating ($P = \sum P_i$) (in Fig. 3) follows the same trend as the I_D-V_{DS} characteristics. WS₂ experiences the most joule heating in the isothermal case, but WSe₂ experiences the most with self-heating. BP has the least isothermally and MoS₂ has the least with self-heating. Next, we look at average temperature rise (ΔT_{avg}) vs V_{DS} in Fig. 4. WS₂ and WSe₂ undergo the most self-heating and BP self-heats the least. We calculate effective thermal conductance using $G_{eff} = P/\Delta T_{avg}$ in Fig. 5. BP is shown to have the highest G_{eff} which makes sense given that BP has the lowest amount of self-heating. MoS₂ has the lowest conductance.

Next, we look at the ratio of carrier mobility in the self-heating case to the isothermal case per layer in Fig. 6. Overall, WS₂ experiences the largest amount of mobility degradation. BP and WSe₂ experience the least. Factoring in phonon-limited mobility, with self-heating, WS₂ and WSe₂ have the highest upper layer mobility and MoSe₂ and BP have the lowest. Thermal boundary resistance (TBR), calculated by taking the inverse of TBC, is plotted for each layer. MoS₂ has the highest TBR and BP has the lowest.

IV. REFERENCES

- [1] H. Liu, A. T. Neal, Z. Zhu, Z. Luo, X. Xu, D. Tomanek and P. D. and Ye, "Phosphorene: An Unexplored 2D Semiconductor with a High Hole Mobility," *ACS N*, vol. 8, no. 4, pp. 4033-4041, 2014.
- [2] Z. Jin, X. Li, J. T. Mullen and K. W. and Kim, "Intrinsic transport properties of electrons and holes in monolayer transition-metal dichalcogenides," *Phys. Rev. B*, vol. 90, no. 4, p. 045422, 2014.
- [3] J. H. Kim, T. H. Kim, H. Lee, Y. R. Park, W. Choi and C. J. and Lee, "Thickness-dependent electron mobility of single and few-layer MoS₂ thin-film transistors," *AIPA*, vol. 6, no. 6, p. 065106, 2016.
- [4] D. Rhodes, S. H. Chae, R. Ribeiro-Palau and J. and Hone, "Disorder in van der Waals heterostructures of 2D materials," *Nat. Mater.*, vol. 18, no. 6, pp. 541-549, 2019.
- [5] A. K. Majee, C. J. Foss and Z. and Aksamija, "Electrical and Electrothermal Properties of Few-Layer 2D devices," *JCE*, vol. 20, no. 1, pp. 2-12, 2021.
- [6] A. K. Majee, Z. Hemmat, C. J. Foss, A. Salehi-Khojin and Z. and Aksamija, "Current Rerouting Improves Heat Removal in Few-Layer WSe₂ Devices," *ACS Applied Materials & Interfaces*, vol. 12, no. 12, pp. 14323-14330, 2020.
- [7] A. Behranginia, Z. Hemmat, A. K. Majee, C. J. Foss, P. Yasaei, Z. Aksamija and A. and Salehi-Khojin, "Power Dissipation of WSe₂ Field-Effect Transistors Probed by Low-Frequency Raman Thermometry," *ACS Applied Materials & Interfaces*, vol. 10, no. 29, pp. 24892-24898, 2018.

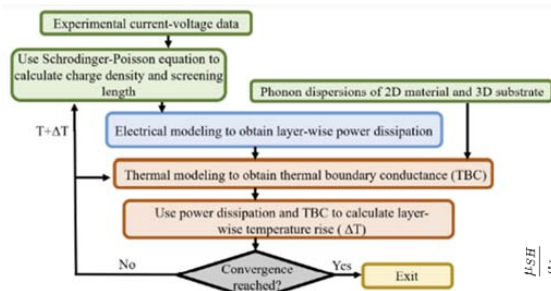


Fig. 1. Flowchart of our self-heating loop showing electronic and thermal components of the simulator.

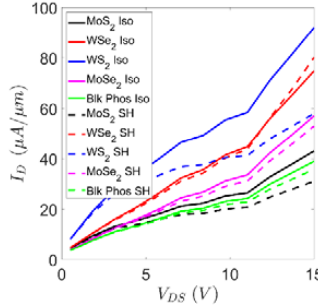


Fig. 2. IV-curve at V_g = 6V for both the isothermal (dashed) and self-heating case (solid lines).

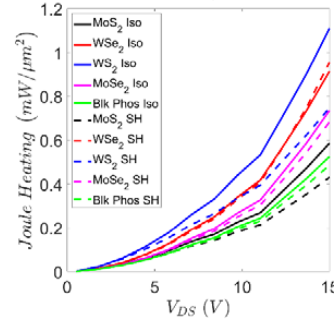


Fig. 3. Joule heating for various V_{DS} at V_g = 6V for both the isothermal (dashed) and self-heating case (solid lines).

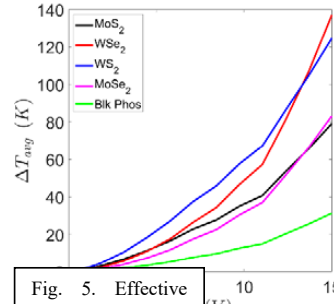


Fig. 4. Average temperature rise as a function of V_{DS} at V_g = 6V for all 5 materials under consideration showing lowest rise in BP and highest in WSe₂.

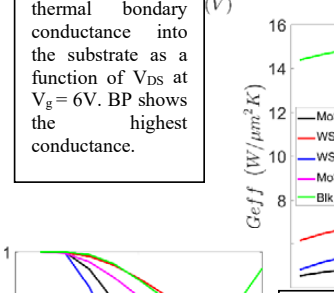


Fig. 5. Effective thermal boundary conductance into the substrate as a function of V_{DS} at V_g = 6V. BP shows the highest conductance.

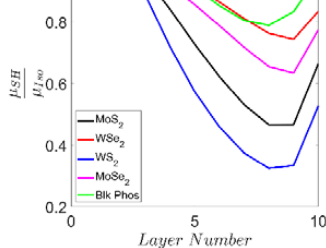


Fig. 6. Ratio of layer-wise mobility in the self-heating case to layer-wise mobility in the isothermal case at V_{DS}=15V and V_g=6V

First-principles study of water molecules at the electrified graphene surface

Hyeonwoo Yeo, Juho Lee, Ryong Gyu Lee, Seunghyun Yu, and Yong-Hoon Kim
 School of Electrical Engineering, Korea Advanced Institute of Science and Technology (KAIST), 291
 Daehak-ro, Yuseong-gu, Daejeon 34141, Korea
 (Email: dndhdrl@kaist.ac.kr)

INTRODUCTION

A detailed understanding of the atomic and electronic structures of electrified electrochemical interfaces has critical implications for the development of advanced energy conversion and storage devices. Here, graphene has been regarded as an ideal component for electrode materials due to its excellent mechanical, electrical, and chemical properties. Recently, for the improved understanding of electrified electrochemical interfaces, first-principles characterizations based on the approach combining density functional theory (DFT) and non-equilibrium Green's function (NEGF) have been utilized with much successes. However, due to the requirement of semi-infinite electrodes, the DFT-NEGF approach so far could not be applied to graphene-based electrochemical interface models. In this presentation, taking the advantage of the multi-space constrained-search DFT (MS-DFT) formalism [1-3] that can handle the electrified finite electrodes, we firstly investigate the total enthalpy change of the water molecule on the electrified graphene electrode surface in a fully first-principles manner. Moreover, by carrying out nonequilibrium molecular dynamics simulations with MS-DFT, we will study the bias-dependent configurations of water molecules at the electrified graphene-water interfaces. Comparing the interfacial water structures with those on metal electrodes, we extract important insight into the water at electrified electrochemical interfaces.

THEORETICAL BACKGROUND

In recent years, we presented a variational approach for non-equilibrium open quantum systems based on the viewpoint that maps quantum transport processes to multi-space excitation counterparts, and established as a practical ab initio computational scheme the multi-space constrained-search DFT (MS-DFT)

formalism [1-3]. Within MS-DFT, the non-equilibrium state of a channel C established by the left electrode L and right electrode R at the electrochemical potentials μ_L and μ_R , respectively, is calculated by variationally minimizing the total energy functional within the constraint of an applied finite bias voltage $eV_b = \mu_L - \mu_R$. Here in, we applied MS-DFT to the electrode-water molecule interface system where a single water molecule, which corresponds to the C , was placed close to one side of the left electrode surface (L). In order to isolate the electrode-water interface from the direct interaction induced by the other side of the right electrode (R), the distance between two electrodes is set to 20 Å.

COMPUTATIONAL DETAILS

All calculations were performed within SIESTA package [4], in which MS-DFT is implemented, and we used the gradient-dependent exchange-correlation (XC) functionals which includes van der waals corrections (vdW) [5]. Double ζ -plus-polarization-level numerical atomic orbital basis sets were employed together with the Troullier-Martins type norm-conserving pseudopotentials [6]. The mesh cutoff of 800 Ry for the real-space integration, and $5 \times 5 \times 1$ and $8 \times 8 \times 1$ Monkhorst-Pack k-points grid of the Brillouin zone were sampled for the Au(111) slab and graphene monolayer electrode, respectively. The atomic geometries were optimized until the total residual force was below 0.005 eV/Å using the conjugate gradient algorithm.

REFERENCES

- [1] J. Lee *et al.* Proc.Natl.Acad.Sci.U.S.A., 117, 10142 (2020)
- [2] J. Lee *et al.* Adv. Sci., 7, 2001038 (2020)
- [3] T.H. Kim *et al.*, Npj Comput. Mater. 8, 50 (2022)
- [4] J. M. Soler *et al.*, J.Phys.:Condens.Matter, 14, 2745 (2002)
- [5] M. Dion *et al.*, Phys. Rev. Lett., 92, 246401 (2004)
- [6] N. Troullier and J. L. Martins, Phys. Rev. B: Condens. Matter Mater. Phys., 43, 1993 (1991)

Wigner Transport in Magnetic Fields

M. Ballicchia, C. Etl, M. Nedjalkov, and J. Weinbub

Institute for Microelectronics, TU Wien, Gußhausstraße 27–29, 1040 Wien, Austria

e-mail: balliccia@iue.tuwien.ac.at

The use of magnetic fields for controlling and manipulating electron states is vital for solid-state quantum systems [1], [2], requiring comprehensive quantum transport models, able to treat multiple dimensions and time dependence. Models based on electromagnetic (EM) potentials depend on the choice of the gauge and thus the same holds for the particular numerical approaches. Recently, a Wigner model has been suggested [3], [4], formulated in terms of general EM fields \mathbf{E}, \mathbf{B} , which is thus gauge-invariant. The transport equation involves the terms $D^F(\mathbf{E})$ and $H^F(\mathbf{B})$, given by the Fourier transform $FT = \int d\mathbf{s} e^{-\frac{i}{\hbar} \mathbf{p} \cdot \mathbf{s}}$ of the quantities $\int_{-1}^1 d\tau (\mathbf{s} \cdot \mathbf{E}(\mathbf{x} + \frac{\mathbf{s}\tau}{2}))$ and $\int_{-1}^1 d\tau (\mathbf{s} \times \mathbf{B}(\mathbf{x} + \frac{\mathbf{s}\tau}{2}))$.

So far, there is no numerical and simulation experience with the general EM equation. In this work, we provide a first step into this direction by considering simplifying assumptions. These consider 2D transport in the $\mathbf{x} = (x, y)$ plane, an inhomogeneous magnetic field normal to the plane $\mathbf{B} = (0, 0, B(y))$ (linear along y : $B(y) = B_0 + B_1 y$), and a general electric field $\mathbf{E}(\mathbf{x})$. If \mathbf{E} is stationary it is possible to redefine the Wigner potential $V_w(\mathbf{p}, \mathbf{x})$ in terms of D^F . The thus obtained equation

$$\left(\frac{\partial}{\partial t} + \frac{\mathbf{p}}{m} \cdot \frac{\partial}{\partial \mathbf{x}} + \mathbf{F} \cdot \frac{\partial}{\partial \mathbf{p}} \right) f_w(\mathbf{p}, \mathbf{x}) = \int d\mathbf{p}' V_w(\mathbf{p} - \mathbf{p}', \mathbf{x}) f_w(\mathbf{p}', \mathbf{x}) + \frac{B_1 \hbar^2}{m} \frac{e}{12} \left(\frac{\partial^2}{\partial p_y^2} \frac{\partial}{\partial x} - \frac{\partial}{\partial p_x} \frac{\partial}{\partial p_y} \frac{\partial}{\partial y} \right) f_w(\mathbf{p}, \mathbf{x}), \quad (1)$$

resembles the common Wigner equation, except the additional terms originating from H^F . On the left is the force-less Liouville operator (Lo), now completed by the magnetic Lorentz force $\mathbf{F} = \frac{e}{m} \mathbf{p} \times \mathbf{B}(y)$. The third row involves higher order mixed derivatives and vanishes with $B_1 \rightarrow 0$. The force-less Lo of the standard theory in conjunction with the Wigner potential gives rise to interference,

nonlocality, tunneling, negativity, and oscillatory behavior of f_w : Despite that Lo involves 'classical' Newtonian trajectories the evolution is fully coherent. In contrast, in equation (1) (i) the trajectories are driven by the inhomogeneous magnetic field $B(y)$, which modifies the interplay with V_w , and (ii) a B_1 -dependent term exists, which interacts with both, $Lo(B(y))$ and V_w . We focus our simulation analysis on (i): A choice of a small B_1 allows to neglect the last term in (1) and considers the interplay between $Lo(B(y))$ and V_w in the process of magnetotunneling. A minimum uncertainty Wigner state is injected at the bottom towards a $0.3eV$ and $1nm$ barrier at $y = 30nm$. We consider four cases of (B_0, B_1) : $(0, 0)$, $(-6T, 0)$, $(-6T, 0.2T/nm)$, and $(-2T, -0.2T/nm)$ (Fig. 1-4). The electron can tunnel into the upper half of the domain. The mean densities follow the classical paths (indicated lines) in accordance with the Ehrenfest theorem. In Fig. 1 the density shows a fine oscillatory structure above the barrier. The latter is destroyed by the constant magnetic field as shown in Fig. 2, which bends the mean path to a particular position. In Fig. 3, the magnetic field changes its direction after the barrier, giving rise to a 'snake' type of evolution. Besides, the fine structure of the density above $y = 30nm$ is recovered. Observing that the magnetic field is zero around the barrier as in Fig. 1, we associate this effect with the existence of a local interplay with the EM fields. Indeed, in Fig. 4, when $B(y)$ around the barrier is particularly large (similar to case 2), the oscillations are again suppressed. The comparison of the four cases, Fig. 5, confirms this conclusion. Despite that in Fig. 4 the electron is guided to the same position as in Fig. 2, the effect on f_w is very different. This is shown by the negativity (Fig. 6), which increases with the magnitude of the magnetic field already far before the barrier. This suggests another, nonlocal effect of the interplay of the EM fields.

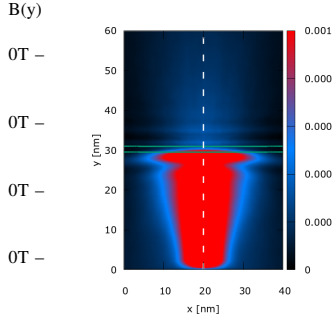


Fig. 1. Case 1: The steady-state electron density $n(x, y)$, obtained after \mathbf{p} integration of f_w , is symmetric and shows a fine oscillatory structure above the barrier. A Wigner state (electron) with a kinetic energy $0.1eV$ and $\sigma_{x,y} = 3nm$ is injected at the bottom, evolving towards $+y$ -direction. Dashed line indicates the mean path of the state's evolution. No magnetic field is applied (see $B(y)$ indicators on the left). Green lines indicate the barrier.

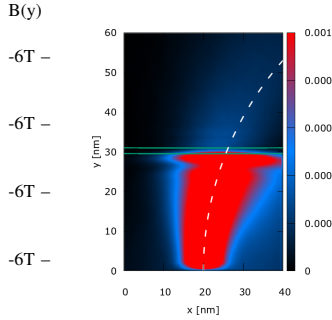


Fig. 2. Case 2: A constant magnetic field bends the density and thus the mean path.

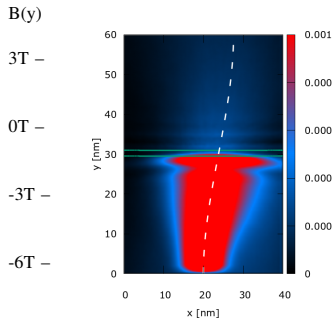


Fig. 3. Case 3: The magnetic field becomes zero at the barrier and switches the sign, giving rise to a snake type of evolution. The density in the upper half of the domain shows again a fine oscillatory structure.

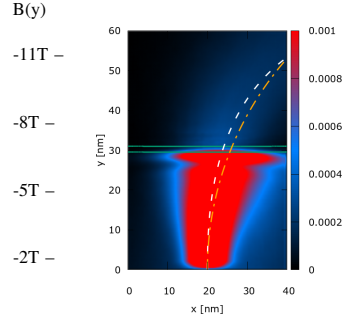


Fig. 4. Case 4: The magnetic field is gradually increased towards $+y$ -direction and is particularly large at and above the barrier. The magnetic field suppresses the oscillations of the density, similar to case 2 (Fig. 2). This is confirmed in Fig. 5. The mean path (white dashed line) is compared to the mean path of case 2 (orange dot-dashed line): Although they differ, they both guide the state to the same final position.

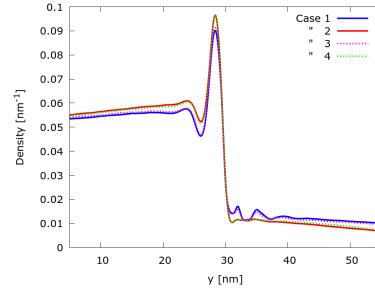


Fig. 5. Density distribution along y -direction, obtained after x -integration of $n(x, y)$: Cases 1&3 and 2&4 clearly group together, suggesting that the oscillations are suppressed in the presence of a magnetic field in the region of the barrier, further indicating that the EM fields interact locally.

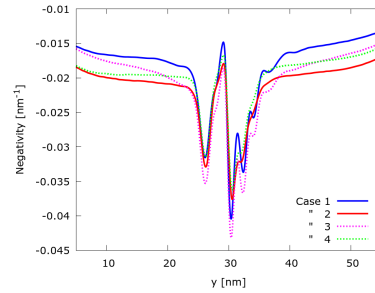


Fig. 6. Negativity obtained after integration of the quantity $f_w\theta(-f_w)$ (θ Heaviside function) on \mathbf{p} and x : The negativity of f_w indicates quantum behavior. The appearance of negative values after the injection of the entirely positive initial state below the barrier ($y < 25nm$) demonstrates the nonlocal action of the barrier already without magnetic field. The negativity increases with the increase of $B(y)$ in this region, which suggests again a nonlocal interplay of the EM fields.

REFERENCES

- [1] P. Hoodbhoy, *J.Phys.Condens.Mat.* **30**, 185303 (2018).
- [2] P. Mondal *et al.*, *Phys.Rev.B* **98**, 125303 (2018).
- [3] M. Nedjalkov *et al.*, *Phys.Rev.B* **99**, 014423 (2019).
- [4] M. Nedjalkov *et al.*, *Phys.Rev.A* **106**, 052213 (2022).

Acknowledgment: The financial support by the Austrian Science Fund (FWF): P33609 is gratefully acknowledged. The computational results have been achieved using the Vienna Scientific Cluster (VSC).

Kirchhoff Coupling Generates ATP, the Chemical Energy of Life

Robert Eisenberg

Illinois Institute of Technology, Rush University, University of Illinois, Chicago IL USA

e-mail: bob.eisenberg@gmail.com

SUMMARY

Electrons flow. Voltages change in biology as in physics. Current — if it includes displacement current — moves according to Kirchhoff's law, on all scales. Current energizes devices and creates signals in biology as in engineering.

In biology, current flow creates chemical energy stored in the form of ATP (adenosine triphosphate) in mitochondria. ATP is the nearly exclusive source of chemical energy in life.

Kirchhoff's current law couples electron flow and proton movement in mitochondria, as our research group, led by Huaxiong Huang, has shown, see Fig. 1 and Ref. [1]. When they are coupled in membrane proteins, electron and proton fluxes form a device — in the strict engineering sense of the word — that produces ATP as an output. See [2] for meaning of biological names.

BACKGROUND

Atomic details control function in these protein devices. Atomic details must be included if models of proteins are to be useful in immensely important medical applications. Those atomic details are manipulated when treatments of disease and drugs are designed in hundreds or thousands of laboratories every day, by 'site directed mutagenesis'. [2]

Atomic details are difficult to include in models and simulations of proteins because biological systems include so many atoms ($>10^{18}$) that move quickly (10^{-15} sec), compared to biology ($>10^{-4}$ sec). Most of the quick motions are irrelevant to biological function but we do not yet have a method ('coarse graining') to reliably take advantage of that fact. Coarse graining of space is dangerous because it so easily hides the reality that a few atoms can control biological function in a quite specific way.

Biological function, including current flow, is thus difficult to compute in simulations with atomic resolution.

Fortunately, it is often not necessary to compute current flow with atomic resolution. Engineers rarely have to consider the atomic details of current flow in wires, for example. Biophysicists rarely have to consider the atomic details of current flow in their 'wires', the interior of long (meters), slender (μm) nerve cells.

Kirchhoff's current law makes it possible to study current without atomic detail in both engineering and biology. Current flow — if it includes displacement current — follows Kirchhoff's current law as implied by taking the divergence of the Maxwell Ampere law [3].

$$\mathbf{div}(\mathbf{curl}\mathbf{B}) = \mathbf{div}\left(\overbrace{\mu_0\mathbf{J} + \mu_0\epsilon_0 \frac{\partial\mathbf{E}}{\partial t}}^{\text{Total Current}}\right) = 0;$$

\mathbf{J} includes flux of *all* charges

Kirchhoff's current law is true on the atomic scale and on the macroscopic scale because Maxwell's equations work on both scales.

Kirchhoff's current law forces current flow in one component of the circuit to depend on current flow in another component. The different components can have entirely different mechanisms of current flow. The mechanism does not matter. The mechanism can vary, with time or conditions. It can depend on other fields, not included in the classical Maxwell equations. Total current is conserved in all cases. Kirchhoff's current law forces a relation between the currents, independent of the mechanism of the movement of electrons, ions, or other charges. Currents are coupled by the Maxwell equations and nothing else — not by chemical or atomic mechanisms. Kirchhoff coupling is as universal as the Maxwell equations themselves.

In particular, Kirchhoff's current law couples electron flow in cytochrome c oxidase to proton flow. Proton flow in turn generates ATP in another protein device, that is a synthase of ATP [2].

Without Kirchhoff's current law it would be difficult if not impossible to simulate or compute coupling of electron and proton flow. Without Kirchhoff's current law, it would be impossible to recognize the physical imperative that currents are coupled, even if currents flow in disjoint components, far separated with unrelated mechanisms, because of the Maxwell equations.

Kirchhoff's current law couples electron, proton, and ATP movements in mitochondria, and it couples electron and proton movements in the two different protein devices of cytochrome c oxidase and ATP synthase [2].

It is no wonder that molecular dynamics simulations of mitochondria have not identified coupling by current flow. The interactions of the $>10^{18}$ atoms that make up macroscopic current flow involve numbers far beyond what can be computed. Stirling's formula says that the number n of pairwise interactions of 10^{18} atoms is something like $n! \approx (10^{18})^{(10^{18})}$, and interactions in a Coulombic fluid are not just pairwise.

CONCLUSION

The laws of circuits are needed to understand the chemical energetics of life. Kirchhoff coupling creates one of the most important processes in life. Kirchhoff coupling of different chemical species is a general mechanism. Kirchhoff coupling generates ATP, a source of chemical energy. Although not widely used in molecular biology, Kirchhoff's current law is as important in biology as in engineering.

REFERENCES

- [1] Xu, Eisenberg, Song, Huang. (2022) Mathematical Model for Chemical Reactions...in Cytochrome c Oxidase: Electro-osmotic Approach. Preprint arXiv:220702215.
- [2] Wikipedia and YouTube provide excellent discussions and comforting visualizations of biological names like ATP, mitochondria, cytochrome c oxidase, ATP synthase, and site directed mutagenesis. 'Proton' is lab jargon for any positively charged form of water, e.g., H_3O^+ or $H_5O_2^+$.
- [3] Eisenberg, Oriols, Ferry. Kirchhoff's Current Law with Displacement Current (2022). arXiv: 220708277.
Eisenberg. A Necessary Addition to Kirchhoff's Current Law of Circuits. (2022) EngArXiv. DOI: 10.31224/2234

Fig. 1. Cytochrome C oxidase and Equivalent Circuit

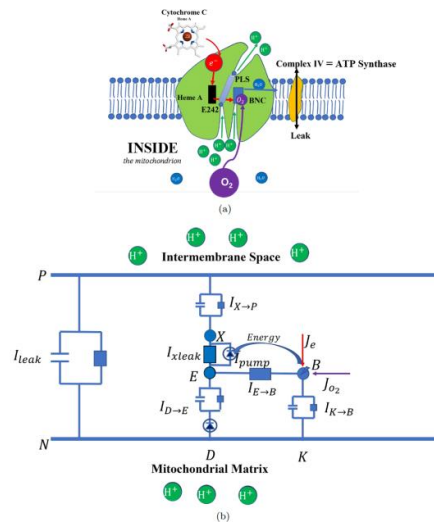
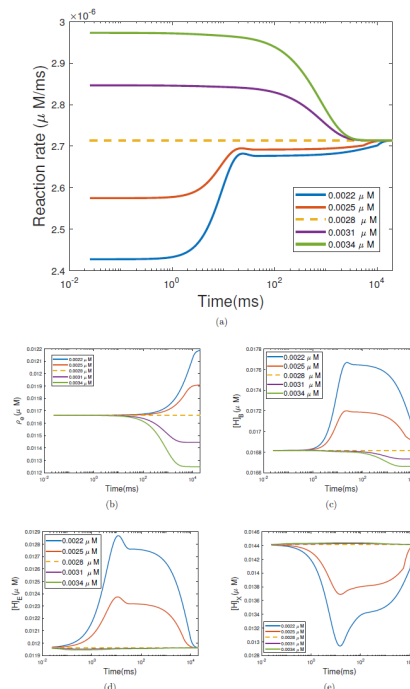


Fig. 2 Representative Result. Different Oxygen concentration. (a) Reaction rate; (b) Electron concentration $_e$; (c) $[H]_B$; (d) $[H]_E$; (e) $[H]_X$. Dashed line — computed from default parameters.



50 Years in the Semiconductor Underground: A Retrospective

Stephen Goodnick (1), Paolo Lugli (2), Dragica Vasileska (3), Irena Knezevic (4), and Wolfgang Porod (5)

(1) Arizona State University (USA), (2) University of Bolzano (Italy), (3) Arizona State University (USA), (4) University of Wisconsin-Madison (USA) and (5) Notre Dame University (USA).

ABSTRACT

This talk wants to be a retrospective on the more than 60 years of research by David K. Ferry, and his main contributions in the fields of physics of semiconductor devices, classical and quantum transport in electron devices and, in general, quantum physics in nanostructures.

Memristors with thousands of conductance levels for analog computing

J. Joshua Yang

University of Southern California, Los Angeles, CA 90089, USA

e-mail: jjoshuay@usc.edu

Abstract:

The analog data deluge issue nowadays call for multipurpose analog computing platforms with great reconfigurability and efficiency, namely, field-programmable analog arrays (FPAAs).[1] FPAAs as the analog counterpart of field-programmable digital arrays (FPGAs) open opportunities for fast prototyping analog designs as well as efficient analog signal processing and neuromorphic computing. Memristors may be the ideal building blocks for FPAAs if they are truly analog with many conductance levels, not just for lab-made devices, but more importantly, devices fabricated in foundries. We have recently demonstrated 2048 conductance levels, a record among all types of memories, achieved with memristors in fully integrated chips with 256×256 memristor arrays monolithically integrated on CMOS circuits in a standard foundry.[2] We have unearthed the underlying physics that previously limited the number of distinguishable conductance levels in memristors and developed electrical operation protocols to circumvent such limitations. These results reveal insights into the fundamental understanding of the microscopic picture of memristive switching and provide approaches to enable high-precision memristors for various applications.

Reference:

- 1 Li, Y., Song, W., Wang, Z., Jiang, H., Yan, P., Lin, P., Li, C., Rao, M., Barnell, M., Wu, Q., Ganguli, S., Roy, A.K., Xia, Q., and Yang, J.J.: 'Memristive Field-Programmable Analog Arrays for Analog Computing', *Advanced Materials*, 2022, pp. 2206648
- 2 Rao, M., Tang, H., Wu, J.-B., Song, W., Zhang, M., Yin, W., Zhuo, Y., Kiani, F., Chen, B., Jiang, X., Liu, H., Chen, H.-Y., Midya, R., Ye, F., Jiang, H., Wang, Z., Wu, M., Hu, M., Wang, H., Xia, Q., Ge, N., Li, J., and Yang, J.J.: 'Thousands of conductance levels in memristors integrated on CMOS', *Nature*, 2023, 615

Probabilistic modeling of resistive switching in emerging ReRAM cells

Y. V. Pershin and V. A. Slipko*

Department of Physics and Astronomy, University of South Carolina, Columbia, SC 29208, USA

*Institute of Physics, Opole University, Opole 45-052, Poland

e-mail: pershin@physics.sc.edu

In this workshop contribution, we present a new model developed to simulate the resistive switching process in resistance-switching random access memory (ReRAM) devices such as electrochemical metallization (ECM) cells. Fig. 1 shows that in ECM cells, under appropriate bias, a conductive metallic filament is formed out of the top electrode (TE) atoms in the insulating layer. Such filament can be dissolved using the voltage of opposite polarity. ECM cells are considered as a promising candidate for the next generation of non-volatile memory, as well as in-memory computing and neuromorphic architectures thanks to their ability to store and process the information on the same physical platform.

The cycle-to-cycle variability is a well-known general property of ECM cells that is not taken into account by standard models. Fundamentally, it originates from the randomness of thermally-assisted atomic rearrangement processes. Quite recently, we demonstrated [1] that the master equation may tremendously simplify the modeling of binary and multi-state ReRAM cells compared to Monte-Carlo simulations (Fig. 2). One of the advantages is that the master equation can be used to find many device/circuit characteristics in a single computation without the need for averaging (see, e.g., Fig. 3).

The main assumption of our new model [2] is that the resistance switching occurs via random markovian jumps in the *continuous* space (CS) of an internal state variable x (see Fig. 1, bottom). The statistical description of a cell is based on the state probability distribution function $p(x, t)$ whose evolution is governed by

$$\frac{\partial p(x, t)}{\partial t} = \int_a^b \gamma(x', x, V(x')) p(x', t) dx'$$

$$-p(x, t) \int_a^b \gamma(x, x', V(x)) dx'. \quad (1)$$

Here, $\gamma(y, z, V(y))$ is the voltage-dependent transition rate density from internal state y to z , and $V(y)$ is the voltage across the device in state y . Eq. (1) is supplemented by statistically averaged Ohm's law

$$\langle I \rangle = \left\langle \frac{V}{R(x, V)} \right\rangle \equiv \bar{R}^{-1}(V) \cdot V, \quad (2)$$

where $\langle I \rangle$ is the mean current, V is the voltage across the device, $R(x, V)$ is the state- and voltage-depend resistance.

Figs. 4-6 present examples of simulations based on the above model with resistance used as the internal state variable. Both the responses to ac-voltage (Figs. 4, 5) and step-like voltage (Fig. 6) demonstrate good agreement with experimental behavior of ECM cells. The suggested approach can be extended to more complex cases such as the description of electronic circuits with several cells.

Overall, our modeling approach is unique and fundamentally different from traditional (deterministic) models of ReRAM cells. In essence, it provides a straightforward way to simulate the response of ReRAM cells *on average*. As such, we expect that this work will contribute to the accelerated development of future information processing and storage devices. Moreover, it may find applications in other fields.

REFERENCES

- [1] V. J. Dowling, V. A. Slipko, and Y. V. Pershin, "Probabilistic memristive networks: Application of a master equation to networks of binary ReRAM cells," *Chaos, Solitons & Fractals*, vol. 142, p. 110385, 2021.
- [2] V. A. Slipko and Y. V. Pershin, "A probabilistic model of resistance jumps in memristive devices," *arXiv preprint arXiv:2302.03079 (submitted for publication)*, 2023.

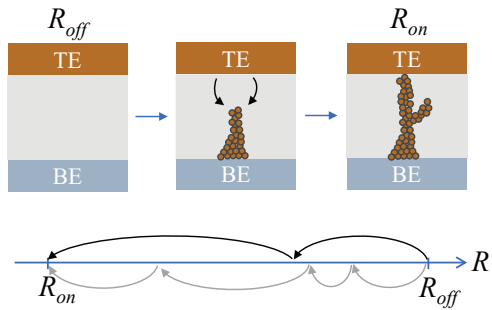


Fig. 1. Schematics of the transition from high- to low-resistance state in an ECM cell. Here, the top (TE) and bottom (BE) electrodes are separated by an insulating layer. Bottom: two different realizations of the resistance switching process.

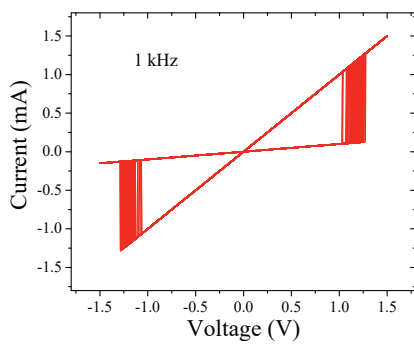


Fig. 2. Monte-Carlo simulations of a two-state resistance switching device [1].

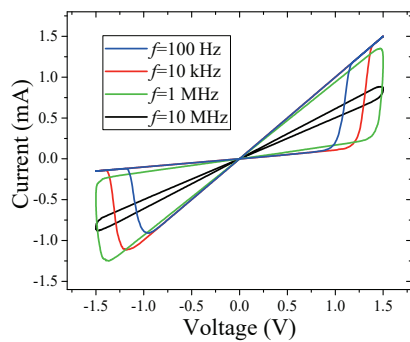


Fig. 3. Two-state model simulations [1]. $\langle I \rangle - V$ curves.

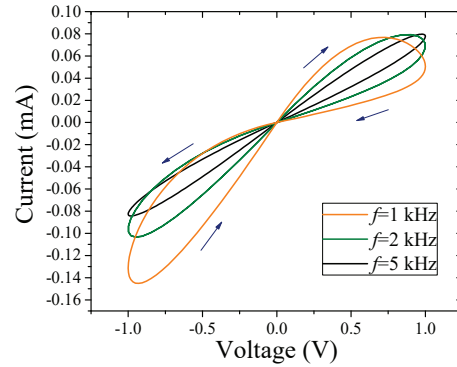


Fig. 4. CS model simulations [2]. $\langle I \rangle - V$ curves.

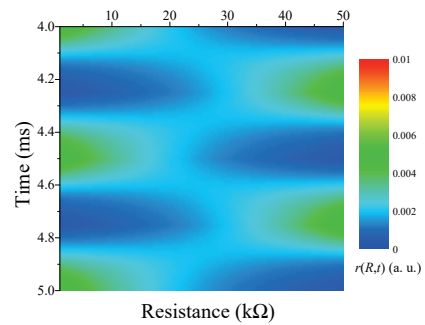


Fig. 5. CS model simulations [2]. Evolution of the resistance probability distribution function.

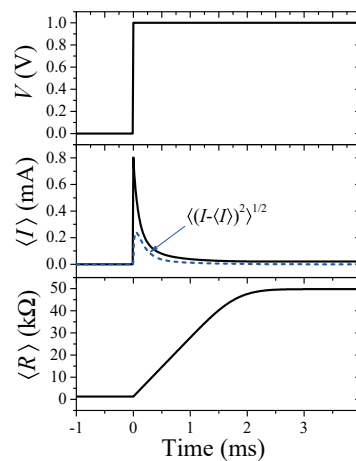


Fig. 6. CS model simulations [2]. Response to a step-like voltage.

Compact modeling of memristors for neuromorphic circuit simulation

F. Aguirre, J. Suñé and E. Miranda

Departament d'Enginyeria Electrònica. Universitat Autònoma de Barcelona
Campus de Bellaterra, 08193-Bellaterra (SPAIN)

e-mail: Jordi.sune@uab.cat

INTRODUCTION

The combination of memristors and CMOS circuits is a promising strategy for the hardware implementation of neural networks (NN) for IoT applications. A compact device model is a simple math. description of its electrical characteristics, to accurately represent its behavior in a circuit. In this work, we present a compact model for filamentary resistive switching (RS) devices with the final goal of simulating memristive circuits. Our model is based on Chua's memristor theory and it includes two coupled equations, one for the current and one for the internal memory parameter (see Fig.1) [1].

MODEL

The memory equation implements the competition of SET and RESET processes with voltage-dependent characteristic times. The current equation is based on the theory of conduction through point contacts. Results of the model for $I(V)$ loops and the conductance hysteron are shown in Fig. 2. Although initially thought for filamentary devices, the model also works for homogeneous RS. Finally, the model has been generalized for memristors showing conductance quantization.

PARAMETER EXTRACTION

The model has ten parameters and we have used a convolutional NN dealing with images of the $I(V)$ loops. The method provides similar results to those of the least-square method (LSM) (Fig. 3) but requires one order of magnitude less time for large number of cycles (10^4 – 10^5), enabling to deal with switching statistics. With the extracted parameters, the model matches the experimental characteristics as shown in Fig. 4.

SIMULATION OF NEURAL NETWORKS

As an example of application to neuromorphic circuits, we have simulated a simple NN for the

recognition of hand-written digits (MNIST database). For the implementation in SPICE, we have converted the memory equation into a very simple equivalent circuit based on a capacitor and two current sources. The NN is a single-layer perceptron with two memristor crossbar arrays for positive and negative weights. Approximately, the simulated circuit contains 16k memristors and about 20k MOSFETs for the control electronics. Training is performed in software and both the writing of weights and the performance during the inference phase have been considered [2]. As an example, Fig. 5 shows the simulated accuracy loss of the network due to wire parasitic resistance (R_w). This is done both as a function of the array size (image resolution) and the ON resistance (R_{ON}). The model performance in terms of memory use and computation time is comparable to much simple models while it provides a much better description of the device behavior (see Fig. 6).

CONCLUSION

A simple compact model for memristors and a novel method for extracting its parameters have been presented. Successful simulation of a memristor based NN has been shown. Extension of the model to devices showing different discrete quantum conductance levels has also been developed and simulation of NN performed.

ACKNOWLEDGMENT

This work was funded by Merck KGaA, in the framework of the project "Sustainability Hub" and by the EU project MEMQuD, code 20FUN06, funded by the EMPIR programme co-financed by the Participating States and the EU Horizon 2020 research and innovation programme.

[1] E. Miranda and J. Suñé, IEEE Trans. Nanotechnol. 2020, 19, 837–840.[2] F. Aguirre et al., Frontiers in Phys.9, 735021 (2021)

$$\frac{d\lambda}{dt} = \frac{1-\lambda}{\tau_S(\lambda, V_C)} - \frac{\lambda}{\tau_R(\lambda, V_C)}$$

$$I = G_0NV + \frac{2e}{h\alpha} \ln \left(\frac{1 + e^{\alpha(\Phi - \beta eV)}}{1 + e^{\alpha[\Phi + (1-\beta)eV]}} \right)$$

Fig. 1. The two equations defining the compact model. The internal memory parameter, λ , is related to ion movement, and it couples both equations. The I(V) equation is related to conduction through a parabolic potential barrier associated to a quantum constriction. Φ is the barrier height, α is related to the barrier width, β describes the possible asymmetry of voltage drops at the interfaces, and N is the number of conducting modes.

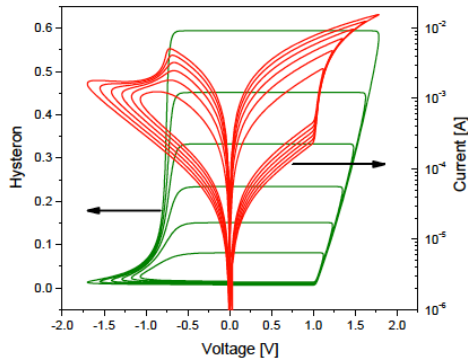


Fig. 2 Switching loops and conductance hysterons (including intermediate states) simulated by the model.

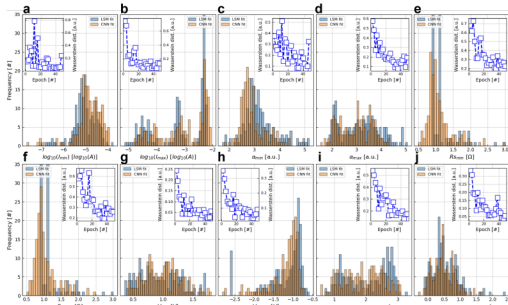


Fig. 3. Statistical distribution of parameters for successive loops in a single device compared to LSM extraction method.

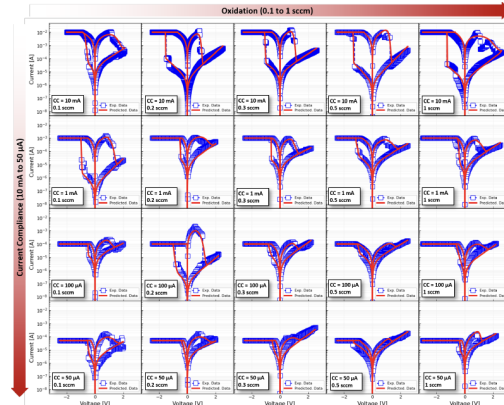


Fig. 4. Simulated I(V) loops with the extracted parameters

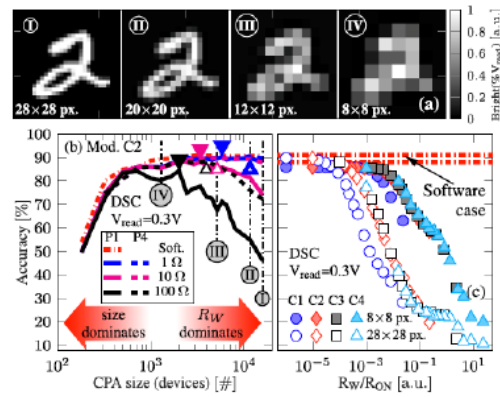


Fig. 5. Effects of the wire resistance on network accuracy as a function of crossbar array size and ON device resistance.

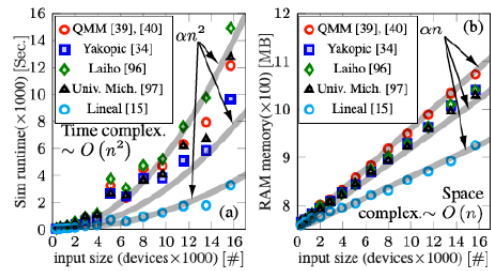


Fig. 6. Performance of different compact models for the simulation of the neural network in terms of memory use and computing time.

Molecular dynamics simulation of the full operation cycle of a HfO₂-based RRAM cell

X. Cartoixa^{*}, M. L. Urquiza^{*†}, Md M. Islam[‡], A. C. T. van Duin[§], and A. Strachan[¶]

^{*}Departament d'Enginyeria Electrònica, Universitat Autònoma de Barcelona,
08193 Bellaterra (Barcelona), Spain, e-mail: Xavier.Cartoixa@uab.es

[†]Laboratoire des Solides Irradiés, École Polytechnique, Institut Polytechnique de Paris, Paris, France

[‡]Department of Mechanical Engineering, Wayne State University, Detroit, Michigan 48202, USA

[§]Department of Mechanical Engineering, Pennsylvania State University,
240 Research East Building, University Park Pennsylvania 16802, USA

[¶]School of Materials Engineering, Purdue University, West Lafayette, Indiana 47907 USA

Resistive random access memories (RRAMs) are considered the most promising candidates for next generation, high-scaling, ultrafast, and low power consumption memories. RRAM cells, that typically consist of a metal-insulator-metal (MIM) stack, store bits by reversibly changing the resistivity of the insulator between a high resistance state (HRS) and a low resistance state (LRS). In order to enable this reversible change, the devices normally require an initial and irreversible process called electroforming, which is basically a current-controlled breakdown of the pristine highly resistive oxide layer [1].

In most RRAM devices, the switching between LRS/HRS originates from the formation/rupture of a nanoscale conductive filament (CF) in the dielectric layer. In the valence change mechanism (VCM) of operation, a variation in local stoichiometry arising from the presence of oxygen vacancies changes the valence of the metallic ions rendering them conductive [1].

In this contribution we present molecular dynamics (MD) simulations of a HfO₂-based RRAM cell evolving in time under the influence of a changing external bias, in order to obtain atomistic information of the filament formation and rupture dynamics during all the stages of operation of the RRAM cell [2]. Our simulations explicitly capture all the relevant processes involved in the switching of the device, including redox reactions, oxygen migration, growth of vacancy-rich regions and the effect of temperature. We studied cells with metallic Hf as AE and our simulations reproduce the substoichiometric layer generated at the oxide/AE interface

during the fabrication of the devices. A detailed, 3D, analysis of the motion of O ions during forming, reset, and set reveal unexpected phenomena. During forming, net oxygen migration towards the active electrode dominates the formation of the CF. Our results support the viewpoint that the filament rupture during reset is governed by lateral oxygen migration, induced by the complex 3D electric fields from the neighboring ions and irregular electrode shape during reverse in the bipolar case, or by effect of temperature under unipolar operating conditions. Finally, simulations of the set process demonstrate negligible vertical oxygen migration, in contrast to the forming process, and the filament forms by the rearrangement of oxygen atoms in the lateral directions.

ACKNOWLEDGMENT

M.L.U and X.C. acknowledge financial support by the Spanish Ministerio de Ciencia e Innovación under Grants No. RTI2018-097876-B-C21 (MCIU/AEI/FEDER, UE) and No. PID2021-127840NB-I00 (MICINN/AEI/FEDER, UE). Computational support from nanoHUB and Purdue University is gratefully acknowledged.

REFERENCES

- [1] R. Waser, R. Dittmann, G. Staikov, and K. Szot, "Redox-based resistive switching memories – nanoionic mechanisms, prospects, and challenges," *Adv. Mater.*, vol. 21, no. 25-26, pp. 2632–2663, 2009.
- [2] M. L. Urquiza, M. M. Islam, A. C. T. van Duin, X. Cartoixa, and A. Strachan, "Atomistic Insights on the Full Operation Cycle of a HfO₂-Based Resistive Random Access Memory Cell from Molecular Dynamics," *ACS Nano*, vol. 15, no. 8, pp. 12 945–12 954, 2021.

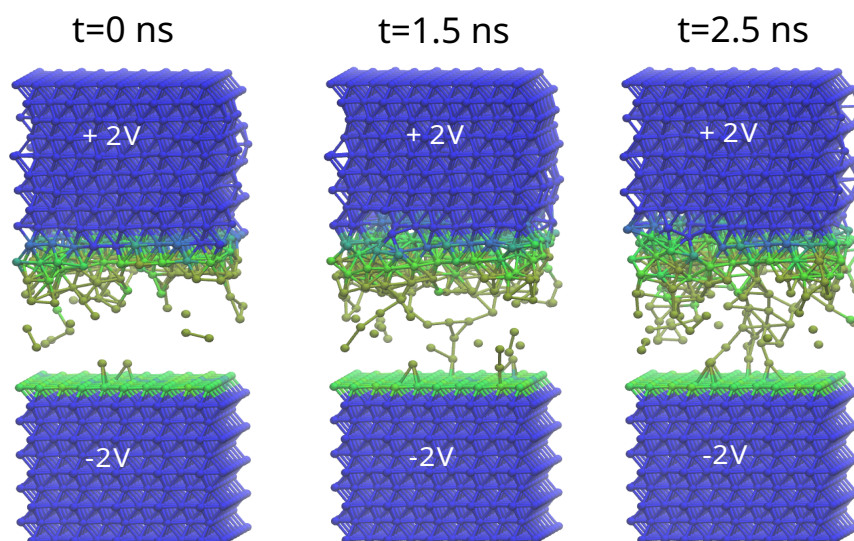


Fig. 1. Snapshots of filament formation during *forming*. Adapted with permission from M. .L. Urquiza et al., ACS Nano vol. 15, 12945 (2021).

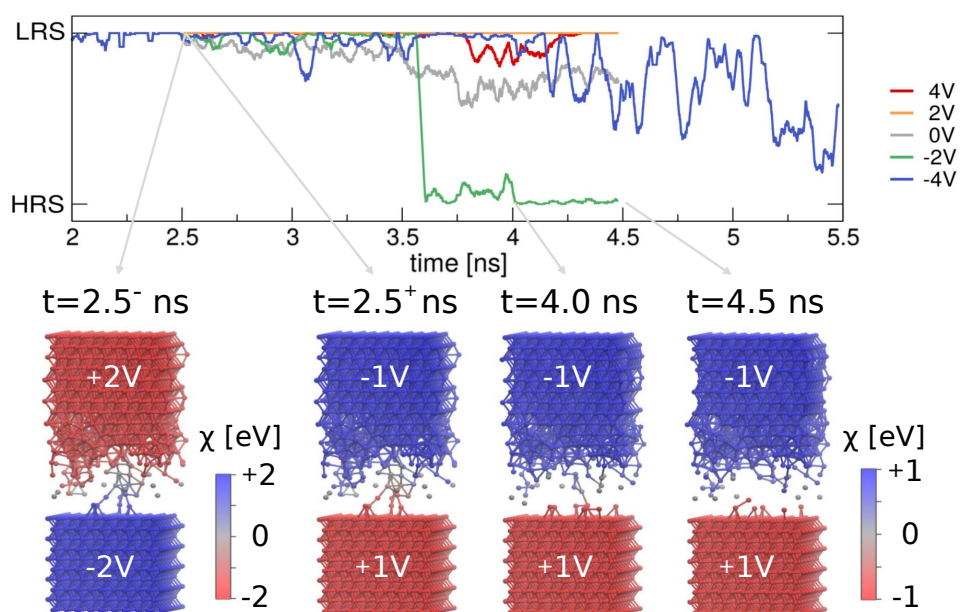


Fig. 2. Snapshots of filament rupture during *reset*. Reproduced with permission from M. .L. Urquiza et al., ACS Nano vol. 15, 12945 (2021).

Multiscale Modelling of Dielectric Breakdown in Amorphous HfO₂

Jack Strand^{1,2} and Alexander Shluger¹

¹Department of Physics and Astronomy, University College London, Gower Street, London WC1E 6BT, UK

²Nanolayers Research Computing Ltd, 1 Granville Court, Granville Road, London, England, N12 0HL

ABSTRACT SUBMISSION

We use a multi-scale modelling approach to study the time-dependent dielectric breakdown (TDDB) of an amorphous (a-) HfO₂ insulator in a metal-oxide-metal (MOM) capacitor. We focus on the role played by electron injection in the creation of oxygen vacancies, which eventually form the percolation path responsible for dielectric breakdown. Energy parameters characterizing the creation of oxygen vacancies and the tunneling process are calculated using Density Functional Theory (DFT), employing a hybrid density functional. The results demonstrate that the formation of oxygen vacancies facilitated by electron injection into the oxide represents a crucial step in the degradation process dominating the kinetics at common breakdown fields.

INTRODUCTION

Micro- and nano-electronic devices based on metal-oxide-metal (MOM) and complementary metal-oxide-semiconductor (CMOS) systems are the basis of modern technology. Over many decades, scaling down of transistor- and memory-device dimensions have led to exponential advances in computing power. This scaling has also led to the replacement of SiO₂ with higher dielectric constant materials, such as HfO₂. However, in spite of decades of perfection, oxides used in CMOS devices, including SiO₂ and HfO₂, are prone to many field-induced reliability issues^[1]. Here, we present the results of multi-scale modelling which link the physical processes responsible for the field induced degradation of a-HfO₂ with the characteristics of time-dependent dielectric breakdown (TDDB), such as temporal evolution of current through the oxide and Weibull plots of TDDB.

MODEL

The model is based on previous work, which shows that electrons trap into deep, intrinsic states in HfO₂^[2] (Fig. 1). The trapping of electrons facilitates the production of vacancies by lowering the activation energy for a vacancy-interstitial pair^[3]. Trapping of electrons at vacancies also facilitates the production of additional vacancies (Fig. 2). We calculate a range of parameters associated with these defects and reactions and use this parameterize a device level simulation in the Ginestra[®]^[4] code. Effects such as TAT, Fowler-Nordheim tunneling, heat generation and vacancy generation et cetera are all included. This allows us to simulate the time evolution current through a TiN/HfO₂/TiN subjected to electrical stress.

RESULTS AND CONCLUSION

The results show that the trap based model agrees well with experiment. We also gain an insight into the formation of the percolation pathway from the spatial distribution of generated vacancies (Fig. 3). This also confirms the Joule feedback mechanism, in which hard breakdown is caused by local heating around the percolation path, leading to a catastrophic increase and current and generation of vacancies.

REFERENCES

- [1] Wu, Ernest Y. "Facts and myths of dielectric breakdown processes—Part I: Statistics, experimental, and physical acceleration models." *IEEE Transactions on Electron Devices* 66.11 (2019): 4523-4534.
- [2] Strand, Jack, et al. "Intrinsic electron trapping in amorphous oxide." *Nanotechnology* 29.12 (2018): 125703.
- [3] Strand, Jack, Moloud Kaviani, and Alexander L. Shluger. "Defect creation in amorphous HfO₂ facilitated by hole and electron injection." *Microelectronic Engineering* 178 (2017): 279-283.
- [4] "Applied Materials Ginestra[®]" [Online] Available: <https://www.appliedmaterials.com/us/en/semiconductor/ginestra-software.html>

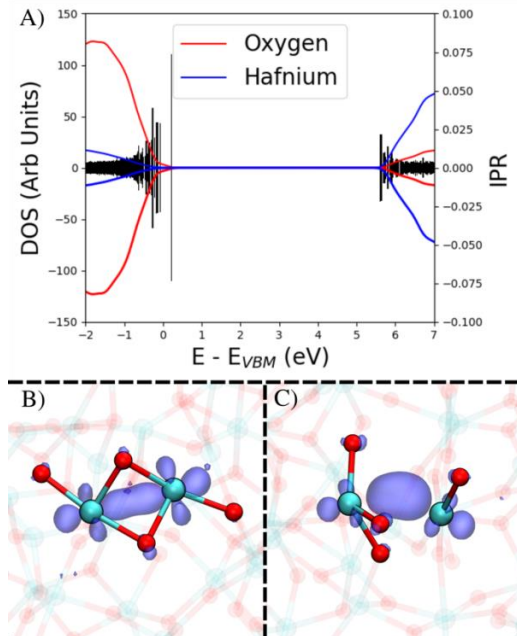


Fig. 1. A) Projected density of states (lineplot) of a bulk, defect free amorphous HfO₂ model. Barplot shows the inverse participation ratio (IPR) of the KS states. High IPR indicates that the electron state is localized. The spectrum shows that there is part-localisation near the valence and conduction band edges. B) A single electron trap and C) A double electron trap in a-HfO₂.

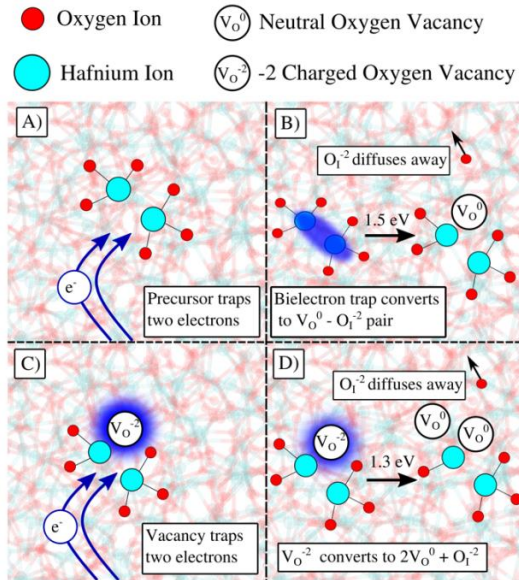


Fig. 2. Degradation model in amorphous HfO₂. A) The injection of electrons into the intrinsic trapping states shown in Fig 1. B) and Fig 1C). B) The creation of a vacancy at the trap site. C) The injection of electrons into the vacancy, leading to negative charging. D) The generation of an additional vacancy.

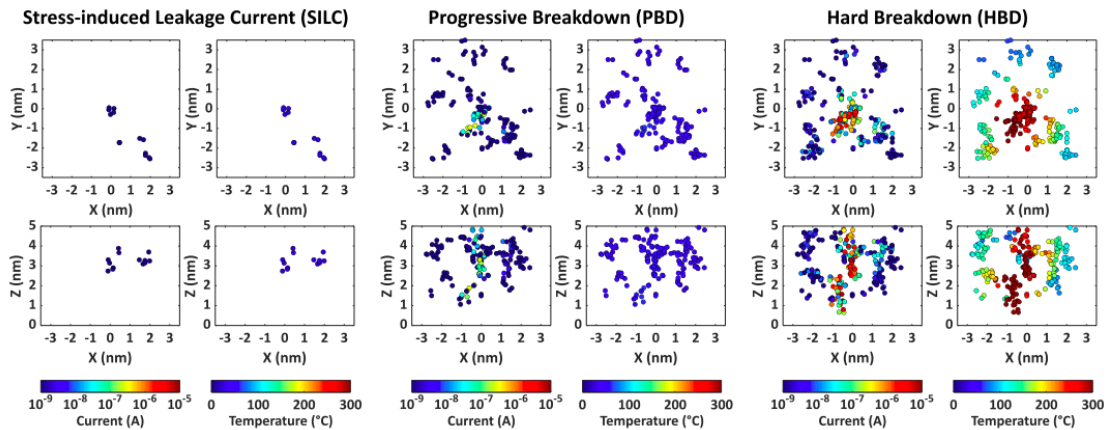


Fig. 3 Position, current and temperature of vacancies in a typical simulated device. Three different stages are shown: SILC, PBD and HBD. For each stage the top two panels show the X-Y projection of the simulation cell whereas the bottom two panels the X-Z projection. The bottom electrode is located at Z=0 and the top electrode is at Z=5 nm. Circles show O vacancies in the oxide. The colour of circles shows the values of current (left panels) and temperature (right panels) according to the colour coding schemes at the bottom of the figure. Initially, there is no clear percolation pathway or filament formation (in SILC and PBD). Eventually, at hard breakdown, a conducting filament indicated by a localised temperature and current increase has developed.

Termination-Dependence of Resistive Switching in SrTiO₃-based Valence Change Memory

M. Mladenović, M. Kaniselyan, C. Weilenmann, A. Emboras, and M. Luisier

*Integrated Systems Laboratory, ETH Zürich, Gloriastrasse 35, 8092, Zürich, Switzerland

e-mail: mmladenovic@iis.ee.ethz.ch

Valence change memories (VCMs) are resistive switching devices that have been recently proposed as solid-state synapses in neuromorphic computing applications. VCM devices typically achieve their switchable resistances through a reversible filamentary dielectric breakdown within an oxide layer [1] (**Fig. 1(a)**, left). Once a transition to the low resistance state (LRS) is complete, the resulting filament of conductive oxygen vacancies leads to linear current-voltage (I-V) characteristics (**Fig. 1(b)**, left). VCM based on SrTiO₃, however, can also exhibit distinctively nonlinear LRS I-V characteristics (**Fig. 1(a)**, right) that have been attributed to the modulation of the Schottky barrier height at the high-work-function contact through an accumulation of oxygen vacancies at that location [2] (**Fig. 1(b)**, right). Previous reports suggest that a conductive filament might also be present in these devices [3], potentially resulting in a combination of both filamentary and interface-type switching. Using *ab-initio* methods, we reveal here that the switching mechanism of these devices may be strongly influenced by the SrTiO₃ edge termination.

We consider a Pt-SrTiO₃-Ti stack (**Fig. 1(c)**) with two different terminations of crystalline SrTiO₃: SrO and TiO₂, as shown in **Fig. 2(a)**. The same termination is used at both interfaces. Optimized atomic device structures are obtained from density functional theory calculations, while the electric currents are calculated with a quantum transport solver [4]. We investigate the effect of oxygen vacancies on the transport properties of SrTiO₃ devices by constructing two distinct models, one with a uniform distribution of the vacancies (**Fig. 2(b)**, top) and one with vacancies accumulated at the Pt electrode (**Fig. 2(b)**, bottom), representing idealized filamentary- and interface-type LRS states, respectively. The resulting I-V characteristics of both

distributions applied to the SrO-/TiO₂-terminated devices are shown in the left/right subplots of **Fig. 2(c)**. In the case of the SrO-terminated device, the uniform distribution exhibits a higher current, indicating a filamentary-type conduction mechanism dominated by hopping through the oxide. In contrast, the device with the TiO₂-terminated surface has a higher current when vacancies are accumulated at the Pt-end, indicating that transport here is limited by the interface.

We analyze the transport mechanism further in **Fig. 3(a)** by plotting the Local Density-of-States (LDOS) and energy-resolved currents for the four cases in **Fig. 2(c)**. The LDOS and current of the SrO-terminated cell indicate that the higher current with uniformly-distributed vacancies (**Fig. 3(a)**, top left) originates from transport through defect states created in the band gap of the oxide. Accumulation of vacancies at the Pt end, meanwhile, still leaves a high tunneling gap which impedes current flow, as illustrated in **Fig. 3(b)**, top right.

The LDOS and current for the TiO₂-termination (**Fig. 3(a)**, bottom) present a different picture in which current is primarily injected into the conduction band from the Ti-contact. The electrons encounter a Schottky barrier at the Pt-end, whose height can be modulated by the accumulation of the oxygen vacancies, as can be seen in **Fig. 3(a) and 3(b)**, bottom.

Our results indicate the possibility of interface-engineering SrTiO₃-based VCM cells to influence the dominant conduction mechanism.

REFERENCES

- [1] W. A. Hubbard, et al, *Adv. Funct. Mater.* **32**, 2102313 (2022).
- [2] D. Cooper, et al, *Adv. Mater.* **29**, 1700212 (2017).
- [3] S. Stille, et al, *Appl. Phys. Lett.* **100**, 223503 (2012).
- [4] M. Luisier, et al, *Phys. Rev. B* **74**, 205323 (2006).

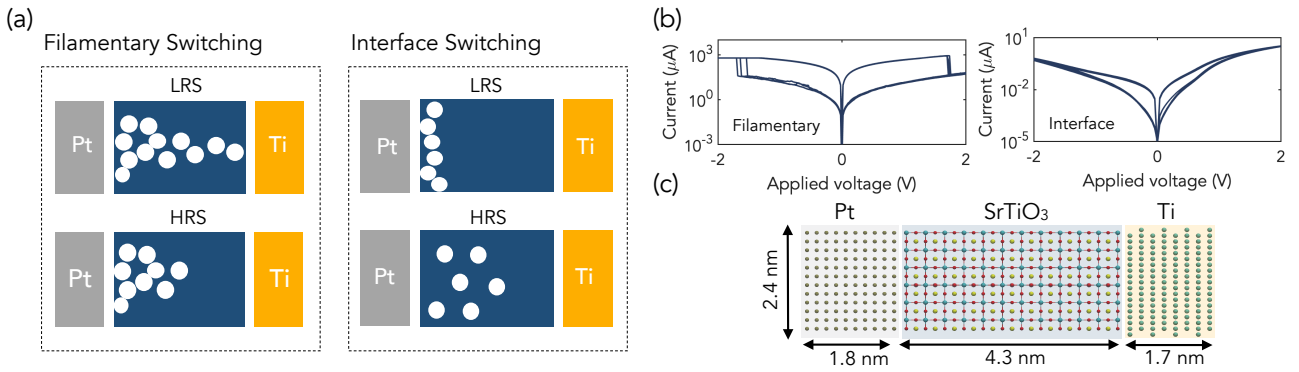


Fig. 1. (a) Illustrations of the low (top) and high resistance state (bottom) corresponding to the interface (left) and filamentary switching (right) of metal-oxide-metal memory cells. White circles refer to oxygen vacancies and the blue region represents the switching material. (b) Experimentally measured I-V characteristics of interface (left) and filamentary switching (right) of Pt-SrTiO₃-Ti memory cells. (c) Atomic structure of the simulated Pt-SrTiO₃-Ti stack. The out of plane direction measures 2 nm.

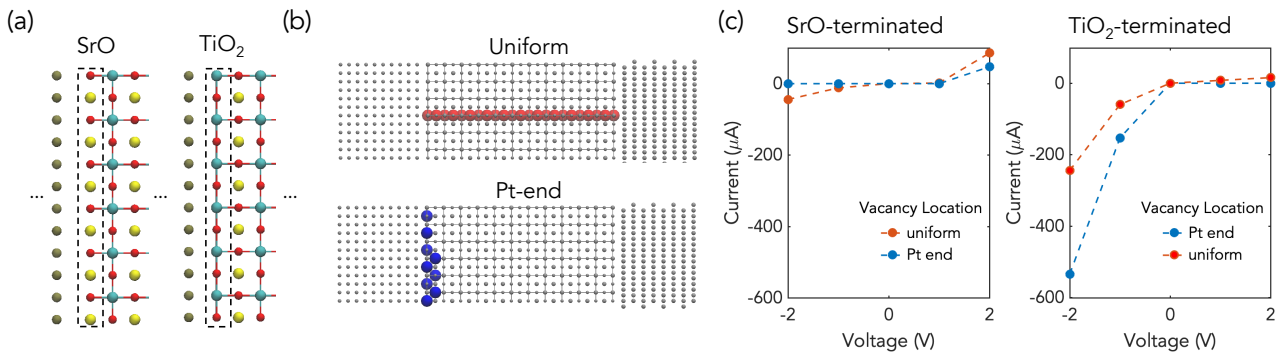


Fig. 2. (a) Atomic structure of a SrO- (left) and a TiO₂-terminated (right) Pt-SrTiO₃-Ti stack. (b) Uniform distribution of vacancies (top) and accumulation of vacancies at the Pt electrode (bottom). (c) I-V characteristics of the SrO- (left) and TiO₂-terminated (right) devices for the two vacancy distributions shown in (b).

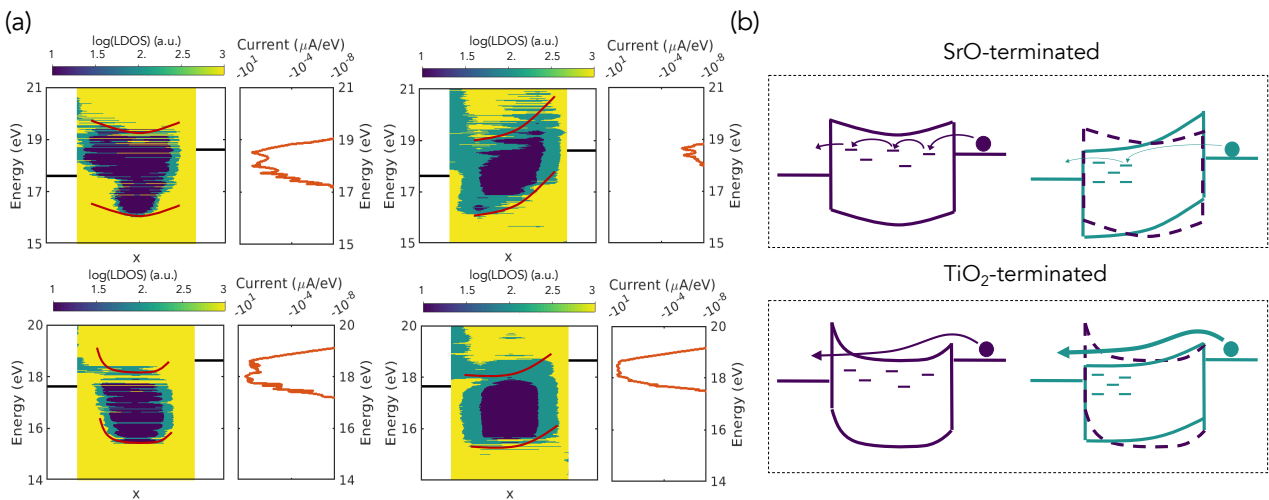


Fig. 3. (a) Local Density-of-States and energy-resolved current of Pt-SrTiO₃-Ti stacks with uniformly distributed vacancies (left) and vacancies accumulated at the Pt electrode (right) for SrO (top) and TiO₂ (bottom) terminations, under an applied bias of -1V. The black horizontal lines indicate the Fermi levels in the contacts, while the red lines are band edges visually approximated from the DOS. (b) Schematic view of the band diagrams and transport regimes corresponding to the four cases depicted in (a). The dashed lines on the right-side diagrams correspond to the band edges of the left-side diagrams for comparison.

Temperature-Dependent Electric Switching of Chalcogenide Memories Below the ns Limit

R. Brunetti, M. Rudan*, and C. Jacoboni

FIM Department, University of Modena and Reggio Emilia, Modena, Italy, rossella.brunetti@unimore.it

*DEI Department, University of Bologna, Bologna, Italy

Abstract — A space- and time-dependent transport model in amorphous chalcogenides, including both localised and mobile electron states, is used here to explore the kinetics of threshold switching of nanoscale structures in the ns–ps time domain. The analysis is carried out in the high-temperature range (below the phase-transition temperature), to test the effect of lattice temperature on the ultrafast switching in view of a possible exploitation in automotive applications.

State of the art and model — Chalcogenide-based Phase Change Memories (PCM) have been studied for many years as a possible replacement for Flash memories [1, Ch. 30 and Refs. therein]. Being two-terminal devices with fast access time and moderate cost, they were easily integrated in 3D cross-point memory arrays [2], with potential breakthroughs in industrial applications; among these, automotive applications [3]. PCM action relies on the fast and reversible structural change of a chalcogenide alloy that switches between the amorphous (*reset*) and crystalline (*set*) states upon the application of an electric pulse [4]. A voltage pulse of suitable intensity, and width of a few ns is often required to surpass an off-to-on threshold switching in the amorphous state (Ovonic Threshold Switching—OTS), precursor of the amorphous-to-crystalline phase change. The limits of a fast electric switching for both selectors and memory elements, based on chalcogenides, are related to the above-mentioned OTS, and to the crystallization kinetics after it [5], [6]. Achieving sub-ns threshold-switching times for nanoscale devices is a goal of both scientific and technological relevance [7], [8]. Preliminary analyses [9] were implemented to interpret recent experimental results in the ns–ps time domain. Here the approach is extended to a range of temperatures of interest for automotive applications, and tested for applied external voltages produced by

optimised electric configurations. Following [10], a homogeneous chalcogenide is considered, in one dimension, assuming unipolar conduction with localised and mobile states. Numerical solutions of the model equations for a time-dependent bias were carried out, varying the thermal-bath temperature from room to high temperatures (always below the amorphous-crystalline transition one). Voltage pulses with finite rise and fall times as fast as 1.5 ns (comparable with the microscopic relaxation times) were considered, as in the experiments of [8].

Results — The transport model has been applied to a 53-nm thick GST-225 chalcogenide layer [9]. Pulses with different plateau values and duration were used, along with different lattice temperatures T , above room temperature and below the crystallization one (425 K); the goal was testing how the transient of the electric current and, in particular, the OTS are affected by an extended temperature range. It was found that the threshold voltage V_{th} decreases at increasing temperatures (specifically, $V_{th} = 2, 1.4, 1.1$ V at $T = 298, 350, 400$ K, resp.); this is due to an increase in the mobile-carrier concentration, whence in the current triggering the onset of OTS. Fig. 1 shows the applied voltage and the current through the device as functions of time, at $T = 350$ K, for one of the simulated voltage profiles. Fig. 2 shows the currents obtained at different temperatures for a given voltage profile. Fig. 3 shows the time evolution of the electron temperature T_e for the same voltage profile as in Fig. 2 (as shown in [12], T_e is almost constant in space). Finally, Fig. 4 shows the delay time as a function of T for two different plateau voltages. To conclude, ultrafast transient characteristics (in the ns scale and below) have been obtained for all temperatures considered. This indicates that ultrafast, sub-ns electric switching of chalcogenide memories can be exploited in automotive applications.

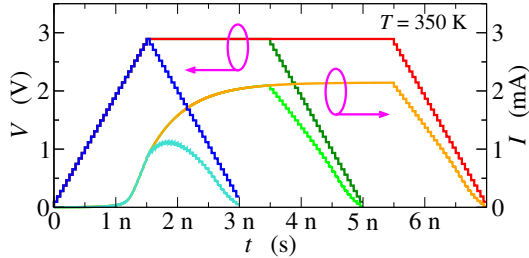


Fig. 1. Current flowing across the PCM device as a function of time (right scale) after the application of voltage trapezoidal profiles of 2.8 V amplitude (left scale), at $T = 350$ K. Rise and fall times are 1.5 ns in all cases, whereas the plateau durations are 0, 2, and 4 ns. The duration of the plateau influences the maximum value of the current, but does not affect the rise time

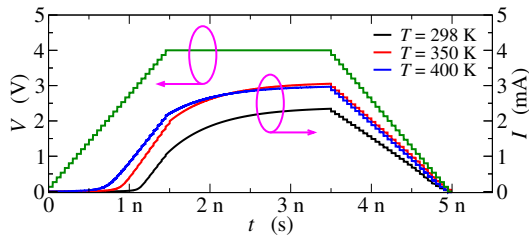


Fig. 2. Currents (right scale) corresponding to a 4-V amplitude and 2-ns plateau duration, at different temperatures. At higher lattice temperatures not only a larger current is obtained, but also the increase in the current occurs earlier: this is due to an increased efficiency of the carrier-heating process at the origin of the OTS effect.

REFERENCES

- [1] M. Rudan, R. Brunetti, and S. Reggiani, Eds., *Springer Handbook of Semiconductor Devices*, 1st ed. Cham: Springer, Nov. 2022.
- [2] J. Choe, “Memory/Selector Elements for Intel Optane™ XPoint Memory,” 2017, <http://techinsights.com/>.
- [3] P. Cappelletti, R. Annunziata, F. Arnaud, F. Disegni, A. Maurelli, and P. Zuliani, “Phase change memory for automotive grade embedded NVM applications,” *J. Phys. D: Appl. Phys.*, vol. 53, pp. 193 002–011, 2020.
- [4] S. Raoux and M. Wuttig, *Phase Change Material — Science and Applications*. Springer, 2009.
- [5] M. Anbarasu, M. Wimmer, G. Bruns, M. Salinga, and M. Wuttig, “Nanosecond threshold switching of GeTe_6 cells and their potential as selector devices,” *Appl. Phys. Lett.*, vol. 100, p. 143505, 2012.
- [6] D. Loke, T. H. Lee, W. J. Wang, L. P. Shi, R. Zhao, Y. C. Yeo, T. C. Chong, and S. R. Elliott, “Breaking the Speed Limits of Phase-Change Memory,” *Science*, vol. 336, New Series, no. 6088, pp. 1566–1569, June 2012.
- [7] M. Wimmer and M. Salinga, “The gradual nature of

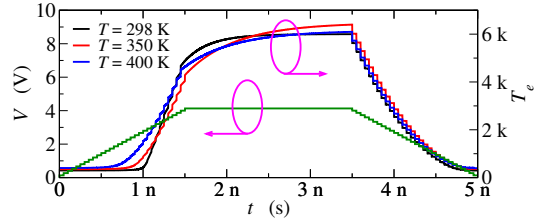


Fig. 3. Time evolution of the electron temperature T_e (right scale) for a 4-V amplitude and 2-ns duration of the voltage plateau. The interpretation derived from Fig. 2 is confirmed by the trend of the electron temperature shown here, where the heating process sets in at shorter times for temperatures above room temperature. As a consequence of the above picture, the

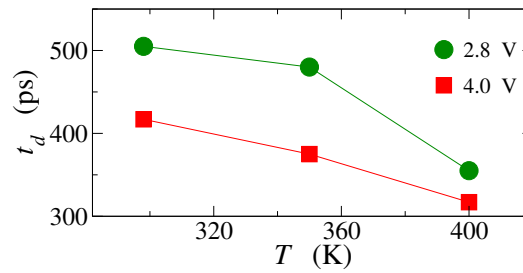


Fig. 4. Simulated delay time t_d as a function of the lattice temperature T for two plateau voltages (2.8 and 4 V); t_d is the time interval between the instant at which the applied voltage exceeds the threshold value and the instant at which a steep rise in the device current begins [7], [11], and is a useful parameter for quantifying the switching speed of the electric response.

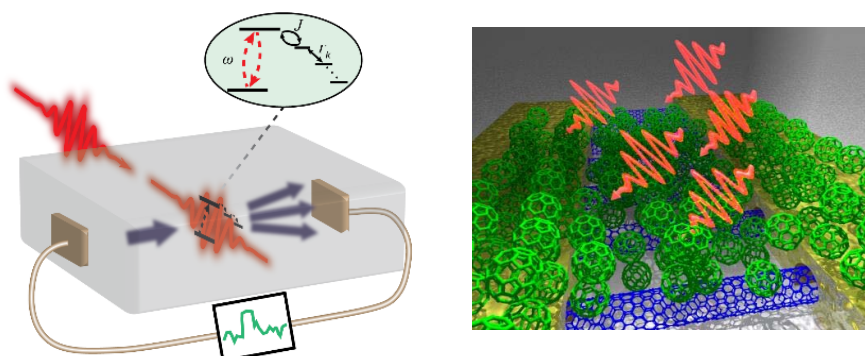
threshold switching,” *New Journal of Physics*, vol. 16, p. 113044, 2014.

- [8] N. Saxena, R. Raghunathan, and A. Manivannan, “A scheme for enabling the ultimate speed of threshold switching in phase change memory devices,” *Sci. Rep.*, vol. 11, p. 6111, 2021.
- [9] R. Brunetti, C. Jacoboni, E. Piccinini, and M. Rudan, “Time-domain analysis of chalcogenide threshold switching: from ns to ps scale,” *Frontiers Phys.*, vol. 10, 2022, doi: 10.3389/fphy.2022.854393.
- [10] —, “Band transport and localised states in modelling the electric switching of chalcogenide materials,” *J. Comput. Electron.*, vol. 19, p. 128, 2020.
- [11] K. D. Shukla, N. Saxena, and A. Manivannan, “An ultrafast programmable electrical tester for enabling time-resolved, subnanosecond switching dynamics and programming of nanoscale memory devices,” *Rev. Sci. Instrum.*, vol. 88, p. 123906, 2017.
- [12] C. Jacoboni, E. Piccinini, R. Brunetti, and M. Rudan, “Time- and space-dependent electric response of Ovonic devices,” *J. Phys. D: Appl. Phys.*, vol. 50, p. 255103, 2017.

Quantum Photodetectors

François Léonard, Sandia National Laboratories, Livermore, California, USA

Photodetection plays a key role in basic science and technology, with exquisite performance having been achieved down to the single photon level. Further improvements in photodetectors would open new possibilities across a broad range of scientific disciplines and enable new types of applications. However, it is still unclear what is possible in terms of ultimate performance, and what properties are needed for a photodetector to achieve such performance. In this presentation, I will discuss recent theoretical and experimental work to address this question. On the theoretical front, we present a new general framework to establish the fundamental properties of photodetectors from a fully quantum perspective, and show what basic features are needed to achieve high performance. Novel photodetector designs emerge from these considerations, and we present initial experiments with nanoscale materials to test these new designs.



Impact of hBN-encapsulation on light absorption in 2D-TMD-based photodetectors

A. A. Díaz-Burgos, A. Toral-López, J. Cuesta, E.G. Marín, F. Pasadas, F.G. Ruiz, A. Godoy
Departamento de Electrónica y Tecnología de Computadores, Universidad de Granada, Granada, Spain
Contact email: angelal@ugr.es

INTRODUCTION

Although the impact of encapsulation ([1]) on electronic properties of monolayer (ML) Transition Metal Dichalcogenides (TMDs) has been addressed in several theoretical and experimental studies ([2], [3]), the assessment of the impact of hBN encapsulation and its van der Waals (vdW) gaps on light propagation and absorption in stacked structures is still pending. To do so, we have adapted and compared several models for light propagation through stacked materials covering a variety of approximation levels, applying them to the light absorption of an hBN-encapsulated ML MoS₂.

DISCUSSION

The impact hBN encapsulation has on the light absorption of MoS₂ is analyzed considering several models for light propagation: from the most simplistic treatments based on the Beer-Lambert (BL) law, that only considers reflection due to the most superficial coating layer, up to the Transfer Matrix Method (TMM), accounting the propagation of normal EM fields, including both multiple reflections and spatial interferences. Moreover, intermediate approximations like Incoherent Path Sum (IPS), that takes into account multiple reflections in each layer but neglects upwards transmission, and Incoherent TMM (ITMM), which assumes spatial incoherence are also discussed. Fig. 1 provides a graphical illustration of each method. The layered nature of the 2D materials is taken into account in the light propagation by the inclusion of the vdW gaps and the reflections originated by them. First, we have compared the propagated energy flux along an hBN-encapsulated ML MoS₂ with two stacks of 20 hBN monolayers for a wavelength $\lambda_0 = 561$ nm. The multiple reflections and interference have a strong impact on the overall intensity inside the material layers, as depicted in Fig. 2.

We have next analyzed the normalized absorption, i.e. the number of absorbed photons in the ML MoS₂ (N_{abs}) with respect to the total number of incident photons (N_0) as a function of the top (n_t) and bottom (n_b) hBN layers for $\lambda_0 = 561$ nm (Figs. 3 and 4). For BL, N_{abs} only changes when a top dielectric layer of hBN is included, as it enhances the optical

coupling between air and MoS₂. No reflections at inner interfaces are included, so vdW gaps are not relevant for this model. For IPS and ITMM, vdW gaps generate additional reflections that reduce the magnitude of propagated light intensity. IPS does not include upward transmissions between adjacent layers. However, these paths, included by ITMM, do not seem to contribute substantially to the net result. TMM, on the contrary, evidences the importance of spatial coherence in this multilayered structure but the effect of varying the thicknesses of the encapsulating layers is rather weak due to how thin these are (6-7 nm at most).

On the other hand, the absorption rate predicted by TMM is very sensitive to the substrate thickness t_s due to interferences. The role of this parameter has been studied in the visible range, in Fig. 5. Tuning t_s can increase N_{abs} in more than one order of magnitude thanks to constructive interferences at ML MoS₂. TMM predicted absorption as a function of t_s for two different wavelengths is presented in Fig. 6, evidencing the periodic nature determined by the ration λ/t_s .

CONCLUSION

We have evaluated the impact of hBN encapsulation on the absorption of ML MoS₂ demonstrating that while vdW gaps have a strong effect on light propagation for models assuming incoherence, they affect in less than 1% to the result predicted by TMM. Interference has a noticeable relevance when thin layers are considered, so TMM stands out as the most appropriate method for characterizing light absorption in optoelectronic devices.

ACKNOWLEDGMENT

This work is funded by FEDER/Junta de Andalucía through projects A-TIC-646-UGR20 and P20-00633 and the Spanish Government through project PID2020-116518GB-I00.

REFERENCES

- [1] Piacentini, A., *et al.* Adv. Electron. Mater., vol. 8, n° 9, 2200123 (2022), DOI: 10.1002/aelm.202200123.
- [2] Magorrian, S.J. *et al.* 2D Materials, vol. 9, n° 4, 045036 (2022). DOI: 10.1088/2053-1583/ac973c.
- [3] Ahn, S. *et al.* ACS Nano, vol. 10, n° 9, 8973-8979 (2016). DOI: 10.1021/acsnano.6b05042.

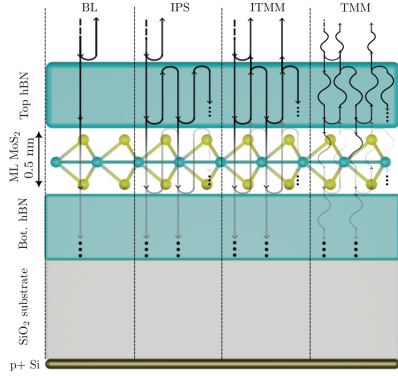


Fig. 1. Sketch of the stacked structure considered. The arrows represent the behavior of light beams according to each model.

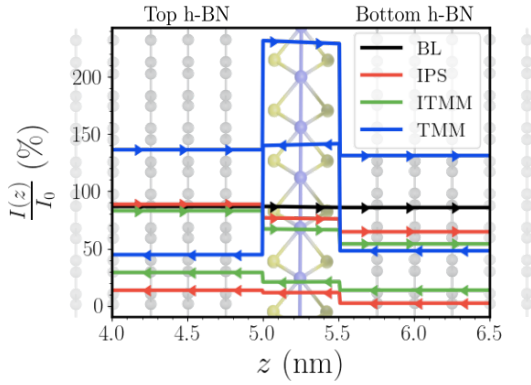


Fig. 2. Net forward and backward propagated energy flux vs. depth in the active region for $\lambda_0 = 561$ nm. Multiple reflections and interference have strong impact on the overall intensity inside material layers. vdW gaps were not included for the sake of clarity, and $n_b = n_t = 20$ and $t_s = 270$ nm were used.

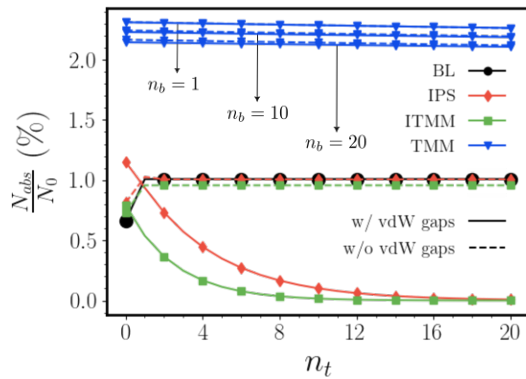


Fig. 3. Photon absorption rate vs. number of top h-BN monolayers calculated with each model. For BL, IPS and ITMM, these curves correspond to $n_b \geq 1$. A substrate thickness of 270 nm was used.

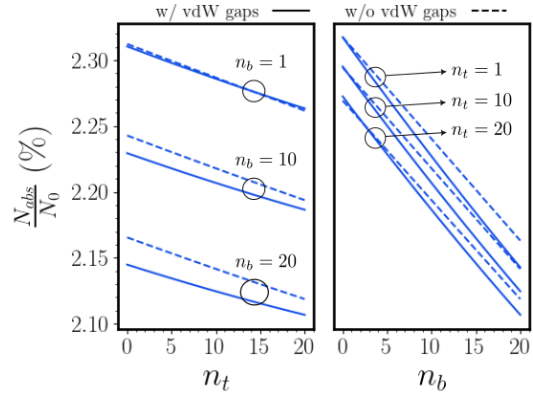


Fig. 4. Absorption rate predicted by TMM for different numbers of top and/or bottom h-BN monolayers, with $\lambda_0 = 561$ nm and $t_s = 270$ nm.

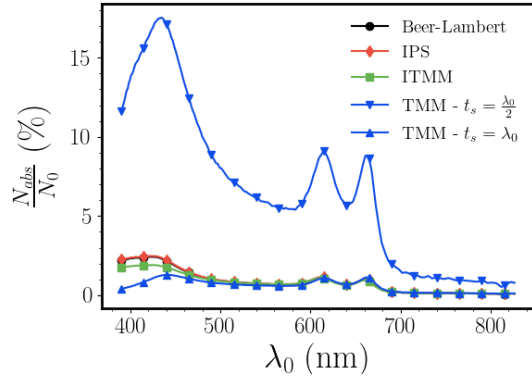


Fig. 5. Comparison of the four models in the visible range. While TMM overlaps with the rest of models for $t_{\text{subs}} = \lambda_0$, it approaches a resonance when $t_s \approx \lambda_0/2$, for which N_{abs} increases in a factor of about 10.

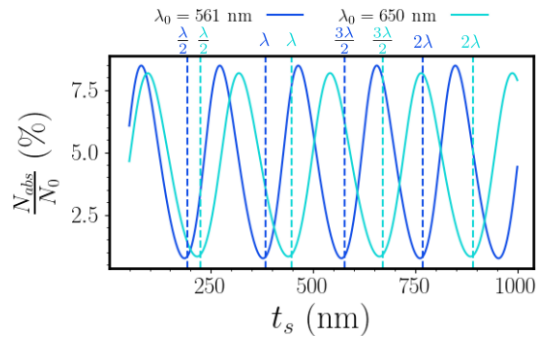


Fig. 6. Normalized N_{abs} vs. t_s for two different wavelengths 561 and 650 nm, according to TMM. The period is $\lambda/2$ in both cases, but resonances do not coincide with multiples of $\lambda/4$ nor $\lambda_0/4$ due to additional phase difference introduced by interfaces.

Dual-Potential Finite-Difference Method for Electrodynamics Within Multiphysics Solvers

S. W. Belling*, L. Avazpour and I. Knezevic

Department of Electrical and Computer Engineering, University of Wisconsin – Madison
Madison, WI 53706

e-mail: swbelling@wisc.edu

ABSTRACT

Many quantum transport simulation tools require the electric and magnetic vector potentials, rather than the electric and magnetic fields. We present a finite-difference time-domain (FDTD) technique for calculating the time-dependent potentials. The equations are first order in space and time, and separate into solenoidal and irrotational parts. The first-order nature of the equations allows us to adapt well-developed techniques for traditional FDTD with fields, such as effective absorbing boundary conditions that allow us to simulate systems in free space within a finite computational domain. We demonstrate coupling of this electrodynamics technique to a ballistic non-equilibrium Green's function transport code.

INTRODUCTION

The coupling of classical electrodynamics to quantum-mechanical charge transport is an essential process to understand for the characterization of time-dependent and high frequency optoelectronic systems. Traditionally, classical electrodynamics is formulated in terms of the electric and magnetic fields, while the key quantity in quantum charge transport, the electronic Hamiltonian, requires the gauge-dependent electric and magnetic potentials. In this work, we present a time-dependent algorithm for calculating the electric and magnetic potentials in the Coulomb gauge, with a focus on coupling to quantum transport codes.

DUAL-POTENTIAL FDTD

The finite-difference time-domain (FDTD) algorithm is a popular choice for solving Maxwell's curl equations. The algorithm marches each component of the electric and magnetic fields forward in time from initial values according to Maxwell's equations. Many problems can be accurately modeled with initial values of all fields

equal to zero, and only a current density driving the time evolution, allowing one to calculate all fields using only the two curl equations. We have produced a similar set of two curl equations for the familiar magnetic vector potential,

$$\nabla \times \mathbf{A} = \mu_0 \epsilon_0 \frac{\partial \mathbf{C}}{\partial t} + \mu_0 \mathbf{F} \quad (1)$$

And the analogous quantity relating to the electric field, the electric vector potential,

$$\nabla \times \mathbf{C} = -\frac{\partial \mathbf{A}}{\partial t} \quad (2)$$

In (1) and (2) \mathbf{A} is the magnetic vector potential, \mathbf{C} is the electric vector potential, and \mathbf{F} is a quantity analogous to current density for the potentials. In this formulation, \mathbf{F} is related only to the solenoidal part of the actual current density. An example of a current density that makes explicit the inclusion of both a solenoidal and conservative part is shown in Fig. 1. Finally, we relate the conservative part of current density to the scalar potential, as

$$\nabla \cdot \mu_0 \mathbf{J} = \frac{\partial}{\partial t} \nabla^2 \phi \quad (3)$$

which is equivalent to the normal continuity equation. To reduce (3) to first order in the spatial derivative, we can track ρ , which is proportional to $\nabla^2 \phi$, and solve Poisson's equation when ϕ is needed. The form of (1) and (2) is just that of Maxwell's curl equations for fields, so the advancements in the FDTD technique for fields, such as the Yee cell [1] and perfectly matched layer boundary condition [2] are easily adapted. We showcase coupling to a ballistic NEGF code (Fig. 2) by initializing a non-zero ϕ and sourcing \mathbf{A} , \mathbf{C} , with a tunneling current between two metallic patches in Fig. 3.

ACKNOWLEDGMENT

This work was primarily funded by the DOE BES award DE-SC0023178 and DE-SC0008712. Additional funding by NSF award 2212011 and the Splinter Professorship.

REFERENCES

- [1] *Computational electrodynamics: the finite-difference time-domain method*, A Taflove and S. C. Hagness, Norwood: Artech House, 3rd ed., 2005
- [2] J. A. Roden and S. D. Gedney, *Convolution PML (CPML): An efficient FDTD implementation of the CFS-PML for arbitrary media*, Microwave and Optical Technology Letters, **27**, 334-339 (200)

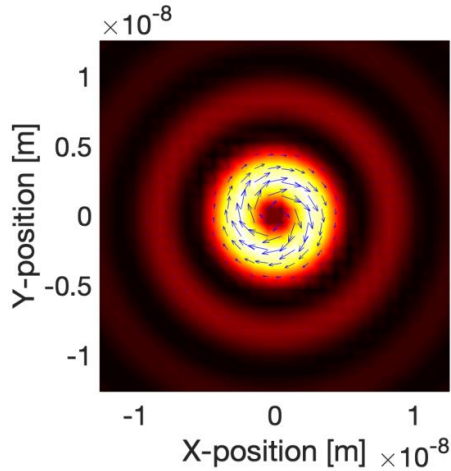


Fig. 1. Current density obtained from an electronic wavefunction for a vortex beam, with an explicitly defined

angular and linear momentum. Color indicates intensity, and blue arrows indicate the solenoidal nature of the beam. The linear momentum is directed into the page.

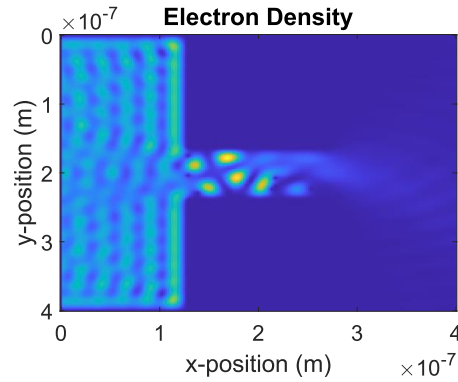


Fig. 2. Demonstration of charge transport through a narrow channel between two contacts (left: full, right: empty) with random disorder using ballistic NEGF.

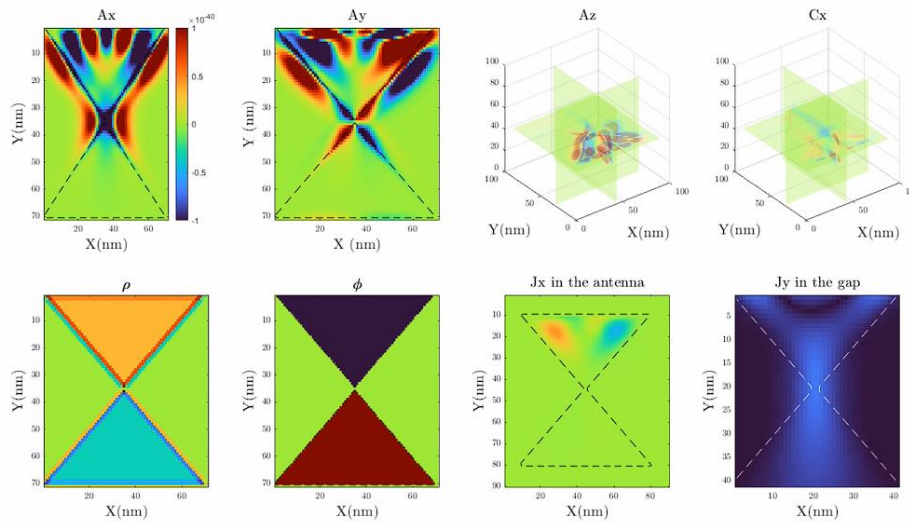


Fig. 3. Snapshot of electric and magnetic potentials sourced by two metallic patches with different initial electric potentials, and a resulting tunneling current through the small gap between the patches. Maxwell solvers on their own cannot capture phenomena such as the tunneling current and must be coupled with quantum transport solvers, as done in this work.

Polaritonic features in the THz displacement current through RTDs in microcavities

C. F. Destefani ^{*}, M. Villani ^{*}, X. Cartoixa ^{*}, M. Feiginov [†], and X. Oriols ^{*}

^{*} Department of Electronic Engineering, Universitat Autònoma de Barcelona, Spain

[†] Department of Electrical Engineering and Information Technology, Technische Universitat Wien, Austria
e-mail: carlos.destefani@uab.cat

Introduction. In electron device modelings, the interaction of electrons and electromagnetic fields is usually tackled by classical or perturbative techniques. In this work, on the contrary, we model electron devices where both degrees of freedom for electrons and electromagnetic fields are described by a unique quantum state solution of a full Hamiltonian. In the resonant strong light-matter coupling regime, our model is able to capture polaritonic signatures in the time-dependent electrical current.

Model. The minimal-coupling Hamiltonian in the Coulomb gauge, for N electrons interacting with an electromagnetic field, is considered [1]. For our qualitative goal, approximations are needed, and among them we consider a single-mode q for the electromagnetic field, in dipole approximation, and a 1D effective single-electron ballistic picture for the transport in the x -direction, in which only the conduction band plays a role, with different electrons meaning different injection times and energies, as handled by the Ramo-Shockley-Pellegrini theorem. Under all these assumptions, the quantized version of the mentioned Hamiltonian reads, for the electron degree x and the single mode degree q [2],

$$H_{xq} = -\frac{\hbar^2}{2m^*} \frac{\partial^2}{\partial x^2} + V(x) - \frac{\hbar\omega}{2} \frac{\partial^2}{\partial q^2} + \frac{\hbar\omega}{2} q^2 + \alpha qx,$$

where $\alpha = \sqrt{e^2 \hbar \omega N / (\epsilon_0 L_c^3)}$ is the coupling constant, with frequency ω and cavity volume L_c^3 . A general solution of the Schroedinger equation with such Hamiltonian H_{xq} in terms of is

$$\psi(x, q, t) = \sum_m^{N_\omega} \Phi_m(x, t) \phi_m^{(\omega)}(q),$$

with $\Phi_m(x, t) = \sum_n^{N_e} c_{n,m}(t) \phi_n^{(e)}(x)$. After integrating out the photon degree of freedom one

obtains, with $H_{xq,e} = -\hbar^2/(2m)\partial^2/\partial x^2 + V(x)$,

$$i\hbar \frac{\partial}{\partial t} \Phi_n(x, t) = [H_{xq,e} + \hbar\omega(n + 1/2)] \Phi_n(x, t) + \alpha x \left[\sqrt{n+1} \Phi_{n+1}(x, t) + \sqrt{n} \Phi_{n-1}(x, t) \right],$$

which is a set of coupled equations for the electron dynamics, each referring to a given photon number.

Results. Effects of a quantized electromagnetic field in the displacement current of a resonant tunneling diode inside a cavity (Fig. 1(a)) are analyzed. The original peaks of the bare electron transmission coefficient split into two new peaks due to the resonant electron-photon interaction (Fig. 2), leading to coherent Rabi oscillations among the polaritonic states that are developed in the system (Fig. 1(d)). This shows how a simultaneous quantum treatment of electrons (Fig. 1(c)) and electromagnetic fields (Fig. 1(b)) may open interesting paths for engineering new THz electron devices. The computational burden involved in the multi-time measurements of THz currents is tackled from a Bohmian description [3] of the light-matter interaction (Fig. 3).

Conclusion. We do believe that our modeling framework may open original unexplored paths for engineering new electron devices and new applications in the THz gap, by taking advantage of the interplay between quantum electrons and quantized electromagnetic fields.

References

- [1] G. Grynberg, A. Aspect, and C. Fabre, Introduction to Quantum Optics (2011).
- [2] C. F. Destefani, M. Villani, X. Cartoixa, M. Feiginov, and X. Oriols, PRB 106, 205306 (2022).
- [3] X. Oriols and J. Mompert, Applied Bohmian Mechanics (2019).

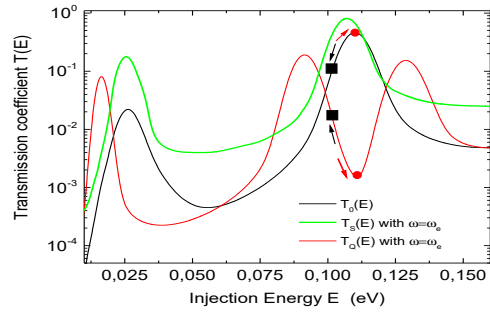
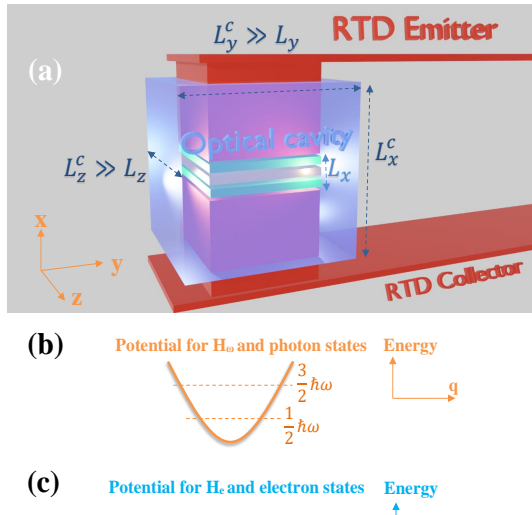


Fig. 2. Transmission coefficients $T(E)$ for: (black) no light-matter interaction $T_0(E)$; (green) resonant semiclassical interaction $T_S(E)$; (red) resonant quantum interaction $T_Q(E)$.

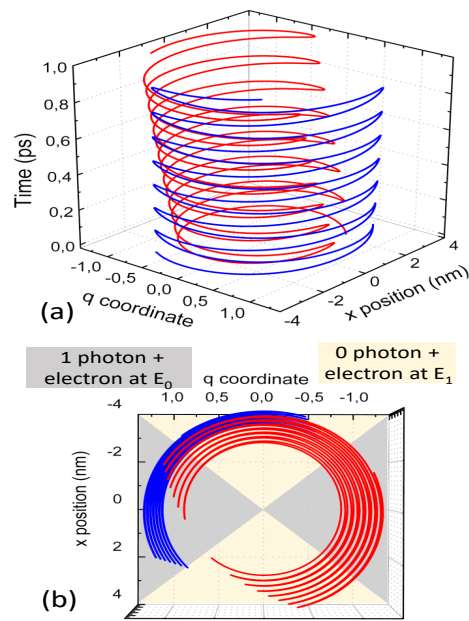


Fig. 3. (a) Example of two Bohmian trajectories in the 2D xq plane guided by the analytical evolution from the quantum scenario. (b) Schematic representation of different regions on the xq configuration space in the quantum well, with white (grey) regions corresponding to the wavefunction occupying the zero (one) photon and excited (ground) electron energy state.

inside the RTD/cavity in the resonant strong coupling regime: state $|0,0\rangle$ almost unaffected; polaritonic states formed out of $(|0,1\rangle \pm |1,0\rangle)/\sqrt{2}$ split by $2E_r = 2\hbar\omega_r$ in comparison to the degenerate decoupled energies (dashed line); state $|1,1\rangle$ would create another polariton subspace, in a larger basis set, with state $|0,2\rangle$; $\omega_r = \alpha L_x/\hbar$ is the Rabi frequency.

Switching Performance of Mo-based pMTJ and dsMTJ structures

B.Pruckner¹ S.Fiorentini¹, N.Jorstad², T.Hadamek¹, S.Selberherr², W.Goes³, and V.Sverdlov^{1,2}

¹ Christian Doppler Laboratory for Nonvolatile Magnetoresistive Memory and Logic at the

² Institute for Microelectronics, TU Wien, Gußhausstraße 27–29, A-1040 Wien, Austria

³ Silvaco Europe, Cambridge, United Kingdom

e-mail: pruckner@iue.tuwien.ac.at

Abstract: We investigate the switching performance of Mo/CoFeB magnetic tunnel junctions depending on the configuration of the magnetization of the ferromagnetic layers and number of fixed layers at low temperatures.

Mo-based perpendicular magnetic tunnel junctions (Mo-pMTJs) have demonstrated superior performance in terms of perpendicular magnetic anisotropy (PMA) and thermal tolerance. Ultrafast sub-ns switching of Mo-pMTJs has been demonstrated at low temperature, making them a potential option for future memory applications [1]. Here we focus on comparing Mo-pMTJs with structures containing two pinned layers (PLs) and a nonmagnetic spacer layer. As the free layer in these structures experiences the torques from both PLs, they are termed double-spin MTJs (dsMTJs). dsMTJs have shown promising results in reducing the switching current and cell size [2]. We used the Finite-Element-Method (FEM) micromagnetic framework which allows evaluating the spin torques produced in bulk as well as at interfaces [3] in multilayered structures which include ferromagnetic layers separated by tunnel barriers and non-magnetic spacers.

We have used [1] to determine material parameters summarized in Table 1. The accuracy of the extracted parameters (saturation magnetization M_s , magnetic anisotropy constant K) is demonstrated in Fig 1, where the experimental hysteresis curve has been accurately reproduced by simulations. Spin drift-diffusion transport model parameters (e.g. spin flip, spin dephasing and exchange lengths) for CoFeB have been taken from [4][5].

We calculate the critical current densities as a function of the switching time for three different structures: (i) a Mo-pMTJ, (ii) a dsMTJ with the two PLs being anti-parallel, and (iii) a dsMTJ* with the two PLs being parallel to each other. We assumed 1nm Mo normal spacer between the free layer and the second PL in the dsMTJ and the dsMTJ*. Fig.2 demonstrates that the critical switching current density is inversely proportional to the switching time τ , which is in agreement with

the experimental [1] observations and theoretical predictions [5]. Fig.2 shows that the pMTJ switching from the anti-parallel to the parallel (AP \rightarrow P) configuration between the free and the pinned layers is faster than the P \rightarrow AP switching, in agreement with [1].

Fig. 2 proves that the (AP \rightarrow P) switching is also faster for dsMTJs. As in dsMTJs the spin torques from the two PLs are additive, the switching is faster than that of pMTJs. Similarly, the torques from the PLs act against each other in a dsMTJ*, which leads to a slower switching than in a pMTJ switching (Fig.2). These results are valid for both P \rightarrow AP and AP \rightarrow P switching.

The switching acceleration in a dsMTJ with a Mo spacer is about 20-40% and is thus not as impressive as in previously studied structures [7] where the gain was two-fold. This is due to reduced spin torque from the second PL as indicated in Fig.3. Finally, Fig.4 and Fig.5 compare the switching times as a function of the voltage applied to Mo-pMTJs and dsMTJs with a Mo spacer for AP \rightarrow P and P \rightarrow AP switching, respectively.

Conclusion: While the dsMTJ using a Mo spacer layer shows faster switching, the speed up depends on the proper choice of materials for the spacer.

REFERENCES

- [1] D. Lyu, P. Khanal, Y. Lv et al., Sub-ns switching and cryogenic-temperature performance of Mo-based perpendicular magnetic tunnel junctions, IEEE Electron Dev. Lett. 43, 1215-1218 (2022). doi: 10.1109/LED.2022.3184278
- [2] G. Hu, C. Safranski, J. J. Sun et al., Double spin-torque magnetic tunnel junction devices for last-level cache applications, in Proceedings IEDM, 10.2.1-10.2.4 (2022) doi: 10.1109/IEDM45625.2022.10019402
- [3] S. Fiorentini, J. Ender, S. Selberherr et al., Coupled spin and charge drift-diffusion approach applied to magnetic tunnel junctions, Solid-State Electron. 186, 108103 (2021). doi: 10.1016/j.sse.2021.108103
- [4] S. X. Huang, T.Y. Chen, C. L. Chien, Spin polarization of amorphous CoFeB determined by point-contact, Andreev reflection, Appl. Phys. Lett. 92, 242509 (2008). doi: 10.1063/1.2949740
- [5] D. M. Lattery, D. Zhang, J. Zhu et al., Low Gilbert Damping Constant in Perpendicularly Magnetized W/CoFeB/MgO Films with High Thermal Stability, Scientific Reports 8, 13395 (2018). doi: 10.1038/s41598-018-31642-9
- [6] J. Z. Sun, Spin-transfer torque switching probability of CoFeB/MgO/CoFeB magnetic tunnel junctions beyond macrospin, Physical Review B 104, 104428 (2021). doi: 10.1103/PhysRevB.104.104428
- [7] W. J. Loch, S. Fiorentini, N. Jorstad, et al., Double reference layer STT-MRAM structures with improved performance, Solid-State Electron. 194, 108335 (2022). doi: 10.1016/j.sse.2022.108335

Table 1: Extracted parameters used in the FEM simulation.

Resistance Anti-Parallel (R_{AP})	6.5	k Ω
Resistance Parallel (R_P)	4	k Ω
Diffusion Coefficient Non-magnetic Layers (D_{NM})	$1.1 \cdot 10^{-2}$	m^2/s
Diffusion Coefficient Ferromagnetic Layers (D_{FM})	$1.1 \cdot 10^{-3}$	m^2/s
Exchange Length (λ_J)	2	nm
Spin-flip Length (λ_{sf})	1	nm
Spin Dephasing Length (λ_ϕ)	0.1	nm
Diffusivity Spin Polarization (β_D)	0.7	
Conductivity Spin Polarization (β_σ)	0.52	
Conductivity Non-magnetic Layers (σ_{NM})	$2 \cdot 10^7$	A/Vm
Conductivity Ferromagnetic Layers (σ_{FM})	$4 \cdot 10^6$	A/Vm
Anisotropy Constant (K)	$7.34 \cdot 10^5$	J/m ³
Exchange Constant (A)	$2 \cdot 10^{-11}$	J/m
Saturation Magnetization (M_S)	$1.47 \cdot 10^6$	A/m
Damping constant (α)	0.02	

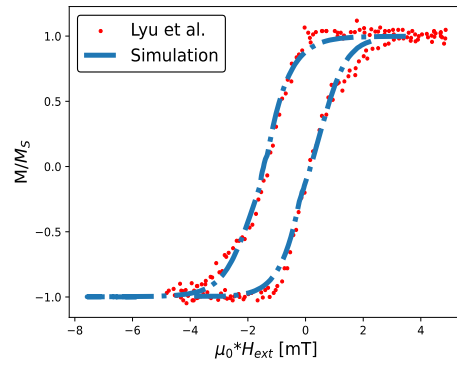


Figure 1: Hysteresis curve for a CoFeB/Mo MTJ by Lyu et al[1] and our simulation

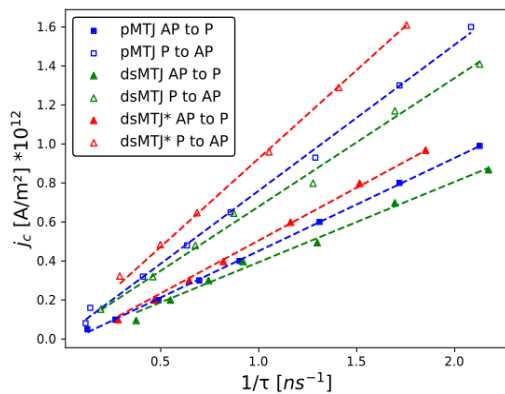


Figure 2: Switching current j_c for AP \rightarrow P and P \rightarrow AP switching respectively. The configuration of the magnetization of the fixed layers was antiparallel (dsMTJ) and parallel (dsMTJ*)

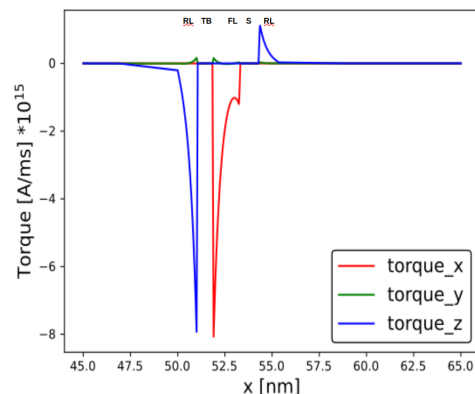


Figure 3: Spin Torque for the structure fixed reference layer (RL) - tunnel barrier (TB) - free layer (FL) - spacer (S) - fixed reference layer (RL)

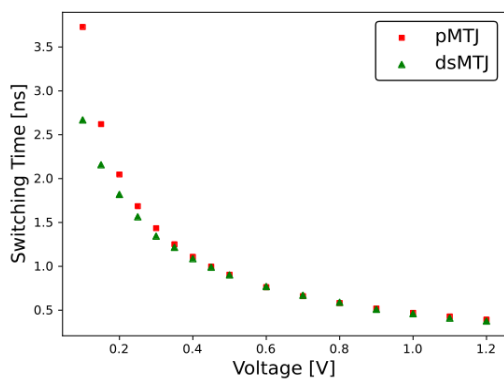


Figure 4: Switching time for AP \rightarrow P switching, at different voltages

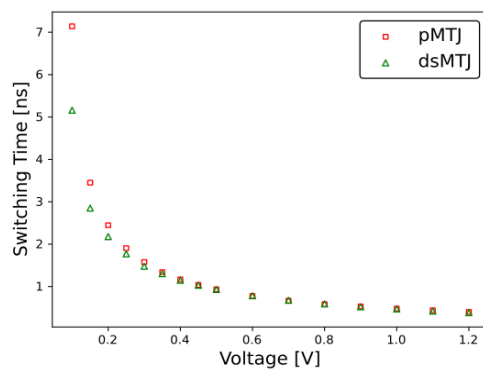


Figure 5: Switching time for P \rightarrow AP switching, at different voltages

Deterministic Approach for Skyrmionic Dynamics at Non-zero Temperatures

C. Navau*, J. Castell-Queralt, L. Gonzalez-Gómez, N. Del-Valle

Departament de Física, Universitat Autònoma de Barcelona, 08193 Bellaterra, Barcelona, Catalonia, Spain

*Presenting author mail: carles.navau@uab.cat

ABSTRACT

The finding of skyrmions at room temperature has boosted the potentiality of skyrmionic devices. From the theoretical point of view, in micromagnetic systems the temperature has been taken into account using stochastic spin dynamics, the stochastic Landau-Lifshitz equation or the Landau-Lifshitz-Block equation. Also, the rigid model can be used to describe the skyrmion dynamics taking into account thermal effects, using the stochastic Thiele equation [1]. All these methods require a statistical study of the obtained data (they rely in stochastic simulations), which results in a large computation time. In addition, analytical tendencies or limits can hardly be obtained.

Here we present a deterministic method to study the skyrmion dynamics[2], a new approach in which the temporal motion of skyrmions can be studied without relying on repetition of stochastic simulations, but on solving once the associated deterministic Fokker-Planck equation. This is a substantial advance, since by finding and solving a single partial differential equation, one could obtain all the relevant probabilistic information of the system. This allows one to evaluate the probability of presence, or survival, or trapping, or escaping, etc., of skyrmions in many practical situations, which is a key information to ensure the viability of applications. In particular, the probability of trapping/escaping of a skyrmion that encounters a pinning site, and the probability of survival of a skyrmion along a track are presented as a function of the temperature. The probability of survival of a skyrmion along a track at room temperature when granularity is considered is also studied.

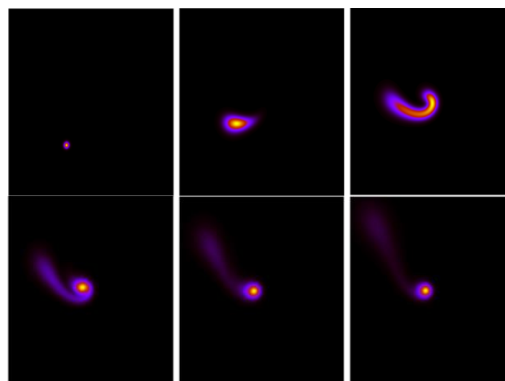


Figure. Time evolution of the probability density of finding a skyrmion which is approaching a pinning site at 150 K.

REFERENCES

- [1] D. Pinna, F. Abreu Araujo, J.-V. Kim, V. Cros, D. Querlioz, P. Bessiere, J. Droulez, and J. Grollier (2018). Skyrmion Gas Manipulation for Probabilistic Computing, *Phys. Rev. Applied* 9
- [2] J. Castell-Queralt, L. González-Gómez, N. del-Valle, C. Navau (2020). Deterministic approach to skyrmionic dynamics at nonzero temperatures: pinning sites and racetracks, *Phys. Rev. B* (R) 101

Mach–Zehnder-like interferometry with graphene nanoribbon networks

Sofia Sanz^{*}, Nick Papior[†], Géza Giedke^{‡,§}, Daniel Sánchez-Portal[¶],
Mads Brandbyge^{*}, Thomas Frederiksen^{‡,§}

^{*}Department of Physics, DTU, DK-2800 Kgs. Lyngby, Denmark

[†]DTU Computing Center DK-2800 Kgs. Lyngby, Denmark

[‡]Donostia International Physics Center (DIPC), E-20018, Donostia-San Sebastián, Spain

[§]IKERBASQUE, Basque Foundation for Science, E-48013, Bilbao, Spain

[¶]Centro de Física de Materiales CSIC-UPV/EHU, E-20018, Donostia-San Sebastián, Spain
e-mail: sofsa@dtu.dk

INTRODUCTION

The similarities between electrons traveling ballistically in graphene nanostructures and photons propagating in waveguides has spawned the novel field of electron quantum optics in graphene constrictions. With the ideas of optics-like experiments in mind, we can think of performing electron interferometry in graphene constrictions, for which some elementary building blocks, e.g., such as electron beam splitters, mirrors, etc., are needed. Remarkably, it has been recently shown that electrons injected in devices formed of two infinite graphene nanoribbons (GNR) placed one on top of the other with a crossing angle of 60° can be split into two outgoing waves without reflection [1], [2], [3]. Moreover, GNRs with zigzag edge topology are expected to host spin polarized states due to magnetic instabilities of the localized states at the edges [4], which make these devices even more interesting since we can think of performing both electron and spin quantum optics experiments [5]. With the advent of on-surface synthesis techniques, now not only atomistic defect-free samples of GNRs can be produced [6], [7] but also they can be manipulated.

In this work we propose interesting networks for studying electron and spin quantum interferometry built from four crossed GNRs in a pairwise setup (see Figure 1) that splits the beam into two possible paths that will self-interfere at the outgoing ports, where, the resulting interference pattern can be further tuned by an external magnetic field [8] as a

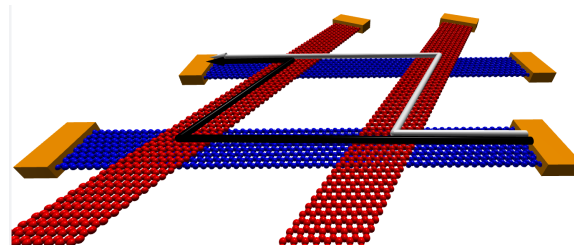


Fig. 1. Geometry of GNR-based interferometer with the two interfering paths sketched.

consequence of the Aharonov-Bohm effect [9]. By means of the mean-field Hubbard model [10], [11] in combination with the non-equilibrium Green's function formalism (NEGF) we are able to describe the spin dependent transport in this multi-terminal device. We further show that the scattering matrix formalism in the approximation of independent scattering at the four individual junctions provides accurate results as compared with the Green's function description, allowing for a simple interpretation of the interference process between two dominant pathways.

REFERENCES

- [1] L. R. F. Lima, A. R. Hernandez, F. A. Pinheiro, and C. Lewenkopf, A 50/50 electronic beam splitter in graphene nanoribbons as a building block for electron optics, *J. Phys.: Condens. Matter* **28**, 505303 (2016).
- [2] P. Brandimarte, M. Engelund, N. Papior, A. Garcia-Lekue, T. Frederiksen, and D. Sanchez-Portal, A tunable electronic beam splitter realized with crossed graphene nanoribbons, *J. Chem. Phys.* **146**, 092318 (2017).

- [3] S. Sanz, P. Brandimarte, G. Giedke, D. Sanchez-Portal, and T. Frederiksen, Crossed graphene nanoribbons as beam splitters and mirrors for electron quantum optics, *Phys. Rev. B* **102**, 035436 (2020).
- [4] Y. W. Son, M. L. Cohen, and S. G. Louie, Half-metallic graphene nanoribbons, *Nature* **444**, 347 (2006).
- [5] S. Sanz, N. Papior, G. Giedke, D. Sanchez-Portal, M. Brandbyge, and T. Frederiksen, Spin-polarizing electron beam splitter from crossed graphene nanoribbons, *Phys. Rev. Lett.* **129**, 037701 (2022).
- [6] J. Cai, P. Ruffieux, R. Jaafar, M. Bieri, T. Braun, S. Blankenburg, M. Muoth, A. P. Seitsonen, M. Saleh, X. Feng, K. Mullen, and R. Fasel, Atomically precise bottom-up fabrication of graphene nanoribbons, *Nature* **466**, 470 (2010).
- [7] P. Ruffieux, S. Wang, B. Yang, C. Sanchez-Sanchez, J. Liu, T. Dienel, L. Talirz, P. Shinde, C. A. Pignedoli, D. Passerone, T. Dumslaff, X. Feng, K. Mullen, and R. Fasel, On-surface synthesis of graphene nanoribbons with zigzag edge topology, *Nature* **531**, 489 (2016).
- [8] S. Sanz, N. Papior, G. Giedke, D. Sanchez-Portal, M. Brandbyge, and T. Frederiksen, Mach-Zehnder-like interferometry with graphene nanoribbon networks, arxiv.org/abs/2302.04821.
- [9] Y. Aharonov and D. Bohm, Significance of Electromagnetic Potentials in the Quantum Theory, *Phys. Rev.* **115**, 485 (1959).
- [10] J. Hubbard, Electron correlations in narrow energy bands, *Proc. R. Soc. A* **276**, 238 (1963).
- [11] S. S. Wuhl, N. Papior, M. Brandbyge, and T. Frederiksen, `hubbard: v0.2.0`, doi.org/10.5281/zenodo.4748765.

Two conductivity regimes in semiconductor δ -layer tunnel junctions

D. Mamaluy¹, and J.P. Mendez¹

¹Cognitive & Emerging Computing, Sandia National Laboratories, Albuquerque, USA

mamaluy@sandia.gov

We present an open-system quantum-mechanical charge self-consistent 3D real-space study of the conduction band structure and conductive properties of phosphorus delta-layer tunnel junctions in silicon shown in Fig. 1. These structures serve as basic building blocks for beyond-Moore (classical digital) (e.g. [1]) and quantum computing applications (e.g. [2]). Recent high resolution ARPES experiments [3, 4] demonstrated that the traditional band structure calculation methods that are based on either periodic or Dirichlet boundary conditions fail to describe the existence of 3Γ subband without adjusting the dielectric constant of Si to 40. Recently we demonstrated that using the open system boundary conditions (for the charge self-consistent Schrodinger equation) that preserve the quantum-mechanical flux allows to explain the existence of 3Γ subband without any fitting parameters and accurately reproduce the sheet resistance values for a wide range of delta-layer doping densities and different experimental groups [5]. Here we extend the open-system charge self-consistent quantum transport analysis to delta-layer tunnel junctions. The performed numerical analysis predicts that *the strong conduction band quantization leads to the existence of two distinct Ohmic conductivity regimes* as shown in Fig. 2. The corresponding mechanism can be understood from Figure 3, where the computed local

density of states is shown. For cryogenic temperatures only the states below Fermi level are occupied. As can be seen from Figure 3, the strong delta-layer confinement leads to the *conduction band quantization*. For low voltages, there is a mismatch between the quasi-discrete states on the left that have to tunnel to the quasi-discrete states on the right side, which reduces the conductivity. For higher applied drain voltages, the quasi-continuum states on the right side become available to tunnel into from the left side that eliminates the mis-match and increases conductivity [6]. Recent experimental data [2] for the I-V characteristics in Si:P delta-layer tunnel junctions support the existence of the two conductivity regimes. The “threshold” voltage (around 0.05-0.07 V in Fig. 2) is a function of doping level and doping thickness, and could be controlled for device applications.

REFERENCES

- [1] He, Y. et al., Nature 571, 371–375 (2019).
- [2] M. B. Donnelly, J. G. Keizer, Y. Chung, and M. Y. Simmons, Nano Letters 21, 10092 (2021).
- [3] A. J. Holt et al., Phys. Rev. B 101, 121402 (2020).
- [4] F. Mazzola, CY. Chen, R. Rahman et al., npj Quantum Mater. 5, 34 (2020).
- [5] D. Mamaluy, J.P. Mendez, X. Gao, et al. Commun Phys 4, 205 (2021).
- [6] J.P.Mendez, D. Mamaluy, Sci Rep 12, 16397 (2022).

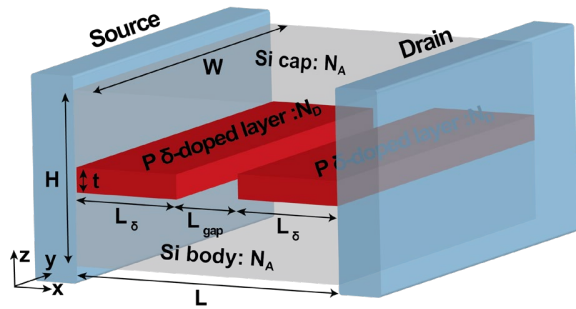


Fig.1: Ideal Si:P δ -layer tunnel junction (TJ) devices. The ideal device consists of a semi-infinite source and drain, in contact with the channel. The channel is composed of a lightly doped Si body and Si cap and a very thin, highly P doped-layer with an intrinsic gap of length L_{gap} .

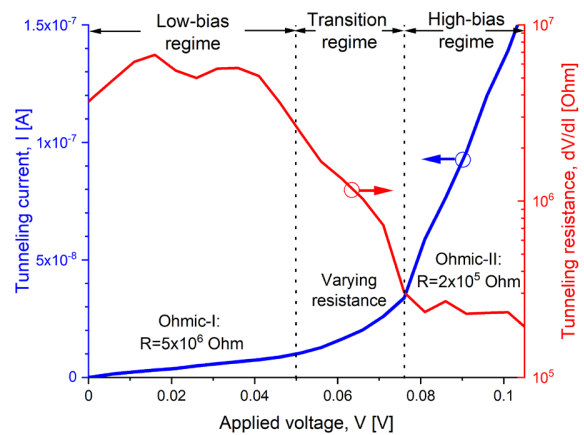


Fig.2: Two conductivity regimes in δ -layer tunnel junctions. Total current vs voltage (blue curve, linear scale) and the corresponding differential resistance dV/dI (red curve, logarithmic scale) are shown for $L_{\text{gap}}=10\text{nm}$, $N_D=1.0 \times 10^{14}\text{cm}^{-2}$, $N_A=5.0 \times 10^{17}\text{cm}^{-3}$ and $t=1\text{nm}$.

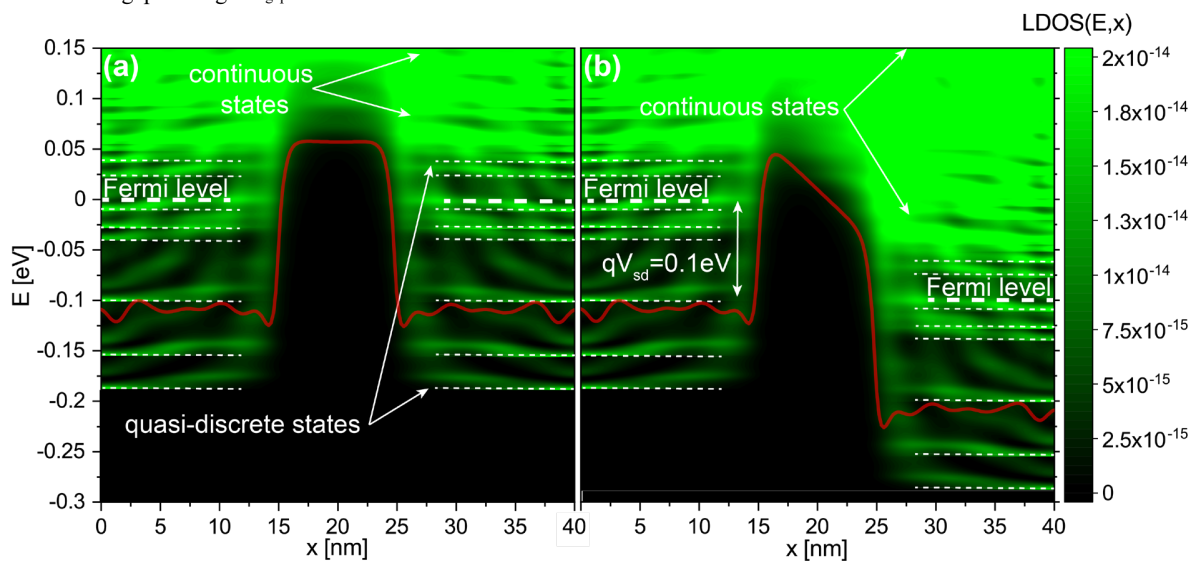


Fig.3: Local Density of States for δ -layer tunnel junctions. The LDOS(E,x) for a tunnel junction of $L_{\text{gap}}=10\text{ nm}$ is shown in (a) and (b) when a voltage of 1 mV and 100 mV is applied to the drain contact, respectively. The Fermi levels indicated in the figures correspond to the Fermi levels of the source and drain contacts. In (a) and (b), the corresponding effective 1D potentials are also shown, calculated by integrating over the (y,z)-plane the actual charge self-consistent 3D potentials weighted with the electron density. $N_D=1.0 \times 10^{14}\text{ cm}^{-2}$, $N_A=5.0 \times 10^{17}\text{ cm}^{-3}$, and $t=1\text{nm}$.

Charge Transport Properties of Cytochrome b₅₆₂ on Gold Interfaces

G.N. Jonnalagadda, Z. Futera

Faculty of Science, University of South Bohemia, Branisovska 1760,
370 05 Ceske Budejovice, Czech Republic
e-mail: jonnag00@prf.jcu.cz

INTRODUCTION

The fundamental processes that drive life, such as respiration, photosynthesis, and various enzymatic catalytic activities, are based on electron transfer reactions facilitated by redox proteins. One such protein, cytochrome b₅₆₂ (Fig. 1) found in *Escherichia coli*, is a metalloprotein, which contains one redox-active heme (Fe^{2+/3+}) cofactor covalently bonded to the protein matrix. The central iron cation at the redox site is coordinated with axial histidine (His102) and methionine (Met7) ligands (Fig. 2). The conductive properties of single cytochrome b₅₆₂ adsorbed on gold surfaces were recently investigated using Electrochemical Scanning Tunneling Microscopy (EC-STM). Here, we examine the related adsorption structures by computational techniques to elucidate the charge transport properties and mechanism.

METHODOLOGY

We employ various computational approaches to study these properties. Classical molecular dynamics (MD) is used for examining the structural aspects of the protein and its configurations on the gold surfaces. On the other hand, the quantum mechanical (QM) approach based on Density Functional Theory (DFT) is applied to investigate the electronic states at the protein/metal interfaces and junctions. [2], [3] These are then used to compute the conductive properties.

PROTEIN ADSORPTION

Following the experimental setup [1], we focus on mutated cytochrome b₅₆₂ (Fig. 3). After validating the stability of a dried protein structure, we simulate spontaneous adsorption to the flat gold (111) surface. The obtained physisorbed structures

are statistically analyzed and representative geometries are selected for further study. These are then chemisorbed and used for the preparation of the cytochrome junction between gold contacts.

TRANSPORT PROPERTIES

For the transport at bio/metallic interfaces, electronic-state alignment is crucial. We use the DFT+ Σ approach for its prediction, followed by the interfacial electronic coupling calculations by the Projector Operator-Based Diabatization (POD) method. These are then used for tunneling current evaluation within the Landauer formalism. [3], [4] For comparison, we also compute the incoherent electronic flux through the heme redox site to show that this mechanism, also dominant in solution, is not competitive with the coherent tunneling in junction configuration. These findings are in accord with previously studied multi-heme cytochrome junctions [4] and have important consequences for the design of novel bioelectronic devices and material development.

REFERENCES

- [1] M. Elliott, D.D. Jones *Approaches to Single-molecule Studies of Metalloprotein Electron Transfer Using Scanning Tunneling Probe-based Techniques*. *Biochem. Soc. Trans.* **46**, 9 (2018).
- [2] O.V. Kontkanen, D. Biriukov, Z. Futera *Reorganization Free Energy of Copper Protein in Solution, in Vacuum and on Metal Surfaces*. *J. Chem. Phys.* **156**, 175101 (2022).
- [3] Z. Futera *et al.* *Coherent Electron Transport across a 3 nm Bioelectronic Junction Made of Multi-heme Proteins*. *J. Phys. Chem. Lett.* **11**, 9766 (2020).
- [4] Z. Futera, X. Wu, and J. Blumberger *Tunneling to Hopping Transition in Multiheme Cytochrome Bioelectronic Junctions*. *J. Phys. Chem. Lett.* **14**, 445 (2023).

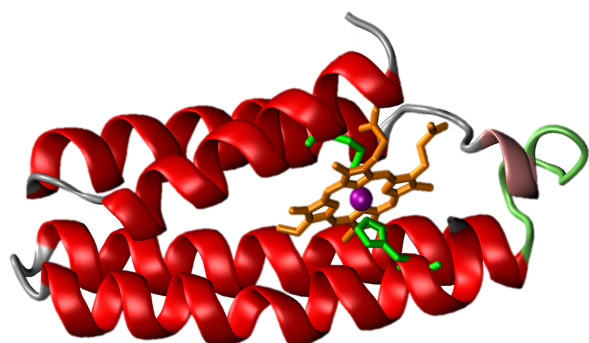


Fig. 1. Crystal structure of the Cytochrome b₅₆₂ protein (PDB id 2BC5)

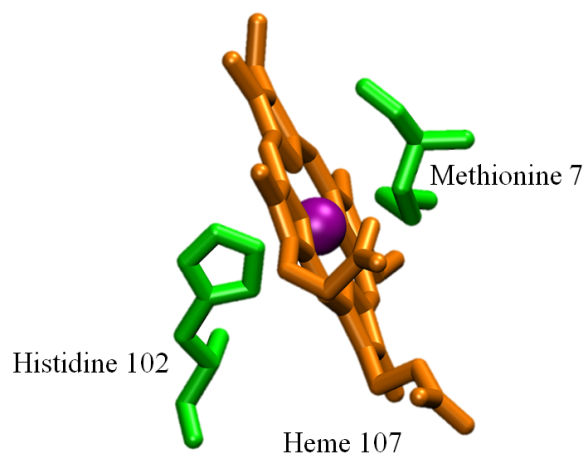


Fig. 2. Details of the redox-active heme site (Purple: Fe, Orange: Porphyrin ring, Green: Axial histidine and methionine)

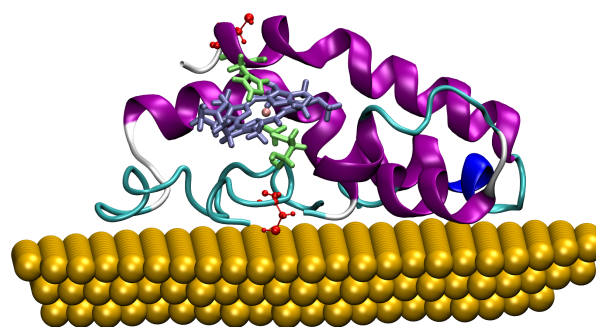


Fig. 4. Mutated cytochrome b₅₆₂ adsorbed onto a gold surface

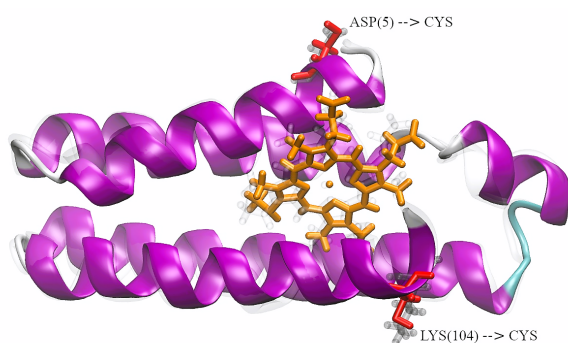


Fig. 3. Mutated (Asp5 to Cys and Lys104 to Cys) vs non-mutated (Native cytochrome b₅₆₂) (Ghost: Native, Color: Mutated)

Coherent and Incoherent Electron Transport through Protein Junctions Investigated by DFT-based Approaches

Z. Futera

Faculty of Science, University of South Bohemia, Branišovská 1760,
370 05 České Budějovice, Czech Republic
e-mail: zfutura@prf.jcu.cz

INTRODUCTION

Electron transfer facilitated by redox-active proteins is utilized in various biological processes, including photosynthesis, respiration cycle, or denitrification reactions. Copper proteins such as Plastocyanin or Azurin and the heme-containing cytochromes often participate in these redox cascades. Recently, these proteins started to be utilized in nanobioelectronic devices due to their suitable electron-transfer properties. However, non-expected physical phenomena were observed when the proteins were incorporated between metal contacts or electrodes. While in a native aqueous environment, the electron flow through the system of redox sites proceeds by the thermally activated hopping mechanism, the temperature-independent currents of relatively high magnitudes were detected on protein/metal junctions. [1], [2] These data suggest that the electrons through protein junctions are transferred by the coherent tunneling mechanism, independently of the redox-active states.

METHODOLOGY

We investigate these electron-transport phenomena by means of computer simulations based on classical molecular dynamics (MD) as well as the first-principles description within the framework of density functional theory (DFT). [3], [4] While the incoherent hopping could be studied by combined quantum-mechanical/molecular-mechanical (QM/MM) techniques, [5] the coherent tunneling requires a quantum description of the whole interface models. Special care is taken to electronic-state alignment on the bio/metallic interfaces for which we apply the DFT+ Σ scheme.

RESULTS

We applied these methodologies on Azurin blue-copper protein and on small tetraheme cytochrome (STC), which were previously studied experimentally. We showed that the transport mechanism in both Azurin and STC junctions between gold electrodes is the coherent tunneling facilitated by valence-band states of the proteins. In contrast to their redox properties in solution, the presence of the metal cations in the protein structures is not essential for their conductivity on the metal interfaces. The reason for this drastically different behavior in solution and on the metal interfaces is the significant electronic-level misalignment between the protein and metallic states. [6] However, the state position, and so the transport mechanism, can be modulated by application of gating potentials.

REFERENCES

- [1] K. Garg *et al.*, *Direct Evidence for Heme-Assisted Solid-State Electronic Conduction in Multi-Heme c-Type Cytochromes*. *Chem. Sci.* **9**, 7304 (2018)
- [2] Z. Futera *et al.*, *Coherent Electron Transport across a 3 nm Bioelectronic Junction Made of Multi-Heme Proteins*. *J. Phys. Chem. Lett.* **11**, 9766 (2020)
- [3] D. Biriukov, Z. Futera *Adsorption of Amino Acids at the Gold/Aqueous Interface: Effect of an External Electric Field*. *J. Phys. Chem. C* **125**, 7856 (2021)
- [4] Z. Futera, *Amino-Acid Interactions with the Au(111) Surface: Adsorption, Band Alignment, and Interfacial Electronic Coupling*. *Phys. Chem. Chem. Phys.* **23**, 10257 (2022)
- [5] O.V. Kontkanen, D. Biriukov, Z. Futera *Reorganization Free Energy of Copper Proteins in Solution, in Vacuum, and on Metal Surfaces*. *J. Chem. Phys.* **156**, 175101 (2022)
- [6] Z. Futera, X. Wu, J. Blumberger *Tunneling-to-Hopping Transition in Multiheme Cytochrome Bioelectronic Junctions*. *J. Phys. Chem. Lett.* **14**, 445 (2023)

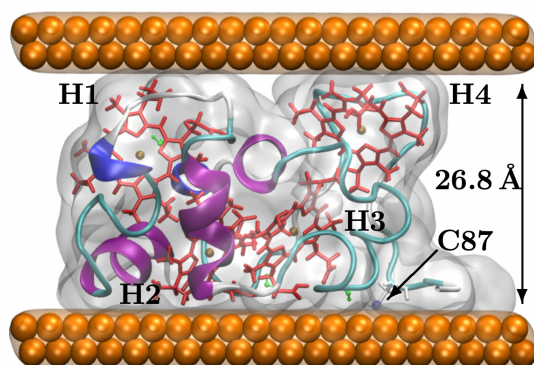


Fig. 1. Model of the STC junction with indicated position of the four redox heme cofactors and chemisorbed Cys87 site. [2]

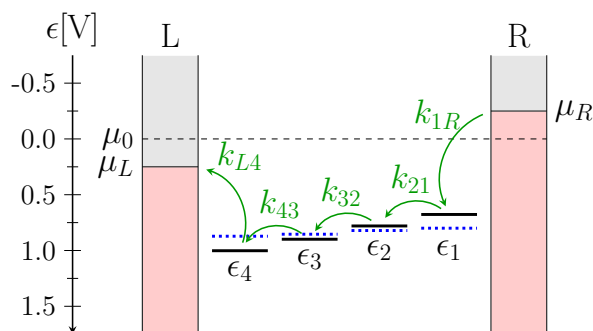


Fig. 2. Schematic illustration of incoherent electron hopping events through four STC redox sites between left (L) and right (R) metal contacts. [6]

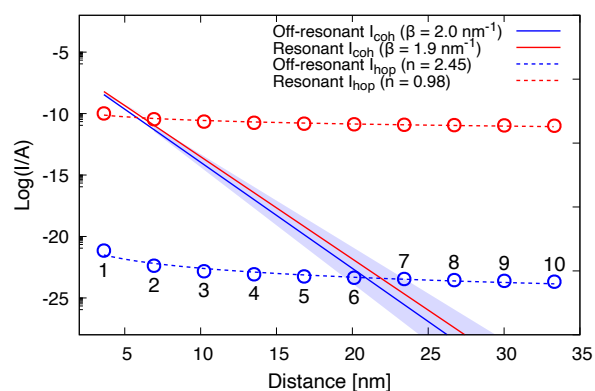


Fig. 3. Distance dependencies of coherent (I_{coh}) and incoherent (I_{hop}) current in multi-STC junctions. [6]

Schrödinger Equation Solver Based on Data-Driven Physics-Informed Generic Building Blocks

Martin Veresko, Ming-Cheng Cheng*

Department of ECE, Clarkson University, 8 Clarkson Ave, Potsdam NT, United States

*e-mail: mcheng@clarkson.edu

This work investigates a physics-informed learning algorithm to solve the multi-dimensional Schrödinger equation for nanostructures based on the quantum element method (QEM) [1]. The QEM selects generic building blocks of a group of nanostructures as *elements*, each of which is trained by proper orthogonal decomposition (POD) to generate its basis functions (or POD modes). To simulate a large structure, these trained elements are then *stitched* together using the discontinuous Galerkin method. Such a multi-element approach minimizes the training effort, optimizes parallel computing efficiency, and offers cost-effective simulation and design of nanostructures.

POD trains the modes to maximize the mean square inner product with the wave function (WF) data collected from direct numerical simulation (DNS) of the Schrödinger equation. Each element is trained to account for variations of electric fields or potentials and adjacent elements. This POD process leads to the Fredholm equation [2],

$$\int_{\Omega'} \langle \psi(\vec{r}) \otimes \psi(\vec{r}') \rangle \vec{\eta}(\vec{r}') d\Omega' = \lambda \vec{\eta}(\vec{r}') \quad (1)$$

where η_j is the POD mode, ψ is the WF and λ is an eigenvalue. The eigenvalues of the POD modes indicate the amount of information captured.

After generating the POD modes, the WF can be formed via a linear combination of M modes,

$$\psi(\vec{r}) = \sum_{j=1}^M a_j \eta_j(\vec{r}) \quad (2)$$

where a_j is the weight. The weights are found via the Galerkin projection of the Schrödinger equation onto the POD modes. This projection provides physical guidance based on first principles to reach an efficient and accurate learning method.

Using the QEM for a system of N_{el} elements, the Hamiltonian equation in POD space is found,

$$\sum_{j=1}^{M_p} (T_{n_p,ij} + U_{\eta_p,ij}) a_{p,j} + \sum_{q=1, q \neq p}^{N_{el}} \sum_{j=1}^{M_p} B_{p,pq,ij} a_{p,j} + \sum_{q=1, q \neq p}^{N_{el}} \sum_{j=1}^{M_q} B_{pq,ij} a_{p,j} = E a_{p,i}, \quad (3)$$

where $T_{n_p,ij}$ and $U_{\eta_p,ij}$ are the interior kinetic energy and potential energy matrixes for the p th element composed of M_p modes. $B_{p,pq,ij}$ is the diagonal boundary kinetic energy matrix and $B_{pq,ij}$ is the off diagonal kinetic matrix [1].

Three GaAs/InAs quantum-dot (QD) structures given in Fig. 1(a) are used to train 3 elements, 2 hexagon QD elements (see E2 and E3 in Fig. 2(a)) and one spacer element (E1 in Fig. 2(a)). Each training structure in Fig. 1(a) is subjected to 10 single component electric fields in x and y varying between $[-35, 35] kV/cm$. At each field, only WFs of the first 6 quantum states (Qs) are collected from DNS with a mesh size of 14966. Data collected from the same elements are combined to generate POD modes to account for more variations of BCs (i.e., adjacent elements).

To test the QEM method, a test electric field $\vec{E} = (25\hat{x} + 15\hat{y}) kV/cm$ was applied to the structure in Fig. 1(b). Around the 7th to 15th mode, the POD eigenvalues of all elements in Fig. 2(a) reduce from the first mode by more than 3 orders of magnitude. Figs. 2(b) and 2(c) reveal that the POD least square (LS) error is near 1% (or 2%) using just 10-15 (or 8-12) modes per element and the eigenenergies from QEM and DNS are nearly identical. $|\psi|^2$ profiles of several Qs given in Fig. 3 illustrate the excellent agreement between the QEM and DNS using only a handful of modes (DoF) per element. This study found that the QEM offers a 2-order reduction in computational time, compared to DNS.

ACKNOWLEDGMENT

This work is supported by NSF OAC-2118079.

REFERENCES

- [1] M.-C. Cheng, "Quantum element method for quantum eigenvalue problems derived from projection-based model order reduction," AIP Advances (2020)
- [2] J. L. Lumley, "The Structure of Inhomogeneous Turbulence," Atmospheric Turbulence & Wave Propagation, A. M. Yaglom and V.I. Tartarski, Ed. Moscow, 166-178 (1967)

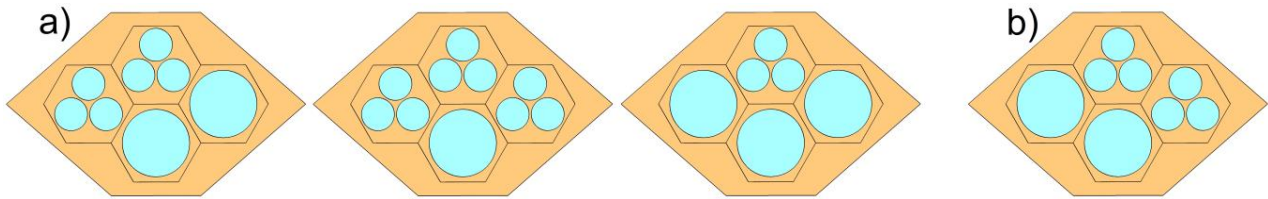


Fig. 1. (a) Three training structures used to train the 3 elements shown in Fig. 2. (b) Test structure used to verify the QEM model.

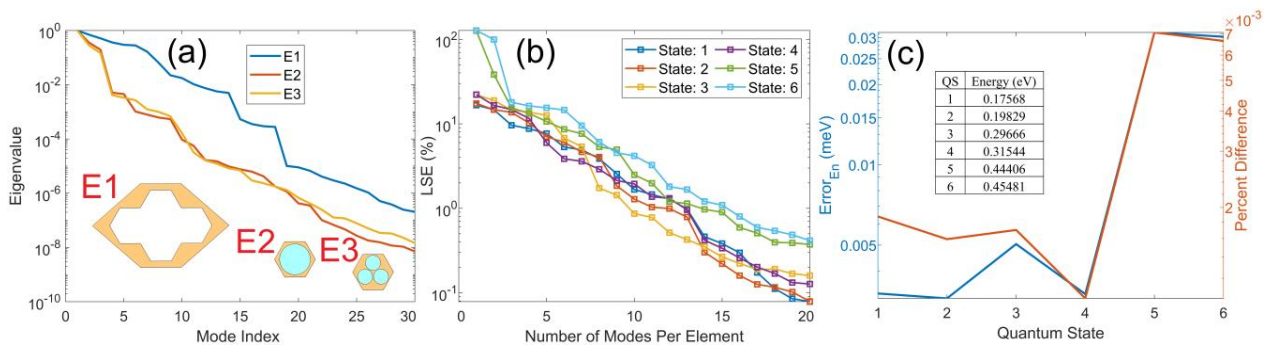


Fig. 2. (a) Eigenvalues of the three generic elements. (b) LS error for QSs 1-6. (c) Error in the QEM eigenenergy relative to DNS.

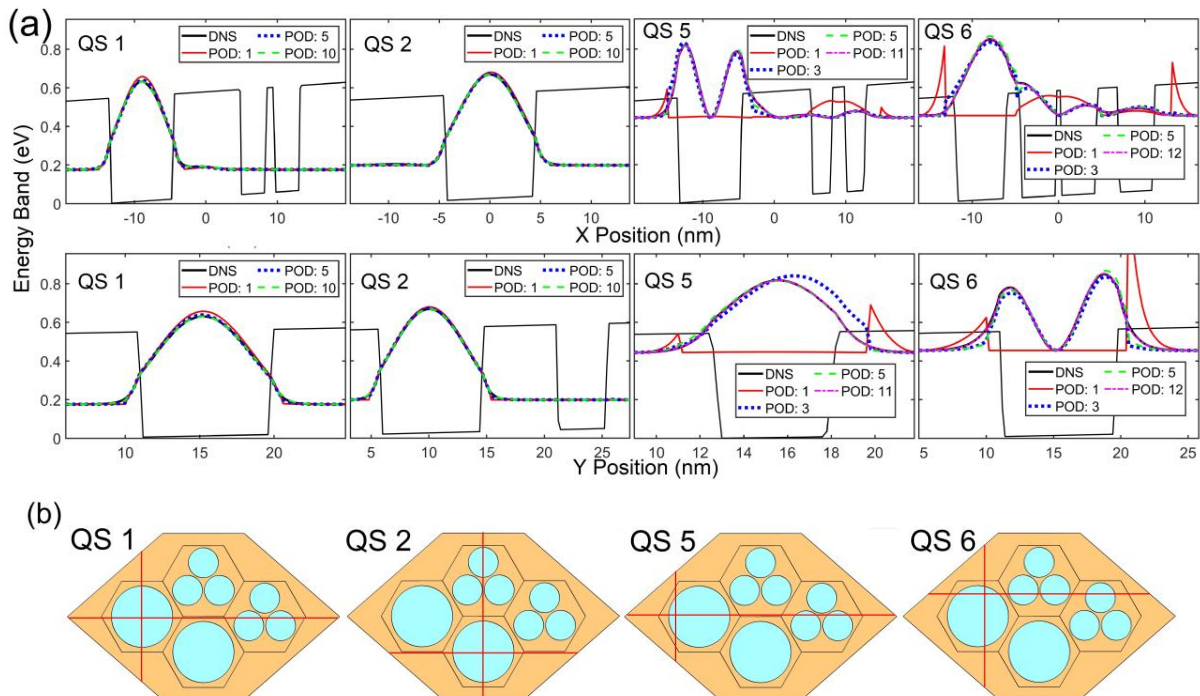


Fig. 3. (a) Profile plots in x (top row) and y (bottom row) for the $|\psi|^2$ of QSs 1,2,5 and 6 along the horizontal and vertical plotting paths (red lines) shown in (b). The paths were selected to show the maximum probability density in the state.

Considerations on Treating Polar-Optical Phonon Scattering in Real Space

D. K. Ferry

School of Electrical, Computer, and Energy Engineering, Arizona State University,
Tempe, AZ 25287-6206 USA
e-mail: ferry@asu.edu

ABSTRACT

For many applications, especially in quantum transport, a more accurate approach to handling scattering by the polar phonons may be had by a treatment in real space rather than by perturbation theory.

INTRODUCTION

In the treatment of carrier transport with quantum transport, non-equilibrium Green's functions are often used. These, however, have difficulty with scattering that arises from Coulombic centers, such as ionized impurities and the polar-optical phonons. In the case of impurities, much improved behavior is found by treating these centers in real space [1]. Importantly, it has been shown that this preserves the quantum coherence of the carriers during scattering [2]. Treating the polar-optical phonons by perturbation theory may well lead to difficulties with use of the non-equilibrium Green's functions, due to a need for the Bethe-Salpeter equation and disconnected diagrams in order to fully account for such phase coherence [3]. On the other hand, it has usually been assumed that optical phonon scattering led to complete phase breaking. Whether or not either view is completely correct only can be determined by treating the polar-optical interaction in real space.

MODEL

Here, semiconductors with the zinc-blende structure are considered. In this case, each atom of the A-B basis set is tetragonally coordinated with 4 nearest neighbors. An important point is that the polar LO mode corresponds to the two atoms in the basis oscillating against one another, as shown by the pair A₁-B in Fig. 1. While this one of the 4 neighbors is involved in the LO mode, it is important to understand that the other three atoms in the tetragonal bonding are moving with TO

motion in conjunction with the B atom. Hence, the LO potential associated with the motion is a dipole potential (Fig. 2), where the dipole moment oscillates in time, and these potentials are oriented along one of the [111] axes of the crystal, and is coherent throughout the crystal due to TO modes.

The number of dipoles present (per unit volume) is given by the product of the Bose-Einstein distribution and the phonon density of states. In a simulation, the simulation volume is determined by the assumed density of carriers and the number of particles in the Monte Carlo simulation. Once the dipoles are introduced, in the same manner as discrete impurities, the particles are guided by the overall potential surface. One important point is that the dipole oscillates with a frequency of the LO mode, and this oscillation modulates the spatial shape of the potential and only weakly its amplitude. This oscillation determines the corresponding time step in the simulation.

Additionally, one has to address the exchange of energy between the carrier and the dipole. Excitation of excess phonons can increase the dipole amplitude, and this excess energy has to be allowed to either recombine or diffuse through the semiconductor.

CONCLUSION

A model for handling the polar-optical phonons in real space is proposed as one approach to such considerations.

REFERENCES

- [1] H. S. Wong and Y. Taur, *Three-Dimensional Atomistic Simulation of Discrete Random Dopant Distribution in 0.1 μm MOSFETs*, IEDM (1993) p.705.
- [2] J. Weinbub *et al.*, *Electron Interference in a Double Dopant Potential Structure*, Phys. Stat. Sol. RRL **12**, 1800111 (2018).
- [3] D. K. Ferry *et al.*, *A Review of Quantum Transport in Field-Effect Transistors*, Semicond. Sci. Technol. **37**, 043001 (2022)

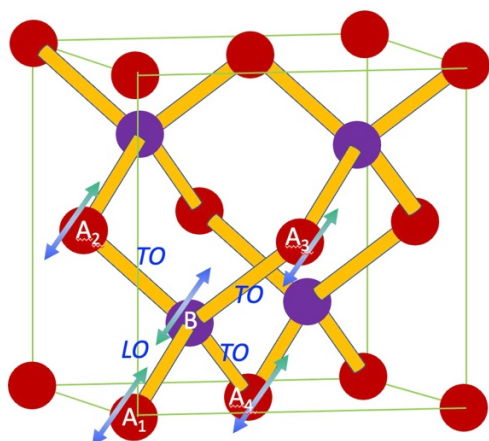


Fig. 1. Motion of the atoms on one basis set may be the LO mode, simultaneously the other atoms in the tetragonal bonding are undergoing TO motion.

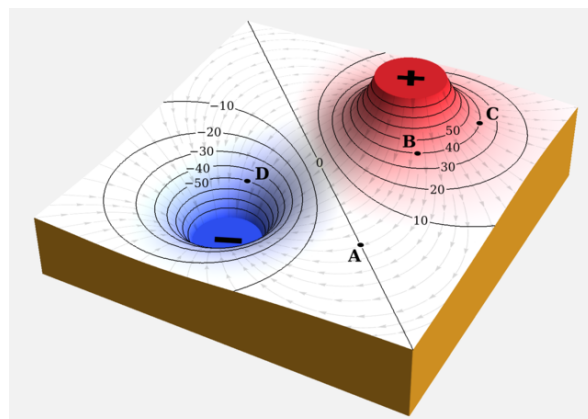


Fig. 2. A dipole potential. The dipole charge is aligned along the (111) crystal axis. (Wikipedia Commons 3.0)

Spin-selective transport phenomena in helical molecular wires

R. Korytár*, Š. Marek*, J. van Ruitenbeek[‡] and F. Evers[†]

* Charles University, Czech Republic, e-mail: korytar@karlov.mff.cuni.cz

[†] Institute of Theoretical Physics, University of Regensburg, Germany

[‡] Huygens-Kamerlingh Onnes Laboratory, Leiden University, Netherlands

Background

Recently various spin-selective phenomena have been reported in transport through helical molecular wires attached to metallic leads[1], [2], [3], see Fig. 1. There is a general consensus that the spin selectivity results due to a combination of the spin-orbit coupling and the helicity. Theoretical understanding of the so called chirality-induced spin selectivity (CISS) is, however, not complete, because most theoretical reports grossly underestimate the magnitude of the effect [4].

We present two approaches to improve the quantitative description of the CISS.

1. Metal-molecular interfaces in the *GW* approximation

First-principles quantum transport simulations rely on an accurate description of electronic charged excitations. The latter are not well described in density functional theory; a natural framework to describe them is Hedin's *GW* approximation. Our calculations show that the *GW* method widens the HOMO-LUMO gap of metallic clusters. We rigorously quantify this observation by investigating an ensemble of disordered metallic clusters [6], see Fig. 2. Our observation has profound impact on the interpretation of standard calculations of molecular adsorbates. Namely, in such studies the infinite metallic surface is always replaced by a finite cluster (with periodic or vacuum boundary conditions). Our results imply that the density of states from the *GW* quasiparticles will be artificially depleted right at the Fermi level.

Therefore, the *GW* method can not be taken as an out-of-the-box improvement over the less

accurate density-functional theory.

2. Spin currents in chiral molecular junctions

Considerations based on time-reversal invariance known in the field of spintronics allow for spin-currents in two-terminal coherent devices even in absence of external magnetic fields and magnetic impurities. Such spin-currents exist even in linear response if the device hosts more than one scattering channel. We exemplify this in a model of a molecular wire of a helical topology, see Fig. 3 for an example. We provide basic principles for designing molecular junctions that generate sizable spin currents [5]. These principles can be verified by ab-initio calculations and experimental setups.

Acknowledgment

R. Korytár acknowledges the Czech Science foundation (project no. 22-22419S).

References

- [1] S. Mishra, A. Kumar Mondal, S. Pal, T. Kumar Das, E. Z. B. Smolinsky, G. Siligardi, and R. Naaman, *J. Phys. Chem. C* 124, 10776 (2020)
- [2] T. Liu, X. Wang, H. Wang, G. Shi, F. Gao, H. Feng, H. Deng, L. Hu, E. Lochner, P. Schlottmann, S. von Molnár, Y. Li, J. Zhao, and P. Xiong, *ACS Nano* 14, 15983 (2020)
- [3] H. Al-Bustami, S. Khaldi, O. Shoseyov, S. Yochelis, K. Killi, I. Berg, E. Gross, Y. Paltiel, and R. Yerushalmi, *Nano Lett.* 22, 5022 (2022)
- [4] F. Evers, et al., *Adv. Mater.* 34(13), 2106629 (2022)
- [5] J. van Ruitenbeek, R. Korytár, F. Evers, Chirality-controlled spin scattering through quantum interference, in preparation (2023)
- [6] Š. Marek and R. Korytár, Pitfalls of ab-initio *GW* calculations for metal-molecular interfaces, in preparation (2023)

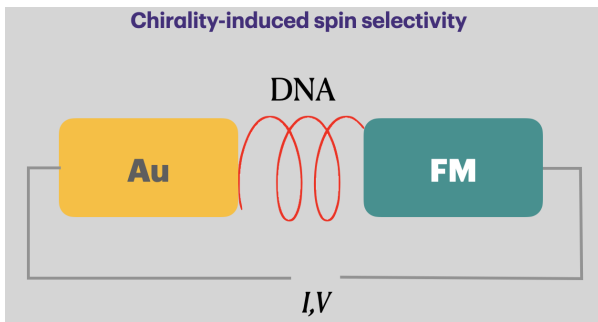


Fig. 1. Typical setup to measure the CISS in electronic current: a non-magnetic lead (Au) attaches to a helical (DNA-like) molecule. The spin selectivity manifests as the the magnetization of the right lead (a ferromagnet) reverses.

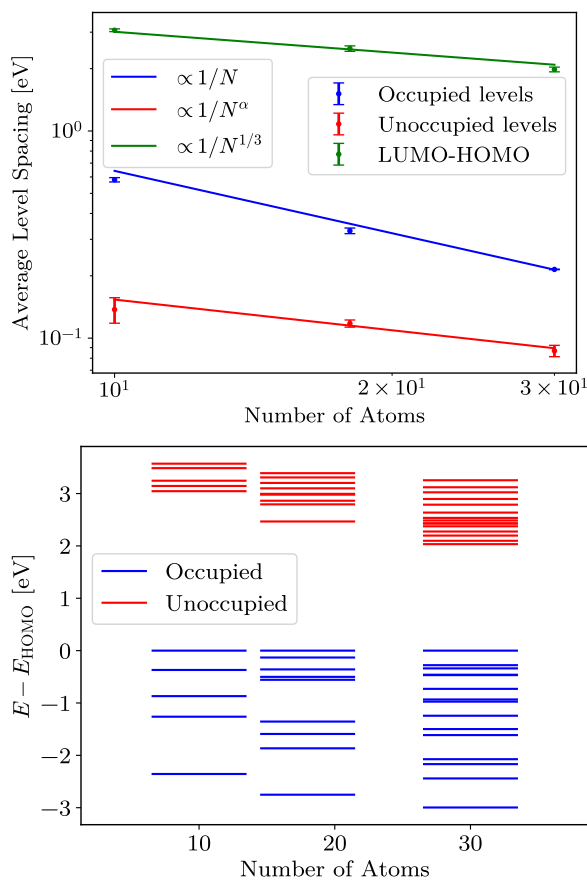


Fig. 2. Scaling of various charged excitations of metallic clusters in $evGW$. Top: average level spacings and gaps in an ensemble of metallic clusters as a function of the number of atoms. Lines are guides to the eye; they reveal that the HOMO-LUMO gaps scale with a slower power law, leading to HOMO-LUMO widening. Right, the energy levels of sample clusters is shown, with HOMO aligned to 0.

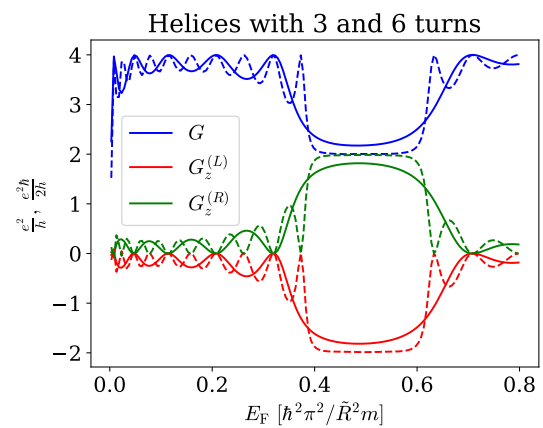


Fig. 3. Charge conductance G and spin left/right spin conductances $G_z^{(L,R)}$ of a model helical wire with 3 (6) turns are depicted by solid (dashed) lines as a function of the Fermi energy. The helix is attached to non-helical leads.

Efficient Method to Obtain Target Bias Solutions of $6F^2$ DRAM Cells with Geometric Fluctuations

Geonho Park, Seung-Cheol Han, and Sung-Min Hong

School of Electrical Engineering and Computer Science, Gwangju Institute of Science and Technology

E-mail: smhong@gist.ac.kr

ABSTRACT

A machine learning (ML)-TCAD algorithm is implemented to obtain the target bias solution of dynamic random access memory (DRAM) cells efficiently, which are generated by introducing geometric fluctuations into the ideal cell structure. The light gradient boosting machine (LGBM) trained on the electrostatic potential profiles of DRAM cells is used to predict the initial solutions at specific bias conditions. The model is trained with 300 simulation results. Using the proposed method, solutions for 1,000 devices at a target bias are obtained quickly.

INTRODUCTION

Geometric fluctuations during DRAM manufacturing obviously affect transistor performance and yield [1]. Therefore, a simulation considering these variations is important, but it requires a lot of computational time. Since the device characteristics are sensitive to geometric fluctuations, a perturbative approach is difficult to apply and we must perform the full device simulation for each device. To overcome this drawback, the ML-TCAD framework has been widely used in this field recently [2]. However, sophisticated and high-level ML/AI models such as CNN and U-net are required.

In this work, we propose an efficient simulation flow using an easy-to-use Light Gradient Boosting Machine (LGBM) [3] to obtain the target bias solutions of DRAM cells with geometric fluctuations.

LGBM MODEL AND RESULTS

We built an LGBM model to predict the electrostatic potential profile of $6F^2$ DRAM in **Fig. 1**. As shown in **Fig. 2**, device parameters ($L_{G1,2}$, L_{ov} , T_{ox} , H_{fin} , R_{iso} , N_{sd} , and N_{ch}) and spatial parameters (x , y , z coordinates) are used as input parameters to the model. The electrostatic potential profile at a given position is obtained as an output. For high accuracy of the model, spatial parameters are preprocessed using the K-means clustering.

The entire simulation procedure to obtain the target bias solution of DRAM cells is shown in **Fig. 3**. First, an LGBM model is trained using the electrostatic potential profiles of 300 DRAM cells, which are generated by introducing geometric fluctuations into the ideal cell structure. These profiles are obtained with our in-house simulator, G-Device [2]. The drift-diffusion model is solved with the doping-dependent mobility model (Ma-

setti), the inversion layer mobility model (Lombardi), the high-field saturation model, the Shockley-Read-Hall recombination (field enhancement) model, and the band-to-band tunneling model [4].

Secondly, for a test set (device and spatial parameters for 1,000 devices), the trained model predicts the initial solutions and these initial solutions are loaded. Finally, a numerical simulation is conducted directly at the target bias step, without any bias ramping procedure. If the simulation does not converge, a solution of the failed device is calculated by a conventional simulation with the bias ramping procedure. The LGBM model is retrained with that solution. This process made it possible to make highly accurate predictions for device with a wide range of parameters.

Figs. 4 and 5 show that our simulation flow is more efficient than the conventional bias ramping method in terms of the number of iterations required to obtain the target bias solution. The computational cost can be significantly reduced by avoiding unnecessary ramping steps. As a result, the target bias solutions of DRAM cells can be calculated within (at least) 13 times fewer Newton iterations.

CONCLUSION

We have proposed the efficient simulation flow to obtain the target bias solutions of $6F^2$ DRAM cells with geometric fluctuation. The proposed simulation flow is highly efficient in analyzing the devices with these variations at a target bias. Compared with the conventional bias ramping procedure, the computational time can be significantly (at least 13 times) reduced.

ACKNOWLEDGMENT

This work was supported by the National Research Foundation of Korea (NRF) through the Korean Government under Grant NRF-2020M3H4A3081800.

REFERENCES

- [1] S. Jeon et al., "Investigation on the local variation in BCAT process for DRAM technology", IEEE IRPS, (2017).
- [2] S.-C. Han et al., "Acceleration of Semiconductor Device Simulation with Approximate Solutions Predicted by Trained Neural Networks", IEEE Trans. Electron Devices, (2021)
- [3] G. Ke et al., "LightGBM: A highly efficient gradient boosting decision tree", in Proc. Adv. Neural Inf. Process. Syst., (2017)
- [4] J. H. Park et al., "Row Hammer Reduction Using a Buried Insulator in a Buried Channel Array Transistor", IEEE Trans. Electron Devices, (2022)

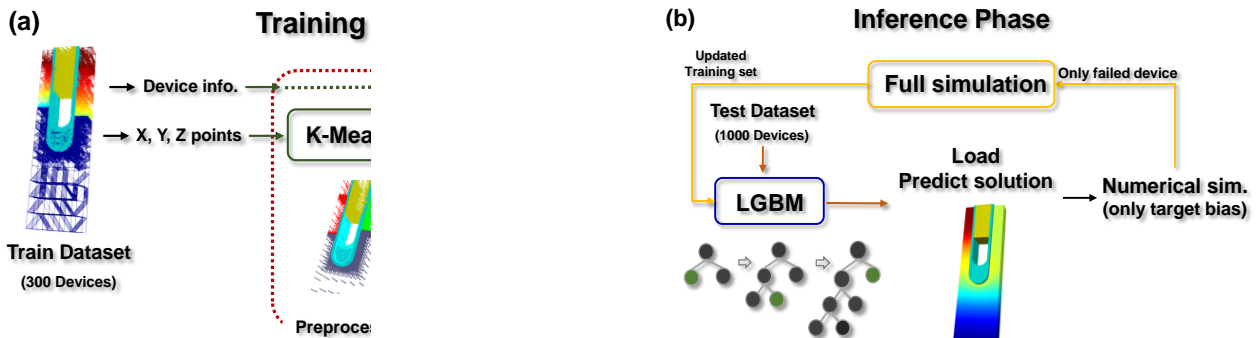
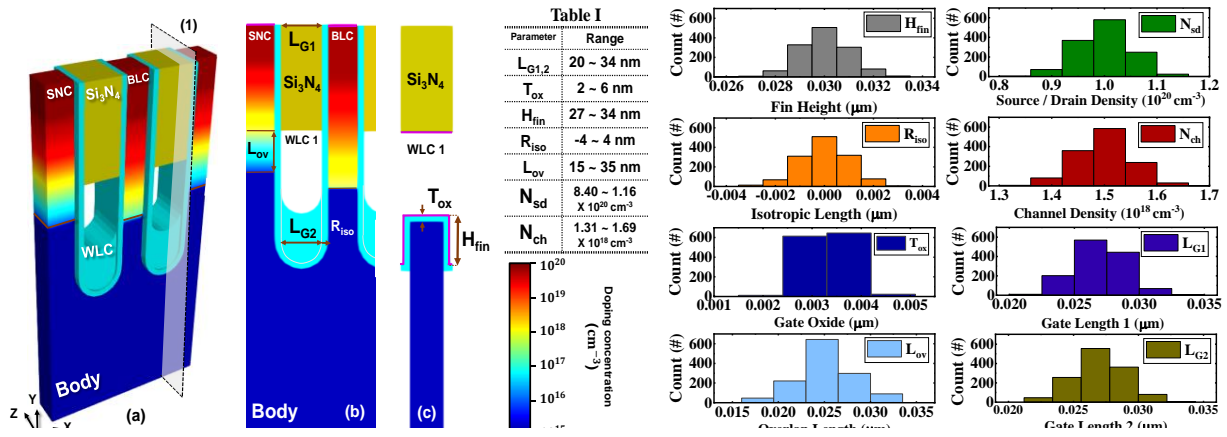


Fig. 3. Schematic for the entire process of ML-TCAD framework. (a) Training phase. The spatial parameters were preprocessed by K-means clustering, and high-accuracy model was built by adding cluster information to the input parameters. (b) Inference phase. The incremental training is used to make highly accurate predictions for device with a wide range of parameters.

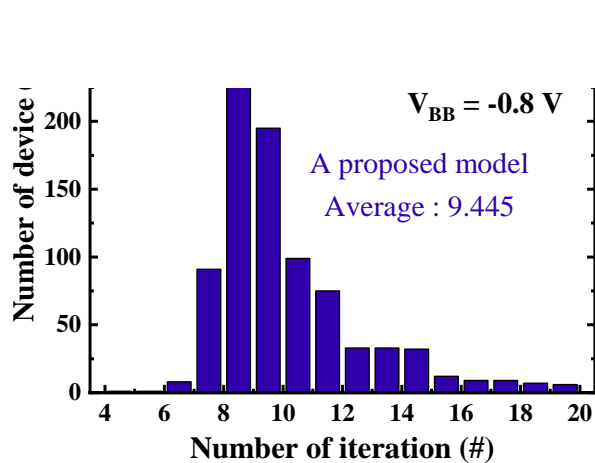


Fig.4. Distribution of the number of iterations for 1,000 devices, when the proposed method is applied at $V_G = 2.0 \text{ V}$, $V_D = 1.5 \text{ V}$, and $V_{BB} = -0.8 \text{ V}$.

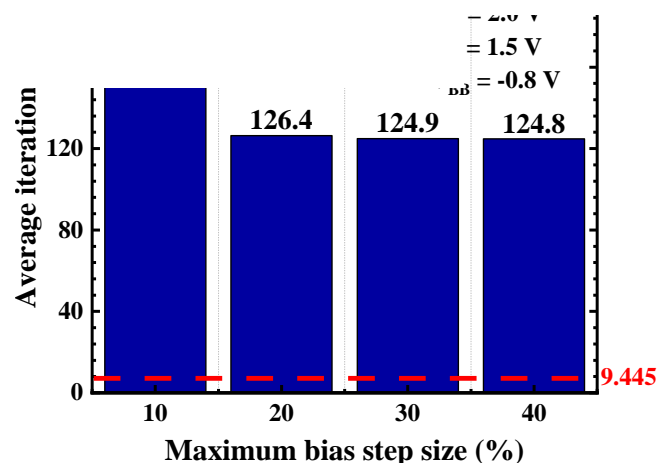


Fig. 5. Comparison of the average number of Newton iterations of the two methods at $V_G = 2.0 \text{ V}$, $V_D = 1.5 \text{ V}$, and $V_{BB} = -0.8 \text{ V}$. Our method converges within (at least) 13 times fewer iterations.

First-principles Study on As Antisites in InGaAs Alloys, GaAs and InAs

Yucheol Cho, Gyeongdo Ham and Daeshik Kim*

School of Electrical Engineering, Korea Advanced Institute of Science and Technology,
Daejeon, 34141, South Korea
e-mail: daeshik@kaist.ac.kr

INTRODUCTION

Due to the high electron mobility of III-V materials, they have been studied as a promising next-generation semiconductor material. However, if there are mid-gap defects, those significantly degrades the device performance. In particular, As antisite is a critical trap state which usually forms their states in the band gap. In this work, we perform first-principles study to rigorously calculate the defect energy level of As antisites in bulk structures of GaAs, InGaAs, and InAs. In addition, we evaluate the energy level while varying the ratio between In and Ga atoms in InGaAs alloys.

SIMULATION AND RESULT

III-V Bulk Structures. We perform density functional theory (DFT) simulations using SIESTA [1] on bulk structures of GaAs, InGaAs and InAs. We first optimize their lattice vectors in conventional unit cells (Fig. 1). We consider various InGaAs alloys such as $\text{In}_{0.25}\text{Ga}_{0.75}\text{As}$, $\text{In}_{0.5}\text{Ga}_{0.5}\text{As}$ and $\text{In}_{0.75}\text{Ga}_{0.25}\text{As}$ with randomly distributed In and Ga atoms. We apply the DFT-1/2 technique [2] to compensate for the fact that general DFT calculations underestimate the band gaps of semiconductor materials as shown in Fig. 2. The relaxed bulk structures with $2 \times 2 \times 2$ supercell of the conventional unit cells are obtained and their band structures are shown in Fig. 3. This shows that the band gap decreases as the ratio of In atoms to Ga atoms increases.

Modeling of As Antisite. We model an As antisite in various III-V materials such as GaAs, $\text{In}_{0.25}\text{Ga}_{0.75}\text{As}$, $\text{In}_{0.5}\text{Ga}_{0.5}\text{As}$, $\text{In}_{0.75}\text{Ga}_{0.25}\text{As}$ and InAs. To minimize the effects of a defect to the near cell, $2 \times 2 \times 2$ supercell with 64 atoms is used.

Then we change an In or a Ga atom to an As atom (As_{In} and As_{Ga} , respectively.). Then we relax the structures with the defect (Fig. 4).

Analysis on As Antisite. As shown in Fig. 5, when compared to defect-free structure (Fig 5 (a)), the band structures of both As_{In} (Fig 5 (b)) and As_{Ga} (Fig 5 (c)) have a trap band, which is in the band gap (above the valence band). Also, it can be seen that the distribution of their density of states (DOS) is almost similar between the conduction band and the valence band (Fig 5 (d)). In the same way, we demonstrated the energy levels of As antisites (both As_{In} and As_{Ga}) in five materials (Fig. 6). For all cases, the energy levels of As antisites are located closer to the valence band than the conduction band. Also, in various InGaAs alloys, the energy level of As_{In} is higher than that of As_{Ga} but the difference of them decreases as the ratio of In atom increases.

CONCLUSION

We performed first-principles simulations for As antisites in several III-V materials. The results show the energy level difference between As_{In} and As_{Ga} is larger in $\text{In}_{0.25}\text{Ga}_{0.75}\text{As}$ than that in $\text{In}_{0.75}\text{Ga}_{0.25}\text{As}$. However, an important finding is that As antisites form a mid-gap state for all the cases we experimented. This means As antisites have the potential to have a fatal effect on device performance by causing leakage current.

REFERENCES

- [1] Soler, et al., "The SIESTA method for *ab initio* order-*N* materials simulation." *Journal of Physics: Condensed Matter* (2002).
- [2] Ferreira, et al., "Approximation to density functional theory for the calculation of band gaps of semiconductors." *Physical Review B* (2008).

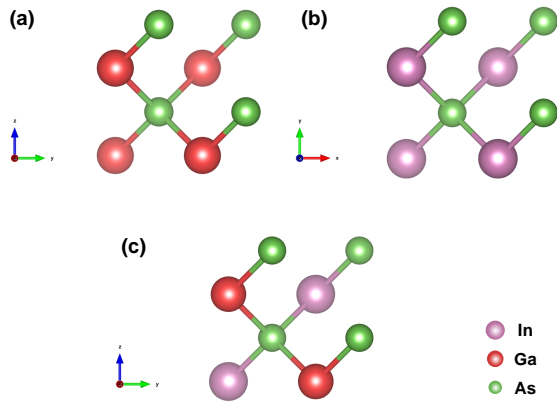


Fig. 1. Atomic structures of conventional unit cells of (a) GaAs, (b) InAs (c) $\text{In}_{0.5}\text{Ga}_{0.5}\text{As}$.

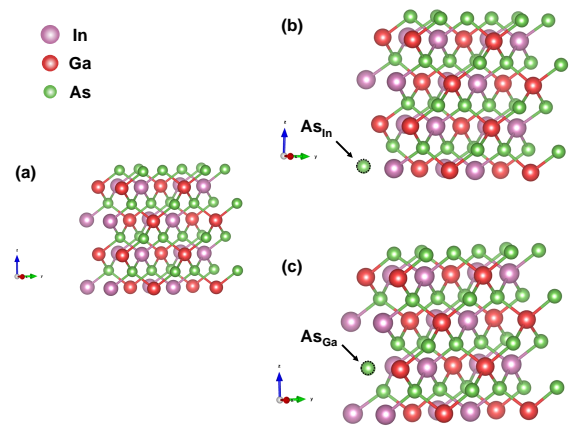


Fig. 4. Relaxed atomic structures of (a) defect-free, (b) w/ As_{In} and (c) w/ As_{Ga} in $\text{In}_{0.5}\text{Ga}_{0.5}\text{As}$.

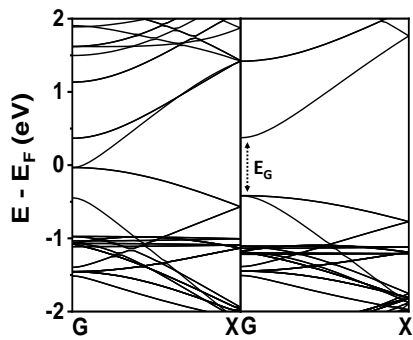


Fig. 2. Band structures of (left) $\text{In}_{0.5}\text{Ga}_{0.5}\text{As}$ and (right) $\text{In}_{0.5}\text{Ga}_{0.5}\text{As}$ with DFT-1/2 technique. E_G is the band gap.

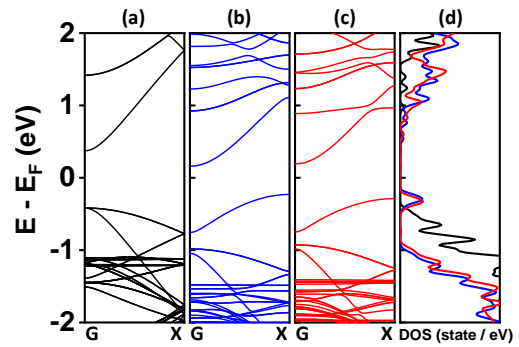


Fig. 5. Band structures of $\text{In}_{0.5}\text{Ga}_{0.5}\text{As}$ (a) defect-free, (b) w/ As_{In} , (c) w/ As_{Ga} and (d) their density of states (DOS).

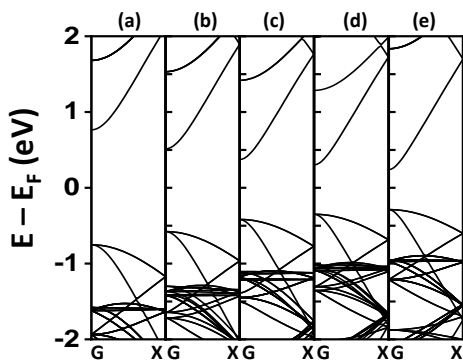


Fig. 3. Band structures of (a) GaAs, (b) $\text{In}_{0.25}\text{Ga}_{0.75}\text{As}$, (c) $\text{In}_{0.5}\text{Ga}_{0.5}\text{As}$, (d) $\text{In}_{0.75}\text{Ga}_{0.25}\text{As}$ and (e) InAs.

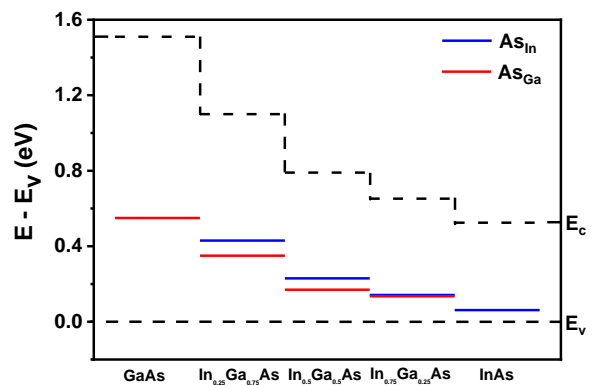


Fig. 6. Charge transition levels of As antisites in various InGaAs alloys.

First-Principles investigation of polytypic defects in InP

Christian Dam Vedel^{1,2,*} , Søren Smidstrup², Vihar P. Georgiev¹ 
 Device Modelling Group, School of Engineering, University of Glasgow, United Kingdom¹
 Synopsys Denmark ApS, Copenhagen, Denmark²
 Correspondence author: christianvedel@hotmail.com*

INTRODUCTION

III-V materials are widely researched as channel material candidates or for photonic applications, but integration of III-Vs leads to numerous defects, such as threading dislocations or Rotational Twin Planes (RTPs). Defects usually degrade the performance of the device they appear in, but they can potentially also be useful if their formation is controlled. For example, RTPs are predicted to work as atomically thin, shallow quantum wells in GaN. In this work we continued the studies of defects in III-Vs, by specifically investigating RTPs and phase-mixing defects in Indium Phosphide (InP). The work reported here is a condensation of the study published in Scientific Reports.¹

SIMULATION METHODOLOGY

The results were acquired using the state-of-the-art first-principles methods implemented in the T-2022.03 version of QuantumATK by Synopsys. We used the "High" version of the PseudoDojo basis sets and their corresponding pseudo-potentials. For the exchange/correlation functional we used the Generalized Gradient Approximation (GGA), by Perdew, Burke and Ernzerhof for solids (PBES). All systems were constructed from supercells of minimal bulk InP systems, which were relaxed until the forces between the atoms were smaller than 0.05 eV \AA^{-1} and the stress was less than 0.1 GPa.

InP crystallises in the Zincblende (ZB) phase, Fig. 1a but can also form the meta-stable Wurtzite (WZ) phase, Fig. 1b. Random transitions between ZB and WZ often occurs, the smallest transition region in a ZB phase, is called a Rotational Twin Plane (RTP), Fig. 1c. If two RTPs form sequentially, the layers form a well-defined WZ phase, Fig. 1d. The stacking sequence of ZB and WZ is shown in Fig. 1, together with an RTP superlattice and a maximally intermixed ZB/WZ system.

RESULTS

Fig. 2 shows the local band gap in a periodic ZB/WZ interface, with different cutoffs of the Local Density of States (LDOS). We see that the transition is far from abrupt, it takes approximately 7 nm, making atomically thin quantum wells from RTPs in InP impossible.

In Fig. 3, the same transition is investigated with a LDOS obtained from a non-equilibrium Greens function calculation. This eliminates the effect from the periodic image of the supercell. Here we found that the transition requires 15 nm.

We next investigated the defects effect on the conductivity. In Fig. 4 the conductivity across the defects are reported, with an intrinsic n-type doping of $1 \times 10^{17} \text{ cm}^{-3}$. We see that WZ has a 5% higher conductivity than ZB, and that the ZB systems with defects have higher conductivities the higher their fraction of WZ is.

In Fig. 5 the relative conductivities are shown again, but with zero bias voltage and varying doping levels instead. We see that increasing the n-doping have similar effects to increasing the applied voltage. But at p-doping levels higher than $4 \times 10^{19} \text{ cm}^{-3}$, the conductivities fall sharply to a mere 5-40% of the ZB reference.

In Fig. 6 we show the conductivities of the systems along the defects. We here see that the defects function as pathways of lesser resistance, thereby increasing the conductivity.

ACKNOWLEDGEMENT

This project has received funding from the European Union's Horizon 2020 research and innovation program under grant agreement No 860095 MSCAITN-EID DESIGN-EID.

REFERENCES

1. Vedel, C., Smidstrup, S. & Georgiev, V. First-principles investigation of polytypic defects in InP. *Scientific Reports* **12** (Nov. 2022).

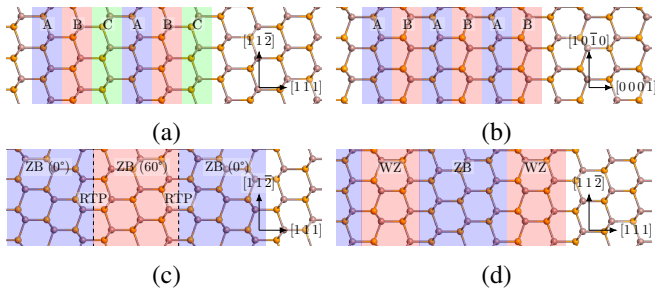


Fig. 1 The 4 different kinds of InP systems investigated in this paper. (a) Pristine Zincblende (ZB). (b) Pristine Wurtzite (WZ). (c) A Rotational Twin Plane (RTP), here shown with a periodicity of 1 RTP every 3 layers of ZB. (d) A mixture of WZ and ZB, here shown with a periodicity of 2 layers WZ every 3 layers ZB.

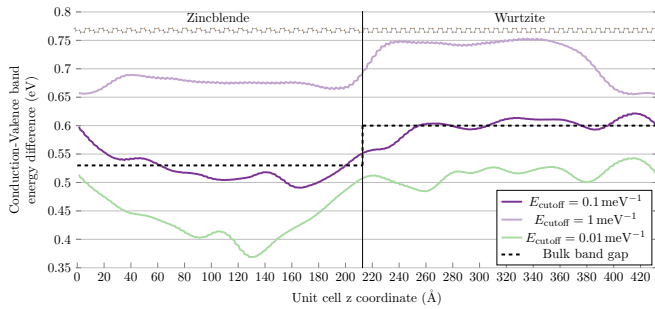


Fig. 2 Conduction-Valence band energy difference in 127 atomic layer long InP ZB/WZ interface system for three different DOS cutoff values.

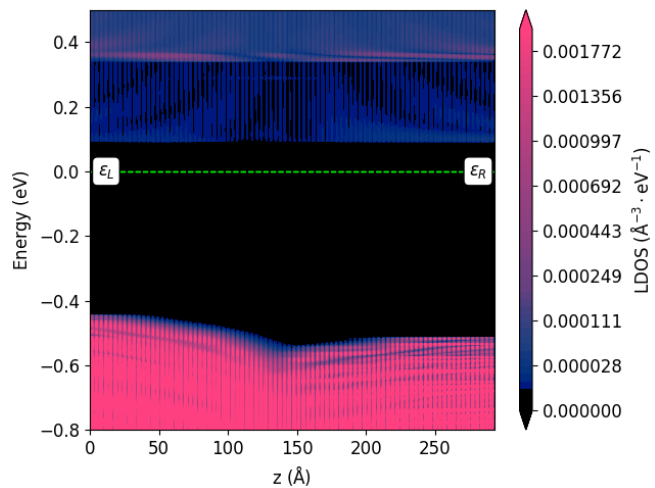


Fig. 3 LDOS of InP interface between Zinblende (on the left) and Wurtzite (on the right).

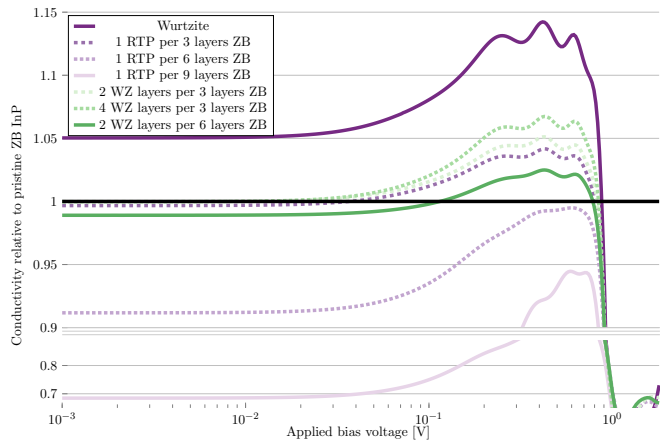


Fig. 4 Conductivity of InP systems along $[1\ 1\ 1]/[0\ 0\ 1]$, relative to pristine ZB InP, at intrinsic doping levels.

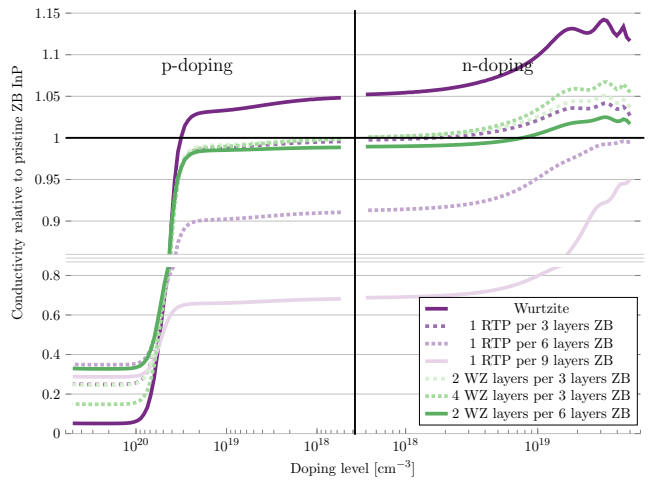


Fig. 5 Conductivity of InP systems along $[1\ 1\ 1]/[0\ 0\ 1]$, relative to pristine ZB InP, at zero bias voltage.

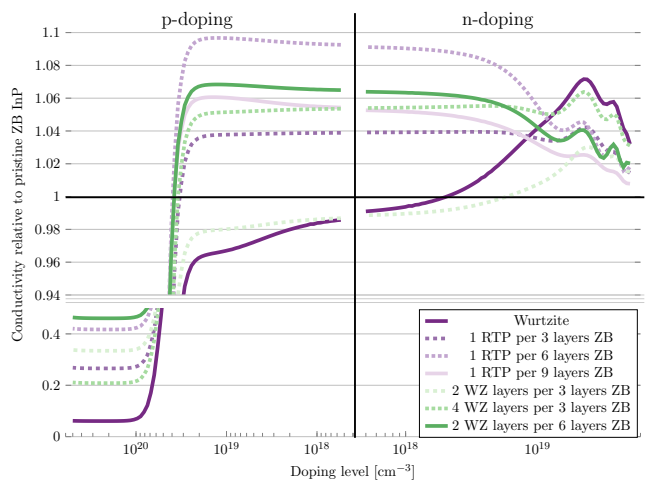


Fig. 6 Conductivity of InP systems along $[1\ 1\ 2]/[1\ 0\ 1]$, relative to pristine ZB InP, at zero bias voltage.

Multiscale simulations of ink-jet printed devices

D. Marian^{†*}, P. K. Dubey[†], M. Perucchini[†], E. G. Marin[‡], and G. Fiori[†]

[†]Dipartimento di Ingegneria dell'Informazione, Università di Pisa, Via G. Caruso 16, Pisa, 16122, Italy

[‡]Departamento de Electrónica, Universidad de Granada, Avenida Fuente Nueva s/n, Granada, 18071, Spain

*e-mail: damiano.marian@gmail.com

INTRODUCTION

In the last few years, the surge of modern portable technologies has boosted the demand for low-power and flexible devices. In this particular niche, printed electronics, raised by the recent advances in two-dimensional materials (2DMs) inks, have emerged as a major enabling technology. Although huge efforts have been made towards the characterization of the electrical properties of the networks of flakes of 2DMs comprising these devices [1], [2], a better theoretical understanding of the physical mechanisms controlling the transport at play in these structures is still needed. In this regard, we present a novel multiscale modeling approach able to simulate printed devices based on 2DMs inks (Fig. 1), and to capture both the microscopic physical mechanisms as well as to extract relevant measurable physical quantities such as the sheet resistance and mobility.

METHOD

The proposed approach consists of three main ingredients. First, the network of flakes of 2DMs forming the semiconducting region of the device is created by a Monte-Carlo algorithm setting the flakes' properties, e.g. lateral dimension, shape, orientation, etc, as well as the network properties, such as the filling factor (FF), i.e., the volume occupied by the flakes with respect to the overall channel volume (see Fig. 2). Second, by means of a precise multiscale methodology, which includes *ab-initio* calculations, we model the anisotropy between the micrometer transport along the flake (in-plane) and the nanometer vertical transport between partially overlapping flakes (inter-flake), as pictorially depicted in Fig. 3 and reported in Ref. [3]. Finally, we solve the transport in the network device by means of the self-consistent solution of the drift-diffusion and the Poisson equation.

DISCUSSION

The model has been validated against graphene-printed structures realized in Refs. [1] and [2]. In Fig. 4 we report the experimental measurements of the sheet resistance versus thickness before (diamonds) and after (squares) annealing, which are compared with the multiscale simulations (circles and triangles), observing an excellent agreement and demonstrating the actual capabilities of the proposed approach [3]. Along with graphene, MoS₂-based devices have been studied [3] as well as printed devices of MoS₂-graphene composite inks [4]. This latter option has been proposed to optimize the performances of MoS₂-printed devices, which severely suffer of reduced mobility due to inter-flake transmissions [4]. In Fig. 5 we report the transfer characteristics of FET devices varying both the graphene ink concentration and the Schottky barrier between graphene and MoS₂, evidencing the impact of the ink mixing.

CONCLUSION

A simulation platform to study the electrical properties and behavior of 2DMs-based ink-printed devices is presented and validated against experimental results, which can constitute valuable support to guide experimental activity in printed electronics.

ACKNOWLEDGMENT

We acknowledge the support from European project grants ERC PEP2D (Contract No. 770047).

REFERENCES

- [1] D. McManus, et al., *Nature Nanotech* **12**, 343 (2017).
- [2] G. Calabrese, et al., *Nanoscale*, **12**, 6708 (2020).
- [3] M. Perucchini, et al., *Adv. Elect. Mat.*, **8**, 2100972 (2022).
- [4] P. K. Dubey, et al., *IEEE TED*, **70**(2), 689 (2023).

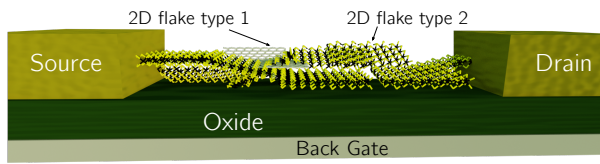


Fig. 1. Schematic depiction of an ink-jet printed network device with 2D materials. Figure adapted from Ref. [4].

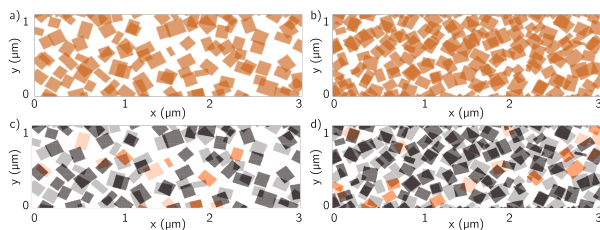


Fig. 2. Network structure sections in two adjacent planes perpendicular to the vertical direction. (a,b) Single material network FF = 0.4 (a) and FF = 0.7 (b). (c,d) Mixed material network, with 90% of material 1 (grey) and 10% of material 2 (orange), with FF = 0.4 (c) and FF = 0.7 (d). In the networks reported we have considered an average lateral size of 150 nm and random orientation. Figure adapted from Refs. [3] and [4].

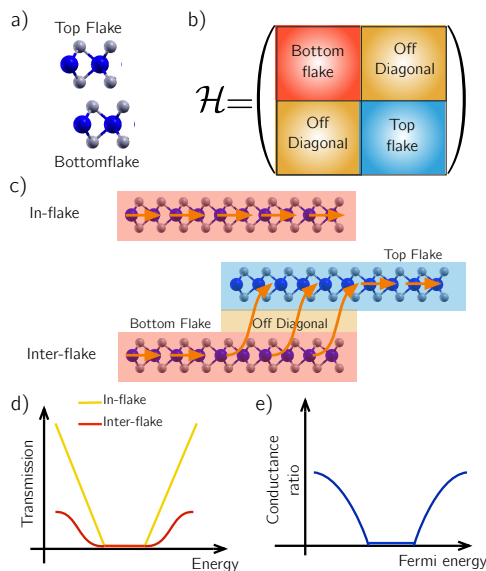


Fig. 3. (a) Bilayer structure used for ab-initio calculations. (b) Schematic wannier Hamiltonian, with indicated the subhamiltonians for the bottom layer, top layer and the coupling between them (off-diagonal). (c) In-flake and inter-flake structures. (d) Pictorial depiction for the in-flake and inter-flake transmission coefficients. (e) Schematic depiction of the conductance ratio as a function of the Fermi energy

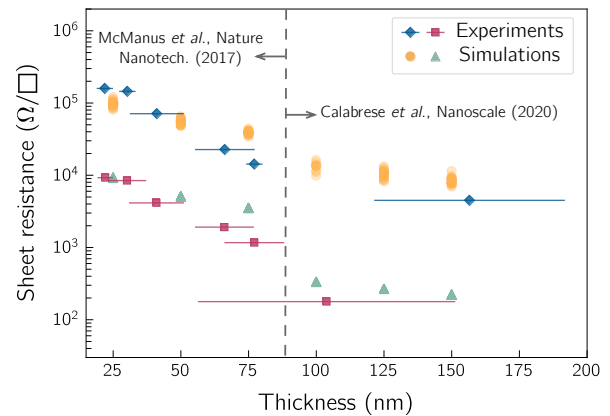


Fig. 4. Extracted sheet resistance for graphene as a function of the channel thickness compared with experimental results obtained in Refs. [1] and [2] before (diamonds) and after (squares) annealing. Two different filling factors FF = 0.35/0.3 for Refs. [1] and [2] and FF = 0.7 are considered in the simulations to reproduce the pre- and after-annealing scenarios. Figure from Ref. [3].

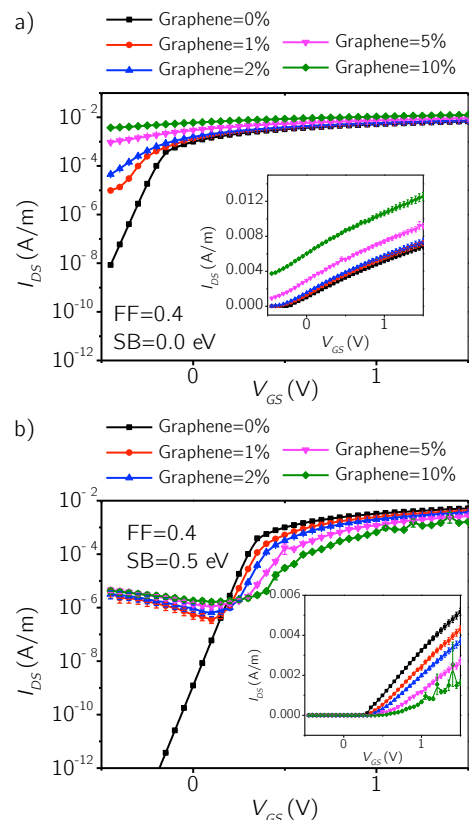


Fig. 5. Transfer characteristics of MoS₂-graphene composite ink-based printed network device with FF = 0.4 and with a Schottky barrier height of (a) 0.0 eV (b) 0.5 eV. Figure adapted from Ref. [4].

An extended Hueckel theory parameterization of Germanium for doped SiGe alloys

D. Dick^{*‡}, F. Fuchs^{†‡}, S. Gemming^{‡§} and J. Schuster^{*†‡}

^{*}Center for Microtechnologies, Chemnitz University of Technology, Chemnitz, Germany

[†]Fraunhofer Institute for Electronic Nano Systems (ENAS), Chemnitz, Germany

[‡]Center for Materials, Architectures and Integration of Nanomembranes (MAIN),
Chemnitz University of Technology, Chemnitz, Germany

[§]Institute of Physics, Chemnitz University of Technology, Chemnitz, Germany

e-mail: daniel.dick@zfm.tu-chemnitz.de

INTRODUCTION

Silicon-germanium (SiGe) heterojunction bipolar transistors (HBTs) have found widespread use in high-frequency applications. Scaling of the HBT base layer thickness to 5 nm and below makes an atomistic treatment indispensable as fluctuations of dopant concentrations play a bigger role. Semi-empirical methods like extended Hueckel theory (EHT) enable us to quickly and efficiently simulate many different permutations of large unit cells with more than a hundred atoms to quantify the influence of atomic-scale fluctuations on the electronic structure and transport properties.

A NEW EHT PARAMETERIZATION OF GE

For crystalline structures, Cerda and Soria [1] provide a wide range of parameterized elements in various phases, but lacking a parameterization of Ge. By fitting the EHT parameters to a Ge bandstructure we fill this gap and provide a parameterization capable of describing the band structure of random SiGe alloys of varying Ge concentrations. It is based on a set of s-, p- and d-orbitals and includes spin-orbit interaction to describe split-off bands. Fig. 2 shows the calculated band gap of unstrained SiGe alloy as a function of Ge content, matching the measurements by Braunstein et al. [2]. Straining the alloy biaxially to match the lattice constant of Si reduces the band gap as expected. Simulations were carried out using the QuantumATK simulation software with the unit cell illustrated in fig. 1.

UNFOLDING SUPERCELL BAND STRUCTURES

Interpretation of band structures from supercell calculations is hampered due to bands folding into the smaller Brillouin zone of the sample cell. We unfold bands back into the Brillouin zone of the primitive cell using the approach from Popescu and Zunger [3] as implemented in QuantumATK. Fig. 3 shows the band density calculated this way. From this, singular bands can be extracted and compared, as shown in Fig. 4 for model cells with varying Ge content.

CONCLUSION

We extend the existing range of EHT parameterizations by providing a new parameterization capable of describing the band structures of random SiGe alloys with varying Ge content. Unfolding the band structure obtained by supercell calculations allows to observe the change in valence band minimum related to Ge content and atomic structure. Studying the influence of structural fluctuations and investigating the effects of C and B doping on band structure by will be issue of future work.

REFERENCES

- [1] J. Cerda and F. Soria. *Accurate and transferable extended hueckel-type tight-binding parameters*. Phys. Rev. B, 61:7965-7971, Mar 2000.
- [2] R. Braunstein, A. R. Moore, and F. Herman. *Intrinsic Optical Absorption in Germanium-Silicon Alloys*. Phys. Rev. 109, 695: 695-710, Feb 1958.
- [3] V. Popescu and A. Zunger. *Effective Band Structure of Random Alloys*, Phys. Rev. Lett. 104, 236403, June 2010

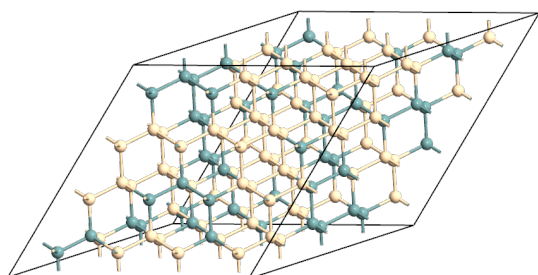


Fig. 1. Example of a SiGe alloy with Ge atoms randomly distributed among the lattice points.

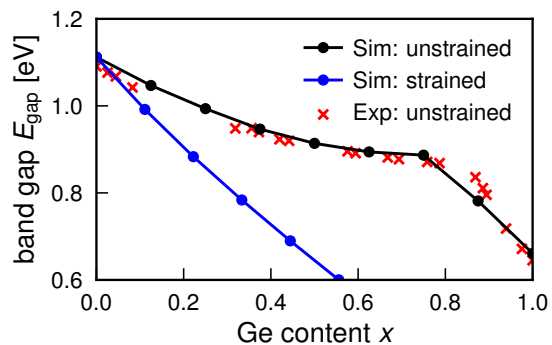


Fig. 2. Comparing the calculated average band gap of unstrained and biaxially strained random SiGe alloys in relation to Ge content. Red crosses show measurements by Braunstein et al. [2] in good agreement with our simulations.

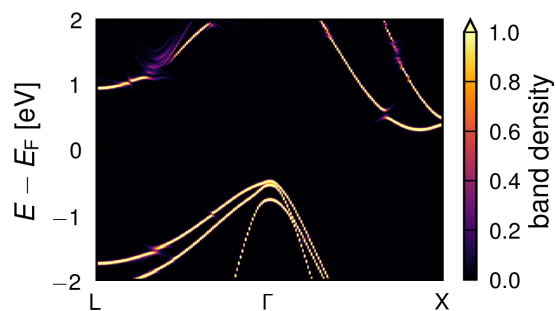


Fig. 3. Unfolded band structure of a random SiGe alloy with 33% Ge content calculated as a band density.

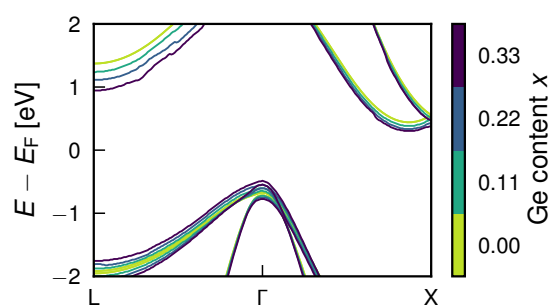


Fig. 4. Extracted band structures of strained SiGe alloy with varying Ge content.

Time-Domain Computation of the Linewidth Enhancement Factor in Multi-Quantum-Well Semiconductor Optical Amplifiers

Ö.E. Aşırım, C. Jirauschek

TUM School of Computation, Information and Technology, Technical University of Munich, Hans-Piloyt Straße 1, 85748 Garching, Germany
e-mail: ozum.asirim@tum.de

ABSTRACT

The linewidth enhancement factor (LWEF) of a semiconductor optical amplifier (SOA) drastically affects the coherence of the amplified beam. Its measurement, however, is complicated due to its sensitivity to the underlying SOA parameters. As practical SOAs are mostly based on multi-quantum-wells (MQWs), this paper aims to introduce a robust algorithm that can be used to compute the time variation of the LWEF of an MQW-SOA. The attained simulation results are confirmed with experimental findings.

INTRODUCTION

The linewidth enhancement factor (LWEF) of a semiconductor optical amplifier (SOA) is a measure of the refractive index fluctuations in its active medium, which distort the coherence of the amplified optical beam [1]. A high LWEF has been shown to heavily degrade the signal quality in optoelectronic devices, such as frequency-swept lasers [2-3], where SOAs are used as the master component. Due to the involved experimental procedure of measuring the LWEF [4-5], a systematic computational algorithm is of great interest for an accurate estimation of the LWEF. Here, we offer a computationally straightforward procedure for evaluating the time variation of the LWEF through the solution of the rate equations for the carrier and the photon densities in the overall active region, and also within each identical quantum-well.

MODEL

The LWEF is a ratio of the variations of the real and imaginary parts of the electric susceptibility against the carrier density

$$\alpha = - \frac{\partial \left(\operatorname{Re} \left\{ 1 + \chi + \frac{\frac{Ne^2}{m\varepsilon_0}}{\omega_0^2 - \omega^2 - i\Omega\omega} \right\} \right) / \partial N}{\partial \left(\operatorname{Im} \left\{ 1 + \chi + \frac{\frac{Ne^2}{m\varepsilon_0}}{\omega_0^2 - \omega^2 - i\Omega\omega} \right\} \right) / \partial N}$$

(1) N : Carrier density, χ : Background susceptibility

m : Electron mass, ω : Ang. frequency, ε_0 : Permittivity

ω_0 : Ang. transition frequency, e : Unit charge

where the transition linewidth Ω depends on the carrier lifetime τ_c and the collision time T_c

$$\Omega = (1/\tau_c) + (1/T_c) \quad (2)$$

In an MQW-SOA, the carriers are mostly confined in the wells. Thus the carrier lifetime and the carrier collision time are computed based on the carrier density within the QWs as $\tau_c = 1/(A + BN_{QW} + CN_{QW}^2 + DN_{QW}^{4.5})$, $T_c = K/N_{QW}$

A : Defect coefficient, N_{QW} : QW carrier density

B : Radiative coefficient, C : Auger coefficient

K : Collision constant, D : Leakage coefficient

Equations 1-2 are functions of the carrier density within the QWs. Therefore, the rate equations for the active medium and the QWs are solved concurrently as they are coupled to each other

$$\frac{dN}{dt} = \frac{\xi_{in}I}{eV} - \frac{N}{\tau_c} - \Gamma G_{ac}(\omega)S \quad (3-4)$$

$$\frac{dS}{dt} = \Gamma G_{ac}(\omega)S - \frac{S}{\tau_p} + \frac{N}{\tau_r}, \quad \tau_p = \frac{n_r L}{c}, \quad \tau_r = \frac{1}{BN_{QD}}$$

$$\frac{dN_{QW}}{dt} = \frac{\Pi_{in}I}{eV_{QW}} - \frac{N_{QW}}{\tau_c} - \Gamma_{QW}G_{QW}(\omega)S_{QW} \quad (5-6)$$

$$\frac{dS_{QW}}{dt} = \Gamma_{QW}G_{QW}(\omega)S_{QW} - \frac{S_{QW}}{\tau_p} + \frac{N_{QW}}{\tau_r}, \Pi_{in} = \frac{\xi_{in}\zeta}{M}$$

$$G(\omega) = \frac{(N - N_{th}) \times \left(\frac{\lambda^2}{8\pi\tau_r}\right) \times \left(\frac{\Omega}{2\pi}\right)}{(\omega - \omega_0)^2 + \left(\frac{\Omega}{2}\right)^2} \quad (7)$$

S : Photon density, N : Carrier density, I : Pump current

Γ : Optical confinement factor, V : Volume, L : Length

G : Small signal gain, λ : Wavelength, c : Speed of light

ξ_{in} : Injection efficiency, τ_p : Photon lifetime

Π_{in} : QW injection efficiency, n_r : Refractive index

ζ : QW carrier confinement ratio ($0 < \zeta < 1$)

N_{th} : Threshold carrier density, M : Number of QWs

An accurate model for computing the LWEF as a time-invariant constant was developed by Vahala et al. [4]. Fig. 1 shows the steady state value of the time-dependent LWEF versus frequency attained by following the outlined procedure, and the frequency variation of the time-independent LWEF based on the experimentally confirmed analytical formulation by Vahala et al. [4]

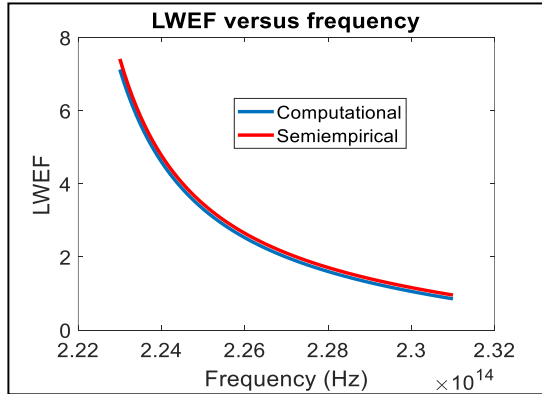


Fig. 1. Comparison of the LWEF variation versus frequency based on numerical computation and semiempirical values. The steady state values of the LWEF are plotted against frequency in Figures 2-3 for different QW carrier densities N_{QW} , and ratios of the active region volume to the total volume occupied by the wells $\kappa = V_{active}/V_{well}$ within the operation bandwidth of InP-InGaAsP MQW-SOAs. The LWEF is observed to decrease with increasing values of N_{QW} and κ , confirming experimental observations [1,4].

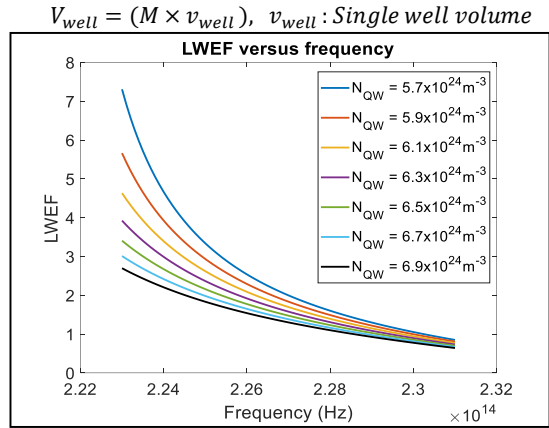


Fig. 1. Variation of the LWEF against frequency for different carrier densities within the quantum wells.

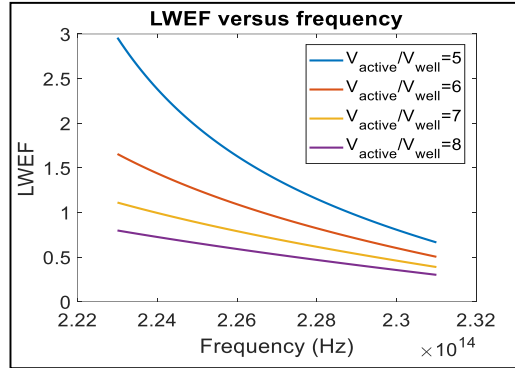


Fig. 2. Variation of the LWEF against frequency for high ratios of the active region volume to the total QW volume.

CONCLUSION

A straightforward computational procedure is outlined for estimating the LWEF of an MQW-SOA in time. The presented procedure enables fast computation of the LWEF with high accuracy and requires fewer input parameters.

REFERENCES

- [1] J. Miloszewski, M. Wartak, P. Weetman, O. Hess, *Analysis of linewidth enhancement factor for quantum well structures based on InGaAsN/GaAs material system*, Journal of Applied Physics. 106, 063102 (2009)
- [2] A. Sobhanan et al., *Semiconductor optical amplifiers: recent advances and applications*, Advances in Optics and Photonics. 14, 571 (2022)
- [3] Aşırım, Ö.E., Huber, R., Jirauschek, C, *Influence of the linewidth enhancement factor on the signal pattern of Fourier domain mode-locked lasers*, Appl. Phys. B. 128, 218 (2022)
- [4] K. Vahala, L. Chiu, S. Margalit, A. Yariv, *On the linewidth enhancement factor a in semiconductor injection lasers*, Applied Physics Letters. 42, 631 (1983)
- [5] C. Ri, C. Kim, Y. Oh, S. Kim, *Immediate estimation of feedback factor and linewidth enhancement factor from measured self-mixing signals under moderate or strong regime*, Measurement Science and Technology. 31, 065204 (2020)

Multiscale simulation of high harmonic generation using artificial intelligence

Javier Serrano, José Miguel Pablos-Marín and Carlos Hernández-García
 Grupo de Investigación en Aplicaciones del Láser y Fotónica, Departamento de Física Aplicada
 Universidad de Salamanca, Pl. Merced s/n, E-37008 Salamanca, Spain
 e-mail: fjaviersr@usal.es

High harmonic generation (HHG) is a laser-matter process that allows to up-convert coherent infrared light into the extreme-ultraviolet or even soft x-rays upon highly nonlinear interaction in a gas or solid target (Fig. 1). The resulting radiation can be synthesized into laser pulses as short as tens of attoseconds, the shortest light pulses ever created, enabling unprecedented studies of ultrafast physics at the nanoscale.

A realistic simulation of HHG requires multiscale calculations from both the quantum microscopic and the macroscopic points of view. At the microscopic level (Fig. 2), the exact calculation of HHG is given by the solution of the time-dependent Schrödinger equation (TDSE), that describes the quantum laser-driven wavepacket dynamics in the vicinity of each atom. However, from the macroscopic point of view, this process has to be considered in all of the atoms involved in the experiment—trillions—and the already time-consuming TDSE has to be coupled with the Maxwell equations to account for propagation. Such calculation is extremely expensive computationally, well beyond the state-of-the-art capabilities, and approximations are required.

In this work we introduce the use of artificial intelligence (AI), and specifically Neural Networks (NN), to obtain complete TDSE-based macroscopic HHG calculations driven by structured laser beams in low density gas jets (Fig. 3). We have implemented a NN using Keras and TensorFlow in Python to predict the microscopic single-atom HHG response, and we have trained it with a dataset of 8×10^4 exact TDSE calculations, achieving a mean square error (MSE) of $\leq 10^{-5}$ (Fig. 4). The dataset was generated with random amplitudes and phases of the driving infrared pulse, covering the whole input range of our simulations, by running a highly

parallelized implementation of the TDSE in CUDA.

Once the NN is trained and validated, we integrate the predicted dipole acceleration into the macroscopic HHG calculation through the exact solution of the Maxwell equations [1]. The macroscopic calculation is parallelized with OpenMP and MPI to allow the prediction of the microscopic HHG in multiple atoms at once. Each OpenMP thread propagates the calculated dipole emission from each atom towards a far-field detector (Fig. 5). We have validated our AI-based HHG method with simulations that compute HHG from structured drivers (Fig. 6), an emerging field with many applications at the nanoscale [2].

Our results [3] demonstrate that AI applied to HHG provides a two-fold advancement: (i) it speeds up the calculations, providing a route towards *in-situ* strong-field simulations that can be performed in parallel to the experiments; and (ii) it allows to perform TDSE-based macroscopic simulations that can reveal hidden signatures neglected in the standard approximations, thus allowing for the exploration of new physics at the nanometer and attosecond scales.

ACKNOWLEDGMENT

This project has received funding from the European Research Council (ERC) under the European Union's Horizon 2020 research and innovation program (Grant Agreement No. 851201) and from Ministerio de Ciencia de Innovación y Universidades (PID2019-106910GB-I00).

REFERENCES

- [1] C. Hernández-García et al. Phys. Rev. A **82**, 033432 (2010).
- [2] A. Forbes et al. Nature Photon. **15**, 253–262 (2021).
- [3] J.M. Pablos-Marín, J. Serrano, C. Hernández-García, *submitted*.

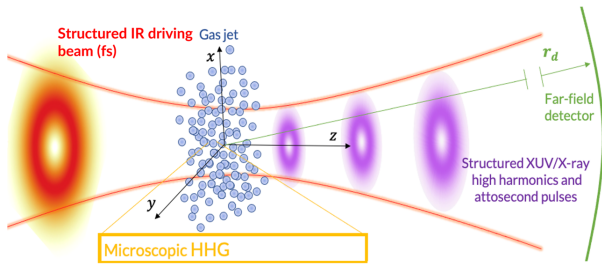


Fig. 1. Scheme of HHG from the macroscopic level. An ultrafast and ultraintense structured IR driving beam is focused in a gas jet. As a result of the highly nonlinear interaction, structured x-ray high-order harmonics, emitted in the attosecond timescale are emitted. The overall emission results from the coherent addition of the dipole acceleration emitted from each atom in the gas target.

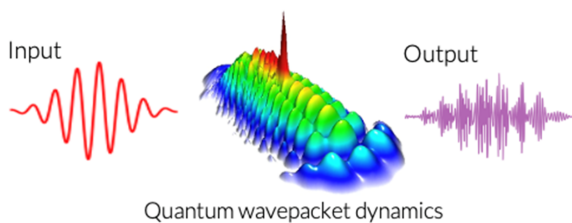


Fig. 2. Scheme of HHG at the microscopic level. An electronic wave packet is ionized by the intense infrared laser pulse. The electronic wave packet is then accelerated, and sent back to the original ionized atom or molecule, driven by the oscillating nature of the laser field. The energy gained by the electronic wave packet during the journey is emitted as high frequency harmonics at recollision. The exact calculation of such process is given by the TDSE.

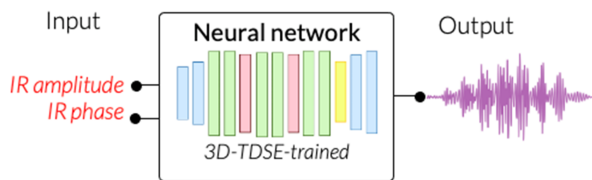


Fig. 3. We introduce the use of neural networks to predict HHG at the microscopic level. The NN is trained to predict the dipole acceleration taking as inputs the amplitude and phase of the driving laser pulse.

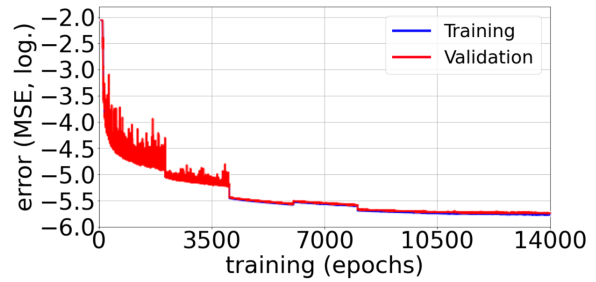


Fig. 4. Neural network training with 14000 epochs, increasing the batch size from 2^3 to the next power of 2 every 2000 epochs up to 2^{10} . The reached MSE of $\leq 10^{-5}$ allows us to get TDSE-based microscopic results in deciseconds instead of minutes-hours using inexpensive hardware

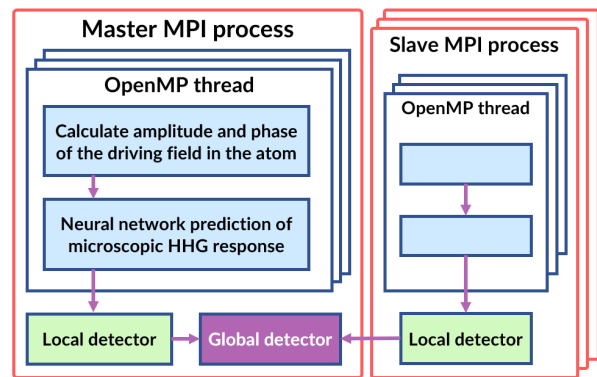


Fig. 5. Highly parallelized simulation platform implemented in C++ that takes advantage of our neural network, MPI and OpenMP to simulate macroscopic HHG. Local detectors with optimized synchronization code reduce synchronization overhead among OpenMP threads and decouples MPI processes until they are reduced in the master at the end of the simulation.

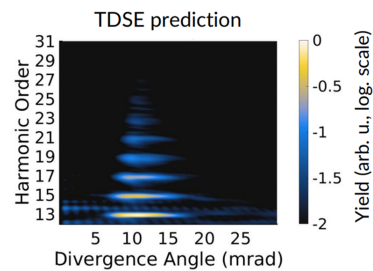


Fig. 6. Sample of macroscopic HHG results obtained with our TDSE-trained NN in combination with our simulation platform. The plot shows the intensity of the far-field high-order harmonics generated in atomic hydrogen as a function of the divergence. The driving laser beam is a combination of two infrared, intense vortex beams with different orbital angular momentum contributions.

Application of Discontinuous Galerkin Methods onto Quantum-Liouville type Equations

V. Ganiu, D. Schulz

Chair for High Frequency Techniques, TU Dortmund, Friedrich-Woehler-Weg 4, 44227 Dortmund, Germany
e-mail: valmir.ganiu@tu-dortmund.de

Abstract—High performance computing methods are needed for the time-dependent analysis of carrier transport within nano structures when using density matrix formulations. For this purpose, a discontinuous Galerkin (DG) method for the numerical approximation of Quantum-Liouville type equations is presented.

INTRODUCTION

The main advantage of the DG method is its dependency on matrix-vector-multiplications when performing transient calculations allowing a parallelization of the resulting algorithms. This has already been successfully demonstrated in other fields of research like in computational fluid dynamics [1]. Hence, the aim of this work is to propose an algorithm based on a Quantum-Liouville type equation not only considering a spatially constant but spatially varying effective mass distribution and a self-consistent Hartree-Fock potential as well.

METHODOLOGY

Starting with the von Neumann equation in center-mass coordinates χ and ξ , a Finite Volume (FV) technique is applied onto the center mass coordinate ξ , followed by an expansion of the density matrix based on plane waves, arriving at a Quantum-Liouville type equation [2]. The DG method is used in χ -direction resulting in a hybrid method [3]. Along with the spatially varying effective mass different numerical fluxes [1] occur, which in combination with boundary conditions as well as the complex absorbing potential (CAP) [4] have a critical influence on the stability of a transient DG method.

DISCUSSION

To assess the stability, the eigenvalues of the resulting system matrix must be analyzed. As depicted in Fig. 1a-1d in combination with Tab. I, two factors have a crucial influence on the stability of the DG scheme: the numerical flux and the CAP. The CAP pushes the eigenvalue spectrum towards the negative half of the

real axis. The choice of an upwind flux further ensures stability by avoiding eigenvalues with a positive real part. Finally, stability can be achieved. To assess the numerical validity of the proposed scheme, a resonant tunneling diode (RTD) is analyzed as depicted in Fig. 2. The self-consistent analysis for the thermal equilibrium is performed for the case of a spatially constant and a spatially varying effective mass. Evidently, from Fig. 3 it can be concluded that the inhomogeneous effective mass leads to a higher local maximum, which is in agreement with the results in [5]. Furthermore, the self-consistent transient simulation of the RTD with a spatially constant effective mass is depicted in Fig. 4 confirming convergence. Finally, from Fig. 5 it can be concluded that performing a transient simulation, a noticeable reduction in computation time compared to a conventional FV approach, as described in [5], can be achieved with the DG and fourth order Runge-Kutta (DGRK4) algorithm.

ACKNOWLEDGMENT

This work was supported by the Deutsche Forschungsgemeinschaft DFG under Grant SCHU 1016/10-1.

REFERENCES

- [1] B. Cockburn, "Discontinuous Galerkin methods for computational fluid dynamics", *John Wiley And Sons, Ltd*, 2017, pp. 1-63, doi: <https://doi.org/10.1002/9781119176817.ecm2053>
- [2] L. Schulz, B. Inci, M. Pech, D. Schulz, "Subdomain-based exponential integrators for quantum Liouville-type equations", *Journal of Computational Electronics*, vol. 20, no. 6, pp. 2070-2090, doi: [10.1007/s10825-021-01797-2](https://doi.org/10.1007/s10825-021-01797-2)
- [3] V. Ganiu, D. Schulz, "Discontinuous Galerkin concept for Quantum-Liouville type equations", *Solid-State Electronics*, vol. 200, p. 108536, 2023, doi: <https://doi.org/10.1016/j.sse.2022.108536>
- [4] L. Schulz, D. Schulz, "Numerical Analysis of the Transient Behavior of the Non-Equilibrium Quantum Liouville Equation", *IEEE Trans. on Nanotech.*, vol. 17, no. 6, pp. 1197-1205, 2018, doi: [10.1109/TNANO.2018.2868972](https://doi.org/10.1109/TNANO.2018.2868972)
- [5] L. Schulz, D. Schulz, "Application of a Slowly Varying Envelope Function Onto the Analysis of the Wigner Transport Equation", *IEEE Trans. on Nanotech.*, vol. 15, no. 5, pp. 801-809, 2016, doi: [10.1109/TNANO.2016.2581880](https://doi.org/10.1109/TNANO.2016.2581880)

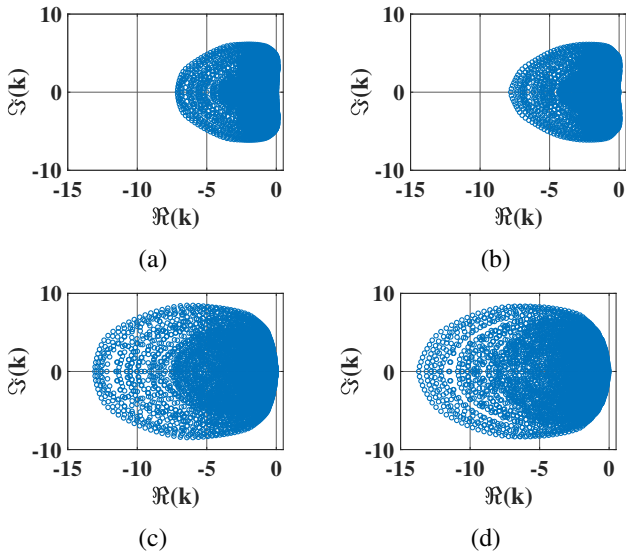


Fig. 1: Stability analysis for the central flux with no CAP (a), central flux with CAP (b), upwind flux with no CAP (c), and upwind flux with CAP (d). The real part of the eigenvalues must be exclusively located in the second and third quadrant of the complex plane. The right vertical line indicates the imaginary axis.

	Fig. a	Fig. b	Fig. c	Fig. d
$\Re_{max}(k)$	0.1265	0.0504	$-3.18e-7$	-0.0015
$\Re_{min}(k)$	-7.1083	-7.7918	-13.0494	-13.6978

TABLE I: Maximum and minimum real part of the eigenvalues from Fig. 1a-1d.

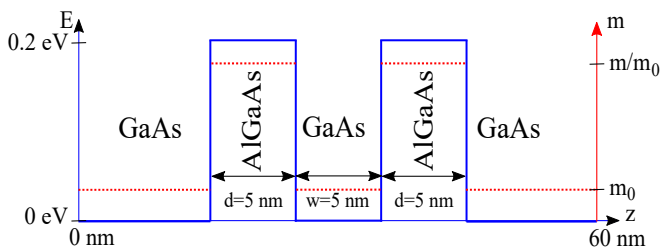


Fig. 2: Schematic representation of a resonant tunneling diode showing the band edge potential and the spatially varying effective mass m_0 .

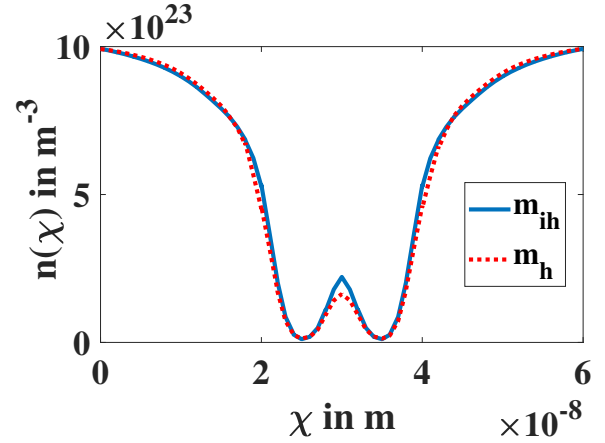


Fig. 3: Self-consistent carrier distribution n dependent on χ in a RTD with homogeneous mass distribution (m_h) and inhomogeneous mass distribution (m_{ih}).

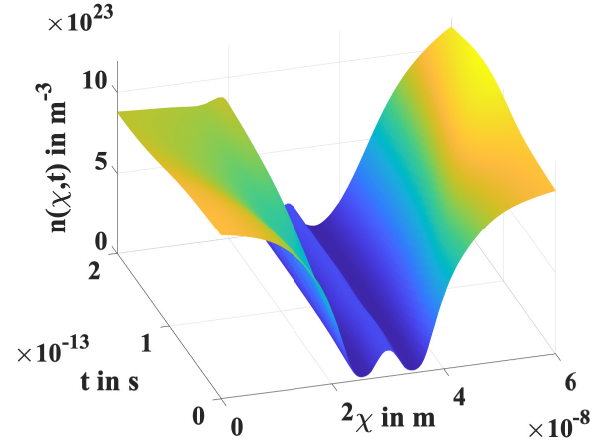


Fig. 4: Spatially time dependent self-consistent carrier distribution n for a mass distribution m_h , dependent on χ .

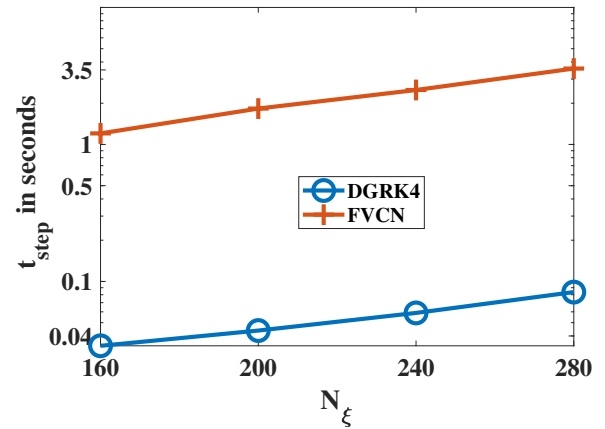


Fig. 5: Comparison of the computation time between the DGRK4 algorithm and the FV-Crank Nicolson (FVCN) scheme [5]. N_ξ indicates the number of ξ -elements.

Full-Band Device Simulator with Real-Space Treatment of the Short-Range Coulomb Interactions for Modeling 4H-SiC VDMOS Devices

Dragica Vasileska and Chi-Yin Cheng
 School of Electrical, Computer and Energy Engineering
 Arizona State University, Tempe, AZ 85287-5706
 e-mail: vasileska@asu.edu

4H-SiC has been widely used in many power electronic applications because of the extremely high critical electric field and good electron mobility. For example, 4H-SiC possesses a critical electric field ten times higher than that of Si, which allows high-voltage blocking layers composed of 4H-SiC to be approximately a tenth of the thickness of a comparable Si device. This, in turn, reduces the device on-resistance and power losses while maintaining the same high blocking capability.

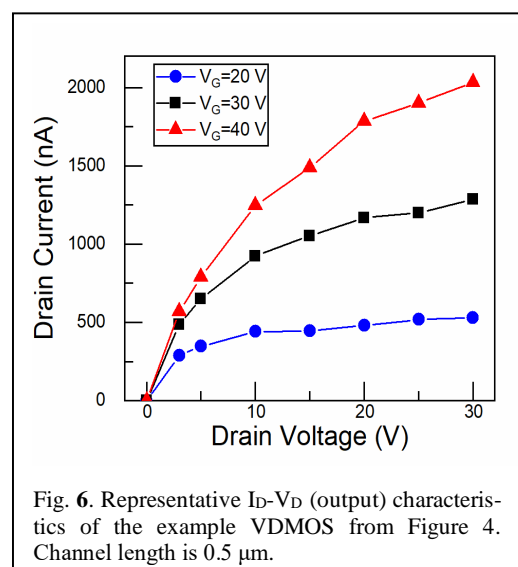
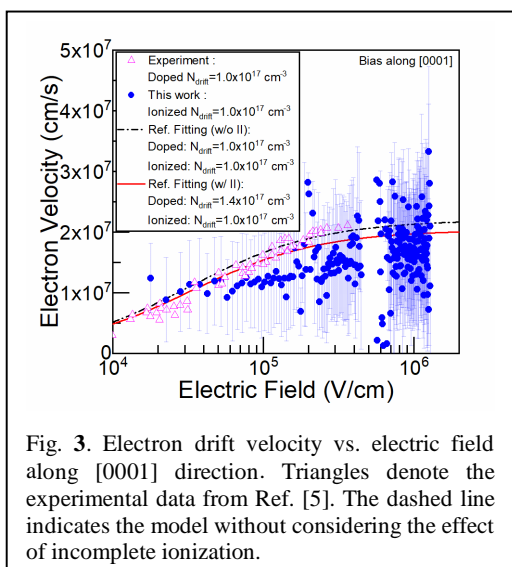
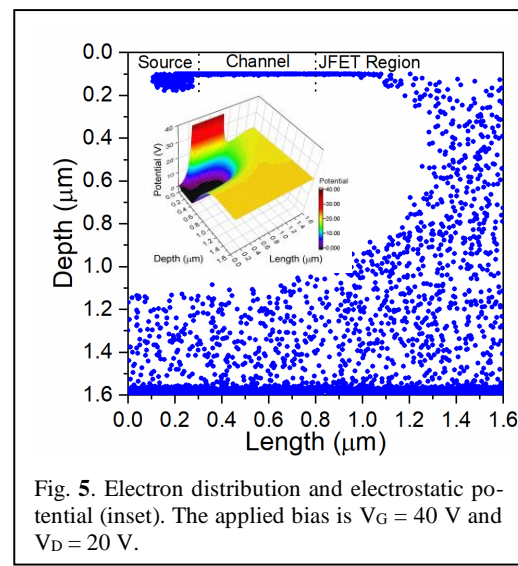
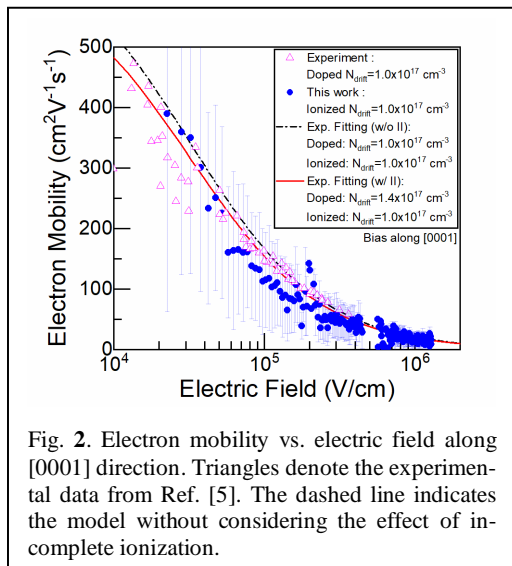
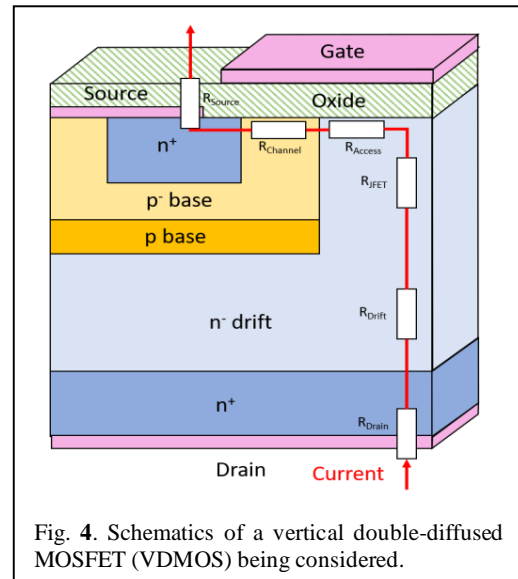
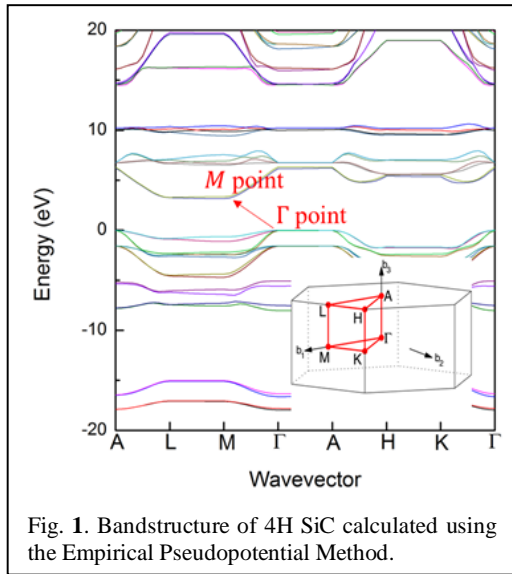
Unfortunately, commercial TCAD tools like Sentaurus and Silvaco are based on the effective mass approximation, while most 4H-SiC devices are operated under high electric fields, so the parabolic-like band approximation does not hold anymore. Hence, to get more accurate and reliable simulation results for these devices, full-band analysis is needed. The first step in the development of a full-band device simulator is the calculation of the band structure. In this work, the empirical pseudopotential method (EPM) is adopted. We follow the approach of Ng [1] who utilizes genetic algorithm to get to a proper set of EPM form factors that match density functional theory (DFT) results. The 4H-SiC band-structure used in this work is shown in Figure 1.

Acoustic, non-polar optical phonon and polar optical phonon are relevant scattering mechanisms for this material system [2]. Impurities are introduced into the model as discrete dopants. Coulomb scattering is treated in real space using the particle-particle-mesh (P³M) approach [3] and represents the major novelty of this work. Proper treatment of the Coulomb interactions is essential for power electronic applications because of the high carrier densities. Bi-CGSTAB method is used for the solution of the 3D Poisson equation.

For proof-of-concept of the methodology adopted here, a 3D resistor is simulated first [4]. From the resistor simulations, the low-field electron mobility dependence upon Coulomb scattering in 4H-SiC devices is extracted. The simulated mobility results agree very well with available experimental data [5], which is clearly seen from the results presented in Figure 2. An anisotropy of mobility along different crystal orientation is also observed. The ratio between [0001] and [1120] direction is found to be between 1.25-1.75. The field dependence of the carrier drift velocity, compared with experimental data from Ref. [5], is shown in Figure 3. The observed excellent agreement validates further the adopted theoretical model. Next, a 3D VDMOS is simulated, a schematic of which is shown in Figure 4. The electron distribution and the potential profile of the VDMOS device are shown in Figure 5. The output characteristics of the VDMOS device are shown in Figure 6. From the results presented we may conclude that, due to its comprehensive nature, the developed tool can serve as a basis for future investigation of 4H-SiC power devices.

REFERENCES

- [1] G. Ng, D. Vasileska, and D.K. Schroder, *Superlattices Microstruct.*, vol. 49, no. 1, pp. 109–115, 2011.
- [2] M. Hjelm, H. E. Nilsson, A. Martinez, K.F. Brennan, and E. Bellotti, *J. Appl. Phys.*, vol. 93, no. 2, pp. 1099–1107, 2003.
- [3] W.J. Gross, D. Vasileska, and D.K. Ferry, *IEEE Trans. Electron Devices*, vol. 47, no. 10, pp. 1831–1837, 2000.
- [4] C.-Y. Cheng and D. Vasileska, *J. Appl. Phys.*, vol. 127, no. 15, p. 155702, 2020.
- [5] I.A. Khan and J.A. Cooper, *IEEE Trans. Electron Devices*, vol. 47, no. 2, pp. 269–273, 2000.



Schottky barriers in one-dimensional field-effect transistors: a model-based characterization

Anibal Pacheco-Sanchez, David Jiménez

Departament d'Enginyeria Electrònica, Escola d'Enginyeria, Universitat Autònoma de Barcelona, Bellaterra 08193, Spain. Email: AnibalUriel@Pacheco.uab.cat

INTRODUCTION

The characterization of the the metal-channel interfaces is of outmost importance for one-dimensional (1D) Schottky field-effect transistor (FET) technologies. The dimensionality of the channel impacts on the injection mechanisms at the Schottky contacts and hence, on the interface characteristics such as the potential barrier height [1]-[4]. The latter device parameter is proven to be underestimated in 1D channel transistors if conventional extraction techniques, e.g., the three-dimensional (3D) activation energy method (AEM), are used. Such approaches rely on the physics of 2D contacts and 3D channels which differ from the phenomena at 3D-metal-1D-channel interfaces [2]-[4]. In this work, a parameter extraction methodology for potential barrier heights in 1D FETs within the context of 1D Landauer-Büttiker transport model is reviewed. The model-based characterization method is applied to fabricated and simulated carbon nanotube (CNT) FETs and nanowire (NW) FETs with single- and multiple-channels (cf. Fig. 1). Studies on the impact of a displaced gate as well as of channel Schottky points on the extracted values are carried out with numerical device simulations.

SCHOTTKY BARRIER HEIGHT EXTRACTION

The thermionic drain current I_D of a 1D FET, corresponding to operation at the subthreshold regime, can be approximated as [1], [5]

$$I_D \approx \Upsilon \exp \left[\frac{n_g}{V_t} (V_{GS} - V_{FB}) + \frac{n_d}{V_t} V_{DS} - \frac{\Phi_{BH,eff}}{V_t} \right], \quad (1)$$

This work has received funding from the European Union's Horizon 2020 research and innovation programme under grant agreement No GrapheneCore3 881603 and from Ministerio de Ciencia, Innovación y Universidades under grant agreements RTI2018-097876-B-C21(MCIU/AEI/FEDER, UE), FJC2020-046213-I and PID2021-127840NB-I00 (MCIN/AEI/FEDER, UE).

where $\Upsilon = (4q^2/h)V_t\mathcal{T}_{th}$ with q as the electronic charge, h the Planck constant, $V_t = k_B T/q$ the thermal voltage with k_B as the Boltzmann constant and T the absolute temperature, \mathcal{T}_{th} is the thermionic transmission probability, n_g and n_d are gate and drain coupling coefficients [5], respectively, V_{GS} and V_{DS} are the gate-to-source and drain-to-source voltage, $\Phi_{BH,eff}$ is an effective potential barrier height at which pure thermionic injection occurs in the 1D device and V_{FB} is the flatband voltage (cf. Fig. 2). Conditions for obtaining Eq. (1) have been explained in detail in [2] and an adapted form for considering multi-1D-channels has been presented in [4]. For quasiballistic 1D devices $\mathcal{T}_{th} \approx 1$ at low-fields and hence, Eq. (1) can be rearranged such as [2], [4]

$$\Phi_{BH,eff} = n_q (V_{GS} - V_{FB}) + \Phi_{SB,eff} \quad (2)$$

where $\Phi_{SB,eff} = n_d V_{DS} - (k_B/q)\alpha$ is an effective Schottky barrier height and α is the slope of an Arrhenius plot ($\ln(I_D T^{-1})$ vs. T^{-1}). $\Phi_{SB,eff}$ is the parameter useful to evaluate the quality of the contacts and it is obtained from Eq. (2) at $V_{DS} = 0$ and $V_{GS} = V_{FB}$. The latter point is obtained at the onset of tunneling phenomena corresponding to a change of slope in a $\Phi_{BH,eff}$ vs. V_{GS} plot. The 1D Landauer-Büttiker extraction method (1D LBM) shown here is visualized in Fig. 3 where it has been applied to experimental data of a CNTFET and a NWFET with multiple 1D channels, as reported elsewhere [4].

NUMERICAL DEVICE SIMULATIONS

Simulations of BG CNTFETs have been performed with an experimentally verified in-house numerical CNT-FET simulator using a self-consistent solution of a transport equation and the Poisson equation, presented elsewhere [6], [7] in order to (i) explore the limits of the methodology (cf. Fig. 4), (ii) propose a test structure to ease the extraction (cf. Fig. 5) and (iii) study specific imperfections affecting the extracted values, e.g., Schottky points within the channel (cf. Fig. 6).

REFERENCES

- [1] A. Pacheco-Sanchez, *TUD Press*, Ph. D. Thesis, CEDIC-TUD, Germany, 2019
- [2] A. Pacheco-Sanchez, et al., *Appl. Phys. Lett.*, 111(16), 163108, 2017
- [3] A. Pacheco-Sanchez, et al., in Proc. *IEEE LAEDC*, 2020
- [4] A. Pacheco-Sanchez, et al., *J. Appl. Phys.*, 132(2), 024501, 2022
- [5] M. Claus, *TUD Press*, Ph. D. Thesis, CEDIC-TUD, Germany, 2011
- [6] M. Claus, et al., *J. Comput. Elect.*, 13(3), 689-700, 2014
- [7] S. Mothes, *TUD Press*, Ph. D. Thesis, CEDIC-TUD, Germany, 2019

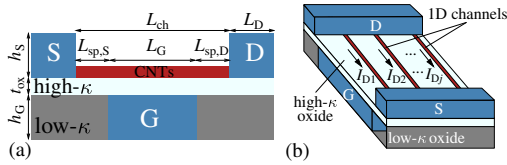


Fig. 1. Schematic (a) cross-section and (b) device structure of a buried-gate CNTFET simulated in this work [2]-[4].

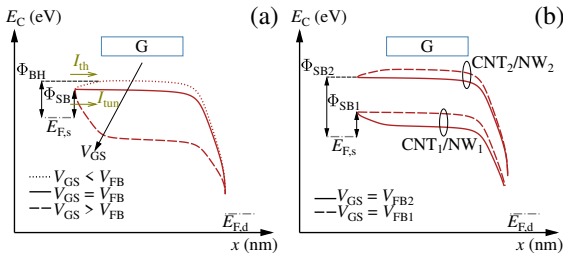


Fig. 2. Conduction band diagrams of a 1D-FET with (a) single-1D-channel and (b) multi-1D-channels at different V_{GS} [4].

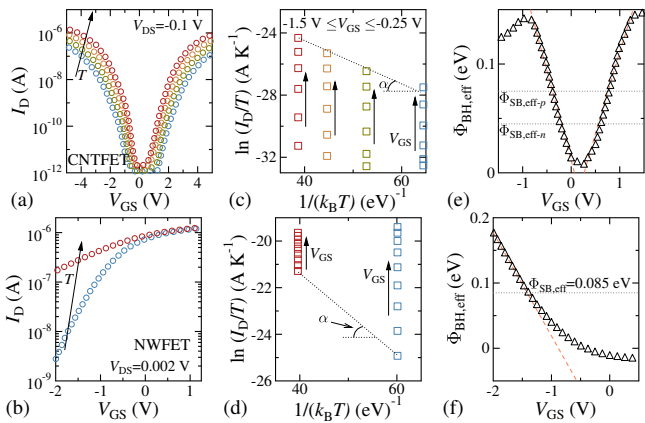


Fig. 3. Extraction of $\Phi_{SB,eff}$ height of (a), (c), (e) a multitube CNTFET and (b), (d), (f) a multiwire NWFET. Further details on experimental data, plots and related discussions are provided in [4].

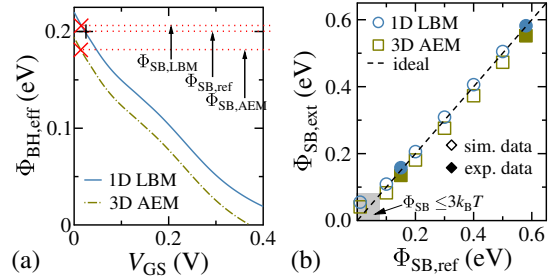


Fig. 4. Comparison between 3D AEM and 1D LBM using simulated BG CNTFETs with (a) 0.2 eV and (b) various values of Schottky barrier height. 1D LBM extracts a value close to the reference value set in simulations. Gray zone in (b) shows that both methods overestimate the value below ~ 0.07 eV. Further details in [2].

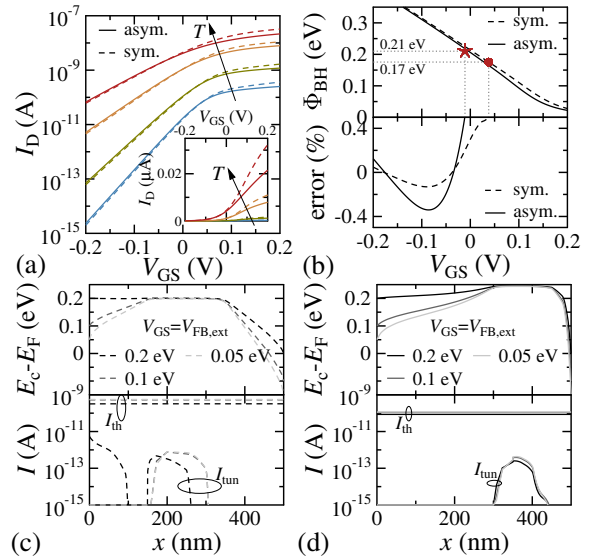


Fig. 5. Simulated symmetric and asymmetric multi-channel BG MT CNTFETs data. (a) Transfer characteristics at $V_{DS}=0.2$ V and different T . (b) $\Phi_{SB,eff}$ extraction from the barrier height potential plot over V_{GS} (top) and relative error related to a linear extrapolation of pure thermionic transport (bottom). Conduction band diagrams (top) and thermionic and tunneling currents along the channel (bottom) of the (c) symmetric and (d) asymmetric CNTFETs. Details in [4].

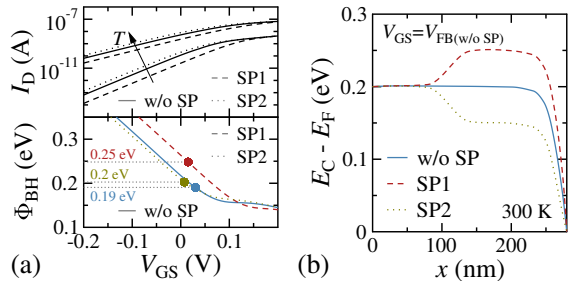


Fig. 6. Simulation results of multi-channel BG CNTFETs with and without different Schottky points. (a) Top: transfer characteristics (300 K and 500 K) at $V_{DS} = 0.2$ V; bottom: potential barrier height versus V_{GS} obtained with 1D LBM. (b) Conduction bands at the V_{FB} of the device without SP. Further details in [4].

Silicon passivation of zigzag graphene edge enabling robust spin-polarized nanogap quantum transport

Juho Lee, Seunghyun Yu and Yong-Hoon Kim*

School of Electrical Engineering, Korea Advanced Institute of Science and Technology (KAIST), 291 Daehak-ro, Yuseong-gu, Daejeon 34141, Korea
(Email: littleyu@kaist.ac.kr)

INTRODUCTION

A major motivation for the research on graphene stems from the ferromagnetically-aligned spin-polarized states appearing at the zigzag graphene edges (ZGEs) in view of spintronic applications [1]. However, in spite of the significant progress made in both top-down and bottom-up synthesis methods, the reliable preparation of magnetic ZGE states in ambient conditions remains a formidable challenge [2]. The preferable condition for the existence of spin-polarized ZGE states is the preservation of sp^2 -type edge C atoms, which liberates the π electrons from p_z orbitals of carbons to populate the edge states. Unfortunately, however, the sp^3 -type hydrogenated ZGE C configurations are thermodynamically favored over their sp^2 counterparts across a wide range of thermodynamic conditions, representing a serious bottleneck in realizing ZGE-based spintronics.

Meanwhile, because Si is an essential element in the existing semiconductor industry, there has been significant interest in elucidating the nature of interactions between Si or its native oxide, SiO_2 , and C nanomaterials in the context of electronic and energy device applications. Particularly, we note recent experiments reported that Si atoms can effectively passivate the edge of graphene nanopores and prevent the healing of nanopores upon the supply of extra C atoms [3]. In related works, an extended linear array of Si atoms along the ZGE was observed by transmission electron microscopy. Given the feasibility of Si-based graphene edge stabilization provided in these experiments, whether the Si edge passivation preserves the ferromagnetic (FM) ZGE states would be an intriguing question. In particular, notable achievements were recently made toward graphene

edge-based tunnel junctions [4], bringing us closer to the realization of atomically thin sensors including DNA sequencers with single-molecule resolution.

COMPUTATIONAL DETAILS

Spin-polarized DFT calculations were performed using the SIESTA code [5] within the Perdew-Burke-Ernzerhof parameterization of generalized gradient approximation. Double ζ -plus-polarization-level numerical atomic orbital basis sets were employed together with the Troullier-Martins type norm-conserving nonlocal pseudopotentials. The mesh cutoff of 200 Ry for the real-space integration, and the $1 \times 1 \times 64$ (32 and 20) \vec{k} -points were sampled for the two (four and six) primitive ZGNR unit-cell models. The atomic geometries were optimized until the total residual forces are converged below 0.02 eV/Å.

For the quantum transport calculation, we used the DFT-based MGF method implemented within the TransSIESTA code [6]. The surface green functions, g_s , for the semi-infinite electrode regions were extracted from separate DFT calculation for the ideal planar graphene structure with 16 \vec{k} -point sampling along the infinite direction (y-axis), and 20 \vec{k} -points sampling along the charge transport direction.

REFERENCES

- [1] Han, W *et al.* Nat. Nanotechnol. 9 (10), 794-807. (2014)
- [2] Magda, G. Z *et al.* Nature 514 (7524), 608-611 (2014)
- [3] Lee, J *et al.* Proc. Natl. Acad. Sci. U. S. A 111 (21), 7522-7526. (2014)
- [4] Bellunato, A *et al.*, Nano Lett. 18 (4), 2505-2510. (2018)
- [5] José, M. S *et al.*, J. Phys. Condens. Matter, 14 (11), 2745. (2002)
- [6] Brandbyge, M *et al.*, Phys. Rev. B: 65 (16), 165401. (2002)

Monte Carlo Simulations of Electrons in Al_4SiC_4 Ternary Carbide

K. Kalna¹ and D. Chaussende²

¹ NanoDeCo Group, Dept. Electronic & Electrical Engineering, Faculty of Science & Engineering, Swansea University, Swansea, SA1 8EN, Wales, United Kingdom

² Université Grenoble Alpes, CNRS, Grenoble INP, SIMaP, 38000 Grenoble, France
Email: k.kalna@swansea.ac.uk

An Al_4SiC_4 ternary carbide has become a promising wide band-gap semiconductor for the semiconductor industry over the last decade because of its emerging properties [1]. A crystal structure of Al_4SiC_4 is illustrated in Fig. 1. The Al_4SiC_4 band-gap has been calculated to be 2.48 eV [2, 3] thus opening a possibility for the design of carbide heterostructure devices in a combination with 4H-SiC or 3C-SiC. These heterostructure carbide devices could potentially resolve issues with the large interface density of states at the semiconductor interface with a dielectric layer leading to a low inversion carrier mobility in SiC MOSFETs [4]. Other remarkable properties include superior oxidation resistance [5], superior wear resistance, low weight, high strength, and high thermal conductivity [6].

In this work, an ensemble Monte Carlo (MC) simulation code is developed to investigate the electron transport in bulk Al_4SiC_4 . Al_4SiC_4 has a wurzite lattice [2, 3] as shown in Fig. 2. We assume that the two lowest valleys will play a role in electron transport. The M -valley has also six locations contributing one-half (a total of 3 equivalent valleys). The K -valley has six locations contributing one-third to the 1st Brillouin zone (a total of 2) as shown in Figs. 3 and 4. Therefore, a two-valley non-parabolic anisotropic bandstructure model is employed with the M -valley to be a minimum and the second K -valley to be 0.52 eV above as illustrated in Fig. 5. The electron interactions with polar and non-polar phonons within and between M - and K -valleys are listed in Table 1. The material parameters in Table 2 use a mix of experimental and theoretical sources like optical phonon energies extracted from IR/Raman spectroscopy [3].

Valley	Transition	Scattering Type
M_1	$M_1 \rightarrow M_1$	Intra Polar
	$M_1 \rightarrow M_{2,3}$	Inter Non-Polar
	$M_1 \rightarrow K$	Inter Non-Polar
M_2	$M_2 \rightarrow M_2$	Intra Polar
	$M_2 \rightarrow M_{1,3}$	Inter Non-Polar
	$M_2 \rightarrow K$	Inter Non-Polar
M_3	$M_3 \rightarrow M_3$	Intra Polar
	$M_3 \rightarrow M_{1,2}$	Inter Non-Polar
	$M_3 \rightarrow K$	Inter Non-Polar
K	$K \rightarrow M_1$	Inter Non-Polar
	$K \rightarrow M_2$	Inter Non-Polar
	$K \rightarrow M_3$	Inter Non-Polar

Table 1: Electron-phonon scattering transitions considered in the MC model.

Finally, M -valley \mathbf{k} -vector (inverse) transformations to a spherical space (denoted by *) within the anisotropic analyt-

Table 2: Al_4SiC_4 material parameters considered in the MC simulations.

Parameter [Unit]	Value
Mass Density [g/cm^3]	3.03 ^a
Lattice Const. [\AA]	3.28 ^a
Piezoelectric Const. [C/m^2]	0.47 ^a
Longitudinal Acoustic Velo. [m/s]	10577 ^a
Transverse Acoustic Velo. [m/s]	6431 ^a
Polar Opt. Phon. Energy [meV]	67.32 ^b , 107.24 ^b
Non-Polar Opt. Phon. Energy [meV]	85.55 ^b
Acoustic Def. Potential [eV]	11.4 ^c
Indirect Band Gap for the M -valley	$E_G^{(M)} = 2.78$
(M) & the K -valley (K) [eV]	$E_G^{(K)} = 3.30$ ^a
Electron Effective Masses [m_e]	$m_l^{*(M)} = 0.568$ ^d
	$m_t^{*(M)} = 0.695$ ^d
	$m_l^{*(K)} = 1.057$ ^d
	$m_t^{*(K)} = 0.936$ ^d

^aRef. [2]. ^bRef. [3]. ^cAverage taken from [7]. ^dExtracted value from DFT calculations [2]. m_e is the rest mass of an electron.

ical model use a combination of Herring-Vogt and rotational transformations [8] as:

$$k_x^*(k_x) = k_x(k_x^*)\cos(\theta) - (+)k_y(k_y^*)\sin(\theta) \quad (1)$$

$$k_y^*(k_y) = k_y(k_y^*)\cos(\theta) + (-)k_x(k_x^*)\sin(\theta) \quad (2)$$

$$k_z^*(k_z) = k_z(k_z^*) \quad (3)$$

The MC simulations in Figs. 6 and 7 predict that Al_4SiC_4 will have a maximum electron drift velocity of $1.35 \times 10^7 \text{ cms}^{-1}$ at an electric field of 1400 kVcm^{-1} and a maximum electron mobility of $82.9 \text{ cm}^2\text{V}^{-1}\text{s}^{-1}$. Fig. 8 shows the electron mobility dependence on ionized impurity concentration. The average electron kinetic energy and valley occupation are plotted in Figs. 9 and 10, respectively.

References

- [1] T. Liao, J. Y. Wang, and Y. C. Zhou, *Phys. Rev. B* **74** (17), 1098-1121 (2006).
- [2] L. Pedesseau et al., *APL Materials* **3** (12), 121101 (2015).
- [3] D. Zevgitis et al., *Synthesis and Characterization of Al_4SiC_4 : A "New" Wide Band Gap Semiconductor Material*, *Materials Science Forum* 821-823, 974-977 (2015).
- [4] S. Forster, D. Chaussende, and K. Kalna, *ACS Appl. Energy Mater.* **2** (9), 3001-3007 (2020).
- [5] K. Inoue and A. Yamaguchi, *J. Am. Ceram. Soc.* **86** (6), 1028-1030 (2003).
- [6] W. Y. Ching, and P. Rulis, *Electronic Structure Methods for Complex Materials: The Orthogonalized Linear Combination of Atomic Orbitals*, OUP Oxford, 2012.
- [7] H. Iwata and K. M. Itoh, *J. Appl. Phys.* **89** (11), 6228-6234 (2001).
- [8] S. Forster, D. Chaussende, and K. Kalna, *ACS Appl. Energy Mater.* **2** (1), 715-720 (2019).

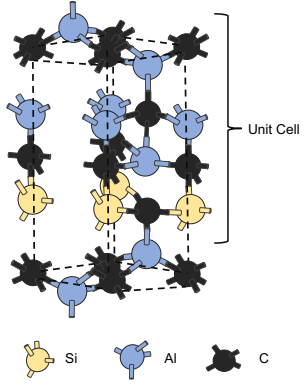


Fig. 1: A crystal structure of Al_4SiC_4 . The blue, yellow, and black spheres represent Al, Si, and C atoms, respectively.

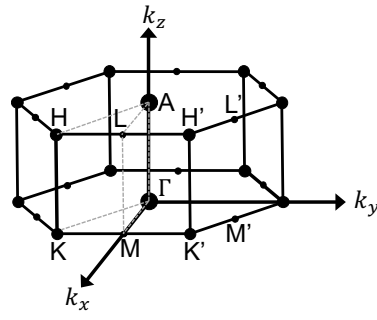


Fig. 2: A schematic of hexagonal bandstructure of Al_4SiC_4 in the k -space showing a location of principal valleys.

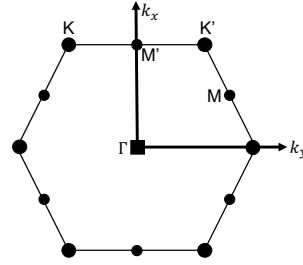


Fig. 3: The hexagonal (0001) $k_x - k_y$ plane of Al_4SiC_4 showing a location of principal valleys.

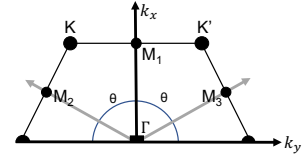


Fig. 4: Detail of locations of the M -valleys in the (0001) plane within the Al_4SiC_4 hexagonal structure, where $\theta = \pm 60^\circ$ or $\pi/3$.

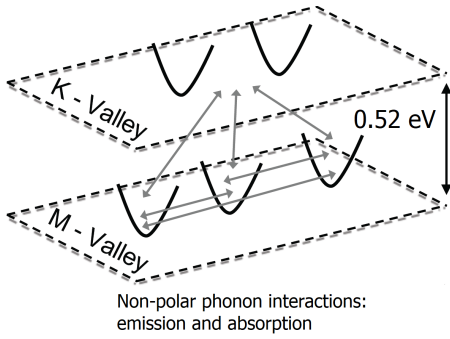


Fig. 5: A schematic of conduction band minimum valleys for Al_4SiC_4 showing details of the number of equivalent M - and K - valleys, the separation between valleys, and the electron—non-polar phonon interactions considered in the transport model.

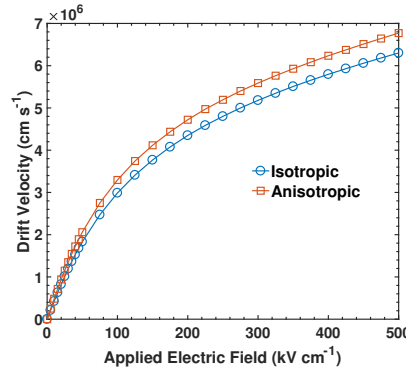


Fig. 6: Electron drift velocity as a function of applied electric field in a bulk Al_4SiC_4 . The velocity obtained assuming an anisotropic (red squares) and a simpler isotropic (blue circles) bandstructure are shown.

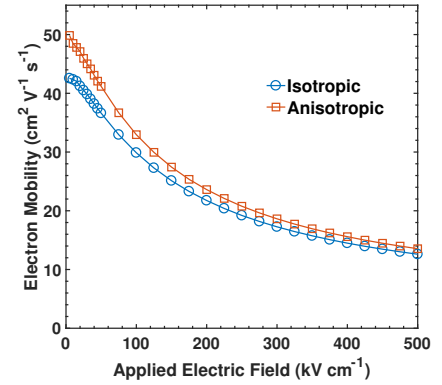


Fig. 7: Electron mobility as a function of applied electric field in a bulk Al_4SiC_4 . The mobility obtained assuming an anisotropic (red squares) and a simpler isotropic (blue circles) bandstructure are plotted.

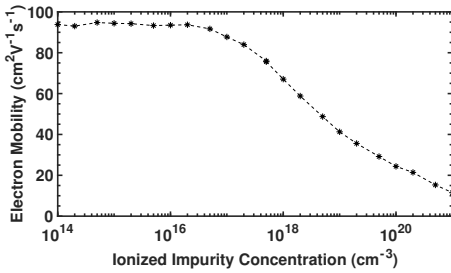


Fig. 8: Electron mobility as a function of ionized impurity concentration in a bulk Al_4SiC_4 .

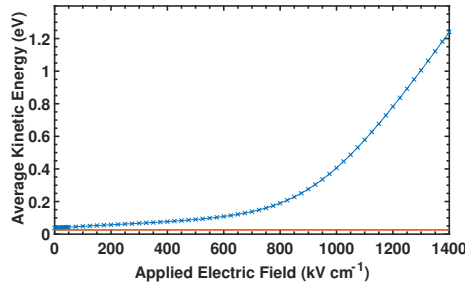


Fig. 9: Average kinetic energy as a function of applied electric field in a bulk Al_4SiC_4 .

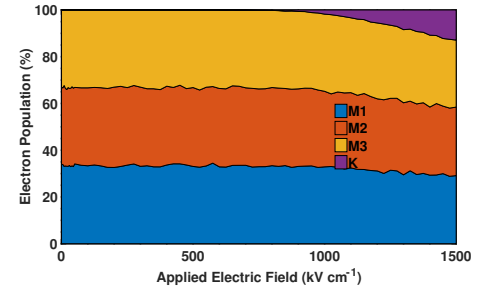


Fig. 10: Valley occupancy of electrons in the M - and K -valleys vs. applied electric field in bulk Al_4SiC_4 .

Ab initio heat dynamics in phonon-based dark matter detectors

M. Raya-Moreno[†], B. J. Kavanagh^{*}, E. Vilanova, L. Fàbrega, and R. Rurali

Institut de Ciència de Materials de Barcelona (ICMAB-CSIC), Campus UAB, 08193 Bellaterra, Spain

^{*}Instituto de Física de Cantabria (IFCA, UC-CSIC), Av. de los Castros, 39005 Santander, Spain

[†]e-mail: mraya@icmab.es

The search for dark matter (DM) is at present one of the most exciting areas of research in Cosmology and Particle Physics. The lack of results for traditional high-mass DM candidates has driven attention to lighter candidates. Recent theoretical work has suggested that such DM may have a relatively strong interaction with polar semiconductors [1]—henceforth called the target—, so that a single optical phonon is created. These phonons could be theoretically collected into a superconductor, from now on referred to as the collector, for subsequent detection using transition edge sensors (TES)—i.e. a detection architecture known as quasiparticle-trap-assisted TES, or QET [3]—; so that phonon-based detectors can be considered (see Fig. 1). However, the rapid decay of this phonon due to intrinsic scattering or the target-collector interface scattering can severely hinder the collected signal or render it below detectable levels. Therefore, phonon dynamics is a limiting factor for the devices' design, making its understanding essential for the optimization of any instrument. Nonetheless, there exist packages to model phonon transport in similar setups [4], they rely on tabulated data or isotropic approximation, limiting their transferability and/or accuracy.

In this work, we have developed tools for the computation of phonon dynamics within the target of a cryogenic phonon-based DM detector allowing for the obtaining of collected thermal signal (phonons) for an Al₂O₃-Al system (target-collector); the developed tools are supplemented with *ab initio* phonon data which allows for the simulation of any pair of materials.

Though arbitrary initial states (single phonon) are allowed, we have selected our initial states based on DM-phonon scattering rates (see Fig. 2) calculated using phonon spectra together with DarkELF [2].

Following the choice of the initial state we obtain the gross flux crossing the target collector interface using a simplified model without spatial resolution, as developed by Swartz *et al.* [5], together with a full band diffusive mismatch model [6] to obtain the mode-dependent transmission coefficient for such a model. The simplified model allows us to check different approaches to the collision operator, showing not only that mode coupling in the scattering is essential, but that linearized and full collision operators provide essentially the same results for our kind of systems (i.e. differences smaller than 0.01%)[see Fig. 3]. This simplified model also allows us to qualitatively investigate the effect that several initial parameters have over the collected signal, namely, the initial phonon state, the isotopic purity of the sample, and/or its volume; showing, for instance, a clear dependence on the collected signal in the initial phonon energy for all the studied target volumes, with higher energies providing better signals. Finally, we have developed an energy deviational Monte Carlo solver [7] which allows us, not only, to obtain more accurate results but also to model spatial effects over the signal.

REFERENCES

- [1] S. Griffin *et al.*, Phys. Rev. D **98**, 115034 (2018).
- [2] S. Knapen *et al.*, Phys. Rev. D **105**, 015014 (2022).
- [3] K. E. Irwin *et al.*, Rev. Sci. Instrum. **66**, 5322 (1995).
- [4] M. Martinez *et al.*, Phys. Rev. Applied **11**, 064025 (2019).
- [5] E. T. Swartz *et al.*, Rev. Mod. Phys. **61**, 605 (1989).
- [6] P. Reddy *et al.*, Appl. Phys. Lett. **87**, 211908 (2005).
- [7] C. Landon *et al.*, J. Appl. Phys. **116**, 163502 (2014).

Acknowledgment: We acknowledge financial support from AEI under grant CEX2019-000917-S, and from the Spanish NRRP through the CSIC PTI-QTEP+. Calculations were performed at the CESGA within action FI-2022-3-0031 of the RES. BJK also acknowledges funding from MCIN/AEI/NGEU/PRTR under grant RYC2021-034757-I.

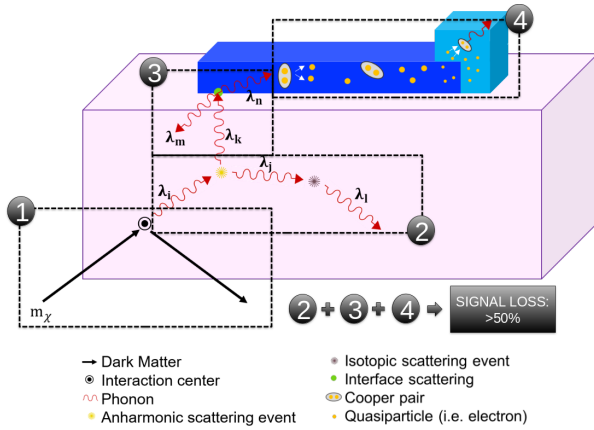


Fig. 1. Sketch of the physical processes within the DM phonon based detector. The related and individual processes—(1) DM -target interaction, (2) phonon downconversion, (3) interface scattering, and (4) pair breaking diffusion and detection—that affect the detected signal are indicated with black-dashed boxes.

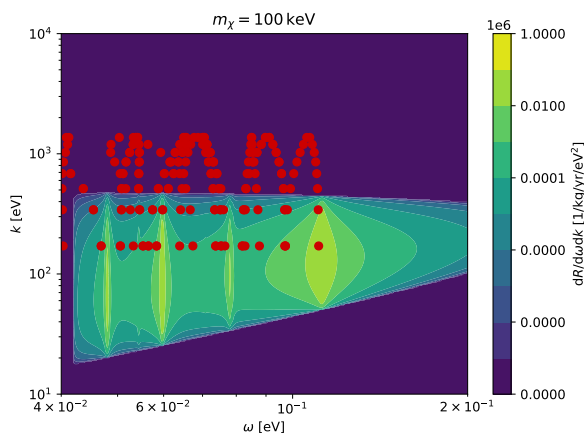


Fig. 2. Spectral and momentum decomposition of DM-phonon scattering rate per unit target mass for Al_2O_3 in the $\langle 0001 \rangle$ direction. Available points for a Γ -centered $17 \times 17 \times 17$ q -mesh are given as reference.

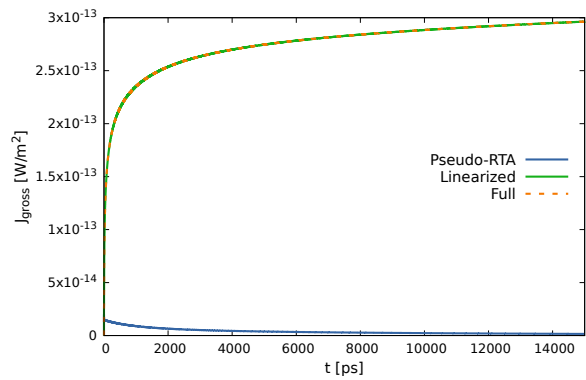


Fig. 3. Gross heat flux computed with Swartz's model [5] traversing the interface as function of time, for $\text{Al}_2\text{O}_3 \langle 0001 \rangle$ - $\text{Al} \langle 111 \rangle$ system at 0.01 K using different approaches for the collision operator. Interface scattering is computed using the diffusive mismatch model. Here, pseudo-RTA refers to an incomplete linearized operator (almost diagonal, that is similar to the relaxation time approximation one), which does not properly model the mode coupling due to the scattering.

Ab initio effective dragged thermoelectric properties in Si nanowires

M. Raya-Moreno[†], R. Rurali, and X. Cartoixà*

Institut de Ciència de Materials de Barcelona (ICMABCSIC), Campus UAB, 08193 Bellaterra, Spain

*Departament dEnginyeria Electrònica, Universitat Autònoma de Barcelona, 08193 Bellaterra, Spain

[†]e-mail: mraya@icmab.es

The growing interest in energy-harvesting has resulted in the research for more efficient thermoelectric systems [1]; as they not only allow to give a practical use to thermal waste of all our devices and/or buildings, but to generate energy for small wearable devices, thus removing the necessity of external batteries [2]. Unfortunately, traditionally those systems offered quite a low efficiency—i.e. they offer low figures of merit zT —, therefore creating a need to enhance their energy conversion ratio [3]. In that context, nanostructuring provides an effective way of reducing the lattice thermal conductivity without deteriorating electrical properties [2], [4], [5], thereby obtaining conversion ratios unachievable using more classical approaches [4]. A paradigmatic example of such an improvement due to nanostructuring can be found in heavily-doped Si nanowires (NWs), which have been found to offer a zT 100 times larger than their bulk counterpart [6]. The quantities necessary for the computation of this figure of merit ($zT = \frac{\sigma S^2 T}{\kappa}$ [4], where σ , S , T and κ are the electrical conductivity, Seebeck coefficient, temperature, and thermal conductivity, respectively) can in principle be obtained from the solution of the mesoscopic linearized Boltzmann Transport Equation for both electrons and phonons (EPBTE). Indeed, the recent development of an iterative solution for these coupled system [7], has resulted in a step forward towards the *ab initio* computation of more accurate thermoelectric properties. Nonetheless the utility of such an approach to accurately describe thermoelectric properties, its practical usage is currently limited to homogeneous systems, namely bulk, thus preventing its use for high- zT systems, as the nanostructured ones.

In this work, we compute the effective thermoelectric properties for nanosystems, namely Si NWs,

by iteratively solving the *ab initio*-informed (i.e. with scattering rates, energies, velocities,... calculated from first principles) linearized EPBTE with the appropriate boundary conditions to correctly model the effect of perfectly diffusive physical boundaries, going for the first time a step beyond the most common approach based on adding a Casimir boundary scattering through Matthiessen's rule. We demonstrate that our methodology provides a higher accuracy than Matthiessen's approach (see Table I) through comparison with recent experimental results [5]. Furthermore, we demonstrate that the effect of the use of Matthiessen's is not straightforward to translate to thermoelectric variables for NWs and that for some cases it provides qualitatively different results than our methodology (see Fig. 1), which provides an exact and physically correct treatment of boundary effects. Consequently, our results not only rise concern of Matthiessen's accuracy for nanosystems, but make it necessary to study its reliability on a case-by-case basis, rendering our approach superior for such systems. Finally, we also discuss the effect of the collision term approach has over thermoelectric properties, as well as the size effect (see Fig. 2); finding that coupling is essential to obtain the accurate dependence of zT with size, as not all radii provide enhancement as predicted by uncoupled approaches.

REFERENCES

- [1] A. J. Minnich *et al.*, Energy Environ. Sci. **2**, 466 (2008).
- [2] A. Shakouri, Annu. Rev. Mater. Res. **41**, 399 (2011).
- [3] C. Wood, Energy Convers. Manag. **24**, 331 (1984).
- [4] M. G. Kanatzidis, Chem. Mater. **22**, 648 (2010).
- [5] G. Gadea Dez *et al.*, Nano Energy **67**, 104191 (2020).
- [6] A. I. Boukai *et al.*, Nature **451**, 168 (2008).
- [7] N. H. Protik *et al.*, Npj Comput. Mater. **8**, 28 (2022).

TABLE I

CALCULATED THERMAL CONDUCTIVITY (κ), ELECTRICAL CONDUCTIVITY (σ), SEEBECK COEFFICIENT (S) AND THERMOELECTRIC FIGURE OF MERIT (zT) AT 300 K, FOR NWS OF RADII RANGING 45-50 nm AND B-DOPINGS OF 2.0×10^{19} AND $5.0 \times 10^{19} \text{ cm}^{-3}$ USING OUR APPROACH, I.E. THE SUPPRESSED DRAGGED EPBTE (SDEPBTE), AND THE DRAGGED EPBTE WITH MATTHIESSEN'S PLUS A CASIMIR SCATTERING TERM (MDEPBTE) TO MODEL THE NW BOUNDARY EFFECT. RESULTS FROM REF. [5] ARE PROVIDED AS REFERENCE.

	κ [$\frac{\text{W}}{\text{m}\cdot\text{K}}$]	σ [$\frac{\text{S}}{\text{cm}}$]	S [$\frac{\mu\text{V}}{\text{K}}$]	zT $\times 10^{-2}$
Experimental	18.3 ± 4.6 (13-25 [†])	270 (247-290 [†])	207 ± 19	1.4-2.5 [†]
SDEPBTE [‡]	25.8-27.3 25.5-26.9	276-280 624-633	276-277 198-199	2.4-2.3 2.7-2.8
MDEPBTE [‡]	39.3-41.4 39.5-41.4	288-291 652-658	282-284 207-209	1.7-1.7 2.1-2.1

[†] These values correspond to the minimum and the maximum of the value for the given temperature of all measurements, including errors.

[‡] These results correspond to the values for NWS of radius 45 (left) and 50 (right) nm, with a B-doping of $2.0 \times 10^{19} \text{ cm}^{-3}$ (top) and $5.0 \times 10^{19} \text{ cm}^{-3}$ (bottom).

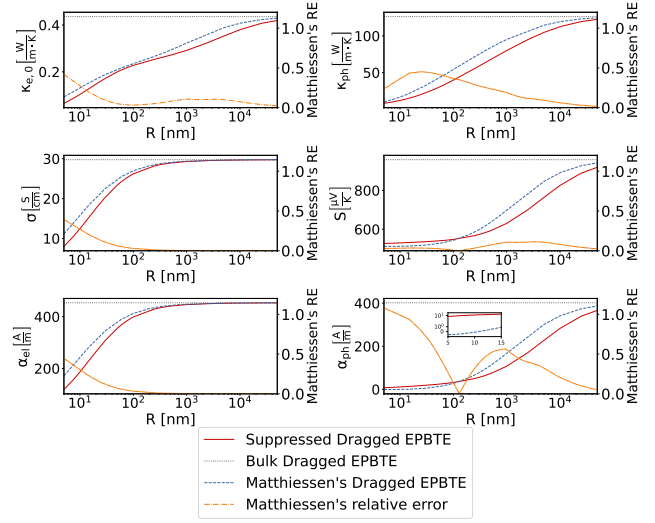


Fig. 1. Left-axis: Electronic (at 0 field; $\kappa_{el,0}$) and phonon (κ_{ph}) thermal conductivity, electrical conductivity, Seebeck coefficient, the electronic (α_{el}) and phonon (α_{ph}) thermal response to an electric field as a function of NW radius at 300 K and a donor concentration (P) of $1.0 \times 10^{18} \text{ cm}^{-3}$ obtained through the suppressed dragged EPBTE (red solid) and dragged EPBTE with Matthiessen's (blue dashed); bulk values (gray dotted) are given as reference. Right-axis: Relative error of Matthiessen's with respect to suppressed solution (orange dot-dash) as function of NW radii. Inset: Zoom at small radii for α_{ph} .

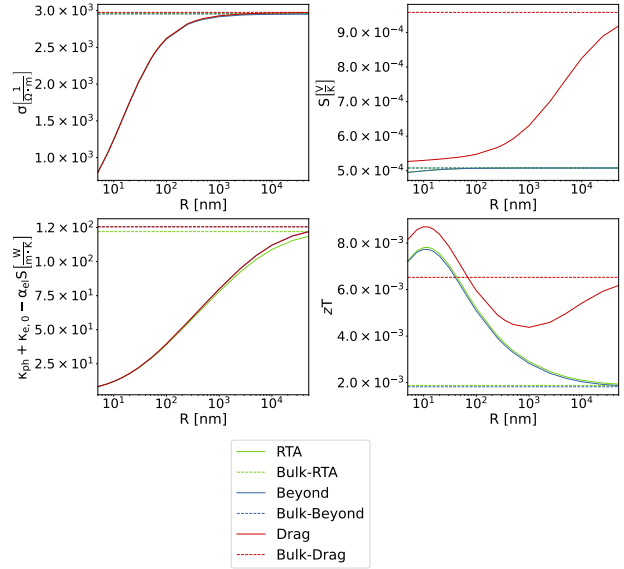


Fig. 2. Electrical conductivity, Seebeck coefficient, total thermal conductivity at zero electric current, and figure of merit as function of NW radius at 300 K and an acceptor concentration (B) of $1.0 \times 10^{18} \text{ cm}^{-3}$ for several approaches to collision operator; namely, relaxation time approximation or RTA (green), uncoupled beyond the RTA (blue), and dragged (red). Bulk values (dashed) are given as reference.

Phonon transport across Ge/GaAs heterojunctions by nonequilibrium molecular dynamics

T. Albrigi¹, R. Rurali¹ Institut de Ciència de Materials de Barcelona (ICMAB–CSIC)
Campus UAB, 08193 Bellaterra, Spain

INTRODUCTION

Thanks to their technological importance, the characterization of solid-state systems made of III-V semiconductor materials represents a well-assessed field of research in the scientific community. Within this context, we focused on the thermal transport properties of the **Ge/GaAs heterojunction** at the nanoscale, investigating their dependence on both geometrical and chemical defects, together with their tunable features. (Fig. 1, 2)

THEORY

The figure of merit of our study is the concept of thermal boundary resistance - or **TBR**, and its pivotal role in engineering thermal transport and dissipation. Second to it, we are interested in the resulting non-linear behavior of the junction itself, thus allowing **thermal rectification** to take place. When we apply some thermal bias - and the system has reached the corresponding steady-state, a non-linear temperature profile appears, which exhibits a sharp temperature drop at the interface between the two materials (Fig. 3). The ratio with the heat flux then yields the basic definition of TBR. When we reverse the bias, the temperature profile doesn't become its mirror image to the interface, and the resulting TBR, as well as the conductivity of the whole system, is different from the forward-bias configuration. The **theoretical framework** to understand these phenomena counts various models, ranging from continuum to atomistic theories, all the way up to the Many Body one, none of which proved capable of explaining all of the data. [1]

NUMERICAL SIMULATION

We constructed a minimal interaction potential to model the physics at the interface and used **NEMD** to compute the TBR and a suitable rectification coefficient in several configurations. We have taken the parameters for Gallium Arsenide from Albe et al., whereas the parameters for Germanium, as well as the empirical rule to combine them with the previous ones, come from Tersoff [2] [3]. Then we varied the cell geometry,

the average temperature, the thermal gradient applied, concentration mixing, and roughness of the interface; and calculated the dependence of the TBR and rectification coefficient on these quantities.

RESULTS

The order of magnitude of our estimates shows fair agreement with the typical values found for other heterojunctions of the like kind [4]. We achieved a relative uncertainty of around 10% for the TBR at 180 nm x 8 nm², which we then used for probing into the other parameters. To a first approximation, different temperature gradients only affect the time needed to reach the steady state; we thus use a value of 1.65 K/nm in order to achieve a reasonable compromise between accuracy and a fast approach to the nonequilibrium steady-state. Mixing enhances the TBR by 0.15 K·m²/W per nanometer of the mixed zone, whereas interface roughness has a relatively minor impact. The temperature dependence of the TBR we obtained is about $T^{-1.6}$. The rectification coefficient crosses zero around 80 nm and stabilizes around 10% when we extrapolate it for the infinite system (Fig. 4, 5).

ACKNOWLEDGMENT

We acknowledge financial support by MCIN/AEI/10.13039/501100011033 under grant PID2020-119777GB-I00, and the Severo Ochoa Centres of Excellence Program under grant CEX2019-000917-S. T.A. acknowledges funding PRE2020-093576

REFERENCES

- [1] J. Chen, X. Xu, J. Zhou, and B. Li *Interfacial thermal resistance: past, present and future*, Review of Modern Physics **94** (2022).
- [2] K. Albe, K. Norlund, J. Nord, and A. Kuronen *Modeling of compound semiconductors: analytical bond-order potential for Ga, As, and GaAs*, Physical Review B **66** (2002).
- [3] J. Tersoff *Modeling solid state chemistry: interatomic potentials for multicomponent systems*, Physical Review B **39** (1989).
- [4] J. Carrete, R. Rurali et al. *Phonon transport across crystal-phase interfaces and twin boundaries in semiconducting nanowires*, Nanoscale **11** (2019).

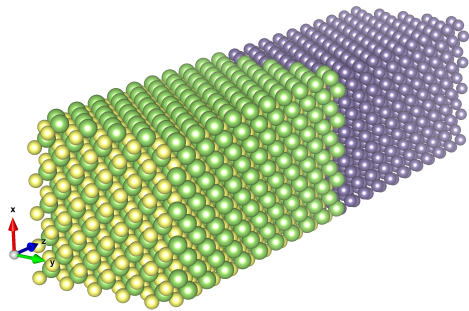


Fig. 1. Ge/GaAs junction with atomically flat interface

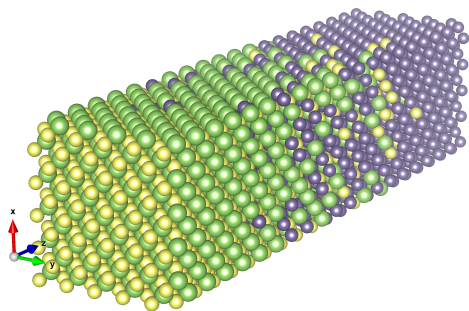


Fig. 2. Ge/GaAs junction with concentration mixing

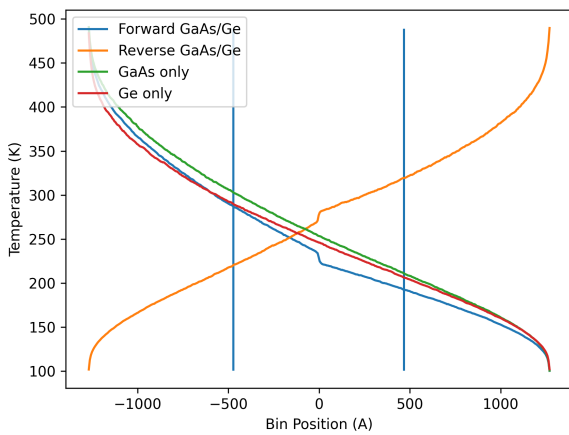


Fig. 3. Temperature profiles comparison for the 260nm x 8nm² cell

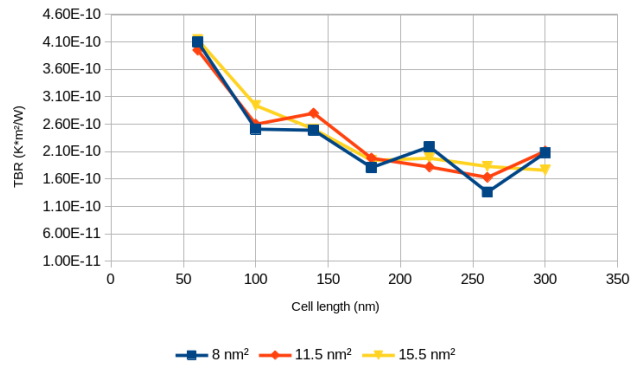


Fig. 4. Thermal boundary resistance dependence on cell length and cross section. A fixed thermal bias of 100K, centered at 300K, has been imposed in every simulation

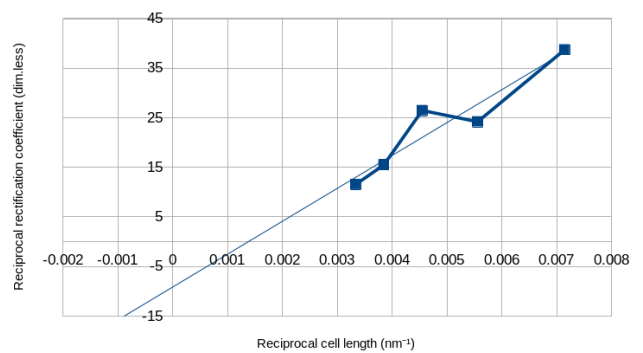


Fig. 5. Thermal rectification dependence on the cell length

Electrothermal simulations of a thermal sensor integrated with a 4H-SiC JFET

F. Monaghan, A. Martinez*, and M. Jennings

Department of Electrical and Electronic Engineering, Swansea University, UK
Swansea, UK

*e-mail: a.e.martinez@swansea.ac.uk

ABSTRACT

In this work we carried out electrothermal simulation of a temperature sensor. The sensor aims to probe the local temperature of a 4H-SiC JFET device during functioning. The change in resistance with the temperature of p-type SiC region is used to provide the sensing capabilities. This change is due to incomplete ionization of P-type *Al* dopants in SiC. The sensor provides a change in resistance of 80 Ohms in the range of temperature studied. We tested the sensor at fixed temperature and using electrothermal simulations. We used an anisotropic and temperature dependent thermal conductivity. The device and sensor doping profile are generated using Monte Carlo simulated implantation.

INTRODUCTION

SiC wafer fabrication technology and device manufacturing have been reach a substantial maturity. Commercial SiC MOSFET and JFET mainly for power application start to populate the markets. Today with an increasing manufacturing of electrical vehicles the need of efficient and compact converters and controllers are paramount.

Even though SiC devices can hold operate at high temperature, it is important to monitor the junction device temperature for protection and reliability purposes. This work aims to design a temperature sensor embedded in JFET. We carried out electrothermal simulations using a Drift-Diffusion/Poisson approach in concomitance with the heat equation.

(1)

MODEL AND RESULTS

The doping and dimensions of JFET devices and embedded sensors are shown in fig. 1. All p+ regions are completed using Monte Carlo

simulations [1] to create realistic implanted profiles with a maximum depth of 1 μ m. The p-dopant used is aluminum with an ionization energy of 265 meV. Fig. 2 shows the dependency of the k_x and k_y with the temperature. k_x is the thermal conductivity in the c-axis (Hexagonal axis) and k_y in the planar direction. For 4H-SiC, thermal conductivity decreases strongly with increasing temperature (approximately 80%). Fig. 3 shows the temperature profile (all the 2D profiles are at $V_d=15V$), following this, the joule heat profile is shown in Fig 4. The joule heat is more concentrated in the JFET channels, which is the high resistance region of the device. The output characteristics of the JFETs using electrothermal and fixed temperature values of 300 K and 450 K are shown in Fig 5. The electrothermal curve matches the 300K curve at low bias, and the 450K at large bias as expected. Fig 6 shows the sensor resistance as a function of temperature. Our calculations show that the sensor current is independent of the drain bias of the device for fixed temperature simulations. This means that there is no influence from the depletion region and device currents to the sensor's resistance. In addition, the resistance is very sensitive to the doping profile and the annealing or activation of dopants. Our sensor resistance sensitivity is around 50 % much larger than [2] and relative of the same order of magnitude than [3], however our design requires fewer implantation steps to fabricate in practice.

REFERENCES

- [1] S. Tian, *Monte Carlo Simulation of Ion Implantation in Crystalline SiC with Arbitrary Polytypes*, IEEE Transactions on Electron Devices, **55**, 1991, (2008)
- [2] K. Han et al. *1.2 kV 4H-SiC SenseFET With Monolithically Integrated Sensing Resistor*, IEEE Electron Device Letters, **41**, 437, (2020)
- [3] M. Berthou et al. *Monolithically Integrated Temperature Sensor in SiC Power Mosfets*, IEEE transactions on Power Electronics, **29**, 4979, (2014)

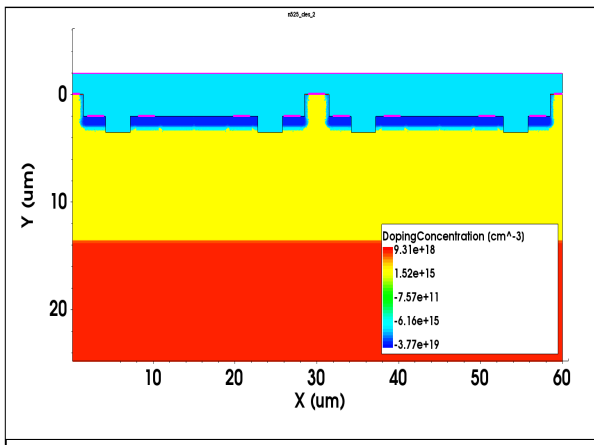


Fig. 1. Doping profile of JFET with embedded sensor. The figure shows a full JFET cell in the centre, with half JFET cells shown at the edges of the image. Two sensor cells are also shown, one either side of the centre JFET.

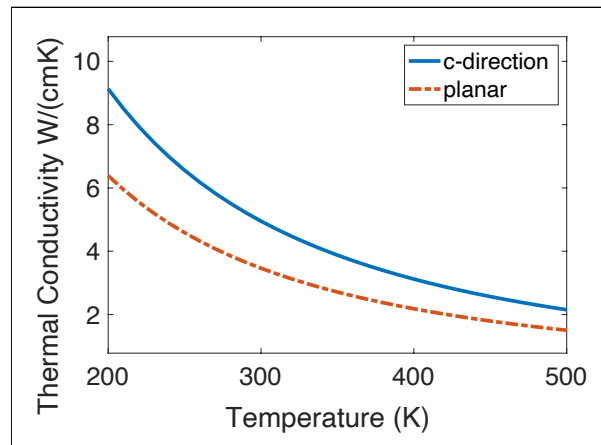


Fig. 2. Thermal conductivity vs temperature for c-axis and planar direction.

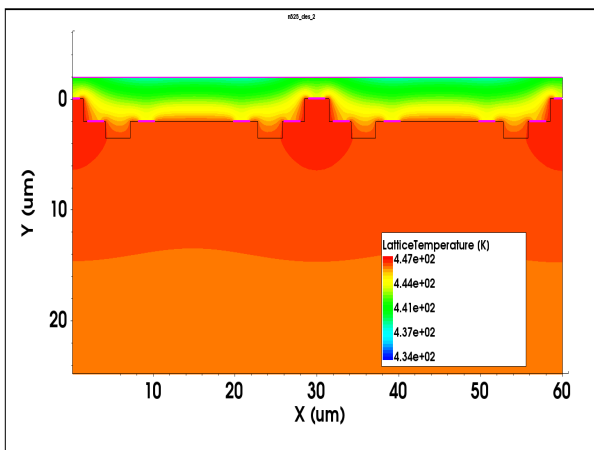


Fig. 3. Temperature profile for $V_{gs} = 0V$, $V_{ds} = 15V$,

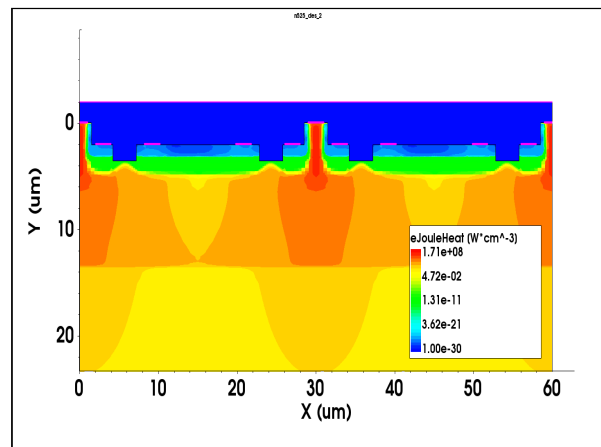


Fig. 4. The Joule heat profile corresponding to the case of Fig. 3.

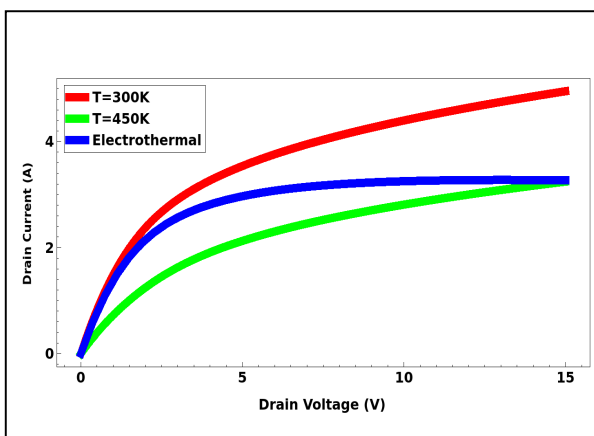


Fig. 5. Output characteristics of the JFET using electrothermal and at fixed temperatures (300K, 450K) at $V_{gs} = 0V$.

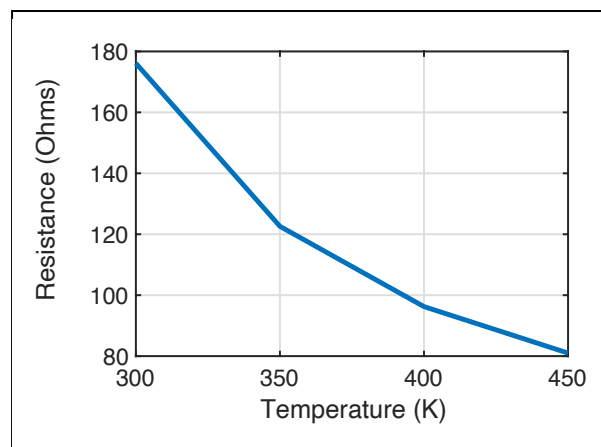


Fig. 6. Sensor resistance as a function of temperature

Effects of structural arrangements on thermoelectric properties of SiX (X=N,P,As,Sb,Bi) monolayers

Subhradip Ghosh, and Himanshu Murari

Department of Physics, Indian Institute of Technology Guwahati, Guwahati-781039, India
e-mail: subhra@iitg.ac.in

INTRODUCTION

Thermoelectric materials are being explored extensively in recent times as they are capable of generating electricity from waste heat of environmental sources. The efficiency of a thermoelectric material at a given temperature T is determined by its figure of merit $ZT = \frac{S^2\sigma}{\kappa}T$; S, σ, κ are Seebeck coefficient, electrical conductivity and thermal conductivity, respectively. The target of most research on thermoelectric materials is to increase ZT upto 3-4. In this work, we present first-principles based investigations into monolayers of hexagonal IV-V semiconductor SiX (X=N,P,As,Sb,Bi) family. We find that the transport properties are substantially affected by atomic arrangements in the planes of the monolayers, an effect observed earlier [1] in another family of two-dimensional materials.

METHODOLOGY

The band structure calculations are done using Density Functional Theory (DFT) as implemented in Vienna Ab initio Simulation Package (VASP) employing the Projector Augmented Wave (PAW) basis set with Generalised Gradient Approximation (GGA) exchange-correlation potential. The band structures are then used along with semi-classical Boltzmann Transport theory to compute the transport parameters S, σ and κ using BoltzTrap2 and ShengBTE packages.

RESULTS AND DISCUSSIONS

Two different stacking patterns, configuration(1) in which the Si atoms occupy the inner planes and configuration(2) where the X atoms occupy the inner planes are used to compute the effects

of atomic arrangements on the thermoelectric properties. We find that the non-conventional stacking pattern (configuration(2)) leads to a maximum ZT of 3.23 at 800 K for electron doped SiP. Overall, the ZT obtained in configuration(2) are 2-6 times higher than those obtained in stacking pattern given as configuration(1). This is due to the combined effect of lower lattice thermal conductivity and higher electronic conductivity in configuration(2). The origin of this lies in the flatness of the bands, weaker bonds and increased anharmonicity in the low frequency acoustic modes when X atoms occupy the inner planes of the SiX monolayers.

The thermoelectric conversion efficiency η of the compounds which is related to the Carnot efficiency are then calculated using ZT

$$\eta = \frac{T_h - T_c}{T_h} \frac{\sqrt{1 + ZT} - 1}{\sqrt{1 + ZT} + T_c/T_h} \quad (1)$$

T_h, T_c are the temperatures of the hot and cold edges of the thermoelectric device, respectively. We find that SiP in configuration(2) has an efficiency of 27% when operated between 300-800K. This efficiency is comparable to that of a home refrigerator.

CONCLUSIONS

Hexagonal Si-X monolayers show substantial dependence of their thermoelectric efficiencies on the structural arrangements. This work demonstrates a route for experimentalists to tweak the stacking to effect significant gains in thermoelectric efficiencies in two-dimensional materials.

REFERENCES

- [1] A. Majumdar, S. Chowdhury, and R. Ahuja, *Drastic reduction of thermal conductivity in hexagonal AX monolayers due to alternative atomic configuration*, Nano Energy **88**, 106248 (2021).

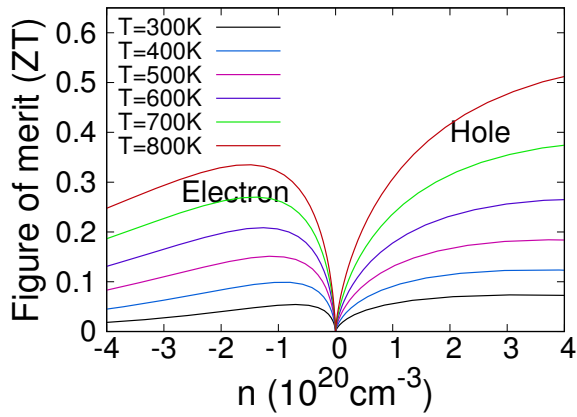


Fig. 1. Thermoelectric figure of merit for SiP in configuration(1)

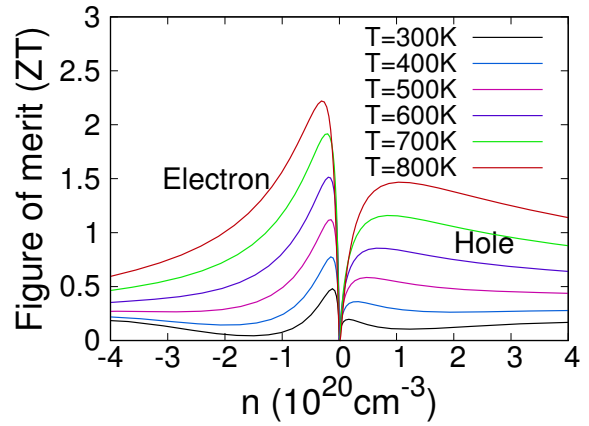


Fig. 4. Thermoelectric figure of merit for SiAs in configuration(2)

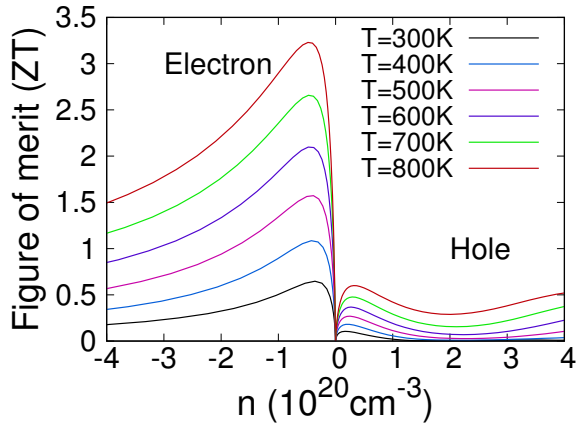


Fig. 2. Thermoelectric figure of merit for SiP in configuration(2)

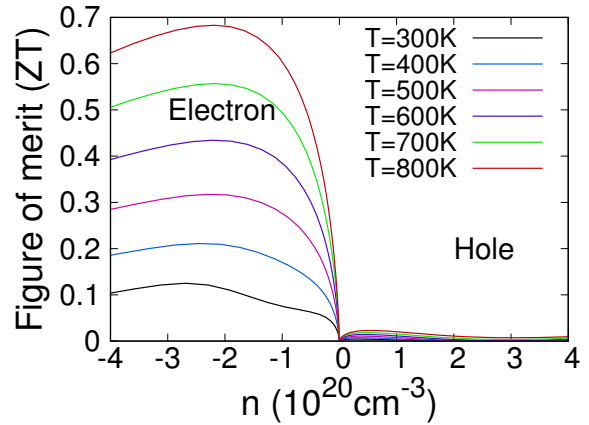


Fig. 5. Thermoelectric figure of merit for SiSb in configuration(1)

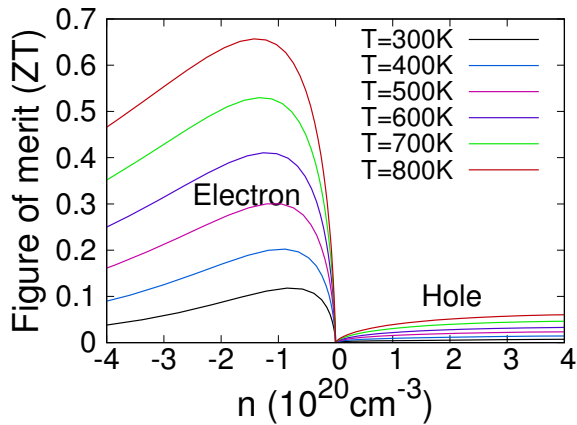


Fig. 3. Thermoelectric figure of merit for SiAs in configuration(1)

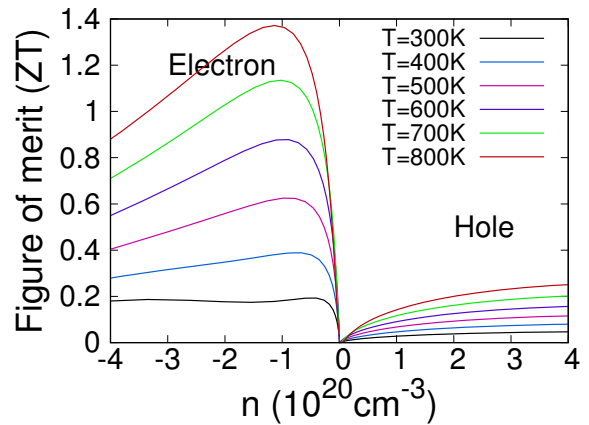


Fig. 6. Thermoelectric figure of merit for SiSb in configuration(2)

Analysis of Wave speed in magneto-thermoelastic nonlocal micropolar orthotropic medium

Anand Kumar Yadav^a and Sangeeta Kumari^b

^aShishu Niketan Model Senior Secondary School, Sector 22-D, Chandigarh, India.

^bDepartment of mathematics, Chandigarh University, Gharuan, Punjab, India

Email: yadavanand977@gmail.com

ABSTRACT

In this article, the governing partial differential equations for nonlocal micropolar orthotropic magneto-thermoelastic half space in context of generalized theory of thermo-elasticity for x-z plane are obtained. The velocity equation is derived and the plane wave solution shows the existence of four coupled quasi plane waves in the plane namely quasi-longitudinal displacement (qCLD) wave, quasi transverse displacement (qCTD) wave, quasi transverse micro-rotational (qCTM) wave and quasi thermal wave (qCT). The speeds of these waves are calculated for a particular material. The variation of speeds of these waves due to magnetic field, nonlocal parameters, micro-polarity is studied and are shown graphically.

Keywords Magneto-thermo-elasticity, micro-polarity, orthotropic.

INTRODUCTION

Orthotropic materials like wood, sheet metal, topaz, unidirectional fibre-reinforced composites, the outer carbon fibres, carbon fibre reinforced polymer (CFRP), glass fibre reinforced plastic (GFRP) and nano-materials. These materials have great engineering importance.

Metamaterials are composite manmade materials that are engineered to have a property that are not found in naturally occurring materials. These are made from assemblies of multiple elements fashioned from composite materials to exhibit unique electromagnetic properties such as negative refractive index. Metamaterials are used optical filters, medical devices, remote aerospace applications, sensor-detection lenses for high-gain antennas, infrastructure monitoring, smart solar power-management, crowd control, redomes, high-frequency, battlefield communication, and even shielding structures from earthquakes. Acoustic, seismic, nano-science and semiconductor metamaterials are also research areas.

Eringen [1,2] established micropolar theory of elasticity to model the behaviour of granular materials, multimolecular bodies, and composite materials, and Eringen [3] proposed a theory, called nonlocal continuum mechanics. The wave propagation in an anisotropic medium is studied by Keith and Crampin [4], Singh and Yadav [5,6] studied wave propagation in rotating magneto-thermoelastic anisotropic solid half space and obtained the reflection coefficients. Yadav [7] studied the reflection of plane waves from the free surface of a rotating orthotropic magneto-thermoelastic solid half-space with diffusion.

MODEL

Plane wave method, Normal mode analysis can be applied to study the waves in micropolar orthotropic medium. Earth modelled for this problem as orthotropic layers are found in the earth.

CONCLUSIONS

Magnetic field, nonlocal parameters and micro-polarity have significant effect on speeds, of these waves.

REFERENCES

- [1] A.C. Eringen, Foundations of micropolar thermoelasticity. International Center for Mechanical Science, Courses and Lectures, Springer, Berlin, 1970;(23).
- [2] A.C. Eringen, Microcontinuum field theory I: Foundations and solids. Springer- Verlag, Berlin, 1999.
- [3] A.C. Eringen, Theory of nonlocal thermoelasticity, Int. J. Eng. Sci. 12, 1063–1077 (1974).
- [4] C.M. Keith, S. Crampin, Seismic body waves in anisotropic media: reflection and refraction at a plane interface. *Geophy. J. Royal Astro. Soc.*, **49**, 181-208(1977).

- [5] B. Singh, A.K. Yadav, Reflection of Plane Waves in a Rotating Transversely Isotropic Magneto-Thermoelastic Solid Half-Space, *J. Theor. App. Mech-Pol., Sofia*, **42(3)**, 33–60(2012b).
- [6] B. Singh, A.K. Yadav, Plane waves in a rotating monoclinic magneto-thermo-elastic medium, *J. Eng. Phy. Thermophys.*, **89**, 428–440(2016).
- [7] A.K. Yadav, Reflection of plane waves from the free surface of a rotating orthotropic magneto-thermoelastic solid half-space with diffusion, *J. Therm. Stresses*, (2020). DOI: 10.1080/ 014957 39.2020.1842273.

Towards a semi-classical simulator for the energy distribution functions in optically excited hot carrier semiconductor devices

J. R. Barker and A. M. Martinez*

James Watt School of Engineering, University of Glasgow, Glasgow G12 8LT, UK ,

* Department of Electrical and Electronic Engineering, Swansea University, Bay Campus , UK

e-mail: john.barker@glasgow.ac.uk

ABSTRACT

Progress is reported on the semi-classical component of a proposed hybrid quantum/classical simulator [1] for the efficient design and analysis of macroscopic photovoltaic semiconductor devices [2,3] with nanoscale insertions and hot photoexcited carriers.

INTRODUCTION AND MODEL

The determination of the energy distributions of carriers, photons and phonons is crucial for photovoltaic device modelling, ideally on time/space scales from very small to very large (fig.1-3). The physical processes involve externally incident photons at high temperature which are absorbed by electron and hole photo-excitation. The excited carriers re-distribute energy and momentum by inter-carrier interactions. Ultimately, the photon and carrier distributions thermalise to the lattice via interaction with optical and acoustic phonons with carrier recombination leading to photon emission processes that produce a steady state photon distribution.. Our long term aim is to couple a simplified version of the NEGF methodology with the semi-classical kinetic equation methodology to obtain a phenomenological parameterised computational model that determines the mobility, diffusion coefficients, and the temperatures and chemical potentials of both carriers *and* photons on multiple time scales for which quasi-steady state processes occur. The aim is to explore nanostructured inserts that provoke *persistent* hot carrier states that improve device efficiency.

We consider coupled transport equations (fig3) for the energy distributions of photons, electrons and holes in the energy-space domain on different

quasi-stationary time scales. Here, we will present results for computation of the electron and hole distributions in a homogeneous slice of an absorber region subject to a quasi-stationary photon distribution intermediate to the incident Bose-Einstein photon flux and the lattice thermalized photon flux at a fixed photon chemical potential. The method involves iterative solving of coupled non-linear integral equations for the carrier energy (E) distribution functions $F[K=(E/k_B T)^{1/2}]$ of Fig.4-5. Fig.6 illustrates a simple sub-case: the energy distribution function of electrons photo-excited by high temperature photons incident on neutral donors in a compensated model semiconductor. Using precise forms for the electron-photon and electron-trap recombination we find that the distributions are non-equilibrium mixtures of the incident excitation function and the scaled thermal electron distribution. Fig. 6 illustrates the typical form of the distributions for weak, intermediate and strong inelastic acoustic phonon scattering. Of course realistic models require optical phonon scattering and phonon and trap-assisted band to band recombination.

REFERENCES

- [1] A. Martinez and J.R. Barker, THIS CONFERENCE.
- [2] M. A. Green, *Third Generation Photovoltaics, Advanced Solar Energy Conversion*, Springer: Berlin Heidelberg New York, (2006).
- [3] P. Würfel and U. Würfel, *Physics of Solar Cells*, (2019).
- [4] J. R. Barker and C. J. Hearn, *A theory of the transport and recombination properties of photoexcited carriers in Ge and Si at low temperatures*, J. Phys. C **6** 3097 (1973).
- [5] A. Martinez and J.R. Barker, *Quantum transport in a silicon nanowire FET transistor: hot electrons and local power dissipation*, Materials, **13** (15), 3326-3368 (2020).

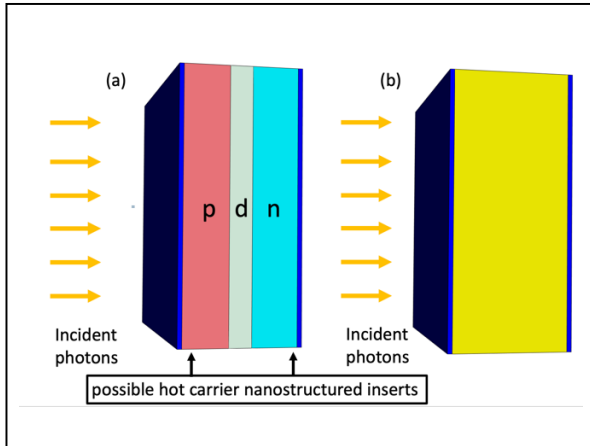


Fig. 1. (a) Schematic of a solar cell; (b) photo-excited compensated semiconductor: trap recombination

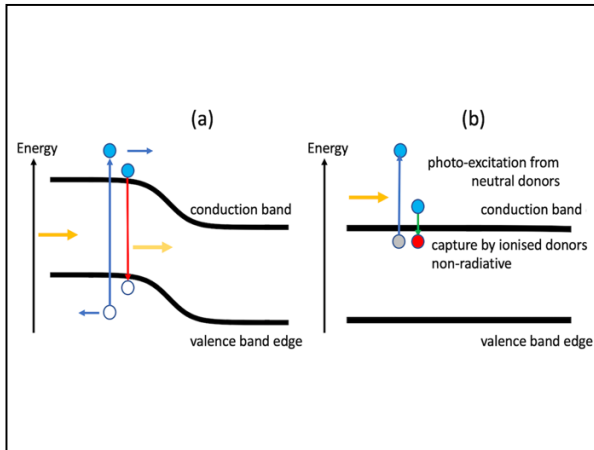


Fig. 2. Band edge profile of (a) solar cell; (b) photo-excited compensated semiconductor

General Coupled Continuity equations for:

n_γ photon density, n_e and n_h electron and hole densities, n_{ph} phonon densities

$$\frac{\partial n_\gamma}{\partial t} + \nabla \cdot \mathbf{j}_\gamma = G_\gamma - R_\gamma$$

$$\frac{\partial n_e}{\partial t} + \nabla \cdot \mathbf{j}_e = G_e - R_e \quad \frac{\partial n_h}{\partial t} + \nabla \cdot \mathbf{j}_h = G_h - R_h$$

$$\frac{\partial n_{ph}}{\partial t} + \nabla \cdot \mathbf{j}_{ph} = G_{ph} - R_{ph}$$

Similarly, the coupled equations for the photon, electron, hole and phonon phase space distribution functions exist with scattering integrals involving

$e - e, e - h, h - h, e - \gamma, h - \gamma, \gamma - \gamma$ - traps/dopants and higher order processes

$e - ph, e h - ph, ph - \gamma, ph - ph, ph - \gamma$ - traps/dopants

STUDY STEADY STATE and SEEK REDUCTION OF THE 6-DIMENSIONAL PHASE SPACE TO LOWER DIMENSIONS

Fig. 3. Coupled system equations

Integral equation for the dimensionless electron energy distribution $F[K]$

$$F[\epsilon_k] \equiv F(K = (\frac{\epsilon_k}{k_B T_{lattice}})^{1/2})$$

$$F(K) = \frac{G(K) + C_{in}[F(K)]}{R(K) + C_{out}(K)}$$

G: Electron photo-excitation rate parameterised by effective photon distribution

R: Electron recombination rate

$F(K)C_{out}(K)$: Electron inelastic phonon scattering - out rate

$C_{in}[F(K)]$: Electron inelastic phonon scattering - in rate

G=R=0 yields the thermalised distribution.

Fig. 4. Energy distribution in a homogeneous region satisfying non-linear Volterra integral equation of second kind

$$C_{in} = C_0 \left\{ \int_{K_1'}^{K_2'} - \int_{K_1''}^{K_2''} \right\} \frac{dK'K'(K^2 - K'^2)}{1 - \exp[K^2 - K'^2]} F(K')$$

$$F(K)C_{out} = C_0 \left\{ \int_{K_1'}^{K_2'} - \int_{K_1''}^{K_2''} \right\} \frac{dK'K'(K^2 - K'^2)}{1 - \exp[K^2 - K'^2]}$$

Fig. 5. Acoustic phonon scattering and boundary conditions.

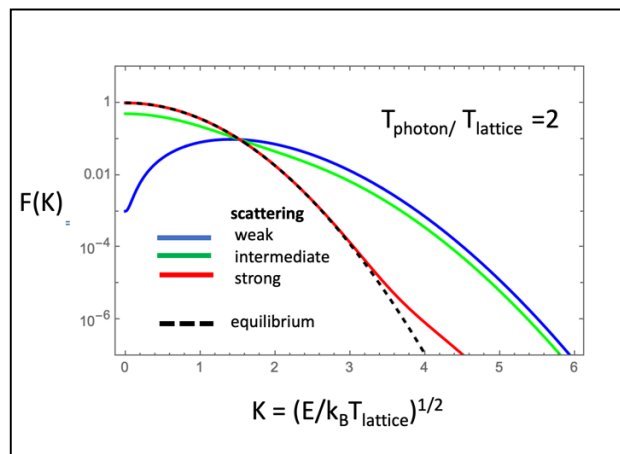


Fig. 6. Energy distributions as a function of recombination and weak to strong energy relaxation parameters.

Breakdown of GaN-based Planar Gunn Diodes investigated through a Combined Deep Learning-Monte Carlo Model

S. García-Sánchez, R. Rengel, S. Pérez, T. González and J. Mateos

Applied Physics Department and NANOLAB, Universidad de Salamanca, Salamanca 37008, Spain
e-mail: sergio_gs@usal.es

ABSTRACT

In this contribution we present a study of GaN Planar Gunn Diodes (PGDs) through a combined deep learning-Monte Carlo (MC) approach. MC simulations will be used to analyze the effect of the leakage current through the buffer, which originates the avalanche breakdown of the diodes due to the onset of impact-ionization (II) phenomena at high-enough voltages. A neural network is then employed to predict the breakdown voltage, thus contributing to optimize the design and reliability of practical GaN PGDs.

INTRODUCTION

The wide bandgap and moderately high mobility of GaN is attracting increasing interest for its use in high-power applications at microwave frequencies [1]. Moreover, given its negative differential mobility, it is being also explored as an interesting material for fabricating high power Gunn diodes. Although only indirect evidence of Gunn oscillations in GaN-based diodes has been experimentally achieved [2,3], MC simulations confirm the possibility of attaining high-power generation in the THz range using PGDs based on highly doped GaN epilayers [4]. However, GaN PGDs fabricated with shaped nanochannels do not display Gunn oscillations, since their breakdown takes place when the applied bias exceeds 20-25V, below the expected threshold for the onset of the oscillations.

MONTE CARLO MODEL AND MAIN RESULTS

A semi-classical ensemble MC tool self-consistently coupled with a two-dimensional (2D) Poisson solver is employed for the simulation of electronic transport in the analyzed structures. II processes are implemented by means of the Keldysh approach. The breakdown voltage V_B at which II mechanisms become relevant is obtained through a model based on a neural network which uses backpropagation, trained with the data obtained from a set of selected MC simulations. This model radically reduces the computational time as compared to MC calculations covering all the possible cases.

Fig. 1(a) sketches the structure of the simulated device, featuring a doped GaN layer with N_D in the range $0.5\text{-}10 \times 10^{18} \text{ cm}^{-3}$. Gunn oscillations are predicted according to our top-view MC simulations, Fig. 1(c). However, when fabricated devices have been characterized, they suffer a catastrophic breakdown before displaying any oscillating behavior. To investigate the origin of the breakdown, in addition to top-view simulations (where electric field hot-spots are observed at the anode corners of the isolating trenches, Fig. 2), we have simulated the lateral cross-section shown in Fig. 1(b). As observed in Fig. 3(a), the electric field reaches values higher than 5 MV/cm at 25 V, also at the same point, but at the bottom corner of the etched trench. Highly energetic electrons, unintentionally leaked across the undoped substrate, are present at that point, Figs. 3(b) and (c), thus leading to II mechanisms, Fig. 3(d). From the data obtained from this type of simulations, our neural network is able to predict the breakdown voltage V_B , determined as the bias at which the average electron energy in the hot spot area surpasses the threshold for the onset of II mechanisms (3.5 eV). Higher values of V_B are predicted by the model for lower N_D and higher permittivity κ_r of the dielectric filling the trenches, as well as at higher T (Fig. 4).

ACKNOWLEDGMENT

This work has been partially supported through grant PID2020-115842RB-I00 funded by MCIN/AEI/10.13039/501100011033.

REFERENCES

- [1] *Power GaN Devices*, edited by M. Meneghini, G. Meneghesso, and E. Zanoni (Springer, Cham, 2017).
- [2] Yilmazoglu O, Mutamba K, Pavlidis D, Karaduman T. *First observation of bias oscillations in GaN Gunn diodes on GaN substrate*, IEEE Trans. Electron Dev. 55, 1563 (2008).
- [3] Hajo AS, Yilmazoglu O, Dadgar A, Küppers F, Kusserow T. *Reliable GaN-based THz Gunn diodes with side-contact and field-plate technologies*, IEEE Access 8, 84116 (2020).
- [4] Garcia-Sanchez S, Íñiguez-de-la-Torre I, Pérez S, González T, Mateos J. *Optimization of the Epilayer Design for the Fabrication of Doped GaN Planar Gunn Diodes*. IEEE Trans. Electron Dev. 69, 514 (2021).

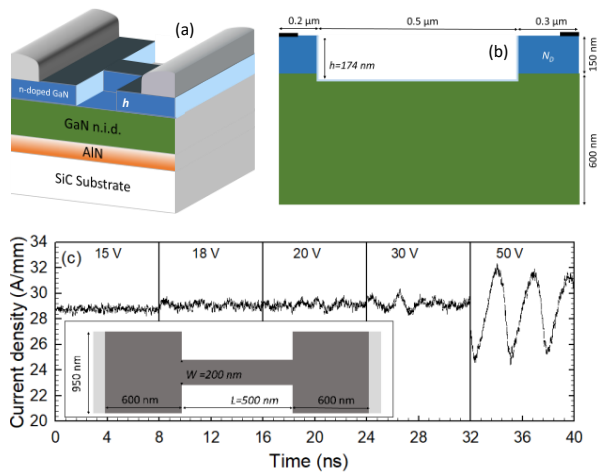


Fig. 1. (a) 3D structure of the simulated device. (b) Longitudinal cut at the etched sides of the channel with an isolation depth of $h=174$ nm. (c) Time-sequence of the current density for $N_D=5 \times 10^{18} \text{ cm}^{-3}$, $\kappa_r=1$ and $T=300$ K for the single channel device shown in the inset.

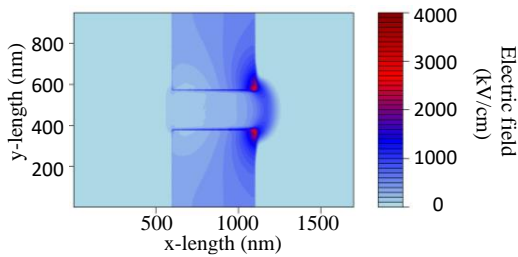


Fig. 2. Map of the electric field modulus obtained with a top-view MC simulation using $N_D=5 \times 10^{18} \text{ cm}^{-3}$, $\kappa_r=1$ and $T=300$ K, for a bias of 25 V.

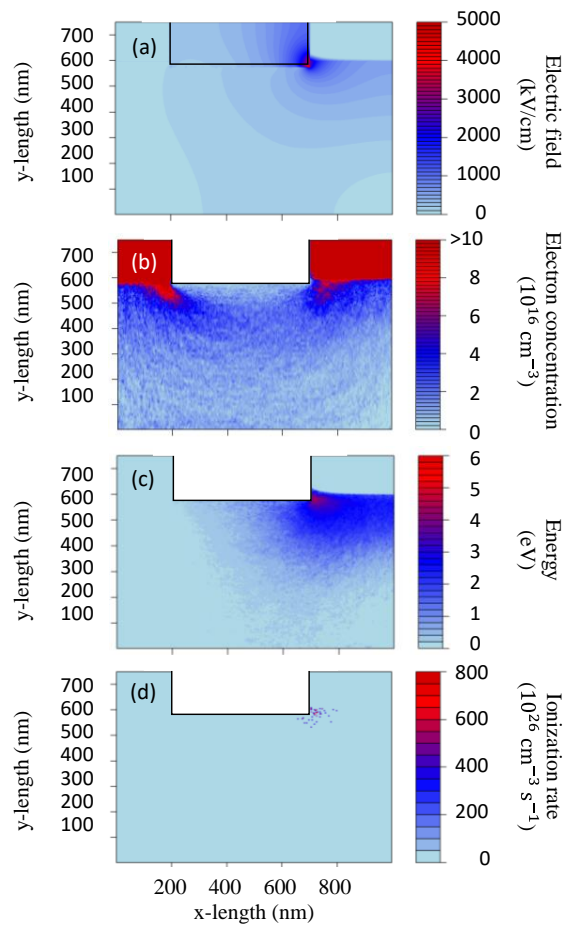


Fig. 3. Maps of (a) electric field modulus, (b) electron concentration, (c) total energy, and (d) II rate obtained with a front-view MC simulation using $N_D=5 \times 10^{18} \text{ cm}^{-3}$, $\kappa_r=1$ and $T=300$ K, for a bias of 25 V.

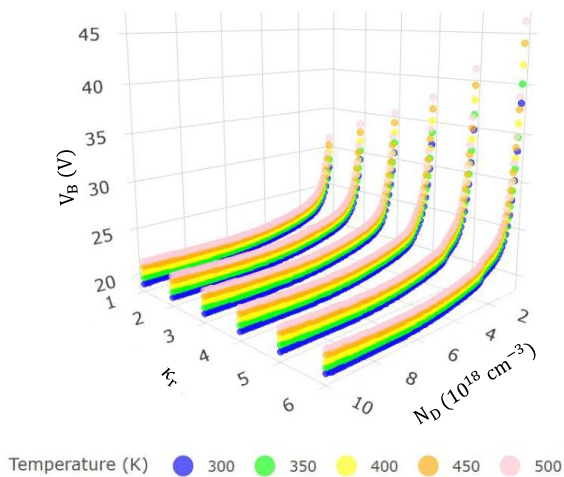


Fig. 4. Dependence of V_B on N_D , κ_r and T obtained with the neural network model.

DECaNT Numerical Tool for Exciton Dynamics in Carbon Nanotube Films

S. S. Sanders, S. W. Belling and I. Knezevic

Department of Electrical and Computer Engineering, University of Wisconsin – Madison
Madison, WI 53706, USA
e-mail: swbelling@wisc.edu

ABSTRACT

Photons incident on carbon nanotube (CNT) films tend to generate tightly bound electron-hole pairs known as excitons. We present a simulation tool for studying exciton diffusion through CNT arrays, based on a microscopic theory of exciton transfer between pairs of CNTs. Utilizing a Monte Carlo algorithm, we can study the diffusion behavior of exciton ensembles based on array properties such as density, composition, and morphology.

INTRODUCTION

Carbon nanotubes are a promising material for several applications, notably including solar-energy harvesting. The process by which solar photons can be converted into useful energy involves absorption by the carbon nanotube, which creates bound electron-hole pairs known as excitons. Excitons must diffuse through the array of CNTs to a harvesting layer, where the electron and hole dissociate and the charge can be captured. The exciton diffusion process is therefore of the utmost importance for understanding the efficiency of energy harvesting in CNT devices. Experimental investigations into exciton diffusion have been fruitful, but here we showcase our unique simulation tool that allows tremendous control over the properties of the CNT array, which can help us to isolate and study the effects of different parameters on exciton diffusion through realistic films [1].

SIMULATION TOOL

We begin the simulation process by generating a realistic 3D array (or “mesh” or “film”) of hundreds to thousands of CNTs. We generate each CNT in several short segments, which are connected with constraints that allow rotation but keep the segments together, like a ball and socket joint. A

group of CNTs is generated and then released from the air into a container of specified size, where they dynamically settle according to Newton’s laws. This dynamic generation process is achieved using the Bullet Physics software library [2]. A snapshot of the mesh generation process is shown in Fig. 1.

We use a Python script to take the coordinates of each tube segment from the mesh generation process and interpolate along the length of each CNT to increase the density of points.

The new set of points, along with the CNT properties (chirality, which determines bandstructure, and relative orientation) are input to a Monte Carlo algorithm. The Monte Carlo code utilizes scattering rates calculated from a detailed microscopic theory [3] of transfer between pairs of CNTs to simulate the movement of thousands of excitons through the array. By studying the aggregate behavior, we discover the diffusion properties of excitons throughout the array. In Fig. 2, we show the diffusion-tensor elements for an array of hundreds of CNTs with a single chirality (this particular chirality is commonly denoted as [4,2]). We note that there is about one order of magnitude difference between in-plane and out-of-plane diffusion constants.

Our mesh generation tool allows us to control several variables—such as film thickness, intertube spacing (Fig 3.) dielectric environment, and array morphology—and study their effect on exciton diffusion. The simulation tool is open source and free to use.

ACKNOWLEDGMENT

This work was primarily funded by the DOE BES award DE-SC0008712. Additional funding was provided by the Splinter Professorship.

REFERENCES

- [1] S. W. Belling, Y. C. Li, A. H. Davoody, A. J. Gabourie, and I. Knezevic, *DECaNT: Simulation tool for diffusion of excitons in carbon nanotube films*, *J. Appl. Phys.* **129**, 084301 (2021)
- [2] E. Coumans, “Bullet Physics Library,” <http://bulletphysics.org> (2020)
- [3] A. H. Davoody, F. Karimi, M. S. Arnold, I Knezevic, “Theory of Exciton Energy Transfer in Carbon Nanotube Composites,” *J. Phys. Chem. C* **120**, 16354-16366 (2016)

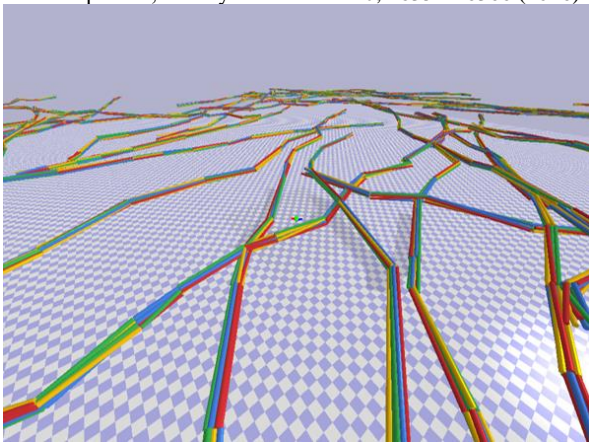


Fig. 1. Snapshot of the CNT mesh generation process using Bullet Physics [1-2]. Each CNT is composed of several segments that are connected together via cone constraints.

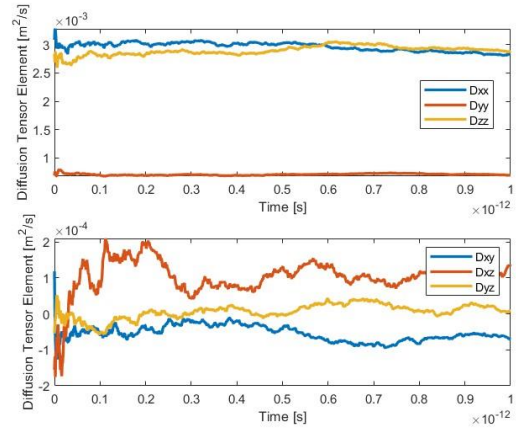


Fig. 2. Mean squared displacements vs. time for each of the components of the diffusion tensor. The diffusion tensor is the long time limit of these plots.

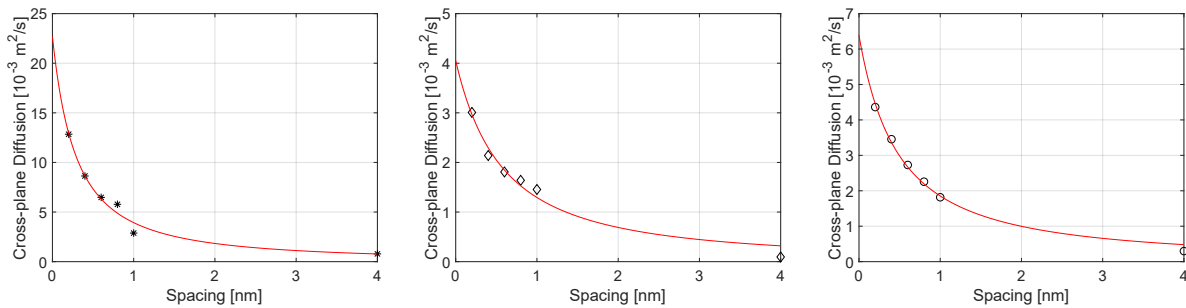


Fig. 3. Effect of additional intertube spacing on cross-plane diffusion constants for three different morphologies of CNT array. Parallel refers to aligned CNTs, “Single Random” refers to randomly oriented unbundled CNTs, and “Bundled Random” refers to randomly oriented bundles of seven CNTs (hexagonally packed) [1].

Efficient Monte Carlo Electron Transport Formalism for Highly Nanostructured Materials

Pankaj Priyadarshi and Neophytos Neophytou

School of Engineering, University of Warwick, Coventry, CV4 7AL, United Kingdom

e-mail: pankaj.priyadarshi@warwick.ac.uk

INTRODUCTION

Nanomaterials and nanostructures are typical in many technologies. One category of benefiting from nanostructuring is thermoelectric (TE) materials [1]. New-generation TE materials are typically highly nanostructured, with the nano-features spanning from macro- to nano-scale (including boundaries, potential barriers, pores, nanoinclusions, atomic defects, second-phasing, etc.) (Fig. 1a, 2a). To theoretically evaluate carrier transport in these cases, a common method is the solution of Boltzmann transport equation (BTE) stochastically using the Monte Carlo (MC) method. However, existing MC methods have many limitations in this setting, the most severe being the huge challenge to gather statistics from two opposite going fluxes under linear response (Fig. 1b) [2]. To make things worse, as geometry complexity increases the simulation time increases exponentially (Fig. 2b). Here we develop an efficient MC transport algorithm tuned specifically for complex nanostructures under linear response.

SIMULATION FORMALISM

Our novel method uses a single-injected flux from the left of the domain only, which traverses through the channel with consecutive free-flight and scattering events (Fig. 3), and stochastically provides the typical flight time (ToF). The ToF is used for the flux calculation (eq. 1) and then the transport distribution function (TDF) (eq. 2), which then evaluates conductivity (eq. 3) as [2].

$$F(E) = \frac{1}{\langle \text{ToF}(E) \rangle} \quad (1)$$

$$\Xi(E) = F(E) \times \text{DOS} \quad (2)$$

$$\sigma = q^2 \int_E \Xi(E) \cdot \left(-\frac{\partial f}{\partial E} \right) \cdot dE \quad (3)$$

Compared to common MC algorithms, our method has the following differences: (i) we employ a mean-free-path approach (mfp), where the carriers scatter definitively after every mfp,

rather than using self-scattering events, thus avoiding the large number of scattering events for low velocity, low energy carriers (Fig. 3). (ii) We map the particle flux from MC to the analytical TDF under acoustic phonon scattering conditions (ADP), thus avoiding the need for super-electron charges and peculiarities in simulating a 2D vs. a 3D channel. Under ADP the TDF is linear, and that is what we capture in our MC flux as well (Fig. 4, 5). The mapping is done using a single constant C (Fig. 6, inset), which maps the conductivities and the TDF. (iii) We use only one flux and mimic the flux differences and applied fields with the df/dE term in BTE, thus avoiding the difficulty in subtracting two opposite fluxes (Fig. 4, red line). Note that this is particularly useful for the Seebeck coefficient where not only the difference of left/right going fluxes needs to be resolved, but simultaneously the ones that flow above/below the Fermi level (Fig. 5, red line).

We have computed the conductivity in Fig. 6 for a pristine channel, a channel with pores, a channel with grain boundaries, and a channel with both nano-features. The latter result is as predicted from Matthiessen's rule using the first two nanostructured channel simulations. We estimated at least an order of magnitude computational savings compared to the current methods.

CONCLUSION

We developed an efficient MC algorithm by overcoming limitations of existing MC methods, tuned specifically for the electronic transport in complex nanostructures under linear response.

REFERENCES

- [1] D. Beretta, et. al. *Thermoelectrics: From history, a window to the future*, Mat. Sci. and Eng.: Reports. **138**, 100501 (2019).
- [2] P. Priyadarshi and N. Neophytou, Computationally efficient Monte Carlo electron transport algorithm for nanostructured thermoelectric material configurations, *Journal of Applied Physics*. **133**, 054301 (2023).

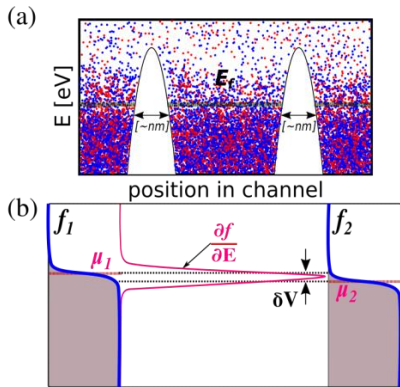


Fig. 1. (a) MC ensemble particles in a nanostructured domain. (b) Energy derivative of the Fermi distribution, which mimics by a small applied potential δV in low-field transport conditions.

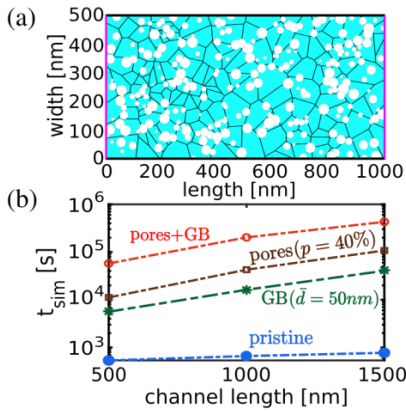


Fig. 2. (a) Complex nanostructured domain populated with grain boundaries and nanoporous features. (b) Simulation time versus device channel length of various nano-featured 2D domains.

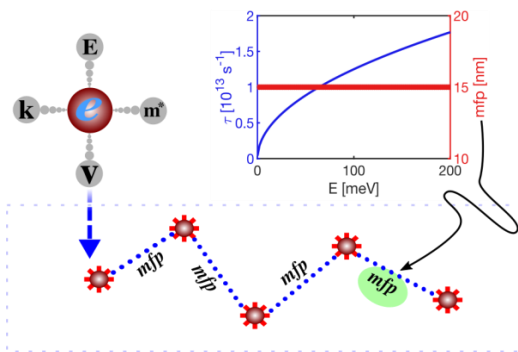


Fig. 3. Developed MC algorithm: need electron parameters, their mean free path, which is constant under ADP scattering.

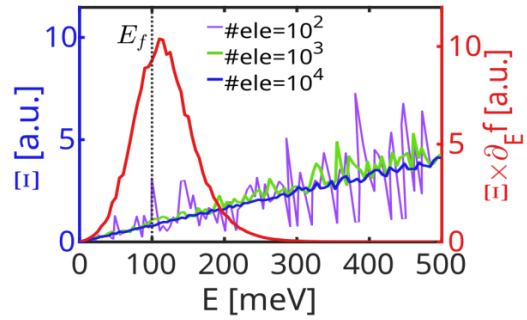


Fig. 4. Transport distribution function, $\Xi(E)$, calculated stochastically using the MC algorithm. The red line (right axis) shows the product of $\Xi(E)$ and the differential Fermi function with respect to energy $\partial f / \partial E$ (the case of 10^4 electrons).

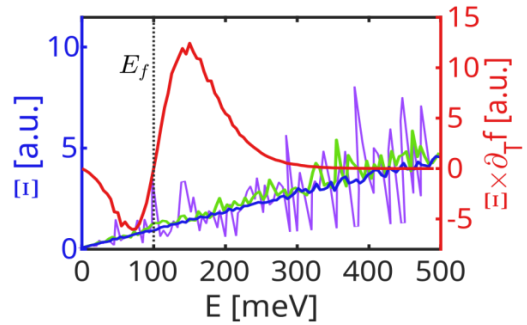


Fig. 5. Transport distribution function using the MC algorithm. The red line (right axis) shows the product of $\Xi(E)$ and the differential Fermi function with respect to temperature $\partial f / \partial T$ (shown for the case of 10^4 electrons).

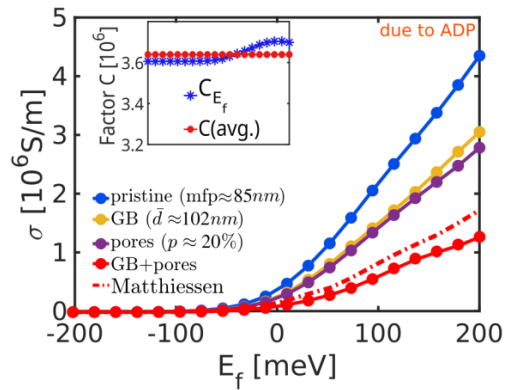


Fig. 6. Electrical conductivity calculated from the MC algorithm in nanostructured material domains populated with grain boundaries, pores, and the combination of both versus the Fermi energy. The red-dotted line shows the calculated conductivity using Matthiessen's rule. Inset: mapping of the analytical to the simulated conductivity.

Thermal and electrical properties of nanocrystalline superionic $\text{Na}_x\text{Cu}_{1.75}\text{S}$ ($x=0.1, 0.15, 0.2, 0.25$) compounds

M.M. Kubenova*, K.A. Kuterbekov, M.Kh. Balapanov, A.M. Kabyshev, K.Zh. Bekmyrza, Zh.A. Mukhan and A.K. Kulanov
L.N. Gumilyov Eurasian National University, 010008 Astana, Kazakhstan
e-mail: kubenova.m@yandex.kz

The paper presents the results of the studies of thermal properties of nanocrystalline superionic $\text{Na}_x\text{Cu}_{1.75}\text{S}$ ($x = 0.1, 0.15, 0.2, 0.25$) compositions, and preliminary results of $\text{Na}_{0.1}\text{Cu}_{1.75}\text{S}$ using as energy stored cathode material in Na-ion half-cell with NaPF_6 electrolyte and Na anode. The compositions contain a few copper sulfide phases: monoclinic chalcocite Cu_2S , orthorhombic anilite $\text{Cu}_{1.75}\text{S}$, triclinic roxbyite $\text{Cu}_{1.74\pm 1.82}\text{S}$, also the compositions can contain monoclinic $\text{Na}_2\text{Cu}_4\text{S}_3$, orthorhombic Na_2S , cubic Cu_2O as inclusion phases. The sizes of powder particles lie in the range from 10 to 113 nm. Differential scanning calorimetry revealed in $\text{Na}_{0.1}\text{Cu}_{1.75}\text{S}$ the endothermic thermal effects with critical temperatures near 123 °C, 422 °C and 442 °C, caused by structural transitions in copper sulfide. Fourth endothermic peak at 323 °C presumably belongs to Na_2S phase. The minimum for the Fermi level at about 420°C is found with using of the e.m.f. E of the electrochemical cell of the $\text{Cu}/\text{CuBr}/\text{Na}_{0.10}\text{Cu}_{1.75}\text{S}/\text{Pt}$, which corresponds to minimum for the carrier concentration. This conclusion correlates well with the observed conductivity minimum at about 410°C. Electrode material $\text{Na}_{0.10}\text{Cu}_{1.75}\text{S}$ achieved a significant specific energy density 146.5 mAh/g in half-cell assembled from the cathode active material, electrolyte (NaPF_6 in 0.5 mol PC) and Na anode.

The results of X-ray phase analysis of the $\text{Na}_{0.15}\text{Cu}_{1.75}\text{S}$, $\text{Na}_{0.20}\text{Cu}_{1.75}\text{S}$ and $\text{Na}_{0.25}\text{Cu}_{1.75}\text{S}$ samples were described in our recent work [1-3], except for the $\text{Na}_{0.10}\text{Cu}_{1.75}\text{S}$ sample. For example, the powder X-ray diffraction pattern of the $\text{Na}_{0.15}\text{Cu}_{1.75}\text{S}$ sample taken at room temperature is shown in Figure 1 a. This alloy contains next phases: triclinic roxbyite, orthorhombic anilite, monoclinic $\text{Na}_2\text{Cu}_4\text{S}_3$, cubic Cu_2O . Analysis of the

spectrum of Figure 1 a revealed that the main phase of $\text{Na}_{0.15}\text{Cu}_{1.75}\text{S}$ sample is the triclinic roxbyite $\text{Cu}_{1.8125}\text{S}$ with space group P and cell parameters, $a = 13.4051(9)$ Å, $b = 13.4090(8)$, $c = 15.4852(3)$ Å, $\alpha = 90.022(2)^\circ$, $\beta = 90.021(2)^\circ$, $\gamma = 90.020(3)^\circ$.

ACKNOWLEDGMENT

This research was funded by the Science Committee of the Ministry of Science and Higher Education of the Republic of Kazakhstan (No. AP14871197).

REFERENCES

- [1] K.A. Kuterbekov et al., *Ionics* **28** (2022) 4311-4319
- [2] M.M. Kubenova et al., *Nanomaterials* **11**(9) (2021) 2238.
- [3] M.M. Kubenova et al., *Eurasian Journal of Physics and Functional Materials* **7**(1) (2023) 60-72

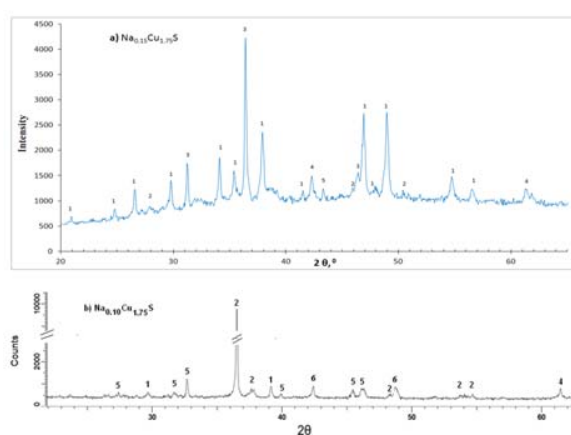


Figure 1. Powder diffraction pattern of the $\text{Na}_{0.15}\text{Cu}_{1.75}\text{S}$ (a), $\text{Na}_{0.10}\text{Cu}_{1.75}\text{S}$ (b) samples taken at room temperature. Digits above pikes denotes: 1- triclinic roxbyite, 2-orthorhombic anilite, 3- monoclinic $\text{Na}_2\text{Cu}_4\text{S}_3$, 4-cubic Cu_2O , 5-monoclinic chalcocite Cu_2S , 6-orthorhombic Na_2S .

Extending the small-signal modeling of GFETs to ambipolarity regime

Nikolaos Mavredakis, Anibal Pacheco-Sanchez, David Jiménez

N. Mavredakis, A. Pacheco and D. Jiménez are with the Departament d'Enginyeria Electrònica, Escola d'Enginyeria, Universitat Autònoma de Barcelona, Bellaterra 08193, Spain. (e-mail: Nikolaos.mavredakis@uab.cat).

1. Abstract

Analog/RF circuit design with Graphene field-effect transistor (GFET) technology, continually grows due to exceptional extrinsic maximum oscillation (f_{\max}) and cut-off frequencies (f_t), recorded for the specific device [1]. We have recently proposed an efficient small-signal GFET parameter extraction procedure, targeting on Quasi-Static regime [2]. Our methodology is based on a charge-based model [3] which ensures charge conservation in the intrinsic device. Both the bias- and frequency- dependence of the total of small-signal parameters have been accurately validated with experiments from a short-channel RF CVD GFET [4], up to 18 GHz for a unipolar (p-type) region of operation. In the present study, the complete ambipolar small-signal response of short-channel GFETs [5], [6] is demonstrated, including the charge neutrality point or Dirac voltage (V_{Dirac}), with remarkable agreement between models and experiments. The bias region around V_{Dirac} is of outmost significance in certain applications of ambipolar devices such as GFET, as it can ensure multifunctionality [7].

2. DUT and Measurement Setup

High frequency measurements are conducted in the present work for two short-channel back-gated RF CVD GFETs with gate width $W=12 \times 2 \mu\text{m}$ (number of gate fingers:2) and gate length $L=200 \text{ nm}$, 300 nm , respectively [5], [6]. They are fabricated by the same group as the device studied in [2], but from a different technology process and thus, they present dissimilar characteristics such as higher contact resistance R_C . They have also been examined in terms of thermal noise experimental characterization and modelling at 1 GHz [6]. In the current work, $S(Y)$ parameters are measured and small-signal parameters are investigated after appropriate de-embedding and R_C -gate resistance R_G elimination procedures [8], [2], [6] up to or even above f_t . Details on the devices' schematics and measurement setups can be found in [5], [6].

3. Results and Discussions

The small-signal sub-circuit model employed in this study, has been presented elsewhere [2 (Fig. 1a)]. As a first step of this work, IV model parameters are extracted, similarly as in [2], for both devices under test

(DUT), and presented in Table I; μ is the carrier mobility, C_{back} the back-gate capacitance, Δ the inhomogeneity of the electrostatic potential, related to the residual charge, u_{sat} the saturation velocity while the rest of the parameters (V_{Dirac} , R_C , R_G) have already been defined. Magnitude and phase of all the measured S_{DEV} parameters for both DUT at a drain voltage $V_{\text{DS}}=0.5 \text{ V}$, are presented vs. V_{GS} at 1 GHz (cf. Fig. 1) and vs. frequency at two V_{GS} values (cf. Fig. 2), near and exactly at V_{Dirac} point, respectively ($V_{\text{GS}}=0.3, 0.5 \text{ V}$ for $L=200 \text{ nm}$, $V_{\text{GS}}=0.4, 0.6 \text{ V}$ for $L=300 \text{ nm}$). The consistency of the extracted models is also highlighted from p- to n-type region including V_{Dirac} , while observed disparities at higher frequencies (cf. Fig. 2) arise from non-quasi-static (NQS) effects due to low f_t of the devices [9]. The recorded model agreement with experiments at V_{Dirac} is prerequisite for reliable circuit design in RF GFET applications such as phase/frequency configurable amplifiers, frequency doublers, in-phase power and inverting amplifiers, which operate near or at the specific neutrality point [7]. Inconsistencies observed in the magnitude of $S_{21\text{DEV}}$ at n-type region are due to measurement asymmetries between hole and electron branches, and can be accounted by considering distinct models for the two conductance regimes [9].

After rigorous removal of $R_{C,G}$ contributions, intrinsic small-signal parameters of the DUT, such as capacitances C_{GG} , C_{GD} , C_{DG} , cut-off frequency f_{INT} , and small-signal current gain $|h_{21\text{INT}}|$, can be extracted [2]. Other significant extrinsic figures of merit, such as f_{EX} , $|h_{21\text{EXT}}|$, and unilateral power gain U , can also be derived directly from de-embedded $S(Y)_{\text{DEV}}$ measurements [2]. C_{GG} , C_{GD} , C_{DG} (cf. Fig. 3), $f_{\text{INT,EX}}$, f_{max} (cf. Fig. 4), and $|h_{21\text{INT,EX}}|$, U (cf. Fig. 5), are depicted for both DUT at 1 GHz for $V_{\text{DS}}=0.5 \text{ V}$, vs. V_{GS} where the models capture precisely the experiments, especially around V_{Dirac} , which is of special interest in the current analysis. Intrinsic capacitances present a minimum at V_{Dirac} and afterwards, increase towards higher carrier densities. Besides, $f_{\text{INT,EX}}$, f_{max} , $|h_{21\text{INT,EX}}|$, U parameters follow an M-shape trend with a minimum at V_{Dirac} while, they are significantly reduced (for the $L=300 \text{ nm}$ device) in comparison with a GFET with same L but much lower R_C in [2]. The latter highlights the negative effect of R_C on small-signal parameters and thus, justifies the aforementioned NQS effects below 5 GHz (cf. Fig. 2).

Table 1. IV extracted parameters

Parameter	Units	L=200 nm	L=300 nm
μ	$\text{cm}^2/(\text{V}\cdot\text{s})$	200	170
u_{sat}	m/s	7×10^5	7×10^5
C_{back}	$\mu\text{F}/\text{cm}^2$	1.87	1.87
V_{Dirac}	V	0.5	0.6
R_c	Ω	130	180
R_G	Ω	18	12
Δ	meV	150	165

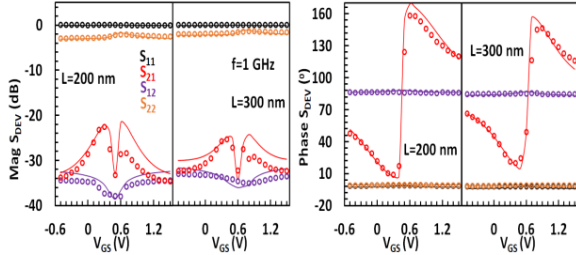


Fig. 1. Magnitude (left plot) and phase (right plot) of de-embedded S-parameters (S_{DEV}) for two GFETs with gate width $W=24 \mu\text{m}$ and length $L=200$ nm (left subplots), $L=300$ nm (right subplots) vs. gate voltage V_{GS} for operation frequency $f=1$ GHz at a drain voltage $V_{\text{DS}}=0.5$ V. Markers: measurements, lines: model.

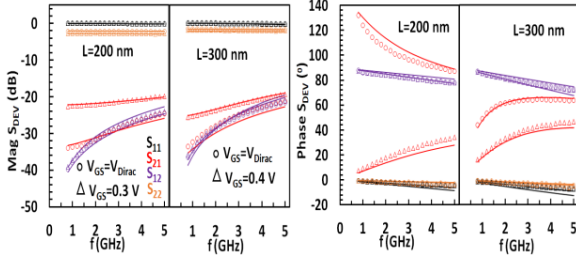


Fig. 2. Magnitude (left plot) and phase (right plot) of de-embedded S_{DEV} for two GFETs with $W=24 \mu\text{m}$ and $L=200$ nm (left subplots), $L=300$ nm (right subplots) vs. f for two V_{GS} values; near and at Dirac Voltage at $V_{\text{DS}}=0.5$ V. Markers: measurements, lines: model.

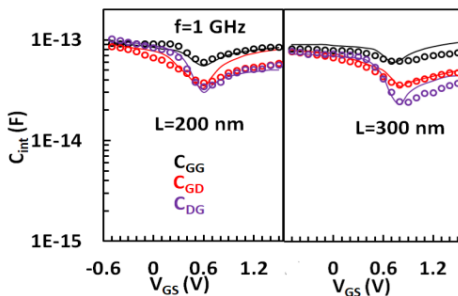


Fig. 3. Intrinsic capacitances C_{GG} , C_{GD} , C_{DG} , respectively for two GFETs with $W=24 \mu\text{m}$ and $L=200$ nm (left subplot), $L=300$ nm (right subplot) vs. V_{GS} for $f=1$ GHz at $V_{\text{DS}}=0.5$ V. Markers: measurements, lines: model.

Acknowledgements

This work has received funding from the European Union's Horizon 2020 research and innovation programme under grant agreement No GrapheneCore3 881603 and from Ministerio de Ciencia, Innovacion y Univer- sidades under grant agreements RTI2018-097876-B-C21(MCIU/AEI/FEDER, UE), FJC2020-046213-I and PID2021-127840NB-I00 (MCIN/AEI/FEDER, UE).

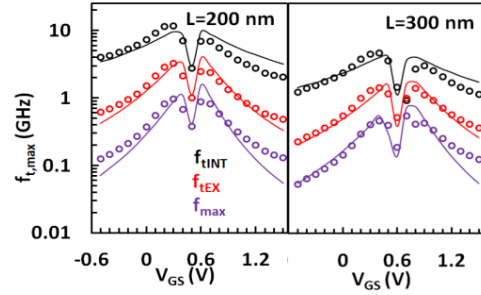


Fig. 4. Intrinsic, extrinsic cut-off and extrinsic maximum oscillation frequencies f_{INT} , f_{EXT} , f_{max} , respectively for two GFETs with $W=24 \mu\text{m}$ and $L=200$ nm (left subplot), $L=300$ nm (right subplot) vs. V_{GS} at $V_{\text{DS}}=0.5$ V. Markers: measurements, lines: model.

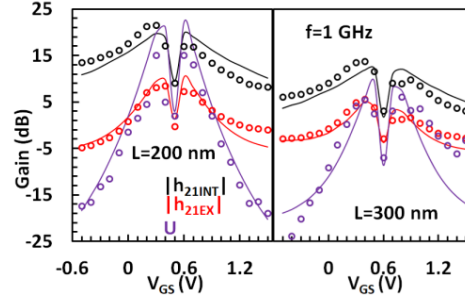


Fig. 5. Intrinsic, extrinsic small-signal current gain and unilateral power gain $|h_{21\text{INT}}|$, $|h_{21\text{EX}}|$, U , respectively for two GFETs with $W=24 \mu\text{m}$ and $L=200$ nm (left subplot), $L=300$ nm (right subplot) vs. V_{GS} for $f=1$ GHz at $V_{\text{DS}}=0.5$ V. Markers: measurements, lines: model.

References

- [1] M. Saeed, P. Palacios, M. D. Wei, E. Baskent, C. Y. Fan, B. Uzlü, K. T. Wang, A. Hemmetter, Z. Wang, D. Neumaier, M. C. Lemme, and R. Negra, *Adv. Mater.*, vol. 34(48), 2108473, 2022.
- [2] N. Mavredakis, A. Pacheco-Sanchez, W. Wei, E. Pallecchi, H. Happy, and D. Jiménez, *Microelectronics J.*, vol. 133, 105715, 2023.
- [3] F. Pasadas, P. C. Feijoo, N. Mavredakis, A. Pacheco-Sanchez, F. A. Chaves, and D. Jiménez, *Adv. Mater.*, vol. 34(48), 2201691, 2022.
- [4] W. Wei, D. Fadil, E. Pallecchi, G. Dambrine, H. Happy, M. Deng, S. Fregonese, and T. Zimmer, in *Proc. IEEE Int. Conf. Noise Fluctuations (ICNF)*, Vilnius, Lithuania, 2017.
- [5] W. Wei, X. Zhou, G. Deokar, H. Kim, M. M. Belhaj, E. Galopin, E. Pallecchi, D. Vignaud, and H. Happy, *IEEE Trans. Electron Devices*, vol. 62(9), pp. 2769-2773, 2015.
- [6] N. Mavredakis, A. Pacheco-Sanchez, P. Sakalas, W. Wei, E. Pallecchi, H. Happy and D. Jiménez, *IEEE Trans. on Microw. Theory Tech.*, 69(11), pp. 4639-4646, 2021.
- [7] A. Pacheco-Sanchez, J. N. Ramos-Silva, N. Mavredakis, E. Ramirez-Garcia, and D. Jiménez, in *proc. IEEE Conf. on Design of Circuits and Integrated Circuits (DCIS)*, Pamplona, Spain, 2022.
- [8] J. N. Ramos-Silva, A. Pacheco-Sánchez, M. A. Enciso-Aguilar, D. Jiménez, and E. Ramirez-Garcia, *Semicond. Sci. Technol.*, vol. 35(4), 045024, 2020.
- [9] J. D. Aguirre-Morales, S. Fregonese, C. Mukherjee, W. Wei, H. Happy, C. Maneux, and T. Zimmer, *IEEE Trans. Electron Devices*, vol. 64(10), pp. 4302-4309, 2017.

Simulation-based Optimization of a Sensor-Indenter System for Thin Layer Crack Detection

F. Tremmel, O. Nagler, C. Kutter¹, and R. Holmer²

Infineon Technologies AG, Am Campeon 1-15, 85579 Neubiberg, Germany

¹Polytronic Systems (EMFT) Institute of Physics, UniBw München, Germany

²Faculty of Electrical Engineering and Information Technology, OTH Regensburg, Germany
e-mail: florian.tremmel@infineon.com

INTRODUCTION

Every semiconductor device is tested for its functionality on wafer level before further processing. Therefore, metal pads on the wafer surface are mechanically contacted with elastic contact springs to provide an electrical connection to external test instruments. The ongoing shrinking of semiconductor structures has increased the risk of generating cracks in brittle layers below the contact pads by applying too much pressure.

The *Infineon Technologies AG* has invented a new method to define the contact force limits during wafer testing [1]. Cracks are generated and acoustically detected with a patented sensor-indenter system (SI system) [2] in situ.

As the released energy of sub-micron cracks is extremely small, the sensitivity of the SI system needs to be as high as possible. This is achieved by analyzing and optimizing the system with a digital twin and simulation studies. To find out the necessary sensor sensitivity, the deflections, which the indenter tip experiences during a crack, are estimated with a laser vibrometer.

SIMULATION & MEASUREMENT RESULTS

The SI system (Fig. 1a) consists of two main components – a steel indenter with a diamond tip and a piezoelectric acoustic sensor (*Vallen VS900-M*). Different to the design of the commercial sensor the indenter geometry is manufactured on custom specifications (*Synton-MDP AG*).

Fig. 1b shows a 3D simulation model of the system in ANSYS that was developed and verified by comparing measurement and simulation results. The corresponding measurement setup (Fig. 2) uses an ultrasound emitter to provide defined excitation signals and records the sensor response. With the setup the frequency characteristic and pulse response of the SI system can be analyzed.

Varying the indenter length causes a shift of the main resonance peak in the simulated frequency characteristics (Fig. 3). This peak is caused by the first longitudinal eigenmode of the indenter.

By moving the indenter peak to frequencies with the highest sensitivity of the sensor component, the SI system can be optimized. Fig. 4 shows measurement and simulation results of adjusted indenter peaks at 125kHz (10mm indenter length) and 300kHz (4.1mm indenter length).

SENSITIVITY ANALYSIS

Using the optimized 10mm indenter, cracks produce a sensor amplitude between 0.1mV and 5mV. With an ultrasound emitter (Fig. 2) similar pulse responses have been created by varying the excitation voltage in the range of 0.15V and 7.5V. Measuring the surface deflection of the ultrasound emitter with a laser vibrometer (Fig. 5) leads to values between 0.02nm and 0.68nm (Fig. 6). The deflections caused by thin brittle layer cracks are estimated to be in the same range.

CONCLUSION

With help of FEM simulation the frequency behavior of a sensor-indenter system was analyzed. The impact of the indenter length on the frequency characteristic was predicted and proven with measurement results.

The sensitivity of the system was determined using an ultrasound emitter to recreate the pulse excitation of the SI system by the semiconductor layer cracks. The emitter and thereby also the crack deflections are in the sub-nanometer range.

REFERENCES

- [1] M. Unterreitmeier, *Contact related Failure Detection of Semiconductor Layer Stacks using an Acoustic Emission Test Method*, Erlangen: FAU University Press, 2020.
- [2] O. Nagler, S. Bernrieder and M. Unterreitmeier, *System and Method for Examining Semiconductor Substrates*, United States Patent US 10,859,534 B2, 8 December 2018.

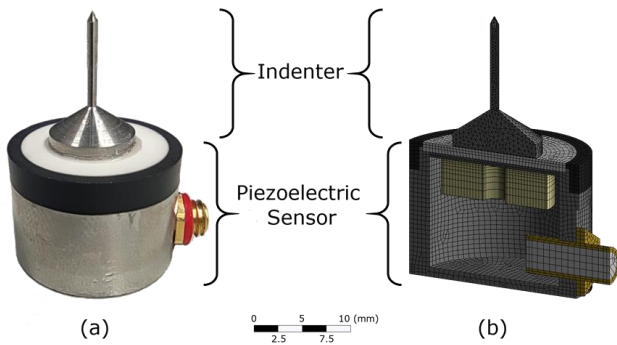


Fig. 1. Sensor-Indenter System – (a) Real Device and (b) Simulation Model (Cut Open)

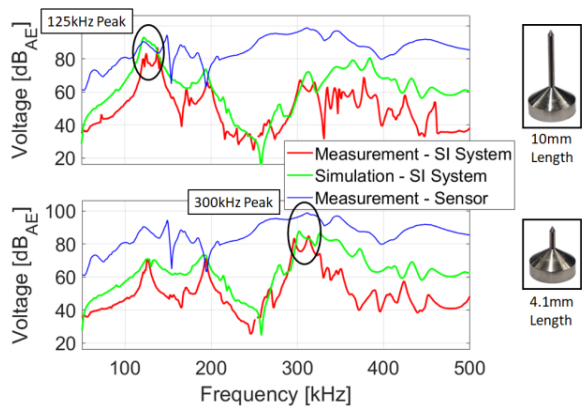


Fig. 4. Comparison between Simulated and Measured Frequency Characteristics with Adjusted Indenter Length

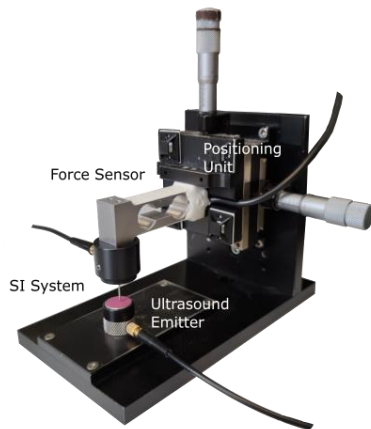


Fig. 2. Measurement Setup with Ultrasound Emitter for SI System Characterization

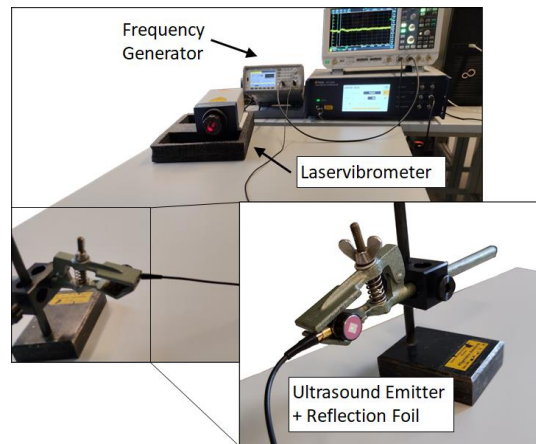


Fig. 5. Laser Vibrometer Setup to Analyze the Ultrasound Emitter Deflection

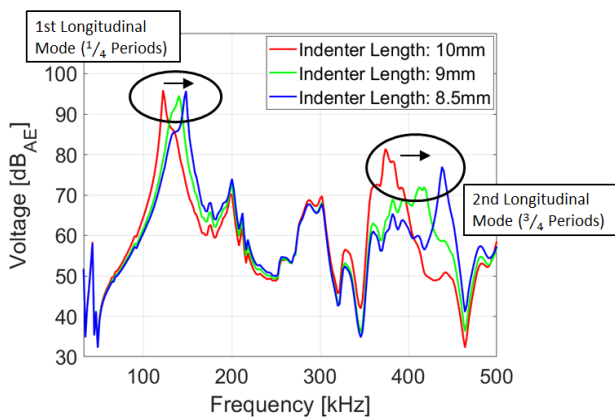


Fig. 3. Simulated Frequency Characteristics of the SI System with Varied Indenter Length

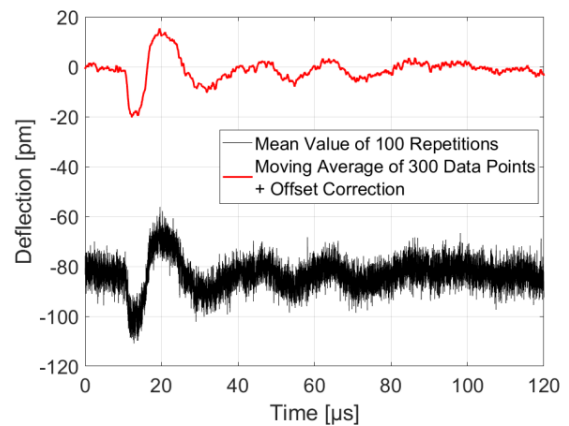


Fig. 6. Measured Ultrasound Emitter Deflection for 180mV excitation voltage (625MHz Sample Rate)

Functionalized TaS₂ for thermoelectric applications: an ab-initio investigation

Francesco Siddi*, Antonio Cappai, Luciano Colombo and Claudio Melis

Department of Physics, University of Cagliari, Italy

*e-mail: francesco.siddi@dsf.unica.it

INTRODUCTION

Thermoelectricity (TE) is a very promising field of research where wasted heat is converted into electricity through the Seebeck effect. The TE efficiency is closely connected to the dimensionless figure of merit ZT that can be written as (1)

$$ZT = \frac{\sigma S^2}{k} T \quad (1)$$

ZT depends on the electrical conductivity (σ), the Seebeck coefficient (S) and inversely on the thermal conductivity (k). Therefore, efficient TE materials should have high σ and S , and low k . In this scenario, many efforts are currently ongoing to optimize ZT by increasing S and and/or by reducing k .

Among different strategies, 2D materials show promising features for TE applications due to their relatively high electronic conduction properties [1]. However, 2D materials still exhibit large thermal conductivities, hindering their possible TE applications. For this reason, great efforts have been recently devoted to reduce their thermal conductivity. A recent experimental study [2] showed that the 2D TaS₂ functionalization with specific covalently-bonded organic side-chains (CBOs) leads to a drastic thermal conductivity reduction without affecting the electronic properties. However, the role of the CBOs in affecting k has not fully yet been clarified. The focus of this work is to investigate this system by proposing a model that comprehensively explains the reduction of thermal conductivity.

METHODS

All the calculations have been performed by means of first principles DFT calculations using the Quantum Espresso package[3]. The characterization of the vibrational and thermal properties

has been performed by means of the Alamode package[4]. The thermal conductivity is obtained using the Boltzmann Transport Equation within the Relaxation Time Approximation (BTE-RTA).

CONCLUSIONS

The calculations showed a dramatic TaS₂ thermal conductivity reduction upon the CBOS functionalization. We attribute such a significant reduction to i) the increase of the TaS₂ inter-layer separation and ii) the role of CBOs as thermal energy-sinks. We finally explore the use of longer and/or chemically different CBOs to further reduce the thermal conductivity of 2D materials therofre increasing the overall ZT .

ACKNOWLEDGMENTS

Francesco Siddi acknowledges that this publication was produced while attending the PhD programme in Physics at the University of Cagliari, Cycle XXXVIII, with the support of a scholarship financed by the Ministerial Decree no. 351 of 9th April 2022, based on the NRRP - funded by the European Union - NextGenerationEU - Mission 4 "Education and Research", Component 1 "Enhancement of the offer of educational services: from nurseries to universities" - Investment 4.1 "Extension of the number of research doctorates and innovative doctorates for public administration and cultural heritage".

REFERENCES

- [1] J. Wu et al. *erspectives on Thermoelectricity in Layered and 2D Materials*, advanced electronic materials, (2018).
- [2] S. Wang et al. *Organic covalent modification to improve thermoelectric properties of TaS₂*, nature communication, (2022).
- [3] P.Giannozzi et al., *Condens.Matter* 21, (2009).
- [4] T. Tadano et al., *Condens.Matter* 26 , (2014).

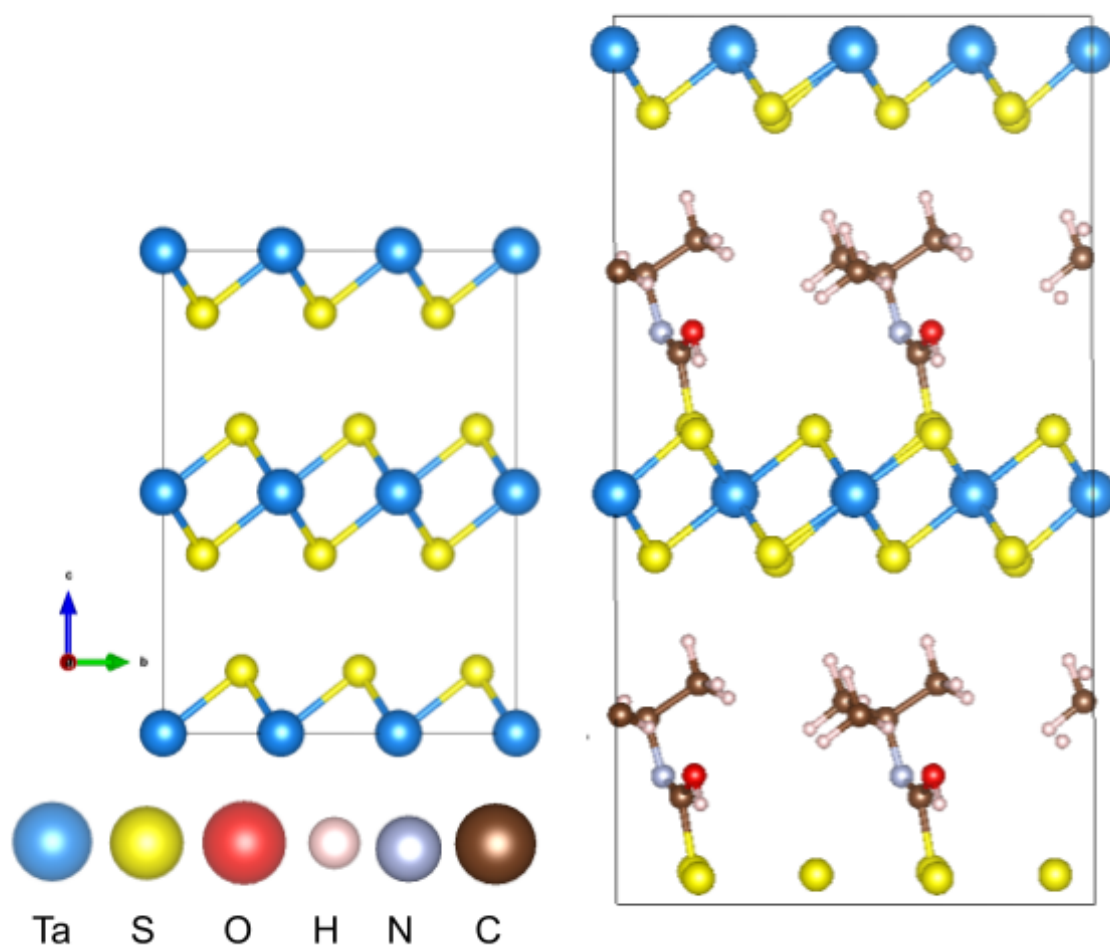


Fig. 1. Left: pristine 2D structure of TaS₂.
Right: CBOSSs-functionalized TaS₂ structure

Monte Carlo Solution to Excess Noise and Spatial Blur in Amorphous Selenium Thin-films

Dragica Vasileska*, Atreyo Mukherjee†, and Amir H. Goldan‡

*School of Electrical, Computer and Energy Engineering, Arizona State University, AZ, US

†Department of Electrical Engineering, Stony Brook University, NY, US

‡Department of Radiology, Weill Cornell Medical College, Cornell University, New York, NY, USA
e-mail: vasileska@asu.edu

Amorphous selenium (*a*-Se) is emerging as a viable solid-state imager with avalanche gain for low-light and low-dose radiation detection applications. [1] At high electric fields, hole transport in *a*-Se can be shifted entirely from localized to extended states, resulting in deterministic and non-Markovian impact ionization avalanche (excess noise factor, $ENF \sim 1$) ~Fig. 1. To understand this behavior, a comprehensive study of the history dependent and non-Markovian nature of the hot hole transport in *a*-Se was performed using a Monte Carlo (MC) random walk of single hole free flights, interrupted by instantaneous phonon, disorder, hole-dipole, and impact-ionization scattering processes.

Our multi-scale simulation approach combines molecular dynamics (MD) simulations with density functional theory (DFT) and MC simulations (using a non-parabolic band model). The energy and phonon band structure ~Fig. 2, along with the valence band density of states (VB-DOS), for trigonal selenium (*t*-Se), was calculated using density functional theory (DFT). Fig. 3 shows the DFT calculated acoustic (first order) and optical (zeroth order) deformation potentials along the perpendicular and parallel directions to the *c*-axis in *t*-Se. According to our knowledge, this work for the first time uses comprehensive quantum mechanical formulation to calculate energy depended phonon scattering (acoustic, polar emission/absorption and non-polar emission/absorption), hole-dipole disorder scattering (caused by valence alternate pair type defects as scattering centers), and impact ionization scattering rates in *a*-Se.[2], [3]

Fig. 4 shows the simulated ENF in 0.1-15 μm *a*-Se thin-films. The non-Markovian nature of hot hole branching dominates for thinner thin films where

the dead space distance (min distance traveled to attain impact ionization) is a multiple of the device length. In ~Fig. 5 (a) and (b) we simulated the threshold distance and gain distributions. The history dependent nature of branching of *Hot* holes is explained using a Gaussian distribution of the avalanche threshold distribution distance which increases determinism in the stochastic impact ionization process. An almost ideal non-Markovian hole ENF of ~ 1 was observed in the case of 100 nm *a*-Se thin-films and avalanche gains of 1000. An inherent limitation to spatial resolution is the lateral blur caused due to the hole drifting process in *a*-Se, and, we calculate and predict the spatial blur and the full width at half max (FWHM) spread of the avalanching charge cloud in 0.5-200 μm *a*-Se films ~Fig. 6. Future detector designs can utilize the non-local/non-Markovian nature of hole avalanche in *a*-Se, to enable a true solid-state photomultiplier with noiseless gain and enhanced signal to noise ratios.

The author D.V. acknowledges the financial support from the National Science Foundation (ECCS 2025490 and ECCS 2048400).

REFERENCES

- [1] A. Mukherjee, D. Vasileska, A. H. Goldan, *et al.*, "Vertical architecture solution-processed quantum dot photodetectors with amorphous selenium hole transport layer," *ACS Photonics*, vol. 10, no. 1, pp. 134–146, 2023.
- [2] A. Mukherjee, D. Vasileska, J. Akis, and A. H. Goldan, "Monte carlo solution of high electric field hole transport processes in avalanche amorphous selenium," *ACS omega*, vol. 6, no. 7, pp. 4574–4581, 2021.
- [3] A. Mukherjee, D. Vasileska, and A. Goldan, "Hole transport in selenium semiconductors using density functional theory and bulk monte carlo," *J. Appl. Phys.*, vol. 124, no. 23, p. 235102, 2018.

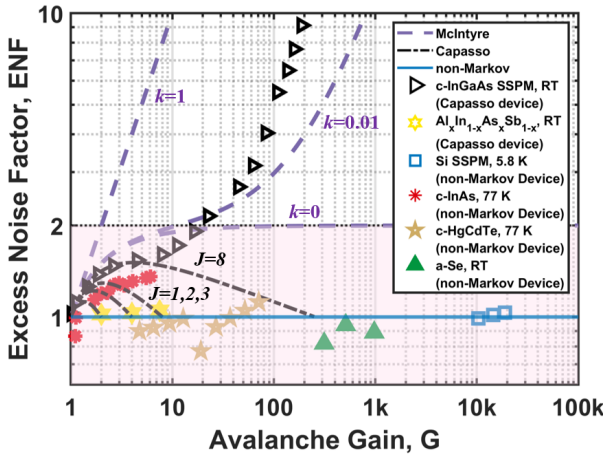


Fig. 1. Excess noise factor in *a*-Se compared with Markov, non-Markov and Capasso type devices.

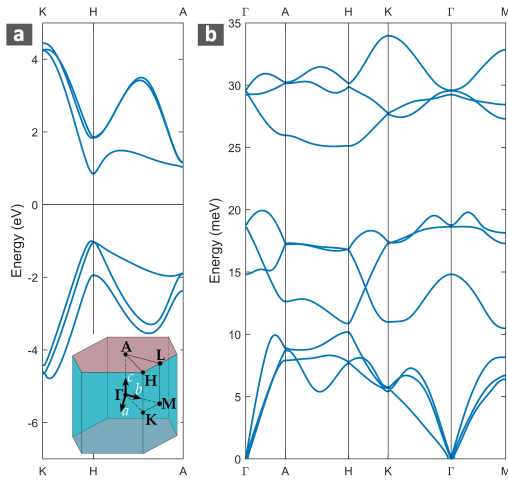


Fig. 2. (a) DFT calculated electronic bandstructure for *t*-Se showing a direct bandgap of 1.9 eV at the H point and (b) phonon dispersion. Inset shows the Brillouin zone for *t*-Se.

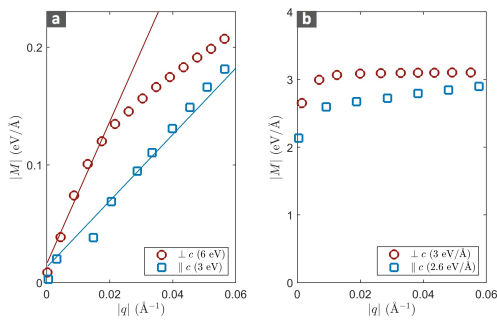


Fig. 3. (a) Acoustic (first order) deformation potentials represented by the slope of solid lines and (b) optical (zeroth order) deformation potential measured via DFT calculations of hole-phonon coupling using a 225-atom supercell of *t*-Se along directions perpendicular and parallel to the *c*-axis.

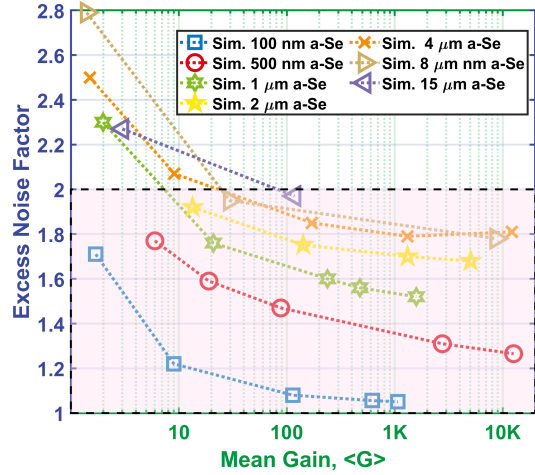


Fig. 4. Plot of *ENF* from single hole MC simulations for 0.1-15 μm *a*-Se bulk drift length as a function of mean gain.

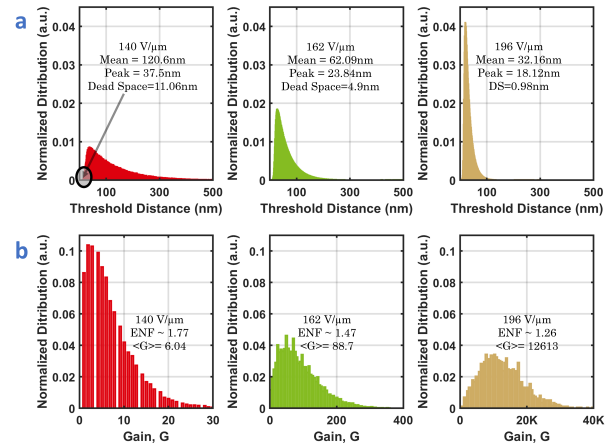


Fig. 5. (a) Threshold distance distributions and (b) avalanche gain distribution for 500 nm *a*-Se bulk drift lengths for electric field strengths of 140, 162 and 196 $\text{V}/\mu\text{m}$, respectively.

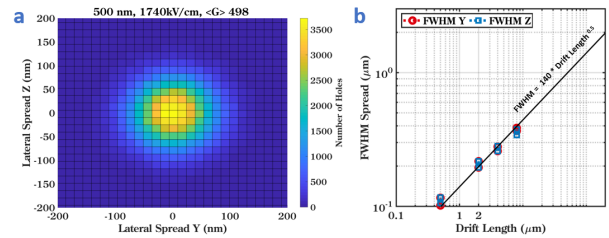


Fig. 6. (a) Increase in the spatial spread of a charge cloud of 500 holes injected at $x = 0$. The lateral spread as a function of electric field at the end of 500 nm of travel in *a*-Se is simulated for 174 $\text{V}/\mu\text{m}$. (b) The FWHM simulated for *a*-Se drift lengths of 500 nm, 2 μm , 4 μm and 8 μm .

Impurity- and remote-phonon-limited mobility in TMD monolayers

Shoaib Mansoori, Sanjay Gopalan, and Massimo V. Fischetti

Department of Materials Science and Engineering,

The University of Texas at Dallas, 800 W. Campbell Rd., Richardson, TX 75080

e-mail: max.fischetti@utdallas.edu

The study of the low-field carrier mobility in monolayer transition metal dichalcogenides (TMDs) is the subject of great interest because of the potential applications of these materials. Whereas most of the studies have been focused on free-standing monolayers [1], in practical applications, these monolayers are supported by an insulating substrate and can also be gated. In this case, in addition to scattering with charged impurities, interactions with interface plasmon/optical-phonons (IPPs) [2], [3], [4] affect transport and these processes may have opposite effects. Specifically, high- κ insulators have been shown, experimentally [5] and theoretically [6], to enhance dielectric screening of the impurity scattering potential, an effect that improves the charge-transport properties. On the other hand, IPP scattering is stronger in the presence of high- κ insulators. Thus, one may ask how ‘pure’ do the TMD monolayers have to be for IPP to control transport and in what range of impurity concentration high- κ insulators improve the mobility.

Here, we address these questions by considering TMD monolayers in a double gate geometry, assuming a SiO₂ substrate and HfO₂ or hBN as examples of high- and low- κ insulators, respectively. The band structure, phonon dispersion, and scattering with the phonons of the TMD layer have been calculated using first-principles methods (Quantum ESPRESSO [9] and EPW [10]), accounting for the screening effects of the insulators as described in Ref. [4]. The dielectric continuum approximation has been used to deal with IPP scattering [4]. We have treated scattering with charged impurities in the TMD using the screened Coulomb potential in

a double-gate geometry [6]:

$$\phi_Q = \frac{e^2 G_Q}{1 - e^2 G_Q^{(22)}(d, d) \Pi_{2D}(Q, \omega = 0)},$$

where G_Q is the Fourier transform of the Poisson Green’s function when the impurity is located at the center of the 2D layer [6]. The quantity $\Pi_{2D}(Q, \omega = 0)$ is the electronic polarizability of the 2D layer given by Stern [7] extended to non-zero temperatures [8]. We show in Fig. 1 the scattering rate calculated using the first Born approximation and the scattering potential given by the above equation.

Our results show that the presence of high- κ insulator results in higher impurity-limited mobility (Fig. 2), as expected from the more effective screening. Figure 3 (top) shows that for the low- κ hBN, IPP scattering controls transport only when the impurity concentration is lower than the mid-10¹¹ cm⁻², whereas for HfO₂ IPP scattering controls transport at any impurity concentration (Fig. 3, bottom). Finally, in Fig. 4 shows that the role of impurity scattering dominates at low temperatures.

REFERENCES

- [1] T. Gunst, T. Markussen, K. Stokbro, and M. Brandbyge, Phys. Rev. B **93**, 035414 (2013).
- [2] N. Ma and D. Jena, Phys. Rev. X **4**, 011043 (2014).
- [3] A. Hauber and S. Fahy, Phys. Rev. B **95**, 045210 (2017).
- [4] S. Gopalan, M. L. Van de Put, G. Gaddemane, and M. V. Fischetti, Phys. Rev. Appl. **18**, 054062 (2022).
- [5] B. Radisavljevic *et al.*, Nat. Nanotech. **6**, 147 (2011).
- [6] Z.-Y. Ong, and M. V. Fischetti, Phys. Rev. B **86**, 121409 (2012).
- [7] Frank Stern, Phys. Rev. Lett. **18**, 546 (1967).
- [8] P. F. Maldague, Surf. Sci. **73**, 296 (1978).
- [9] P. Giannozzi *et al.*, J. Phys. Cond. Matt. **21**, 395502 (2009).
- [10] S. Ponc e, E. R. Margine, C. Verdi, and F. Giustino, Comp. Phys. Commun. **209**, 116 (2016).

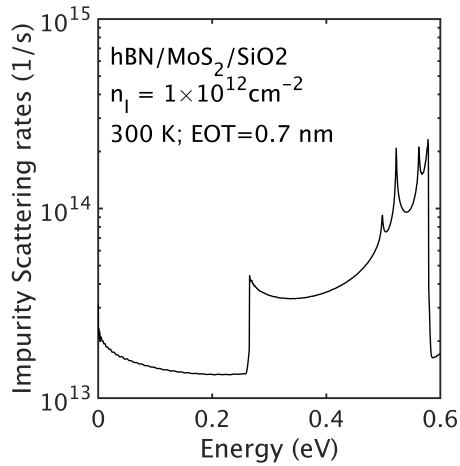


Fig. 1. Impurity scattering rates vs. electron kinetic energy in the hBN/MoS₂/SiO₂ stack calculated for an impurity concentration of 10^{12} cm^{-2} at 300 K. The insulators have been assumed to have an equivalent SiO₂ thickness of (EOT) 0.7 nm.

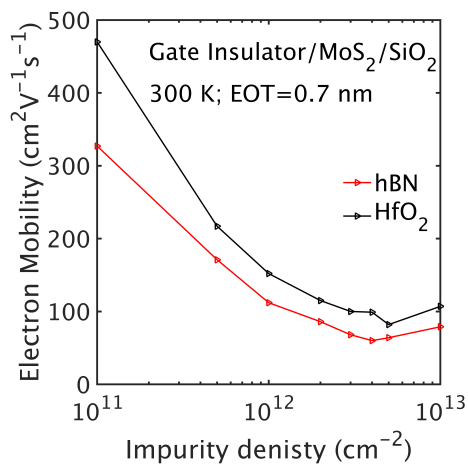


Fig. 2. Impurity-limited mobility vs. impurity density in the hBN/MoS₂/SiO₂ and HfO₂/MoS₂/SiO₂ stacks at 300 K.

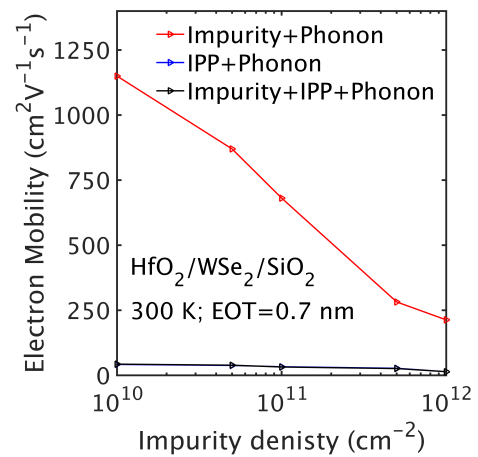
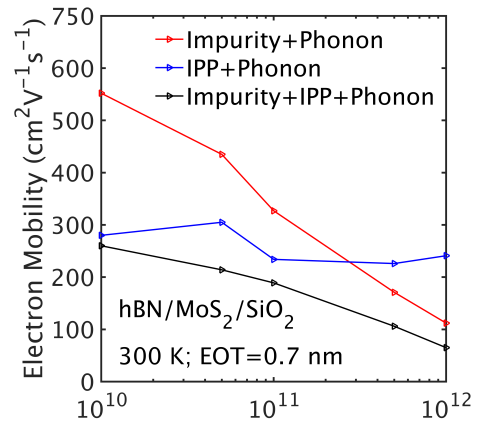


Fig. 3. Calculated electron mobility vs. impurity density for hBN/MoS₂/SiO₂ (top) and HfO₂/WSe₂/SiO₂ (bottom) stacks.

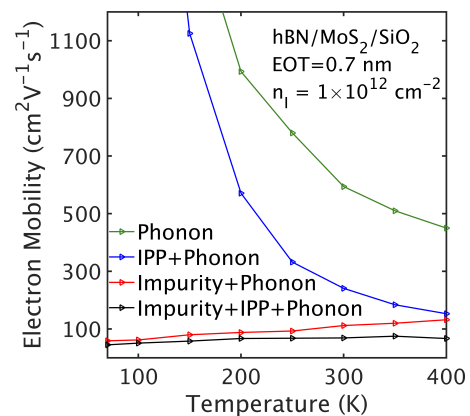


Fig. 4. Calculated electron mobility vs. temperature for hBN/MoS₂/SiO₂ stack. The Impurity-limited mobility increases with increasing temperature. This can be attributed to the temperature-independent screening by the insulator(s), by the increasing thermal carrier energy at high temperatures and the reduced scattering rates at high energy, as shown in Fig. 1.

Self-consistent $k.p$ band structure in doped core-shell nanowires with type-I, type-II and broken-gap radial heterointerfaces.

A. Vezzosi¹, A. Bertoni², and G. Goldoni^{1,2}

¹ Università di Modena e Reggio Emilia, via Campi, 213/A, Modena, Italy

² Istituto Nanoscienze - CNR, Modena, Italy

e-mail: andrea.bertoni@nano.cnr.it

INTRODUCTION

Tailoring spin-orbit coupling and valence-band mixing in nano-fabricated semiconductors is critical to engineer scalable spintronic devices. Here, we present our numerical investigations on the electronic band structure of modulation-doped GaAs/AlGaAs and InAs/GaSb core-shell nanowires (CSNW) with both n - and p -type doping. Calculations are performed by a recently developed self-consistent finite-element library able to treat a broad class of CSNWs which will be described.

MODEL AND METHOD

We adopt an 8-band Burt-Foreman $k.p$ Hamiltonian approach which describes coupled conduction and valence bands in heterostructured nanowires of arbitrary radial composition, growth directions, and doping. Coulomb interactions with the electron/hole gas are taken into account within a mean-field self-consistent approach. We map the ensuing multi-band envelope function and Poisson equations to optimized, nonuniform real-space grids (fig. 1). Self-consistent charge-density, single-particle subbands, density of states, and absorption spectra are obtained at different doping regimes[1]. We extend previous investigations to realistic descriptions of modulation-doped samples. The use of a flexible numerical approach, with nonuniform grids, proved to be critical to treat doping levels at comparable numerical loads.

RESULTS

For n -doped GaS/AlGaAs samples, a large restructuring of the electron gas for increasing doping takes place and results in the formation of quasi-1D electron channels at the core-shell interface (fig. 2). For p -doped samples, strong heavy-hole/light-hole coupling of valence states

leads to non-parabolic dispersions with mass inversion (fig. 3), similar to planar structures, which persist at large doping, giving rise to both heavy-hole and light-hole gaps. In addition, the hole gas forms an almost isotropic, ringlike cloud for a large range of doping. We will also show that signatures of the evolution of the band structure can be singled out in the anisotropy of linearly polarized optical absorption[1].

In InAs/GaSb CSNWs a type-II/broken gap alignment transition takes place, which changes the topological nature of the gap, depending on structural parameters[2,3], making this system a building block for topological quantum gates and for non-abelian physics. Based on our library, we propose a numerical protocol to calculate the self-consistent charge in broken-gap materials, where band alignment induces charge transfer also at charge neutrality. Therefore, we are able to expose the role of the self-consistency field in assessing the metallic or semiconductor character of the nanostructure (fig. 3) and driving the topological transition both by structural parameters and external gates.

ACKNOWLEDGMENT

AB acknowledges partial financial support from the EU project IQubits (Call No. H2020-FETOPEN-2018-2019-2020-01, Project ID 829005). The authors acknowledge CINECA for HPC computing resources.

REFERENCES

- [1] A. Vezzosi, A. Bertoni, G. Goldoni, *Band structure of n - and p -doped core-shell nanowires*, Phys. Rev. B 105, 245303 (2022).
- [2] Luo, N., et al. *Band-inverted gaps in InAs/GaSb and GaSb/InAs core-shell nanowires*, Sci Rep 6, 38698 (2016).
- [3] M. Rocci et al., *Tunable Esaki Effect in Catalyst-Free InAs/GaSb Core-Shell Nanowires*, Nano Lett. 16, 7950, (2016).

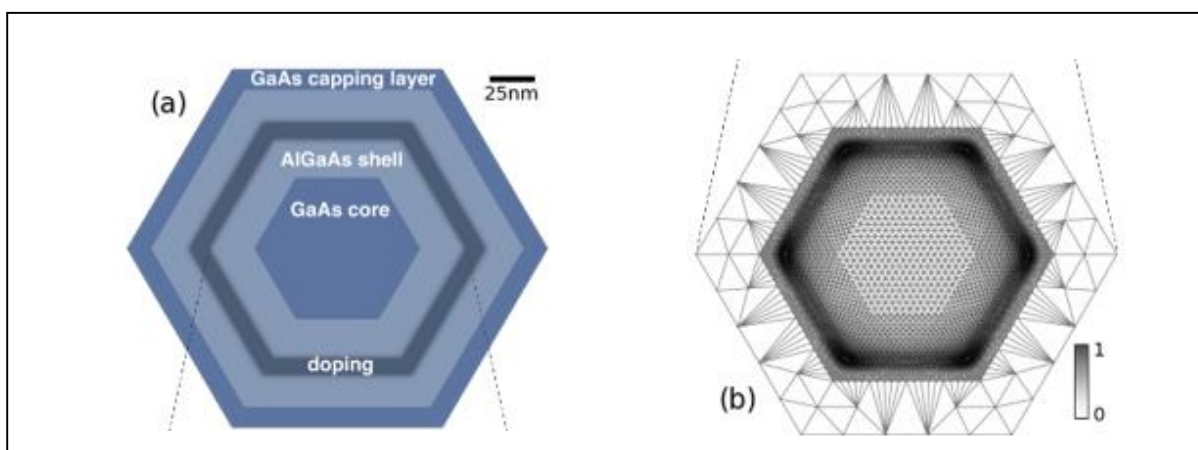


Fig. 1. (a) Cross-section of the GaAs/AlGaAs CSNW illustrating the different materials and the doped region. (b) Example of an optimized FEM grid used to solve the $k \cdot p$ equation of motion with superimposed self-consistent charge density (in grey scale arbitrary units). The grid is limited to the core and first shell, as indicated by the dashed lines.

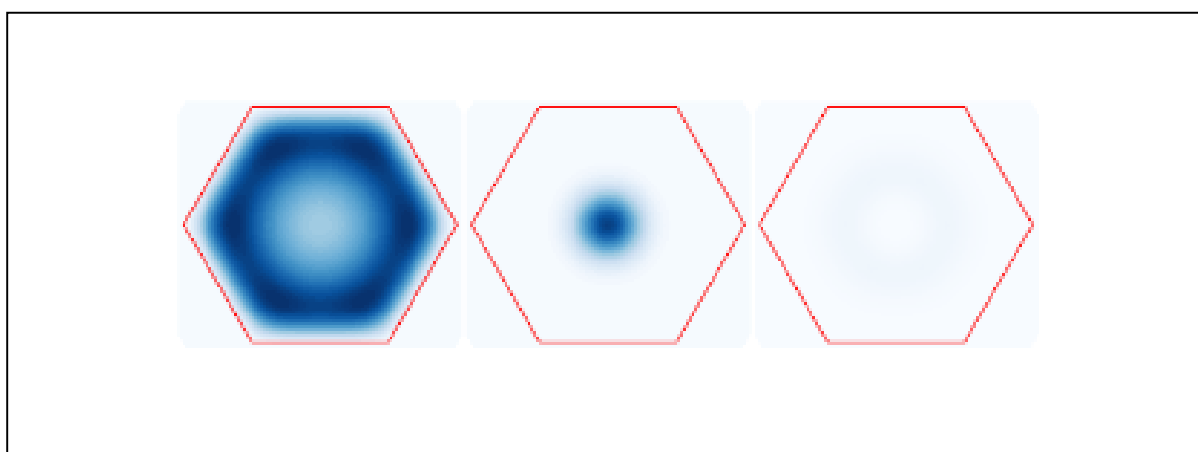


Fig. 2. Electron (left), light-hole (center) and heavy-hole (right) density for the ground of a heavily doped GaAs/AlGaAs sample, with doping density $1.9 \times 10^{18} \text{ cm}^{-3}$.

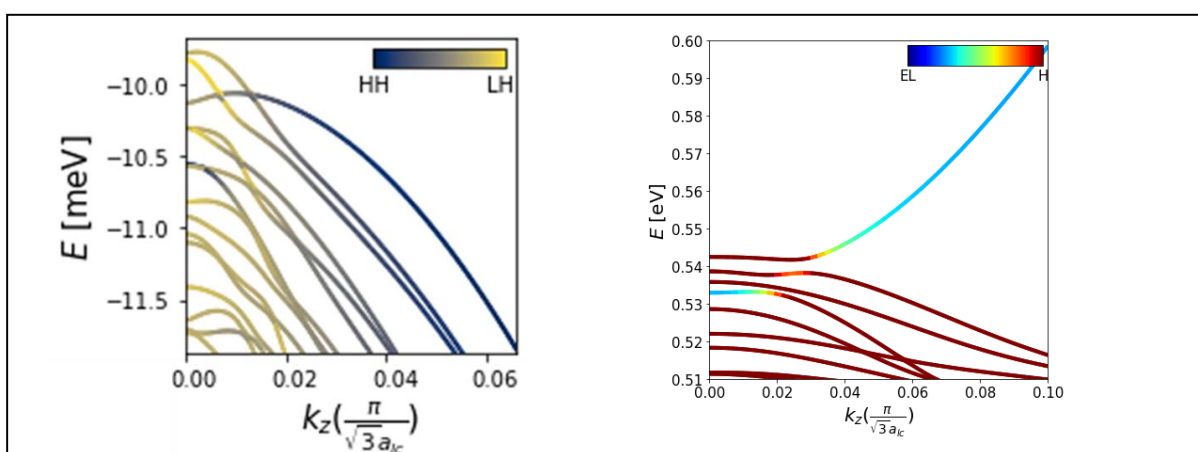


Fig. 3. Left: valence bandstructure of a GaAs/AlGaAs sample with doping density $1.73 \times 10^{18} \text{ cm}^{-3}$ showing mass inversion. Right: Bandstructure of an InAs/GaSb sample showing band hybridization and the opening of an energy gap induced by the spin-orbit coupling and the self-consistent field. The color respectively indicates the weight of the heavy/light hole or electron/hole character of the states.

A Sunlight Cooling Device Based on a 2D van der Waals Heterojunction

P. Dalla Valle, M. Bescond, F. Michelini, and N. Cavassilas.

Aix Marseille Université, CNRS, Université de Toulon, IM2NP UMR 7334, 13397, Marseille, France.

e-mail: paul.dalla-valle@im2np.fr

INTRODUCTION

The quantum yield (QY) defines the number of electron-hole pairs generated in a semiconductor (gap E_g) by the absorption of a photon of energy $h\nu$. In the simplest model we have $QY=1$ when $h\nu>E_g$. However, $QY>1$ occurs when the excess energy generates extra electron-hole pairs by Coulomb carrier-carrier interaction. This is the impact ionization (II) behaviour [1]. In the ideal case, shown in Fig. 1, a photon of energy $h\nu>nE_g$ gives $QY=n$ (with n a integer). Recent works show that, due to large Coulomb screening, II is particularly strong in few-layers transition metal dichalcogenides (TMD) [2].

In a previous study, we used *ab initio* calculations to compute the electronic band structure of MoS₂/WSe₂, a van der Waals heterojunction based on monolayers of TMD. The absorption coefficient is shown Fig. 2. The gap of this heterojunction is small since $E_g=0.4$ eV [3]. Here, we show that in contact with a large bandgap reservoir (Fig. 3), under solar radiation and considering an ideal II, it is possible to cool this small gap heterojunction. The sun light generates electron-hole pairs with a large kinetic energy, involving a strong II. The consequence is an accumulation of carriers at the band edges. This excess of carriers can be extracted in a well-designed reservoir by absorbing phonon. We then obtain an evaporative cooling.

MODEL

To model the carriers in the heterojunction, we assume that their distribution function is a Fermi function at temperature T_c with a difference between the Fermi levels of electrons and holes given by $\Delta\mu=\mu_c-\mu_v$, where μ_c (μ_v) is the Fermi level of electrons (holes) in the conduction (valence) band. To calculate T_c and $\Delta\mu$, we consider a detailed balance model:

$$\begin{cases} J_{gen} = J_{rec} + J_{contact} \\ P_{gen} = P_{rec} + P_{contact} + P_{phonon} \end{cases}$$

We present the different terms of this equations in Fig. 4. J_{gen} is the carrier flux generated by the sun light, considering the absorption of the heterojunction (Fig. 2) and an ideal II. J_{rec} is the

recombination flux, considering both radiative and non-radiative recombinations. $J_{contact}$ is the flux of carriers between the heterojunction and the reservoir. P_{gen} , P_{rec} and $P_{contact}$ are respectively the power flux-densities corresponding to the fluxes J_{gen} , J_{rec} and $J_{contact}$. P_{phonon} is the exchanged power between the carriers and the phonons and is assumed proportional to the difference of carrier and phonon temperatures [4]. When the carrier temperature $T_c<300$ K, the carriers absorb phonons and $P_{phonon}<0$. If this heat absorption is greater than the heat emitted by the non-radiative recombination, the heterojunction is cooled. We define the cooling efficiency as:

$$\eta_{cooling} = \frac{-P_{phonon} - P_{rec,non\ rad}}{P_{gen}}$$

RESULTS

Fig. 5 shows the temperature T_c as a function of E_{cv} , the gap of the reservoir. We get $T_c<300$ K ($P_{phonon}<0$) if both $E_{cv}<0.98$ eV and the II is considered. The detailed balance equation shows that P_{phonon} is more negative as $P_{contact}$ is larger. $P_{contact}$ is proportional to the flux of extracted carriers, multiplied by the extraction energy. The II increases the number of carriers and the energy increases with E_{cv} . Nevertheless, if E_{cv} is too high, the flux is reduced. The best trade-off is obtained for $E_{cv}=0.85$ eV. As shown Fig. 6, where $\eta_{cooling}$ is represented versus E_{cv} , this corresponds to a maximum efficiency of 61%.

CONCLUSION

We propose a cooling device which uses the sun as the only source of energy. This concept could have practical applications in nanoscale cooling.

REFERENCES

- [1] W. Spirkel and H. Reis, *Luminescence and efficiency of an ideal photovoltaic cell with charge carrier multiplication*, Phys. Rev. B **52**, (1995)
- [2] J-H. Kim et al., *Carrier multiplication in van der Waals layered transition metal dichalcogenides*, Nature Comm. **10**, (2019)
- [3] P. Dalla Valle and N. Cavassilas, *A van der Waals heterojunction based on monolayers of MoS₂ and WSe₂ for overall solar water splitting*, Nanoscale Adv. **13**, (2022)
- [4] M. Giteau et. al., *Identification of surface and volume hotcarrier thermalization mechanisms in ultrathin GaAs layers*, JAP, **128**, (2020)

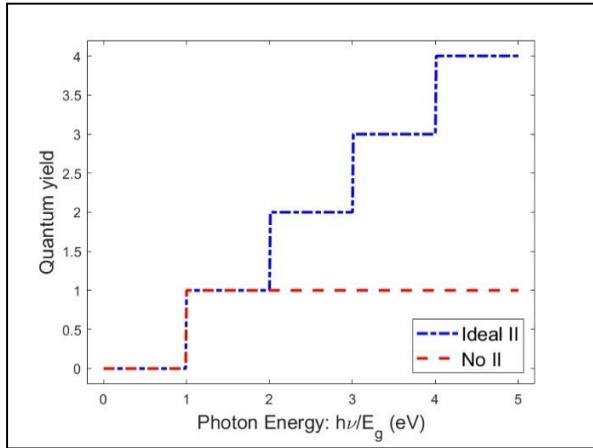


Fig. 1. The quantum yield (QY) is shown as a function of $h\nu/E_g$ where $h\nu$ is the photon energy and E_g is the gap of the semiconductor. The blue curve shows the QY under ideal impact ionisation (II) and the red curve shows the QY without II.

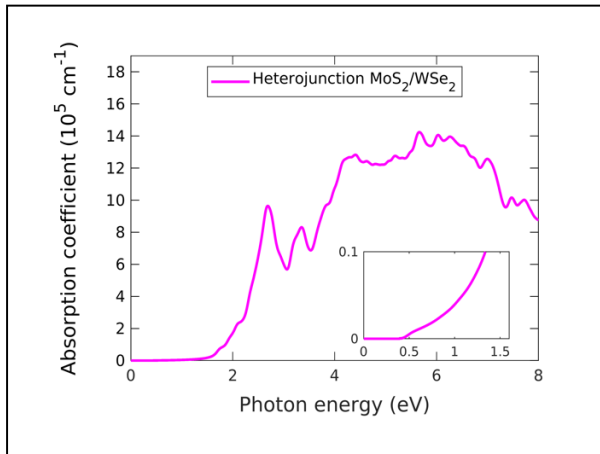


Fig. 2. Absorption coefficient of the MoS₂/WSe₂ heterojunction, computed with DFT calculation. The inset plot is a zoom in the low energy range.

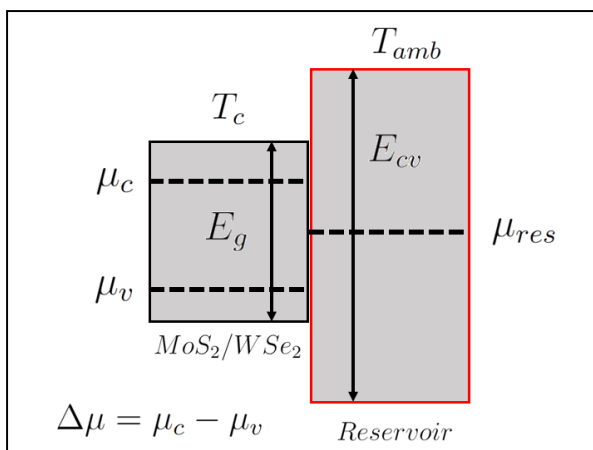


Fig. 3. Band diagram of our device where the MoS₂/WSe₂ heterojunction (bandgap $E_g = 0.4$ eV) is in contact with a reservoir (bandgap $E_{cv} \geq E_g$). μ_c (μ_v) is the Fermi level of electrons (holes) in the conduction (valence) band. μ_{res} is the Fermi level in the reservoir. T_c is the carrier temperature in the heterojunction. $T_{amb} = 300$ K is the ambient temperature.

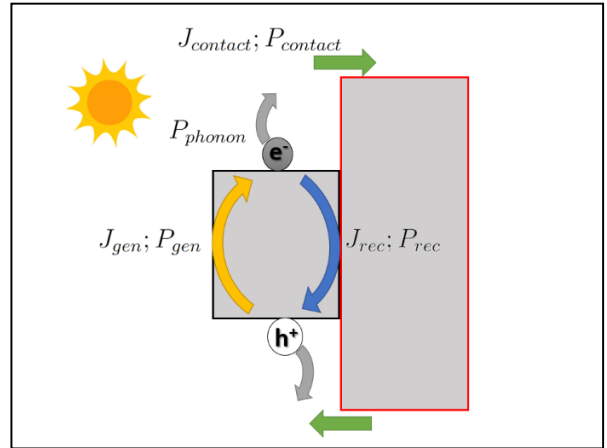


Fig. 4. Carriers fluxes and power flux densities displayed on the band diagram of the device. We consider an isolated system. Thus, carrier exchanges occur only between the small gap heterojunction and the reservoir.

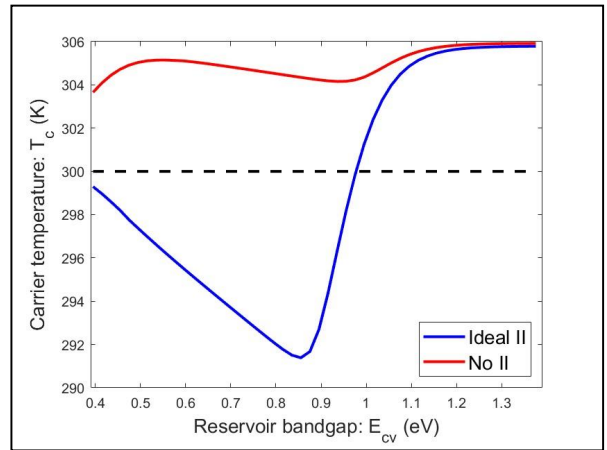


Fig. 5. The carrier temperature T_c is shown with ideal (blue curve) and without (red curve) II, as a function of the reservoir bandgap E_{cv} . The black dashed line stands for $T_c = 300$ K.

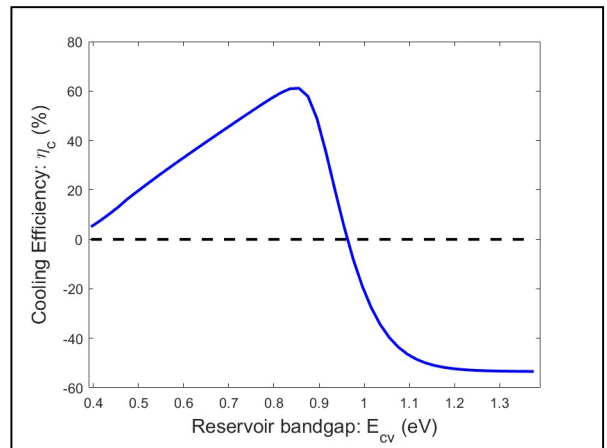


Fig. 6. The cooling efficiency $\eta_{cooling}$ is shown with ideal II as a function of the reservoir bandgap E_{cv} . The black dashed line stands for $\eta_c = 0$ %.

Revealing the Thermal and Mechanical Properties of Amorphous Boron Nitride

Onurcan Kaya, Ivan Cole and Stephan Roche

Catalan Institute of Nanoscience and Nanotechnology (ICN2), CSIC and BIST,

Campus UAB, Bellaterra, 08193 Barcelona, Spain

stephan.roche@icn2.cat

ABSTRACT

Interconnect materials with ultralow dielectric constant, good thermal and mechanical properties are crucial for further miniaturization of electronic devices. Recently, it is demonstrated that ultrathin amorphous boron nitride (aBN) films have very low dielectric constant ($\kappa < 2$), high density (above 2.1 g/cm^3), high thermal stability and mechanical properties. Additionally, it is more suitable for large area deposition compared to its crystalline counterparts, since it can be grown lower temperature, which opens new integration opportunities with 2D materials into flexible devices for nanoelectronics and spintronics [1,2].

The excellent properties of aBN derives from the nature and degree of disorder, which can be controlled at fabrication, allows to tune the physical properties for desired applications. In this context, new fabrication strategies to modify the structural properties and a systematic theoretical characterization of the impact of structural properties on the performance of the material is crucial.

In this work, we will present a systematic analysis to screen out possible realistic morphologies as a function of growth parameters, such as temperature, quenching rate and presence of dopant, and their corresponding thermal and mechanical properties using classical molecular dynamics simulations. We ensure the reliability of results by introducing Gaussian Approximation Potentials which are trained on a large dataset of atomic structures generated by ab-initio calculations. We found that quenching rate and level of dopants causes a significant change in structural properties of aBN, which is strongly reflected in the resulting mechanical and thermal properties of the compounds. We believe the extensive simulations of large quantity of possible structures presented in this work will guide

experimental research and provide trends of scaling behavior as a function of experimentally controllable parameters. We will also mention the anticorrosive properties of the material against oxidation.

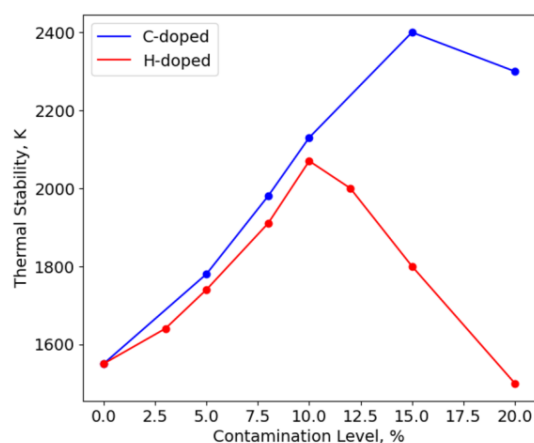


Fig. 1. Thermal stability of amorphous boron nitride as a function of level of contamination.

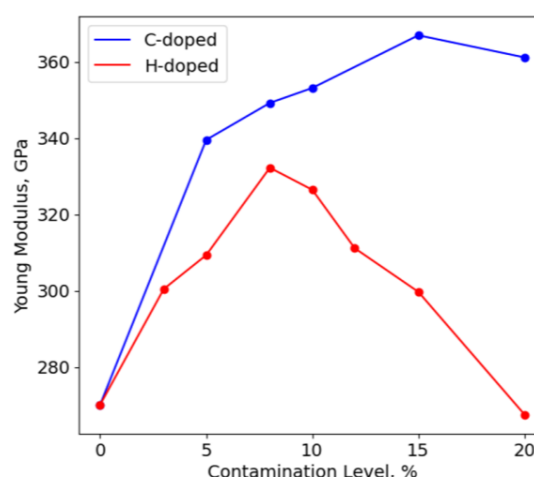


Fig. 2. Young's Modulus of amorphous boron nitride as a function of level of contamination.

ACKNOWLEDGEMENT

This project has been supported by Samsung Advanced Institute of Technology and is conducted under the REDI Program, a project that has received funding from the European Union's Horizon 2020 research and innovation programme under the Marie Skłodowska-Curie grant agreement no. 101034328. Simulations were performed at the Center for Nanoscale Materials, a U.S. Department of Energy Office of Science User Facility, supported by the U.S. DOE, Office of Basic Energy Sciences, under Contract No. DE-AC02-06CH11357. Additional computational support was received from the King Abdullah University of Science and Technology-KAUST (Supercomputer Shaheen II Cray XC40) and Texas Advanced Computing Center (TACC) at The University of Texas at Austin.

REFERENCES

- [1] Hong, S et al. *Nature* 582 (2020) 511–514.
- [2] Sattari-Esfahlan, S. M, et al., *ACS App. Mat. & Int.* (2023) (2023), doi: 10.1021/acsami.2c18706.
- [3] Bartók, A. P., et al., *Physical Review Letters*, 104 (2010) 136403.
- [4] Kaya, O., et al., *Nanoscale Horizons* (2023), doi: 10.1039/D2NH00520D.
- [5] Kaya, O. et al (in preparation).
- [6] Lin, C-M., et al., *Adv. Mater. Technol.* (2022), doi: 10.1002/admt.202200022.

Resistance calculation in metal-2D contacts: Accuracy of numerical integration

Peter Reyntjens^{Ⓜ*†‡}, Pranay Baikadi^{Ⓜ†}, Raseong Kim^{Ⓜ§},
Maarten Van de Put^{Ⓜ‡}, Bart Sorée^{Ⓜ*‡¶}, William G. Vandenberghe^{Ⓜ†}

* Department of Electrical Engineering, KULeuven

† Department of Materials Science, UT Dallas

‡ Imec

§ Components Research, Intel Corporation, Hillsboro, OR 97124 USA

¶ Department of Physics, Universiteit Antwerpen

INTRODUCTION

Ab-initio modelling techniques provide ways to estimate the contact resistance of metal-2D contacts, and are important tools to understand and design these structures. However, due to the complicated nature of metal - 2D semiconductor contacts, the task of obtaining accurate, physically sound results that are consistent with experiment is daunting.

In this work, we investigate the validity of a widely used method for the calculation of contact resistance. Using our in-house quantum transport solver [1], [2], we compare the calculation of the transmission coefficient and contact resistance through a metal-2D contact using an analytical integration [2] and trapezoidal integration commonly used in ab-initio modelling approaches [3], [4]. It is necessary to carefully choose the integration method for the transmission coefficient [5].

CALCULATION OF CONTACT RESISTANCE

Figure 1a shows the structure of the Au-MoS₂ contact we simulate, with the Au ($\phi_{\text{Au}} = 5.2$ eV) in blue and the MoS₂ ($\chi_{\text{MoS}_2} = 4.2$ eV) in red. Figures 1b and 1c show the Hartree potential and free charge density, respectively, obtained by self-consistently solving the Poisson and Schrödinger equations [1].

Figure 2 shows the band structures of the Au and MoS₂ at the left and right edges of the simulation domain, where semi-infinite leads provide electron baths from which electrons are injected in the simulated structure. We describe the materials using a continuum effective mass model. Therefore, the bandstructures are those of free electrons with an effective mass m^* ($m^* = 1$ in this work).

We calculate the conductance from the transmis-

sion coefficient using

$$\sigma = \frac{2q^2}{h} \int_{-\infty}^{+\infty} dE \int_{-\infty}^{+\infty} dk_y T(E, k_y) \frac{\partial f_{\text{FD}}(E)}{\partial E}. \quad (1)$$

Here, $\frac{\partial f_{\text{FD}}(E)}{\partial E}$ is the derivative of the Fermi-Dirac distribution, and $T(E, k_y)$ is the transmission coefficient in the transport (x) direction at a certain energy E sampled at a value of k_y of the wave vector in the transverse direction.

Figure 3 shows the comparison between the analytical and trapezoidal integration methods for the calculation of $T(E) = \int dk_y T(E, k_y)$. Using our effective mass model, we are able to perform a transformation where we obtain $T(E)$ analytically [2]. Crucially, Fig. 3 shows that a small N_{k_y} can result in over- as well as underestimation of the transmission coefficient.

CONCLUSION

Figure 4 shows the convergence of the contact resistance w.r.t. the number of samples taken in the transverse (k_y) direction. We see that the trapezoidal integration is able to capture the behavior of the contact well when N_{k_y} is well-chosen.

Figure 5 shows that the relative error in the calculated contact resistance is strongly dependent on the choice of N_{k_y} . The choices for N_{k_y} that do not include the conduction band minimum are particularly erroneous at insufficiently large N_{k_y} . We conclude that even in advanced models, e.g. DFT+NEGF, it is important to carefully choose N_{k_y} .

ACKNOWLEDGEMENT

This material is based upon work supported by Intel Corporation. We acknowledge the Texas Advanced Computing Center (TACC) at The University of Texas at Austin for providing the HPC resources.

REFERENCES

- [1] M. L. Van de Put *et al.* *Comp. Phys. Comm.*, vol. 244, pp. 156–169, 2019.
- [2] P. Reyntjens *et al.*, “In preparation,” 2023.
- [3] D. Lizzit *et al.* in (*IEDM*), pp. 28.2.1–28.2.4, 2022.
- [4] M. G. Pala *et al.* *Phys. Rev. B*, vol. 102, p. 045410, Jul 2020.
- [5] J. T. Falkenberg and M. Brandbyge *Beilstein journal of nanotechnology*, vol. 6, no. 1, pp. 1603–1608, 2015.

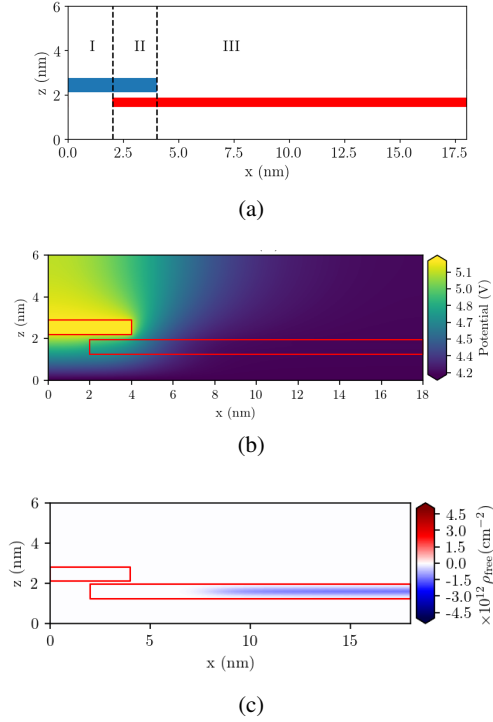


Fig. 1: (a) Schematic representation of our metal-2D semiconductor contact. Self-consistently calculated Hartree potential (b) and free charge density (c). The calculated Schottky barrier is 0.57 eV. We add a sheet doping of $\rho_{\text{sheet}} = 5 \times 10^{12} \text{ cm}^{-2}$.

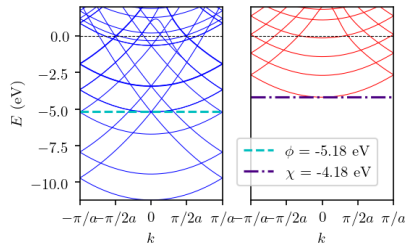


Fig. 2: Bandstructure of the materials at the left and right edges of the simulation domain and in the corresponding semi-infinite leads. The metal and semiconductor are at the left and right sides, respectively.

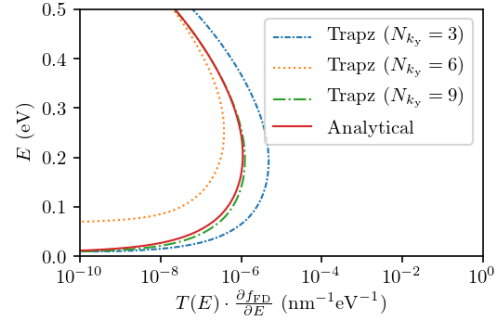


Fig. 3: The transmission coefficient, multiplied by the derivative of the Fermi-Dirac distribution, calculated using trapezoidal and analytical integration of $T(E) = \int dk_y T(E, k_y)$ for $N_{k_y} = 3$, $N_{k_y} = 6$ and $N_{k_y} = 9$.

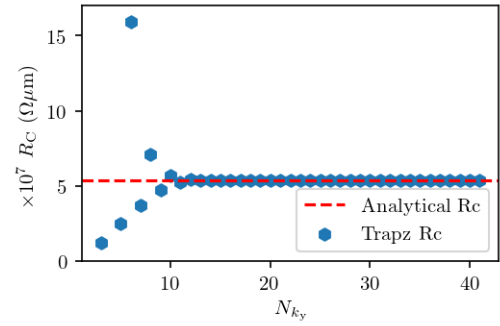


Fig. 4: Convergence of the contact resistance calculated using trapezoidal integration of the transmission coefficient, with varying number of samples in the transverse (k_y) direction. The analytically calculated value is shown as the dashed red line.

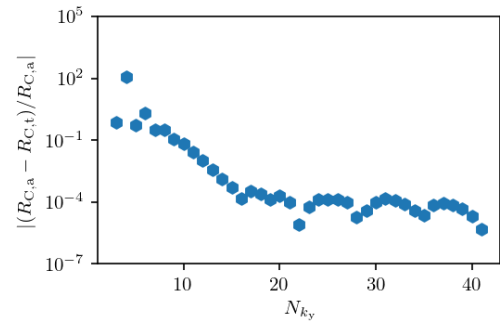


Fig. 5: Convergence of the relative error in the contact resistance between the trapezoidal and analytical integration methods for the transmission coefficient.

FiPo FDTD Algorithm: Modeling Electric and Magnetic Fields with Potentials \mathbf{A} and ϕ for Quantum Transport Solvers

L. Avazpour, M.L. King, S.W. Belling, and I. Knezevic

Department of Electrical and Computer Engineering
University of Wisconsin-Madison, Madison, WI 53706, USA
e-mail: laleh.avazpour@wisc.edu

ABSTRACT

We present the FiPo FDTD algorithm, which can solve a set of first-order equations for the electric and magnetic fields (\mathbf{E} and \mathbf{H}), as well as the magnetic vector potential \mathbf{A} and the scalar electric potential ϕ in the Lorenz gauge. We also provide the derivation and implementation of a state-of-the-art convolutional perfectly matched layer absorbing boundary condition for this new set of equations. Knowing that potentials \mathbf{A} and ϕ can be utilized as input for the single-particle electron Hamiltonian in quantum transport solvers, we demonstrate that by initializing \mathbf{A} and ϕ we can extract information about electric and magnetic fields (\mathbf{E} and \mathbf{H}). The FiPo FDTD algorithm can provide a balance between computational expense and accuracy and has significant potential applications in various fields such as optics, photonics, and quantum transport.

INTRODUCTION

Computational electromagnetics has traditionally focused on the Lorenz gauge to model electromagnetic fields for quantum transport applications. However, the decoupled second-order wave equations for the magnetic vector potential \mathbf{A} and the scalar electric potential ϕ in this gauge pose significant challenges when it comes to boundary conditions and sourcing. Instead of pursuing the decoupled second-order equations, we propose a new algorithm that utilizes first-order field-potential (FiPo) hybrid algorithm, which utilizes the \mathbf{A} - ϕ formulation combined with traditional \mathbf{E} - \mathbf{H} Maxwell's equations. It can be solved using the finite-difference time-domain (FDTD) technique on a staggered spatial grid and using the leapfrog method [1].

This model can accurately and efficiently calculate both electromagnetic fields and quantum transport response in devices with tunneling or nonlinear optical properties. We also present a complex-frequency shifted form of the convolutional perfectly matched layer (CFS-CPML) medium to terminate the FDTD domain.

HYBRID FIELD AND POTENTIAL TECHNIQUE: FIPO HYBRID

The FiPo equations are derived from Maxwell's equations and the Lorenz gauge. The full set of equations reads:

$$\epsilon \partial_t \mathbf{E} = \nabla \times \mathbf{H} - \mathbf{J}, \quad (1a)$$

$$\mu \partial_t \mathbf{H} = -\nabla \times \mathbf{E}, \quad (1b)$$

$$\partial_t \mathbf{A} = -\mathbf{E} - \nabla \phi, \quad (1c)$$

$$\epsilon \nabla \cdot \partial_t \mathbf{A} = -\nabla \cdot (\epsilon \mathbf{A}), \quad (1d)$$

They are updated in the order shown in Figure 1.

Furthermore, we present a complex-frequency shifted form of the convolutional perfectly matched layer (CFS-CPML) for the termination of the finite-difference time-domain (FDTD) simulation region, based on the approach described in reference [2]. In the standard FDTD method, the number of arrays required for relevant variables and auxiliary PML variables is eighteen in a three-dimensional domain, while the proposed FiPo FDTD method requires twenty-eight arrays for the same purpose and this number is much higher for traditional second-order potential wave equation approach. The effectiveness of our CFS-CPML is demonstrated by the low reflection error of -100dB for FiPo Hybrid, as shown in Figure 2.

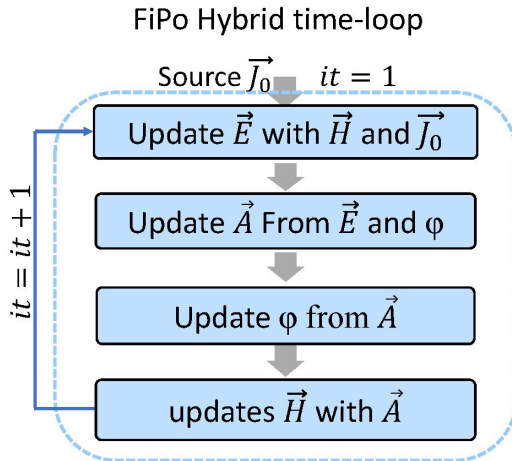


Fig. 1. Flowchart of the ϕ , \mathbf{E} , \mathbf{A} , and \mathbf{H} time-stepping loop for the FiPo Hybrid algorithm. Field and potential updates are consecutive. Arrows show the progression of field or potential values through the update equations.

Additionally, we provide an example showcasing the capabilities of using a combination of \mathbf{A} and ϕ to initialize the simulation (Fig. 3). This technique can be coupled with a quantum solver to use the potentials as an input for FDTD or export the potentials to the quantum solver, enabling a better understanding of the light-matter interaction in quantum effects such as tunneling.

CONCLUSION

In conclusion, we have presented the FiPo FDTD algorithm with a new convolutional perfectly matched layer medium that can efficiently terminate the FDTD domain. By utilizing a set of first-order equations for the electric and magnetic fields, along with the magnetic vector potential and scalar electric potential in the Lorenz gauge, we have demonstrated the potential for coupling with quantum transport solvers. The ability to use the potentials as input for the single-particle electron Hamiltonian, and the fields for standard FDTD purposes with phenomenological materials parameters or coupled with semiclassical transport solvers, makes FiPo a versatile tool for future multiphysics simulations.

REFERENCES

- [1] A. Taflov and S. C. Hagness, *Computational electrodynamics: the finite-difference time-domain method*, 3rd ed. Norwood: Artech House, (2005).
- [2] J. A. Roden and S. D. Gedney, *Convolution PML (CPML): An efficient FDTD implementation of the CFS-PML for arbitrary media*, *Microwave and Optical Technology Letters*, **27**, 334 (2000).

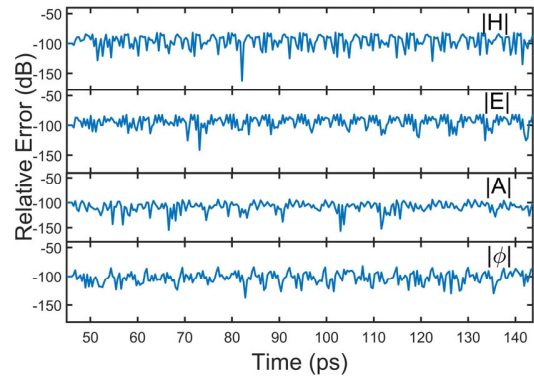


Fig. 2. Relative reflection error for the magnitudes of fields and potentials with CPML implemented for \mathbf{H} , \mathbf{E} , \mathbf{A} , and ϕ . Reference simulation is $300 \times 300 \times 300$ where the PML is 10 cells thick. FiPo simulation was run on a $100 \times 100 \times 100$ grid with a PML of 10 cells.

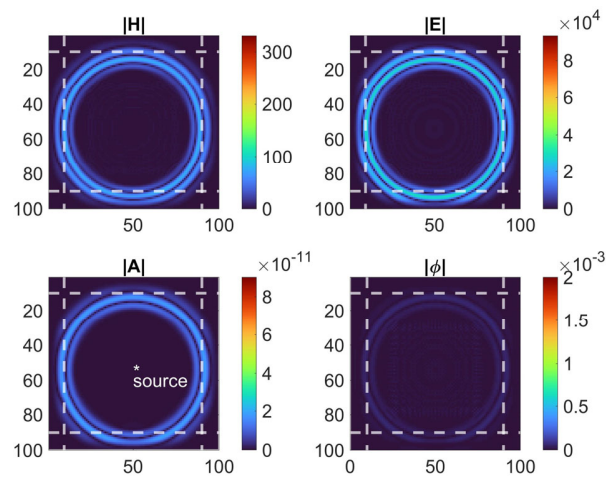


Fig. 3. Visualization of fields and potentials amplitude showing axial x-y cross-section of a 3D simulation domain, sourced by a first derivative of a Gaussian wave packet vector potential (\mathbf{A}) at the center and enclosed by an active CPML region, demonstrating the algorithm's vector-potential-sourcing capabilities. FiPo simulation was run on a $100 \times 100 \times 100$ grid with a PML of 10 cells, z-axis is normal to the plane of the figure.

Noise impact on memristor performance: improvement of neuromorphic binary STDP

E. Salvador¹, R. Rodriguez¹, E. Miranda¹, J. Martin-Martinez¹, A. Rubio², V. Ntinis², G. Ch. Sirakoulis³,
A. Crespo-Yepes¹, M. Nafria¹

¹Electronic Engineering Department, Universitat Autònoma de Barcelona, 08193 Bellaterra, Spain

²Electronic Engineering Department, Universitat Politècnica de Catalunya, 08034, Barcelona, Spain

³Dept. of Electrical & Computer Engineering, Democritus University of Thrace, 67100, Xanthi, Greece
email: emili.salvador@uab.cat

ABSTRACT

Stochastic Resonance (SR) phenomenon has been experimentally observed in Hf-based memristors. The addition of an external noise increases the OFF/ON resistances ratio of the current-voltage (I-V) memristor characteristic. The SR impact on the binary spike time dependent plasticity (STDP) learning rule, when implemented in memristors, has been experimentally analyzed. The two memristor conductance states, which represent the synaptic weights in neuromorphic systems, can be better distinguished if Gaussian noise is added to the bias signal.

INTRODUCTION

Memristors are of great interest in a wide range of applications due to their properties, as low power consumption and large integration density [1]. Memristors exhibit non-linear current-voltage characteristic, so that the properties associated to nonlinear systems can be explored in these devices. In nonlinear systems, noise can have a beneficial role, improving the device performance. This phenomenon is often referred to as stochastic resonance (SR) and it is present in nature in fields as biology, physics, engineering, etc [2-3]. In memristor-based neuromorphic computing spike time dependent plasticity (STDP) learning approach is commonly accepted in the scientific community as a descriptor of the biological synapse [4]. In this work, we analyze the effect of adding an external noise to the memristor bias on binary STDP, where only '1' or '0' values are assigned for each synaptic weight [4].

STOCHASTIC RESONANCE IN MEMRISTORS

Fig. 1 shows the used memristor structure [5] and a typical I-V curve. From 200 I-V cycles, statistical characterization of the resistance ratio

between the OFF and ON memristor states (R_{OFF}/R_{ON}) in the presence of noise is performed [6]. Gaussian noise, whose standard deviation (σ) ranged between 50 mV and 150 mV, is introduced. Fig. 2.a shows that the addition of noise increases the mean values of R_{OFF}/R_{ON} , and the typical SR curve is observed. The memristor I-V curves without adding noise (Fig.2.b) and with a noise of 90 mV σ summed to the bias (Fig.2.c) show that the memristor I-V characteristic is clearly more open when noise is added, leading to the larger R_{OFF}/R_{ON} resistance ratios.

NOISE-INDUCED BINARY STDP

Samples used in this study slightly differ from the previously ones (Fig. 3). To switch devices conductance, set and reset pulses were applied, constructed from the difference between a pulse applied to the top electrode (pre-synaptic pulse, V_{pre}) and a pulse applied to the bottom electrode (post-synaptic pulse, V_{post}) (Fig 4.a). Conductance state was registered, at a reading voltage, $V_{read} = -0.5V$. The reset pulse (V_{reset}) is always a 150ms pulse of -1V, to ensure the reset process (Fig. 4.b). For the set pulse (V_{set}), lower voltage than the one needed to trigger the set process is applied, in this case $V_{set}=0.35V$. V_{set} amplitude is changed every 20 cycles by delaying the post-synaptic pulse (Figure 4.c), generating different overlap situations [7]. Noise addition (with $\sigma_{noise} = 150mV$) becomes essential for the identification of the two resistive states: when noise is not added, there is no state separation (Fig. 5.a), whereas, with the inclusion of noise (Fig. 5.b), an increase in the mean current after the set pulses, proportional to the overlap between the pre- and post-synaptic pulses (Fig. 5c), is observed.

CONCLUSION

The beneficial role of an external noise in the performance of HfO₂ based memristors is

experimentally demonstrated. Noise inclusion increases the OFF/ON resistance ratio and the typical SR curve is obtained. This work presents a first experimental approach for the evaluation of SR in memristors-based neuromorphic systems. The noise addition allows the switching between two resistance states, not initially identified without noise, being the OFF/ON resistance ratio proportional to the pre- and post-synaptic pulses overlap. Further studies on the exploitation of the SR phenomenon in neuromorphic systems are mandatory to perform.

ACKNOWLEDGMENT

The authors acknowledge the Spanish MCIN/AEI/10.13039/501100011033, Project PID2019-103869RB and The ‘Departament de Recerca i Universitats de la Generalitat de Catalunya’.

REFERENCES

- [1] I.H. Im et al., *Advanced Intelligent Systems*, 2020.
- [2] R Benzi et al., *Journal of Physics A: Mathematical and General*, 1981.
- [3] K. Wiesenfeld et al., *Nature*, 1995.
- [4] C. Mohan et al., *ISCAS 2021*
- [5] S. Poblador et al., *Microelectronic Engineering*, 2018.
- [6] R. Rodriguez et al., *ISCAS 2021*.
- [7] E. Salvador et al., *IEEE NANO*, 2022.

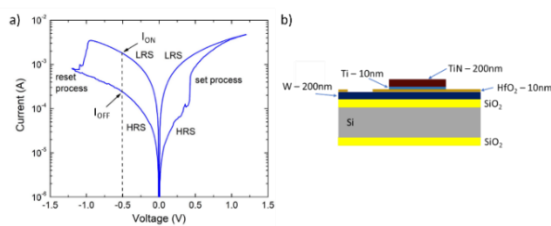


Fig. 1: Typical I-V characteristic (left) and device structure (right) of the memristors used to study the impact of SR on memristors I-V.

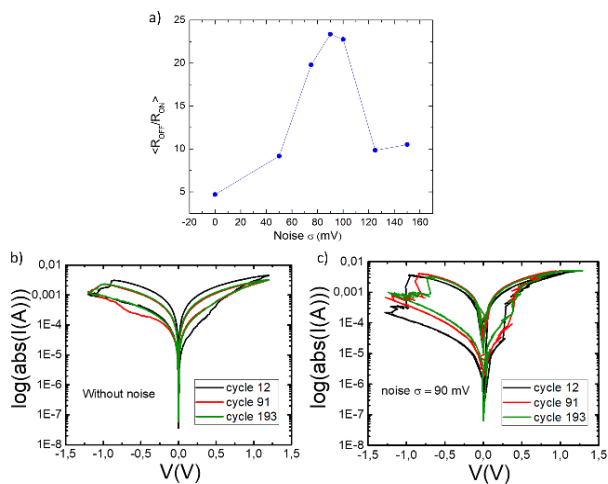


Fig. 2: a) Mean memristor ratio R_{OFF}/R_{ON} as a function of the noise (σ). The typical stochastic resonance curve is observed. Memristor I-V curves at cycles 12, 91 and 193 b) without and c) with 90 mV noise σ .

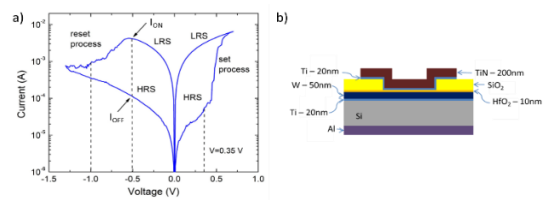


Fig. 3: Typical I-V characteristic (left) and device structure (right) of the memristors used to study noise-induced binary STDP.

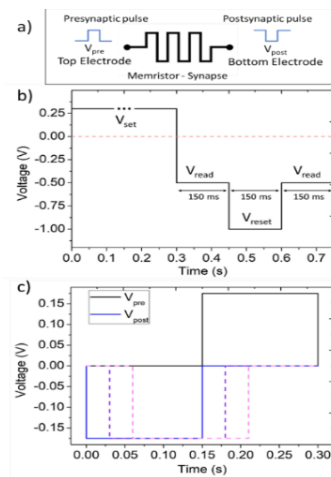


Fig. 4: a) Pre- and post-synaptic pulses were applied to the top and bottom memristor electrodes, respectively b) voltage waveform (cycle) applied to measure the set and reset currents (20 times) for a given V_{set} . (c) Amplitude and duration of V_{set} has been changed by delaying the post-synaptic pulse. Solid lines: pre- and post-synaptic pulses, without overlapping. Dashed lines: examples of delayed post-synaptic pulses.

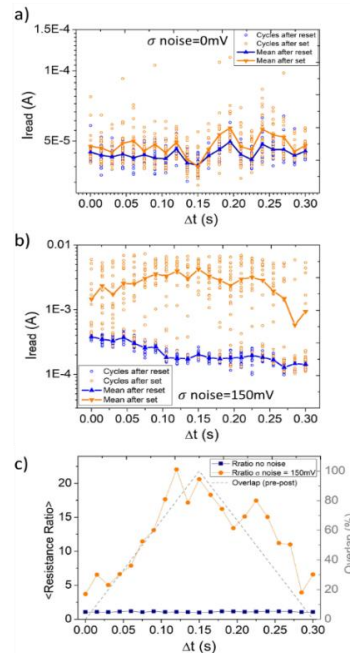


Fig. 5: Current during the 20 cycles for each Δt shift (post-synaptic pulse delay) and mean current evaluated after a set pulse (orange) and after a reset pulse (blue) a) for the case w/o noise and b) adding a $\sigma = 150\text{mV}$ Gaussian noise. c) Mean resistance ratio versus the post-synaptic pulse delay without noise (blue) and with noise (orange).

Control of the local magnetic states in graphene with voltage and gating

Fei Gao^{1,2}, Yu Zhang³, Lin He³, Shiwu Gao⁴ and Mads Brandbyge^{1*}

¹Department of Physics, Technical University of Denmark, DK-2800 Kongens Lyngby, Denmark

²Donostia International Physics Center (DIPC), 20018 Donostia-San Sebastián, Spain

³Center for Advanced Quantum Studies, Department of Physics, Beijing Normal University, 100875 Beijing, China

⁴Beijing Computational Science Research Center, 100193 Beijing, China

ABSTRACT SUBMISSION

Magnetism of graphene can be created by atomic defects, either hydrogen adsorption or single-carbon vacancy formation, owing to the unpaired π electrons around the defects. Based on rigorous first principles calculations, we explore the possibility of voltage manipulation of two such types of π magnetism in graphene via a scanning tunneling microscope tip. For the hydrogen, the magnetic moment can be switched on and off with voltage-induced doping, whereas, for the carbon vacancy, the spin splitting of the π bands persists, almost independent of the extent of doping, due to the coupling between the π and the σ bonds. Furthermore, the local atomic structures near the vacancy can be reversibly manipulated by a coordination mechanism between an intermediate tip-defect distance and a moderate tip voltage, consequently leading to the reversal of spin polarization of the π bands. Voltage control of the local magnetic states may open a new avenue for potential applications in spintronics.

INTRODUCTION

Voltage control of magnetism at the atomic scale is one of the grand challenges in spintronics and has the potential to bring about revolutionary new spintronic devices down to subnanometer scale^[1]. It is known that graphene can become magnetic by hydrogen adsorption^[2], or vacancy formation^[3], which introduces defect states in the π band through its unpaired p_z orbitals. These defect states are localized in space and show preference to one sublattice, according to Lieb's theorem, and can offer a unique candidate for atomic-scale magnetic operation and qubits.

MODEL

The SIESTA/TRANSSIESTA code was employed for the spin polarized calculations. All the calculations were carried out with a low electronic temperature of 50 K. Physical quantities like density of states, transmission, current, and spin density were extracted by using SISL.

SAMPLE SECTION

Figure 1 shows the transport setup for one H atom adsorbate on graphene. The total magnetic moment is 1 and 0 μ_B at 0.0 and 0.4 V with $g = 0$ gating, respectively. This means the spin states of such system can be switched on and off with voltage-induced doping. Moreover, the calculated current is around 0.016 μA at 0.4 V, which implies the mechanism here is governed by the tip-induced field or potential shift with little current effect. The tip acts as a local electrostatic gate, akin to local doping or gating and tunes the energy of the localized defect state.

Figure 2 shows the transport properties of graphene with single-carbon vacancy. At zero bias, three magnetic states, HS, LS, and the non-magnetic state (NS), can be realized as the Au tip-CV distance. Interestingly, a spin transition from the LS to HS states occurs at a bias of -0.4 V, corresponding to the atomic geometry changing from a nonplanar structure to a nearly flat structure. Moreover, the charge-induced forces on the carbon atoms close to the vacancy suggest that it remains an out-of-plane structure at 0.4 V and favors a planar structure at -0.4 V, as shown in Fig. 4(c).

CONCLUSION

In conclusion, we have performed first-principles DFT- non-equilibrium Green's function calculations to study the manipulation of the

localized π magnetism at two types of defects in graphene by using a STM tip. It is found that the magnetism of the π states strongly depend on both the tip voltage and the tip-defect distance. Our findings support the prospect of the local control of graphene magnetism on the atomic scale. We believe that it is versatile and could find potential applications in spintronics and magnetic sensing.

ACKNOWLEDGMENT

We would like to express our sincere thanks to all the contributors to the conference.

REFERENCES

- [1] W. Han, R. K. Kawakami, M. Gmitra, and J. Fabian, *Graphene spintronics*, Nat. Nanotechnol. **9**, 794 (2014).
- [2] H. González-Herrero *et al.*, *Atomic-scale control of graphene magnetism by using hydrogen atoms*, Science **352**, 437 (2016).
- [3] Y. Zhang *et al.*, *Scanning Tunneling Microscopy of the π Magnetism of a Single Carbon Vacancy in Graphene*, Rev. Lett. **117**, 166801 (2016).
- [4] F. Gao *et al.*, *Control of the local magnetic states in graphene with voltage and gating*, Phys. Rev. B **103**, L241402 (2021).
- [5] Y. Zhang *et al.*, *Characterization and Manipulation of Intervalley Scattering Induced by an Individual Monovacancy in Graphene*, Phys. Rev. Lett. **129**, 096402 (2022).

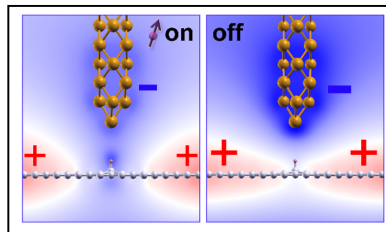


Fig. 1. Hydrogen adsorbate on graphene. Electrostatic potential profile at 0.0 and 0.4 V with $g = 0$ gating.

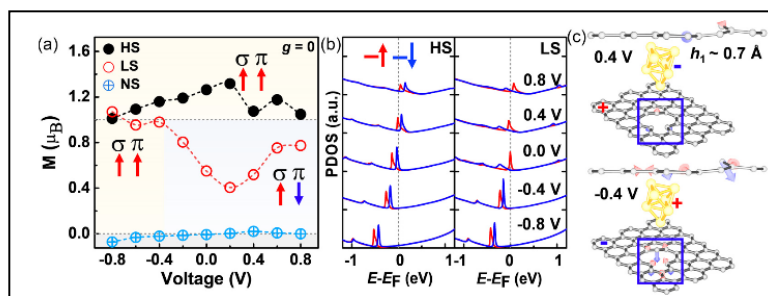


Fig. 2. Carbon vacancy. (a) The magnetic moment as a function of applied voltage for the three different vacancy spin states and conformations, HS, LS, and NS, respectively. (b) The density of states projected on the p_z orbitals. The red and blue lines represent the spin-up and spin-down states. (c) Charge-induced force in the LS state at ± 0.4 V. The absolute force on the C atom is 0.24 nN at -0.4 V.

General Maxwell-Bloch modelling of self-induced transparency in N-level atom

A. Demić*, T.B Gill*, M.A. Talukder**, D. Indjin*, P. Dean*

*School of Electronic and Electrical Engineering, University of Leeds, Leeds LS2 9JT, UK

**Electrical and Electronic Engineering, Bangladesh University of Engineering and Technology, Dhaka-1205, Bangladesh
e-mail: A.Demic@leeds.ac.uk

INTRODUCTION

We investigate self-induced transparency (SIT) effect caused by Rabi oscillations in N -level atom systems implemented in multiple quantum well superlattice. The common models typically implement a two-level Maxwell-Bloch model [1] and consider SIT effect in quantum systems that ideally match with theoretical predictions. The realistic quantum system, as a heterostructure superlattice, however have design-dependent parameters and a ladder of quantum states which cannot be justified by only two levels. We develop a model in which we couple full Maxwell equations to Bloch equations comprised of N levels. We consider scattering of electrons with longitudinal optical phonons, acoustic phonons, interface roughness, impurities and other electrons that provide a realistic disipater within Bloch equations which is similar to the modelling of transport in terahertz quantum cascade lasers [2]. Our model allows propagation of arbitrary input signal and offers detail information of dynamics within N -level atom. This model opens new insights in developing strategies for passive mode locking of THz QCLs via SIT effect.

We analyse ideal two level atom (Fig. 1 and 2) and an exemplary superlattice (Fig. 3) with calculated dephasing time of 0.6 ps, and driven by 3 ps optical pulse at 2 THz frequency (Fig. 4). The system generates partial Rabi flops between the levels at the pump's frequency and complex multiphoton absorption (Fig. 5) that can only be modelled by N -level model.

MODEL

The general formulation of Maxwell-Bloch model for N -level atom consists of two Maxwell equations:

$$\begin{aligned} \frac{\partial H}{\partial t} &= \frac{1}{\mu} \frac{\partial E}{\partial z} \\ \frac{\partial E}{\partial t} &= \frac{1}{\epsilon} \frac{\partial H}{\partial z} - \frac{\sigma}{\epsilon} E - \frac{1}{\epsilon} \frac{\partial P}{\partial t} \end{aligned} \quad (1)$$

where the polarisation term is calculated by coupling this equation to the minimal set of $N(N+1)/2$ Bloch equations:

$$\begin{aligned} \frac{\partial P}{\partial t} &= 2en_{3D} \sum_j \sum_{i>j} \left(\frac{z_{ji}}{\tau_{||ij}} X_{ij} - z_{ji} \omega_{ij} Y_{ij} \right) \\ \frac{\partial \rho_{ii}}{\partial t} &= -\frac{\rho_{ii}}{\tau_i} + \sum_{j \neq i} \left(\frac{2eE}{\hbar} z_{ij} Y_{ji} \text{sgn}(j-i) + \frac{\rho_{jj}}{\tau_{ji}} \right) \end{aligned}$$

Write only for $i > j$ on the left hand side :

$$\begin{aligned} \frac{\partial X_{ij}}{\partial t} &= \omega_{ij} Y_{ij} - \frac{X_{ij}}{\tau_{||ij}} \\ &+ \frac{eE}{\hbar} \sum_{k \neq i,j} (z_{ik} Y_{kj} \text{sgn}(k-j) - z_{jk} Y_{ik} \text{sgn}(i-k)) \\ \frac{\partial Y_{ij}}{\partial t} &= -\omega_{ij} X_{ij} - \frac{Y_{ij}}{\tau_{||ij}} - \frac{eE}{\hbar} \sum_{k \neq i,j} (z_{ik} X_{kj} - z_{jk} X_{ik}) \\ &- \frac{ez_{ij}E}{\hbar} (\rho_{jj} - \rho_{ii}) \end{aligned} \quad (2)$$

where ρ_{ii} (populations) are diagonal elements of the density matrix, while the off-diagonal elements are written as $\rho_{ij} = X_{ij} + jY_{ij}$ allowing a system of equations in real plane, τ_i represent the state lifetimes, τ_{ij} are scattering times while $\tau_{||ij}$ are dephasing times modelled as in [2], z_{ij} are dipole elements and n_{3D} is volume doping density. The Maxwell equations are solved on a Yee grid in order to ensure numerical stability of the system. The normalisation condition $\sum_i \rho_{ii} = 1$ is implemented by replacing Bloch equation for the last state as $\rho_{NN} = 1 - \sum_{i \neq N} \rho_{ii}$ and in order to increase the numerical accuracy of the system, Bloch equations are solved within predictor-corrector algorithm. For $N = 2$, this system directly folds into two level atom model [1]. Quantum system parameters ($z_{ij}, \tau_i, \tau_{ij}, \tau_{||ij}$) are calculated by self-self consistent Schrödinger-Poisson algorithm [2] which offers realistic values as this model provides high degree of accuracy for modelling transport in THz QCLs. The input field $E(z=0, t)$ can take an arbitrary function, and we analysed secant signal for ideal two level atom and experimental pulse for superlattice quantum system.

REFERENCES

- [1] R.W. Ziolkowski *et.al*, PRA 52, 4, 3082 (1995).
- [2] A. Demić *et.al*, AIP Advances 9 no. 9, 095019 (2019).

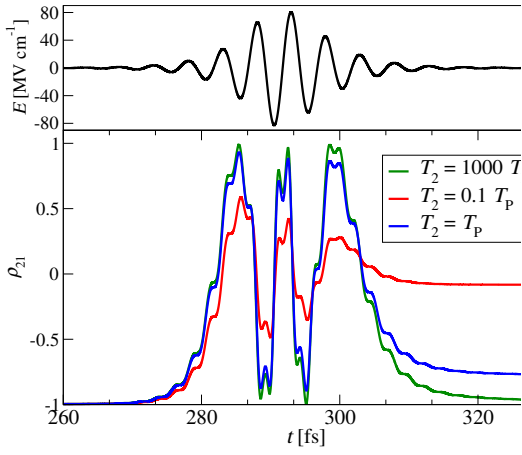


Fig. 1: Top: Secant signal $E_0^{6\pi} = 63 \text{ MV cm}^{-1}$ that analytically causes three Rabi SIT flops of an ideal two level atom from [1]. Bottom: Population inversion when dephasing time (T_2) is larger, equal and smaller than signal width T_P .

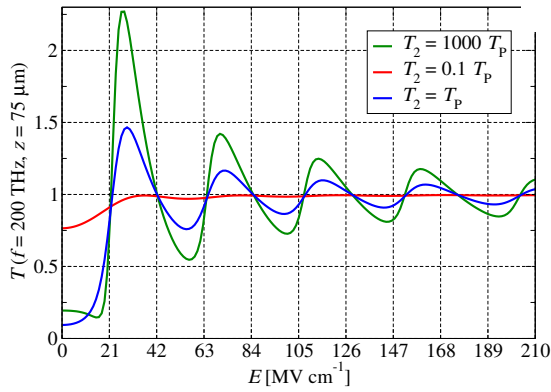


Fig. 2: Transmittance at resonant frequency (200 THz) of ideal two level atom from [1] for different electrical field amplitudes when dephasing time (T_2) is larger, equal and smaller than signal width T_P . Oscillations at $E_0^{2\pi} = 21 \text{ MV cm}^{-1}$ can be clearly observed.

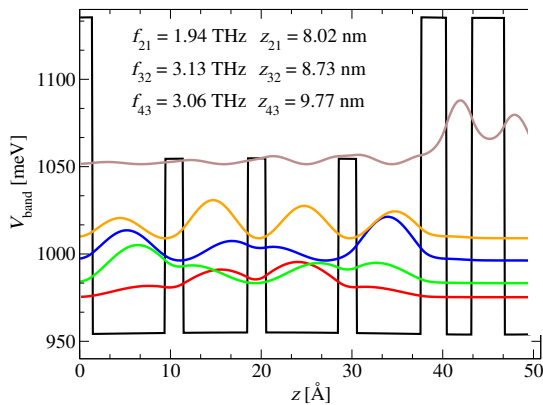


Fig. 3: Bandstructure of superlattice GaAs/Al_xGa_{1-x}As. designed for absorption at 1.94 THz. Conduction band profile and wafefunction moduli squared are presented. The layer structure is **28/80/20/71/20/80/20/71/28/28/36/28**, barriers are shown in bold text ($x=0.11$ and 0.2) and underlined wells are doped by 2 cm^{-1} .

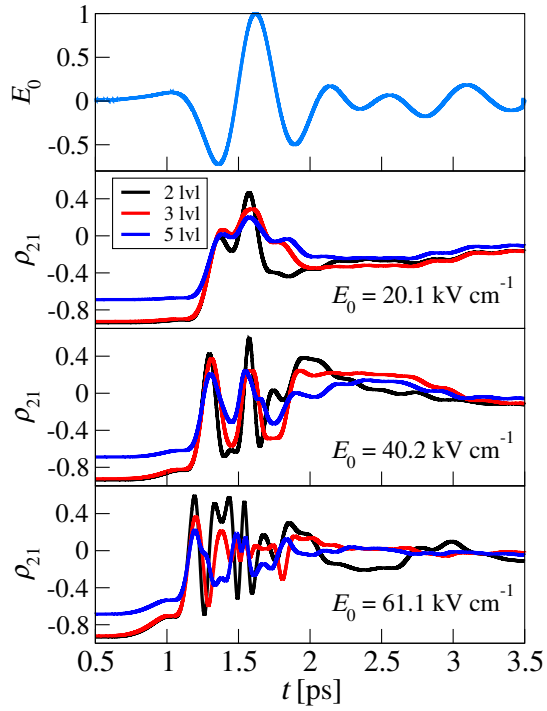


Fig. 4: Top: Experimental input signal generated at resonance of $\sim 2 \text{ THz}$ presented with normalised amplitude that can be varied experimentally and within the model. Bottom: Population inversion at different input field amplitudes when 2,3 and 5 levels are considered in model in Eqs. (1) and (2). Quantum system parameters are calculated for the structure in Fig. 3, displaying dephasing time $\tau_{||21} = 0.6 \text{ ps}$.

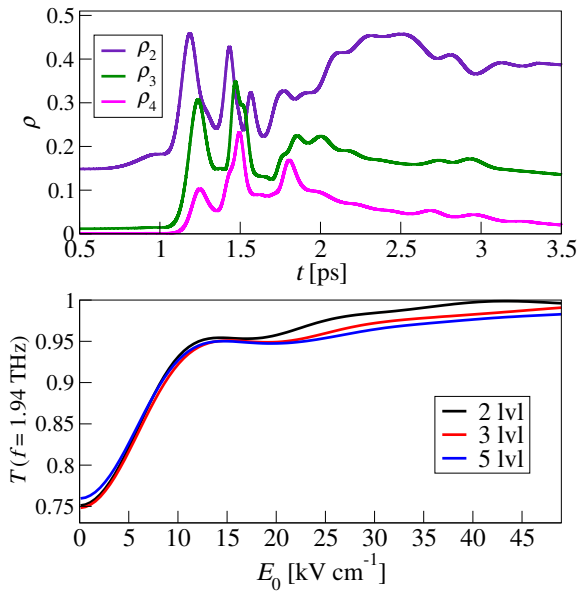


Fig. 5: Top: Populations (in %) at input electric field $E_0 = 40.2 \text{ kV cm}^{-1}$ when five levels are considered in the model. As the signal has spectral contributions $\sim 3 \text{ THz}$ and structure's dipole elements are significantly large, complex multiphoton absorption is observed. This, combined with short dephasing time is responsible for the incomplete Rabi oscillations in Fig. 4. Bottom: Transmittance at resonant frequency (1.94 THz) for different electrical field amplitudes when 2,3 and 5 levels are considered in the model.

Electronic and Magnetic Properties of Eu doped GaN nanowires: An Ab-initio study for spin-optoelectronic applications

V. K. Gudelli[#] and I. S. Roqan^{*}

Physical Sciences and Engineering Division, King Abdullah University of Science and Technology, Thuwal-23955-6900, Saudi Arabia

[#]Presenting author ^{*}Corresponding author e-mail: iman.roqan@kaust.edu.sa

ABSTRACT SUBMISSION

The properties of Eu-doped GaN nanowires (NWs) grown along the wurtzite orientation are calculated using density functional theory (DFT) based on the generalized gradient approximation (GGA) including the Hubbard (U) parameter. Our simulation reveals that Eu impurities (Eu_s) prefer to locate on the NW surface, while they are more stable than the native point defects. Further increase in the Eu density, opens the lattice, thus reducing the energy of the formation of point defects. The density of states (DOS) shows the Eu impurities state in the NWs bandgap, which can be the factor responsible for interesting optical, electrical, and magnetic properties of Eu-doped GaNNWs. The unique magnetic properties are revealed, indicating in-plane and out-of-plane magnetic anisotropy energy (MAE), depending on Eu_s - defect configuration.

INTRODUCTION

The nanostructure of rare earth (RE) doped wide band gap nitrides are of interest in optoelectronic applications, such as in visible lasers due to the 4f partial transition states, resulting in sharp emission that is not affected by temperature. GaN doped with RE impurities has attracted many researchers. Eu-doped GaN is fascinating due to its potential magnetic and optical properties [1]. However, the mechanism behind the magnetic behaviour of Eu in GaN NWs is not well investigated in the literature

MODEL

VASP is used to carry out the computations. The projected augmented wave (PAW) basis set with GGA in the Perdew-Burke-Ernzerhof (PBE) form is used to describe the exchange and correlation effects [2] along with the GGA+U method. The on-site Coulomb parameter $U=6.7\text{eV}$

with a J value of 0.7eV is used for Ga, and $U=7.4\text{eV}$ with a J value of 1.109eV is used for Eu.

RESULTS AND DISCUSSION

We see that the Eu atom is a stable defect as indicated by the negative formation energy values. The total and projected density of states of the NWs are calculated with Eu dopant along with point defects and is presented in Fig. 1 and 2. The DOS indicates that the Eu f -states is located in the band gap of GaN NWs, activating impurity states, while the valence band maximum (VBM) moves towards/away from the Fermi-level in presence of N and Ga vacancies (V_N and V_{Ga}). The calculated magnetic moment of Eu-doped GaN NWs increases in the presence of the N and Ga vacancies. Further, as the density of Eu impurity increases in NWs with intrinsic defects leads to out-of-plane magnetic anisotropy energy (MAE) for all Eu-intrinsic defect doped GaNNW configurations apart from Eu- V_{Ga} , which shows in-plane MAE. The out-of-plane MAE is found to increase with the increase in the number of Eu atoms in NWs this could have valuable applications in high-density data storage devices.

CONCLUSION

The intra-band f - f transitions from the electronic structure calculations and higher value MAE makes the Eu-doped GaN nanowires a favourable candidate for optoelectronic and data storage device applications.

ACKNOWLEDGMENT

We would like to thank the KAUST baseline fund and supercomputing facility fund.

REFERENCES

- [1] Hite, J., et al., *Optical and magnetic properties of Eu-doped GaN*. Appl. Phys. Lett., **89**, 132119 (2006).
- [2] P. E. Blöchl, *Projector augmented-wave method*. Physical Review B, **50**, 17953(1994).

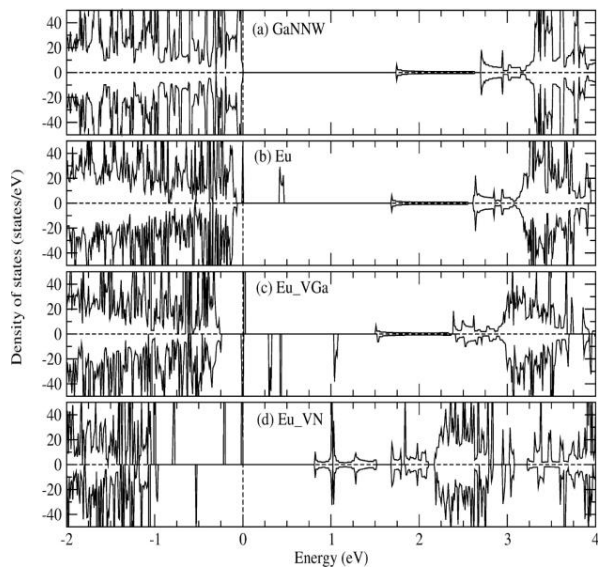


Fig. 1. The Density of states of GaN NW with Eu doping and point defects.

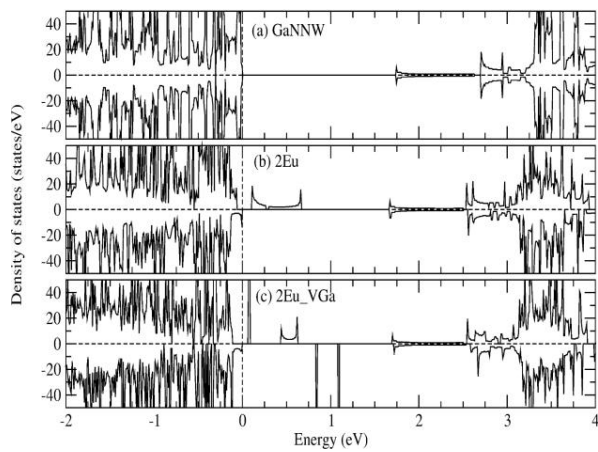


Fig. 2. The Density of states of GaN NW with 2Eu doping and point defects.

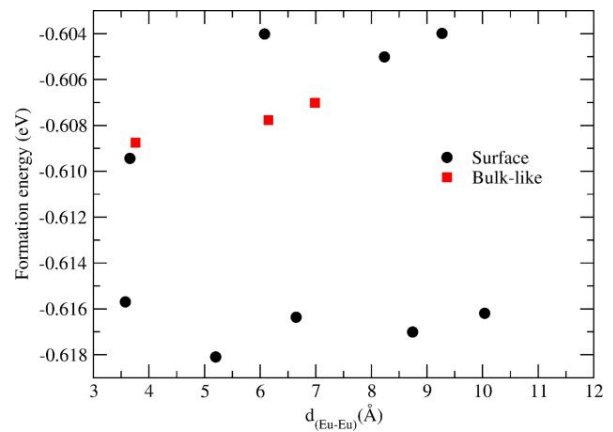


Fig. 3. The formation energy of Eu-doped GaN NW with the variation of Eu distance in NW.

From radiofrequency to infrared antennas: downscaling a rectangular loop geometry

Daniyal Khosh Maram, Joan Garcia, Raul Ruiz, Xavier Cartoixà, Gabriel Abadal

Dept. Enginyeria Electrònica, Campus UAB, 08193-Bellaterra, Spain;

e-mail: Daniyal.KhoshMaram@uab.cat

ABSTRACT

A millimeter scale rectangular loop antenna has been selected as a reference geometry to analyze the effects of downscaling to the infrared range on the impedance and resonance frequency of the antenna. CST and COMSOL numerical simulators have been used to calculate impedance and S_{11} vs. frequency curves of the reference loop antenna, to calibrate their predictions with measured curves. Once model simulators have been calibrated, the reference antenna has been downscaled by a 10^5 scaling factor to predict the behavior of the resulting IR nanoantenna.

INTRODUCTION

In the design process of an antenna, impedance vs. frequency calculation in the range of interest will give information about antenna's resonances and antiresonances. Zero crossing frequencies of the impedance imaginary part (antenna reactance, X_A) define antiresonances when crossing is produced from positive to negative X_A values and resonances in the opposite case. Only in resonances, a constructive interference effect (which is destructive in the antiresonance case) is produced on the antenna's current stationary wave since the loop perimeter is a multiple of the wavelength. Consequently radiation of the antenna is in this case maximized. Reactance, resistance (R_A , real part of the impedance), as well as the reflection coefficient curves (S_{11}) derived from impedance can be obtained numerically by standard electromagnetic simulations (CST) or analytically from RLC models [1]. In the present work we want to analyze the effect on the impedance curves and resonance frequencies of the dimensional reduction to the nanometer scale by means of CST simulations, but also using COMSOL simulator because it allows coupling to other relevant domains as mechanics [2]. This kind of coupling will be useful to describe novel

transduction mechanisms between electromagnetic and mechanical domains, such as the ones reported in MEMSTENNA structures [3].

RADIOFREQUENCY RECTANGULAR LOOP ANTENNA

A 2.5 GHz cylindrical Cu wire rectangular loop antenna has been chosen as a reference structure to calibrate the simulated predictions of CST and COMSOL with S_{11} measured curves. The geometry of the antenna, as defined in figure 1, is characterized by its perimeter, p , and the radius of the wire, r . A slenderness ratio, p/r , can be defined to parametrize the relative thickness of the cylindrical wire. In figure 2 the measured and simulated S_{11} vs. frequency curves are shown. As predicted by classical RF antenna theory, the first resonance frequency, f_{res} , is produced when its corresponding wavelength, $\lambda_{res}=c/f_{res}$, equals the loop perimeter, being c the speed of light. This is evidenced by the notch frequency in the S_{11} curve or by the second zero crossing of the reactance curve (fig.3).

INFRARED RECTANGULAR LOOP ANTENNA

The 2.5 GHz reference structure has been uniformly reduced by a scaling factor $k=10^5$. Consequently, the loop perimeter is reduced from 120.4 mm to 1.204 μm , wire radius is also reduced from 0.5 mm to 5 nm and the classically expected resonance frequency would be expected to increase from 2.5 GHz to 250 THz (wavelength decreased from 120 mm to 1200 nm). However, as it was previously reported [1], the first resonance, as indicated by the second zero crossing of the reactance curve (fig. 4), is produced at a lower frequency, 170 THz, or, equivalently, at a larger wavelength, 1765 nm. Such a shift in the resonance frequency is due to the different phase velocity of currents at optical frequencies in metals. [4]

CONCLUSION

A COMSOL model of a 2.5 GHz wire rectangular loop antenna has been calibrated from CST simulated and measured S_{11} vs. frequency curves. The reference antenna has been subsequently downscaled to the IR region and the effects of metal properties at optical frequencies on the resonance frequency have been analyzed.

ACKNOWLEDGMENT

This work was funded by Spain’s Ministerio de Ciencia, Innovación y Universidades under Grant No. PID2021-127840NB-I00 (MICINN/AEI/FEDER, UE).

REFERENCES

- [1] A.F. McKinley, T.P. White and K.R. Catchpole. *Theory of the circular closed loop antenna in the terahertz, infrared, and optical regions*, J. Appl. Phys. **114**, 4, 044317 (2013).
- [2] R. Ruiz, J. Bonache, G. Abadal. *A flexible dipole antenna for direct transduction of microwave radiated power into DC mechanical deflection*, Sensors and Actuators A: Physical **340**, 113536 (2022).
- [3] R. Ruiz, G. Abadal. "Direct Transduction from Radiofrequency Radiated Power to Static and Dynamic Flexural Mechanical Modes." 2021 21st International Conference on Solid-State Sensors, Actuators and Microsystems (Transducers). IEEE, 2021.
- [4] J. Dorfmueller, R. Vogelgesang, W. Khunsin, C. Rockstuhl, C. Etrich, K. Kern. *Plasmonic nanowire antennas: experiment, simulation, and theory*, Nano letters **10**, 9, 3596-3603 (2010).

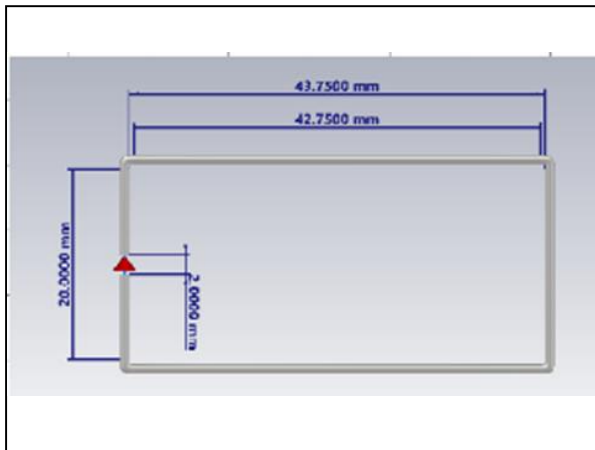


Fig. 1. Rectangular loop antenna geometry designed to resonate at 2.5 GHz.

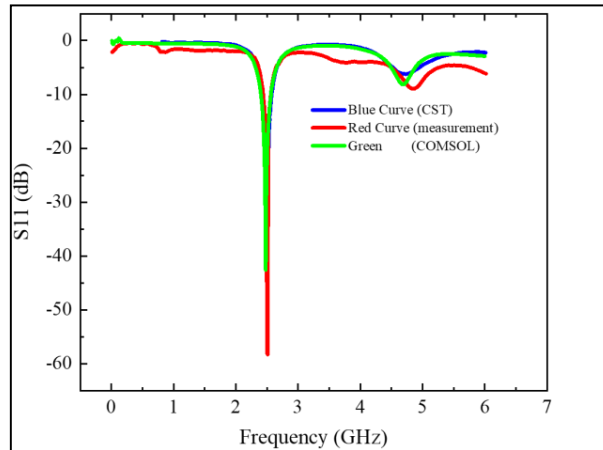


Fig. 2. Measured and simulated S_{11} vs. frequency curves of the 2.5 GHz rectangular loop antenna defined in figure 1.

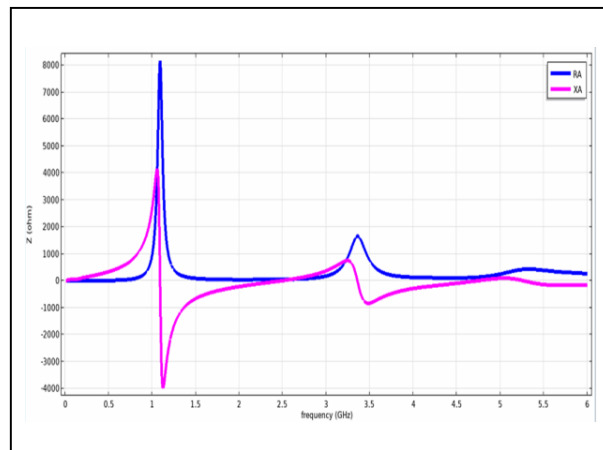


Fig. 3. Real (R_A) and imaginary (X_A) parts of the impedance vs. frequency curves obtained by COMSOL simulations, corresponding to the reference 2.5 GHz antenna of figure 1.

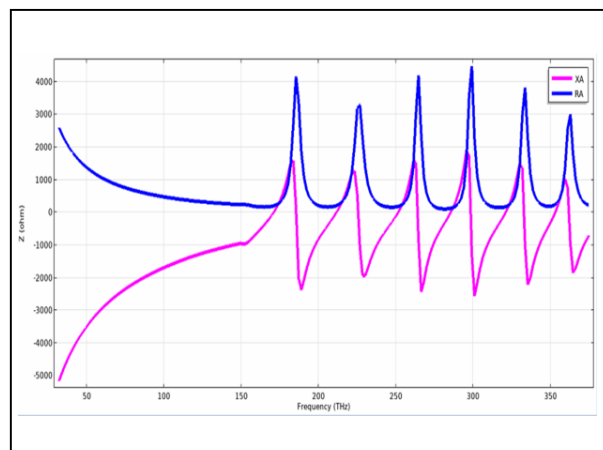


Fig. 4. Real (R_A) and imaginary (X_A) parts of the impedance vs. frequency curves obtained by COMSOL simulations, corresponding to the IR antenna.

Artificial Intelligence at FC Barcelona

Jordi Mompart

Director of Research at FC Barcelona,

ABSTRACT

FC Barcelona excels in data and digital assets, including information on 400 million fans, stadium attendees, and player positions. By utilizing AI and blockchain technologies, the club leads in innovation, generating knowledge, products, and services. Examples include personalized fan engagement using social media data, AI-driven player performance analysis, AI-assisted organization of historical digital assets, blockchain-based authenticity and security measures, and data-driven optimization of ticketing and e-commerce. FC Barcelona leverages these technologies to enhance the fan experience and stay at the forefront of sports innovation.

INDEX OF AUTHORS CONTRIBUTING TO THE IWCN 2023

G.Abadal 234
A.Abdi 92
F.Aguirre 127
Z.Aksamija 116
T.Albrigi 188
I.Alcon 108
M.Alducin 98
O.E.Asirim 171
L.Avazpour 54,112,140,224
A.BachLorentzen 11
P.Baikadi 222
J.Bailey 86
M.K.Balapanov 204
M.Ballicchia 90,119
J.R.Barker 21,196
K.Z.Bekmyrza 204
C.Belabbas 58
S.W.Belling 140,200,224
A.Bertoni 82,216
M.Bescond 25,58,218
S.Birner 19
T.Biswas 68
P.Blaise 74
R.Bombin 98
P.Bordone 82
M.Brandbyge 11,147,228
P.Brandimarte 9
R.Brunetti 135
E.Cannavo 15
L.M.CanonicoArmas 10
A.Cappai 56,104,210
J.Carrete 48,52
X.Cartixa 52,129,142,186,234
J.Castell-Queralt 146
N.Cavassilas 25,58,218
C.Cazorla 36
D.Chaussende 182
F.A.Chaves 110
E.Chen 13
M.C.Cheng 155
C.Y.Cheng 177
Y.Cho 163
I.Cole 220
L.Colombo 56,104,210
A.Crepieux 58
A.Crespo-Yepes 226
G.Csaba 32
J.Cuesta 138
A.W.Cummings 10,108
J.E.Cunningham 86
P.DallaValle 218
A.G.Davies 86
P.Dean 86,230
E.Degoli 42
N.Del-Valle 146
A.Demic 86,230
C.F.Destefani 27,142
E.Deylgat 13
C.H.Diaz 72
A.A.Diaz-Burgos 138
D.Dick 169
P.Dollfus 34
D.K.Dubey 15,167
T.R.Durrant 102
R.Eisenberg 121
A.Emboras 133
L.Ermoneit 88
M.K.Eryilmaz 54
G.Etesse 25,58
C.Etl 119
S.R.Evans 13
F.Eversy 159
L.Fabrega 184
A.Fazzio 8
M.Feiginov 142
P.C.Feijoo 110
D.K.Ferry 17,157
L.Filipovic 38
S.Fiorentini 144
G.Fiori 15,167
M.V.Fischetti 78,214
D.M.Fleetwood 78
G.Forghieri 82
T.Frederiksen 147
F.Fuchs 169
J.Fuhrmann 88
G.F.Furtado 80
Z.Futera 151,153
V.Ganiu 175
D.Z.Gao 102
S.Gao 228
F.Gao 228
J.H.Garcia 4
J.Garcia 234
A.Garcia-Lekue 9
S.Garcia-Sanchez 198
S.Gemming 169
V.P.Georgiev 165
S.Ghosh 192
G.Giedke 147
T.BGill 230
Y.Giret 102
A.Godoy 138
W.Goes 144
A.H.Goldan 212
G.Goldoni 216

T.Gonzalez 66,198
L.Gonzalez-Gamez 146
M.Gonzalez-Silveira 104
S.M.Goodnick 68,123
S.Gopalan 214
T.Grange 19
P.Graziosi 64
J.Grebot 34
V.K.Gudelli 232
E.Guichard 74
J.Gull 62
R.GyuLee 118
Z.Wang 76
T.Hadamek 144
G.Ham 163
S.C.Han 161
P.Harrison 86
L.He 228
R.Helleboid 34
K.Hermansson 94
C.Hernandez-Garcia 173
K.Hirakawa 25,58
R.Holmer 208
S.M.Hong 44,161
H.W.Hsiao 96
J.M.Iglesias 70
D.Indjin 230
M.M.Islam 129
C.Jacoboni 135
M.Jennings 190
D.Jimenez 110,179,206
C.Jirauschek 19,171
G.N.Jonnalagadda 151
N.Jorstad 144
J.I.Juaristi 98
A.M.Kabyshev 204
C.Kalin 100
K.Kalna 70,182
M.Kaniselman 133
M.Kantner 88
B.J.Kavanagh 184
O.Kaya 220
A.Kent 86
Y.H.Kim 5,46,118,181
I.K.Kim 44
D.Kim 163
R.Kim 222
M.L.King 224
S.Klein 116
G.Klimeck 2
T.Kloss 1
I.Knezevic 54,112,123,140,200,224
T.Koprucki 88
R.Korytar 159
H.Kosina 62
M.M.Kubanova 204
T.Kubis 74,96
A.K.Kulanov 204
S.Kumari 194
K.A.Kuterbekov 204
C.Kutter 208
J.Lee 46
R.G.Lee 46
J.Lee 118,181
F.Leonard 84,137
Z.Li 64
L.H.Li 86
E.H.Linfield 86
D.Logoteta 106
C.Lopez-Alvarez 36
E.E.Lorenz 40
P.Lugli 123
M.Luisier 100,133
M.Macucci 106
R.Magri 42
D.Mamaluy 23,149
S.Mansoori 214
D.K.Maram 234
P.Marconcini 106
A.Marek 159
D.Marian 15,167
E.G.Marin 15,138,167
D.Marongiu 56
A.Martinez 21,190,196
J.Martin-Martinez 226
J.Mateos 66,198
N.Mavredakis 206
C.Melis 56,104,210
R.E.Menchon 9
J.P.Mendez 23,149
F.Michelini 25,58,218
E.Miranda 127,226
S.Mitra 112
M.Mladenovic 133
J.Mompart 236
F.Monaghan 190
N.Mori 60
B.Mortazavi 30
G.Mugny 34
Z.A.Mukhan 204
A.Mukherjee 212
H.Murari 192
A.S.Muzas 98
M.Nafria 226
O.Nagler 208
N.Narendra 96
C.Navau 146
M.Nedjalkov 90,119
N.Neophytou 64,202
I.Nicholson 34
D.O.Nielsen 78
A.Nonaka 84
D.Novko 98
V.Ntinis 226

X.Oianguren-Asua 27
P.Ordejon 6
B.Orfao 66
X.Oriols 27,142
J.M.Pablos-Marin 173
A.Pacheco-Sanchez 179,206
M.Pala 34,50
S.T.Pantelides 78
N.Papior 147
J.Park 50
G.Park 161
F.Pasadas 138
E.Pascual 70
L.Paulatto 50
M.A.Pavanello 76
M.Pech 92
S.Perez 66,198
Y.V.Pershin 125
M.Perucchini 167
W.Porod 32,123
M.Povolotskyi 76
P.Priyadarshi 202
B.Pruckner 144
F.Quochi 56
M.Raya-Moreno 184,186,52
P.K.ReddyBaikadi 114
R.Rengel 70,198
P.Reyntjens 114,222
D.Rideau 34
S.Roche 10,108,220
R.Rodriguez 226
M.Rodriguez-Lopez 104
J.Rodri-guez-Viejo 104
I.S.Roqan 232
A.C.J.Rossetto 80
A.Rubio 226
M.Rudan 135
T.Rudner 32
A.Ruini 42
F.G.Ruiz 138
R.Ruiz 234
R.Rurali 36,184,186,188
M.Saba 56
J.Saint-Martin 34,50
C.Salhani 25,58
M.A.Salvador 42
E.Salvador 226
D.Sanchez-Portal 9,147
S.S.Sanders 200
S.Sanz 147
M.Saraniti 68
T.Sato 19
S.S.Sawant 84
B.Schmidt 88
L.R.Schreiber 88
R.D.Schrimpff 78
D.Schulz 92,175
J.Schuster 40,169
S.Selberherr 144
J.Serrano 173
A.L.Shluger 102,131
J.Shoemaker 68
F.Siddi 210
M.Simoncelli 7
A.Singh 68
G.C.Sirakoulis 226
V.A.Slipko 125
S.Smidstrup 165
C.S.Soaes 76,80
B.Soree 222
D.Soriano 15
A.Strachan 129
J.Strand 131
J.Suñe 127
VSverdlov 144
M.A.Talukder 230
A.Toral-Lopez 138
F.Tremmel 208
M.L.Urquiza 129
A.Valavanis 86
M.L.VandePut 114,222
C.G.VandeWalle 78
A.C.T.vanDuin 129
J.vanRuitenbeekz 159
W.G.Vandenbergh 13,114,222
B.G.Vasallo 66
D.Vasileska 76,80,123,177,212
R.Vatan 68
C.D.Vedel 165
M.Veresko 155
A.Vezzosi 216
E.Vilanova 184
M.Villani 142
A.B.Walker 29
C.Weilenmann 133
J.Weinbub 90,119
G.I.Wirth 76,80
A.K.Yadav 194
J.J.Yang 124
J.Yao 84
H.Yeo 46,118
S.Yu 118,181
Y.Zhang 228
X.Zhu 25,58
X.Zhuang 30